Highlights in Theoretical Chemistry 12
Series Editors: Carlo Adamo · Ilaria Ciofini · Donald G. Truhlar

Ágnes Szabados
Mihály Kállay
Péter G. Szalay *Editors*

Péter R. Surján

A Festschrift from Theoretical Chemistry Accounts

Springer

Highlights in Theoretical Chemistry

Vol. 12
Series Editors: Carlo Adamo • Ilaria Ciofini • Donald G. Truhlar

More information about this series at http://www.springer.com/series/11166

Ágnes Szabados • Mihály Kállay • Péter G. Szalay
Volume Editors

Péter R. Surján

A Festschrift from Theoretical Chemistry Accounts

With contributions from

Khaled Abdel-Maksoud • Diego R. Alcoba • Anna Andreou
János G. Ángyán • X. Assfeld • Pierre Beaujean • Jessica E. Besaw
Roberto C. Bochicchio • Ferenc Bogár • Janine Boodram • Petr Čársky
Patrick Cassam-Chenaï • Koushik Chatterjee • Jerzy Cioslowski
András Csehi • József Csontos • Roman Čurík • Richard Dronskowski
György G. Ferenczy • V. N. Glushkov • Bálint Gyimesi • Gábor J. Halász
Laurence Hamdan • Bence Hégely • Johan Holmberg • Tomasz Janowski
Péter Jeszenszki • F. Kalincsák • Mihály Kállay • Miklos Kertesz
Masato Kobayashi • János Koltai • Lukáš Krivosudský • Jenő Kürti
Luis Lain • István László • Ingvar Lindgren • Xabier Lopez • Kwan Y. Man
Gustavo E. Massaccesi • I. Mayer • Iain McGregor • Dávid Mester
Paul G. Mezey • Catherine Munteanu • Bastien Mussard • Kishan Muthu
Péter R. Nagy • Károly Németh • Jozef Noga • Gabriela Orešková
Ofelia B. Oña • Katarzyna Pernal • Mario Piris • Jannat Poddar • G. Pongor
Raymond A. Poirier • Peter Pulay • Riya Radia • Joanna Roberts
Zoltán Rolik • Edina Rosta • Stephanie Sadler • Sten Salomonson
Oren A. Scherman • Nabeela Siddiqi • Ján Šimunek • Ágnes Szabados
Péter G. Szalay • Tetsuya Taketsugu • Sianne Tam • Andrei L. Tchougréeff
Andrey M. Tokmachev • Alicia Torre • Zsuzsanna Tóth • L. Udvardi
Ágnes Vibók • Peter L. Warburton • Krzysztof Wolinski • Viktor Zólyomi

Springer

Volume Editors
Ágnes Szabados
Laboratory of Theoretical Chemistry
Eötvös Loránd University
Budapest, Hungary

Mihály Kállay
Budapest University of Technology and Economics
Department of Physical Chemistry and Material Science
Budapest, Hungary

Péter G. Szalay
Laboratory of Theoretical Chemistry
Eötvös Loránd University
Budapest, Hungary

Originally published in Theor Chem Acc, Volume 134 (2015), volume 135 (2016),

ISSN 2194-8666 ISSN 2194-8674 (electronic)
Highlights in Theoretical Chemistry
ISBN 978-3-662-49824-8 ISBN 978-3-662-49825-5 (eBook)
DOI 10.1007/978-3-662-49825-5

Library of Congress Control Number: 2016936688

Printed on acid-free paper

This Springer imprint is published by Springer Nature
The registered company is Springer-Verlag GmbH Berlin Heidelberg

Contents

Theor Chem Acc (2016) 135:19
DOI 10.1007/s00214-015-1771-y

PREFACE

Preface to the special collection of theoretical chemistry accounts in honour of Péter R. Surján

Ágnes Szabados[1] · Mihály Kállay[2] · Péter G. Szalay[1]

Published online: 31 December 2015

This collection of papers presents a special cross section of recent advances in Theoretical Chemistry. It gives a fingerprint of the scientific interest of Péter R. Surján, contributors having either interacted with him and/or working on topics closely related to his expertise.

A study on optical rotatory strength calculation, published in 1980 in Theoretica Chimica Acta, marks the beginning of the documented scientific career of Péter R. Surján. His interest has always been shared between fundamental problems in electronic structure theory and theoretical applications in material structure research. Localizability of electron pairs and weak intermolecular interactions were his first research topics besides characterization of conjugate polymers by semiempirical methods. During his visit at the Memorial University of Newfoundland, St. John's, Canada, he started lecturing on the theory of second quantization, applied in quantum chemistry. This was the origin of the book titled "Second Quantized Approach to Quantum Chemistry", published by Springer in 1989. The easy to follow elaboration of a complicated subject is characteristic not only to this book but also to the lectures he has been giving at the Eötvös Loránd University (ELTE) of Budapest, Hungary, since 1991. Working as a professor at ELTE, he pursued his long-term investigations on the theoretical characterization of the chemical bond by geminal wave functions as well as on model Hamiltonians for the description of pi-electron systems. He also extended his research activity to the field of many-body methods, Green's function theory, electronic excited states and linear scaling methods in quantum chemistry.

The research work of Péter R. Surján is characteristically rich in scientific interactions. He has been a successful Ph.D. advisor, raising generations of graduate students. He has also been actively cooperating both on the national and international level and was proud to host his distinguished colleagues at his laboratory in Budapest. This collection was initiated by students and colleagues of Péter R. Surján, on the occasion of his reaching 60. It is not intended to be a celebration, however. It is rather a tribute to the colleague and the friend. But mostly, it is a snapshot of current research in quantum chemistry. The Editors of this Collection strongly hope that the reader will find these papers instructive and inspirational. *Tolle*, *lege et procede!*

Budapest, 7 November, 2015.

Published as part of the special collection of articles "Festschrift in honour of P. R. Surjan".

✉ Ágnes Szabados
szabados@chem.elte.hu

[1] Laboratory of Theoretical Chemistry, Institute of Chemistry, Eötvös Loránd University, P.O. Box 32, Budapest 1518, Hungary

[2] MTA-BME Lendület Quantum Chemistry Research Group, Department of Physical Chemistry and Materials Science, Budapest University of Technology and Economics, POB 91, Budapest 1521, Hungary

Theor Chem Acc (2015) 134:123
DOI 10.1007/s00214-015-1707-6

REGULAR ARTICLE

Combination of many-body perturbation theory and quantum electrodynamics

Ingvar Lindgren[1] · **Johan Holmberg**[2] · **Sten Salomonson**[1]

Received: 22 May 2015 / Accepted: 25 July 2015 / Published online: 6 October 2015

Abstract A procedure for energy-dependent perturbation expansion has been developed, based upon the covariant evolution operator method. This makes it possible to treat energy-dependent perturbations very much like the energy-independent ones in standard many-body perturbation theory. This has been applied to the non-radiative QED perturbations (retardation and virtual electron–positron pairs) as well as the radiative ones (electron self-energy, vacuum polarization and vertex correction). The combination of QED and electron correlation, beyond two-photon exchange, has been evaluated, using the Coulomb gauge. It turned out that in that gauge the extremely time-consuming model-space contributions of the self-energy and vertex corrections do not have to be evaluated in full. In the Feynman gauge no sensible results could be obtained in this way, as is demonstrated by the numerical results.

Keywords Perturbation theory · Quantum electrodynamics · Electron correlation · Electron self-energy · Green's operator · Covariant evolution operator

Published as part of the special collection of articles "Festschrift in honour of P. R. Surjan".

✉ Ingvar Lindgren
ingvar.lindgren@physics.gu.se

[1] Department of Physics, University of Gothenburg, Gothenburg, Sweden

[2] Physikalisches Institut, Universität Heidelberg, Heidelberg, Germany

1 Introduction

The procedures for many-body perturbation calculations (MBPT) for atomic and molecular systems are nowadays very well developed, and the dominating electrostatic as well as magnetic perturbations can be taken to essentially all orders of perturbation theory (see, for instance, [1]). Less pronounced, but in many cases still quite significant, are the quantum electrodynamical (QED) perturbations—retardation, virtual pairs, electron self-energy, vacuum polarization and vertex correction. Sophisticated procedures for their evaluation have also been developed, but for practical reasons such calculations are prohibitive beyond second order (two-photon exchange). Pure QED effects beyond that level can be expected to be very small, but the *combination* of QED and electrostatic perturbations (electron correlation) can be significant. However, none of the previously existing methods for MBPT or QED calculations is suited for this type of calculation.

We have during the past decade developed an energy-dependent perturbation procedure, based on a "*covariant evolution operator method*" [2–5], that will make it possible to handle energy-dependent QED perturbations very much in the same way as the energy-independent ones in MBPT.

2 Covariant evolution operator

The time-evolution operator for the Schrödinger wave function transforms the wave function from one time to another

$$\Psi(t) = U(t, t_0)\Psi(t_0). \tag{1}$$

In the *interaction picture* the wave function has the time dependence

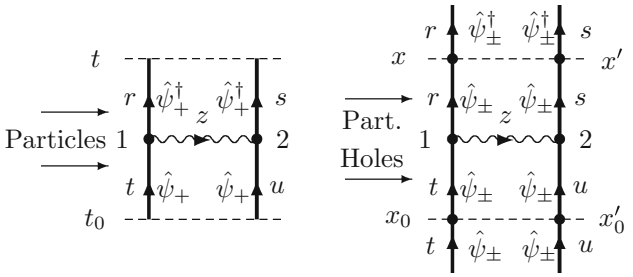

Fig. 1 Comparison between the standard evolution operator and the covariant evolution operator for single-photon exchange in the equal-time approximation

$$\Psi(t) = \mathrm{e}^{-it(E-H_0)/\hbar}\Psi(0) \tag{2}$$

with the Hamiltonian in the *Schrödinger representation* $H = H_0 + V$ and E being the exact energy of the state. An equation for the evolution operator follows from the time-dependent Schrödinger equation.

The non-relativistic evolution operator is in first order represented by the first Feynman diagram in Fig. 1. It is non-covariant, since time flows only in the positive direction. If we insert electron propagators in the in- and outgoing orbital lines, time can flow in both directions, and we get a covariant form of the evolution operator, represented by the second diagram.

The *covariant evolution operator* for a ladder of retarded interactions between the electrons is given by

$$U(t,-\infty)\,P_{\mathcal{E}} = \mathrm{e}^{-it(\mathcal{E}-H_0)}[1 + \Gamma(\mathcal{E})\,V(\mathcal{E}) + \Gamma(\mathcal{E})\,V(\mathcal{E})\,\Gamma(\mathcal{E})\,V(\mathcal{E}) + \cdots]P_{\mathcal{E}}, \tag{3}$$

assuming that we have a small damping factor on the perturbation so that $t = -\infty$ corresponds to an unperturbed state. Here, $P_{\mathcal{E}}$ is the projection operator for the part of the model space of energy $\mathcal{E}$. $\Gamma(\mathcal{E})$ is the resolvent

$$\Gamma(\mathcal{E}) = \frac{1}{\mathcal{E} - H_0}.$$

The evolution operator is (quasi)singular, when an intermediate or final state lies in the model space.

The evolution operator without intermediate model-space states is

$$U_0(t,-\infty)\,P_{\mathcal{E}} = \mathrm{e}^{-it(\mathcal{E}-H_0)}[1 + \Gamma_Q(\mathcal{E})\,V(\mathcal{E}) + \Gamma_Q(\mathcal{E})\,V(\mathcal{E})\,\Gamma_Q(\mathcal{E})\,V(\mathcal{E}) + \cdots]P_{\mathcal{E}}, \tag{4}$$

which is regular. Here, Γ_Q is the reduced resolvent

$$\Gamma_Q = \frac{Q}{\mathcal{E} - H_0}.$$

and Q is the projection operator for the space outside the model space.

We define a *Green's operator* by

$$U(t,-\infty)P = \mathcal{G}(t,-\infty)\cdot PU(0,-\infty)P, \tag{5}$$

which is free from singularities and analogous to the Green's function in field theory. In the definition the heavy dot indicates that the Green's operator acts on the intermediate model-space state. The evolution operator and the Green's operator depend on the energy of the model-space states they are operating on. We then write the relation

$$U(t,\mathcal{E})P_{\mathcal{E}} = \mathcal{G}(t,\mathcal{E}')\cdot P_{\mathcal{E}'}U(0,\mathcal{E})P_{\mathcal{E}},$$

leaving out the initial time $t_0 = -\infty$ and assuming that the model-space energies might be slightly different.

The definition leads to *counterterms*, which form *model-space contributions* (MSC) that eliminate the singularities so that the Green's operator becomes regular for all times.

The Green's operator transforms the unperturbed state in the model space, Ψ_0, to the corresponding exact (target) state, $\Psi(t)$, at a given time t

$$\Psi(t) = \mathcal{G}(t,\mathcal{E})\Psi_0(\mathcal{E}) \tag{6}$$

and hence acts as a time-dependent wave operator. For $t = 0$ it is the energy-dependent analogue of the standard wave operator in standard MBPT [1]

$$\Omega(\mathcal{E}) = \mathcal{G}(0,\mathcal{E}). \tag{7}$$

2.1 Model-space contributions

Including the counterterm, the first-order Green's operator becomes

$$\mathcal{G}^{(1)}(t,\mathcal{E})P_{\mathcal{E}} = \mathcal{G}^{(0)}(t,\mathcal{E})\,U^{(1)}(0,\mathcal{E})P_{\mathcal{E}} - \mathcal{G}^{(0)}(t,\mathcal{E}')P_{\mathcal{E}'}U^{(1)}(0,\mathcal{E})P_{\mathcal{E}}, \tag{8}$$

where we observe that the Green's operator in the counterterm has the energy parameter $\mathcal{E}'$. Here,

$$\mathcal{G}^{(0)}(t,\mathcal{E}) = \mathrm{e}^{-it(\mathcal{E}-H_0)} \tag{9}$$

is the zeroth-order Green's operator.

When there is an intermediate model-space state $P_{\mathcal{E}'}$ in the first term, we have a MSC given by

$$\begin{aligned}\Big[\mathcal{G}^{(0)}(t,\mathcal{E}) - \mathcal{G}^{(0)}(t,\mathcal{E}')\Big]P_{\mathcal{E}'}U^{(1)}(0,\mathcal{E})P_{\mathcal{E}} &= \Big[\mathcal{G}^{(0)}(t,\mathcal{E}) - \mathcal{G}^{(0)}(t,\mathcal{E}')\Big]P_{\mathcal{E}'}\frac{V(\mathcal{E})}{\mathcal{E}-\mathcal{E}'}P_{\mathcal{E}} \\ &= \frac{\delta\mathcal{G}^{(0)}(t,\mathcal{E})}{\delta\mathcal{E}}\,P_{\mathcal{E}'}V(\mathcal{E})P_{\mathcal{E}}.\end{aligned} \tag{10}$$

In the case of exact degeneracy, the difference ratio goes over into a partial derivative. The complete first-order Green's operator then becomes

$$\mathcal{G}^{(1)}(t,\mathcal{E})P_{\mathcal{E}} = \mathcal{G}^{(0)}(t,\mathcal{E})\Gamma_Q V P_{\mathcal{E}} + \frac{\delta\mathcal{G}^{(0)}(t,\mathcal{E})}{\delta\mathcal{E}} P_{\mathcal{E}'} V(\mathcal{E}) P_{\mathcal{E}}, \tag{11}$$

where the second term is the MSC.

The *effective interaction* that gives rise to the energy shift is given by

$$W = P\left(i\frac{\partial}{\partial t}\mathcal{G}(t,-\infty)\right)_{t=0} P, \tag{12}$$

and applied to the first-order Green's operator we find that the first-order effective interaction is as expected

$$W^{(1)} = PVP. \tag{13}$$

Continuing this process we find that the second-order Green's operator becomes

$$\mathcal{G}^{(2)}(t,\mathcal{E})P_{\mathcal{E}} = \Gamma_Q V_2 \Gamma_Q V_1 + \frac{\delta\Gamma_Q V_2}{\delta\mathcal{E}} P V_1 P, \tag{14}$$

where we have assumed that the interactions might be different. If the interactions are energy independent, this goes over into the second-order wave operator of standard MBPT [1]

$$\Omega^{(2)} = \Gamma_Q V_2 \Gamma_Q V_1 - \Gamma_Q \Omega^{(1)} W^{(1)}. \tag{15}$$

The second-order effective interaction becomes

$$W^{(2)} = P V_2 \Gamma_Q V_1 + P\frac{\delta V_2}{\delta\mathcal{E}} P V_1 P. \tag{16}$$

The last terms in Eqs. (14) and (16) are MSC.

The Green's operator satisfies a Bloch-like equation

$$\mathcal{G} = \mathcal{G}^{(0)} + \Gamma_Q V \mathcal{G} + \frac{\delta^*\mathcal{G}}{\delta\mathcal{E}} W, \tag{17}$$

where the asterisk represents derivation with respect to the last interaction $\Gamma_Q V$ and with respect to $\mathcal{G}^{(0)}$ when no factor of $\Gamma_Q V$ is present. When the interactions are energy independent, this equation goes over into the Bloch equation in standard MBPT [1, 6, 7].

3 Application to Helium-like ions

The procedure sketched above has recently been applied to the ground state of medium-heavy helium-like ions. We have evaluated the effect of QED combined with electron correlation, defined as the interaction with at least two Coulomb interactions. The QED part is here restricted to first order and consists of "non-radiative" effects (retardation of the electromagnetic interaction and effect of virtual electron–positron pairs) as well as "radiative" effects (electron self-energy, vacuum polarization and vertex correction).

It is true that in this procedure we miss some second-order QED effects which can be evaluated by standard QED methods. To mix these in a general way with electron correlation is beyond reach for the moment. We have found, however, that higher-order correlation is considerably more important than second-order QED effects for medium-heavy elements. Therefore, this procedure does include the most important effects of many-body QED in the cases studied.

The effect of retardation in combination with electron correlation was evaluated by Daniel Hedendahl in his PhD thesis [8], including the effect of crossing Coulomb interaction and the effect of virtual pairs. The effect was found to be of the order of 5–10 meV for the ground state of helium-like ions in the range $Z = 20$–40. This is one order of magnitude smaller than the corresponding two-photon effect.

To evaluate the corresponding radiative effects is considerably more difficult. First or all, these effects are divergent and the effects have to be regularized and renormalized, which has to be done in a covariant way. Several schemes for this procedure exist, but the most effective scheme is the dimensional regularization, where the calculations are performed in $(4-\epsilon)$ dimensions, ϵ being a small positive number. Then all integrals are finite, and finally the limit $\epsilon \to 0$ is taken.

All calculations of radiative QED effects have until very recently been performed using the Feynman gauge. The procedure for dimensional regularization was developed for that gauge around 1990 mainly by Snyderman at Livermore Nat. Lab. [10], and the procedure has been applied by several laboratories [11, 12]. We have demonstrated that it is more advantageous to use the Coulomb gauge in combination with electron correlation. Here, the dimensional regularization is more complicated, but a working procedure was developed a few years ago by Hedendahl and Holmberg [9] at our laboratory, based upon the work of Adkins [13, 14]. This procedure was tested for hydrogen-like ions, and the result is given in Table 1, showing the results in terms of the $F(Z\alpha)$ function,

$$\Delta E^{SE} = \frac{\alpha}{\pi}(Z\alpha)^4 mc^3 F(Z\alpha), \tag{18}$$

Table 1 Values of the function $F(Z\alpha)$ in Eq. (18) for the self-energy of the ground state of hydrogen-like ions (from Hedendahl and Holmberg [9])

Z	Coulomb gauge	Feynman auge
18	3.444 043(9)	3.444 04(3)
26	2.783 762(3)	2.783 77(1)
36	2.279 314(2)	2.279 316(7)
54	1.181 866 2(6)	1.781 868(3)
66	1.604 461 5(4)	1.604 462(2)
82	1.487 258 4(4)	1.487 259(1)
92	1.472 424 1(4)	1.472 425(1)

Table 2 Two-photon electron self-energy and vertex correction for the ground state of He-like argon ion, using the Coulomb and Feynman gauges, from Holmberg et al. [5] (in meV)

Gauge	Wave function contr.		MSC	VTX	MCS,VTX	Total SE
	Zero-pot.	Beyond	Zero-pot	Zero-pot	Beyond	
Coulomb	−115.8(7)	11.55(1)	−24.8(1)	16.2(1)	−1.1(1)	−113.8(8)
Feynman	1620.8(6)	−1707.7(1)	3819.0(1)	−3653.3(1)	−192.2(6)	−113(1)

Z being the nuclear charge and α the fine-structure constant. The gauge invariance is here clearly demonstrated, and it is interesting to note that the accuracy is actually higher in the Coulomb gauge, the reason being that in the Feynman gauge there are large cancellations between different contributions, making the result less accurate.

Very recently these calculations have been extended to helium-like systems by Holmberg et al. [5]. Complete two-photon calculations have been performed in the Coulomb as well as the Feynman gauge, again demonstrating the gauge invariance. It is very striking to observe how different the various contributions behave in the two gauges, as shown in Table 2 for $Z = 18$. In the Coulomb gauge one can see that the wave function contribution dominates and the remaining model-space (MSC) and vertex (VTX) contributions are considerably smaller. In the Coulomb gauge this is not at all the case. Here all contributions are of the same order. In the Coulomb gauge the MSC and VTX beyond zero-potential represent about one per cent of the total effect, while in the Feynman gauge it represents about 200 %. This will have important consequences in higher orders.

The evaluation of the full MSC and VTX correction in combination with electron correlation (beyond second order) is prohibitive in any gauge for computational reason. Fortunately, however, one can conclude from the second-order results that these contributions should be relatively small in the Coulomb gauge and be well approximated by the zero-potential part. This gives the result shown in Table 3 for He-like argon (Z = 18). It is obvious from the results in the table that no sensible results can be deduced by using this approximation in the Feynman gauge.

Table 3 Correlation effect beyond two-photon exchange for the electron self-energy and vertex correction for the ground state of He-like argon ion, using the Coulomb and Feynman gauges, from Holmberg et al. [5] (in meV)

Gauge	Wave function contr.		MSC	VTX	Total SE
	Zero-pot.	Beyond	Zero-pot	Zero-pot	
Coulomb	4.8	−0.5	1.2	−0.7	4.6
Feynman	−142	71	−24	54	

4 Summary and conclusions

Quite extensive calculations on helium-like ions on the two-photon level have been performed by Artemyev et al., using the Two-Time Green's function [15], and related calculations have been performed by Plante et al., using the relativistic MBPT with first-order QED energy corrections to the energy [16]. The calculations of Artemyev et al. leave out effects beyond second order and those of Plante et al. include them in a very restricted way. We have for the first time performed calculations of combined QED-correlation effects *beyond* the two-photon level on the ground states of a number of helium-like ions, using the recently developed Green's operator method.

The X-ray transition energies of type $1s$–$2p$ for helium-like ions can in many cases be measured with high accuracy, and this can be used to test various computational results and possibly also the QED theory itself.

The agreement between the experiments results and the theoretical results of Artemyev et al. and Plante et al. is in most cases quite good. Nevertheless, Chantler et al. have in a series of papers claimed that there are significant discrepancies between theory and experiments in a number of cases [17, 18]—up to the order of 100 meV. We have found in our calculations that the effects beyond second order for the ground states of medium-heavy ions are only of the order of a few meV (the effect on the excited state should be even smaller), thus considerably smaller than the effects that Chantler et al. claim to have found. Therefore, if these discrepancies are real, they must have other causes than higher-order QED effects.

The findings of Chantler have recently been challenged by Kubiček et al. [19], who found excellent agreement between their experiments and the above-mentioned theoretical calculations. Our numerical results are consequently quite consistent with those of Kubiček et al.

The effect of interactions beyond two-photon exchange has been estimated in a crude way in the publication by Artemyev et al. [15]. We have found that these estimations agree roughly with our accurate calculations for light elements, while there is significant disagreement for heavier elements [5].

In some cases the X-ray energies can be measured with extreme accuracy, and in such cases effects beyond second

order might be relevant. Here the comparison between theory and experiment can be carried out on a higher level in order to find out whether there are effects that cannot be accounted for.

The Green's operator procedure was primarily developed for investigating *static* problems, but it has recently been demonstrated that also *dynamical* processes, such as scattering processes or transitions between atomic states, are governed by the Green's operator and can be handled by a similar procedure [20].

Acknowledgments The authors want to congratulate Peter Surjan to his 60th birthday, and I.L. wants in particular to thank Peter for his hospitality during several visits to Budapest. This work has been financially supported by the Helmholtz Association and the Gesellschaft für Schwerionenforschung under the project VH-NG-421.

References

1. Lindgren I, Morrison J (1986) Atomic many-body theory, 2nd edn. Springer, Berlin reprinted 2009
2. Lindgren I, Salomonson S, Åsén B (2004) Phys Rep 389:161
3. Lindgren I, Salomonson S, Hedendahl D (2010) Recent progress coupled cluster methods: theory and applications. In: Čársky P, Paldus J, Pittner J (eds) Springer, New York, pp 357–374
4. Lindgren I (2011) Relativistic many-body theory: a new field-theoretical approach. Springer, New York
5. Holmberg J, Salomonson S, Lindgren I (2015) Phys Rev A 92:012509
6. Bloch C (1958) Nucl Phys 6/7:329/451
7. Lindgren I (1974) J Phys B 7:2441
8. Hedendahl D (2010) Ph.D. thesis, University of Gothenburg, Gothenburg, Sweden
9. Hedendahl D, Holmberg J (2012) Phys Rev A 85:012514
10. Snyderman NJ (1991) Ann Phys (NY) 211:43
11. Artemyev AN, Shabaev VM, Yerokhin VA (1997) Phys Rev A 56:3529
12. Sunnergren P (1998) Ph.D. thesis, Department of Physics, Chalmers University of Technology and University of Gothenburg, Gothenburg, Sweden
13. Adkins G (1983) Phys Rev D 27:1814
14. Adkins G (1986) Phys Rev D 34:2489
15. Artemyev AN, Shabaev VM, Yerokhin VA, Plunien G, Soff G (2005) Phys Rev A 71:062104
16. Plante DR, Johnson WR, Sapirstein J (1994) Phys Rev A 49:3519
17. Chantler CT et al (2012). arXiv-ph0988193
18. Chantler CT (2012) Phys Rev Lett 109:153001
19. Kubiček K, Mokler PH, Mäckel V, Ullrich J, López-Urrutia JC (2014) PRA 90:032508
20. Lindgren I, Salomonson S, Holmberg J (2014) Phys Rev A 89:062504

Theor Chem Acc (2016) 135:6
DOI 10.1007/s00214-015-1761-0

REGULAR ARTICLE

Efficient calculation of the density response function from generalized polarizabilities

Tomasz Janowski[1,2] · Krzysztof Wolinski[3] · Peter Pulay[1]

Received: 26 June 2015 / Accepted: 7 November 2015 / Published online: 21 December 2015

Abstract We present a method to calculate the density response function (DRF), also known as the density response kernel or the polarization propagator in the static limit. Our method uses generalized polarizabilities (GPs) which are second derivatives of the molecular energy with respect to two arbitrary perturbations of the external electrostatic potential. They are generalizations of the common multipole polarizabilities. The latter use solid spherical harmonics as perturbing potentials, while GPs can use any function. We use a sine function expansion of the electrostatic potential. Generalized polarizabilities were originally introduced for a different project, ultrafast quantum/molecular mechanics calculations. By transforming the GPs to a (discretized) direct space representation, we obtain the DRF in the static limit. The method has been implemented for single-determinant (Hartree–Fock and density functional theory) wavefunctions, but can be generalized to more accurate wavefunctions. The number of coupled-perturbed self-consistent field (CP-SCF) calculations in our method is proportional to the molecular volume at a given spatial resolution, i.e., scales linearly with the system size, and is independent of the basis set size. The best previous method has the number of CP-SCF calculations proportional to the product of the number occupied and virtual orbitals, and therefore scaling quadratically with the system size at constant basis set quality. The diagonal elements of the DRF (local polarizabilities) of water and butadiene in the molecular plane are displayed. An example of non-diagonal DRF is presented for butadiene 0.77 Å above the molecular plane, with one point fixed over the midpoint of a C=C bond. We obtain a fairly localized DRF, even in this conjugated system. The values become quite small if the distance of the two local perturbations exceeds a bond length. By using frequency-dependent polarizabilities, one could readily calculate the dynamic DRF.

Keywords Density response function · Polarization propagator · Density response kernel · Generalized polarizability · Polarizability · Conceptual density functional theory · Random phase approximation

1 Introduction

The density response function (DRF), also known as polarization propagator or density response kernel, $\chi(\mathbf{r}, \mathbf{r}', \omega)$, [1, 2] is an important quantity in electronic structure theory, particularly in evaluating dispersion energies, in conceptual density functional theory (DFT) and in random phase approximation (RPA) and GW (approximate Green's function) methods. The static ($\omega = 0$) limit of this function is defined as the second functional derivative of the molecular energy E with respect to the external potential u at constant electron number N. Its frequency-dependent form is widely used, as its poles give the electronic excitation energies. The zero-frequency limit [3] can be used to define electric response in larger molecules and is useful in conceptual density functional theory [4, 5]. The first functional

Published as part of the special collection of articles "Festschrift in honour of P. R. Surjan."

✉ Peter Pulay
pulay@uark.edu

[1] Department of Chemistry and Biochemistry, The University of Arkansas, Fayetteville, AR 72701, USA

[2] Present Address: Department of Chemistry, Duke University, Durham, NC 27708, USA

[3] Department of Chemistry, Marie Curie-Sklodowska University, 20-031 Lublin, Poland

derivative of the energy with respect to $u(\boldsymbol{r})$ is $\rho(\boldsymbol{r})$, the electronic charge density at $\boldsymbol{r}$. Therefore, χ can be written as the functional derivative of the approximate electron density (corresponding to the quantum chemical method used) at a point $\boldsymbol{r}$, $\rho(\boldsymbol{r})$ with respect to $u(\boldsymbol{r}')$, the potential at another point $\boldsymbol{r}'$, at constant electron number N:

$$\chi(\mathbf{r},\mathbf{r}',0) = \chi(\mathbf{r},\mathbf{r}') = \left(\frac{\delta^2 E}{\delta u(\mathbf{r})\delta u(\mathbf{r}')}\right)_N = \left(\frac{\delta\rho(\mathbf{r})}{\delta u(\mathbf{r}')}\right)_N \quad (1)$$

In this paper, we will concentrate on the static limit, but generalization to the frequency-dependent case is straightforward at the Hartree–Fock and DFT levels, and we plan to implement it.

Although the density response function is a fundamental quantity in theory, see, e.g., [6–12], there have been few numerical studies of it, partly because it is a function of 7 real variables (6 in the static limit), but also because the difficulty of its calculation. Yang [13], Kudrnovsky and coworkers [14], Senet [15], and Ayers [16] discuss the numerical evaluation of this quantity, but have apparently not found a practical formulation, as none of these papers has a single numerical result or example. The problem is connected with the fact that evaluating $\chi(\mathbf{r}, \mathbf{r}')$ at a single pair of points $(\mathbf{r}, \mathbf{r}')$ involves a numerically awkward delta function perturbation in the potential. Kudrnovsky and coworkers [14] discuss a simplified version of this function in which the potential perturbation consists of varying the nuclear charge of the atoms which can be evaluated simply using analytical derivative methods. This leads us to naturally coarse-grained approximations to the DRF. The foremost of these is the distributed multipole polarizability expansion of Stone and coworkers [3, 17]. This method partitions the DRF to local atomic multipole polarizabilities by using weight functions to define the atomic regions. Le Sueur and Stone [18] reported difficulties in calculating physically meaningful distributed polarizabilities from ab initio calculations, although these have been at least partially resolved by the density fitting method and its latest modification [19–21]. Nevertheless, Rob and Szalewicz [21] remark that the values obtained using the Misquitta–Stone method [19] for distributed polarizabilities are still not satisfactory, often containing large cancelling terms. A further radical simplification was introduced by Morita and Kato [22, 23]. In their technique, the charges and the electric potential are condensed to atoms, and thus polarization effects are described as charge flowing from one atom to another. This method was applied very successfully by Hu and Yang [24]. Condensing the charges to the nuclear positions greatly simplifies both the calculations and the presentation, reducing χ from a function of 6 real variables to an $M \times M$ matrix, where M is the number of atoms in the system. However, its limits are clear. Consider, for instance, planar molecules like benzene and naphthalene (Table 1). A polarizability model, expressed as derivatives of atomic charges, gives obviously zero polarizability perpendicular to the molecular plane. The calculated static dipole polarizability of benzene is 76.5 atomic units in-plane and 41.4 au out-of-plane at the PW91/aug-cc-pVTZ level. The second value is clearly not negligible compared to the first, showing the importance of the atomic polarizability which is neglected in the Morita–Kato–Yang scheme. The situation is similar for naphthalene (Table 1). This limitation does not apply to the distributed polarizability method.

Table 1 Electric dipole polarizabilities of benzene and naphthalene in the coupled and uncoupled Kohn–Sham perturbation theory

Molecule	Method	$\alpha(xx)$	$\alpha(yy)$	$\alpha(zz)$
Benzene	CPKS	76.5	76.5	41.4
Benzene	UCKS	134.9	134.9	67.5
Naphthalene	CPKS	163.3	117.9	61.2
Naphthalene	UCKS	293.4	224.3	105.5

Geometry optimized using the BP86/cc-pVTZ level. Aug-cc-pVTZ basis set

The first numerical results for the DRF we are aware of were published by Savin et al. [25] for He and Be isoelectronic series. However, the method they used is restricted to spherical electron densities and potentials, and thus its applicability in chemistry is limited. A practical method, based on standard coupled-perturbed Kohn–Sham, CPKS, or its predecessor, the coupled-perturbed Hartree–Fock, CPHF [26, 27], was introduced recently by Yang et al. [28]. This paper presents a lucid rederivation of the CPHF/CPKS equations and uses the fact that, in a finite basis set, the only possible first-order changes in the density are linear combinations of $\phi_i(\mathbf{r})\phi_a(\mathbf{r})$, where ϕ_i and ϕ_a are occupied and virtual (vacant) orbitals, respectively. The results were used extensively by Geerlings and coworkers who have done the most significant work in calculating the density response function numerically at the single-determinant level, and correlating the results with chemical concepts. Their results, with a number of chemical applications, are summarized in a recent review article [29] which also gives a detailed exposition of such time-honored techniques as the CPHF and CPKS methods. The method used [28] avoids the problem with the delta functions by carrying out the perturbations in molecular orbital (MO) basis and transforming it to real space. In agreement with the number of possible first-order density variations, this procedure leads to nV distinct perturbations, where n is the number of occupied and V is the number of virtual orbitals. Each perturbation requires the solution of the coupled-perturbed Hartree–Fock or Kohn–Sham (CPHF and CPKS) equations, giving $34 \times 610 = 20740$ CPHF equations in the

naphthalene example (for comparison, the calculation of the nuclear Hessian or force constant matrix requires only 54 CPHF equations). While the effort is still manageable in this case, the method of Ref. [29] has a steep formal scaling of $O(N^2)$ solutions of the CPHF/CPKS equations, each of which scales formally as $O(N^4)$. This leads to an overall formal scaling of $O(N^6)$ and becomes impractical for large molecules and basis sets. This method does not lend itself to truncation because it is formulated in delocalized canonical MO basis.

The large computational effort associated with the solution of the CPHF/CPKS equations can be avoided by neglecting the change of the effective one-electron (Fock) operator caused by the orbital perturbations. This is known in the chemistry literature as the uncoupled Hartree–Fock (UCHF) approximation, and in physics as the independent particle approximation. With this approximation, the zero-frequency propagator is given, assuming real orbitals, as

$$\chi^0(\mathbf{r},\mathbf{r}') = \frac{\delta\rho(\mathbf{r})}{\delta u(\mathbf{r}')} = 4\sum_{i,a}\frac{\phi_i(\mathbf{r})\phi_i(\mathbf{r}')\phi_a(\mathbf{r})\phi_a(\mathbf{r}')}{\varepsilon_i-\varepsilon_a}. \quad (2)$$

Unlike the true propagator, the UCHF approximation is given by a simple closed formula and requires only minimum computational effort to evaluate "on the fly" if the orbitals are available. The uncoupled Hartree–Fock/Kohn–Sham approximation has almost completely vanished from the chemistry literature about 40 years ago when modern derivative techniques became available because of the poor results it produced for second-order properties. Some systematic expositions of analytical derivative methods still use it as a starting point, but it is in our opinion pedagogically inappropriate, as it requires considerable effort to recover the coupled-perturbed Hartree–Fock results which can be derived in a simpler way. UCHF/UCKS is still used in some approximate theories, but we suspect that its only merit is easy computability. According to Geerlings et al. [29], the polarizabilities derived from the uncoupled density response function correlate well with accurate results but can be off by up to a factor of 2, and thus they are only qualitatively useful. Our results in Table 1 confirm this.

2 Generalized polarizabilities for ultrafast quantum/molecular mechanics simulations

Recently we developed a quantum/molecular mechanics (QM/MM) method for the accurate statistical simulation of molecules in polar environments such as in aqueous solutions [30, 31], which speeds up the calculations by 4 or more orders of magnitude or more, even for relatively small solutes and at the inexpensive DFT level. The generalized polarizabilities in our protocol can be used for the efficient evaluation of the density–density response function. In this section, we give a brief description of our ultrafast QM/MM method to clarify the connection between the two very different methods. However, only the generalized polarizabilities of the quantum system (and not the models for the solvent or the statistical sampling) are relevant for the calculation of the DRF.

In our simulations, a small molecule or region, which we will call the "solute," is described by a quantum mechanical method, and its much larger environment (the "solvent") is modeled by simpler and much faster molecular mechanics. The most important and computationally most expensive interaction between the two subsystems is long-range electrostatics. Van der Waals interaction has a much shorter range. In general, the environment is very flexible and must be statistically sampled for thermodynamic properties like free energy. For reliable statistical predictions, particularly of entropic properties, 1–50 million solvent configurations have to be sampled [32]. This is straightforward if the polarization of the quantum subsystem by the solvent is neglected, as it reduces to the evaluation of the electrostatic interaction between the solute and the solvent (usually represented by point charges), and does not require quantum mechanical calculations for each solvent configuration. However, the polarizability of the solute is important, particularly in polar solvents. Statistical (for instance, Monte Carlo) simulation becomes extremely time-consuming if the polarization energy of the quantum system in the field of the solvent molecules is calculated by quantum mechanics, even if a single calculation takes only a fraction of a minute.

We eliminate the need for separate QM calculations for each solvent configuration by approximating the electric potential of the solvent within the solute molecule as linear combination of predefined basis functions *for the potential*:

$$U(\mathbf{r}) \approx \sum_k c_k g_k(\mathbf{r}) \quad k = 1,\ldots M \quad (3)$$

The potential *within the volume of the solute molecule* is a smooth function and can be expanded in an appropriate set of expansion functions $g_k(\mathbf{r})$. This is a generalization of the usual multipole expansion. The latter uses Cartesian monomials 1, x, y, z, x^2, xy, y^2, xz, yz, z^2, x^3, …, or the corresponding solid spherical harmonics to expand the potential. However, for reasons explained in [17], the origin-centered multipole expansion is unsuitable for most systems. We experimented with several expansion sets. One important requirement is that the expansion functions should not diverge to infinity like the solid harmonics do. We finally settled on a sine function expansion of the potential. It is conveniently defined in an outer box that is larger than the extent of the molecular electronic density, to avoid problems with the periodic nature of the sine expansion. Other

choices such as distributed (atom-centered) Gaussian-damped spherical harmonics would also work. The latter provide an alternative definition of distributed polarizabilities [3]. A plane wave expansion of the electric potential has been used successfully for atoms a long time ago by Koide [33].

In the ultrafast QM/MM method, we precalculate *generalized polarizabilities*, i.e., second derivatives with respect to electrostatic perturbations representing the potential. For single-determinant wavefunctions, this requires the solution of the coupled-perturbed Hartree–Fock (or Kohn–Sham) (CPHF/CPKS) equations for each perturbation g_k, i.e., for each function used to expand the potential. The solution is simplified by the fact that the perturbation is a one-electron operator. The CPHF procedure [27, 34] is routinely included in most quantum chemistry programs; for a review, see [35]. As the potential is irregular within the molecule, a fairly large number of expansion (in our case, sine) functions (several hundred to a few thousand for a drug-sized molecule) are required to represent the electrostatic potential accurately. The result of the second derivative calculation in the field-free ($\lambda = 0$) case is a matrix of generalized polarizabilities:

$$\alpha_{kl} = -\left(\frac{\partial^2 E}{\partial c_k \partial c_l}\right)_{\lambda=0} \tag{4}$$

This is analogous to the usual dipole polarizability tensor which has only 3×3 components, corresponding to the perturbations $g(\mathbf{r}) = x, y, z$. The second-order part of the energy in the electric field is given as

$$E^{(2)} = -\frac{1}{2}\sum_{kl} c_k c_l \alpha_{kl} = -\frac{1}{2}\mathbf{c}^T \alpha \mathbf{c} \tag{5}$$

We calculate the electric potential within the molecular box on a grid, and these values are fitted by a linear combination of the potential basis functions, Eq. (3), by a weighted least-squares procedure. This gives the coefficients of the expansion functions, c_k in Eq. (3), as

$$\mathbf{c} = [(\mathbf{A}^T\mathbf{W}\mathbf{A})^{-1}\mathbf{A}^T\mathbf{W}]\mathbf{u} = \mathbf{L}\mathbf{u} \tag{6}$$

Here, $\mathbf{c}$ is the (column) vector of the expansion coefficients, $\mathbf{A}$ is a rectangular matrix, $\mathbf{A}_{\mu k} = g_k(\mathbf{r}_\mu)$, $\mu = 1,\ldots N$, i.e., the value of the expansion (in our case, sine) function g_k at grid point $\mathbf{r}_\mu$. To ensure a unique solution, the number of grid points N should exceed the number of expansion functions M. $\mathbf{W}$ is a weight matrix, see [31] for a discussion about appropriate weights. For the calculation of DRFs, no weights were used. The vector $\mathbf{u}$ contains the values of the electrostatic potential at the grid points within the molecule, $\mathbf{u}_\mu = U(\mathbf{r}_\mu)$, and $\mathbf{L}$ is the $N \times M$ matrix $(\mathbf{A}^T\mathbf{W}\mathbf{A})^{-1}\mathbf{A}^T\mathbf{W}$. Calculating the coefficients $\mathbf{c}$ and the second-order energy, Eq. (5) involves only linear algebra manipulations and is very fast on modern CPUs.

3 Calculation of the density response function from generalized polarizabilities

We will discuss in this section the determination of the density response function from generalized polarizabilities. This has lower formal scaling, $O(N^5)$, than the method of Yang et al. [28], and its spatial resolution can be easily adjusted. One possibility is taking the 3-D Fourier (actually, sine) transform of the generalized polarizability expressed by sine waves. We have implemented an alternative, more general method. Substituting Eq. (6) into Eq. (5) gives

$$E^{(2)} = -\frac{1}{2}\mathbf{u}^T(\mathbf{L}^\mathbf{T}\alpha\mathbf{L})\mathbf{u} \tag{7}$$

where $\mathbf{L}$ is defined in Eq. (6) and in the text. Recall that $\mathbf{u}$ contains the values of the electrostatic potential at the grid points and $\boldsymbol{\alpha}$ is the matrix of generalized polarizabilities (second derivatives with respect to modulated perturbations in the potential). Equation (7) gives the second-order (polarization) energy as a discretized sum over the values of the potential on the grid points. By considering this discrete sum as a quadrature formula for the two-dimensional integral

$$E^{(2)} = -\frac{1}{2}\int \mathrm{d}\mathbf{r}^3 \int \mathrm{d}\mathbf{r}'^3 u(r)\chi(r,r')u(r') \tag{8}$$

where $u(\mathbf{r})$ is the (continuous) electric potential, we can identify the density response function at the grid points as

$$\chi(\mathbf{r}_\mu, \mathbf{r}_\nu) = -[\mathbf{L}^T\alpha\mathbf{L}^T]_{\mu\nu}(\Delta \mathrm{v}_\mu)^{-1}(\Delta \mathrm{v}_\nu)^{-1} \tag{9}$$

where the Δv's are the weights, i.e., grid cell volumes corresponding to the points μ and ν. We use a regular grid (with grid points where the electron density is practically zero removed), with all cells of the same volume for our sine function expansion, and thus the density response function at the pair of points ($\mathbf{r}_\mu$, $\mathbf{r}_\nu$) is simply $(\Delta v)^{-2}$ times the $\mu\nu$ matrix element in Eq. (9).

The computational cost of the transformation in Eq. (9) is negligible compared to the cost of calculating the generalized polarizabilities, $\boldsymbol{\alpha}$. Compared to the method used by Geerlings et al. [29], the advantage of our method is that its resolution, i.e., the size of the sine basis, can be defined by the user and is not given by the atomic orbital basis set. The main features of the DRF do not require high resolution. The number of the expansion (sine) basis is proportional to the molecular volume and at a constant resolution scales linearly with molecular size. This quantity determines the main computational cost, the calculation of the first-order perturbed wavefunctions by the CPHF or CPKS procedure

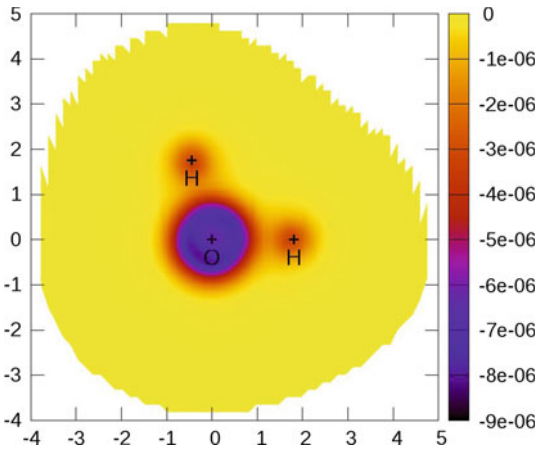

Fig. 1 Diagonal elements of the density response function for water in the molecular plane. Coordinates are expressed in atomic units. The wavefunction is restricted Hartree–Fock with the 6-31G** basis set. The figure shows raw values of the response function. These must be multiplied by 1.0012×10^5 (twice the inverse square of the volume element) to get the values in atomic units

for Hartree–Fock or DFT wavefunctions. This is proportional to the number of the expansion functions for the potential. By contrast, the number of CPHF/CPKS calculations in the method of Ref. [28] is nV, where n is the number of occupied and V is the number of virtual orbitals, i.e., it scales quadratically with the molecular size at constant basis set quality. For this reason, it becomes impractical for larger molecules and basis sets.

Verifying the correctness of the DRF program is somewhat challenging because there are few published numerical results. A simplest test was introduced by Liu et al. [10]. It states that the integral of the DRF with respect to one of its coordinates ($\mathbf{r}$ or $\mathbf{r}'$) over the whole space gives zero. It can be easily proven from the second equality in Eq. (1), by noting that the electron density is unchanged if the potential is changed uniformly. It is particularly easy to apply in our case because of our uniform rectangular grid. Satisfying this test is not, of course, a proof for the correctness of the program, but a random programming error is unlikely to preserve this property.

4 Examples

Although the main content of this paper is to describe our technique to calculate the DRF, we give a few numerical examples. Figure 1 shows the diagonal elements of the density response function (DRF) in the water molecule, shown as color contours in the molecular plane. These are in essence local polarizability densities. The values of the diagonal elements $\chi(\mathbf{r},\mathbf{r})$ are negative as expected because polarization always lowers the molecular energy in the second order.

Figure 2 shows the diagonal elements of χ (the local polarizability) for the butadiene molecule in a plane 0.77 Å above the molecular plane. The diagonal elements of the DRF mimic the electron density. Of more interest is Fig. 3 which shows the off-diagonal elements, with $\mathbf{r}$ fixed 0.77 Å above the midpoint of the C=C bond and $\mathbf{r}'$ sweeping in a plane parallel to the molecular plane at the same height. It

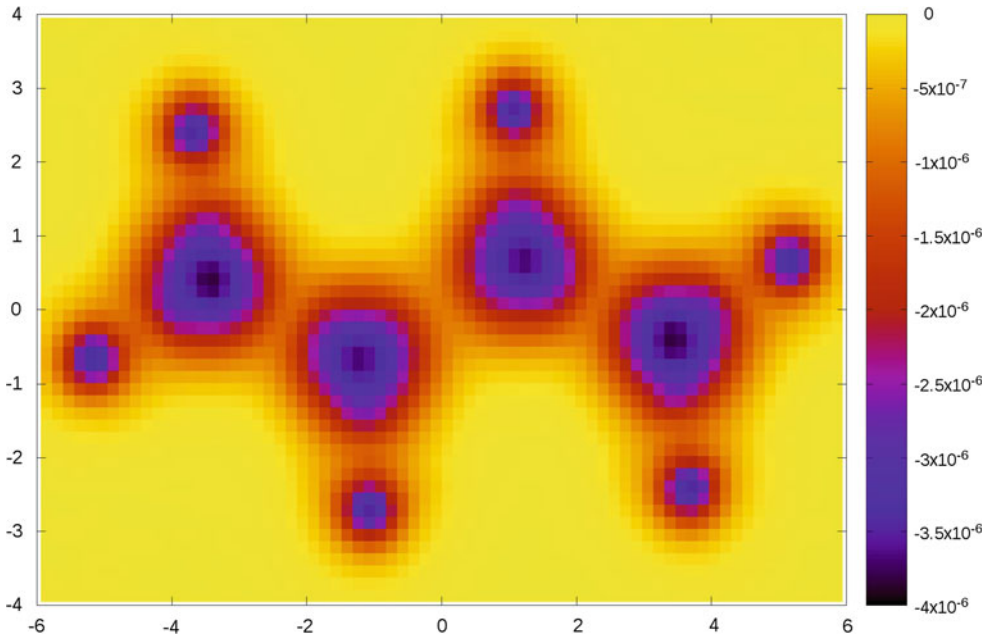

Fig. 2 Diagonal elements of the density response function for butadiene in the molecular plane. Coordinates are expressed in atomic units. The wavefunction is restricted Hartree–Fock with the 6-311G** basis set. The atomic coordinates are C: ($\pm$3.4673, $\mp$0.4178, 0) and ($\pm$1.1939, $\pm$0.6839, 0); H: ($\pm$5.1952, $\pm$0.6801,0), ($\pm$3.6663, $\mp$2.4596,0), ($\pm$1.0674, $\pm$2.7366, 0). The figure shows raw values of the response function. These must be multiplied by 1.0012×10^5 to get the values in atomic units

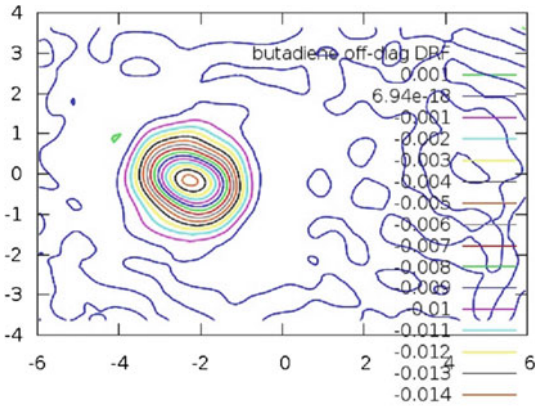

Fig. 3 Non-diagonal elements of the density response function for butadiene in a plane 1.4573 a_0 (0.77 Å) above the molecular plane. See the caption of Fig. 2. Coordinates and values are expressed in atomic units

shows that the DRF, even in this conjugated molecule, is quite localized, its value becoming small if the distance $|\mathbf{r}-\mathbf{r}'|$ is larger than the C=C bond length.

Acknowledgments This work was supported by the US National Science Foundation under Grant number CHE-1213870. It was also supported by the National Institutes of Health under grant number GM103450, the Arkansas Biosciences Institute, and the Mildred B. Cooper Chair in Bioinformatics and Computational Research at the University of Arkansas. We acknowledge the resources of the Arkansas High Performance Computing Center.

References

1. Maaskant WJA, Oosterhoff LJ (1964) Mol Phys 8:319
2. Hunt KLC (1983) J Chem Phys 78:6149
3. Stone AJ (1985) Mol Phys 56:1065
4. Berkowitz M, Parr RG (1988) J Chem Phys 88:2554
5. Parr RG, Yang W (1989) Density functional theory of atoms and molecules. Oxford University Press, New York
6. Casida EM (1995) In: Chong DP (ed) Recent advances in density functional methods. World Scientific, Singapore, pp 155–193
7. Petersilka M, Gossman UJ, Gross EKU (1996) Phys Rev Lett 76:1212
8. Furche F (2001) J Chem Phys 114:5982
9. Ayers PW, Parr RG (2001) J Am Chem Soc 123:2007
10. Liu S, Li T, Ayers PW (2009) J Chem Phys 131:114106
11. Sablon N, De Proft F, Solá M, Geerlings P (2010) Chem Phys Lett 498:192
12. Ángyán JG (2011) Curr Org Chem 15:3609
13. Yang W (1988) Phys Rev A 38:5512
14. Cohen HH, Ganduglia-Pirovano MV, Kudrnovsky J (1995) J Chem Phys 103:3543
15. Senet P (1997) J Chem Phys 107:2516
16. Ayers PW (2001) Theor Chem Acc 106:271
17. Stone AJ (2013) The theory of intermolecular forces. Oxford University Press, Oxford
18. Le Sueur CR, Stone AJ (1993) Mol Phys 78:1267
19. Misquitta AJ, Stone AJ (2006) J Chem Phys 124:024111
20. Hättig C, Jansen G, Hess BA, Ángyán JG (1896) Can J Chem 74:976
21. Rob F, Szalewicz K (2013) Chem Phys Lett 572:146
22. Morita A, Kato S (1997) J Am Chem Soc 119:4021
23. Morita A, Kato S (2002) J Phys Chem A 106:3909
24. Hu H, Yang W (2008) Annu Rev Phys Chem 59:573
25. Savin A, Colonna F, Allavena M (2001) J Chem Phys 115:6827
26. Bratož S (1958) Colloq Int CNRS 82:287
27. Gerratt J, Mills IM (1968) J Chem Phys 49:1719
28. Yang W, Cohen A, De Proft F, Geerlings P (2012) J Chem Phys 136:144110
29. Geerlings P, Fias S, Boisdenghien Z, De Proft F (2014) Chem Soc Rev 43:4989
30. Janowski T, Pulay P (2009) Intern J Quantum Chem 109:2113
31. Janowski T, Wolinski K, Pulay P (2012) Chem Phys Lett 530:1
32. Jorgensen WL, Tirado-Rivers J (2005) J Comput Chem 26:1689
33. Koide A (1976) J Phys B Atom Mol Phys 9:3173
34. Pople JA, Raghvachari K, Schlegel HB, Binkley JS (1979) Int J Quantum Chem Symp 13:225
35. Pulay P (1987) Adv Chem Phys 67:241

Theor Chem Acc (2015) 134:102
DOI 10.1007/s00214-015-1701-z

REGULAR ARTICLE

Use of graphics processing units for efficient evaluation of derivatives of exchange integrals by means of Fourier transform of the 1/*r* operator and its numerical quadrature

Petr Čársky[1] · Roman Čurík[1]

Received: 20 May 2015 / Accepted: 8 July 2015 / Published online: 7 August 2015

Abstract In this paper, we propose an efficient way for evaluation of derivatives of exchange integrals. We propose an approach in which we factorize the non-local exchange kernel into a sum of separable terms. We exploit a discretized Fourier transform for the 1/*r* operator, and we devise a method that allows us to employ a manageable number of plane-wave functions in the Fourier expansion while still keeping necessary accuracy. Resulting formulas are amenable for efficient evaluation on graphics processing units (GPU). We discuss the GPU implementation for derivatives of two-electron repulsion integrals of the (*gk*|*gk*) type in the hybrid Gaussian and plane-wave basis. Derivatives of such integrals are needed for computation of cross sections in vibrationally inelastic electron scattering by polyatomic molecules. Speedup and accuracy achieved are demonstrated for cross sections of selected vibrational modes of cyclopropane, benzene and adamantane. The proposed factorization method is general and may be applied to any type of exchange integrals. We note briefly on its possible application to exchange integrals and their derivatives in quantum chemical computational methods.

Keywords Use of graphical processing units · Derivatives of exchange integrals · Fourier transform of 1/*r* · Electron scattering

1 Introduction

In our recent paper [1], we presented a way of evaluation of exchange integrals that is based on the use of Fourier transform of the 1/*r* operator and its subsequent numerical quadrature. In this way, we succeeded [1] to reduce the computational time for exchange integrals considerably. The stimulus for undertaking that study arose from our urgent need to calculate efficiently exchange integrals in electron–molecule scattering calculations. These integrals are of the $[g(1)k(1)|g(2)k(2)]$ type, where g and k symbols, respectively, refer to Gaussians and plane-wave functions. Lengthy evaluation of theses integrals has been a bottleneck in the scattering theory [2], and it hampers ab initio applications to larger polyatomic molecules. The use of the Fourier transform of the 1/*r* operator itself

$$\frac{1}{r_{12}} = \frac{1}{2\pi^2}\int \frac{1}{k^2} e^{-\mathrm{i}\mathbf{k}.\mathbf{r}_1} e^{i\mathbf{k}.\mathbf{r}_2}\,\mathrm{d}\mathbf{k} \tag{1}$$

and its subsequent numerical quadrature

$$\frac{1}{r_{12}} = \frac{1}{2\pi^2}\sum_{pj} \omega_p\omega_j e^{-\mathrm{i}\mathbf{k}_{pj}.\mathbf{r}_1} e^{i\mathbf{k}_{pj}.\mathbf{r}_2} \tag{2}$$

brought only a minor computer time-saving. However, the merit of Fourier transformation is that it can express exchange integrals for a Hartree–Fock exchange potential V_{ex} as a scalar product of two vectors with one-electron elements

Published as part of the special collection of articles "Festschrift in honour of P. R. Surjan".

✉ Roman Čurík
roman.curik@jh-inst.cas.cz; curik@jh-inst.cas.cz

Petr Čársky
carsky@jh-inst.cas.cz

[1] J. Heyrovský Institute of Physical Chemistry, v.v.i., Academy of Sciences of the Czech Republic, Dolejškova 3, 18223 Prague 8, Czech Republic

$$N_{k_1}N_{k_2}(k_1|V_{\mathrm{ex}}|k_2) = \sum_{i}^{\mathrm{occ}} \sum_{q} (A_{iq}^{k_1})^*(A_{iq}^{k_2}), \tag{3}$$

which is an ideal task for general-purpose computation on graphics processing units (GPU). The indices p and j in Eq. (2) refer to radial and angular numerical quadrature, respectively, ω_p and ω_j are weights of the grid points, N_{k1} and N_{k2} in Eq. (3) are normalization constants for plane-wave functions k_1 and k_2, the first summation in Eq. (3) is over occupied molecular orbitals, and q is a collective index for numerical quadrature

$$q \equiv pj \tag{4}$$

Vectors A in Eq. (3) were obtained as

$$A_{iq}^{k} = \sum_{\mu} c_{i\mu} a_{\mu q}^{k}, \tag{5}$$

where $c_{i\mu}$ stands for expansion coefficients of the ith molecular orbital, and

$$a_{\mu q}^{k} = N_k \sqrt{\frac{\omega_p \omega_j}{2\pi^2}} (\mu k k_q), \tag{6}$$

where the notation $(\mu k k_q)$ denotes the overlap integral between the gaussian μ and a plane-wave function $\exp[\mathrm{i}(k + k_q)]$. By substituting the A terms in Eq. (3) from Eqs. (5) and (6), we obtain the working form of Eq. (3)

$$N_{k_1}N_{k_2}(k_1|V_{\mathrm{ex}}|k_2) = N_{k_1}N_{k_2}\frac{1}{2\pi^2} \sum_{\mu}\sum_{\nu}\sum_{p,j} \omega_p\omega_j(\mu k_1 k_{p,j})^*(\nu k_2 k_{p,j})P_{\mu\nu}, \tag{7}$$

which is ready for differentiation. $P_{\mu\nu}$ is a density matrix element.

In our original code [1, 3], the $(gk|gk)$ integrals were evaluated by means of complex Shavitt functions $F_n(z)$. When the Fourier transform of the $1/r$ operator was used together with graphics processing units, the calculation of exchange integrals for adamantane could be accomplished in 2 min, whereas it lasted previously about 4 days and half on the same computer. Our primary interest has been calculations of cross sections for vibrationally inelastic electron scattering, for which, in contrast to elastic electron scattering, also derivatives of exchange integrals with respect to atomic coordinates has to be evaluated [3]. Their evaluation by Fourier transform and the use of GPU are the subject of this paper.

The paper is organized as follows. In Sect. 2, we present derivation of formulas for derivatives of $(gk|gk)$ integrals suitable for computer coding. Sections 3 and 4 are dealing with test calculations on the molecules of cyclopropane, benzene and adamantane. By its size, adamantane is a molecule considerably larger than molecules for which calculations on vibrationally inelastic scattering have been reported. In 2004, Itikawa [4] characterized the situation as that "a lot of problems are still to be solved" and that "compared to the large number of theoretical studies of vibrational excitation of diatomic molecules, the number of theoretical works for polyatomic molecules is very limited." Hence, in this paper we wish to show that the use of Fourier transform of the $1/r$ operator and the use of GPU open a way to treatments of polyatomic molecules considerably larger than it was possible so far. Section 3 comprises technical details of calculations, and in Sect. 4, we check performance and accuracy of the proposed computational scheme. The technique presented in this paper is general and can be also applied to exchange integrals of other types. In Sect. 5, we note on its possible use for integrals and their derivatives in quantum chemical methods.

2 Derivatives of exchange integrals

Our task is to differentiate Eq. (7) with respect to a nuclear coordinate denoted as variable y,

$$\begin{aligned} &N_{k_1}N_{k_2}\frac{\partial}{\partial y}(k_1|V_{\mathrm{ex}}|k_2) \\ &\quad = N_{k_1}N_{k_2}\frac{1}{2\pi^2}\sum_{\mu}\sum_{\nu}\sum_{p,j}\omega_p\omega_j\left[\left(\frac{\partial}{\partial y}(\mu k_1 k_{p,j})^*\right)(\nu k_2 k_{p,j})P_{\mu\nu}\right. \\ &\qquad \left. + (\mu k_1 k_{p,j})^*\left(\frac{\partial}{\partial y}(\nu k_2 k_{p,j})\right)P_{\mu\nu} + (\mu k_1 k_{p,j})^*(\nu k_2 k_{p,j})\frac{\partial}{\partial y}P_{\mu\nu}\right] \end{aligned} \tag{8}$$

The first two terms on the r.h.s. of Eq. (8), representing the Hellmann–Feynman contribution, can be easily factorized. Substituting (5) and (6) into (8) and defining

$$D_{i,q}^{k,y} = \sum_{\mu}\left(\frac{\partial}{\partial y}a_{\mu,q}^{k}\right)c_{i\mu}, \tag{9}$$

we obtain

$$\begin{aligned} &N_{k_1}N_{k_2}\frac{1}{2\pi^2}\sum_{\mu}\sum_{\nu}\sum_{p,j}\omega_p\omega_j\left[\left(\frac{\partial}{\partial y}(\mu k_1 k_{p,j})^*\right)(\nu k_2 k_{p,j})P_{\mu\nu}\right. \\ &\quad \left. + (\mu k_1 k_{p,j})^*\left(\frac{\partial}{\partial y}(\nu k_2 k_{p,j})\right)P_{\mu\nu}\right] \\ &\quad = 2\sum_{i}^{occ}\sum_{q}[(D_{i,q}^{k_1,y})^*A_{i,q}^{k_2} + (A_{i,q}^{k_1})^*D_{i,q}^{k_2,y}]. \end{aligned} \tag{10}$$

Factorization of the last term on the r.h.s. of Eq. (8) is harder, but it is facilitated by availability of quantum chemical software. From the coupled perturbed Hartree–Fock part of quantum chemical programs, it is possible to extract the first-order transformation matrix $\mathrm{P}^{(1)}$ which is needed for evaluation of derivatives of density matrix elements.

In notation of the paper by Pople et al. [5], they can be expressed as

$$\frac{\partial P_{\mu\nu}}{\partial y} = \sum_{rs} 2\mathrm{P}_{\mathrm{rs}}^{(1)} c_{r\mu} c_{s\nu}, \tag{11}$$

but in contrast to Ref. [5], the subscripts r and s are used here for molecular orbitals (both occupied and virtual) instead of spin orbitals. Comparison with

$$\frac{\partial P_{\mu\nu}}{\partial y} = \sum_{i}^{occ} 2\left(\frac{\partial}{\partial y} c_{i\mu}\right) c_{i\nu} + \sum_{i}^{\mathrm{occ}} 2 c_{i\mu}\left(\frac{\partial}{\partial y} c_{i\nu}\right), \tag{12}$$

provides us the expression for derivatives of expansion coefficients

$$\frac{\partial}{\partial y} c_{i\mu} = \sum_{a}^{\mathrm{virt}} 2\mathrm{P}_{\mathrm{ia}}^{(1),\mathrm{y}} c_{a\mu} + \sum_{j}^{\mathrm{occ}} \mathrm{P}_{\mathrm{ij}}^{(1),\mathrm{y}} c_{j\mu}. \tag{13}$$

Subscripts i and j are used for occupied molecular orbitals and a for virtual molecular orbitals. Equations (11) and (12) can be used for factorization of the derivatives of the density matrix elements, giving the following expression for the last term on the r.h.s. of Eq. (8)

$$N_{k_1} N_{k_2} \frac{1}{2\pi^2} \sum_{\mu} \sum_{\nu} \sum_{p,j} \omega_p \omega_j (\mu k_1 k_{p,j})^* (\nu k_2 k_{p,j}) \frac{\partial}{\partial y} P_{\mu\nu}$$
$$= 2 \sum_{i}^{occ} \sum_{q} [(C_{i,q}^{k_1,y})^* A_{i,q}^{k_2} + (A_{i,q}^{k_1})^* C_{i,q}^{k_2,y})], \tag{14}$$

where the C terms are defined as

$$C_{i,q}^{k,y} = \sum_{\mu} a_{\mu,q}^{k} \frac{\partial}{\partial y} c_{i\mu}. \tag{15}$$

Addition of C and D terms

$$B_{i,q}^{k,y} = C_{i,q}^{k,y} + D_{i,q}^{k,y} \tag{16}$$

gives the following compact factorized expression for derivatives of exchange integrals

$$N_{k_1} N_{k_2} \frac{\partial}{\partial y} (k_1 | V_{\mathrm{ex}} | k_2) = 2 \sum_{i}^{\mathrm{occ}} \sum_{q} [(B_{i,q}^{k_1,y})^* A_{i,q}^{k_2} + (A_{i,q}^{k_1})^* B_{i,q}^{k_2,y}]. \tag{17}$$

As reported in our previous paper [1], a straightforward conventional coding of the $A^*.A$ scheme for integrals brought only a small time-saving when compared to rigorous calculation of integrals by means of complex Shavitt functions. With derivatives and the $B^*.A + A^*.B$ scheme, the situation is even less favorable. As a matter of fact, the CPU implementation of derivatives based on the factorization approach lasted longer than the calculation performed with our original version of the program using complex Shavitt functions. However, the merit of the factorization approach is that the plain multiplication of two long vectors **B***.**A** and **A***.**B** is an ideal task for general-purpose computation on graphics processing units (GPU). Processing of elementary mathematical operations is considerably faster on GPU than processing a general Fortran code on CPU. In Sect. 4, we show that the bottleneck of generation of **B** matrix and the **B***.**A**, **A***.**B** multiplications is largely eliminated by the use of GPU. This bottleneck emerges due to sheer number of ($\mathbf{k}_1$, $\mathbf{k}_2$) pairs (~10^8) needed by realistic scattering calculations.

Details on the CPU and GPU implementations are discussed below in Sect. 3.4.

3 Computational details

3.1 Scattering calculations

Our theoretical model for scattering calculations [3, 6] is a two-channel approach in the discrete momentum representation (DMR) expressed for each vibrational mode by the following two equations

$$\mathbf{T_{10}} = \mathbf{U_{10}} + \mathbf{U_{10}G_0T_{00}} + \mathbf{U_{11}G_1T_{10}}, \tag{18}$$

$$\mathbf{T_{00}} = \mathbf{U_{00}} + \mathbf{U_{00}G_0T_{00}} + \mathbf{U_{01}G_1T_{10}}. \tag{19}$$

We found that cross sections for elastic scattering evaluated by means of Eq. (19) for different vibrational modes differ very little and this fact permits us to simplify Eq. (19) as

$$\mathbf{T_{00}} = \mathbf{U_{00}} + \mathbf{U_{00}G_0T_{00}}, \tag{20}$$

and to obtain the $\mathbf{T_{00}}$ matrix by a standard single-channel calculation for elastic scattering. The $\mathbf{T_{00}}$ matrix so obtained is then used in Eq. (18) for all vibrational modes. Hence, the two-channel approach is so converted to a pseudo-single-channel Lippmann–Schwinger equation, where subscripts 10 and 00 mean the transitions $1 \leftarrow 0$ and $0 \leftarrow 0$, respectively [6]. The T_{10} elements were obtained from Eq. (18) by a standard method of matrix inversion. The calculations are of the SEP (static-exchange-plus-polarization) type [7]. The SE part is calculated rigorously in an ab initio manner by using the density matrix, its analytical derivatives with respect to atomic coordinates of the target, normal modes, and dipole moment derivatives from Hartree–Fock calculations. The polarization–correlation potential is approximated by a model based on the DFT (density functional theory) as described previously [7]. As in photon spectroscopy, the harmonic approximation seems to be the only

manageable approach to polyatomic molecules. Hence, the U_{10} matrix elements for the ith normal mode can be taken as the derivative of the electron–molecule interaction potential with respect to the ith normal coordinate,

$$U_{10} = 1/\sqrt{2}\,\partial U/\partial q_i \tag{21}$$

The calculations were performed for the incident electron energy of 10 eV. The one-electron A and B terms were evaluated for 62 680 806 k_1,k_2 pairs, with the absolute value of k vectors within the range from 0 to 17 a.u. For more details, we refer to the quoted papers.

3.2 Hartree–Fock calculations

For Hartree–Fock calculations of cyclopropane, benzene and adamantane, we used the Gaussian valence-shell double-zeta-and-polarization (9*s*5*p*/4*s*1*p*)/[3*s*2*p*1*d*/2*s*1*p*] basis set of Dunning and Hay [8]. The geometries of the three molecules were optimized with this DZP basis set and then used for analytical evaluation of normal modes, harmonic frequencies, dipole moment and its derivatives, and density matrix and its derivatives with respect to atomic coordinates.

3.3 Numerical quadrature

In the x^y notation of Chien and Gill [9], the quadrature used for *UGT* terms in Eq. (18) may be denoted as 6^{12} 12^1 38^1 590^2 146^1 194^2 302^1 434^2 770^7 2030^1, indicating that x point angular Lebedev grid [10, 11] was used for y successive radial points of the Gauss–Legendre quadrature. The total number of radial points was 31. The 31st radial point with 770 angular grid points was assigned to k_0 of the incoming electron. The total number of grid points was 11,196. The quadrature used for factorization of the $1/r$ operator in Eq. (2) was of the Laguerre–Lebedev type. After some experimentation, we found that a scaled adaptive Laguerre quadrature with 15 grid points can be used as an universal radial quadrature for low-energy electron–molecule scattering calculations. The radial points were obtained as scaled Laguerre grid points

$$k_i = x_{15,i}R, \tag{22}$$

where $x_{15,i}$ is the ith grid point in the 15-point Laguerre quadrature and the scaling factor R was obtained as

$$R = R_{\max}/x_{15,15}, \tag{23}$$

with the fixed $R_{\max} = 11$ a.u. The weights were also scaled as

$$\omega_i = w_i e^{x_i} R, \tag{24}$$

where w_i's are weights of Laguerre grid points. The scaled radial points k_i were ordered in five ranges (0, 0.2), (0.2, 0.4), (0.4, 0.8), (0.8, 1.0) and (1.0, 11.0) and assigned to Lebedev angular quadratures with 26, 50, 86, 194 and 302 grid points, respectively. The total number of grid points was 3402. In the x^y notation of Chien and Gill, the quadrature may be denoted as 26^2 50^1 86^1 194^1 302^{10}. Some calculations were performed with a larger quadrature with a total number of 31,516 grid points, to see if the accuracy of the calculated integrals and derivatives can be improved to the μHartree range. $R_{\max}$ was fixed at 20, and 50 Laguerre radial points were ordered in six ranges (0, 0.5), (0.5, 3.0), (3.0, 7.5), (7.5, 9.5), (9.5, 15.0) and (15.0, 20.0) as 50^9 302^{14} 590^{14} 770^1 2030^8 302^4. It should be noted that this quadrature with 31,516 grid points is used here only for testing. For practical calculations, it is too large as it increases the computational time so much that the merit of time-saving is lost.

3.4 GPU implementation of the method

The bottleneck of the computational scheme, as it is represented by Eqs. (8)–(17), is the calculation and storage of the B terms defined by Eq. (16). For a somewhat larger molecular system, the size of the B array may quickly exceed common disk capacities; moreover, a manipulation with such a large data object (represented by necessary input/output operations) quickly becomes a dominant hindrance in the calculations. For example, in case of adamantane, which serves as one of the benchmark molecules in the present paper, the physical size of the B array that is necessary to form the $\mathbf{U_{10}}$ matrix in Eqs. (18), (19), is larger than 1 TB of data. Therefore, we do not recommend a typical CPU implementation of presented method. Instead, we propose an implementation in which the elements of the B array are not saved on any storage device. In fact, they never even enter the memory space of the computer. This idea is implemented as follows.

Let M be a collective index for plane-wave k_1 and the nuclear coordinate we differentiate with respect to. Thus, M represents two upper indices of the B array in Eq. (16). Let N be a contraction index in Eq. (17); i.e., N represents a collective index for occupied orbital i and plane-wave q (4), denoted as lower indices of B array in Eq. (16). Then, the first term in Eq. (17) represents a simple matrix multiplication

$$\sum_N B^*(M,N)A\left(N,M'\right), \tag{25}$$

while the second term is a Hermitian conjugate of the first term. Since the array B is too large to be stored in the GPU memory, the multiplication (25) must be done in more passes. For each pass, we first calculate a sub-matrix B^* for a subset of rows M_1–M_2. This computation is carried out by a simultaneous launch of a CUDA kernel on

several thousands of GPU threads. The role of the computational kernel is to perform operations summarized by Eqs. (8)–(16). Once the sub-matrix B^* is generated in the GPU memory, we carry out the matrix multiplication (25) by the use of the CUBLAS library. Results are then transferred into the CPU memory space (RAM of the computer that hosts the GPU card) and saved on the disk. Size of the segment computed in one pass is determined by the size of the GPU memory, which was 6 GB in the present case. As can be seen, the proposed algorithm for the derivatives of the exchange integrals requires, in general, very large data blocks denoted as B^* in Eq. (17). However, in the presented GPU implementation these data blocks are generated on the GPU card, they are used on the GPU device, and they are deleted from the GPU memory once they are of no use for the following calculations. Therefore, there is no overhead time connected with their manipulation.

From our personal experience, an exploitation of GPU for its efficient use is not an easy and straightforward task. Large parts of the programs designed for CPU must be rewritten, and algorithms must be rethought. For example, an alignment of data in the GPU memory plays a very important role in the speed of the program. A GPU implementation often requires (as in the present case) programming of a GPU kernel that is designed to be launched in thousands of instances. The available programing and especially the debugging tools are still very limited. Even, with all these difficulties, the GPGPU implementations presently undergo very rapid development in software and hardware and thus they offer a promising environment for computational quantum chemistry and physics.

4 Performance and accuracy

For testing purposes, we performed calculations for all vibrational modes of cyclopropane, benzene and adamantane in two different ways. In the first approach, the exchange integrals and their derivatives were evaluated rigorously by means of complex Shavitt functions $F_n(z)$ by the original (CPU parallelized) version of the program [1, 3]. We used 12 CPU cores, because on a single core the calculations would be excessively long, in particular for adamantane.

In the second approach, a single CPU was used but with the help of GPU for factorization given by Eqs. (3) and (17). The entries in Table 1 are the respective timings for the evaluation of all integrals and their derivatives that were needed for computation of differential cross sections for all vibrational modes. The CPU execution times, t_0, shown in Table 1 on the first line were obtained by using 12 cores of Intel Xeon 3 GHz workstation. The entries on the second line are execution times on a single CPU core code where the evaluation steps shown in Eqs. (3) and (17) were offloaded to Tesla card K20m with 2496 cuda cores clocked at 710 MHz. Single-core rigorous calculations for benzene and adamantane would be excessively long, and therefore, they were only performed with our parallelized version of the program for 12 CPU's. Speedups are therefore expressed as ratios t_0/t_{FT}. They may be multiplied by a factor of 11.1, which was the ratio of timings for rigorous calculations we obtained for cyclopropane on 1 and 12 CPU's.

Table 1 CPU time (in seconds) and speedup in calculations of a preselected set of exchange integrals $(k_1|V_{ex}|k_2)$ and their derivatives $\partial/\partial A_x(k_1|V_{ex}|k_2)$ (denoted as $\partial/\partial y$ in Sect. 2), needed for computation of vibrational cross sections of cyclopropane, benzene and adamantane

	C_3H_6	C_6H_6	$C_{10}H_{16}$
Rigorous calculation[a], 12 CPU's, t_0	19,894	67,330	515,100
FT calculation[b], GPU used, 1 CPU, t_{FT}	1398	3610	19,460
Speedup, defined as (t_0/t_{FT})	14	19	26

[a] Calculation by means of complex Shavitt functions $F_n(z)$

[b] Calculation by means of the Fourier transform of $1/r$

For checking the loss in accuracy connected with the numerical discretization of the $1/r$ term, we selected the cyclopropane molecule and derivatives with respect to the C_{2y} atomic coordinate, as it is defined in Fig. 1. Testing was done for many combinations of k_1 and k_2, keeping the $\mathbf{k}_2$ vectors fixed at 12 orientations, whereas the $\mathbf{k}_1$ vectors were varied.

The result of the testing is shown graphically in Figs. 2 and 3. Figure 2 shows a case when variation of k_1 is limited to small values of $|\mathbf{k_1}|$. For plots, we selected the regions of k_1 and k_2 combinations, where the error was the largest. With a smaller numerical quadrature used in Eq. (2), the maximum error was found for $\mathbf{k_2} \equiv (0; 10; 0)$ and it was in the range of 10^{-4} a.u. The purpose of this figure is to show that on increasing the number of grid points from 3402 to 31,516, the maximum error was reduced to the range of microhartrees.

Figure 3 shows the only region where the factorization method does not work well. If both $\mathbf{k}_1$ and $\mathbf{k}_2$ are large in absolute value and parallel or close to be parallel in orientation, the error is in the millihartree range. On increasing the number of grid points from 3402 to 31,516, the maximum error was reduced, but only to the range of 10^{-4} a.u. If a higher accuracy is requested, this small number of integrals and their derivatives must be evaluated by some other more rigorous method. It is unlikely that the mere use of the double-precision arithmetics would solve the problem. We reached the limit in accuracy of single-precision arithmetics that is sufficient for our scattering codes, and therefore, we did not attempt to optimize the numerical FT quadrature further.

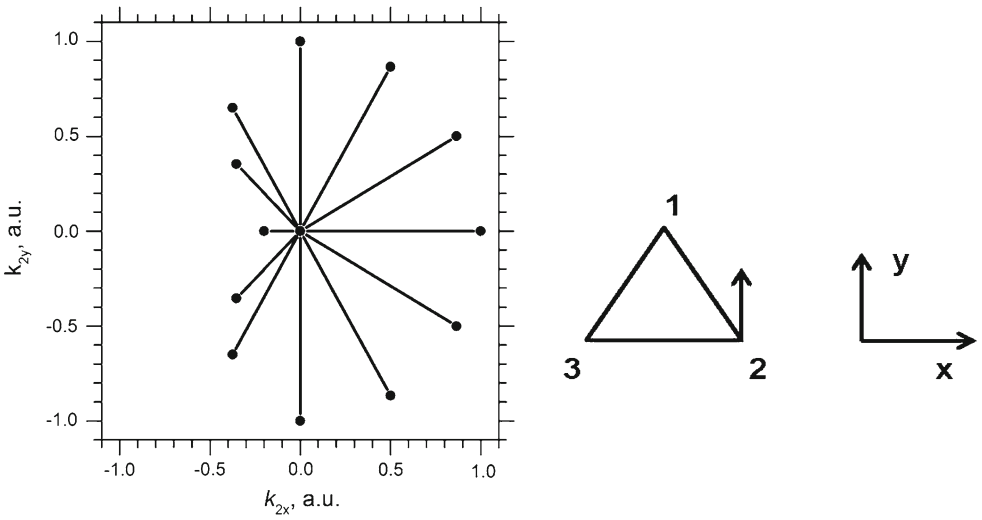

Fig. 1 Two sets of 12 fixed orientations of the $\mathbf{k}_2$ vectors used for testing the accuracy of derivatives $\partial/\partial A_x(k_1|V_{ex}|k_2)$ for cyclopropane. The absolute values of $\mathbf{k}_2$ vectors were either those shown in the figure or ten times greater. All derivatives were with respect to the C_{2y} atomic coordinate, as shown on the right side of the figure

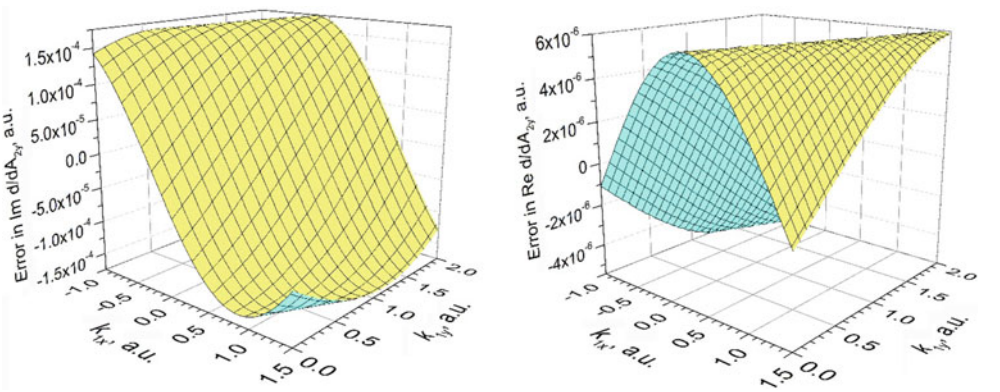

Fig. 2 Error in derivatives $\partial/\partial A_x(k_1|V_{ex}|k_2)$ with respect to values obtained by regular calculations. The $\mathbf{k}_1$ vectors are bound to lie in the σ_{xy} plane of cyclopropane, and its k_{1x} and k_{1y} components are varied with a grid of 0.01 a.u. The $\mathbf{k}_2$ vector is kept fixed at the position (0; 10; 0). *Left* A smaller numerical quadrature with 3402 grid points was used for Eq. (2). The largest error was in the imaginary part of derivatives. *Right* A larger numerical quadrature with 31,516 grid points was used for Eq. (2). For this quadrature, the largest error was in the real part of derivatives

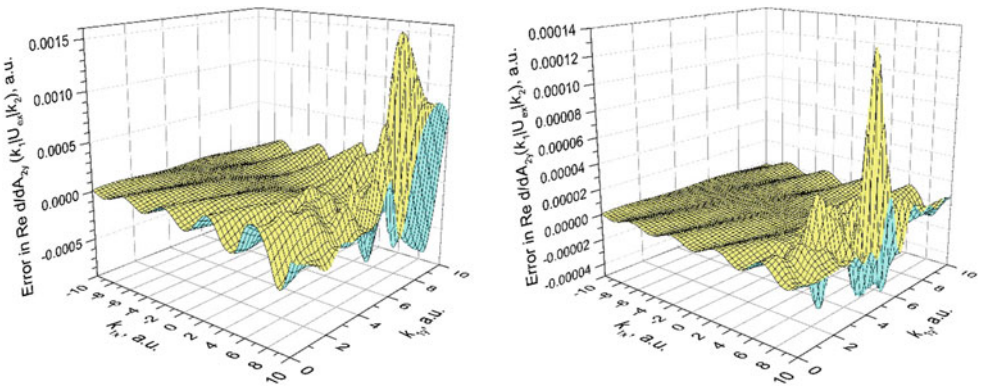

Fig. 3 Error in the real part of derivatives $\partial/\partial A_x(k_1|V_{ex}|k_2)$ with respect to values obtained by the regular calculations. The $\mathbf{k}_1$ vectors are bound to lie in the σ_{xy} plane of cyclopropane, and its k_{1x} and k_{1y} components varied with a grid of 0.1 a.u. The $\mathbf{k}_2$ vector is kept fixed at the position (8.66, 5, 0). The left plot was obtained with a smaller quadrature with 3402 grid points, whereas the right plot was obtained with a larger quadrature with 31,516 grid points

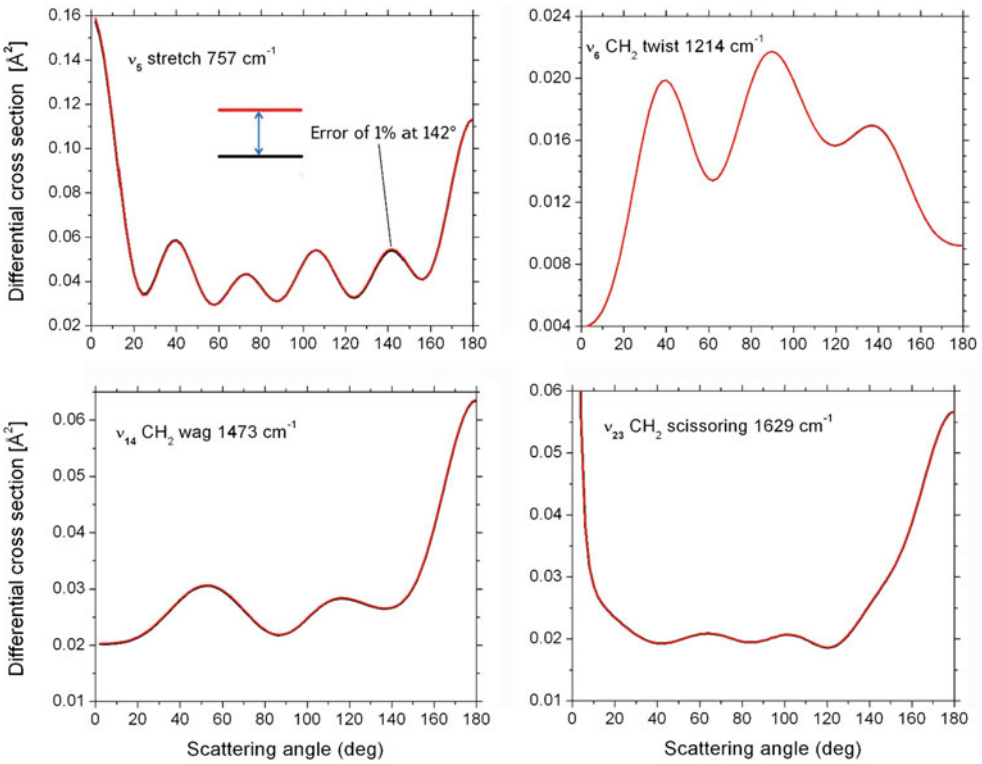

Fig. 4 Angular dependence of the vibrationally inelastic differential cross sections for adamantane and its CC stretch breathing ν_5 mode (*top left*), CH_2 twist ν_6 (*top right*), CH_2 wag ν_{14} (*bottom left*) and the IR-active CH_2 scissoring ν_{23} mode (*bottom right*). The black curves are the result of calculations with factorized exchange integrals, whereas red lines were obtained by rigorous calculations. The calculations were done for the collision energy of 10 eV. The corresponding black and red lines are not distinguishable in the scale of plots. The maximum error found is shown in the upper left plot for ν_5

Next, we show that the smaller numerical quadrature with 3402 grid points is good enough for scattering calculations. As an illustration, we present in Fig. 4 the angular dependence of the differential cross sections for four selected vibrational modes of different types for adamantane. We note that even for such a large multicenter system, results obtained by factorizing the exchange kernel are practically indistinguishable from results obtained rigorously. In the four plots in Fig. 4, the largest error was found for the ν_5 at 142°. In absolute value, it is 0.0005 Å^2 which is negligible for any kind of practical application.

5 Possible use in quantum chemistry

The factorization method presented in this paper may be beneficial for the computational approach proposed by Füsti-Molnar and Pulay [12]. In 2002, they came up with the idea that modern computers have overcome the severe memory limitations of their predecessors, and thus alternative basis sets such as plane waves are becoming attractive alternatives. Up to now, this statement applies to Coulomb integrals only, whereas the exchange energy has to be treated in a traditional way by using a Gaussian basis set or by using a DFT-type functional. However, even for Coulomb integrals a Gaussian basis set cannot be substituted fully by a plane-wave basis because compact molecular orbitals (core orbitals) are not suited to be expanded in a plane-wave basis. Therefore, Füsti-Molnar and Pulay [12] used for expansion of molecular orbitals a mixed Gaussian and plane-wave basis. This led to appearance of $(gk|gk)$ and $(gg|gk)$ integrals in their computational scheme. Evaluation of these integrals by standard methods, using complex Shavitt functions or some other variant of the incomplete Gamma function, is lengthy, and it represents therefore a drawback in the full exploitation of the Fűsti-Molnar and Pulay's idea. We considered it therefore expedient to mention a possible use of the factorization method in this context, though we cannot take it for granted that it is a remedy for this problem. Although factorization of $(gk|gk)$ and $(gg|gk)$ integrals gives readily obtainable overlap integrals (ggk) and (gkk), it may bring profit only in conjunction with the use of GPUs, which reduces considerably the CPU time of originally lengthy multiplication of long vectors with (ggk) and (gkk) elements. A point in favor of the factorization method presented in this paper may be anticipated when derivatives of integrals are to be calculated. A link of the program for derivatives can be coded in such a way that execution of many elementary operations can be passed from CPU to GPU.

The factorization technique presented in this paper is general, and it can be, at least in principle, applied to any type of two-electron integrals. Hence, a question can be asked, if its use could also be profitable for quantum chemistry methods that are using pure Gaussian basis sets. Here, the situation is less clear-cut. A few years ago, the potential

of GPUs in quantum chemistry has been recognized, and since then, their merits in applications to evaluation of two-electron repulsion integrals [13–17], semiempirical methods [18, 19], Hartree–Fock calculations [19, 20], DFT [21, 22], CIS [23], MP2 [24–26], CCSD and CCSD(T) [27, 28] and Quantum Monte Carlo calculations [29] were reported. Nevertheless, we considered it expedient to note a possible use of our computational scheme also for post-Hartree–Fock methods. We mention post-Hartree–Fock methods on purpose, because for energy gradients our factorization approach needs the coupled perturbed Hartree–Fock calculation for evaluation of derivatives of expansion coefficients of molecular orbitals [in Eq. (15)]. It is assumed that evaluation of the gradient at the correlated level is considerably more time-consuming than the coupled perturbed Hartree–Fock calculation. Provided that evaluation of derivatives would be done on GPU in double-precision arithmetics and with an optimized FT quadrature, the calculations may be effective. Below, we indicate how it could work.

Consider an integral of the type $[p(1)q(1)|r(2)s(2)]$, where p, q, r, s are molecular orbitals, constructed from a Gaussian atomic basis set. Direct application of the Fourier transform of $1/r$ by means of Eqs. (1) and (2) leads to the following expression

$$(pq|rs) = \frac{1}{2\pi^2} \sum_t \sqrt{\omega_t}(pqk_t)|(k_t rs)\sqrt{\omega_t}, \tag{26}$$

where (pqk) and (krs) are one-electron overlap integrals that are easy to evaluate. Provided that we have good computational facilities at our disposal, and that GPUs can be effectively applied, we can expect considerable time-saving with respect to a standard evaluation, as we demonstrated it with $(gk|gk)$ integrals [1]. Obviously, the utility of this approach cannot be taken for granted and it should be tested against well-established quantum chemical methods, known under specifications such as RI (resolution of identity), density fitting, Cholesky decomposition or chain-of-spheres approach which employs factorization based on a mixed analytical and numerical evaluation of the exchange integrals [30]. They all use sort of a factorization, and for most of them, the factorization of $(pq|rs)$ integrals can be expressed as

$$(pq|rs) = \sum_P B^P_{pq} B^P_{rs}, \tag{27}$$

where

$$B^P_{pq} = \sum_Q (pq|Q)|(Q|P)^{-1/2}. \tag{28}$$

The $(pq|Q)$ and $(Q|P)$ are, respectively, three- and two-index two-electron repulsion integrals. The overlap integrals (pqk) in our approach in Eq. (26) are easier to evaluate, but this need not be a substantial advantage because performance of factorization depends mainly on efficient coding the matrix multiplication operations. Three-center overlap integrals in pure Gaussian basis were also exploited in tensor hypercontraction density fitting applied perturbation approaches [31] and coupled clusters method [32]. Recent experience with the development of quantum chemical methods shows that when an ingenious use is made of GPUs, not depending on linear algebra libraries only, unprecedented progress in the evaluation of exchange integrals can be achieved [13, 14, 20, 21]. Hence, the factorization method presented in this paper for derivatives of exchange integrals is worth of further exploration, if it is a viable alternative to RI-type methods.

6 Conclusions

We have shown that the factorization method, proposed in our earlier paper [1] for exchange integrals of the $(gk|gk)$ type, can also be applied to their derivatives. We found that the Fourier transform of $1/r$ alone does not bring an advantage of speedup. However, its merit is its ability to cast mathematical expressions into a form which is suited ideally for use of GPUs. Net result of such a combination is considerable computer time-saving. In this paper, the test calculations were extended for evaluation of derivatives. The calculations were done for a set of exchange integral and their derivatives that were needed for a treatment of electron scattering by cyclopropane, benzene and adamantane. The data on timing of calculations are listed in Table 1. The mere Fourier transform by means of Eqs. (1) and (2) did not bring any profit. But, if on top of that the $A^*.A$ and $B^*.A + A^*.B$ multiplications in Eqs. (3) and (17) were performed on GPU, the CPU time dropped by more than an order of magnitude. It is important to note that the present speedup achieved for the derivatives of the $(gk|gk)$ integrals is smaller when comparing to speedup of the GPU implementation for the $(gk|gk)$ integrals alone [1]. A reason for this is due to very efficient implementation of the nuclear derivatives in the original rigorous method that uses tabulated Shavitt functions while the present algorithm scales linearly with the number of nuclear degrees of freedom.

The factorization method in a form presented in this paper is general and can be, at least in principle, applied to any type of two-electron integrals. To become an alternative to existing established quantum chemical methods, the computer code has to enable an efficient use of GPU. Although reorganization of the program for this purpose is tedious and requires programming skill, the result may be rewarding. The factorization method may also have a merit in supporting the idea of Füsti-Molnar and Pulay [12] to substitute Gaussians by plane-wave functions. So far, their

method is limited to Coulomb energy only because of the problem to calculate efficiently integrals of (*gk*|*gk*) and (*gg*|*gk*) types. The factorization method may be profitable in this context.

Finally, a brief remark on economy is noteworthy. At the present price level, a single CPU with a GPU (used in the present setup) is 2–3 times cheaper than a computer with 12 CPU's (also used in the present demonstration), still providing more than one order of magnitude better performance.

Acknowledgments This work was conducted in the framework of the COST Action CM1301 (CELINA), supported also by the Czech Ministry of Education, Youth and Sports (Grant LD14088) and Grant Agency of the Czech Republic (Grant P208/11/0452).

References

1. Čársky P, Čurík R (2014) Theor Chem Acc 133:1466
2. Winstead C, McKoy V (1995) In: Yarkony DR (ed) Modern electronic structure theory part II. World Scientific, Singapore
3. Čársky P, Čurík R (2012) In: Čársky P, Čurík R (eds) Low-energy electron scattering from molecules, biomolecules and surfaces. CRC Press, Taylor@Francis Group, Boca Raton
4. Itikawa Y (2004) J Phys B 37:R1
5. Pople JA, Krishnan R, Schlegel HB, Binkley JS (1979) Int J Quantum Chem Quantum Chem Symp 13:225
6. Čurík R, Čársky P (2003) J Phys B 36:2165
7. Čurík R, Šulc M (2010) J Phys B 43:175205
8. Dunning TH Jr, Hay PJ (1977) In: Schaefer HF III (ed) Modern theoretical chemistry, vol 3. Plenum Press, New York
9. Chien SH, Gill PMW (2006) J Comput Chem 27:730
10. Lebedev VI (1975) Zh Vychisl Mat Mat Fiz 15:48
11. Lebedev VI (1976) Zh Vychisl Mat Mat Fiz 16:293
12. Füsti-Molnar L, Pulay P (2002) J Chem Phys 116:7795
13. Ufimtsev IS, Martinez TJ (2008) J Chem Theory Comput 4:222
14. Yasuda K (2008) J Comput Chem 29:334
15. Kussmann J, Ochsenfeld C (2013) J Chem Phys 138:134114
16. Kussmann J, Ochsenfeld C (2015) J Chem Theory Comput 11:918
17. Asadchev A, Allada V, Felder J, Bode BM, Gordon MS, Windus TL (2010) J Chem Theory Comput 6:696
18. Wu X, Koslowski A, Thiel W (2012) J Chem Theory Comput 8:2272
19. Carvalho Maia JD, Carvalho GAU, Mangueira CP Jr, Santana SR, Cabral LAF, Rocha GB (2012) J Chem Theory Comput 8:3072
20. Ufimtsev IS, Martinez TJ (2009) J Chem Theory Comput 5:1004
21. Yasuda K (2008) J Chem Theory Comput 4:1230
22. Luehr N, Ufimtsev IS, Martinez TJ (2011) J Chem Theory Comput 7:949
23. Isborn CM, Luehr N, Ufimtsev IS, Martinez TJ (2011) J Chem Theory Comput 7:1814
24. Vogt L, Olivares-Amaya R, Kermes S, Shao Y, Amador-Bedolla C, Aspuru-Guzik A (2008) J Phys Chem A 112:2049
25. Olivarez-Amaya R, Watson MA, Edgar RG, Vogt L, Shao Y, Aspuru-Guzik A (2010) J Chem Theory Comput 6:135
26. Maurer SA, Kussmann J, Ochsenfeld C (2014) J Chem Phys 141:051106
27. DePrince AE III, Hammond JR (2011) J Chem Theory Comput 7:1287
28. Bhaskaran-Nair K, Ma W, Krishnamoorthy S, Villa O, van Dam HJJ, Apra E, Kowalski K (2013) J Chem Theory Comput 9:1949
29. Anderson AG, Goddard WA III, Schröder P (2007) Comput Phys Commun 177:298
30. Neese F, Wennmohs F, Hansen A, Becker U (2009) Chem Phys 356:98
31. Hohenstein EG, Parrish RM, Martinez TJ (2012) J Chem Phys 137:044103
32. Hohenstein EG, Kokkila SIL, Parrish RM, Martinez TJ (2013) J Chem Phys 138:124111

Theor Chem Acc (2015) 134:134
DOI 10.1007/s00214-015-1728-1

REGULAR ARTICLE

Relations between real molecules through abstract molecules: the reference cluster approach

Paul G. Mezey[1,2,3]

Received: 15 June 2015 / Accepted: 13 September 2015 / Published online: 16 October 2015

Abstract Replacing integer atomic numbers representing nuclear charges by continuous variables has already provided some rigorous quantum chemical relations between real molecules, using a formal interpolation through non-physical abstract molecules of continuously varying nuclear charges. Extending this approach to the more general "universal molecule" model, where all discrete parameters of molecules are generalized and replaced by continuous variables, provides further relations, actually interconnecting all real molecules through abstract, non-physical "molecules," involving, for example, non-integer number of electrons. One simplifying idea of this model is the so-called "reference cluster," originally defined for isoelectronic systems of a fixed number N of nuclei, where each nucleus is replaced by a possibly fictive nucleus with a nuclear charge equal to the average of the N nuclear charges. Based on the earlier results, some new relations are derived interrelating energies and some other properties of some real molecules, and also providing a unifying framework for the utilization of both symmetry and energy relations of the universal molecule model.

Published as part of the special collection of articles "Festschrift in honour of P. R. Surjan".

✉ Paul G. Mezey
paul.mezey@gmail.com

[1] Scientific Modeling and Simulation Laboratory (SMSL), Department of Chemistry and Department of Physics and Physical Oceanography, Memorial University of Newfoundland, 283 Prince Philip Dr., St. John's, NF A1B 3X7, Canada

[2] Institute of Chemistry, Eötvös University, Budapest, Hungary

[3] Institute of Chemistry, Babes-Bolyai University, Cluj-Napoca, Romania

Keywords Nuclear charge space · Electronic energy inequalities · Reference cluster · Universal molecule model

1 Introduction

Originally motivated by the United Atom studies of Thirring, Narnhofer, and Lieb [1–3], the idea of exploiting nuclear charge convexity relations between electronic energies of molecules, without involving the extreme case of uniting all nuclei of the molecule into a single, formal nucleus of the United Atom, has lead to a variety of rigorous quantum chemical energy inequalities for various sets of molecules, starting with simple diatomic cases [4, 5].

After the very first examples of such electronic energy inequalities [4, 5], including one of the simplest cases, the N_2 and CO pair, the concept of the nuclear charge space was elaborated [6] and the level set topology approach was introduced [7]. A generalization to other linear parameters besides the nuclear charges was described [8], followed by several additional applications [9–15]. As one important generalization, geometry-independent relations were also derived [9, 14]. Analogous relations for isomerisation energies [10], as well as for potential surfaces for higher multiplicities, were derived [11], and applications to clusters [13], an early step toward the more recent reference cluster model, relevant to this study, were also described. Exploiting the quadratic dependence of the nuclear repulsion on the nuclear charges, in some cases, for example, in the prototype case of N_2 and CO, analogous inequalities were derived for molecular total energies [12, 15]. Special applications, for example, to polymers of different unit cell sizes [16], and to special problems of vibrational spectra [17], have also been described.

In the present study, the earlier relations are extended to cases involving larger number of "anchor structure" points of the relevant nuclear charge space, that is, higher-dimensional convex sets will be used than in earlier studies. These higher-dimensional cases are not as easily visualized; however, they can provide more options for interrelations between molecules. Some new connections to the reference cluster and the universal molecule models, especially in the context of symmetry, will also be elaborated.

A common feature of most of the earlier approaches is the replacement of the formal nuclear charges by continuous variables, and considering the resulting values as components of a "nuclear charge vector" $\mathbf{z}$ in a formal nuclear charge space $\mathbf{Z}$, of dimension equal to or greater than the number of nuclei in the molecules studied. Note that formal dummy nuclei of zero nuclear charges could always be added without affecting the validity of the physical laws applied, and hence very general treatments, interrelating rather diverse molecules and ionic systems, have become possible.

Although the specific linear dependence of the electronic Hamiltonian on the nuclear charges has been the primary tool applied, it has been also natural to extend the approach by replacing other discrete, integer parameters of molecules by continuous variables. Clearly, no such fractional nuclear charges correspond to real molecules, and similarly, allowing, for example, the number of nuclei and the number of electrons to vary continuously, many "non-physical," abstract entities can result. For example, just as there exists no molecule "halfway between" N_2 and CO, as far as the nuclear charge vectors of (7, 7) and (6, 8) are concerned, similarly, no actual molecules exist, for example, with 10.3 nuclei or with some non-integer number of electrons. Nevertheless, just as the mathematical approaches extended to the complex plane can provide useful shortcuts (such as contour integration), even if no actual physical quantities can ever take complex values, similarly, such an extension of the family of real molecules to fictitious "objects" with non-physical properties also has provided useful shortcuts. This way, new relations can be derived between actual, physically valid molecules, such as the simplest of these rigorous electronic energy inequalities for N_2 and CO using continuous nuclear charge variations, the earliest example that will be briefly reviewed and also extended in the next section.

By following this idea to the extreme case, where all such parameters of individual molecules are considered continuous variables, a rather general model has been established. The resulting formal "universal molecule" model [18–21] provides a formal link between any two actual molecules, by some continuous changes in all those parameters which distinguish these molecules. This universal molecule model offers not only conceptual tools, but also new relations on energy or other properties of actual, real molecules. In this contribution, the advantages of this model are used to obtain new results for both energy interpolation, as well as energy extrapolation, resulting in both upper and lower bounds for energies. Besides this result, the central role of the so-called "reference cluster" [22, 23], a formal molecular entity with all nuclei having the same nuclear charge, is discussed. The reference cluster has a distinguished role in terms of its transformations to real, actual molecules, and also in terms of the maximal symmetry properties of the associated potential energy surfaces, where somewhat counter-intuitive, "opposing" trends exist between transformations reducing symmetry and reducing energy.

2 Nuclear charge space convexity relations and their extensions

In the Born–Oppenheimer approximation, the molecular total energy, E_t, is regarded as a sum of the nuclear repulsion energy, E_n, and the electronic energy E_e,

$$E_t = E_n + E_e \tag{1}$$

where the latter is associated with the electronic Hamiltonian H_e (N, k, $\mathbf{z}$, $\mathbf{r}$) given as

$$H_e(N,k,\mathbf{z},\boldsymbol{r}) = -1/2 \sum_{t=1,k} \Delta_t - \sum_{i=1,N} \sum_{t=1,k} z_i/|\boldsymbol{r}_i - \boldsymbol{r}_t| + \sum_{t<t'\le k} 1/|\boldsymbol{r}_t - \boldsymbol{r}_{t'}| \tag{2}$$

The z_i nuclear charges of the N nuclei of nuclear positions $\mathbf{r}_i$ are collected into a formal nuclear charge vector $\mathbf{z}$ (usually considered as a column vector, although often the transpose, $\mathbf{z}'$, is used), and the index t refers to the electrons of a k-electron molecule.

In order to derive the general, $(n-1)$-dimensional convexity relation for nuclear charge vectors, consider $n+1$ isoelectronic molecular systems,

$$M, M^{(1)}, M^{(2)}, \ldots M^{(i)}, \ldots M^{(n)} \tag{3}$$

in their electronic ground states (or in some common, lowest state of some electronic manifold), where the nuclear locations match, but the nuclear charges can be different and even zero nuclear charges, that is, "dummy nuclei" are allowed.

For each of these molecular systems, the nuclear charge vector $\mathbf{z}$ contains the individual nuclear charges as components, following some fixed ordering.

Let us denote the corresponding nuclear charge vectors by

$$\mathbf{z}, \mathbf{z}^{(1)}, \mathbf{z}^{(2)}, \ldots \mathbf{z}^{(i)}, \ldots \mathbf{z}^{(n)}, \tag{4}$$

respectively, where the ordering of the nuclei as components of these vectors is consistent with the common nuclear geometry *r*.

If **z** is a convex combination of the other n nuclear charge vectors, $\mathbf{z}^{(1)}$, $\mathbf{z}^{(2)}$,…$\mathbf{z}^{(i)}$,…$\mathbf{z}^{(n)}$, that is, if

$$\mathbf{z} = \alpha^{(1)}\mathbf{z}^{(1)} + \alpha^{(2)}\mathbf{z}^{(2)} + \cdots + \alpha^{(i)}\mathbf{z}^{(i)} + \cdots + \alpha^{(n)}\mathbf{z}^{(n)}, \quad (5)$$

where

$$0 \leq \alpha^{(i)} \leq 1, \quad \text{for every } i, \quad (6)$$

and where

$$\alpha^{(1)} + \alpha^{(2)} + \cdots + \alpha^{(i)} + \cdots + \alpha^{(n)} = 1 \quad (7)$$

then due to linearity of the electronic Hamiltonians $H_e(\mathbf{z}, r)$ in components of **z**, a relation analogous to Eq. (5) must apply for their corresponding electronic Hamiltonians as well,

$$H_e(\mathbf{z}, r) = \alpha^{(1)}H_e\left(\mathbf{z}^{(1)}, r\right) + \alpha^{(2)}H_e\left(\mathbf{z}^{(2)}, r\right) + \cdots + \alpha^{(i)}H_e\left(\mathbf{z}^{(i)}, r\right) + \cdots + \alpha^{(n)}H_e\left(\mathbf{z}^{(n)}, r\right), \quad (8)$$

If the electronic wavefunction of system *M* is Ψ_e, then based on the above, the electronic energy expectation value of system *M* can be written as

$$\langle\Psi_e|H_e(\mathbf{z}, r)|\Psi_e\rangle = \sum_{i=1,n} \alpha^{(i)} \left\langle \Psi_e|H_e\left(\mathbf{z}^{(i)}, r\right)|\Psi_e \right\rangle \quad (9)$$

However, the wavefunction Ψ_e of system *M* is not in general variationally optimal for any of the other molecular systems $M^{(1)}$, $M^{(2)}$,… $M^{(i)}$,… $M^{(n)}$. Consequently, according to the variational theorem, the right-hand side of Eq. (9) cannot increase if in the expectation value expression for each of the right-hand side Hamiltonians H_e ($\mathbf{z}^{(i)}$, *r*), we replace Ψ_e with the actual wavefunction $\Psi_e^{(i)}$ of the respective molecular system $M^{(i)}$.

Consequently, we obtain that

$$\langle\Psi_e|H_e(\mathbf{z}, r)|\Psi_e\rangle \geq \sum_{i=1,n} \alpha^{(i)} \left\langle \Psi_e^{(i)}|H_e\left(\mathbf{z}^{(i)}, r\right)|\Psi_e^{(i)} \right\rangle \quad (10)$$

But, inequality (10) is in fact an inequality for the electronic energies,

$$E_e \geq \sum_{i=1,n} \alpha^{(i)} E_e^{(i)} \quad (11)$$

That is, convexity for the set of nuclear charge vectors, which in our case form a simplex in an $(n-1)$-dimensional nuclear charge space **Z**, implies convexity for the respective electronic energies.

Specifically, if the nuclear charge vector **z** falls on or inside of the **Z**-space simplex defined by the nuclear charge vectors $\mathbf{z}^{(1)}$, $\mathbf{z}^{(2)}$,… $\mathbf{z}^{(i)}$,… $\mathbf{z}^{(n)}$, then the electronic energy relation (11) must hold.

The special case of $n = 2$ has been studied in most detail, and one of the simplest applications that has been already discussed is the comparison of the electronic energies of N_2, CO, and the equivalent OC molecule. If $M = N_2$, $M^{(1)} = CO$, and $M^{(2)} = OC$, with identical bond lengths, and with the following 2D nuclear charge vectors $z = (7, 7)'$, $z^{(1)} = (6, 8)'$ and $z^{(2)} = (8, 6)'$, respectively, then these nuclear charge vectors fulfill the convexity condition

$$z = \alpha z^{(1)} + (1-\alpha)\, z^{(2)}$$

where, as in general, $0 \leq \alpha \leq 1$, now with the simple special choice of $\alpha = 0.5$.

Consequently, the theorem applies, hence for every common bond length, that is, for the entire electronic potential energy curves

$$E_e \geq 0.5E_e^{(1)} + (1-0.5)E_e^{(2)}$$

$$E_e(N_2) \geq 0.5E_e^{(1)}(CO) + (1-0.5)E_e^{(2)}(OC),$$

that is,

$$E_e(N_2) \geq E_e(CO) \text{ for every common bond length.}$$

Note that this is a rigorous (although simple) quantum chemical result, as derived entirely by using nuclear charge variations.

However, convexity, if used in a judicious way, can also be used for extrapolation!

Consider now the case of $M = CO$, $M^{(1)} = N_2$, and $M^{(2)} = BF$ triple of diatomics, again, with identical bond lengths, and with the following 2D nuclear charge vectors $z = (6, 8)$, $z^{(1)} = (7, 7)$, and $z^{(2)} = (5, 9)$, respectively.

Again, we obtain that

$$z = \alpha z^{(1)} + (1-\alpha)\, z^{(2)}$$

where $0 \leq \alpha \leq 1$, with the current special choice of $\alpha = 0.5$.

Hence, just as before, the theorem applies, consequently, for every common bond length, that is, for the entire electronic potential energy curves

$$E_e \geq 0.5E_e^{(1)} + 0.5E_e^{(2)}$$

$$E_e(CO) \geq 0.5E_e^{(1)}(N_2) + 0.5E_e^{(2)}(BF).$$

However, now we can combine this result with the previous one,

$$E_e(N_2) \geq E_e(CO),$$

and we get

$$E_e(N_2) \geq E_e(CO) \geq 0.5E_e^{(1)}(N_2) + 0.5E_e^{(2)}(BF),$$

that implies

$E_e(N_2) \geq 0.5E_e(N_2) + 0.5E_e(BF)$.

After subtracting 0.5 $E_e(N_2)$ from both sides, we get

$0.5E_e(N_2) \geq 0.5E_e(BF)$,

that is,

$E_e(N_2) \geq E_e(BF)$,

for every common bond length, that is, for the entire electronic potential energy curves.

We might note that the same result can also be obtained, not through the above extrapolation, but considering the triple of FB, N_2, and BF.

These two simple examples also can serve as illustrations of the reference cluster concept. For both CO and BF, the reference cluster is in fact the molecule N_2, since in each of these systems the average nuclear charge is 7.

For many molecular families, the reference cluster, having identical nuclei with the average nuclear charge present in the family, is a chemically viable system, which happens to have integer nuclear charges, just as in the above example. For example, for all carbohydrates, such as those with the formula $[C(H_2O)]_6$, the reference cluster is made up by Be atoms: Be_{24}, or in general, for carbohydrates $[C(H_2O)]_m$, the reference cluster is Be_{4m}.

Similarly, for both methanol, CH_3OH, and hydrazine, H_2NNH_2, the reference cluster is Li_6, again, a chemically viable entity, with integer nuclear charges.

The advantage of such reference clusters is the fact that their potential energy surfaces typically show the highest symmetry, as well as the most elaborate distribution of 3D symmetries along the usually multidimensional energy surface, an important advantage in the analysis of such potential surfaces. This has consequences also for the lower symmetry cases represented by the molecules which generate the actual reference cluster, for example, methanol, CH_3OH, and hydrazine, H_2NNH_2, in the Li_6, reference cluster case (a problem discussed from a different perspective in Ref. [22]).

We call these integer-charge cases the "realizable reference clusters."

However, it is far more common to obtain a reference cluster with non-integer formal nuclear charge, that is, a "non-realizable reference cluster," but even in such cases, the principle of continuous nuclear charge variations can lead to new results, for actual, existing molecular systems.

As an example, consider some four-atom clusters composed from some of the metal atoms from the sequence

Re(75), Os(76), Ir(77), Pt(78), Au(79),

where the atomic numbers are given in the parentheses.

One such example:

Take the following five isoelectronic atomic clusters with a common nuclear geometry assumed to be some irregular tetrahedron in the 3D space:

M = [Ir(77) Ir(77) Ir(77) Pt(78)]

$M^{(1)}$ = [Os(76) Au(79) Os(76) Pt(78)]

$M^{(2)}$ = [Pt(78) Re(75) Ir(77) Au(79)]

$M^{(3)}$ = [Re(75) Ir(77) Au(79) Pt(78)]

$M^{(4)}$ = [Au(79) Ir(77) Os(76) Ir(77)]

The reference cluster $M^{(ref)}$ in this case is a fictitious entity, an isoelectronic cluster of four atoms with nuclear charges equal to 77.25, in protonic units, clearly, a non-physical entity. It is evident that the formal potential energy hypersurface for this reference cluster $M^{(ref)}$ shows the highest symmetry among all of the actual potential energy hypersurfaces that can be associated with the given nuclear charge space $\mathbf{Z}$, including, of course, the potential energy hypersurfaces of the actual clusters, M, $M^{(1)}$, $M^{(2)}$, $M^{(3)}$, and $M^{(4)}$, an issue we shall discuss briefly in the closing segment of this paper.

For these five actual clusters, their respective 4D nuclear charge vectors are

$\mathbf{z}$ = [77 77 77 78]

$\mathbf{z}^{(1)}$ = [76 79 76 78]

$\mathbf{z}^{(2)}$ = [78 75 77 79]

$\mathbf{z}^{(3)}$ = [75 77 79 78]

$\mathbf{z}^{(4)}$ = [79 77 76 77],

whereas for the reference cluster $M^{(ref)}$ the nuclear charge vector is

$\mathbf{z}^{(ref)}$ = [77.25 77.25 77.25 77.25].

One can easily verify by direct substitution that nuclear charge vector $\mathbf{z}$ is a convex combination of the other four nuclear charge vectors:

$$\mathbf{z} = 0.25\,\mathbf{z}^{(1)} + 0.25\,\mathbf{z}^{(2)} + 0.25\,\mathbf{z}^{(3)} + 0.25\,\mathbf{z}^{(4)}$$

Consequently, the 4D version of the electronic energy convexity theorem applies, and one obtains the quantum-chemically rigorous result that

$$E_e(Ir_3Pt) \geq 0.25\,E_e(OsAuOsPt) + 0.25\,E_e(PtReIrAu) + 0.25\,E_e(ReIrAuPt) + 0.25\,E_e(AuIrOsIr),$$

valid for any common nuclear geometry, that may be taken as any irregular tetrahedron in the 3D space.

Note, however, that if the common geometry of the tetrahedra chosen shows some symmetry, then some simplifications are possible, for example, structures of molecules $M^{(2)}$ and $M^{(3)}$ may become equivalent, that can lead to a more concise energy relation.

That is, symmetry, in this case, indeed, provides simplification.

3 Some comments about the universal molecule aspects of potential energy hypersurface symmetry and energy relations connected to the reference cluster

If in a molecule all parameters are taken as continuous variables, one obtains the abstract "universal molecule model" that connects all real molecules, even seemingly unrelated molecules, to one another through impossible, non-physical models within a single mathematical framework [18–21]. Turning discrete variables into continuous ones amounts to "anti-quantization," and if these variables again take up one of the allowed (often integer) values, this amounts to "re-quantization." This anti-quantized and re-quantized "universal molecule model" provides new, valid relations on energy and other properties of real molecules, and all actual molecules may then be regarded as special cases of the "universal molecule."

In a formal sense, it is possible to define a *universal molecule*

$$M(N, k, r, \mathbf{z}, \mathbf{s}, \mathbf{w})$$

of N nuclei and k electrons, with nuclear configuration vector variable r, nuclear charge vector $\mathbf{z}$, electronic state label $\mathbf{s}$, and possible additional variables $\mathbf{w}$, where all these variables are allowed to take non-integer values, even if for some of them only integer values (and very limited values) may actually correspond to physically possible entities.

We have seen that for the case of nuclear charges, such a generalization provides rather quick and rigorous results. Although taking advantage of other such variables appears less straightforward, this general framework provides the tools for such investigations. One field that can benefit from such a model is using comparisons of various realizations of the universal molecule to the level of reference clusters [22, 23], where the potential energy surface, PES, of the reference clusters typically shows the highest symmetry when compared to molecules of equal total nuclear charge, as a consequence of permutational equivalences of atoms, being the highest possible for the reference clusters. On the other hand, as shown also by the diatomic example with N_2 being the reference cluster, the energy of the reference cluster is typically higher than the energy of the related other molecules with the same total nuclear charge.

That is, in this case, higher symmetry is associated with higher energy, a combination of properties that in other contexts often considered counter-intuitive.

Specifically, we are concerned with two symmetry problems along PES [22, 23]:

(a) the distribution of the three-dimensional, 3D, symmetries of molecular structures along PES
(b) the actual $(3N + 1)$D symmetry of the $(3N)$D PES itself, defined by the $3N$ laboratory-frame Cartesian coordinates of the N nuclei; such a PES is a $(3N)$D hypersurface embedded in a $(3N + 1)$D space, where one may formally regard energy as the "vertical coordinate."

It is often advantageous to use the $(3N - 6)$D reduced nuclear configuration space, a metric space M obtained as the quotient space of equivalence classes of (chemically equivalent) internal configurations related to one another by rigid translations and rigid rotations within the $(3N)$D Euclidean space of all, mass-weighted Cartesian coordinates of the nuclei. If the PES is defined over M, then it is a $(3N - 6)$D hypersurface embedded in a $(3N - 5)$D space, where, as before, one may formally regard energy as the "vertical coordinate."

In general, if the dimension of a Euclidean space is W, then all reflections in such high-dimensional spaces can be constructed by some series of reflections with reference to some $(W - 1)$D hyperplanes, and all rotations can be generated by a series of rotations according to some $(W - 2)$D rotation axes. It is advantageous to use for each of these reflections and rotations specific coordinate systems aligned with the reflection planes and rotation axes, in such a way that the origin falls on the reflection plane or rotation axis, and one coordinate axis is orthogonal to the $(W - 1)$D reflection hyperplane, and two coordinate axes are orthogonal to the $(W - 2)$D rotation axis. Then, reflection is accomplished by a sign change in all coordinate values along the coordinate axis orthogonal to the reflection hyperplane. Rotation by some angle α is accomplished by keeping all coordinates along the $(W - 2)$D rotation axis unchanged, and by the $\cos(\alpha)$, $\sin(\alpha)$ linear combination of the remaining two coordinate values for the new first such coordinate, and the $-\sin(\alpha)$, $\cos(\alpha)$ linear combinations of the remaining two coordinate values for the new second such coordinate. This is in exact analogy with the rotation along the z axis in 3D, where x and y take the roles of the two "remaining" coordinates, becoming $x\cos(\alpha) + y\sin(\alpha)$ for the new "first" coordinate value, and $-x\sin(\alpha) + y\cos(\alpha)$ for the new "second" coordinate value.

These very tools, higher-dimensional reflections and rotations are those which are gradually "degraded" from their symmetry element status as the reference cluster is

gradually replaced by molecular structures of fewer and fewer equivalences among their nuclear charges. To follow these changes, it is advantageous to use the 3*N*-dimensional configuration space (instead of the reduced nuclear configuration space *M* of $(3N - 6)$ dimensions), for the following reasons:

The case of (3*N*)D PES allows for such Euclidean representation; however, in the case of PES defined over *M*, no such representation is possible generally, and in fact one deals with not an Euclidean space but with a manifold with boundary, involving many, only locally valid coordinate systems. Therefore, in this context, it is advantageous to use for reference cluster studies the full, 3*N*-dimensional configurational space.

A contrast exists between two effects of increasing symmetry. If the symmetry of nuclear charges is maximal in *Z* space, as it happens for the reference cluster, then this typically implies the highest energy among all isoprotonic species within the same nuclear charge space *Z* for these clusters. Yet, if an increase in the actual 3D symmetry of the nuclear framework renders two, previously non-equivalent clusters equivalent, then the energy inequalities, such as those for the clusters produced by the metals atoms Re(75), Os(76), Ir(77), Pt(78), Au(79) of the examples above, become simpler, often implying tighter energy bounds.

An interesting problem arises concerning the manifestation of the gradual reductions in the 3*N*-dimensional symmetries of the reference cluster to actual molecule transformations as these are represented in the reduced internal configuration space of $(3N - 6)$ dimensions. In this lower-dimensional space, the recognition of such symmetries is less straightforward; however, the information is fully preserved in some different form. These relations will be the subject of a forthcoming study.

Acknowledgments This study has been supported by the Canada Research Chair (CRC) Program of Canada, the Scientific Modeling and Simulation Laboratory (SMSL), and the Memorial University of Newfoundland.

References

1. Thirring W (1975) Acta Phys Austriaca (Suppl) 14:631–635
2. Narnhofer H, Thirring W (1975) Acta Phys Austriaca 41:281–287
3. Lieb EH, Simon B (1978) J Phys B 11:L537–L542
4. Mezey PG (1981) Theor Chim Acta 59:321–332
5. Mezey PG (1981) Int J Quant Chem Symp 15:279–285
6. Mezey PG (1982) Mol Phys 47:121–126
7. Mezey PG (1982) Int J Quant Chem 22:101–114
8. Mezey PG (1982) Chem Phys Lett 87:277–279
9. Mezey PG (1983) Int J Quant Chem 24:523–526
10. Mezey PG (1984) Can J Chem 62:1356–1357
11. Mezey PG (1984) J Chem Phys 80:5055–5057
12. Mezey PG (1985) J Am Chem Soc 107:3100–3105
13. Mezey PG (1985) Surf Sci 156:597–604
14. Mezey PG (1986) Int J Quant Chem 29:85–99
15. Mezey PG (1986) Int J Quant Chem 29:333–343
16. Otto P, Ladik J, Mezey PG (1987) J Math Chem 1:85–96
17. Cassam-Chenaï P, Chiaramello J-M, Mezey PG (2008) J Math Chem 44:981–987
18. Mezey PG (2007) AIP Conf Proc 963:513–516
19. Mezey PG (2012) AIP Conf Proc 1504:725–728
20. Mezey PG (2015) J Phys Chem A 119:5305–5312
21. Mezey PG (2015) Topological tools for the study of families of reaction mechanisms: the fundamental groups of potential surfaces in the universal molecule context. In: Alikhani E, Chauvin R, Lepetit C, Silvi B (eds) Applications of topological methods in molecular chemistry. Springer, New York (in press)
22. Mezey PG (1987) Potential energy hypersurfaces. Elsevier, Amsterdam
23. Mezey PG (1989) Topology of molecular shape and chirality. In: Bertran J, Csizmadia IG (eds) New theoretical concepts for understanding organic reactions. Kluwer Academic, The Netherlands

Theor Chem Acc (2015) 134:86
DOI 10.1007/s00214-015-1682-y

REGULAR ARTICLE

Hermitian "chemical" Hamiltonian: an alternative ab initio method

I. Mayer[1]

Received: 21 April 2015 / Accepted: 6 June 2015 / Published online: 4 July 2015

Abstract Some previous results of the present author are combined in order to develop a Hermitian version of the "Chemical Hamiltonian Approach." In this framework the second quantized Born–Oppenheimer Hamiltonian is decomposed into one- and two-center components, if some finite basis corrections are omitted. (No changes are introduced into the one- and two-center integrals, while projective expansions are used for the three- and four-center ones, which become exact only in the limit of complete basis sets.) The total molecular energy calculated with this Hamiltonian can then presented as a sum of the intraatomic and diatomic energy terms which were introduced in our previous "chemical energy component analysis" scheme. The corresponding modified Hartree–Fock–Roothaan equations are also derived; they do not contain any three- and four-center integrals, while the non-empirical character of the theory is conserved. This scheme may be useful also as a "layer" in approaches like ONIOM.

Keywords Chemical Hamiltonian Approach · Alternative non-empirical SCF formalism · Second quantized Hamiltonian · Excluding three- and four-center integrals · Projective integral approximation

Published as part of the special collection of articles "Festschrift in honour of Péter R. Surjan."

Dedicated to the 60th birthday of Professor Péter R. Surján.

✉ I. Mayer
mayer@chemres.hu

[1] Research Centre for Natural Sciences, Hungarian Academy of Sciences, P.O.Box 286, Budapest 1519, Hungary

1 Introduction

Three decades ago the present author studied the apparent contradiction that one has one- and two-electron integrals up to four-center ones in the ab initio quantum chemical theory, while the empirical chemical facts indicate that the intramolecular interactions are basically of atomic and diatomic character [1]. In chemical practice, one needs not to assume the existence of any *primary* three- and four-atom effects in a molecule, while the presence of the three- and four-center integrals in the theory would indicate the opposite. The problem was approached by introducing a "projected" integral approximation scheme [1], permitting to present each three- and four-center integral as a sum of a leading "physical" term containing only one- and two-center integrals, and a finite basis correction to it (this integral approximation scheme has some resemblance with Ruedenberg classical proposition [2]). Combined with a special "mixed" second quantized formalism for non-orthogonal basis orbitals, this permitted to present the finite basis version of the Born–Oppenheimer Hamiltonian as a sum of atomic and diatomic "physical" terms and finite basis correction ones. An interesting theoretical property of these atomic Hamiltonians was that—despite the interatomic overlap of the basis functions—the antisymmetrized product of atomic full CI solutions was an eigenfunction of the respective sum of the atomic Hamiltonians, and the eigenvalues were the sums of the atomic full CI energies [1] (no analogous property could be proved, however, for the Hartree–Fock wave functions). The diatomic terms of the Hamiltonian have been also decomposed into terms of different physical nature, like electrostatic and overlap effects.

These properties motivated us to call this formalism as "Chemical Hamiltonian Approach" (CHA). The disadvantage of the formalism was the non-Hermiticity of the

"physical" terms [1], obviously causing complications in the practical applications. This non-Hermiticity originated from the asymmetric treatment of "bra"-s and "ket"-s constituting the different one- and two-electron integrals, as different functions in the integrands were analyzed by assuming that every operator acts "to right."

The intramolecular CHA formalism received no direct numerical applications. However, the application of the same philosophy to the BSSE problem of intermolecular interactions has been found rather useful [1, 3, 4]. An energy decomposition formalism has also been developed [1], in which the different energy components were defined as the expectation values of the corresponding "physical" terms of the Hamiltonian; the analysis of one of them (that of the diatomic electrostatic interactions in a point-charge approximation) had led to the definition of the bond order index [5–8], which has been widely applied in studying different chemical problems.

Later a somewhat different energy decomposition scheme—called "chemical energy component analysis" (CECA)—has been introduced [9, 10]. It differed from the scheme in [1] in two aspects. First all two-center integrals were conserved, including those that in [1] were considered as finite basis correction terms with respect to the intra-atomic Hamiltonians, and were omitted from the "physical terms." Second, the projective integral approximations were symmetrized with respect the "bra"-s and "ket"-s. Although for the energy decomposition this symmetrization probably would have a true significance only if one admitted the use of complex basis functions, it is the conceptual starting point for our present analysis, because it permits to build up a Hermitian version of the "chemical" Hamiltonian.

In the CECA scheme, the energy of a molecule calculated at the SCF level is expressed *approximately but to a good accuracy* as a sum of atomic and diatomic contributions, the computation of which requires the use of *one- and two-center integrals only* [9]. It seems important that the error of this approximation apparently has the character of a "white noise" and does not reflect any actual intramolecular effects of physical or chemical significance.

For the CECA scheme, several (more or less successful) improvements and refinements have been developed (see e.g., [11–14]); we are not going to discuss them here in any detail. All of them (including, of course, CECA itself) are *a posteriori* means of analysis, that is, they can be applied *after* a conventional ab initio SCF calculation has been performed, in order to elucidate the results of the latter. The aim of the present paper is to use the same integral approximation scheme in order to develop an approximate ab initio scheme of a priori calculations, in which one needs not to calculate any three- and four-center integrals. In this respect, the scheme could be put in parallel with the semiempirical quantum chemical methods. However, the projective integral approximations are improving with increasing basis sets; thus, one may expect that the proposed scheme will exhibit convergence to the conventional Hartree–Fock limit. (The proposed scheme may be useful also as a "layer" in schemes like ONIOM [15].)

2 Integral approximation

Let us first consider the three-center one-electron integral $\langle\chi_\mu^A|\frac{Z_C}{r_C}|\chi_\nu^B\rangle$, where A, B and C represent three *different* atoms. Here the superscripts A and B indicate that the basis orbitals χ_μ and χ_ν are centered on the atoms A and B, respectively. Thus the integral describes the interaction of the diatomic overlap population $\chi_\mu^{A*}(\mathbf{r})\chi_\nu^B(\mathbf{r})$ with the nucleus of atom C. This integral can also be written in the symmetrized form

$$\langle\chi_\mu^A|\frac{Z_C}{r_C}|\chi_\nu^B\rangle = \frac{1}{2}\left[\langle\chi_\mu^A|\frac{Z_C}{r_C}|\chi_\nu^B\rangle + \langle\chi_\nu^B|\frac{Z_C}{r_C}|\chi_\mu^A\rangle^*\right]. \quad (1)$$

(All the one- and two-electron integrals, if the opposite is not stated, include also summations over the spin variables). Considering the "bra" $\frac{Z_C}{r_C}|\chi_\nu^B\rangle$ in the first integral, one may pictorially consider it as describing the "scattering" of the electron occupying orbital χ_ν^B on the nucleus of atom C; it is a function that may be considered a diatomic entity related to the atoms B and C. By writing a resolution of identity in the form

$$1 \equiv \hat{P}_{BC} + (1 - \hat{P}_{BC}), \quad (2)$$

where $\hat{P}_{BC}$ is the projector on the subspace of orbitals centered on atoms B and C, this function can be written as a sum of two components: One which is in the subspace BC of the basis orbitals centered on atoms B and C, and another which is orthogonal to that subspace. The first component appears always when atoms B and C are at the given configuration with respect to each other, while the question whether the second plays any role in the molecular problem depends on the particular configuration of the other atoms of the molecule. That term is simply neglected in any calculations of the diatomic molecule BC.) As the basis set on atoms B and C improves, the term in the orthogonal complement becomes smaller and smaller; experience shows that for reasonable basis sets—but not for the minimal ones—one may neglect these terms without causing serious problems [9, 11].

According to the above discussion, we shall replace the function $\frac{Z_C}{r_C}|\chi_\nu^B\rangle$ in the first integral by its projection $\hat{P}_{BC}\frac{Z_C}{r_C}|\chi_\nu^B\rangle$, and analogously, the function $\frac{Z_C}{r_C}|\chi_\mu^A\rangle$ in the second integral by its projection $\hat{P}_{AC}\frac{Z_C}{r_C}|\chi_\mu^A\rangle$ on the subspace of the basis orbitals centered on atoms A and C:

$$\langle\chi_\mu^A|\frac{Z_C}{r_C}|\chi_\nu^B\rangle \Longrightarrow \frac{1}{2}\left[\langle\chi_\mu^A|\hat{P}_{BC}\frac{Z_C}{r_C}|\chi_\nu^B\rangle + \langle\chi_\nu^B|\hat{P}_{AC}\frac{Z_C}{r_C}|\chi_\mu^A\rangle^*\right]. \quad (3)$$

Here and further on we use the symbol $\Longrightarrow$ to indicate the replacements caused by the projective integral approximations of the type discussed. We recall in this connection, that in the case of an overlapping basis, the projection on the subspace of orbitals centered on some subunit X can be presented as

$$\hat{P}_X = \sum_{\kappa,\lambda\in X} |\chi_\kappa\rangle S^{-1}_{(X)\kappa\lambda}\langle\chi_\lambda|. \tag{4}$$

Here and further on we use the shorthand $S^{-1}_{(X)\kappa\lambda}$ for the elements of the *inverse* overlap matrix of the subunit X:

$$S^{-1}_{(X)\kappa\lambda} = (\mathbf{S}^{-1}_{(X)})_{\kappa\lambda}. \tag{5}$$

One should proceed analogously with the three- and four-center two-electron integrals. The two-electron function $\frac{1}{r_{12}}\chi^C_\kappa(1)\chi^D_\rho(2)$ can be considered as belonging primarily to the diatomic fragment CD where the basis orbitals are centered; accordingly, we introduce projectors on the CD subspace *for both electrons*. We shall again perform the symmetrization, thus we obtain the projective integral approximation for the two-electron integral

$$\begin{aligned}&\langle\chi^A_\gamma(1)\chi^B_\nu(2)|\frac{1}{r_{12}}|\chi^C_\kappa(1)\chi^D_\rho(2)\rangle\\ &\quad\Longrightarrow \frac{1}{2}\Big[\langle\chi^A_\gamma(1)\chi^B_\nu(2)|\hat{P}_{CD}(1)\hat{P}_{CD}(2)\frac{1}{r_{12}}\chi^C_\kappa(1)\chi^D_\rho(2)\rangle\\ &\qquad+\langle\chi^C_\kappa(1)\chi^D_\rho(2)|\hat{P}_{AB}(1)\hat{P}_{AB}(2)\frac{1}{r_{12}}\chi^A_\gamma(1)\chi^B_\nu(2)\rangle^*\Big].\end{aligned} \tag{6}$$

It is assumed that at least three of the four atoms A, B, C and D are different. (If it happens that for a three-center integral $A = B$ or $C = D$, then the projector $\hat{P}_{AB}$ or $\hat{P}_{CD}$ obviously reduces to $\hat{P}_A$ or $\hat{P}_C$, respectively.)

We introduce the matrices $\mathbf{A}^X$ closely related to the projectors, with the elements

$$A^X_{\mu\nu} = \sum_{\rho\in A} S_{\mu\rho}S^{-1}_{(X)\rho\nu}. \tag{7}$$

Note that the intra-fragment block of matrix $\mathbf{A}^X$ (i.e., that corresponding to both $\mu,\nu\in X$) is a unit matrix, according to the definition.

Utilizing the definition (7) when substituting the expression (4) of the projection operators in the integral approximation formulae (3) and (6), the latter become

$$\begin{aligned}\langle\chi^A_\mu|\frac{Z_C}{r_C}|\chi^B_\nu\rangle &\Longrightarrow \frac{1}{2}\left[\sum_{\rho\in BC}A^{BC}_{\mu\rho}\langle\chi_\rho|\frac{Z_C}{r_C}|\chi_\nu\rangle + \sum_{\rho\in AC}\left(A^{AC}_{\nu\rho}\langle\chi_\rho|\frac{Z_C}{r_C}|\chi_\mu\rangle\right)^*\right]\\ &= \frac{1}{2}\left[\sum_{\rho\in BC}A^{BC}_{\mu\rho}\langle\rho|\frac{Z_C}{r_C}|\nu\rangle + \sum_{\rho\in AC}\langle\mu|\frac{Z_C}{r_C}|\rho\rangle A^{AC\dagger}_{\rho\nu}\right],\end{aligned} \tag{8}$$

and

$$\begin{aligned}&\langle\chi^A_\gamma(1)\chi^B_\nu(2)|\frac{1}{r_{12}}|\chi^C_\kappa(1)\chi^D_\rho(2)\rangle\\ &\quad\Longrightarrow \frac{1}{2}\left[\sum_{\lambda,\tau\in CD}A^{CD}_{\gamma\lambda}A^{CD}_{\nu\tau}\langle\chi_\lambda(1)\chi_\tau(2)|\frac{1}{r_{12}}|\chi_\kappa(1)\chi_\rho(2)\rangle\right.\\ &\qquad\left.+\left(\sum_{\lambda,\tau\in AB}A^{AB}_{\kappa\lambda}A^{AB}_{\rho\tau}\langle\chi_\lambda(1)\chi_\tau(2)|\frac{1}{r_{12}}|\chi_\gamma(1)\chi_\nu(2)\rangle\right)^*\right]\\ &\quad= \frac{1}{2}\left[\sum_{\lambda,\tau\in CD}A^{CD}_{\gamma\lambda}A^{CD}_{\nu\tau}[\lambda\tau|\kappa\rho] + \sum_{\lambda,\tau\in AB}[\gamma\nu|\lambda\tau]A^{AB\dagger}_{\lambda\kappa}A^{AB\dagger}_{\tau\rho}\right].\end{aligned} \tag{9}$$

respectively. Here, and further on, † denotes the adjoint, and we have introduced the short-hand notations for the one- and two-electron integrals

$$\begin{aligned}&\langle\mu|\frac{Z_C}{r_C}|\nu\rangle = \langle\chi_\mu|\frac{Z_C}{r_C}|\chi_\nu\rangle;\\ &[\mu\nu|\rho\tau] = \langle\chi_\mu(1)\chi_\nu(2)|\frac{1}{r_{12}}|\chi_\rho(1)\chi_\tau(2)\rangle,\end{aligned} \tag{10}$$

which, in general, include also summations over the spin variables.

The integral approximations (8) and (9) are the same as were used in the energy decomposition scheme [9]; we hope that here we succeeded to present them in a more compact and transparent manner.

The accuracy of the integral approximations introduced may be guessed on the basis of comparing the exact SCF energies and the sum of the CECA one- and two-center energy components of a given molecule. In Ref. [9] such a comparison was done for ethane molecule, by using a wide variety of basis sets from 6-31G to 6-311++G** and cc-pVDZ, and it was found that the total energy of about −79.2 Hartree-s of this molecule in all cases was approximated within 15 *milli*Hartree-s, and the deviation was less than 20 mH even for 4-31G. Considering the refined version of the CECA scheme [11] in which these remaining three- and four-electron effects were distributed among the one- and two-center components by using a special scheme, one could conclude that this error is scattered in a random fashion among the numerous energy components, so it does not carry any physical or chemical significance

(this conclusion was drawn not only for ethane molecule, but for every system considered as yet).

3 The LCAO Hamiltonian

In the followings we shall use, besides the non-orthogonal set of original basis orbitals $\{\chi_\mu\}$, also the respective *Löwdin-orthogonalized* set $\{\psi_\nu\}$ of orbitals:

$$\psi_\nu = \sum_\mu S^{-\frac{1}{2}}_{\mu\nu}\chi_\mu, \tag{11}$$

where $S^{-\frac{1}{2}}_{\mu\nu}$ is an element of the $-\frac{1}{2}$th power of the overlap matrix, as well as the biorthogonal set $\{\varphi_\rho\}$:

$$\varphi_\rho = \sum_\mu S^{-1}_{\mu\rho}\chi_\mu. \tag{12}$$

All the three sets span the same subspace of the one-electron functions.

We introduce creation and annihilation operators corresponding to each set of these orbitals. In order to distinguish to what type of orbitals the given creation or annihilation orbital is pertinent, we shall use Longuet-Higgins' [16] notations $\hat\psi^+_\nu$, $\hat\chi^+_\mu$ and $\hat\varphi^+_\rho$ for the creation operators and $\hat\psi^-_\nu$, $\hat\chi^-_\mu$ and $\hat\varphi^-_\rho$ for the annihilation ones. The annihilation operators are defined as the adjoints of the respective creation operators:

$$\hat\psi^-_\nu = (\hat\psi^+_\nu)^\dagger \quad \hat\chi^-_\mu = (\hat\chi^+_\mu)^\dagger \quad \hat\varphi^-_\rho = (\hat\varphi^+_\rho)^\dagger. \tag{13}$$

The creation operators transform in the same manner as the respective orbitals do, i.e., according to Eqs. (11) and (12). However, standard Fermion anticommutation rules hold only for the creation and annihilation operators defined for the orthonormalized set $\{\psi_\nu\}$

$$\{\hat\psi^+_\nu;\hat\psi^-_\mu\} = \hat\psi^+_\nu\hat\psi^-_\mu + \hat\psi^+_\mu\hat\psi^-_\nu = \delta_{\mu\nu}, \tag{14}$$

while

$$\{\hat\chi^+_\nu;\hat\chi^-_\mu\} = \hat\chi^+_\nu\hat\chi^-_\mu + \hat\chi^+_\mu\hat\chi^-_\nu = S_{\mu\nu}, \tag{15}$$

and

$$\{\hat\varphi^+_\nu;\hat\varphi^-_\mu\} = \hat\varphi^+_\nu\hat\varphi^-_\mu + \hat\varphi^+_\mu\hat\varphi^-_\nu = S^{-1}_{\mu\nu}, \tag{16}$$

respectively. Owing to the presence of the (inverse) overlap matrix elements in the anticommutators (15) and (16), Fermion anticommutation rules hold for the *mixed* anticommutators

$$\{\hat\chi^+_\nu;\hat\varphi^-_\mu\} = \delta_{\mu\nu}. \tag{17}$$

and

$$\{\hat\varphi^+_\nu;\hat\chi^-_\mu\} = \delta_{\mu\nu}. \tag{18}$$

This means that when acting *to right* on a string of creation operators $\hat\chi^+_\mu$ in a "ket", operator $\hat\varphi^-_\mu$ behaves as a conventional annihilation operator does, and analogously, when acting *to left* on a string of annihilation operators $\hat\chi^-_\mu = (\hat\chi^+_\mu)^\dagger$ in a "bra", operator $\hat\varphi^+_\mu$ behaves as a conventional creation operator.

The LCAO version of the Born–Oppenheimer Hamiltonian has a standard form in terms of the creation and annihilation operators referring to the Löwdin-orthogonalized basis [16, 17]:

$$\hat H = \sum_{A<B}\frac{Z_A Z_B}{R_{AB}} + \sum_{\mu,\nu} h^\lambda_{\mu\nu}\hat\psi^+_\mu\hat\psi^-_\nu + \frac{1}{2}\sum_{\mu,\nu,\rho,\tau}[\psi_\mu\psi_\nu|\psi_\rho\psi_\tau]\,\hat\psi^+_\mu\hat\psi^+_\nu\hat\psi^-_\tau\hat\psi^-_\rho. \tag{19}$$

Here the first sum describes the internuclear repulsion, $h^\lambda_{\mu\nu} = \langle\psi_\mu|\hat h|\psi_\nu\rangle$ is the matrix element of the one-electron Hamiltonian

$$\hat h = -\frac{1}{2}\Delta - \sum_A\frac{Z_A}{r_A}, \tag{20}$$

in the Löwdin-orthogonalized basis, and $[\psi_\mu\psi_\nu|\psi_\rho\psi_\tau]$ is a two-electron integral in that basis and the [12|12] convention.

Using the transformations (11), (12) connecting the different sets of the orbitals (and thus also the respective creation and annihilation operators,) one can transform the Hamiltonian (19) into several equivalent forms. We shall present here two of them.

Using "biorthogonal" operators

In one version we collect pairs of matrices $\mathbf{S}^{-\frac{1}{2}}$ into matrices $\mathbf{S}^{-1}$, and express the Hamiltonian in terms of the one- and two-electron integrals over the original *overlapping* basis orbitals and of the "biorthogonal" creation and annihilation operators $\hat\varphi^+_\mu$, $\hat\varphi^-_\nu$:

$$\hat H = \sum_{A<B}\frac{Z_A Z_B}{R_{AB}} + \sum_{\mu,\nu} h_{\mu\nu}\hat\varphi^+_\mu\hat\varphi^-_\nu + \frac{1}{2}\sum_{\mu,\nu,\kappa,\rho}[\mu\nu|\kappa\rho]\hat\varphi^+_\mu\hat\varphi^+_\nu\hat\varphi^-_\rho\hat\varphi^-_\kappa. \tag{21}$$

where $h_{\mu\nu}$ and $[\mu\nu|\kappa\rho]$ are the one- and two-electron integrals calculated for the overlapping set of basis orbitals $\{\chi_\mu\}$.

As it is known [17], the expectation value E of operator $\hat H$ can be expressed through the matrix representations

P and **Γ** of the first- and second-order density matrices, respectively:

$$E = \langle \hat{H} \rangle = \sum_{A<B} \frac{Z_A Z_B}{R_{AB}} + \sum_{\mu,\nu} h_{\mu\nu} P_{\nu\mu} + \frac{1}{2} \sum_{\mu,\nu,\kappa,\rho} [\mu\nu|\kappa\rho]\, \Gamma_{\kappa\rho\mu\nu}. \tag{22}$$

Comparison with Eq. (21) indicates that in *overlapping basis* the elements of the spin-dependent first- and second-order density matrix can be obtained as expectation values of operator strings constructed from "biorthogonal" creation and annihilation operators:

$$\left\langle \hat{\varphi}_\mu^+ \hat{\varphi}_\nu^- \right\rangle = P_{\nu\mu}; \tag{23}$$

and

$$\left\langle \hat{\varphi}_\mu^+ \hat{\varphi}_\nu^+ \hat{\varphi}_\rho^- \hat{\varphi}_\kappa^- \right\rangle = \Gamma_{\kappa\rho\mu\nu}, \tag{24}$$

calculated for the actual wave function (note that $\Gamma_{\kappa\rho\mu\nu} = \Gamma_{\rho\kappa\nu\mu} = -\Gamma_{\rho\kappa\mu\nu}$ etc.) As it is known, in the case of *single-determinant* (SD) wave functions the second-order density matrix can be expressed through the first-order one, so one has

$$\left\langle \hat{\varphi}_\mu^+ \hat{\varphi}_\nu^+ \hat{\varphi}_\rho^- \hat{\varphi}_\kappa^- \right\rangle_{SD} = P_{\kappa\mu} P_{\rho\nu} - P_{\kappa\nu} P_{\rho\mu}. \tag{25}$$

Using "mixed" set of operators

In this version, first presented in [1], we collect the matrices $\mathbf{S}^{-1}$ necessary to form operators $\hat{\varphi}_\mu^-$, but let the other matrices $\mathbf{S}^{-1}$ to appear explicitly (this increases the number of summation indices to be explicitly written out). Thus we obtain an expression of $\hat{H}$ that contains individual terms that are not Hermitian—although the overall $\hat{H}$, of course, is:

$$\hat{H} = \sum_{A<B} \frac{Z_A Z_B}{R_{AB}} + \sum_{\mu,\nu,\rho} S^{-1}_{\rho\mu} h_{\mu\nu} \hat{\chi}_\rho^+ \hat{\varphi}_\nu^- + \frac{1}{2} \sum_{\mu,\nu,\rho,\tau,\lambda,\sigma} S^{-1}_{\lambda\mu} S^{-1}_{\sigma\nu} [\mu\nu|\rho\tau]\, \hat{\chi}_\lambda^+ \hat{\chi}_\sigma^+ \hat{\varphi}_\tau^- \hat{\varphi}_\rho^- \tag{26}$$

The advantage of this form is that it permits to work only with quantities related to the original, non-orthogonal basis orbitals; we recall in that respect that operators $\hat{\varphi}_\mu^-$ can be considered as the "true" annihilation operators, in light of the anticommutation rule (17)—they *act* (to right) in the non-orthogonal framework exactly in the manner as usual annihilation operators do in the orthogonal case. This approach has been utilized when CHA has been applied to the BSSE problem of intermolecular interactions [1, 3, 4].

As for a Hermitian Hamiltonian $\hat{H}$ one obviously has $\hat{H} \equiv \frac{1}{2}(\hat{H} + \hat{H}^\dagger)$, one can symmetrize each term of (26), and get:

$$\hat{H} = \sum_{A<B} \frac{Z_A Z_B}{R_{AB}} + \frac{1}{2} \sum_{\mu,\nu,\rho} \left(S^{-1}_{\rho\mu} h_{\mu\nu} \hat{\chi}_\rho^+ \hat{\varphi}_\nu^- + h_{\nu\mu} S^{-1}_{\mu\rho} \hat{\varphi}_\nu^+ \hat{\chi}_\rho^- \right) + \frac{1}{4} \sum_{\mu,\nu,\rho,\tau,\lambda,\sigma} \Big(S^{-1}_{\lambda\mu} S^{-1}_{\sigma\nu} [\mu\nu|\rho\tau]\, \hat{\chi}_\lambda^+ \hat{\chi}_\sigma^+ \hat{\varphi}_\tau^- \hat{\varphi}_\rho^- + [\rho\tau|\mu\nu] S^{-1}_{\mu\lambda} S^{-1}_{\nu\sigma} \varphi_\rho^+ \hat{\varphi}_\tau^+ \hat{\chi}_\sigma^- \hat{\chi}_\lambda^- \Big) \tag{27}$$

This possibility was not considered previously. To save space, we shall not develop it in any detail either here, only note that the respective formulae of this type can be obtained from those discussed in the forthcoming sections by substituting for every creation operator $\hat{\varphi}_\mu^+$ its explicit expansion

$$\hat{\varphi}_\rho^+ = \sum_\mu S^{-1}_{\mu\rho} \hat{\chi}_\mu^+. \tag{28}$$

and, if necessary, symmetrize like it was done for Eq. (27).

4 The "chemical" Hamiltonian

The different forms of the "chemical Hamiltonian" are obtained if one introduces into formulae (21), (26) and (27), the integral approximations discussed previously.

When introducing the projective integral approximations into these equations, we shall group the terms according to the centers involved. The one-electron matrix elements $h_{\mu\nu}$ do not contain any three-center integrals if $\mu, \nu \in A$, i.e., both basis orbitals χ_μ and χ_ν are centered on the same atom A. In this case, no approximation is needed. If, however, $\mu \in A$, $\nu \in B$ $(A \neq B)$, then $h_{\mu\nu}$ will contain both two-center integrals and three-center ones—and the latter should be approximated according to Eq. (8). For treating the genuine two-center contributions in this case, it is worth introducing the one-electron Hamiltonian $\hat{h}^{AB}$ corresponding to the diatomic fragment AB:

$$\hat{h}^{AB} = -\frac{1}{2}\Delta - \frac{Z_A}{r_A} - \frac{Z_B}{r_B}. \tag{29}$$

The two-electron integrals need be grouped not only according to the number of centers involved, but also depending on whether the two orbitals in the "ket" part of the integral in (21) are centered on the same or on different atoms.

Performing the grouping of the terms, one obtains the approximation to the Hamiltonian (21) as

$$
\begin{aligned}
\hat{H} \Longrightarrow & \sum_{A} \sum_{\mu,\nu\in A} h_{\mu\nu}\hat{\varphi}_{\mu}^{+}\hat{\varphi}_{\nu}^{-} + \sum_{\substack{A,B\\A\neq B}} \sum_{\substack{\mu\in A\\ \nu\in B}} \Bigg[h_{\mu\nu}^{AB} - \frac{1}{2} \sum_{\substack{C\\ C\neq A,B}} \left(\sum_{\rho\in BC} A_{\mu\rho}^{BC} \langle\rho|\frac{Z_C}{r_C}|\nu\rangle + \sum_{\rho\in AC} \langle\mu|\frac{Z_C}{r_C}|\rho\rangle A_{\rho\nu}^{AC\dagger} \right) \Bigg] \hat{\varphi}_{\mu}^{+}\hat{\varphi}_{\nu}^{-} \\
& + \frac{1}{2}\sum_{A} \sum_{\mu,\nu,\kappa,\rho\in A} [\mu\nu|\kappa\rho]\, \hat{\varphi}_{\mu}^{+}\hat{\varphi}_{\nu}^{+}\hat{\varphi}_{\rho}^{-}\hat{\varphi}_{\kappa}^{-} + \frac{1}{4}\sum_{\substack{A,B\\A\neq B}} \Bigg[\sum_{\kappa,\rho\in A} \sum_{\substack{\mu,\nu\in AB\\ (\mu\notin A)\vee(\nu\notin A)}} \left([\mu\nu|\kappa\rho]\, \hat{\varphi}_{\mu}^{+}\hat{\varphi}_{\nu}^{+}\hat{\varphi}_{\rho}^{-}\hat{\varphi}_{\kappa}^{-} + [\rho\kappa|\nu\mu]\, \hat{\varphi}_{\kappa}^{+}\hat{\varphi}_{\rho}^{+}\hat{\varphi}_{\nu}^{-}\hat{\varphi}_{\mu}^{-} \right) \\
& + \sum_{\substack{\kappa\in A\\ \rho\in B}} \sum_{\mu,\nu\in AB} \left([\mu\nu|\kappa\rho]\, \hat{\varphi}_{\mu}^{+}\hat{\varphi}_{\nu}^{+}\hat{\varphi}_{\rho}^{-}\hat{\varphi}_{\kappa}^{-} + [\rho\kappa|\nu\mu]\, \hat{\varphi}_{\kappa}^{+}\hat{\varphi}_{\rho}^{+}\hat{\varphi}_{\nu}^{-}\hat{\varphi}_{\mu}^{-} \right) \\
& + \sum_{\kappa,\rho,\tau,\eta\in A} \sum_{\mu\in B} \sum_{\substack{\nu\\ (\nu\notin AB)}} \left(A_{\mu\tau}^{A} A_{\nu\eta}^{A} [\tau\eta|\kappa\rho] \hat{\varphi}_{\mu}^{+}\hat{\varphi}_{\nu}^{+}\hat{\varphi}_{\rho}^{-}\hat{\varphi}_{\kappa}^{-} + [\rho\kappa|\eta\tau] A_{\eta\nu}^{A\dagger} A_{\tau\mu}^{A\dagger} \hat{\varphi}_{\kappa}^{+}\hat{\varphi}_{\rho}^{+}\hat{\varphi}_{\nu}^{-}\hat{\varphi}_{\mu}^{-} \right) \\
& + \sum_{\substack{\kappa\in A\\ \rho\in B}} \sum_{\tau,\eta\in AB} \sum_{\substack{\mu,\nu\\ (\mu\notin AB)\vee(\nu\notin AB)}} \left(A_{\mu\tau}^{AB} A_{\nu\eta}^{AB} [\tau\eta|\kappa\rho] \hat{\varphi}_{\mu}^{+}\hat{\varphi}_{\nu}^{+}\hat{\varphi}_{\rho}^{-}\hat{\varphi}_{\kappa}^{-} + [\rho\kappa|\eta\tau] A_{\eta\nu}^{AB\dagger} A_{\tau\mu}^{AB\dagger} \hat{\varphi}_{\kappa}^{+}\hat{\varphi}_{\rho}^{+}\hat{\varphi}_{\nu}^{-}\hat{\varphi}_{\mu}^{-} \right) \Bigg]
\end{aligned}
\tag{30}
$$

This is a Hermitian Hamiltonian that does not contain explicitly three- and four-center integrals any more. It requires some further regrouping in order to present it as a sum of terms that can be assigned to the individual atoms and pairs of atoms. For that reason, we introduce the atomic one-electron Hamiltonian $\hat{h}^A$

$$
\hat{h}^A = -\frac{1}{2}\Delta - \frac{Z_A}{r_A}. \tag{31}
$$

and perform projections of all relevant quantities to atomic subspaces in order to separate out effective atomic Hamiltonians. However, the error of projecting two-center quantities on the one-center ones is not neglected but is assigned to the diatomic terms of the Hamiltonian. In this manner we get

$$
\hat{H} \Longrightarrow \sum_{A} \hat{H}_A + \sum_{A<B} \hat{H}_{AB}, \tag{32}
$$

where

$$
\begin{aligned}
\hat{H}_A = & \frac{1}{2} \sum_{\nu,\tau\in A} \sum_{\mu} \left(A_{\mu\tau}^{A} h_{\tau\nu}^{A} \hat{\varphi}_{\mu}^{+}\hat{\varphi}_{\nu}^{-} + h_{\nu\tau}^{A} A_{\tau\mu}^{A\dagger} \hat{\varphi}_{\nu}^{+}\hat{\varphi}_{\mu}^{-} \right) \\
& + \frac{1}{4} \sum_{\eta,\kappa,\tau,\rho\in A} \sum_{\mu,\nu} \left(A_{\mu\tau}^{A} A_{\nu\eta}^{A} [\tau\eta|\kappa\rho] \hat{\varphi}_{\mu}^{+}\hat{\varphi}_{\nu}^{+}\hat{\varphi}_{\rho}^{-}\hat{\varphi}_{\kappa}^{-} \right. \\
& \left. + [\kappa\rho|\tau\eta] A_{\tau\mu}^{A\dagger} A_{\eta\nu}^{A\dagger} \hat{\varphi}_{\kappa}^{+}\hat{\varphi}_{\rho}^{+}\hat{\varphi}_{\nu}^{-}\hat{\varphi}_{\mu}^{-} \right)
\end{aligned}
\tag{33}
$$

and

$$
\begin{aligned}
\hat{H}_{AB} = & \frac{Z_A Z_B}{R_{AB}} - \frac{1}{2} \sum_{\tau\in AB} \sum_{\nu} \Bigg[\sum_{\mu\in A} \left(A_{\nu\tau}^{AB} \langle\tau|\frac{Z_B}{r_B}|\mu\rangle \hat{\varphi}_{\nu}^{+}\hat{\varphi}_{\mu}^{-} + \langle\mu|\frac{Z_B}{r_B}|\tau\rangle A_{\tau\nu}^{AB\dagger} \hat{\varphi}_{\mu}^{+}\hat{\varphi}_{\nu}^{-} \right) + \sum_{\mu\in B} \left(A_{\nu\tau}^{AB} \langle\tau|\frac{Z_A}{r_A}|\mu\rangle \hat{\varphi}_{\nu}^{+}\hat{\varphi}_{\mu}^{-} + \langle\mu|\frac{Z_A}{r_A}|\tau\rangle A_{\tau\nu}^{AB\dagger} \hat{\varphi}_{\mu}^{+}\hat{\varphi}_{\nu}^{-} \right) \Bigg] \\
& + \frac{1}{2} \sum_{\substack{\kappa\in A\\ \rho\in B}} \sum_{\eta,\tau\in AB} \sum_{\mu,\nu} \left(A_{\mu\tau}^{AB} A_{\nu\eta}^{AB} [\tau\eta|\kappa\rho] \hat{\varphi}_{\mu}^{+}\hat{\varphi}_{\nu}^{+}\hat{\varphi}_{\rho}^{-}\hat{\varphi}_{\kappa}^{-} + [\kappa\rho|\tau\eta] A_{\tau\mu}^{AB\dagger} A_{\eta\nu}^{AB\dagger} \hat{\varphi}_{\kappa}^{+}\hat{\varphi}_{\rho}^{+}\hat{\varphi}_{\nu}^{-}\hat{\varphi}_{\mu}^{-} \right) \\
& + \frac{1}{2} \sum_{\substack{\nu\in A\\ \mu\in B}} \left[\left(h_{\mu\nu}^{A} - \sum_{\tau\in A} A_{\mu\tau}^{A} h_{\tau\nu}^{A} + h_{\mu\nu}^{B} - \sum_{\tau\in B} h_{\mu\tau}^{B} A_{\tau\nu}^{B\dagger} \right) \hat{\varphi}_{\mu}^{+}\hat{\varphi}_{\nu}^{-} + \left(h_{\nu\mu}^{A} - \sum_{\tau\in A} h_{\nu\tau}^{A} A_{\tau\mu}^{A\dagger} + h_{\nu\mu}^{B} - \sum_{\tau\in B} A_{\nu\tau}^{B} h_{\tau\mu}^{B} \right) \hat{\varphi}_{\nu}^{+}\hat{\varphi}_{\mu}^{-} \right] \\
& + \frac{1}{2} \Bigg\{ \sum_{\kappa,\rho\in A} \sum_{\substack{\mu,\nu\in AB\\ (\mu\notin A)\vee(\nu\notin A)}} \left[\left([\mu\nu|\kappa\rho] - \sum_{\eta,\tau\in A} A_{\mu\tau}^{A} A_{\nu\eta}^{A} [\tau\eta|\kappa\rho] \right) \hat{\varphi}_{\mu}^{+}\hat{\varphi}_{\nu}^{+}\hat{\varphi}_{\rho}^{-}\hat{\varphi}_{\kappa}^{-} + \left([\kappa\rho|\mu\nu] - \sum_{\eta,\tau\in A} [\kappa\rho|\tau\eta] A_{\tau\mu}^{A\dagger} A_{\eta\nu}^{A\dagger} \right) \hat{\varphi}_{\kappa}^{+}\hat{\varphi}_{\rho}^{+}\hat{\varphi}_{\nu}^{-}\hat{\varphi}_{\mu}^{-} \right] \\
& + \sum_{\kappa,\rho\in B} \sum_{\substack{\mu,\nu\in AB\\ (\mu\notin B)\vee(\nu\notin B)}} \left[\left([\mu\nu|\kappa\rho] - \sum_{\eta,\tau\in B} A_{\mu\tau}^{B} A_{\nu\eta}^{B} [\tau\eta|\kappa\rho] \right) \hat{\varphi}_{\mu}^{+}\hat{\varphi}_{\nu}^{+}\hat{\varphi}_{\rho}^{-}\hat{\varphi}_{\kappa}^{-} + \left([\kappa\rho|\mu\nu] - \sum_{\eta,\tau\in B} [\kappa\rho|\tau\eta] A_{\tau\mu}^{B\dagger} A_{\eta\nu}^{B\dagger} \right) \hat{\varphi}_{\kappa}^{+}\hat{\varphi}_{\rho}^{+}\hat{\varphi}_{\nu}^{-}\hat{\varphi}_{\mu}^{-} \right] \Bigg\}
\end{aligned}
\tag{34}
$$

In this presentation, the monoatomic terms of the Hamiltonian contain only one-center integrals and the diatomic terms contain one- and two-center ones. While the first few terms in Eq. (34) describe direct diatomic interactions (electron-nuclear and electron-electron), most of the terms contain differences between a two-center integral related to *intra*atomic interactions and its approximation by one-center integrals and projection-related matrices $\mathbf{A}^X$, like the term

$$h^A_{\mu\nu} - \sum_{\tau\in A} A^A_{\mu\tau} h^A_{\tau\nu}. \tag{35}$$

These terms account for the effects of the basis extension from the atomic description to the diatomic fragments. Their role should diminish as the basis set increases, and in Ref. [1] terms of this type were assigned to the finite basis correction ones. Here they are conserved as to provide that the diatomics (diatomic fragments) are treated without any approximations.

Contrary to the integrals, a part of the creation and annihilation operators run over the whole basis, so there occur operator strings involving three and four centers. When the energy is calculated as the expectation value of the Hamiltonian, the expectation values of the operator strings give the density matrix elements according to Eqs. (23)–(25). Combined with the elements of the matrices $\mathbf{A}^X$, in the single-determinant case they lead to the *projected density matrices* [9] $\mathbf{B}^X$ and $\mathbf{C}^{\sigma X}$, $\sigma = \alpha$ or β:

$$B^X_{\mu\nu} = \sum_\gamma D_{\mu\gamma} A^X_{\gamma\nu}; \quad C^{\sigma X}_{\mu\nu} = \sum_\gamma P^\sigma_{\mu\gamma} A^X_{\gamma\nu} \quad (\nu \in X), \tag{36}$$

which implicitly account for the three- and four-center effects—without the need to deal with them explicitly. In Eq. (36)

$$\mathbf{D} = \mathbf{P}^\alpha + \mathbf{P}^\beta, \tag{37}$$

is the usual spinless density matrix, while $\mathbf{P}^\sigma$ is the density matrix for spin σ ($\sigma = \alpha$ or β). The expectation values of the operators $\hat{H}_A$ and $\hat{H}_{AB}$ are equal to the energy components $\hat{E}_A$ and $\hat{E}_{AB}$, respectively, quoted in [9]; we shall not display them here explicitly. (We note, however, that a further decomposition of these energy components into terms of different physical origin has also been accomplished in [18].)

We shall mention that using the "mixed" second quantized formalism of Ref. [1], already mentioned, it is possible to present the "chemical" Hamiltonian (32)–(34) in a form in which each term of the Hamiltonian contains only creation and annihilation operators assigned to the corresponding atom or pair of atoms. To save place, we shall illustrate that only by considering the first term of Eq. (33)—all the other terms can be treated analogously. The first term in question is

$$\sum_{\nu,\tau\in A} \sum_\mu A^A_{\mu\tau} h^A_{\tau\nu} \hat{\varphi}^+_\mu \hat{\varphi}^-_\nu. \tag{38}$$

We substitute the explicit expansions $\hat{\varphi}^+_\mu = \sum_\rho S^{-1}_{\rho\mu} \hat{\chi}^+_\rho$, and $A^A_{\mu\tau} = \sum_{\lambda\in A} S_{\mu\lambda} S^{-1}_{(A)\lambda\tau}$, and get

$$\begin{aligned}\sum_{\nu,\tau\in A} \sum_\mu A^A_{\mu\tau} h^A_{\tau\nu} \hat{\varphi}^+_\mu \hat{\varphi}^-_\nu &= \sum_{\lambda,\nu,\tau\in A} \sum_{\mu,\rho} S_{\mu\lambda} S^{-1}_{(A)\lambda\tau} h^A_{\tau\nu} S^{-1}_{\rho\mu} \hat{\chi}^+_\rho \hat{\varphi}^-_\nu \\ &= \sum_{\lambda,\nu,\tau\in A} \sum_\rho \delta_{\rho\lambda} S^{-1}_{(A)\lambda\tau} h^A_{\tau\nu} \hat{\chi}^+_\rho \hat{\varphi}^-_\nu \\ &= \sum_{\lambda,\nu,\tau\in A} S^{-1}_{(A)\lambda\tau} h^A_{\tau\nu} \hat{\chi}^+_\lambda \hat{\varphi}^-_\nu. \end{aligned} \tag{39}$$

When calculating expectation values, the three- and four-center effects will again be accounted for through the "projected density matrices" Eq. (36), owing to the fact that for the expectation values of the "mixed" pairs of creation and annihilation operators one has (in the single-determinant case) [1, 6]

$$\left\langle \hat{\chi}^+_\mu \hat{\varphi}^-_\nu \right\rangle = (\mathbf{PS})_{\nu\mu} = \sum_\tau P_{\nu\tau} S_{\tau\mu}, \tag{40}$$

and

$$\left\langle \hat{\chi}^+_\mu \hat{\chi}^+_\nu \hat{\varphi}^-_\varrho \hat{\varphi}^-_\kappa \right\rangle_{SD} = (\mathbf{PS})_{\kappa\mu} (\mathbf{PS})_{\varrho\nu} - (\mathbf{PS})_{\kappa\nu} (\mathbf{PS})_{\varrho\mu}. \tag{41}$$

The overlap matrix elements appearing in these expressions, combined with the elements of matrices $\mathbf{S}^{-1}_{(X)}$ in the terms like (39) give elements of matrices $\mathbf{A}^X$, occurring in the definitions (36).

Equation (33) contains also the adjoint of the term considered in Eq. (38). After the transformations analogous to those in Eq. (39), it will contain the subscripts of the matrices interchanged (complex conjugation) and the operator string $\hat{\chi}^+_\lambda \hat{\varphi}^-_\nu$ replaced by $\hat{\varphi}^+_\nu \hat{\chi}^-_\lambda$; its expectation value will be the complex conjugate of that for the term (38).

Based on these consideration, it is easy to see that the atomic Hamiltonians Eq. (33) can be obtained by Hermitizing the non-Hermitian atomic Hamiltonians $\hat{H}'_A$ defined in Ref. [1]:

$$\hat{H}_A = \frac{1}{2}\left(\hat{H}'_A + \hat{H}'^\dagger_A\right). \tag{42}$$

As a consequence of this Hermitization, the antisymmetrized products of the full CI atomic solutions is not an eigenfunction of the sum of atomic operators $\hat{H}_A$, as was the case for the sum of non-Hermitian operators $\hat{H}'_A$. However, considering $\hat{H}'_A$ acting to right and $\hat{H}'^\dagger_A$ acting to left, one can easily see that the *expectation value* of that operator sum calculated with the antisymmetrized product of the atomic full CI solutions will be equal to the sum of atomic full CI energies.

The possibility to write down an (even if approximate) Hermitian Hamiltonian representing the sum of monoatomic and diatomic terms has a significant conceptual importance, in particular because the expectation values of these terms of the Hamiltonian reproduce the one- and two-center energy components in the CECA analysis [9]. We hope that this way of writing the Hamiltonian will permit to accomplish some a priori approaches to molecular structure problems, and not only a posteriori ones like the energy decomposition. In the next section, we shall consider the application of our approach at the SCF level of theory; it is not utilizing explicitly the detailed form (32)–(34) of the Hamiltonian.

5 SCF equations

The fact that the projective integral approximations discussed in Sect. 2 lead to the approximate Hermitian Hamiltonian (30), opens a quite straightforward way to introduce the respective approximate SCF equations. As the Hamiltonian in the second quantized framework is defined by the *integrals* over the basis orbitals, one should simply introduce the same integral approximations in the SCF equations as were used for the Hamiltonian.

Admitting unrestricted Hartree–Fock (UHF) case, the Hartree–Fock–Roothaan (HFR) equations are

$$\mathbf{F}^{\sigma}\,\mathbf{c}_i^{\sigma} = \varepsilon_i^{\sigma}\,\mathbf{S}\mathbf{c}_i^{\sigma} \tag{43}$$

where $\mathbf{c}_i^{\sigma}$ is the vector of the LCAO coefficients of the i-th molecular orbital of spin σ ($\sigma = \alpha$ or β), ε_i^{σ} is its orbital energy, and the matrix elements of the Fockian are given in terms of the *integrals over the spatial orbitals* by

$$F^{\sigma}_{\mu\nu} = h_{\mu\nu} + \sum_{\rho,\tau}\big(D_{\tau\rho}[\mu\rho|\nu\tau] - P^{\sigma}_{\tau\rho}[\mu\rho|\tau\nu]\big). \tag{44}$$

When introducing here the projective integral approximations, one should treat separately the cases, when the subscripts μ and ν of $F^{\sigma}_{\mu\nu}$ correspond the same atom ($\mu,\nu \in A$) and when they refer to different atoms ($\mu \in A,\ \nu \in B$; $A \neq B$). By performing somewhat lengthy derivations outlined in the "Appendix", and turning to the convention (11|22) for the two-electron integrals, usually preferred in the programming work, we get for the one-center Fock-matrix elements:

$$\begin{aligned} F^{\sigma}_{\mu\nu}\big|_{\mu,\nu\in A} \Longrightarrow\ & h_{\mu\nu} + \sum_{\rho,\tau\in A}\left[\, D_{\rho\tau}(\mu\nu|\rho\tau) - P^{\sigma}_{\rho\tau}(\mu\rho|\nu\tau)\,\right] \\ & + \sum_{\rho\in A}\sum_{\substack{B\\ B\neq A}}\sum_{\tau\in B}\left\{ D_{\rho\tau}(\mu\nu|\rho\tau) - \frac{1}{2}P^{\sigma}_{\rho\tau}[(\mu\rho|\nu\tau) + (\mu\tau|\nu\rho)]\right\} \\ & + \sum_{\substack{B\\ B\neq A}}\sum_{\tau\in B}\sum_{\eta\in AB}\left\{ B^{AB}_{\tau\eta}(\mu\nu|\eta\tau) - \frac{1}{2}\,C^{\sigma AB}_{\tau\eta}[(\mu\tau|\eta\nu) + (\mu\eta|\nu\tau)]\right\}. \end{aligned} \tag{45}$$

In the case of two-center Fock-matrix elements, it is also possible to add and subtract terms as to get an expression with the "projected density matrices" $\mathbf{B}^{AB}$ and $\mathbf{C}^{\sigma AB}$; however, that expression would contain a number of correction terms with sums containing one-center to two-center corrections, like the difference $[\mu\rho|\nu\tau] - \sum_{\eta,\lambda\in B} A^{B}_{\mu\eta}A^{B}_{\rho\lambda}[\eta\lambda|\nu\tau]$, essentially similar to those occurring in Eq. (34). For that reason we separate out only the terms containing only one- and two-center integrals and conserve explicitly the projective expansion of the three- and four-center ones:

$$\begin{aligned} & F^{\sigma}_{\mu\nu}\big|_{\mu\in A,\ \nu\in B\ (A\neq B)} \\ & \Longrightarrow h^{AB}_{\mu\nu} - \frac{1}{2}\sum_{\substack{C\\ C\neq A,B}}\left[\sum_{\tau\in BC} A^{BC}_{\mu\tau}\langle\tau|\frac{Z_C}{r_C}|\nu\rangle + \sum_{\tau\in AC} A^{AC}_{\nu\tau}\langle\mu|\frac{Z_C}{r_C}|\tau\rangle\right] \\ & \quad + \sum_{\rho,\tau\in AB}\left[D_{\rho\tau}(\mu\nu|\rho\tau) - P^{\sigma}_{\rho\tau}(\mu\rho|\nu\tau)\right] \\ & \quad + \frac{1}{2}\sum_{\substack{C,D\\ \{C,D\}\neq\{A,B\}}}\sum_{\rho\in C}\sum_{\tau\in D}\left[\left(D_{\rho\tau}\sum_{\eta,\lambda\in BD} A^{BD}_{\mu\eta}A^{BD}_{\rho\lambda}\right.\right. \\ & \quad \left. - P^{\sigma}_{\tau\rho}\sum_{\eta,\lambda\in BD} A^{BD}_{\mu\lambda}A^{BD}_{\rho\eta}\right)(\eta\nu|\lambda\tau) \\ & \quad \left. + \left(D_{\rho\tau}\sum_{\eta,\lambda\in AC} A^{AC}_{\nu\eta}A^{AC}_{\tau\lambda} - P^{\sigma}_{\tau\rho}\sum_{\eta,\lambda\in AC} A^{AC}_{\nu\lambda}A^{AC}_{\tau\eta}\right)(\mu\eta|\rho\lambda)\right] \end{aligned} \tag{46}$$

Here the notation $\{C,D\} \neq \{A,B\}$ is used to indicate that at least one of the centers C, D is different from both A and B. When three-center integrals are expanded, it happens that $D = B$ or $C = A$; then obviously one should assume $\mathbf{A}^{AA} \equiv \mathbf{A}^{A}$ and $\mathbf{A}^{BB} \equiv \mathbf{A}^{B}$.

An interesting property of these equations is that the respective SCF energy—the expectation value of the Hamiltonian (30)—will be an exact sum of the one- and two-center CECA energy components. The SCF energy may be calculated by using the standard formula

$$E = \sum_{A<B}\frac{Z_A Z_B}{R_{AB}} + \frac{1}{2}\left\{ Tr\left[\mathbf{P}^{\alpha}(\mathbf{h}^{eff} + \mathbf{F}^{\alpha})\right] + Tr\left[\mathbf{P}^{\beta}(\mathbf{h}^{eff} + \mathbf{F}^{\beta})\right]\right\} \tag{47}$$

Here the effective core matrix $\mathbf{h}^{eff}$ is defined by the one-electron components of the Fock-matrix elements (45), (46).

The conceptual approach behind these equations is quite similar to that we used [3, 4] with success in the theory of intermolecular interactions in order to get wave functions which are free of the so-called basis set superposition error. However, in contrast to that case, the present SCF equations are Hermitian and, as a consequence, may be directly used also to calculate the energy.

The actual programming of these equations may require introduction of different intermediate matrices; the effectiveness of the whole procedure may depend decisively on

what quantities may be stored in the computer's memory. However, we think that the exclusion of the explicit appearance of the three- and four-center integrals will worth of these complications. A promising special applications of these equations may be their use as a special intermediate layer in the ONIOM-type approaches between the parts used with full ab initio and those treated at the semiempirical level.

6 Conclusions

An attempt is made to develop a new scheme of non-empirical SCF-LCAO-MO calculations, which may represent an alternative for both the "orthodox" ab initio scheme and the semiempirical theories (it may also be a useful intermediate layer in the ONIOM-type approaches). For that reason it is suggested to treat all the one- and two-center integrals in a strict ab initio manner and to use approximate projective expansions for the three- and four-center ones—the same as were used in the CECA energy decomposition scheme [9]. These projective integral expansions permit to express the leading "physical" components of the three- and four-center integrals through one- center and two-center integrals and the overlap ones. These expansions are utilized to rewrite the second quantized Born–Oppenheimer LCAO Hamiltonian in an approximate form not containing any three- and four-center integrals and to write down a Hermitian version of the "Chemical Hamiltonian" [1], containing only mono- and diatomic terms. Incorporating these projective integral approximations in the HFR equations, one obtains some modified SCF equations. The calculations will require only one- and two-center integrals and some quantities calculated by using the overlap matrix. Nevertheless, for large basis sets, this method should converge to the usual Hartree–Fock limit. The approach is in the spirit of the CHA–SCF equations [3, 4] used with success to exclude basis set superposition error in the theory of intermolecular interactions, but here the Fockian is Hermitian and can also directly be applied to calculate energy.

Appendix: Derivation of Eq. (45)

When considering the integral approximations, we should stick to the [12|12] convention for the integrals permitting to distinguish the terms originating from the "bra"-s and "ket"-s, respectively; in the final formulae we have turned to the (11|22) convention more convenient in programming.

Systematizing the terms according to the centers of the orbitals involved, for the one-center matrix elements of matrix $\mathbf{F}^\sigma$ one has

$$\begin{aligned} F^\sigma_{\mu\nu}\big|_{\mu,\nu\in A} = h_{\mu\nu} &+ \sum_{\rho,\tau\in A}\left(D_{\tau\rho}[\mu\rho|\nu\tau] - P^\sigma_{\tau\rho}[\mu\rho|\tau\nu]\right) \\ &+ \sum_{\substack{B\\B\neq A}}\sum_{\rho\in B}\sum_{\tau\in A}\left(D_{\tau\rho}[\mu\rho|\nu\tau] - P^\sigma_{\tau\rho}[\mu\rho|\tau\nu]\right) \\ &+ \sum_{\substack{B\\B\neq A}}\sum_{\tau\in B}\sum_{\rho\in A}\left(D_{\tau\rho}[\mu\rho|\nu\tau] - P^\sigma_{\tau\rho}[\mu\rho|\tau\nu]\right) \\ &+ \sum_{\substack{B,C\\B,C\neq A}}\sum_{\rho\in B}\sum_{\tau\in C}\left(D_{\tau\rho}[\mu\rho|\nu\tau] - P^\sigma_{\tau\rho}[\mu\rho|\tau\nu]\right) \end{aligned} \tag{48}$$

Only the last sum of Eq. (48) contain three- or four-center integrals that need to be approximated, therefore we shall consider its terms in detail. At first, we substitute the approximations (6) in the first term of that sum:

$$\begin{aligned} &\sum_{\substack{B,C\\B,C\neq A}}\sum_{\rho\in B}\sum_{\tau\in C} D_{\tau\rho}[\mu\rho|\nu\tau] \\ &\Longrightarrow \sum_{\substack{B,C\\B,C\neq A}}\sum_{\rho\in B}\sum_{\tau\in C} D_{\tau\rho}\frac{1}{2}\left(\sum_{\lambda,\eta\in AC} A^{AC}_{\mu\lambda}A^{AC}_{\rho\eta}[\lambda\eta|\nu\tau]\right. \\ &\quad\left. + \sum_{\lambda,\eta\in AB} A^{AB\dagger}_{\lambda\nu}A^{AB\dagger}_{\eta\tau}[\mu\rho|\lambda\eta]\right) \end{aligned} \tag{49}$$

Both subscripts of the coefficient $A^{AC}_{\mu\lambda}$ in the first term are belonging to the diatomic fragment AC; as noted above, the intra-fragment blocks of the matrices $\mathbf{A}$ are unit-matrices; therefore, this coefficient reduces to the Kronecker delta $\delta_{\mu\lambda}$. Similarly, in the second term $A^{AB\dagger}_{\lambda\nu} = \delta_{\lambda\nu}$. Utilizing this we get:

$$\begin{aligned} &\sum_{\substack{B,C\\B,C\neq A}}\sum_{\rho\in B}\sum_{\tau\in C} D_{\tau\rho}[\mu\rho|\nu\tau] \\ &\Longrightarrow \sum_{\substack{B,C\\B,C\neq A}}\sum_{\rho\in B}\sum_{\tau\in C} D_{\tau\rho}\,\frac{1}{2}\left(\sum_{\eta\in AC} A^{AC}_{\rho\eta}[\mu\eta|\nu\tau]\right. \\ &\quad\left. + \sum_{\eta\in AB} A^{AB\dagger}_{\eta\tau}[\mu\rho|\nu\eta]\right). \end{aligned} \tag{50}$$

In the followings we shall assume that we use real basis orbitals and orbital coefficients—as it is usually the case in the practice. Then $D_{\tau\rho} = D_{\rho\tau}$, $A^{AB\dagger}_{\eta\tau} = A^{AB}_{\tau\eta}$, $[\mu\rho|\lambda\eta] = [\lambda\eta|\mu\rho]$, and interchanging some summation

indices we can conclude that the two sums are equal. Thus we have in the real case

$$\sum_{\substack{B,C\\B,C\neq A}}\sum_{\rho\in B}\sum_{\tau\in C} D_{\tau\rho}[\mu\rho|\nu\tau] \Longrightarrow \sum_{\substack{B,C\\B,C\neq A}}\sum_{\rho\in B}\sum_{\tau\in C} D_{\tau\rho}\sum_{\eta\in AC} A^{AC}_{\rho\eta}[\mu\eta|\nu\tau]. \tag{51}$$

The summation over $\rho \in B;\ B \neq A$ in the right-hand side of Eq. (51) means that ρ runs over all the orbital indices, except those assigned to atom A; we may add and subtract the sum for the case $\rho \in A$:

$$\sum_{\substack{B,C\\B,C\neq A}}\sum_{\rho\in B}\sum_{\tau\in C} D_{\tau\rho}[\mu\rho|\nu\tau] \Longrightarrow \sum_{\substack{C\\C\neq A}}\sum_{\rho}\sum_{\tau\in C} D_{\tau\rho}\sum_{\eta\in AC} A^{AC}_{\rho\eta}[\mu\eta|\nu\tau] - \sum_{\substack{C\\C\neq A}}\sum_{\rho\in A}\sum_{\tau\in C} D_{\tau\rho}\sum_{\eta\in AC} A^{AC}_{\rho\eta}[\mu\eta|\nu\tau]. \tag{52}$$

In the first term on the right-hand side, we can sum over ρ to get the "projected density matrix element" $B^{AC}_{\tau\eta}$, while in the second term the coefficient $A^{AC}_{\rho\eta}$ again reduces to the Kronecker delta $\delta_{\rho\eta}$. Thus we get, changing the summation index C to B in the right-hand side:

$$\sum_{\substack{B,C\\B,C\neq A}}\sum_{\rho\in B}\sum_{\tau\in C} D_{\tau\rho}[\mu\rho|\nu\tau] \Longrightarrow \sum_{\substack{B\\B\neq A}}\sum_{\tau\in B}\sum_{\eta\in AB} B^{AB}_{\tau\eta}[\mu\eta|\nu\tau] - \sum_{\substack{B\\B\neq A}}\sum_{\rho\in A}\sum_{\tau\in B} D_{\tau\rho}[\mu\rho|\nu\tau]. \tag{53}$$

The second sum just cancels the respective term in the third line of Eq. (48).

The second (exchange) term in the fourth line of Eq. (48) transforms analogously. However, in that case the two terms are not equal, as were in Eq. (50), and there is no full canceling of the second term in the third line of Eq. (48); instead the *half* of the respective terms in both second and third lines is canceled.

References

1. Mayer I (1983) Int J Quantum Chem 23:341
2. Ruedenberg K (1951) J Chem Phys 19:1433
3. Mayer I (1998) Int J Quantum Chem 70:41
4. Salvador P, Asturiol D, Mayer I (2006) J Comput Chem 27:1505
5. Mayer I (1983) Chem Phys Lett 97:270
6. Mayer I (2007) J Comput Chem 28:204
7. Mayer I (2012) Chem Phys Lett 544:83
8. Programs BORDER, NEWBORDER etc. http://occam.ttk.mta.hu
9. Mayer I (2000) Chem Phys Lett 332:381
10. Program APOST. http://occam.ttk.mta.hu
11. Mayer I (2006) Phys Chem Chem Phys 8:4630
12. Mayer I (2007) Faraday Discuss 135:439
13. Mayer I (2012) Phys Chem Chem Phys 14:337
14. Programs APEX4, ENPART, NEWENPART. http://occam.ttk.mta.hu
15. Maseras F, Morokuma K (1995) J Comput Chem 16:1170
16. Longuet-Higgins HC (1966) In: Löwdin P-O (ed) Quantum theory of atoms, molecules and the solid state. Academic Press, New York, p 105
17. Surján PR (1989) Second quantized approach to quantum chemistry. Springer, Berlin
18. Hamza A, Mayer I (2003) Theor Chem Acc 109:91

Theor Chem Acc (2015) 134:108
DOI 10.1007/s00214-015-1713-8

REGULAR ARTICLE

Internal coordinates and orthogonality: features of the pseudoinverse of the Eliashevich–Wilsonian *B*-matrix

F. Kalincsák[1] · G. Pongor[1]

Received: 16 June 2015 / Accepted: 3 August 2015 / Published online: 18 August 2015

Abstract It is shown that the system of unit vectors corresponding to the internal coordinates is non-orthogonal generally. The deduction starts with the well-known orthonormality of unit vectors of the Cartesian coordinates. The crucial point of the GDIIS method is discussed regarding a "partially isomorphic" relationship between two vector spaces. Some features of the pseudoinverse of the Eliashevich–Wilsonian matrix B are deduced and discussed: these are analogous to the conditions formulated originally for the elements of the $\boldsymbol{B}$-matrix.

Keywords Internal coordinates · Reciprocal internal displacement coordinates · Non-orthogonal · *B*-matrix · Pseudoinverse · Sayvetz conditions · GDIIS

1 Introduction

The use of the internal coordinates is a relevant and interesting topic both in the field of the vibrational calculations [1–3] and in quantum chemistry [4]. Though vibrational calculations could be carried out in terms of Cartesians as well, the system of valence-type internal coordinates gives the most significant and physically meaningful description of the vibrational potential energy. Internal coordinates are often used in quantum chemical calculations not directly in the quantum mechanical determination of single-point energies rather in representing the equilibrium and transition-state geometries. The dimension of a complete and non-redundant set of the internal coordinates is smaller than the number of the Cartesians, but this is not the main reason for their application. Their most important feature is that in terms of internal coordinates, the Hessian matrix could be well approximated with a simple diagonal matrix [4] in gradient geometry optimization procedures. In this paper, we will deal with the system of internal coordinates, in order to give a deeper insight and characterize some interesting features of the pseudoinverse of the Eliashevich–Wilsonian matrix $\boldsymbol{B}$ [1, 2].

2 Theory

Instead of the usual Cartesians, we can also apply a complete and non-redundant set of the so-called internal coordinates. In order to understand their application in vibrational calculations, let us consider a molecular system consisting of N nuclei; let the Cartesian displacement vectors of the nuclei be $\boldsymbol{d}_1, \boldsymbol{d}_2, \ldots, \boldsymbol{d}_N$ around their equilibrium geometry in the usual three-dimensional Euclidean space E_3. (The expression for the n-th Cartesian displacement vector is $\boldsymbol{d}_n = \boldsymbol{\rho}_n - \boldsymbol{\rho}_n^0$, where $\boldsymbol{\rho}_n$ is the instantaneous position vector of the n-th nucleus, and $\boldsymbol{\rho}_n^0$ is the position vector of the same nucleus at equilibrium. Hereafter, these position vectors correspond to an arbitrary origin. Note that for simplicity, we omit the explicit use of the atomic masses, i.e., do not use mass-weighted Cartesians.) A single-point $\boldsymbol{\delta}$ of a hypothetical $3N$-dimensional space $\Re_{3N}$ ($\boldsymbol{\delta} \in \Re_{3N}$), defined as

Published as part of the special collection of articles "Festschrift in honour of P. R. Surjan".

✉ G. Pongor
pongor@chem.elte.hu

[1] Department of Inorganic Chemistry, Institute of Chemistry, Eötvös Loránd University, Pázmány Péter sétány 1/A, Budapest 1117, Hungary

$$\begin{pmatrix} \boldsymbol{d}_1 \\ \boldsymbol{d}_2 \\ \cdots \\ \boldsymbol{d}_N \end{pmatrix} \rightarrow \begin{pmatrix} \delta_1 \\ \delta_2 \\ \cdots \\ \delta_{3N} \end{pmatrix} \tag{1}$$

can be used as an equivalent of the set $\boldsymbol{d}_1, \boldsymbol{d}_2, \ldots, \boldsymbol{d}_N$. (Note the difference between the components of vector $\boldsymbol{\delta}$ and the Kronecker-delta symbol: the former have just one index in subscript, the latter has two!) Let us denote an orthonormal (Cartesian) basis set of the $\Re_{3N}$ space by $\{\boldsymbol{e}_k\}_1^{3N}$, for which the well-known equations hold:

$$\langle \boldsymbol{e}_k \mid \boldsymbol{e}_l \rangle = \delta_{kl} \quad (k, l = 1, 2, \ldots, 3N) \tag{2}$$

(that is, the Gram-matrix of the $\boldsymbol{e}_k$ unit vectors is the unit matrix). Naturally,

$$\boldsymbol{\delta} = \sum_k^{3N} \delta_k \boldsymbol{e}_k. \tag{3}$$

Let us construct another space in order to determine the vibrational displacements of the molecule without referring the external coordinates, that is, without the data of the center-of-mass (COM) and the rotations. In the general case, the dimension of the latter space is $3N - 6$, according to the well-known Sayvetz (or, Eckart) conditions [5–7] (the special case of the linear molecules is exceptional with its $3N - 5$ dimension). Hereafter, this Euclidean space will be denoted by $\Re_{3N-6}$, and let us denote the internal displacement vector by $\boldsymbol{s} \in \Re_{3N-6}$ which can be expressed in terms of the basis set $\{\boldsymbol{\kappa}_i\}_1^{3N-6}$ according to the following equation:

$$\boldsymbol{s} = \sum_i^{3N-6} s_i \boldsymbol{\kappa}_i \tag{4}$$

(here the s_i − s are the well-known internal coordinates; moreover, $\boldsymbol{s} = \boldsymbol{\sigma} - \boldsymbol{\sigma}^0$, where $\boldsymbol{\sigma}$ is the instantaneous internal coordinate vector and $\boldsymbol{\sigma}^0$ is the internal coordinate vector at the equilibrium). Unit vectors $\boldsymbol{\kappa}_i \in \Re_{3N-6}$ are constructed as fixed linear combinations of the primitive curvilinear valence coordinates (bond lengths, bond angles, out-of-plane and dihedral angles), similarly to the contracted Gaussian basis sets in quantum chemistry. [Naturally, there is a significant difference between the unit vectors of the "internal vector space" $\Re_{3N-6}$ and the Cartesian unit vectors (or the Gaussian primitives): each of the latter is attached to (centered on) a single nucleus, while the former ones are non-local]. Let us express the $\boldsymbol{\kappa}_i$ unit vectors of $\Re_{3N-6}$ by a simple *linear* transformation around the molecular equilibrium:

$$\boldsymbol{\kappa}_i = \sum_k^{3N} \boldsymbol{e}_k A_{ki} \tag{5}$$

(here the role of linear coefficients A_{ki} is not known yet). Let us collect the $\boldsymbol{\kappa}_i$ unit vectors of $\Re_{3N-6}$ and the $\boldsymbol{e}_k$ unit vectors of $\Re_{3N}$ into the row matrices $(\boldsymbol{\kappa}_1\, \boldsymbol{\kappa}_2 \cdots \boldsymbol{\kappa}_{3N-6})$ and $(\boldsymbol{e}_1\, \boldsymbol{e}_2 \cdots \boldsymbol{e}_{3N})$, respectively. Now we can write the following expression, obviously:

$$(\boldsymbol{\kappa}_1\, \boldsymbol{\kappa}_2 \cdots \boldsymbol{\kappa}_{3N-6}) = (\boldsymbol{e}_1\, \boldsymbol{e}_2 \cdots \boldsymbol{e}_{3N})\boldsymbol{A}, \tag{6}$$

{here $\boldsymbol{A}$ is a matrix of dimension $3N \times (3N - 6)$}. Also, let us consider the following equation:

$$\begin{aligned} &(\boldsymbol{e}_1\, \boldsymbol{e}_2 \cdots \boldsymbol{e}_{3N})\boldsymbol{E}\boldsymbol{\delta} \rightarrow (\boldsymbol{e}_1\, \boldsymbol{e}_2 \cdots \boldsymbol{e}_{3N})\boldsymbol{A}\boldsymbol{B}\boldsymbol{\delta} = \\ &(\boldsymbol{\kappa}_1\, \boldsymbol{\kappa}_2 \cdots \boldsymbol{\kappa}_{3N-6})\boldsymbol{B}\boldsymbol{\delta} = (\boldsymbol{\kappa}_1\, \boldsymbol{\kappa}_2 \cdots \boldsymbol{\kappa}_{3N-6})\boldsymbol{s}, \end{aligned} \tag{7}$$

where $\boldsymbol{E}$ is the full-rank ($3N$) projector (i.e., the unit matrix), whereas the rectangular matrix $\boldsymbol{B}$ multiplied from the left by its pseudoinverse $\boldsymbol{A}$ (see below in details) results a projector $\boldsymbol{AB}$ of rank lower by 6. In Eq. (7), the order of the matrices $\boldsymbol{A}$ and $\boldsymbol{B}$ in the product follows from Eq. (6) and the relation $\boldsymbol{s} = \boldsymbol{B}\boldsymbol{\delta}$ equation (see, e.g., Ref. [3]) where matrix $\boldsymbol{B}$ of dimension $(3N - 6) \times 3N$ is that of Eliashevich [8] and Wilson [9]. It is well known that there exists no better approximation to the left "inverse" of matrix $\boldsymbol{B}$ than matrix $\boldsymbol{A}$. In other words, $\boldsymbol{AB}$ is the closest possible to the unit matrix $\boldsymbol{E}$ of dimension $3N \times 3N$. Projector $\boldsymbol{AB}$ could thus be a replacement of $\boldsymbol{E}$ in Eq. (7). The expression for the matrix $\boldsymbol{A}$ is:

$$\boldsymbol{A} = \boldsymbol{U}\boldsymbol{B}^{+}\left(\boldsymbol{B}\boldsymbol{U}\boldsymbol{B}^{+}\right)^{-1}. \tag{8}$$

(In our case, the adjoint of a matrix is equivalent to the transpose of it since we use real arithmetics. We denote it with a + symbol according to the conventions.) In Eq. (8), $\boldsymbol{U}$ is an arbitrary $3N \times 3N$ non-singular matrix; we use the unit matrix for $\boldsymbol{U}$ in the simplest case; the matrix $\boldsymbol{A}$ is the Moore–Penrose pseudoinverse [10, 11] of the rectangular $\boldsymbol{B}$-matrix. To our best knowledge, the aforementioned matrix $\boldsymbol{A}$ was originally introduced exactly in the same way as in Eq. (8) by Pulay et al. [12, 13] who referred to generalized inverse. The notation $\boldsymbol{A}$ itself originates from Crawford [14]. The definitions for the elements of both matrices $\boldsymbol{A}$ and $\boldsymbol{B}$ are:

$$\left(\frac{\partial \boldsymbol{\kappa}_i}{\partial \boldsymbol{e}_k}\right)_{\boldsymbol{\sigma}^0} = A_{ki} \quad \text{and} \quad \left(\frac{\partial s_i}{\partial \boldsymbol{e}_k}\right)_{\boldsymbol{\sigma}^0} = B_{ik}, \tag{9}$$

at a special nuclear configuration $\boldsymbol{\sigma}^0$. [Note that in Eq. (9) $\boldsymbol{\kappa}_i$ is a vector and s_i is a component of a vector]. Moreover, for another internal unit vector, one can write $\boldsymbol{\kappa}_j = \sum_l^{3N} \boldsymbol{e}_l A_{lj}$ [c.f. Eq. (5)], so we get for a typical $\langle \boldsymbol{\kappa}_i \mid \boldsymbol{\kappa}_j \rangle$ element of the Gram-matrix of the $\boldsymbol{\kappa}_i$ unit vectors (with the help of Eq. (8) setting $\boldsymbol{U}$ to the unit matrix):

$$\begin{aligned}\langle \boldsymbol{\kappa}_i \mid \boldsymbol{\kappa}_j \rangle &= \left\langle \sum_k^{3N} \boldsymbol{e}_k A_{ki} \,\middle|\, \sum_l^{3N} \boldsymbol{e}_l A_{lj} \right\rangle \\ &= \sum_k^{3N}\sum_l^{3N} A_{ki}A_{lj}\langle \boldsymbol{e}_k \mid \boldsymbol{e}_l \rangle \\ &= \sum_k^{3N}\sum_l^{3N} A_{ki}A_{lj}\delta_{kl} = \sum_k^{3N} A_{ki}A_{kj} \\ &= \sum_l^{3N-6}\sum_m^{3N-6} \left(\boldsymbol{BB}^+\right)^{-1}_{li}\left(\boldsymbol{BB}^+\right)^{-1}_{mj}\sum_k^{3N} B_{lk}B_{mk}, \end{aligned} \tag{10}$$

that is, the $\{\boldsymbol{\kappa}_i\}_1^{3N-6}$ basis set is generally *not orthogonal* in the $\Re_{3N-6}$ space. (Nevertheless, it is possible to *define* the internal coordinate system as an orthogonal one; this statement is acceptable on the basis that the Eliashevich–Wilson-type $\boldsymbol{B}$-matrix can be regarded as a sparse matrix.) Note that $\boldsymbol{s} = \boldsymbol{B\delta}$ is valid in linear approximation only, thus Eq. (6) is true in the same approximation as well. Consequently, our proof given above also assumes a linear approximation. If considering higher terms, the basis $\{\boldsymbol{\kappa}_i\}_1^{3N-6}$ will still not be orthogonal. In a strict sense, the linear approximation is valid using infinitesimal displacements, but in practice we can consider it to be effective using "small enough" displacements in molecular vibration calculations as well as determination of stationary states in quantum chemistry. The first (minor) consequence of this non-orthogonality is that the terminology of internal *coordinates* itself is improper according to the rules of the linear algebra (see, e.g., [15]): in the case of a non-orthonormal metrics, it is correct to mention *components* instead of coordinates. However, we will use the terminology of "internal coordinates" in the following, as it is widely accepted.

Let us consider a physical system consisting of N points of masses representing the nuclei of a molecule. Let us choose a complete and non-redundant system of the internal coordinates (such coordinates are, e.g., the so-called natural internal coordinates (NICs) [4, 16]) and consider the linear approximation valid at a given reference point. Now, let us consider two different vector spaces X and Y, both of them being of $3N-6$ dimensional. Vector space X possesses the $\boldsymbol{s}$' vectors describing the molecular conformations in terms of the internal coordinates chosen (later the apostrophe can be left). Vector space Y contains the forces acting on the nuclei in the same system of internal coordinates, evaluated in the corresponding $\boldsymbol{s}$' points. An X to Y mapping $\hat{C}$ can be created between the two vector spaces that connect to each internal coordinate vector of the X space to the internal force vector of Y space:

$$\hat{C}\boldsymbol{s}' = -\left(\frac{\partial E}{\partial \boldsymbol{s}}\right)_{\boldsymbol{s}'} \tag{11}$$

(where E is the total molecular energy and $\boldsymbol{s}$ is the internal coordinate vector). It is obvious that the operator $\hat{C}$ has no inverse: if the molecule has more than one energy minima the operator connects at least two different vectors of the X space to the same (zero) vector of the Y space. In this way, it is evident that the X and Y spaces are not isomorphic. In spite of this, the vector spaces mentioned before are *"partially isomorphic"* in the vicinity of a chosen molecular equilibrium geometry. This "reduced-level" isomorphism does not apply in a strict sense to any subspaces of X and Y, only to not well-defined subsets whose borders are somewhat blurred. This serves as the basis of the Eqs. (6) and (7) of the paper on geometry optimization by direct inversion in the iterative subspace (GDIIS) [17]: Eq. (6) of Ref. [17] refers to the X space, and Eq. (7) of Ref. [17] corresponds to the Y vector space; the same coefficients in both linear combinations are coming from the existing "partial isomorphism" mentioned above.

As it is well known, Malhiot and Ferigle [18] have proven two interesting characters of the elements of the $\boldsymbol{B}$-matrix in their classical paper. Let us write the i-th internal coordinate in linear approximation in a somewhat modified form:

$$s_i = \sum_{k=1}^{3N} B_{ik}\delta_k = \sum_{n=1}^{N} \boldsymbol{b}_{in}\cdot\boldsymbol{d}_n. \tag{12}$$

In Eq. (12), the terms occurring in the first summation are grouped into N terms in the second one where each term corresponds to a certain nucleus only. Let the vector $\boldsymbol{b}_{in}$ contains three consecutive elements of the i-th row of matrix $\boldsymbol{B}$ corresponding to nucleus n, and let the components of vector $\boldsymbol{d}_n$ be the three Cartesian displacements of the same nucleus [see Eq. (1) in E$_3$]. With these notations, the following equations are valid [18]:

$$\sum_{n=1}^{N} \boldsymbol{b}_{in} = \boldsymbol{0} \tag{13A}$$

$$\sum_{n=1}^{N} \boldsymbol{\rho}_n \times \boldsymbol{b}_{in} = \boldsymbol{0}, \tag{13B}$$

that is, the $\boldsymbol{b}_{in}$ elements fulfill conditions similar to the Sayvetz ones. In Eq. (13B) $\boldsymbol{\rho}_n$ means the position vector of nucleus n for an arbitrary origin. It can be mentioned that the assumption of Malhiot and Ferigle [18]—Eq. (13B) is valid in a COM system only—was too strict. Due to Eq. (13A), it can be easily realized that Eq. (13B) is valid in an arbitrary coordinate system as well.

We will show that an equation similar to Eq. (13) holds for the columns of the matrix $\boldsymbol{A}$ mentioned before. In order to prove this, let us consider the following partition:

$$\begin{pmatrix} \boldsymbol{B} \\ \boldsymbol{C} \end{pmatrix} (\boldsymbol{A}\ \boldsymbol{K}) = \begin{pmatrix} \boldsymbol{E}_{NQxNQ} & \boldsymbol{0} \\ \boldsymbol{0} & \boldsymbol{E}_{6x6} \end{pmatrix}, \tag{14}$$

here NQ equals to $3N - 6$, $\boldsymbol{B}$ is the aforementioned Eliashevich–Wilsonian matrix, $\boldsymbol{C}$ is the submatrix of the additional six rows descripting the transformations between the Cartesian displacement coordinates and the external coordinates, $\boldsymbol{A}$ is the pseudoinverse of the rectangular $\boldsymbol{B}$-matrix, $\boldsymbol{K}$ is the pseudoinverse of the submatrix $\boldsymbol{C}$, $\boldsymbol{E}_{NQxNQ}$ is a diagonal unit block corresponding to elements for the internal coordinates separately, $\boldsymbol{E}_{6x6}$ is the unit block corresponding to elements for the external coordinates only. Note that a similar partition was used in Refs. [19] and [20] earlier. The internal coordinates are chosen in a way that the following requirements are satisfied [c.f., Eq. (12) of Ref. [18] in somewhat different transcription]:

$$\sum_{k}^{3N} B_{ik} C_{pk} = 0, \tag{15}$$

where index p refers to any of the six external coordinates coming from the Sayvetz conditions, i.e., $p = 1, 2,\ldots, 6$ in submatrix $\boldsymbol{C}$. It is easy to prove that an equation analogous to Eq. (15) is valid for the elements of the ($\boldsymbol{A}$ $\boldsymbol{K}$) matrix as well:

$$\sum_{k}^{3N} A_{ki} K_{kp} = 0. \tag{16}$$

In fact,

$$\sum_{k}^{3N} A_{ki} K_{kp} = \sum_{l}^{NQ} \sum_{q}^{6} \left(\boldsymbol{B}\boldsymbol{B}^{+}\right)^{-1}_{li} \left(\boldsymbol{C}\boldsymbol{C}^{+}\right)^{-1}_{qp} \sum_{k}^{3N} B_{lk} C_{qk} = 0, \tag{17}$$

where we have taken into consideration Eq. (15) and used the pseudoinverse of the submatrix $\boldsymbol{C}$ to express the elements of submatrix $\boldsymbol{K}$ [similarly to Eq. (8)]. Now let us group the elements of each column of the ($\boldsymbol{A}$ $\boldsymbol{K}$) matrix into triplets corresponding to the various nuclei. With the help of these, we can define the new set of *reciprocal internal displacement coordinates* $\bar{s}_i$ ($i = 1, 2,\ldots, 3N - 6$) according to the equation:

$$(\bar{\boldsymbol{s}})_i \equiv \left(\boldsymbol{A}^{+}\boldsymbol{\delta}\right)_i = \sum_{n=1}^{N} \boldsymbol{a}_{ni} \cdot \boldsymbol{d}_n \tag{18}$$

(the reciprocity refers to the "inverse" transformation in connection with Eq. (12), instead of matrix $\boldsymbol{B}$ with $\boldsymbol{A}^{+}$; however, it is only a terminology). In Eq. (18) each term corresponds to a certain nucleus only in summation like in Eq. (12), that is, the vector $\boldsymbol{a}_{ni}$ contains three consecutive elements in the i-th column of the matrix $\boldsymbol{A}$ corresponding to nucleus n, and the components of vector $\boldsymbol{d}_n$ contain the three Cartesian displacements of the same nucleus again. A similar expression is valid for the new *reciprocal external coordinates* $\bar{s}_p$ ($p = 1, 2,\ldots, 6$ in case of the submatrix $\boldsymbol{K}$) as well:

$$\bar{s}_p = \sum_{n=1}^{N} \boldsymbol{k}_{np} \cdot \boldsymbol{d}_n = 0, \tag{19}$$

respectively. (Note, that Eq. (19) is valid for the reciprocal external coordinates; one can easily realize taking into account

$$\bar{s}_p = \sum_{k=1}^{3N} K^{+}_{pk} \delta_k = \sum_{k=1}^{3N} \left[\left(\boldsymbol{C}\boldsymbol{C}^{+}\right)^{-1}\boldsymbol{C}\right]_{pk}$$
$$\delta_k = \sum_{q=1}^{6} \left(\boldsymbol{C}\boldsymbol{C}^{+}\right)^{-1}_{pq} \sum_{k=1}^{3N} C_{qk} \delta_k = 0; \tag{20}$$

the last summation of Eq. (20) is obviously zero because of the zero values of the "usual" external coordinates, see, e.g., p. 28 of Ref. [3]). Thus, the orthogonality condition Eq. (16) can be reformulated with Eqs. (18) and (19) as follows:

$$\sum_{n=1}^{N} \boldsymbol{a}_{ni} \cdot \boldsymbol{k}_{np} = 0, \tag{21}$$

Now, we can turn to the characterization of the elements of matrix $\boldsymbol{A}$.The Sayvetz conditions [3] are

$$\sum_{n=1}^{N} m_n \boldsymbol{d}_n = \boldsymbol{0}, \tag{22A}$$

$$\sum_{n=1}^{N} m_n \boldsymbol{\rho}^{0}_{n} \times \boldsymbol{d}_n = \boldsymbol{0}, \tag{22B}$$

where m_n is the atomic mass of the n-th nucleus. (Note that hereafter we will omit the masses, as it was mentioned earlier.) Since the selected $\bar{s}_p$ and $\bar{s}_q$ reciprocal external coordinates can be expressed as

$$\bar{s}_p = \boldsymbol{e}_p \cdot \sum_{n=1}^{N} \boldsymbol{d}_n = 0 \quad p = 1, 2, 3, \tag{23A}$$

$$\bar{s}_q = \boldsymbol{e}_q \cdot \sum_{n=1}^{N} \boldsymbol{\rho}^{0}_{n} \times \boldsymbol{d}_n = 0 \quad q = 4, 5, 6, \tag{23B}$$

one can easily express the required $\boldsymbol{k}_{np}$ and $\boldsymbol{k}_{nq}$ elements [c.f., Eq. (19)] as

$$\boldsymbol{k}_{np} = \boldsymbol{e}_p, \tag{24A}$$

$$\boldsymbol{k}_{nq} = \boldsymbol{e}_q \times \boldsymbol{\rho}_n^0, \tag{24B}$$

respectively. Now we can substitute Eq. (24) into Eq. (21) leading to

$$\sum_{n=1}^{N} \boldsymbol{e}_p \cdot \boldsymbol{a}_{ni} = 0, \tag{25A}$$

$$\sum_{n=1}^{N} \boldsymbol{e}_q \cdot \boldsymbol{\rho}_n^0 \times \boldsymbol{a}_{ni} = 0. \tag{25B}$$

[In Eq. (25B) the rules for the scalar triple product were used]. The equations above are valid for any value of p and q thus our final result is

$$\sum_{n=1}^{N} \boldsymbol{a}_{ni} = \boldsymbol{0}, \tag{26A}$$

$$\sum_{n=1}^{N} \boldsymbol{\rho}_n^0 \times \boldsymbol{a}_{ni} = \boldsymbol{0}\,. \tag{26B}$$

It can be clearly seen that similar expressions are valid for the $\boldsymbol{a}_{ni}$ column-elements of the pseudoinverse of the $\boldsymbol{B}$-matrix as the $\boldsymbol{b}_{in}$ row-elements of matrix $\boldsymbol{B}$ itself.

3 Conclusion

We prove that the unit vectors associated with the valence-type internal coordinates are not orthogonal generally. It can be expected that the metrics deduced is suitable for the acceleration of the obstinate bad convergence of gradient geometry optimization procedure GDIIS [17] in case of very shallow potential surfaces. For instance, such situations are the torsional modes around single bonds (e.g., the rotations of methyl groups). The possible gain can be significant if using a complete and non-redundant set of internal coordinates. In our next paper, we will deal with this project.

Acknowledgments The authors are grateful to Dr. László Párkányi (Research Centre for Natural Sciences of the Hungarian Academy of Sciences) and to Dr. Lajos László, Dr. Tibor Pasinszki and János Előri (Eötvös Loránd University, Budapest) for the valuable discussions and help.

References

1. Wilson EB Jr, Decius JC, Cross PC (1955) Molecular vibrations. McGraw-Hill, New York
2. Волькенштейн МВ, Грибов ЛА, Ельяшевич МА, Степанов БИ (1972) Колебания молекул. Наука, Москва **(in Russian)**
3. Califano S (1976) Vibrational states. Wiley, London
4. Fogarasi G, Zhou X, Taylor PW, Pulay P (1992) J Am Chem Soc 114:8191
5. Casimir HBG (1931) Dissertation, Leyden
6. Eckart C (1935) Phys Rev 47:552
7. Sayvetz A (1939) J Chem Phys 6:383
8. Eliashevich M (1940) C. R. Acad Sci URSS 28:605
9. Wilson EB Jr (1941) J Chem Phys 9:76
10. Moore EH (1920) Bull Am Math Soc 26:394
11. Penrose R (1955) Proc Cambridge Phil Soc 51:406
12. Pulay P, Fogarasi G, Pang F, Boggs JE (1979) J Am Chem Soc 101:2550
13. Fogarasi G, Pulay P (1985) Ab initio calculation of force fields and vibrational spectra. In: Durig JR (ed) Vibrational spectra and structure, vol 14. Elsevier, Amsterdam, p 125
14. Crawford B Jr (1952) J Chem Phys 20:977
15. Mirsky L (1990) An introduction to linear algebra. Dover, New York
16. Pulay P, Fogarasi G, Zhou X, Taylor PW (1990) Vibr Spectrosc 1:159
17. Császár P, Pulay P (1984) J Mol Struct 114:31
18. Malhiot RJ, Ferigle SM (1954) J Chem Phys 22:717
19. Woodward LA (1972) Introduction to the theory of molecular vibrations and vibrational spectroscopy. Oxford University Press, Oxford
20. Winnewisser BP, Watson JKG (2001) J Mol Spectrosc 205:227

Theor Chem Acc (2015) 134:147
DOI 10.1007/s00214-015-1750-3

REGULAR ARTICLE

Helical molecular redox actuators with pancake bonds?

Pierre Beaujean[1,2] · **Miklos Kertesz**[2]

Received: 23 July 2015 / Accepted: 22 October 2015 / Published online: 12 November 2015

Abstract In an attempt to design molecular electromechanical actuators with large deformation response, we present here three helicene-like compounds, which offer significant strain above 5 % due to two-electron charge transfer (CT). The shrinking induced by CT is a quantum mechanical orbital effect. A good π–π overlap across the helical pitch is critical for this type of actuation. The relevant overlap refers to frontier orbitals that are involved in the CT, and it has some features common with π–π stacking pancake bonds; however, these molecules do not represent all aspects of typical pancake bonding. This overlap is accompanied by a change in the bond length alternation pattern indicating significant change in π-conjugation. Additionally, two further helicene-like molecules included in this study also indicate large electromechanical actuation, but a simple orbital interpretation is not available in those cases.

Keywords Molecular actuators · Charge transfer · Helical structure · π–π Overlap · Density functional theory computations

Published as part of the special collection of articles "Festschrift in honour of P. R. Surjan".

Electronic supplementary material The online version of this article (doi:10.1007/s00214-015-1750-3) contains supplementary material, which is available to authorized users.

✉ Miklos Kertesz
kertesz@georgetown.edu

[1] Laboratoire de Chimie Théorique, Unité de Chimie Physique Théorique et Structurale, Université de Namur, rue de Bruxelles 61, 5000 Namur, Belgium

[2] Department of Chemistry and Institute of Soft Matter, Georgetown University, 37th and O Streets, NW, Washington, DC 20057-1227, USA

1 Introduction

Molecular actuators present large and reversible structural changes triggered by an external stimulus [1, 2]. The potential applications of such systems range from molecular electronics to nanotechnology [3, 4]. Actuation mechanism is based on the ability of the system to transform this external stimulus into mechanical work. The signal can take many forms: optical [5], chemical, or electrical [6], which allows a wide range of systems to be used, such as synthetic foldamers [7–9] or functional molecular rotaxanes [10, 11]. The review by Baughman et al. [1] summarized various advantages and limitations of those systems.

In particular, the external stimuli can be a consequence of chemical or electrochemical doping, for example in the case of conducting polymers (polypyrroles [12, 13], polyanilines [14, 15] or polythiophenes [16]) or single-walled carbon nanotubes [17]. Electromechanical actuators, in which the conformational or configurational change is caused by a redox event, have attracted significant attention [18–21]. This class also includes, for example, redox-controlled S···N interactions [22] and π-dimers formation [23–25]. In these cases, the redox event triggers a modification of the frontier orbital pattern which is a quantum mechanical (QM) orbital effect. The overlap of the singly occupied molecular orbitals (SOMOs) creates multicenter/2-electron bonds (mc/2e), which are generally found in π-radical dimers, where they are called *pancake* bonds [26–33]. These multicenter π-stacking bonds present a number of unusual characteristics, one being that the contact distances are shorter than the classical van der Waals (vdW) distances [34]. They also present some characteristics of covalent bonds: These bonds are typically significantly stronger than vdW contacts and have ESR-silent diamagnetic character providing evidence for

electron pairing [35]. Those observations are coherent with the molecular orbital description of the phenomenon, where two singly occupied molecular orbitals (SOMOs) overlap to form a bonding inter-molecular orbital between the two molecules, like the electron pair in a covalent bond (Fig. 1), in a *trough space* fashion across the vdW separation. However, those bonds are much weaker than conventional bonds and are longer than covalent ones (for example, the CC covalent distance is 1.54 Å, while pancake bonds are around 3.1 Å). They also often retain a diradicaloid character [35].

Combining these two concepts, it may be interesting to look into highly π-conjugated molecules for intramolecular orbital interactions with significant overlap across the vdW separation triggered by a redox charge transfer (CT) process. The candidates must present possibilities of π–π stacking, and therefore, aromatic helical molecules are very appealing. In the past, helical structures were already envisaged for molecular actuation, for example helicene [36] and *o*-phenylene [37–39]. The helical architecture is attractive because the helical molecule holds the π-electron network in place and is ready made for through space bonding and antibonding interactions that is then exploited for redox actuation. The critical question is whether for any given helix, there is sufficient frontier orbital overlap matching across the pitch. Given the subtle dependency of this overlap as a function of the molecular architecture, only computations at the appropriate level can help select systems for this goal.

In this paper, we will present computational results for helicene-like molecules testing the idea whether such an architecture could be exploited for molecular redox actuation using the π–π overlap across the space of the helical pitch. We selected systems from components for which crystal structures have been reported in the literature (Fig. 2).

A quantitative measure of a molecular actuator is the magnitude of geometrical change as function of the amount and sign of the charge transferred to the molecule, q, in terms of the number of electrons added ($X^{|q|-}$, reduction) or removed ($X^{|q|+}$, oxidation), and the following formula can be used to characterize them:

$$s(q) = \frac{\Delta l(q)}{l} \times 100\,\% \tag{1}$$

where s is the (linear) strain, defined as the ratio of the change $\left[\Delta l = l(q) - l(0)\right]$ to the length (l) in a given direction [42]. Addition or removal of electrons leads normally to Coulombic repulsion ($\propto 1/r$, where r is the distance between two charges), and therefore, for most systems, this strain is positive. We will then show that the systems listed in Fig. 2 display significant s values for at least one direction of CT, which can be used to design molecular actuators triggered by redox processes with strain values comparable to those obtained previously for other systems [1].

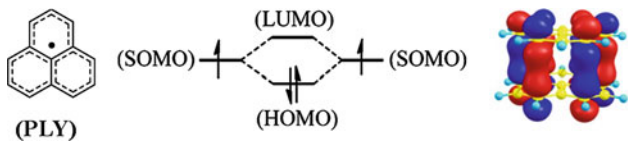

Fig. 1 Orbital interaction diagram between two π-radicals, example of the phenalenyl (PLY) with the representation of the HOMO with strong bonding interaction across the vdW separation in the dimer [35]

2 Computational methodology

In this paper, we will focus on molecules **1b**, **2b**, and **3**. **1b** was chosen instead of **1a**, for which the methyl units can cause steric hindrance, and **2b** is longer than the experimentally available **2a** presenting a minimal length so that at least part of the molecule overlaps with another part of the molecule in a π–π stacking fashion. All structures were

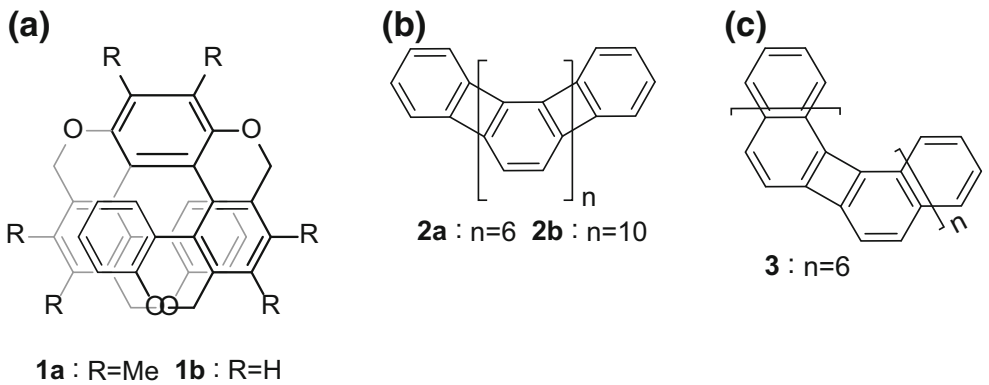

Fig. 2 Structures of the helicene-like molecules: **a** sketch of helicene incorporating saturated sp^3 carbons, distorted metric shows connectivity (**1a** from Kimura et al. [40]). **b** Heliphene (**2a** from Han et al. [41]) and **c** heliphene with naphthalene units

optimized using density functional theory at the UM05-2X/6-31G(d,p) level, for charges going from +2 to −2, except for **2b**, which was optimized at the (R)M05-2X/6-31G(d,p) level. The M05-2X functional is a hybrid functional with 52 % of Hartree–Fock exchange [43], which was previously found to give accurate results for conjugated systems with pancake bonds [44]. We found that the restricted and unrestricted levels give geometries in close agreements with each other. We obtained zero spin densities in all cases when there was a good overlap across the helical pitch. For this reason, calculations at the unrestricted level provided no new information. The structures present a C_2 symmetry, except for $\mathbf{1b}^{2+}$. All calculations were performed using the Gaussian 09 package [45]. We used the graphics program ChemCraft [46].

To characterize such structures, we have used three different approaches which are listed below. The Cartesian coordinates (x, y, z) of the ith atom of a helix are given by the parametric Eq. (2),

$$\begin{cases} x_i = r_i \cos\theta_i \\ y_i = r_i \sin\theta_i \\ z_i = \dfrac{p_i}{2\pi}\theta_i \end{cases} \tag{2}$$

where θ_i is the angle (in radian), r_i is the radius (in Å), and p_i the pitch (in Å) of the helix (width of one complete helical turn, measured parallel to the axis of the helix along the axis, Fig. 3) [47].

Many helical molecules lack perfect "helical staircases" in which repeat units would be perpendicular to the helical axis making it necessary to define an average pitch value. Due to this and due to end effects, we used three alternative measures for the change of the pitch and l: $\bar{p}$, Δz, and $\overline{d_{CC}}$, as defined below. These are based on the atomic numbering for the carbon atoms located in the inner part of the helices (Figs. 4, 5, 6), because we found that those carbons showed the largest changes in contact distances as they respond to CT. Note that the two first and last carbons of **2b** and **3** are not considered, because the terminal regions deviate most from the helical symmetry.

The three measures used for the quantitative description of the changes of the helical geometry are $\bar{p}$, Δz, and $\overline{d_{CC}}$, and they are defined below. The following algorithm was used to obtain average pitch, $\bar{p}$. First, we used Eq. (2) in order to find r_i, θ_i, and p_i for each carbon in each molecular (repeat) units; their indices are listed in Table 1. Then, the average radius, $\bar{r}$, is retrieved from the average of all r_i values. $\bar{p}$ is calculated by taking the slope (and forcing the trend line to pass through zero) of the graph of z_i with respect to θ_i. The reason for choosing this algorithm is that we observed that directly averaging p_i leads to a strong dependency on the choice of the Z axis for the molecule producing large standard deviations. In this paper, the Z axis is chosen by taking

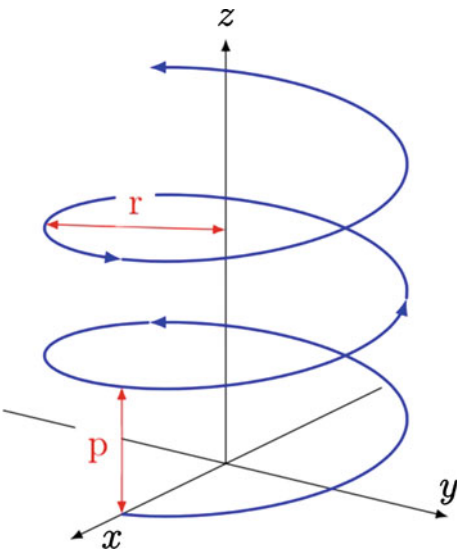

Fig. 3 Definition of the helical axis and parameters, with r the radius and p the pitch

the mean vector that passes through the centers of the circles determined for each consecutive three carbons listed in Table 1. $\bar{p}$ and $\bar{r}$ give therefore quantitative measures of the global conformational changes induced by CT.

Another metric is Δz, the difference in the z coordinates of the first and the last atom considered in the previous process (bold indices in Table 1). Finally, since the lowest intramolecular C···C through space contact distances across the pitch were found to be on the inner part of the molecules, the shortest C···C distances, d_{CC}, were measured, by taking the three shortest contacts for each inner atom (Table S1). An average of these three values, $\overline{d_{CC}}$, was then be evaluated, giving an insight into the overall length change of the molecule. This value should correlate with the average pitch, $\bar{p}$.

To validate this analysis, an error was estimated by measuring the average deviation from helicity, $\bar{D}$, between the coordinates of the carbon in the structure $(x_{C,i}, y_{C,i}, z_{C,i})$ and the one obtained by using Eq. (2) with our $\bar{r}$ and $\bar{p}$, which is the position if the structure was a "perfect helix" (x_i, y_i, z_i):

$$\bar{D} = \frac{1}{N}\sum_i^N D_i \quad \text{with} \qquad D_i = \sqrt{\left(x_i - x_{C,i}\right)^2 + \left(y_i - y_{C,i}\right)^2 + \left(z_i - z_{C,i}\right)^2}. \tag{3}$$

$\bar{D}$ is zero if the structure is a perfect helix, and $\bar{r}$ and $\bar{p}$ fit perfectly, and a large value means structure deviates significantly from a helix.

To characterize the optimized structures, another structural parameter was also used: the bond length alternation (BLA), defined as the mean difference between the

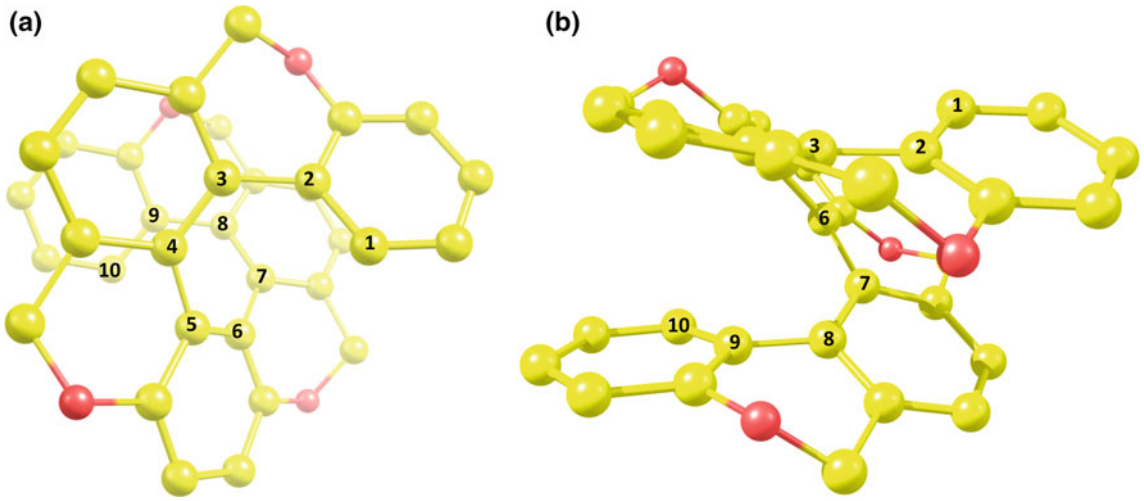

Fig. 4 **a** Top and **b** side view of **1b** with the numbering of the carbons of the inner part. Hydrogens were omitted for clarity. Carbons are in *yellow*, and oxygens in *red*

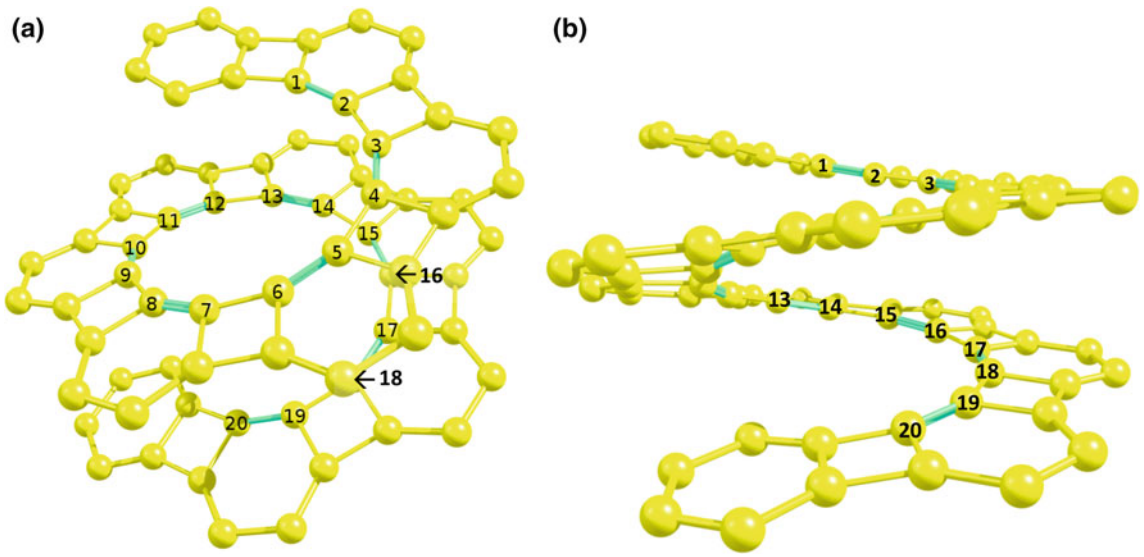

Fig. 5 **a** Top and **b** side view of **2b** with the numbering of the carbons of the inner part. Hydrogens were omitted for clarity. The *green bonds* are shorter than the *yellow ones*, indicating a bond length alternation pattern

single- and double-bond lengths [48]. For a π-conjugation path containing N carbon–carbon bonds, it reads

$$\mathrm{BLA} = \frac{1}{N-1}\sum_{j=1}^{N-1}\left(l_{j+1} - l_j\right)(-1)^j \tag{4}$$

where l_i is the length of bond i. For an aromatic structure, BLA > 0, and for quinonoid ones, BLA < 0 starting with a short bond along the conjugation path. Significant changes in BLA due to oxidation or reduction indicate significant electronic structure changes. We note that due to a relatively large exact exchange contribution in the M05-2X functional, the computed BLA values are expected to be somewhat overestimated [49].

Considering a CT of adding electrons to the lowest unoccupied molecular orbital, LUMO, or removing them from the highest occupied molecular orbital, HOMO, two major effects should be considered. The orbital effect can lead to both positive and negative strain depending on the bonding or antibonding nature of the frontier orbital in

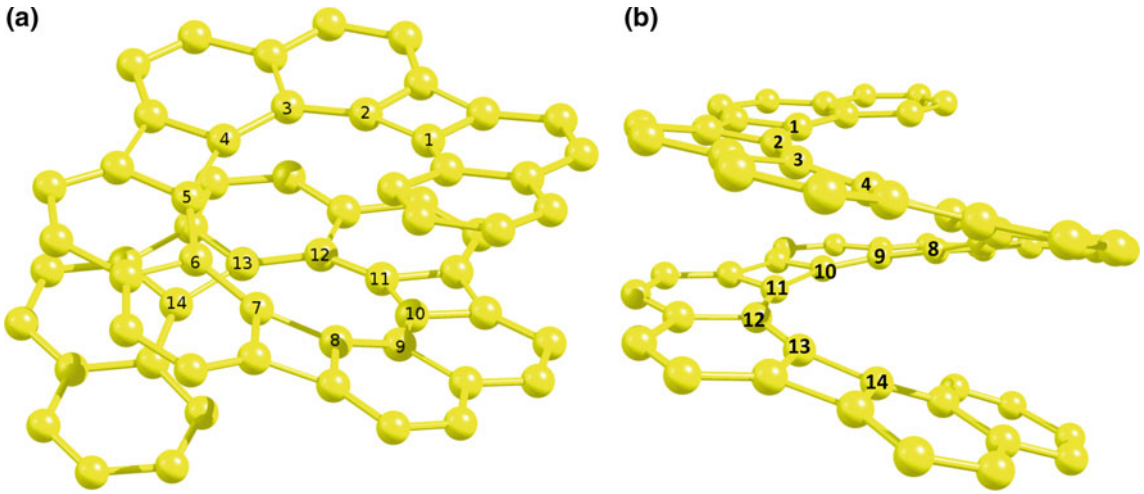

Fig. 6 **a** Top and **b** side view of **3** with the numbering of the carbons in the inner part. Hydrogens were omitted for clarity

Table 1 Index of the carbons (numbering as defined in Figs. 4, 5, and 6) considered in the helix analysis, and total number of carbons included in the average radius, $\bar{r}$

	Index of the carbons	Total number
1b	**1**, 3, 5, 7, **9**	5
2b	**2**, 4, 6, 8, 10, 12, 14, 16, **18**	9
3	**2**, 5, 8, 11, **14**	5

Initial and final carbons for the calculation of Δz are bolded

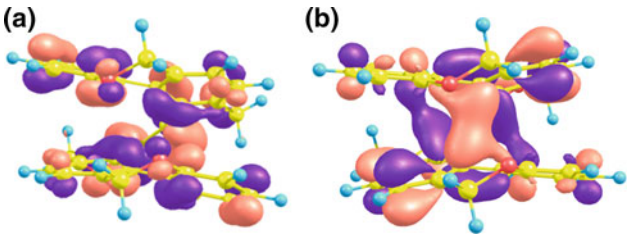

Fig. 7 HOMO of **a 1b** and **b** $\mathbf{1b}^{2-}$. Isosurface was generated with a contour value of 0.030 a.u

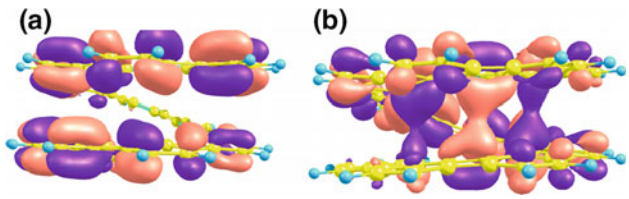

Fig. 8 HOMO of **a 2b** and **b** $\mathbf{2b}^{2-}$. Isosurface was generated with a contour value of 0.021 a.u

question. In addition to the orbital effect, the additional charge is delocalized according to the HOMO or LUMO.

3 Results and discussion

3.1 Changes of the geometry due to CT

All three target molecules show actuation effects upon charging as reflected by the differences of the optimized geometries compared to the $q = 0$ optimized geometry as a reference. One feature of pancake bond is the overlap of the two SOMOs to form mc/2e bonds. Figures 7, 8, 9 show that this is also the case in those molecules when optimized with a modification of the number of electrons. Molecules **1b** and **2b** show this behavior under reduction, while **3** present an overlap for both oxidation and reduction.

Note that the corresponding HOMO–LUMO gaps are large (more than 2.0 eV, see Table S3), while they tend to be small in the case of pancake bonding (Fig. 1). Also, the presence or absence of overlap does not seem to affect the energy levels significantly. As a result, other metrics are to be used for these systems.

3.2 Comparison of the different metrics

Table 2 reports the radius and the average deviation from helicity, using Eq. (3), for each charge state of the 3 molecules. As mentioned, the overlap goes with a shrinking of the distances along the Z axis, as reported in Table 3 for the metric defined in the previous section.

From Table 2, one can see that the CT affects the radius by a few %. Note that the larger radius difference between **2b** and **3** is due to the change from the phenyl units to naphthalenes, and those two molecules have a larger radius than **1b**, due to the presence of unsaturated carbons in

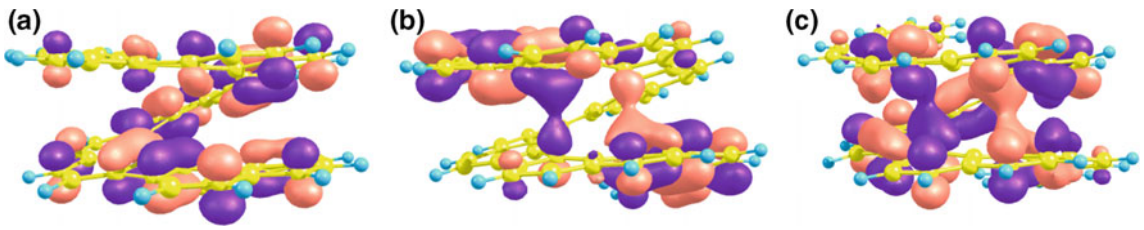

Fig. 9 HOMO of **a 3**, **b** $\mathbf{3^{2+}}$ and **c** $\mathbf{3^{2-}}$. Isosurface was generated with a contour value of 0.030 a.u. for the neutral and oxidized molecule (**a**, **b**), and 0.025 a.u. for the reduced molecule (**c**)

Table 2 Average radius, $\bar{r}$ (Å), and its standard deviation, $\sigma_{\bar{r}}$ (Å), average deviation from helicity, $\bar{D}$ (Å), and its standard deviation, $\sigma_{\bar{D}}$, for **1b**, **2b**, and **3** in different charge states

	Neutral				$q = +2$				$q = -2$			
	$\bar{r}$	$\sigma_{\bar{r}}$	$\bar{D}$	$\sigma_{\bar{D}}$	$\bar{r}$	$\sigma_{\bar{r}}$	$\bar{D}$	$\sigma_{\bar{D}}$	$\bar{r}$	$\sigma_{\bar{r}}$	$\bar{D}$	$\sigma_{\bar{D}}$
1b	1.347	0.040	0.033	0.023	1.345 (−0.2)	0.046	0.042	0.025	1.384 (2.7)	0.038	0.030	0.023
2b	2.903	0.040	0.054	0.027	2.784 (−4.1)	0.174	0.156	0.082	3.120 (7.5)	0.058	0.109	0.062
3	2.189	0.100	0.092	0.049	2.129 (−2.8)	0.100	0.082	0.062	2.011 (−8.1)	0.168	0.165	0.051

For the charged molecules, the percentages of change in the radius from the neutral ones are given in parentheses

Table 3 Changes upon charge transfer of various measures of the molecular length: average pitch, $\bar{p}$ (Å), Δz (Å), and carbon–carbon intramolecular distances, $\overline{d_{CC}}$ (Å), for **1b**, **2b** and **3**

	Neutral			$q = +2$			$q = -2$		
	$\bar{p}$	Δz	$\overline{d_{CC}}$	$\bar{p}$	Δz	$\overline{d_{CC}}$	$\bar{p}$	Δz	$\overline{d_{CC}}$
1b	3.299	4.352	3.378	3.258	4.254	3.334	3.130	4.046	3.182
2b	3.561	4.431	3.688	3.402	4.415[a]	3.884	3.437	3.982	3.500
3	3.308	4.030	3.422	3.148	3.939	3.273	3.246	4.283	3.373

[a] Underlined numbers refer to cases where the helicity is partially lost due to CT (see text)

Table 4 Computed strain due to CT, $s(q)$ (in %), using the three different metrics for **1b**, **2b**, and **3**

	$q = +2$			$q = -2$		
	$s_{\bar{p}}$	$s_{\Delta z}$	$s_{\overline{d_{CC}}}$	$s_{\bar{p}}$	$s_{\Delta z}$	$s_{\overline{d_{CC}}}$
1b	−1.24	−2.25	−1.30	**−5.11**	**−7.02**	**−5.81**
2b	−4.45[b]	−0.35	5.31	**−3.49**	**−10.13**	**−5.09**
3	**−4.82**[a]	**−2.26**	**−4.34**	−1.86	6.28	−1.43

[a] Numbers in bold indicate large actuation (see text)

[b] Underlined numbers indicate partial loss of helicity upon CT (see text)

the latter, which gives more flexibility to the molecule to change its conformation and form the overlap. Under CT, **2b** and **3** undergo a larger change in radius than **1b**. Also, the large standard deviations of the radius for $\mathbf{2b^{2+}}$ and for $\mathbf{3^{2-}}$ (>0.15 Å) indicate that the use of Eq. (2) is more approximate in these cases. This statement is confirmed by the larger average deviations from helicity for those two cases ($\bar{D} > 0.15$ Å).

In Table 3, $\overline{d_{CC}}$ and $\bar{p}$ provide a comparable metric, as expected, but $\overline{d_{CC}}$ is usually larger than $\bar{p}$. The exception is for $\mathbf{2b^{2+}}$ for the reasons mentioned above. It is important to note that in **1b** and **3**, the average pitch is smaller than the carbon–carbon vdW distance (3.4 Å [34]), even for the neutral case. This small through space contact distance is partially responsible for the large actuation effect on the pitch due to CT.

Table 4 lists the strain data for all three systems and both directions of the CT based on Eq. (1) using a subscript to identify which of the three measures of elongation are used. Large strain is obtained for $\mathbf{1b^{2-}}$, $\mathbf{3^{2+}}$, and $\mathbf{2b^{2-}}$. Most of the $s(q)$ values are negative, indicating that the effect is mostly quantum mechanical, and, when negative, in opposition to the Coulombic repulsion due to the extra charge on the molecule. The numbers in bold identify

Table 5 Carbon–carbon intramolecular through space contact distance, d_{CC} (Å), between overlapping carbons (see text for definition) and smallest contact distances for each molecule

	Overlapping carbon number[c]	d_{CC} between overlapping carbons			Smallest d_{CC}		
		Neutral	$q=+2$	$q=-2$	Neutral	$q=+2$	$q=-2$
1b[a]	2···8, 3···9	3.256	3.163, 3.242	**3.030**	3.021	2.975	**2.898**
2b[b]	3···16, (4···17)	3.532	3.822	**3.272**	3.439	3.339	**3.260**
3[b]	2···11, (3···12)	3.188	**3.036**[d]	3.192	3.188	**3.036**	3.137

[a] Due to broken symmetry, two values are given

[b] Due to the C_2 symmetry, only one distance is given (the other pair is given in parentheses)

[c] Carbon numbers refer to Figs. 4, 5, and 6

[d] Numbers in bold indicate large actuation (see text)

Table 6 BLA (Å) for **1b**, **2b** and **3**, calculated by using Eq. (4) for different charge states

	Path definition[a]	BLA		
		Neutral	$q=+2$	$q=-2$
1b	2–9	0.069	0.051	**−0.011**
2b	2–18	0.142	0.136	**0.092**
3	3–6; 6–9; 9–12	0.143	**0.091**[b]	0.089

[a] Carbon numbers refer to Figs. 4, 5, and 6

[b] Bolded numbers indicate the three highest strain systems (see Table 4)

relatively large actuation strains. The number in italics refer to two cases where the helicity is partially lost upon charge transfer, and therefore, the three measures indicate significant discrepancies as we pointed out in connection with the data in Table 4. The large actuation effect is the result of the antibonding nature of the LUMO for **3**, and due to the bonding nature of the HOMO for **1b** and **2b**. The lack of charge symmetry is also apparent as expected for a quantum mechanical mechanism of CT actuation. Molecule $\mathbf{1b^{2-}}$ gives the largest strain values, followed by $\mathbf{3^{2+}}$ and $\mathbf{2b^{2-}}$, if one considers $\bar{p}$ as the measure of the elongation of the molecule. Considering $\overline{d_{CC}}$ confirms that $\mathbf{1b^{2-}}$ is first, but exchanges the order of strains for $\mathbf{3^{2+}}$ and $\mathbf{2b^{2-}}$.

The most significant *through space orbital overlap* is located in the inner part near the C_2 axis of the helix and involves at least four carbons for all three systems, with two pairs of *overlapping carbons* (relation between a pair of overlapping carbon i and j is $\theta_j \approx \theta_i + 360°$, so j is "on top" of i, together with the presence of overlap as shown in Figs. 7, 8, 9). Contact distances are given in Table 5, along with the shortest and/or overlapping contact distances. The values are lower than the average pitch and carbon–carbon distances in Table 4, so one can conclude that local changes are larger than the global changes. Also, except for the reduced $\mathbf{3^{2-}}$, the distances are shorter for the charged molecules with respect to the neutral ones, even if the change is more important when there is an overlap, in comparison with the opposite sign CT (for example, 3.03 Å for $\mathbf{1b^{2-}}$, which present a short contacts with a possibility of a good overlap, vs 3.16 Å for $\mathbf{1b^{2+}}$). Contact distances between overlapping carbons are compatible with the hypothesis of pancake bonds: about 3.00 Å for $\mathbf{1b^{2-}}$ and $\mathbf{3b^{2+}}$ and 3.25 Å for $\mathbf{2b^{2-}}$. The smallest d_{CC} values do not always refer to pairs of overlapping carbons (good overlap would require also the appropriate orientation of the two $2p_z$ atomic orbitals), but short contacts imply that at least one of the four has a good overlap. Therefore, this is the interesting area of the molecule to look at: this is where the actuation is concentrated on.

3.3 Analysis of the molecular strain generated by CT

In Table 6, the BLA values were displayed for both **1b** and **2b**, using Eq. (4) along the path defined by the inner carbons (note that carbons 1 and 10 were omitted in **1b** to start the BLA path with the "short" bond). This analysis is not possible for **3**, because the alternation of single and double bonds is modified by the presence of the naphthalene units. Therefore, another approach was used for **3**: For each 4-membered ring that links two naphthalene units, the inner bond was considered along with its two neighbors, and the average of the length of the two double bonds were subtracted from the length of the single bond. Then, these three values were averaged.

The BLA is lower in the charged systems, so those systems tend to change toward their quinonoid forms, but this decrease in the BLA is more significant if there is an overlap as it is the case for the tree bolded values in Tables 4 and 6 . A BLA change is interpreted as an increase in the π-conjugation, and one can conclude that the form which presents an overlap is more π-conjugated, which is coherent with the large delocalization of the HOMOs in Figs. 7, 8 and 9. For example, a representation of the quinonoid structure of $\mathbf{1b^{2-}}$ is illustrated in Fig. 10.

In Table 7, results from a Mulliken population analysis are given on the respective HOMOs of each three q values, in order to quantify the overlap pictured in Figs. 7, 8, and 9. This sheds light on the participation of the inner part of the structure (see Figs. 4, 5, 6 for the definition) and the 4 atoms that were reported to overlap above in Table 5.

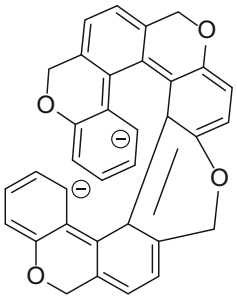

Fig. 10 A representation of the quinonoid structure of $\mathbf{1b}^{2-}$. Distorted metric is used to show the connectivity

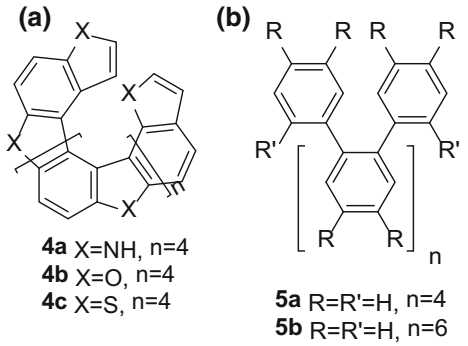

Fig. 11 Alternative helicene-like molecule considered in this work: **a** heterohelicenes (Nakagawa et al. [50] for $n = 3$, X = S) and **b** polymeric *o*-phenylenes (Ohta et al. [39] for $n = 6$, R = OMe and $R' = NO_2$)

This population analysis gives a percentage which is proportional to the presence of the HOMO electrons in a given region of the space. In Table 7, the values for the neutral molecule are low, but when there is CT, a non-negligible part of the population (between 10 and 25 %) is located on the four carbons mentioned in Table 5 in correlation with the presence of an overlap. In that case, the participation of the inner part of the helix accounts for between 38 and 54 % of the population of the orbital. This is in agreement with the previous presented observations as well as the presence of overlaps across the helical pitch as pictured in Figs. 7, 8, and 9.

4 Further systems studied

We have studied (at the same level of theory) five analogous conjugated helical systems with similar architectures which are illustrated in Fig. 11.

Table 8 lists the average deviation from helicity for each systems which is quite large for these systems (larger than in Table 2), making the values difficult to interpret in terms of a helix.

Table 9 gives the calculated strain values using $\bar{p}$, as well as BLA values at different oxidation states. For BLA, the same path definition was used as before: only the inner part of the helix was considered, with the exclusion of the first and the last repeat unit.

The main result from this table is that two systems display large computed actuation values: $\mathbf{4b}^{2+}$ and $\mathbf{5a}^{2-}$. The large positive actuation value for $\mathbf{5a}^{2-}$ indicates that the electrostatic repulsion is not being reduced by an orbital effect which partially explains the actuation in this case. The significant negative actuation value for $\mathbf{4b}^{2+}$ is in concordance with strong bonding interaction displayed in Fig. 12. Except for this case, structures **4** and **5** miss an overlap in their frontier orbitals with CT.

While we did not find one general reason for the lack of orbital overlap-based charge transfer actuation for the molecules in Fig. 11, a pattern arises: Heteroatoms (for example sulfur) on the periphery in **4** tend to have X···X contacts larger than vdW distances, and for this reason, the overlap across the pitch is small. In the case of **5**, the actuation reported by Ohta et al. [39] via oxidation is confirmed by our calculations (**5b**), but this is probably due to a reduction in the length of inter-phenyl bond lengths, as shown by the reduction in the BLA value. Note that the large positive strain value for $\mathbf{5a}^{2-}$ is partially related to the large deviation from the helical structure (as shown in Table 8, with $\bar{D} > 0.90$ Å), probably due to the presence of less phenyl rings to constrain the structure. Concerning $\mathbf{4b}^{2+}$, the strain is negative, but the large $\bar{D} = 0.14$ Å value for **4b** indicates a large deviation from helicity. Also, the pitch

Table 7 Percentage of the HOMO localized on the 4 carbons that present a direct overlap ("4 carbons" as defined in Table 5) and localized on the inner part of the helix ("Inner part" as defined in Figs. 4, 5, 6) for molecules **1b**, **2b**, and **3**, using a Mulliken population analysis

	Neutral		$q = +2$		$q = -2$	
	4 carbons	Inner part	4 carbons	Inner part	4 carbons	Inner part
1b	7(2)	26 (10)	11 (2)	20 (5)	**16 (4)**	**48 (10)**
2b	0 (0)	1 (1)	0 (0)	4 (1)	**10 (4)**	**54 (18)**
3	6 (2)	34 (10)	**22 (4)**[a]	**38 (7)**	14 (4)	30 (10)

The number of carbons involved in this percentage is given in parentheses

[a] Bolded numbers refer to the three highest strain systems

Table 8 Average deviation from helicity, $\bar{D}$ (Å), and its standard deviation, $\sigma_{\bar{D}}$, for **4a–c**, and **5a**–**b** in different charge states

	Neutral		$q = +2$		$q = -2$	
	$\bar{D}$	$\sigma_{\bar{D}}$	$\bar{D}$	$\sigma_{\bar{D}}$	$\bar{D}$	$\sigma_{\bar{D}}$
4a	0.122	0.066	0.107	0.053	0.107	0.055
4b	0.140	0.068	0.090	0.039	0.106	0.039
4c	0.125	0.051	0.112	0.045	0.127	0.055
5a	0.350	0.042	0.441	0.063	0.914	0.144
5b	0.051	0.022	0.077	0.039	0.122	0.024

Table 9 Strain values due to CT $[s_{\bar{p}}(q)$ in %$]$ and bond length alternation (BLA, in Å) for **4a**–**4c** and **5a**–**5b** for different charge states

	$s_{\bar{p}}$		BLA		
	$q = +2$	$q = -2$	Neutral	$q = +2$	$q = -2$
4a	0.09	0.20	0.029	0.047	−0.005
4b	**−7.34**[a]	−2.85	0.040	0.005	−0.008
4c	−0.89	1.07	0.034	0.023	−0.011
5a	−1.95[b]	**14.77**	0.082	0.040	0.043
5b	−2.74	3.52	0.082	0.051	0.049

[a] Numbers in bold indicate large actuation (see text)

[b] Underlined numbers indicate partial loss of helicity upon CT (based on the values in Table 8, see text)

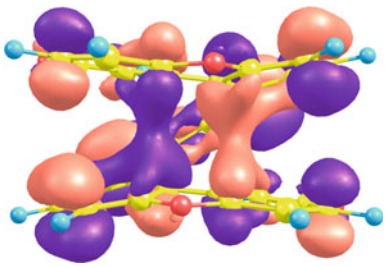

Fig. 12 HOMO of $\mathbf{4b}^{2+}$ (isosurface was generated with a contour value of 0.021 a.u.)

as measured by $\bar{p}$ is 3.24 Å for $\mathbf{4b}^{2+}$, which is larger than $\mathbf{3}^{2+}$ and $\mathbf{1b}^{2-}$ (<3.2 Å, see Table 3) presented before. This partially explains why the effect of the overlap is smaller in this case.

5 Conclusions

In this paper, we discussed the charge transfer actuation mechanism in helical conjugated molecules. We find significant actuation values for molecules with repeat units that appear to be synthesizable.

Molecules **1b** and **2b** present a large strain under reduction, while a large strain is obtained under oxidation for **3**. This change of the number of electrons is accompanied with a modification of the radius of the molecule. We discussed three alternative measures for strain in a helix pointing out the limitations of these metrics when the structure deviates from an exactly helical shape. The strains are significant and larger than 5 % with two electrons added or removed, which is comparable to other values in the literature.

The shrinking generated by CT is accompanied by a large modification of the BLA, with a clear shift toward a quinonoid structure. The strain caused by CT is strongly correlated with the presence of an across the pitch overlap in the relevant frontier orbital. This overlap is concentrated in the inner parts of the molecules.

In the oxidized or reduced systems, there are some hints of the presence of a pancake bonding, but there are some significant differences. First, the structure presents no spin densities when there is an overlap. It was also mentioned that the HOMO–LUMO gaps are large in these systems, which is generally not the case with pancake bonds. Therefore, what is observed for **1b**, **2b**, and **3** should be more thought of as a *through space* interactions rather than pancake bonds.

$\mathbf{4b}^{2+}$ and $\mathbf{5a}^{2-}$ also show large actuation values. While the mechanisms vary, the presented examples indicate that various helical molecules should show electromechanical actuation effects similar to the ones described in this paper and that the order of this effect should be several percent strain per electron transferred.

Acknowledgments P. B. is grateful to the *Fond d'aide à la mobilité étudiante* (FAME) for a FAME/BMI traineeships grant and a Visiting Scientist Fellowship to Georgetown University. We thank the U S National Science Foundation for its support of this research at Georgetown University (Grant Number CHE-1006702). MK is member of the Georgetown Institute of Soft Matter.

References

1. Baughman RH (2005) Science 308:63–65
2. Mirfakhrai T, Madden JDW, Baughman RH (2007) Mater Today 10:30–38
3. Göpel W (1991) Sens Actuators B Chem 4:7–21

4. Smela E (2003) Adv Mater 15:481–494
5. Terao F, Morimoto M, Irle M (2012) Angew Chem Int Ed 51:901–904
6. Ebron VH, Yang Z, Seyer DJ, Kozlov ME, Oh J, Xie H, Razal J, Hall LJ, Ferraris JP, MacDiarmid AG, Baughman RH (2006) Science 311:1580–1583
7. Yu HH, Swager TM (2004) IEEE J Ocean Eng 29:692–695
8. Marsella MJ, Reid RJ (1999) Macromolecules 32:5982–5984
9. Barboiu M, Vaughan G, Kyritsakas N, Lehn JM (2003) Chem Eur J 9:763–769
10. Juluri BK, Kumar AS, Liu Y, Ye T, Yang YW, Flood AH, Fang L, Stoddart JF, Weiss PS, Huang TJ (2009) ACS Nano 3:291–300
11. Huang TJ, Brough B, Ho C-M, Liu Y, Flood AH, Bonvallet PA, Tseng H-R, Stoddart JF, Baller M, Magonov S (2004) Appl Phys Lett 85:5391
12. Madden JD, Cush RA, Kanigan TS, Brenan CJ, Hunter IW (1999) Synth Met 105:61–64
13. Madden JD, Cush RA, Kanigan TS, Hunter IW (2000) Synth Met 113:185–192
14. Qi B, Lu W, Mattes BR (2004) J Phys Chem B 108:6222–6227
15. Tahhan M, Truong V-T, Spinks GM, Wallace GG (2003) Smart Mater Struct 12:626–632
16. Han G, Shi G (2004) Sens Actuators B Chem 99:525–531
17. Baughman RH (1999) Science 284(80):1340–1344
18. Bissell RA, Córdova E, Kaifer AE, Stoddart JF (1994) Nature 369:133–137
19. Credi A, Balzani V, Langford SJ, Stoddart JF (1997) J Am Chem Soc 119:2679–2681
20. Tseng HR, Vignon SA, Stoddart JF (2003) Angew Chem Int Ed 42:1491–1495
21. Badjic JD, Balzani V, Credi A, Silvi S, Stoddart JF (2004) Science 303:1845–1849
22. Tian YH, Kertesz M (2009) Chem Mater 21:2149–2157
23. Song C, Swager TM (2008) Org Lett 10:3575–3578
24. Chebny VJ, Shukla R, Lindeman SV, Rathore R (2009) Org Lett 11:1939–1942
25. Scherlis DA, Marzari N (2005) J Am Chem Soc 127:3207–3212
26. Goto K, Kubo T, Yamamoto K, Nakasuji K, Sato K, Shiomi D, Takui T, Kubota M, Kobayashi T, Yakusi K, Ouyang JY (1999) J Am Chem Soc 121:1619–1620
27. Zheng SJ, Lan J, Khan SI, Rubin Y (2003) J Am Chem Soc 125:5786–5791
28. Small D, Rosokha SV, Kochi JK, Head-Gordon M (2005) J Phys Chem A 109:11261–11267
29. Zaitsev V, Rosokha SV, Head-Gordon M, Kochi JK (2006) J Org Chem 71:520–526
30. Haddon RC (2012) ChemPhysChem 13:3581–3583
31. Suzuki S, Morita Y, Fukui K, Sato K, Shiomi D, Takui T, Nakasuji K (2006) J Am Chem Soc 128:2530–2531
32. Tian YH, Kertesz M (2010) J Am Chem Soc 132(31):10648–10649
33. Cui ZH, Lischka H, Beneberu HZ, Kertesz M (2014) J Am Chem Soc 136:5539–5542
34. Bondi A (1964) J Phys Chem 68:441–451
35. Mou Z, Uchida K, Kubo T, Kertesz M (2014) J Am Chem Soc 136:18009–18022
36. Rempala P, King BT (2006) J Chem Theory Comput 2:1112–1118
37. Mathew SM, Hartley CS (2011) Macromolecules 44:8425–8432
38. Mathew SM, Engle JT, Ziegler CJ, Hartley CS (2013) J Am Chem Soc 135:6714–6722
39. Ohta E, Sato H, Ando S, Kosaka A, Fukushima T, Hashizume D, Yamasaki M, Hasegawa K, Muraoka A, Ushiyama H, Yamashita K, Aida T (2011) Nat Chem 3:68–73
40. Kimura Y, Fukawa N, Miyauchi Y, Noguchi K, Tanaka K (2014) Angew Chem Int Ed 53:8480–8483
41. Han S, Bond AD, Disch RL, Holmes D, Schulman JM, Teat SJ, Vollhardt KPC, Whitener GD (2002) Angew Chem Int Ed 114:3357–3361
42. Sun G, Kürti J, Kertesz M, Baughman RH (2002) J Am Chem Soc 124:15076–15080
43. Zhao Y, Schultz EN, Truhlar DG (2006) J Chem Theory Comput 2:364–382
44. Beneberu HZ, Tian TH, Kertesz M (2012) Phys Chem Chem Phys 14:10713–10725
45. Frisch MJ et al (2013) Gaussian 09, Revision D.01. Gaussian Inc., Wallingford
46. Zhurko GA, Zhurko DA Chemcraft, Version 1.8 (2015). http://Chemcraftprog.com
47. Helix, in Wolfram Mathworld. http://mathworld.wolfram.com/Helix.html. Accessed on 13 May 2015
48. Longuet-Higgins HC, Salem L (1959) Proc R Soc A Math Phys Eng Sci 251:172–185
49. Kertesz M, Choi CH, Yang SJ (2005) Chem Rev 105:3448–3481
50. Nakagawa H, Yoshino J, Yamada K, Shiro M (2003) Chem Lett 32:90–91

Theor Chem Acc (2015) 134:117
DOI 10.1007/s00214-015-1717-4

REGULAR ARTICLE

Atoms and bonds in molecules: topology and properties

Jessica E. Besaw[1] · Peter L. Warburton[1] · Raymond A. Poirier[1]

Received: 12 June 2015 / Accepted: 1 September 2015 / Published online: 18 September 2015

Abstract The atoms and bonds in molecules (ABIM) theory Warburton et al. (J Phys Chem A 115:852, 2011) partitions the molecular electron density into atomic and bonding regions using radial density. The concept is motivated by the radial distribution function of atoms which exhibit shell structure, where each shell contains a realistic number of electrons. In this paper, we define molecular radial density and investigate its topology in 2D planes of halogens, diatomics, and hydrides. The terminology employed to classify the radial density topology of atoms and molecules is then presented. The ABIM model quantifies both the molecular atom and bond. Here, we describe and calculate properties of ABIM and discuss how these properties correlate with expected trends. ABIM makes it possible to calculate the properties of atoms and bonds in molecules including number of electrons, shape, volume, dipole, and expectation values. The radial density model provides an intuitive description of ABIM.

Published as part of the special collection of articles "Festschrift in honour of P. R. Surjan".

Electronic supplementary material The online version of this article (doi:10.1007/s00214-015-1717-4) contains supplementary material, which is available to authorized users.

✉ Raymond A. Poirier
rpoirier@mun.ca

Jessica E. Besaw
jeb150@mun.ca

Peter L. Warburton
peterw@mun.ca

[1] Department of Chemistry, Memorial University, St. John's, NL A1B 3X7, Canada

Keywords Atoms in molecules · Bonds in molecules · Molecular radial electron density · Topology

1 Introduction

The concept of atoms and bonds is ubiquitously employed to predict, interpret, and communicate chemistry [2]. In pursuit of a well-defined molecular atom, numerous atoms in molecules (AIM) theories were developed [1, 3–5]. An AIM theory partitions the molecular electron density into atomic contributions, revealing the properties of each molecular atom [3]. One downfall of most AIM theories is that they fail to explicitly define the bond. In this paper, we seek to develop an atoms and bonds in molecules (ABIM) theory that elucidates the physical and chemical properties of both molecular atoms and bonds.

There are many benefits to quantify atoms and bonds. One motivation for defining molecular atoms is the potential to construct the electron density of larger molecules from a database of appropriate AIM representations, thus greatly reducing computational time and cost [1]. Furthermore, if molecules can be built from AIM representations, it follows that molecular properties could be determined as a combination of AIM properties [1]. We are also motivated to quantify the physical and chemical properties of the bond, such as number of electrons, strength, order (single, double, or triple), type (ionic or covalent), shape, and volume. With this knowledge, we can acquire greater insight into chemical reactions by noting changes in the molecular atom and bond properties.

Many approaches have been developed to define atoms in molecules [3, 6], resulting in much debate about which model is the most realistic. One contentious issue is whether or not the electron density of the AIM overlaps.

The most widely used approach is Bader's quantum theory of atoms in molecules (QTAIM), which depicts AIM as nonoverlapping [3, 7–10]. Other popular models, such as those of Stewart [4, 11] and Hirshfeld [5], depict AIM as overlapping spherical fuzzy electron densities. Both the advantages and disadvantages of these methods have been previously discussed [1].

This paper builds upon the preliminary findings by Warburton et al. [1], which suggest that employing molecular radial density to partition molecules into atomic and bonding contributions may provide a more intuitive scheme to define atoms and bonds. The ABIM model represents AIM as atoms with overlapping electron densities and bonds in molecules (BIM) as the region where this overlap occurs.

Radial density provides a good starting point for an ABIM theory because the atomic radial density, $\mathbf{r}^2\rho(\mathbf{r})$, of a free atom in space has shell structure and contains a realistic number of electrons in each shell. The connection between the number and position of the critical points in the atomic radial density distribution function and the atomic shell structure has been well established [12, 13]. In 1976, Politzer and Parr [12] showed that the minimum in the atomic radial density provides a well-defined and physically meaningful separation of electron density into a core and valence region for the second period atoms. Boyd [13] then established that analogous minimum surfaces are also found for heavier atoms and further showed that the first 54 neutral atoms in their ground state have the expected shell-occupation numbers. Therefore, partitioning the electron density of atoms based on the minimum in radial density is quite effective. By extension, we postulate that a molecular radial density function may effectively partition the molecular electron density in an intuitive and physically meaningful way. However, as Smith pointed out, extension of atomic radial density to molecular systems is not straightforward [14].

Recently, the molecular radial density, $\rho_{\mathrm{rad}}(\mathbf{r}_i)$, at a grid point, $\mathbf{r}_i$, was defined as the sum of the radial densities of all molecular atoms at that grid point as given by Equation 1 [1]. The weight, $W_A(\mathbf{r}_i)$, is a partition function that represents the fraction of density owned by a particular atom in a molecule at each grid point in space at a distance $\mathbf{r}_{iA}$ from atom A. The weight allows us to calculate the electron density distribution associated with each AIM ($W_A(\mathbf{r}_i)\,\rho(\mathbf{r}_i) = \rho_A(\mathbf{r}_i)$). In particular, the Becke weight is employed in this paper, which defines the ownership of each point in the molecular space based on $\mathbf{r}_{iA}$ and the atomic Bragg–Slater radii [15].

$$\begin{aligned}\rho_{\mathrm{rad}}(\mathbf{r}_i) &= \sum_{A}^{N_A} \mathbf{r}_{iA}^2\; W_A(\mathbf{r}_i)\;\rho(\mathbf{r}_i) \\ &= \sum_{A}^{N_A} \mathbf{r}_{iA}^2\;\rho_A(\mathbf{r}_i) \quad 0 \le W_A(\mathbf{r}_i) \le 1\end{aligned} \tag{1}$$

It is necessary to point out that any weighting scheme that partitions the molecular space into atomic contributions can be used, and the Becke weight is just one of many possible choices. Other possibilities include Hilbert space decomposition (e.g., Mulliken) and 3D space partitioning (e.g., QTAIM [3]). The Becke weight was originally chosen to partition the molecular space because of its simplicity and ease of implementation. One additional benefit of the Becke weight is that it does not employ spherical averaging, and thus, distortion of atoms upon bonding can be investigated.

The molecular radial density along the internuclear axis has been studied previously [1]. This paper looks at the radial density in 2D planes of various molecules which reveal topologically interesting features residing off the internuclear axis. We also present the terminology employed to classify the radial density topology of atoms and molecules. Most importantly, properties of ABIM will be calculated and discussed.

2 Methodology

All the calculations were performed with the program MUNgauss [16]. The molecular electron and radial densities were calculated at HF/6-311++G(d,p)// HF/6-311++G(d,p), specifically using RHF for closed shell and ROHF for open-shell molecules. All of the visual aids, including contour, relief, and gradient plots, were created using the Mathematica version 9.0 graphing package. The gradient vector field plots were calculated in Mathematica from input radial density data.

Throughout this paper, length is given in bohr, radial density (ρ_{rad}) is given in e/bohr, the gradient of radial density ($\nabla\rho_{\mathrm{rad}}$) is given in e/bohr^2, and electron density is in e/bohr^3. The terms ρ_{rad}, $\nabla\rho_{\mathrm{rad}}$, and $\nabla^2\rho_{\mathrm{rad}}$ are all calculated analytically using MUNgauss. Please see supporting information for the derivation of $\nabla\rho_{\mathrm{rad}}$ and $\nabla^2\rho_{\mathrm{rad}}$.

For both atoms and bonds, the shape ($\mathbf{S}'_{\mathbf{o}}$ in bohr) and volume (V_o in bohr^3) were calculated using Eqs. 2–5. In Eq. 2, $\mathbf{S_o}$ is calculated at a specified origin: the nuclear position for AIM and the radial bond critical point for BIM. $\mathbf{S}_o$ can be diagonalized as in Eq. 3, which results in the diagonal matrix shown in Eq. 4. The eigenvalues correspond to principal axes of the electronic second moment. The shape of the atom or bond is defined as (S_x^o, S_y^o, S_z^o), where $S_i^o = \sqrt{\langle i^{2\prime}\rangle_o}$. Using the eigenvalues of shape, we can calculate the volume of an atom using Eq. 5. All of the investigated properties (shape, volume, dipole, number of electrons, $\langle r\rangle$ and $\langle r^2\rangle$), are calculated through numerical integration using the standard SG-1 grids [17]. In particular, $\langle r\rangle$ and $\langle r^2\rangle$ can be calculated for atoms using Eqs. 6 and 7, as well as for bonds using Eqs. 8 and 9.

$$\mathbf{S}_o = \begin{pmatrix} \langle x^2\rangle_o & \langle xy\rangle_o & \langle xz\rangle_o \\ & \langle y^2\rangle_o & \langle yz\rangle_o \\ & & \langle z^2\rangle_o \end{pmatrix} \tag{2}$$

$$\mathbf{Q}^{+}\mathbf{S_o}\mathbf{Q} = \mathbf{S}'_o \tag{3}$$

$$\mathbf{S}'_o = \begin{pmatrix} \langle x^{2'}\rangle_o & 0 & 0 \\ & \langle y^{2'}\rangle_o & 0 \\ & & \langle z^{2'}\rangle_o \end{pmatrix} \tag{4}$$

$$V_o = \frac{4\pi}{3} S_x^o S_y^o S_z^o \tag{5}$$

$$\langle r\rangle_A = \int W_A(\mathbf{r})\ \rho(\mathbf{r})\ \mathbf{r}\ d\mathbf{r} \tag{6}$$

$$\langle r^2\rangle_A = \int W_A(\mathbf{r})\ \rho(\mathbf{r})\ \mathbf{r}^2\ d\mathbf{r} \tag{7}$$

$$\langle r\rangle_{A-B} = \int \sqrt{W_A(\mathbf{r})\ W_B(\mathbf{r})}\ \rho(\mathbf{r})\ \mathbf{r}\ d\mathbf{r} \tag{8}$$

$$\langle r^2\rangle_{A-B} = \int \sqrt{W_A(\mathbf{r})\ W_B(\mathbf{r})}\ \rho(\mathbf{r})\ \mathbf{r}^2\ d\mathbf{r} \tag{9}$$

3 Results and discussion

3.1 Radial density

3.1.1 Atomic radial density

The atomic radial density of hydrogen, fluorine, and chlorine is shown in Fig. 1 to illustrate shell structure and electron distribution. The 2D, 3D, contour, and gradient paths of radial density are shown for each atom. The plots reveal that H, F, and Cl have one, two, and three shells, respectively, which matches their period position. An atomic shell is defined here as the region of space bounded between

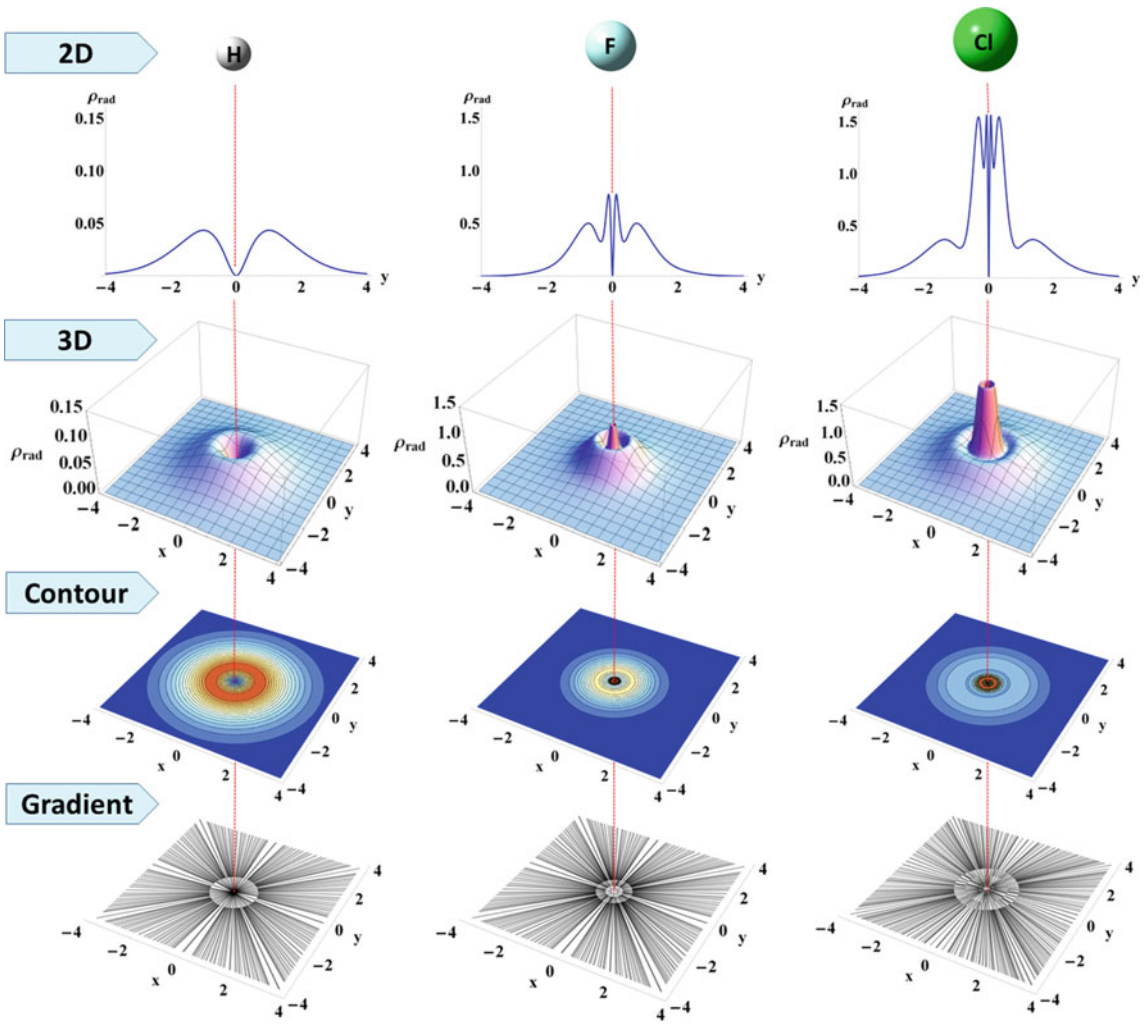

Fig. 1 The 2D (ρ_{rad} vs. x) , 3D (ρ_{rad} vs. x , y) contour (ρ_{rad} vs. x , y), and gradient path ($\nabla\rho_{\text{rad}}$ vs. x , y) plots for the H, F, and Cl atoms

adjacent minima in radial density (numerical values found in Table S1). The outermost shell is the valence shell, while any remaining inner shells are termed core shells. The number of electrons, N_e, found within each shell can be determined by integrating the electron density in the spherical regions between two adjacent radial minima, r_1 and r_2, as shown in Eq. 10. It has been shown that a realistic number of electrons is found within each shell [12, 13]. For example, a neutral chlorine atom has approximately two, eight, and seven electrons in the first, second, and third shells, respectively. The topology, shell structure, and electron distribution of atomic radial density motivated us to define a molecular equivalent for use in the ABIM model.

$$N_e = 4\pi \int_{r_1}^{r_2} r^2 \rho(r) \mathrm{d}r \tag{10}$$

3.1.2 Molecular radial density

The central idea in ABIM is when atoms bond, it is primarily the valence electron density of the bonding atoms that undergoes distortion and overlap to form a bond, while the core electron density remains mostly unaffected [1]. Therefore, the core region of each molecular atom should maintain the same shell structure and electron density as its free-atom counterpart, whereas the distorted valence shell can be investigated to define bonding and nonbonding regions. This makes it possible to determine the number of electrons in each region.

3.1.2.1 Halogens Figure 2a shows the molecular radial density of F_2 along the internuclear axis, alongside the atomic radial density of two undistorted, free F atoms placed at $y = 0$ and $y = 2.509$ bohr to coincide with the fluorine nuclei of the molecule. As expected, the atomic radial density of each fluorine atom has one core and one valence shell. When two fluorine atoms combine to form F_2, three regions are formed: the core, bonding, and nonbonding valence regions. Intuitively, the core regions in the molecular atoms are identical to the core shells in the atom, except close to the interface between the core and the valence regions. The bonding region is found between the nuclei, where the valence shells of the fluorine atoms overlap to form a single shared maximum, which we term the radial bond critical point (RBCP). Note that the ABIM RBCP should not be confused with the BCP based on electron density (DBCP). The nonbonding valence is classified as the region outside the internuclear region where the valence shells of the fluorine atoms do not overlap.

The molecular radial density in a plane of the F_2 molecule is shown in Fig. 2c, which uncovers more topologically interesting features. For clarity, the radial density along the internuclear axis has been superimposed on this

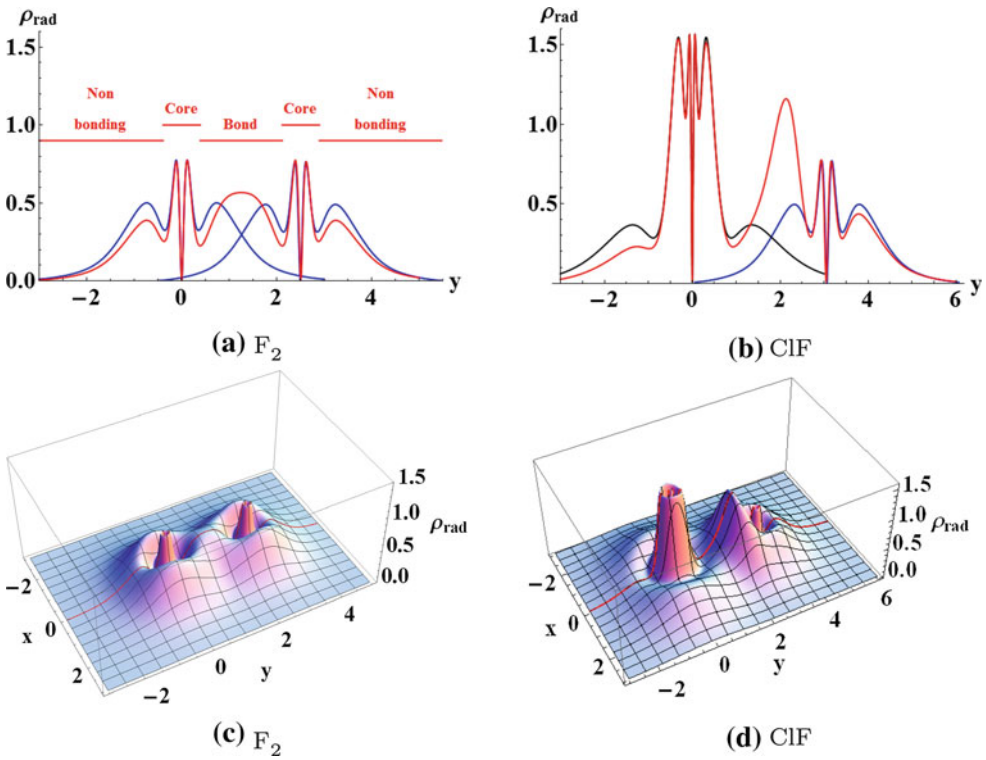

Fig. 2 **a** The radial density of a F_2 molecule along the internuclear axis, with two free F atoms superimposed on the two fluorine nuclei. **b** The radial density of a ClF (*red*) molecule along the internuclear axis, with a F atom (*blue*) and Cl atom (*black*) superimposed on their corresponding two nuclei. **c** The radial density of an *xy* cross section of F_2 with the plot from **a** superimposed on it. **d** The radial density of an *xy* cross section of ClF with the plot from **b** superimposed on it

graph in red. The core region of each nucleus is easily identified in this cross section as the symmetrical, volcano-shaped cones that surround the nuclei. The core is separated from the distorted valence by a minimum in radial density. Thus, the boundary between the core and valence shells still exists for the atoms in the molecule.

Unlike the homonuclear diatomic F_2, which has a symmetrical distribution of radial electron density, the heteronuclear diatomic ClF has an asymmetric distribution as predicted due to the unequal sharing of electron density. When Cl (at $y = 0$ bohr) and F (at $y = 3.050$ bohr) combine to form ClF, the single core shell in the F atom and both core shells in the Cl atom remain mostly unchanged in the bonded molecule as shown in Fig. 2b. This figure also shows that the RBCP is skewed toward the fluorine nucleus. This feature makes sense because F is more electronegative than chlorine, and Cl is fairly polarizable. In Fig. 2d, the cross section of the ClF molecule depicts the two core shells for Cl and the single core shell for F.

As shown in Fig. 2, F_2 and ClF show very interesting and intuitive features with respect to the core, bonding, and the nonbonding regions. In the core region, we see that the core shells are transferable from an atom to a molecular atom. In the bonding region, the distorted valence shells overlap to form a bond with a single-bond critical point. There are also topological features, such as the peaks off the internuclear axis that require further investigation.

3.1.2.2 Second period hydrides Hydrogen atoms in molecules can often be problematic to model and detect due to their relatively low electron density. However, although small, hydrogen can undergo very diverse chemistry depending on whether it is anionic, cationic, or neutral. Molecular radial electron density provides an aesthetic way to model hydrogen containing compounds and qualitatively determine the nature of the hydride in these molecules.

The molecular radial density of hydrogen containing compounds is more aesthetically pleasing to model and visualize than electron density. When plotting molecular electron density of hydrogen containing compounds, one must readjust the scale and truncate the electron density of heavier atoms in order to identify the electron density peak of a hydrogen constituent. On the other hand, the molecular radial density function of both hydrogen and heavy atoms can be viewed on the same scale. This is a consequence of the balance between the electron density and the squared distance from the nucleus that allows the valence region to become emphasized and the nuclear region to become less overwhelming in comparison with plotting solely the electron density function. As a result, radial density is generally shown on a scale between 0 and $2\,e/a_o$.

Hydrogen AIM can be easily identified in Figs. 3 and 4, which show the radial density (ρ_{rad}) and the gradient paths of radial density ($\nabla\rho_{\text{rad}}$), respectively, for the second period hydrides. Since hydrogen does not have any core shells, we can easily identify the hydrogen nuclei as points of zero radial density that are surrounded by a single distorted valence shell as shown in Fig. 3. This leads to the depressions ('dimples') seen in the radial density graphs. In Fig. 4, there exists a distinct boundary path that completely encircles each hydrogen nucleus that results in hydrogen having a very similar and easily identifiable shape. Larger versions of the plots found in Figs. 3 and 4 can be found in Figure S1–S16 of the supporting information.

The nature of hydrogen in the second row hydrides is chemically diverse. Crossing the second period from LiH to HF, hydrogen shifts from being anionic in LiH to more covalently bonded in CH_4 to cationic in HF. Ultimately, we would expect the molecular radial density to give insight into the type of bonding (ionic/covalent) and the nature of the hydrogen (cationic/anionic/neutral) in these types of molecules. One promising method for identifying bond type is by analyzing the curvature of the RBCP. In the $\nabla\rho_{\text{rad}}$ plots, the boundary path at the RBCP is concave for LiH and BeH_2, fairly flat for BH_3, CH_4, and NH_3, and convex for H_2O and HF, all with respect to the hydrogen. The observed trend is concave curvature for anionic hydrogen, flat curvature for covalently bonded hydrogen, and convex curvature for cationic hydrogen.

3.2 Topology

3.2.1 Terminology

The radial density of atoms and molecules is rich in topological features such as critical points, critical rings, and critical spheres. These critical architectures can be identified and characterized using the gradient and diagonalized Hessian of radial density, respectively. Each critical feature includes points where the gradient of radial density vanishes ($\nabla\rho_{\text{rad}} = 0$). The classification (point, ring, sphere) and magnitude (maximum, minimum, or saddle) of a critical feature is found by evaluating the diagonalized Hessian of radial density at these points to yield three characteristic eigenvalues that are invariant to coordinate rotation.

The set of eigenvalues $\{\ \lambda_1, \lambda_2, \lambda_3\ \}$ is referred to as a spectrum. For consistency, the following convention is employed to order the eigenvalues: $\lambda_1 \leq \lambda_2 \leq \lambda_3$. The rank and the signature are crucial for classifying critical architecture. The rank (r) is the number of nonzero eigenvalues. A rank of one, two, or three represents a critical sphere, ring, and point, respectively. The signature (s) is the sum of the signs of the three eigenvalues. The sign is $+1$ for a positive eigenvalue, -1 for a negative eigenvalue, or zero for a vanishing eigenvalue. The signature relative to the rank determines whether the

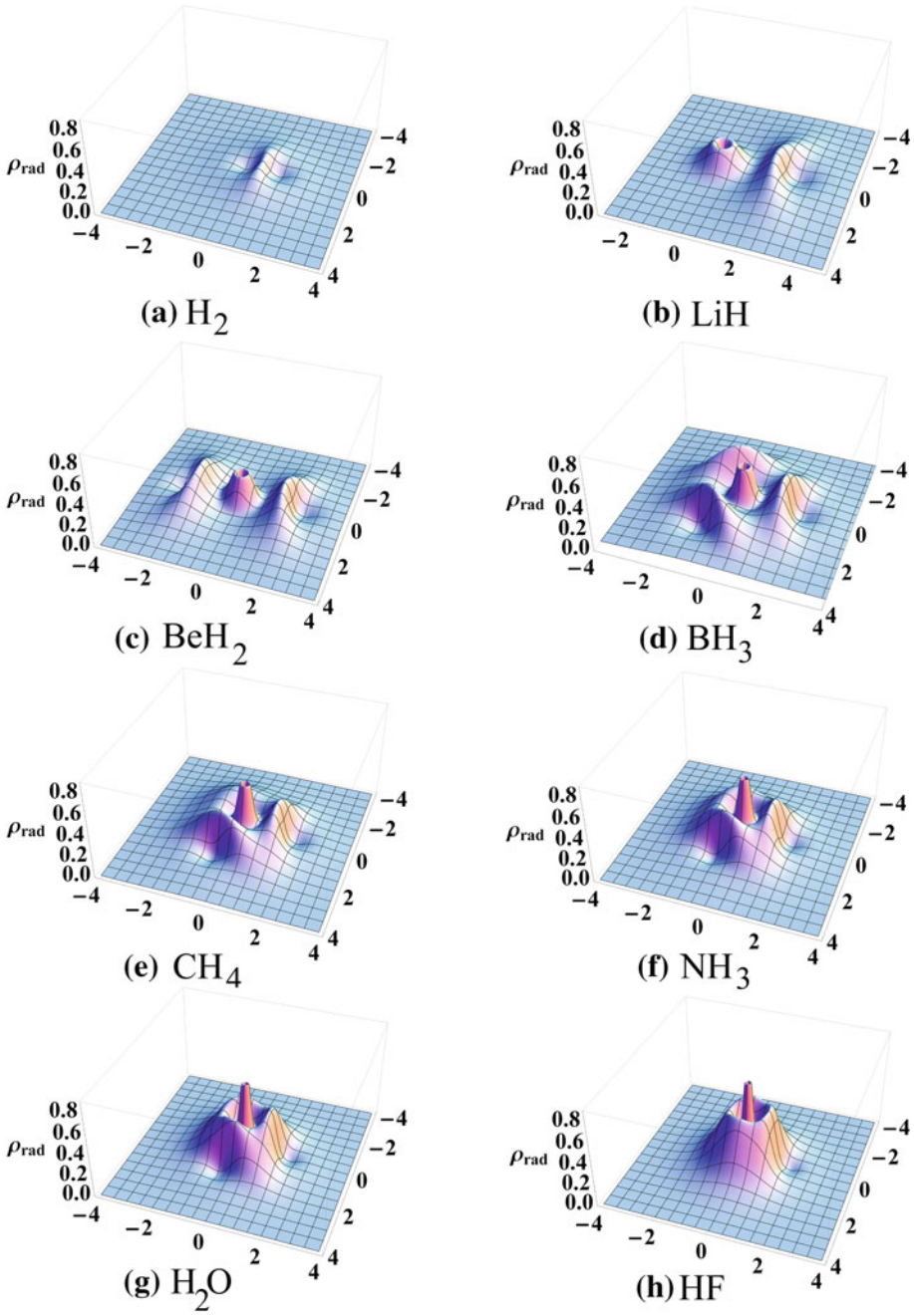

Fig. 3 Radial density in the *xy*-plane of H_2 and the second period hydrides. The central atom is located at (0, 0). The hydrogen nuclei are clearly identified by the distinct depressions (dimples) in the graphs

topological feature is a maximum, minimum, or saddle. If $s = +r$ a minimum results; $s = -r$ denotes a maximum; if $-r < s < r$, a saddle results. The trivial case occurs when rank and signature are identically zero. This represents a critical point at infinity and occurs in all systems at an infinite distance away from the molecule. Table 1 summarizes the ABIM classification of radial density critical architectures.

3.2.2 *Atomic topology*

The radial density topology of atoms is fairly simple, though not featureless. At the nucleus, the radial distance is zero, and thus, a minimum critical point (PM) occurs. Radially outward from the nucleus, a series of maximum critical spheres (SX) and minimum critical spheres (SM) are observed. For atoms in the first three periods, the

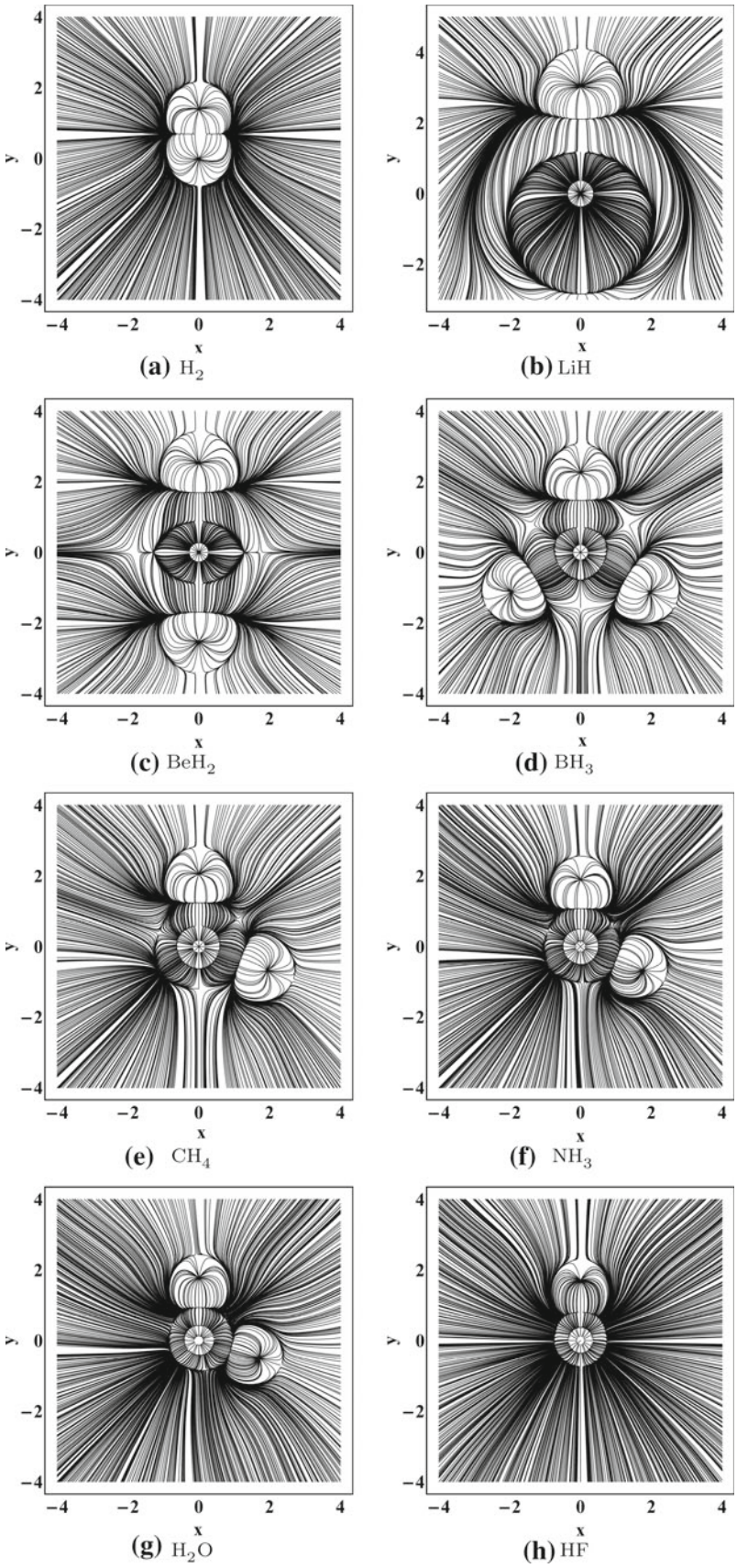

Fig. 4 Map of the gradient vector field of the radial density for the plane containing the maximum number of nuclei. Each line represents a trajectory traced out by the vector $\nabla\rho_{\mathrm{rad}}$. Gradient paths of radial density in the *xy*-plane of the second period hydrides. The central atom is located at (0, 0). The hydrogen nuclei are clearly identified by the distinct boundary path that encloses the nucleus

number of critical spheres observed is related to its period. The number of SX is equivalent to its atomic period, while the number of SM equals one less than the period. The boundary traced out by the minimum critical spheres marks the boundary between adjacent shells for an atom. It can be readily inferred from both the spherical symmetry of atoms and Fig. 1 that the radial density topology for a H, F, and Cl atom have 1, 2, and 3 SXs, as well as 0, 1, and 2 SMs, respectively.

We emphasize that the trend between the atomic period and the number of observed SXs and SMs is limited to the first three periods [14]. In a study by Smith et. al. of the radial density of neutral atoms from hydrogen through uranium, the radial density of atoms that were heavier than the third period exhibited fewer SXs than the actual number of shells [18].

3.2.3 *Molecular topology*

The radial density topology of molecules is more complex than atoms. The topology of the simple F_2 diatomic has numerous critical points and critical rings as depicted in Fig. 5 and described in Table 1. A PM occurs at each F nucleus. Two more PM arise adjacent each F nucleus along the internuclear axis which marks the boundary between the core and valence regions. Also along the internuclear axis, residing in the middle of the two nuclei, is the maximum bond point (PX) depicted in red. This shows a buildup of radial density at the center of the bond. A saddle minimum point (PSM) is found in the nonbonding region for each F atom on the internuclear axis, which is shown as a green point. More interesting features also arise off the internuclear axis including two maximum rings (RX) and two saddle rings (RS).

Table 1 Name, acronym, sign of eigenvalue, rank, and signature for each critical architecture in ABIM

Architecture	Name	Acronym	λ_1	λ_2	λ_3	r	s
Point	Max point	PX	−	−	−	3	−
	Saddle max point	PSX	−	−	+	3	−1
	Saddle min point	PSM	−	+	+	3	+1
	Min point	PM	+	+	+	3	+3
Ring	Max ring	RX	−	−	0	2	−2
	Saddle ring	RS	−	0	+	2	0
	Min ring	RM	0	+	+	2	+2
Sphere	Max sphere	SX	−	0	0	1	−
	Min sphere	SM	0	0	+	1	+
Trivial case	Infinite point	IP	0	0	0	0	0

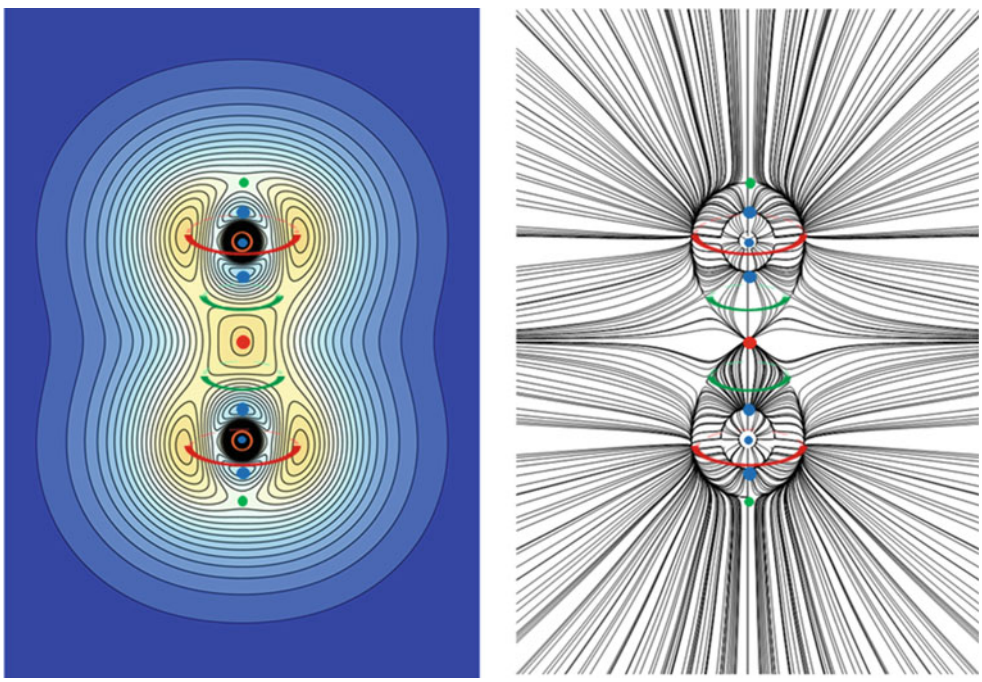

Fig. 5 The contour (*left*) and gradient vector field (*right*) of $\rho_{\mathrm{rad}}(\mathbf{r})$ for F_2 shows numerous critical points (PX = *red*, PSM = *green*, PM = *blue*) and critical rings (RX = *red*, RS = *green*)

Table 2 Shape, volume, $\langle r \rangle$, and $\langle r^2 \rangle$, of AIM

Atom	Molecule	Shape			Volume	$\langle r \rangle$	$\langle r^2 \rangle$
		S_x^o	S_y^o	S_z^o			
Hydrogen	H_2^-	2.15	2.15	3.02	58.38	3.94	18.36
	H^- ion	2.35	2.35	2.35	54.59	4.83	16.61
	LiH	1.21	1.21	1.08	6.65	1.88	4.11
	H atom	1.00	1.00	1.00	4.20	1.50	3.01
	H_2	0.88	0.88	0.68	2.19	1.22	2.00
	$B_2H_6^a$	0.69	0.78	0.79	1.79	1.08	1.71
	CH_4	0.80	0.80	0.65	1.76	1.11	1.71
	CH_3F	0.77	0.75	0.63	1.52	1.05	1.58
	NH_3	0.75	0.59	0.82	1.51	1.05	1.57
	HCl	0.76	0.76	0.58	1.42	0.97	1.51
	HF	0.76	0.76	0.59	1.42	1.07	1.49
	CH_3Cl	0.75	0.72	0.61	1.39	1.00	1.46
	C_2H_2	0.76	0.76	0.56	1.36	0.98	1.47
	H_2O	0.77	0.72	0.56	1.29	0.99	1.42
	$B_2H_6^b$	0.68	0.52	0.63	0.93	0.80	1.12
	H_2^+	0.56	0.56	0.49	0.64	0.58	0.87
Lithium	Li atom	2.50	2.50	2.50	65.12	5.02	18.69
	Li_2	2.52	2.52	2.07	54.99	4.82	16.96
	LiCl	1.66	1.66	2.45	28.18	4.54	11.50
	LiF	1.42	1.42	2.54	21.40	4.77	10.46
	LiH	1.57	1.57	1.78	18.40	3.38	8.10
	Li^+ ion	0.55	0.55	0.55	0.68	1.15	0.89
Boron	B atom	2.30	2.30	2.30	51.12	6.82	15.90
	B_2H_6	2.10	1.95	2.02	34.56	6.56	12.27
Carbon	C atom	2.15	2.15	2.15	41.57	7.16	13.85
	C_2	2.17	2.17	1.83	36.08	6.91	12.77
	CO	1.97	1.97	2.05	33.23	6.78	11.94
	C_2H_2	2.15	2.15	1.71	32.95	6.83	12.13
	CH_3F	1.85	1.85	2.01	28.79	6.75	10.87
	CH_4	1.86	1.86	1.86	26.85	6.49	10.35
	CH_3Cl	1.77	1.77	1.74	22.86	5.99	9.30
Nitrogen	N atom	2.01	2.01	2.01	34.09	7.36	12.14
	N_2	1.95	1.95	1.86	29.71	7.07	11.09
	NH_3	1.80	1.80	2.19	29.69	7.27	11.26
Oxygen	O atom	1.93	1.93	1.93	30.28	7.62	11.22
	H_2O	2.10	1.91	1.71	28.68	7.30	10.35
	O_2	1.92	1.92	1.77	27.36	7.43	10.51
	CO	1.92	1.92	1.72	26.65	7.30	10.35
Fluorine	F^- ion	2.28	2.28	2.28	49.38	9.91	15.54
	F atom	1.85	1.85	1.85	26.53	7.79	10.27
	HF	1.91	1.91	1.66	25.30	7.71	10.03
	F_2	1.87	1.87	1.72	25.24	7.72	9.97
	CH_3F	1.86	1.86	1.66	24.10	7.54	9.68
	LiF	1.80	1.80	1.65	22.32	7.07	9.18
	ClF	1.79	1.79	1.57	21.02	7.09	8.86

Table 2 continued

Atom	Molecule	Shape			Volume	$\langle r \rangle$	$\langle r^2 \rangle$
		S_x^o	S_y^o	S_z^o			
Chlorine	Cl^- ion	3.57	3.57	3.57	190.12	18.87	38.17
	CH_3Cl	3.21	3.21	3.01	129.87	16.67	29.66
	ClF	3.13	3.13	3.12	127.95	16.64	29.31
	Cl atom	3.04	3.04	3.04	118.08	15.84	27.79
	HCl	3.15	3.15	2.82	117.40	16.02	27.83
	Cl_2	3.09	3.09	2.85	114.00	15.74	27.23
	LiCl	3.09	3.09	2.76	110.31	15.37	26.69

Each group of AIM are ordered from largest to smallest volume

[a] Terminal H

[b] Bridging H

Table 3 Dipole (a.u.) of Li AIM

Molecule	μ_z
Li_2	±0.68
LiH	−1.28
LiF	−2.83
LiCl	−2.39

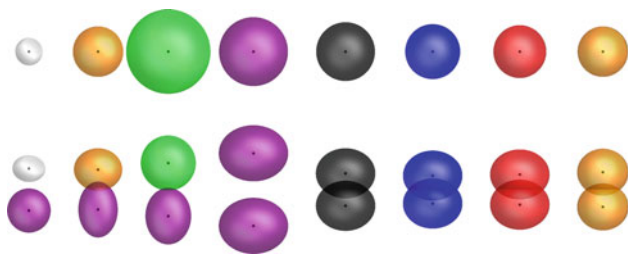

Fig. 6 The relative size and shape of atoms (*top*) and AIM (*bottom*). The atoms, from left to right, are H, F, Cl, Li, C, N, O, and F, while the molecules are LiH, LiF, LiCl, Li_2, C_2, N_2, O_2, and F_2

Table 4 The number of electrons each AIM contributes to the bond and the total bonding electrons

Molecule	No. electrons by atom		Total	Bond length
A–B	A	B		
$H–H^+$	0.17	0.17	0.34	1.98
H–H	0.35	0.35	0.71	1.39
Li–H	0.35	0.40	0.75	3.04
H–H	0.39	0.39	0.79	1.43
Li–Li	0.46	0.46	0.92	5.26
Cl–H	0.61	0.37	0.98	2.40
F–H	1.02	0.49	1.51	1.70
$C–C_{C_2H_6}$	0.83	0.83	1.65	2.89
F–F	1.06	1.06	2.12	2.51
$C–C_{C_2H_4}$	1.11	1.11	2.21	2.49
Cl–F	0.91	1.45	2.36	3.05
$C–C_{C_2}$	1.26	1.26	2.52	2.35
Li–F	0.91	1.65	2.56	2.98
$C–O_{CO_2}$	1.09	1.48	2.57	2.15
Li–Cl	0.82	1.76	2.58	3.85
$C–C_{C_2H_2}$	1.34	1.34	2.69	2.24
O–O	1.29	1.29	2.58	2.18
Cl–Cl	1.34	1.34	2.68	3.77
C–O	1.20	1.53	2.72	2.09
N–N	1.40	1.40	2.81	2.02

Molecules are ordered in terms of increasing total number of electrons

The critical architectures in molecular radial density provide information on the probability of finding electrons in a particular region such as at a point or along a ring or sphere. In the neighborhood of a critical architecture, the probability of finding electrons at a maximum is higher than at a minimum, while finding electrons at a saddle has intermediate probability.

The critical features shown on the contour and gradient vector field of radial density for F_2 in Fig. 5 are an excellent example of the electron probability distribution information provided by the critical architectures. For comparison, the atomic radial density of a free fluorine atom is shown in Fig. 1. The most significant topological change occurring in the free fluorine atom is the distortion of the maximum sphere in the valence shell. The distortion yields numerous critical features in F_2 that are connected by a teardrop-shaped gradient path. The most intuitive feature is the red maximum bond point which shows a higher probability of electrons in the bonding region. Another intuitive feature is the red maximum spherical ring, which shows a high probability of electrons in the nonbonding region. A buildup of charge probability in the bonding and nonbonding regions cannot occur without a subsequent depletion from another region. The physical significance of the green saddle ring is to show a lower probability of finding

Table 5 Expectation values ($\langle r\rangle$ and $\langle r^2\rangle$), dipole, size, and volume of BIM calculated at both the RBCP (top row) or DBCP (bottom row) origin (Z_o)

Molecule					Size		Volume
A–B	Z_o	$\langle r\rangle$	$\langle r^2\rangle$	μ_Z	$X = Y$	Z	
Homonuclear bonds							
$H–H^+$	0.99	0.41	0.63	0.00	0.53	0.28	0.33
H–H	0.69	0.92	1.61	0.00	0.85	0.39	1.19
$C–C_{C_2H_6}$	1.44	2.53	4.60	0.00	1.41	0.79	6.55
F–F	1.25	2.72	4.36	0.00	1.29	1.01	7.07
H–H	0.71	1.42	4.83	0.00	1.42	0.90	7.57
O–O	1.09	3.27	5.40	0.00	1.49	0.97	9.05
N–N	1.01	3.70	6.44	0.00	1.67	0.93	10.84
$C–C_{C_2H_4}$	1.25	3.47	6.96	0.00	$X \neq Y$[a]	0.89	11.33
$C–C_{C_2H_2}$	1.12	4.23	8.80	0.00	1.98	0.97	16.01
$C–C_{C_2}$	1.18	4.14	8.69	0.00	1.95	1.04	16.61
Cl–Cl	1.89	4.97	11.46	0.00	2.08	1.69	30.41
Li–Li	2.63	3.13	13.67	0.00	2.47	1.23	31.37
Heteronuclear bonds							
F–H	0.80	1.71	2.56	−0.07	1.06	0.55	2.58
	1.44	1.96	3.08	0.89	1.06	0.90	4.28
Cl–H	1.49	1.40	2.65	−0.28	1.08	0.58	2.80
	1.72	1.37	2.58	−0.06	1.08	0.51	2.47
Li–H	2.11	1.46	3.80	−0.38	1.28	0.74	5.03
	1.35	1.71	4.80	−0.95	1.28	1.24	8.48
$C–O_{CO_2}$	1.21	3.29	5.50	−0.29	1.54	0.87	8.61
	0.74	3.62	6.35	−1.51	1.54	1.27	12.57
Li–F	2.18	3.18	5.32	−0.84	1.49	0.93	8.67
	1.15	4.68	9.73	−3.46	1.49	2.29	21.45
Cl–F	2.14	3.07	5.21	−0.44	1.46	0.99	8.75
	1.33	3.87	7.46	−2.34	1.46	1.79	15.94
C–O	1.19	3.54	6.11	−0.13	1.62	0.91	10.09
	0.70	3.86	6.89	−1.46	1.62	1.27	14.03
Li–Cl	2.48	4.71	11.03	−0.88	2.16	1.30	25.41
	1.30	6.09	16.65	−3.91	2.16	2.70	52.91

Note that RBCP = DBCP for homonuclear bonds when the BCP coincides with the molecule's center of inversion. The BIM are ordered from largest to smallest volume at the RBCP

[a] $S_X = 1.90, S_Y = 1.60$

electrons along this ring, due to the electrons residing close to the bond point or the nonbonding regions.

Critical features can be more easily identified using contour plots of the gradient length of radial density, $|\nabla\rho_{\text{rad}}|$, as shown in Figure S17–S22 of the supporting information.

3.3 Atoms in molecules

AIM properties can be quickly and easily calculated, including shape, volume [19], $\langle r\rangle$, $\langle r^2\rangle$ (Table 2), and dipole (Table 3). For comparison, these properties are also given for free atoms and ions in Table S2.

Several intuitive trends can be extracted from these calculated properties. First of all, as given in Table 2, volume is generally proportional to $\langle r^2\rangle$. This is consistent with results found by Blair and Thakkar, who determined that the best correlation between volume and $\langle r^2\rangle$ for a set of 1641 organic molecules could be approximated by $V \approx 29.073\langle r^2\rangle^{1/2}$ [20]. Another observation is that the volume of an AIM in comparison with the free atom and ions follows the same trend as its ionic state. For example, hydrogen AIM ordered by volume result in: $H_2^- > H^- > LiH > H$ atom $> H_2 > CH_4 > H_2O > H_2^+$. As expected, this trend shows anionic hydrogen tend to be larger than covalently bonded hydrogen which are subsequently larger than cationic hydrogen. For other heavy atoms, the AIM is generally smaller in volume than the free neutral atom because

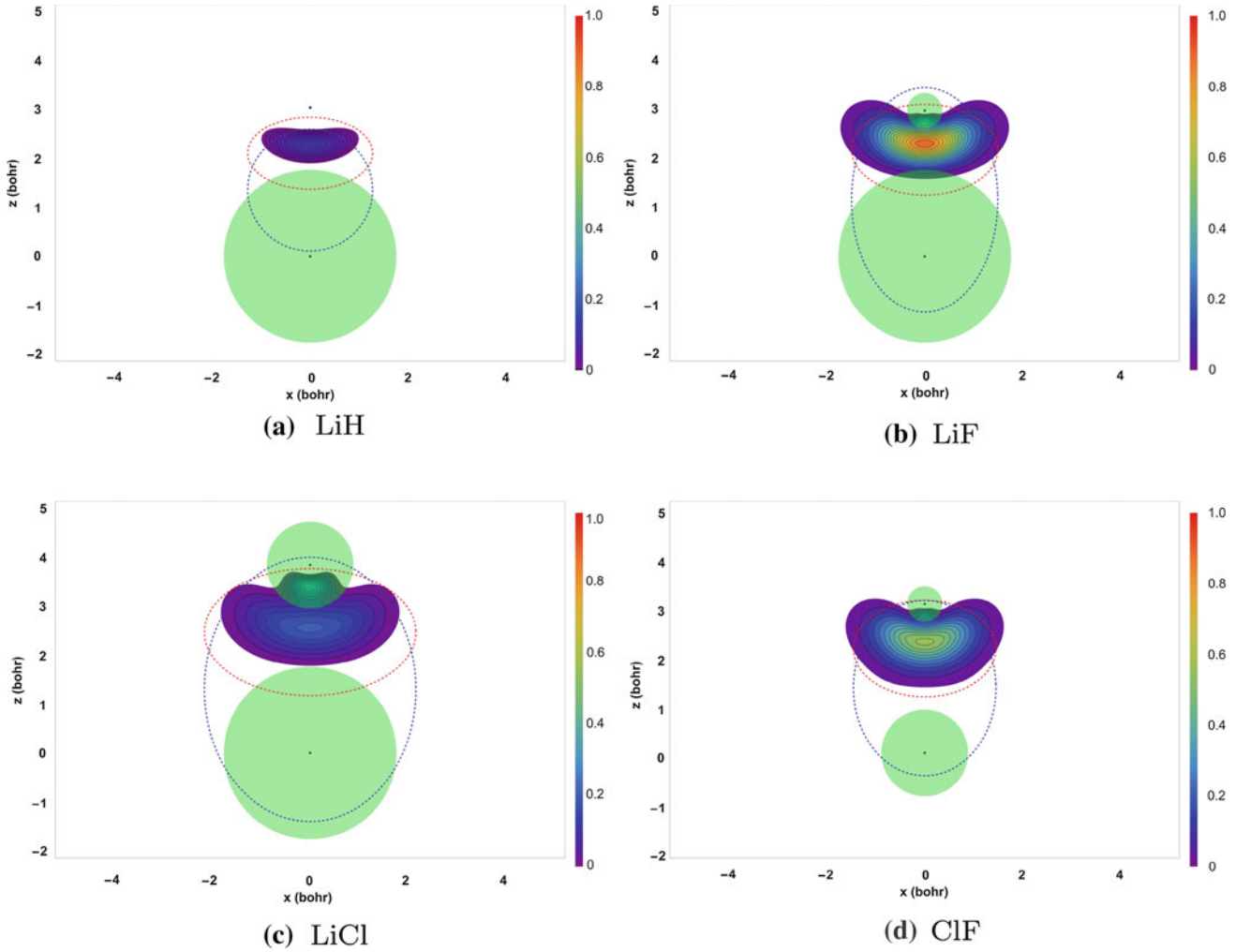

Fig. 7 Contours of bond density for several molecules. The outermost contour has a magnitude of 0.05. The position of each nucleus is given as a *black dot*. Spherical cores, defined as the position of the last minimum in the atomic radial density of the free atom (see Table S1), are depicted by a *green circle* for the heavy atoms. The superimposed ellipses show the shape and size of the bond calculated at the RBCP (*red*) and DBCP origin (*blue*), respectively. The RBCP origin better approximates bond density than the DBCP origin

the process of bonding places electrons into the bonding region decreasing the volume of the AIM. As well, we can easily distinguish between bridging and terminal hydrogen in B_2H_6 from volume differences. The bridging hydrogen each share electron density among two bonds making its AIM volume significantly smaller than the singly bonded terminal hydrogen.

The average shape and volume of several AIM also reveal electron density distortion for molecular atoms. Figure 6 shows that Li AIM shrinks in size relative to the Li atom, consistent with lithium's low electronegativity and its propensity to lose electron density upon bonding. Moreover, there is little overlap observed between the Li AIM and its bonded atom, indicative of the cationic character of Li. In contrast, there is much more overlap in the covalently bonded atoms. The overlap, which increases in the order $F_2 \approx C_2 < O_2 < N_2$ correlates with the increase in bond order.

Another property that can be calculated is the dipole, which is a measure of charge polarization of the atom in a molecule. The dipole of several Li AIM in LiX molecules is given in Table 3. These dipole values correlate well with electronegativity differences: the greater the electronegativity difference between Li and X, the larger the dipole of the Li AIM.

The benefit of AIM go beyond determining atomic properties. We seek to create an AIM database where the electron density and properties of larger molecules can be built and approximated from the appropriate combination of AIM. Since molecular atoms in ABIM are represented as overlapping AIM, then the electron density can be built to a first approximation as a linear combination of AIM.

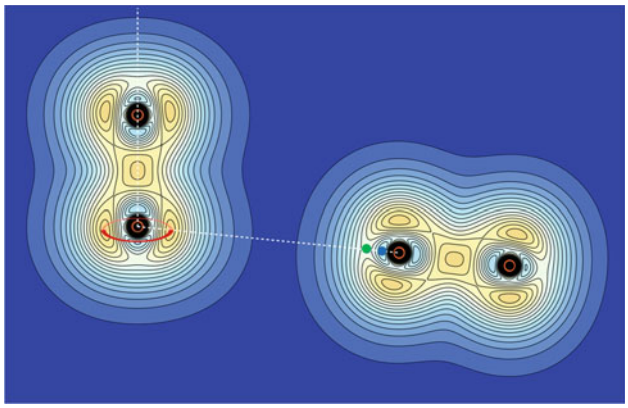

Fig. 8 The radial density for a F_2 dimer. The maximum radial density ring (*red*) of one F_2 is oriented toward a saddle minimum (*green*) and a minimum critical point (*blue*) of the other F_2

Table 6 The orientation of halogen dimers predicted from the radial density topology of the monomer

Dimer	Predicted angle from monomer (°)	Computed dimer angle (°)
$F_2 \cdots F_2$	96.56	95.72
$Cl_2 \cdots Cl_2$	98.50	98.52

3.4 Bonds in molecules

One integral aspect of chemistry is that *chemical bonds*, formed from the interaction of electron density, hold the atoms of a molecule together. Therefore, it is essential for any AIM model to explicitly define the bond.

We define a bond as the region of space between a pair of atoms where the joint probability of finding electron density owned by each atom is nonzero. In the bonding region, the weighting function of both nuclei (W_A and W_B) must be nonzero (and nonnegligible) since both the space and electron density are shared. Thus, the bond density is defined in Eq. 11. Similarly, the radial bond density can be defined as in Eq. 12.

$$\rho_{A-B}(\mathbf{r}) = \sqrt{W_A(\mathbf{r})\, W_B(\mathbf{r})}\, \rho(\mathbf{r}) \tag{11}$$

$$\rho_{\mathrm{rad}_{A-B}}(\mathbf{r}) = \sqrt{W_A(\mathbf{r})\, W_B(\mathbf{r})}\, \rho_{\mathrm{rad}}(\mathbf{r}) \tag{12}$$

We denote the number of electrons in the bond A–B contributed from atom A as N^A_{A-B} and calculate this value by Eq. 13. Therefore, the total number of bonding electrons in A–B is the sum of the contributions from A and B as seen in Eq. 14. When performing the numerical integration for Eq. 13, we use the combined grid points of both atom A and B.

$$N^A_{A-B} = \int W_A(\mathbf{r})\, \rho_{A-B}(\mathbf{r}) \mathrm{d}r \tag{13}$$

$$N_{A-B} = N^A_{A-B} + N^B_{A-B} \tag{14}$$

The number of bonding electrons for several molecules is given in Table 4, which show some very intuitive trends. First, for diatomics, the number of bonding electrons increases with increasing total charge as seen by H_2^+ (0.34) < H_2 (0.71) < H_2^- (0.79). The addition of an electron to H_2 to form H_2^- does not significantly increase the number of bonding electrons, which is the expected result from molecular orbital theory. Another trend observed is the number of bonding electrons increases with bond order, such as the C–C bond in $H_3C - CH_3$ (1.65) < $H_2C{=}CH_2$ (2.21) < $HC{\equiv}CH$ (2.69). Similarly, more electrons are observed in stronger bonds than weaker bonds, such as: F_2 (2.12) < O_2 (2.58) < CO (2.72) ≈ N_2 (2.81). However, there are several exceptions such as ClF (2.36), LiCl (2.56), and Cl_2 (2.68), which do not follow these trends as discussed below.

Similar to AIM, we can also quantify the properties of BIM. The shape, volume, and expectation values of BIM in various molecules are calculated using either the RBCP or DBCP as the origin as shown in Table 5. Figure 7 shows the shape and size of the bond density calculated at both the RBCP and DBCP origin superimposed on a contour plot of bond density for several diatomics. This figure reveals that the RBCP origin better approximates bond density. Larger versions for these diatomics, as well as three additional examples, are shown in Figures S23–S29 of the supporting information. Unfortunately, for a number of cases, the core of the atom is included in the bond. This is an artifact of the Becke weight, where the step function partitions the density too early and causes the core to be included in the bond. As observed in Fig. 7, the Cl core contributes to the bond in both ClF and LiCl, which results in the number of bonding electrons in ClF (2.36) and LiCl (2.56) to be of the same order as the double bond O_2 (2.58) as given in Table 4.

One particularly interesting case is the hydrogen-bridged B_2H_6 molecule. A figure of the contours of radial density for B_2H_6 suggests that there is no B–B bond, as shown in Figure S30 of the supporting information. This is consistent with a QTAIM analysis which finds no bond path between the boron atoms. Unfortunately, the machinery does not yet exist in MUNgauss to quantitatively calculate the number of bonding electrons for 3-centered bonds.

3.5 Applications

Is molecular radial density chemically significant? One application is predicting the orientation of molecular

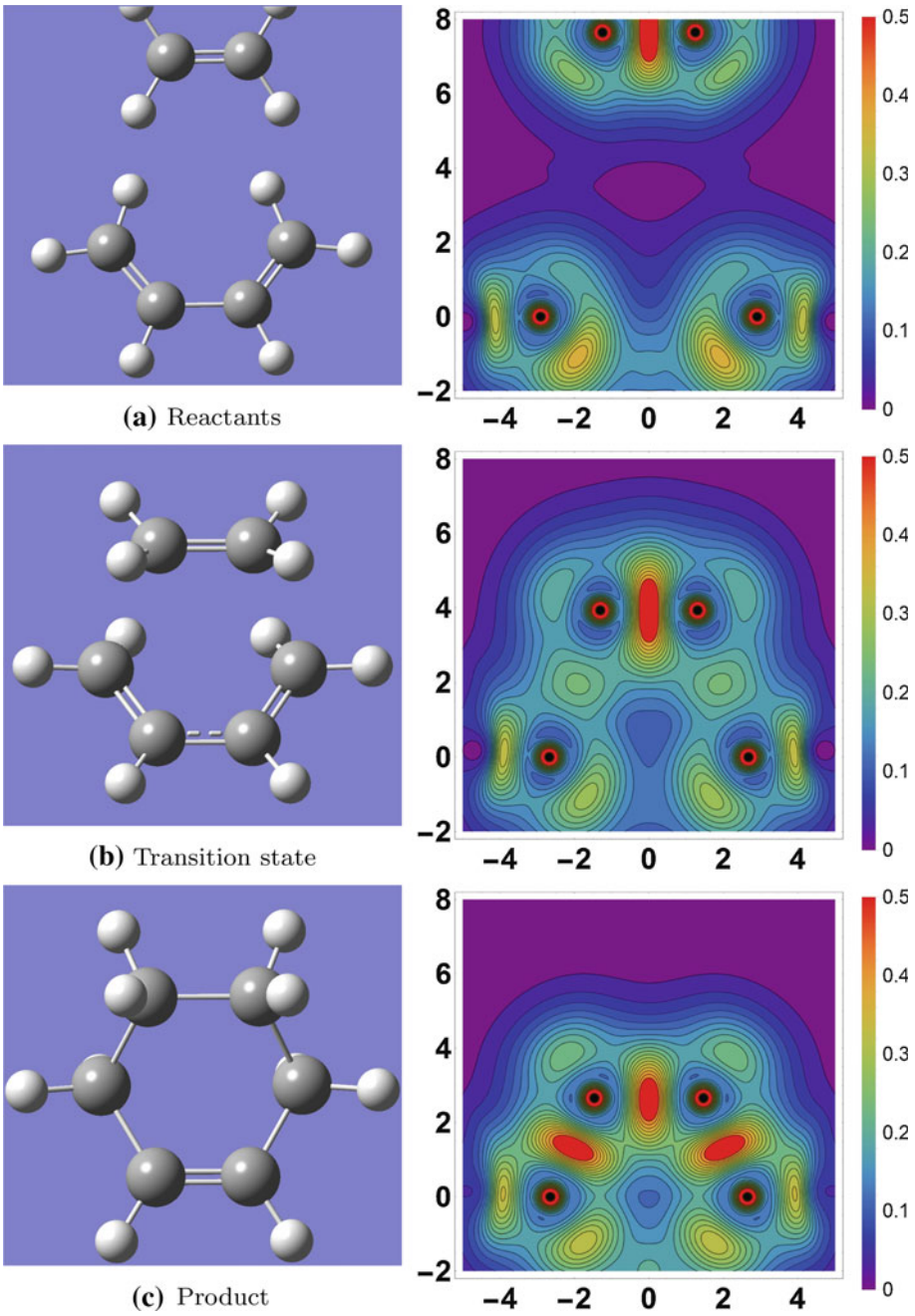

Fig. 9 The molecular radial density during the Diels–Alder reaction between ethene and 1,3-butadiene showing **a** the reactant complex, **b** the transition state, and **c** the product of the reaction. See text for explanation

dimers from the radial density topology of the monomers. This is based on the linear alignment of a maximum in radial density (charge accumulation) on one molecule with a minimum or saddle in radial density (charge depletion) for the other molecule. For example, the RX of one F_2 orients itself toward the line between the PSM and PM of the other as illustrated in Fig. 8. The same trend was also found in Cl_2. The predicted angles fall within one degree of the computationally determined dimer angle in the lowest energy dimer structure as shown in Table 6.

Another application of molecular radial density is monitoring and gaining insight into changes in bonding during a reaction. For example, changes in the molecular radial density during the intrinsic reaction coordinate of the Diels–Alder reaction between ethene and 1,3-butadiene can be seen in Fig. 9 and also in a video available at: http://www.chem.mun.ca/homes/plwhome/files/DielsAlderanimate20.mp4.

In this video, the contours of molecular radial density are presented in the plane that contains the two carbon atoms of ethene and the two outermost carbon atoms of 1,3-butadiene. There are 35 points in total along the IRC, where point 1 represents the reactant complex, point 18 reflects the transition state, and point 35 is the product of the reaction.

As the IRC proceeds from reactants to product, molecular radial density is seen to move from the π bond systems of the ethene and butadiene molecules into the regions of space between the ethene and butadiene carbon atoms to form sigma bonds. In the transition state, there is molecular radial density between these carbon atoms that is about half of the molecular radial density found in the product of the reaction. However, the ethene bond in the transition state has maintained much of its double bond character in the transition state as compared to the reactant complex, which is consistent with an early transition state for the reaction as expected through the Hammond postulate.

4 Conclusions

We have demonstrated that the molecular electron density can be partitioned into atomic and bonding contributions using radial density and electron density. The Becke weight was employed to partition the molecular space. Although the Becke weight works well in a number of cases, there are several drawbacks. First, the reliance on fixed Bragg–Slater radii makes the Becke weight less versatile in dealing with AIM that can have different charged states. Another problem arises when there is a large difference between the Bragg–Slater radii of the atoms. In the first step of the Becke weight calculation, if the ratio of the Bragg–Slater radii of two atoms is larger than 2.4 (or smaller than 0.41), the ratio will be capped to these extremes. For example, the ratio of the Bragg–Slater radii for LiH and LiF is 4.15 (=2.74/0.66) and 2.91 (=2.74/0.94), respectively, and both become capped to 2.4. Consequently, H and F are effectively treated as the same size when paired with Li. The restriction on the range of the ratio is a problem of the Becke weight because the properties of AIM and BIM can change significantly depending on the ratio of the Bragg–Slater radii. This is illustrated in Tables S3–S5, where changing the radius of Li from its Bragg Slater radii (2.74) to $\langle r \rangle$ of Li^+ (1.15) changes its AIM and BIM properties. This motivates the need to explore or develop alternative partition functions to replace or modify the Becke weight.

The topology of ABIM is rich in features such as critical points, rings, and spheres, which can be identified and characterized using the gradient and diagonalized Hessian of radial density, respectively. ABIM is able to quickly and easily determine the properties of atoms and bonds, including shape, volume, dipole, and expectation values and link them to chemically intuitive properties such as electron density distortion and bond orders. Two of the most important features arising from the ABIM model is that the bonding region is explicitly defined and the number of electrons in the bonding region can be calculated.

Acknowledgments We gratefully acknowledge the support of the Natural Sciences and Engineering Council of Canada and the Atlantic Excellence Network (ACEnet) and Compute Canada for the computer time. We would also like to dedicate this paper to Marco Häser, who was the first to define molecular radial density [21]. The authors express their best wishes to Peter Surjan on the occasion of his 60th birthday.

References

1. Warburton PL, Poirier RA, Nippard D (2011) J Phys Chem A 115:852
2. Pauling L (1960) The nature of the chemical bond, 3rd edn. Cornell University Press, Ithaca, NY
3. Bader RFW (1990) Atoms in molecules: a quantum theory. Clarendon, Oxford
4. Yáñez M, Stewart RF, Pople JA (1978) Acta Cryst A34:641
5. Hirshfeld FL (1977) Theor Chim Acta 44:129
6. Moffitt W (1951) Proc R Soc Lond Ser A 210:245
7. Bader RFW (1985) Acc Chem Res 18:9
8. Bader RFW, Larouche A, Gatti C, Carroll MT, MacDougall PJ, Wiberg KB (1987) J Chem Phys 87(2):1142
9. Bader RFW, Matta CF (2004) J Phys Chem A 108:8385
10. Bader RFW (2010) J Phys Chem A 114:7431
11. Stewart RF (1970) J Chem Phys 53(1):205
12. Politzer P, Parr RG (1976) J Chem Phys 64:4634
13. Boyd RJ (1977) J Chem Phys 66:356
14. Schmider H, Sagar RP, Smith VH (1991) J Chem Phys 94:8627
15. Becke AD (1988) J Chem Phys 88(4):2547
16. Poirier RA, Hollett JW, Warburton PL, MUNgauss, Memorial University, Chemistry Department, St. John's, NL A1B 3X7. With contributions from Alrawashdeh A, Becker J-P, Besaw JE, Bungay SD, Colonna F, El-Sherbiny A, Gosse T, Keefe D, Kelly A, Nippard D, Pye CC, Reid D, Saputantri K, Shaw M, Staveley M, Stueker O, Wang Y, Xidos J
17. Gill PMW, Johnson BG, Pople JA (1993) Chem Phys Lett 209:506
18. Simas AM, Sagar RP, Ku ACT, Smith VH (1988) Can J Chem 66:1923
19. Hollett JW, Kelly A, Poirier RA (2006) J Phys Chem A 110(51):13884
20. Blair SA, Thakkar AJ (2014) Chem Phys Lett 609:113
21. Häser M (1996) JACS 118:7311

Theor Chem Acc (2015) 134:104
DOI 10.1007/s00214-015-1708-5

REGULAR ARTICLE

Topological coordinates for bar polyhex carbon structures

István László[1]

Received: 11 June 2015 / Accepted: 25 July 2015 / Published online: 12 August 2015

Abstract Very often, the basic information about a nanostructure is a topological one. Based on this topological information, we have to determine the Descartes coordinates of the atoms. In the present paper, we review first the previous results obtained by drawing graphs with the help of various matrices as the adjacency matrix, the Laplacian matrix and the Colin de Verdière matrix. We explain why they are applicable if the atoms are on spherical surfaces. We have found recently a matrix **W** which could generate the Descartes coordinates for fullerenes, nanotubes and nanotori and also for nanotube junctions and coils as well. Here will be shown with examples of bar polyhex structures that using the matrix elements of smaller structures, the **W** matrix of larger structures can be generated.

Keywords Drawing · Eigenvectors · Embedding · Graphs · Molecular structures · Nanostructures

1 Introduction

In order to perform a quantum chemical calculation, usually one of the most important input data is the initial position of the atoms. This information is an inevitable requirement for a molecular viewer as well. In many cases, however, only the neighbouring structure of the atoms is given. That is, we know the adjacency matrix $\mathbf{A} = \mathbf{A}(G) = (a_{uv})$ of the structure which is represented by a graph $G(V, E)$. Here V is the set of vertices, and E is the set of edges, the adjacency matrix element $a_{uv} = 1$ if $(u, v) \in E$ and $a_{uv} = 0$; otherwise, we suppose further that the graph has $n = |V|$ vertices. In this graph, the atoms correspond to the vertices and the first-neighbour bonds to the edges. The topology can be described with the help of the $\mathbf{Q}(G) = \mathbf{D} - \mathbf{A}$ Laplacian matrix as well, where $\mathbf{D} = (d_{vv})$ is the diagonal matrix with $d_{vv} = \sum_{u:(u,v)\in E} a_{uv}$. In the topological coordinate method, some eigenvectors of the adjacency matrix (or the Laplacian matrix) are used to generate the Descartes coordinates of the atoms. These eigenvectors are the so-called bi-lobal eigenvectors. An eigenvector c^k is bi-lobal, if in the graph of the atomic structure after deleting the vertices i if $c_i^k = 0$ and the edges (i, j) if the signs of c_i^k and c_j^k are different, the resulting graph will have two components. The increasing index k for the eigenvector c^k corresponds to decreasing λ_k eigenvector for the adjacency matrix and increasing eigenvector to the Laplacian matrix. The first systematic application of this method was presented by Fowler and Manolopoulos [1, 2] for general fullerene isomers C_{20} to C_{50} and isolated-pentagon isomers C_{60} to C_{100}. Similar method was found by Pisanski and Shaw-Taylor [3–5]. All of these methods were applicable where the carbon atoms were on a spherical or near-spherical surface. In mathematics, the problem was stated and proved as embedding graphs into the Euclidean space R^3 or R^2 [5–7]. Under embedding a graph $G(V, E)$ into R^k, we mean a mapping $\tau : V(G) \to R^k$. Let τ_i be the n-dimensional vector formed by taking the i-th coordinate $\tau(v)_i$ of $\tau(v)$ for all $v \in V$.

This paper is dedicated to Professor P. R. Surján on the occasion of his 60th birthday.

Published as part of the special collection of articles "Festschrift in honour of P. R. Surján".

✉ István László
laszlo@eik.bme.hu

[1] Department of Theoretical Physics, Institute of Physics, Budapest University of Technology and Economics, Budapest 1521, Hungary

As an example in R^3, we introduce $\mathbf{X} = \tau_1$, $\mathbf{Y} = \tau_2$ and $\mathbf{Z} = \tau_3$, then $(x_v, y_v, z_v) = \big(\tau(v)_1, \tau(v)_2, \tau(v)_3\big)$. The question arises if there is a topological coordinate method for toroidal structures as well. In these structures, the carbon atoms are on a surface of a torus. It seemed that three bi-lobal eigenvectors of the adjacency matrix cannot describe the torus [8]. It turned out that a formula constructed from four bi-lobal eigenvectors yields reasonable Descartes coordinates for the atoms on the surface of a torus [9]. According to our shape analysis [10], 16 bi-lobal eigenvectors are necessary to describe the position of the carbon atoms in a nanotube junction of 1165 atoms. This result showed that there is not a general method for constructing topological coordinates for any structures. Successful algorithm was found only spherical and toroidal structures. The torus is the Cartesian product of two circles (spheres in two dimensions). Thus, it can be said that the topological coordinate method works only structures which are in some way related to the sphere.

Some kind of breakthrough happened when it turned out that there exists a matrix **W** which has the property that its three eigenvectors of zero eigenvalue can reproduce the Descartes coordinates of the atoms [11–14]. This matrix has further nonzero matrix elements only in the diagonal and for first and second neighbours or at most third neighbours. In the following paragraphs, we review the topological coordinate method and show its applicability to bar polyhex carbon structures. Bar polyhex carbon structures are very simple ones, and its Descartes coordinates can be produced very easily. Here we are using them to test our method in these structures. The other problem is that although the matrix **W** exists for its precise construction, we need the Descartes coordinates of the atoms as well. In this article, we present an algorithm for constructing an approximation of the matrix **W** without knowing the Descartes coordinates. The bar polyhex carbon structures are very good for testing this algorithm.

2 Topological coordinates for spherical structures

Pisanski and Showe-Taylor [3, 4] obtained $\tau_i = \mathbf{c}^{i+1}$ with $i = 1, \ldots k$ for the optimal embedding $\tau : V(G) \to R^k$ by minimizing the following energy functional

$$E(\tau) = \sum_{(u,v)\in E} a_{uv}\|\tau(u) - \tau(v)\|^2 - \beta \sum_{(u,v)\notin E} \|\tau(u) - \tau(v)\|^2 \tag{1}$$

where β is a positive constant and $\|\tau(u) - \tau(v)\|$ is the Euclidean norm of the vector $\tau(u) - \tau(v)$. The solutions have further the constraints $\|\tau_i\| = 1$, $\tau_i^T \mathbf{c}^1 = 0$ for $i = 1,\ldots,k$ and $\tau_i^T \tau_j = 0$ for $1 \le i < j \le k$.

Fowler and Manolopoulos [1, 2] have found that the first few eigenvectors of the fullerene adjacency matrix contain three bi-lobal eigenvectors $\mathbf{c}^{k_1}$, $\mathbf{c}^{k_2}$ and $\mathbf{c}^{k_3}$ which determine the (x_v, y_v, z_v) coordinates of the atoms as

$$x_v = S_1 c_v^{k_1} \tag{2}$$

$$y_v = S_2 c_v^{k_2} \tag{3}$$

$$z_v = S_3 c_v^{k_3} \tag{4}$$

where the scaling factors are $S_\alpha = S_0$ or $S_\alpha = \frac{S_0}{\sqrt{\lambda_1 - \lambda_{k_\alpha}}}$.

In the majority of fullerenes, these three bi-lobal eigenvectors are the second, third and fourth eigenvector of the adjacency matrix.

Lovász and Schrijver [6] proved that the null space of the Colin de Verdière matrix **M** gives a proper embedding of a three-connected planar graph $G(V, E)$ in the sphere S^2 as $\tau_i = \mathbf{c}^{i+1}$ for $i = 1, 2, 3$, and $\|\tau_i\| = 1$. The matrix **M** defined with the following properties:

1. **M** has exactly one negative eigenvalue, and its multiplicity is 1;
2. for all $(u, v) \in E$: $m_{uv} < 0$ and if $u \neq v$ for $(u, v) \notin E$: $m_{uv} = 0$;
3. **M** has rank $n - 3$.

The null space of **M** is defined as the vector space of its eigenvectors with $\lambda = 0$ eigenvalue.

Graovac et al. [8] have shown that three bi-lobal eigenvectors of the torus adjacency matrix are not sufficient to generate the Descartes coordinates for such kind of structures. The torus always became flat from some point of view. Laszlo et al. [9] have found that four bi-lobal eigenvectors of the adjacency matrix are sufficient for embedding the torus into R^3 as

$$x_v = S_1 c_v^{k_1}\left(1 + S_4 c_v^{k_4}\right) \tag{5}$$

$$y_v = S_2 c_v^{k_2}\left(1 + S_4 c_v^{k_4}\right) \tag{6}$$

$$z_v = S_3 c_v^{k_3} \tag{7}$$

where $\mathbf{c}^{k_1}$, $\mathbf{c}^{k_2}$, $\mathbf{c}^{k_3}$ and $\mathbf{c}^{k_4}$ are the four bi-lobal eigenvectors of the adjacency matrix of the torus.

Although the torus is a genus = 1 surface and the genus of the sphere is 0, we classified here the torus to the spherical structure. It is namely the Descartes product of the two-dimensional spheres (circles). Thus, in this paragraph under spherical structures, we mean atomic arrangements where the atoms are on surfaces which are homeomorphous to the sphere or to the torus.

3 Topological coordinates for nonspherical structures

Under nonspherical structure, we mean a structure where the position of the atoms is not restricted to any kind of surfaces. That is, there is not a special restriction to the atomic positions. On the one side, it was presented that there is not a simple rule based on the bi-lobal eigenvectors of the adjacency matrix for generating the Descartes coordinates of the carbon atoms in nanotube junctions [10]. On the other side, however, we have proved that a matrix (or matrices) **W** can be constructed for any atomic arrangement and the eigenvectors of the null space of **W** construct the Descartes coordinates of the atoms [11]. In general cases, we know only the existence of such a matrix and it can be constructed with the help of an energy minimization process. In the next paragraphs, we shall show which way can we construct good approximations to this matrix without minimizing the total energy. Our method will be shown on the bar polyhex structures.

First, let us see the construction of the matrix **W**. We describe the total energy of the system of n atoms with the potential function

$$E(r) = E(r_{12}, \ldots r_{uv}, \ldots) \tag{8}$$

where r_{uv} is the interatomic distance between the atoms u and v. The condition that in equilibrium, the forces acting on the atoms are zero, can be written in the following form:

$$\mathbf{WX} = 0, \quad \mathbf{WY} = 0, \quad \mathbf{WZ} = 0 \tag{9}$$

where

$$w_{uv} = -\frac{\partial E(r)}{r_{uv}\partial r_{uv}} - \frac{\partial E(r)}{r_{vu}\partial r_{vu}} \tag{10}$$

and

$$\begin{aligned} w_{uu} &= \sum_{v\neq u}^{n} \left(\frac{\partial E(r)}{r_{uv}\partial r_{uv}} + \frac{\partial E(r)}{r_{vu}\partial r_{vu}} \right) \\ &= -\sum_{v\neq u}^{n} w_{uv}. \end{aligned} \tag{11}$$

Thus, in equilibrium, the Descartes coordinates of the atom v are (x_v, y_v, z_v) where x_v, y_v and z_v are the v-th components in order of the vectors **X**, **Y** and **Z**. The matrix elements of the matrix **W** are calculated at the equilibrium position of the atoms. If the centre of mass of the molecule is in the origin and the molecule is directed in such a way that the eigenvectors of its tensor of inertia are showing to the directions of the x, y and z axis, then the vectors **X**, **Y** and **Z** are orthogonal eigenvectors of the matrix **W**. From the construction of the w_{uu}, matrix elements follow that $\mathbf{WU} = 0$ if $u_v = \frac{1}{\sqrt{n}}$. If the centre of mass is the origin of the coordinate system, **U** is orthogonal to the vectors **X**, **Y** and **Z**. It can be seen very easily that if in the potential function $E(r) = E(r_{12}, \ldots r_{uv}, \ldots)$ we suppose only first-neighbour interactions, the structure cannot be determined because of the freedom of the bond angles. In most of the cases, the first and second neighbours completely determine the structure. In some cases, we have to take into account the third neighbours as well [12, 15, 16].

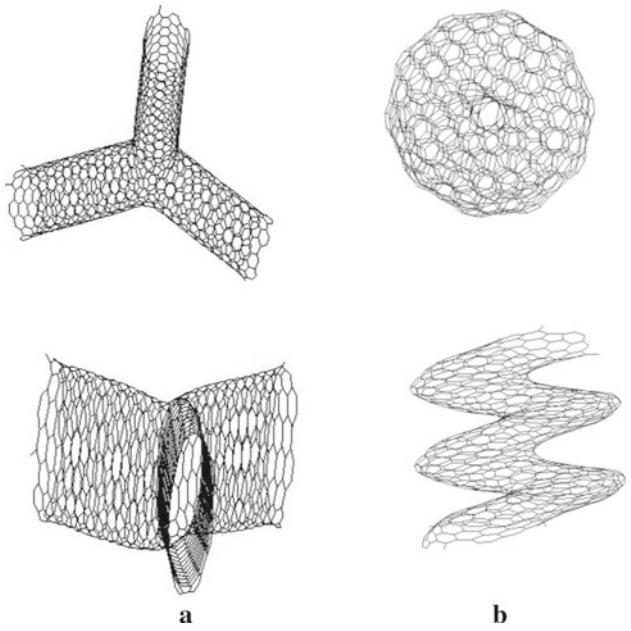

Fig. 1 *Side* and *top view* of nanotube junction (**a**) and helical structure (**b**) of atoms obtained by three zero eigenvalue of the matrix **W**

If we determine in some way the matrix **W**, and the underlying graph is sufficiently rigid, the degeneracy of the zero eigenvalue is four. We can chose that one of them is the vector **U**. As any linear combination of the other three eigenvectors is also eigenvector of the zero eigenvalue, the vectors **X**, **Y** and **Z** establish an affine transformation of the molecule. In order to obtain some given realistic interatomic distances, an appropriate scaling can be found. First, using Brenner potential [17], we could generate the matrix **W** for nanotube junction and helical structures as well. Figure 1 shows the corresponding structures obtained by the zero eigenvalues of **W**.

The Brenner potential can be seen as a potential where first- and second-neighbour interactions are taken into account in the potential function $E(r) = E(r_{12}, \ldots r_{uv}, \ldots)$. Later, we replaced this potential by the much simpler one the harmonic potential [12–14],

$$E(r) = E(r_{12}, r_{21}, \ldots r_{uv}, r_{vu} \ldots) = \sum_{u,v=1}^{n} \frac{1}{2} k_{uv}(r_{uv} - a_{uv})^2 \tag{12}$$

and

$$w_{uv} = -2k_{uv}\left(1 - \frac{a_{uv}}{r_{uv}}\right). \quad (13)$$

Here $k_{uv} = k_{vu}$ are the spring constants, and $a_{uv} = a_{vu}$ are parameters. The summation goes for all the pairs (u, v) which are sufficient for determining the equilibrium position of the atoms. The eigenvalue problem of the matrix **W** has meaning only if it is not the zero matrix.

Thus, the parameters a_{uv} must be different from the corresponding equilibrium values of r_{uv}.

The next step is to find a good approximation to the matrix **W**. But if this matrix is approximated, only the vector **U** will be an eigenvector with zero eigenvalue. Then, the question is to find the eigenvectors which are good approximations to the **X**, **Y** and **Z** zero eigenvectors of the exact matrix **W**. According to our experiences, the lobality of the eigenvectors helps us to find the good approximating eigenvectors to **X**, **Y** and **Z**.

Let us see which explanation can we give to the formula of Eqs. (2–4) applied for fullerenes [1, 2]. Let the matrix **W** be constructed for the fullerene under study. We suppose first- and second-neighbour interactions. As each carbon atom has 3 neighbours, symmetry gives that w_{uv} equals to a constant w for the first neighbours and let us choose $w_{uv} = 0$ for the second neighbours. Usually, it has only one eigenvector with zero eigenvalue. It is the eigenvector **U**. If we put the centre of mass of a fullerene into the origin of a Descartes coordinate system, we can see that the **X**, **Y** and **Z** vectors are bi-lobal. Namely, **X** is bi-lobal as one connected set of atoms is on one side of the plane yz and the other connected set is on the other side. If some atoms are on this plane, usually this does not disturb the lobality. On similar way, can we see that the vectors **Y** and **Z** are also bi-lobal. Thus, we have to choose the three bi-lobal eigenvectors of our matrix for approximating the eigenvectors **X**, **Y** and **Z**. In the fullerenes, each carbon atom has three neighbours and thus $w_{uu} = -3w$. From this reasoning follow Eqs. (2–4); namely by taking the value $w = 1$ and shifting the diagonals by 3, we obtain the adjacency matrix of the fullerene and the eigenvectors will not be changed.

By inspecting Fig. 1b, it can be seen that not all of the vectors **X**, **Y** and **Z** of a helical structure are bi-lobal. The helical structure of this figure was obtained by two bi-lobal and on 4-lobal eigenvectors of the matrix **W**.

4 Topological coordinates for bar polyhex structures

The bar polyhex structure defined as a polyhex consisting of hexagons arranged along a line. A polyhex containing h hexagons has $n = 4h + 2$ vertices (or atoms). In

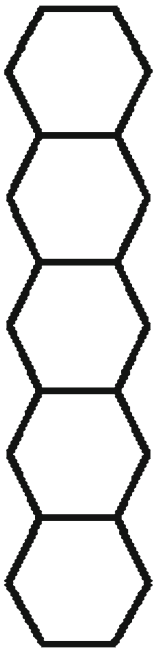

Fig. 2 A bar polyhex structure containing $h = 5$ hexagons and $n = 22$ vertices

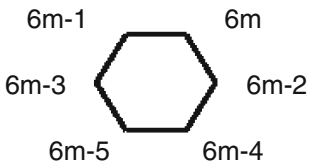

Fig. 3 Numbering of the vertices of the m-th hexagon in a bar polyhex. The first hexagon is the lowest one

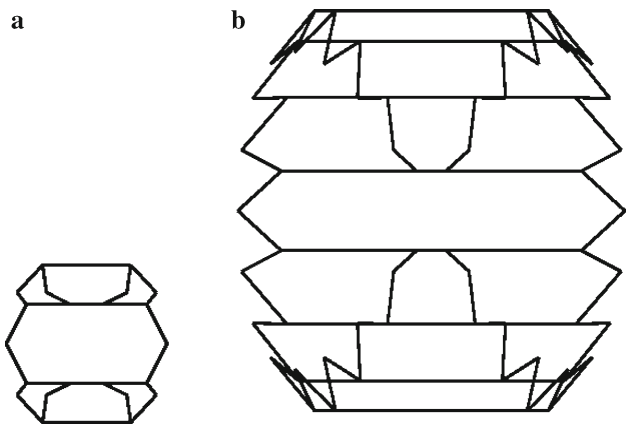

Fig. 4 Bar structures of $h = 5$ (**a**) and $h = 15$ (**b**) hexagons obtained with the help of the two bi-lobal eigenvectors of the corresponding adjacency matrices using Eqs. (2, 3)

Fig. 2a, polyhex structure of five hexagons and 22 vertices is shown.

Figure 3 shows our numbering of the vertices. The m -th hexagon has the vertices $6m$, $6m-1$, $6m-2$, $6m-3$, $6m-4$ and $6m-5$.

In Fig. 4, we present two structures obtained by the topological coordinates of Eqs. 2 and 3. For hexagons $h=5$, we obtained the second and the 5th eigenvectors as bi-lobal eigenvectors. For the adjacency matrix of the bar structure of 15 hexagons, we obtained the second and the 12th adjacency matrix bi-lobal eigenvectors. In both structures, we can see that the bonds at the ends of the bars are much smaller than those in the central part. The other peculiarity is that the structure turns back at the ends. If we increase the number of hexagons, these problems of the structures are much more pronounced.

In Fig. 5, we used once more the same relations of Eqs. 2 and 3, but we replaced the adjacency matrix with the Laplacian matrix. The bond lengths are still smaller at the ends of the bars, but the structure does not turns back at the ends. The bi-lobal eigenvectors of the Laplacian are the second and 12th in the case of 5 hexagon bar, and they are the second and the 10th eigenvectors in the case of the 15 hexagon structure.

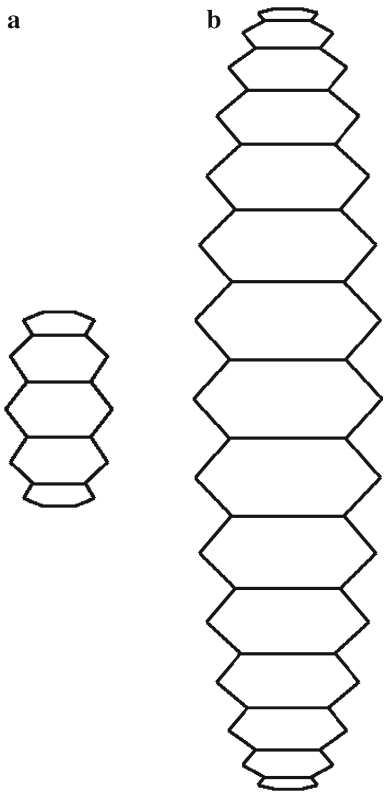

Fig. 5 Bar structures of $h=5$ (**a**) and $h=15$ (**b**) hexagons obtained with the help of the two bi-lobal eigenvectors of the corresponding Laplacian matrices using Eqs. (2, 3)

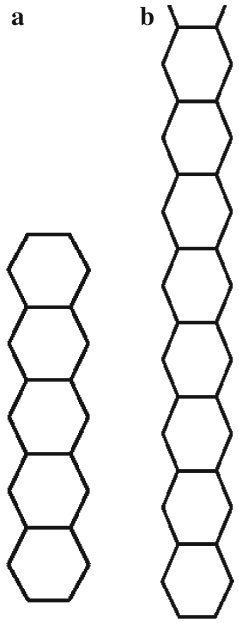

Fig. 6 Bar structure of $h=5$ (**a**) and $h=15$ (**b**) hexagons obtained with the help of the energy minimization of the harmonic potential of Eq. (12). The same structures were obtained from the zero-eigenvalue bi-lobal eigenvectors of the corresponding **W** matrix of Eq. (13)

Figures 4 and 5 show that the eigenvectors of the adjacency matrix and of the Laplacian matrix cannot be used for constructing topological coordinates for bar polyhex structures. Here we study the eigenvectors of the matrix **W**. We shall use the harmonic potential of Eq. (12). We take $k_{\mu\nu}=k=1$ for each bond. In the potential function, we suppose only first- and second-neighbour interactions. We use the value $a1=1.4$ for the first neighbours and $a2=3.0$ for the second neighbours. Here we remark that $a2=a1\sqrt{3}$ should give $w_{uv}=0$ for each matrix elements of **W**. In Fig. 6, we can see the bar polyhex structures of five and 15 hexagons obtained by energy minimization of the harmonic potential of Eq. (12). Using the equilibrium positions of the vertices, we constructed the **W** matrix. The first, second and third eigenvectors have the zero eigenvalue. We obtained that the first eigenvector is one-lobal and the second and third eigenvectors are the bi-lobals. The two bi-lobal eigenvectors with appropriate scaling reconstructed the structures of Fig. 6.

The $a1=1.4$ and $a2=3.0$ parameters produced the following interatomic distances (edge lengths) $r_{1,2}=1.6541$, $r_{5,6}=1.7813$, $r_{9,10}=1.7865$, $r_{13,14}=1.7869$, $r_{17,18}=1.7869$, $r_{21,22}=1.7869$, $r_{25,26}=1.7869$, $r_{29,30}=1.7869$ for the bar polyhex of 15 hexagons. For four digits, we obtained the same corresponding values with 5 hexagons as well. That is, increasing the number of hexagons, the distances in the central part of the polyhex do not depend strongly on the number of hexagons. This

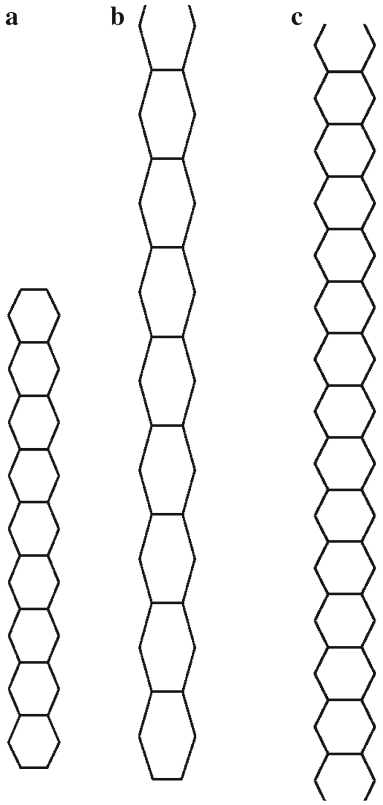

Fig. 7 Bar structures of $h = 9$ (**a**) and $h = 109$ hexagons with the *bottom* (**b**) and *central* (**c**) part of 109 hexagon structure. The matrix **W**(**9**) obtained with the help of the energy minimization of the harmonic potential of Eq. (12), and the matrix elements of **W**(**109**) were constructed with the help of the matrix **W**(**9**)

property gives the possibility to construct an approximate matrix **W** for a larger number of hexagons using the matrix elements obtained for a smaller number of hexagons. In Fig. 7, we can see the results obtained for bar polyhex structures of 9 and 109 hexagons. For the structure of 9 hexagons, we constructed the matrix **W**(**9**) by minimizing the total energy of Eq. (12) and using matrix elements of Eq. (13). The matrix **W**(**109**) was calculated with the help of **W**(**9**). We imagined that the central hexagon $m = 5$ of the structure of hexagons $h = 9$ was repeated 100 times in the structure of hexagons $h = 109$ and the corresponding matrix elements of **W**(**109**) were taken from the matrix **W**(**9**). Thus, we could construct an approximation for the exact matrix **W**(**109**). We obtained that the first and third eigenvector of this **W**(**109**) was bi-lobal. Using this bi-lobal eigenvectors, we could construct the topological coordinates of the structure with 109 hexagons.

Although at the end of the 109 hexagon structure, the distances are different of the distances from the central part, the matrix **W**(**109**) could reproduce rather well the corresponding structure. Using the **W**(**21**) matrix, we could approximate well the **W**(**421**) matrix as well and could construct topological coordinates for the bar polyhex structure of 421 hexagons.

5 Conclusions and outlook

Using the well-known structures of bar polyhexes, we presented approximation for the **W** matrices of large number of hexagon structures. Using the calculated matrix elements of smaller structures, we constructed **W** matrices without minimizing the total energy of large polyhex. These results can be generalized for any complicated atomic (or graph) structures as well. First, we divide the large structure for smaller ones and the **W** matrices of these smaller parts can be used for constructing the **W** matrix of the large system. Using these ideas, topological coordinates can be constructed for any large molecular structures.

The topological coordinate method was successfully applied for fullerenes [1], and there are promising results for helical structures as well [18–21].

References

1. Fowler PW, Manolopulos DE (1995) An atlas of Fullerenes. Clarendon Press, Oxford
2. Manolopoulos DE, Fowler PW (1992) Molecular graphs, point groups, and fullerenes. J Chem Phys 96:7603–7614
3. Pisanski T, Shawe-Taylor JS (1993) Characterising graph drawing with eigenvectors. In: Technical report CSD-TR-93-20, Royal Holloway, University of London, Department of Computer Science, Egham, Surrey TW200EX, England
4. Pisanski T, Shawe-Taylor JS (2000) Characterising graph drawing with eigenvectors. J Chem Inf Comput Sci 40:567–571
5. Godsil CD, Royle GF (2001) Algebraic graph theory. Springer, Heidelberg
6. Lovász L, Schrijver A (1999) On the null space of the Colin de Verdière matrix. Annales de l'Institute Fourier (Grenoble) 49:1017–1026
7. Lovász L, Vesztergombi K (1999) Representation of graphs. In: Halász L, Lovász L, Simonovits M, Sós V (eds) Paul Erdős and his mathematics. Bolyai Society – Springer, Berlin
8. Graovac A, Plavšić D, Kaufman M, Pisanski T, Kirby EC (2000) Application of the adjacency matrix eigenvectors method to geometry determination of toroidal carbon molecules. J Chem Phys 113:1925–1931
9. László I, Rassat A, Fowler PW, Graovac A (2001) Topological coordinates for toroidal structures. Chem Phys Lett 342:369–374
10. Graovac A, Lászlo I, Plavšić D, Pisanski T (2008) Shape analysis of carbon nanotube junctions, MATCH. Commun Math Comput Chem 60:917–926
11. László I, Graovac A, Pisanski T, Plavšić D (2011) Graph drawing with eigenvectors. In: Putz MV (ed) Carbon bonding and structures: advances in physics and chemistry. Springer, New York, pp 95–115
12. László I, Graovac A, Pisanski T (2013) Nanostructures and eigenvectors of matrices. In: Ashrafi AR, Cataldo F, Graovac A, Iranmanesh A, Ori O, Vukicevic D (eds) Carbon materials chemistry and physics: topological modelling of nanostructures and extended systems. Springer, New York

13. László I, Graovac A, Pisanski T (2013) Drawing diamond structures with eigenvectors. In: Diudea MV, Nagy CL (eds) Carbon materials chemistry and physics: diamond and related nanostructures. Springer, New York
14. László I (2013) Geometry of nanostructures and eigenvectors of matrices. Phys Status Solidi B 250:2732–2736
15. Jackson B, Jordán T (2007) Rigid components in molecular graphs. Algorithmica 48:399–412
16. Jackson B, Jordán T (2008) On the rigidity of molecular graphs. Combinatorica 28:645–658
17. Brenner DW (1990) Empirical potentials for hydrocarbons for use in simulating the chemical vapor deposition of diamond films. Phys Rev B 42:9458–9471
18. László I, Rassat A (2003) The geometric structure of deformed nanotubes and the topological coordinates. J Chem Inf Comput Sci 43:519–524
19. Popovic ZP, Damnjanovic M, Milosevic I (2013) Anisotropy of thermal expansion of helically coiled carbon nanotubes. Phys Status Solidi B 250:2535–2538
20. Dmitrovic S, Popovic ZP, Damnjanovic M et al (2013) Structural model of semi-metallic carbon nanotubes. Phys Status Solidi B 250:2627–2630
21. Dmitrovic S, Popovic ZP, Damnjanovic M et al (2013) Strain engineering of electronic band structure and optical absorption spectra of helically coiled carbon nanotubes. J Nanoelect Optoelektr 8:160–164

Theor Chem Acc (2015) 134:114
DOI 10.1007/s00214-015-1709-4

REGULAR ARTICLE

Hydrocarbon chains and rings: bond length alternation in finite molecules

Jenő Kürti[1] · János Koltai[1] · Bálint Gyimesi[1] · Viktor Zólyomi[2,3]

Received: 19 June 2015 / Accepted: 28 July 2015 / Published online: 9 September 2015

Abstract We present a theoretical study of Peierls distortion in carbon rings. We demonstrate using the Longuet-Higgins–Salem model that the appearance of bond alternation in conjugated carbon polymers is independent of the boundary conditions and does in fact appear in carbon rings just as in carbon chains. We use the Hartree–Fock approximation and density functional theory to show that this behaviour is retained at the *first principles* level.

Keywords Peierls distortion · Conjugated polymers · Annulenes · Longuet-Higgins–Salem model · Density functional theory

1 Introduction

Peierls distortion [1] in one dimension (1D) is an inherent trait of linear conjugated polymers, leading to a bond length alternation (BLA). The usual chemical nomenclature for it is conjugation. Examples include polyacetylene and polyyne, two materials which have been studied by the physics and chemistry community for a very long time (see, e.g. the book [2] and the papers cited therein). For more recent publications about the BLA in carbon chains, see, e.g. Refs. [3–6] and references therein. Polyyne in particular remains a hot topic experimentally and theoretically, in part due to the difficulty in determining the band gap of this material [6]. One reason why it is difficult to correctly calculate the band gap in Peierls distorted systems is that the bond length alternation directly determines the band gap, i.e. if the bond length alternation is underestimated (as is often the case in, e.g. density functional theory), the band gap will be underestimated as well. As such, the matter of correctly describing bond length alternation is a current and important topic.

In addition, Peierls distortion brings with it some interesting fundamental questions, such as whether the bond length alternation appears in carbon *rings*. It is known that in long linear chains, as we increase the length of the chain, we approach the infinite polymer where the Peierls distortion is realized. However, the effect cannot depend on the boundary conditions, and hence, a hydrogen terminated finite chain and a cyclic carbon ring must converge to the same Peierls distorted geometry in the infinite limit. All that can be different is the speed of convergence. In this work, we discuss the question of Peierls distortion in carbon rings and at what number of carbon atoms the alternation appears.

The BLA in conjugated polymers can be very well described by an improved Hückel-type method, the semiempirical Longuet-Higgins–Salem (LHS) model [7, 8].[1] The corresponding solid-state physics approximation is the Su–Schrieffer–Heeger model [9, 10]. The relationship between the LHS and the SSH models was pointed out in Ref. [11].

Published as part of the special collection of articles "Festschrift in honour of P. R. Surjan".

✉ Jenő Kürti
kurti@virag.elte.hu

[1] Department of Biological Physics, Eötvös University Budapest, Budapest, P.O.B. 32, 1518, Hungary

[2] Physics Department, Lancaster University, Lancaster LA1 4YB, UK

[3] Wigner Research Institute, Hungarian Academy of Sciences, Budapest, P. O. B. 49, 1525, Hungary

[1] Developing the model and the corresponding HUGEH code and applying it to various conjugated polymers was a very fruitful collaboration between P.R. Surján and J. Kürti.

To further demonstrate the robustness of the appearance of the Peierls distortion, we also use ab initio (Hartree–Fock, HF) and *first principles* (density functional theory, DFT) methods.

We start our investigation with the benzene molecule, where no BLA appears. We increase the number of carbon atoms by four atoms in each step in order to topologically allow the potential appearance of a BLA. Our goal is to find the critical number of carbon atoms where the ring becomes Peierls distorted. As it will turn out, it is not enough to consider only the simplest planar rings. Therefore, we consider various possible ring-type structures, determining their optimized geometries. The next section discusses which molecules come into question. This is followed by the results for the energies and for the BLA, starting with the LHS model, continuing with HF and DFT results. The paper is concluded by a summary.

2 Investigated molecules

Theoretically, the simplest possible carbon systems showing BLA are linear carbon chains with sp^1 hybridization. Imagine a row of carbon atoms where each atom is covalently bonded to its left and right neighbours. The question is, are the bond lengths uniform, or do they vary? Theoretically the purest case is the infinite long carbon chain. It can be shown, based on solid-state physics arguments, that for the infinite long chain the structure with alternating bond lengths (polyyne) is energetically more favourable than the structure with uniform bond lengths (polycumulene)—this is an example of the well-known Peierls distortion [1, 12]. However, this is only a speculative situation. In fact the longest isolated linear carbon chain consists of 'only' 44 carbon atoms [13], which is still far from a length which can be considered as infinite. The structure of a finite chain is strongly influenced by how it is terminated. The chain can be stabilized by relatively large end groups [13] or it can simply have a nitrogen atom or a hydrogen atom at the end [14]. There is even the possibility that the chain has no end groups, consisting of only carbon atoms [15, 16]. However, the accurate treatment of pure carbon molecules is a delicate problem which is outside the scope of this paper. We just mention that a linear C_n molecule is unstable against bending, crosslinking, forming fused rings or cage-like molecules, depending on the number of carbon atoms. The relatively long carbon chains are stable and accessible for experiments only if they exist inside carbon nanotubes [3, 17] or if they are separated from each other by alkali fluoride particles when preparing them from polytetrafluoroethylene [18, 19]. In any case the end groups have a drastic influence on the bond length alternation. For example, H–C≡ group or N≡C– group at the end immediately triggers the BLA starting from the end of the chain. Therefore, the BLA is always present in linear carbon chains, and only its amount changes (decreases) when going from finite molecules to the infinite limit. We can say, with some exaggeration, that qualitatively nothing special happens in this case.

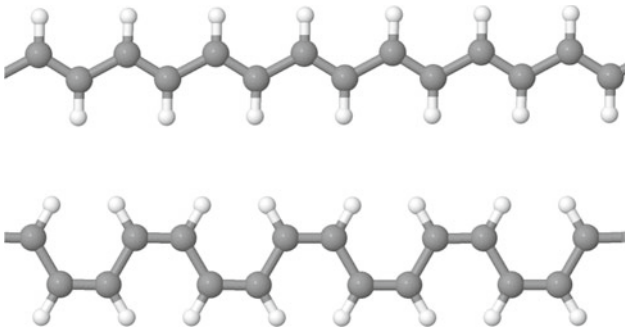

Fig. 1 *Trans* (*trans-transoid*) and *cis* (*cis-transoid*) isomers of polyacetylene, *above* and *below*, respectively

The situation is more intriguing if we go from sp^1 to sp^2 molecules, that is, to hydrocarbons. Polyacetylene $(C_2H_2)_x$ is the prototype of the whole family of conjugated polymers. It has two isomers, the *trans* and *cis* forms (see Fig. 1). The *trans* isomer is more stable than the *cis* one. The experimentally observed bond lengths are 136/144 and 137/144 pm for *trans* and *cis* isomers, respectively. [Note that these bond lengths differ from that of 'true' double bond (133 pm) and single bond (154 pm)].

The BLA of the infinitely long polyacetylene can be reproduced theoretically on different computational levels: the LHS model gives a result of 136/144 pm for the bond lengths [8, 20], whereas the DFT method with B3LYP functional results in a BLA of 5 pm [12]. The BLA of short conjugated oligoenes is larger than this, again due to the chain end effects. The shortest oligoene 1,3-butadiene (C_4H_6) has bond lengths of 134 and 145 pm at the end and in the middle, respectively [12]. The next non-radical oligoene is 1,3,5-hexatriene (C_6H_8) with bond lengths of 134, 146 and 137 pm, starting from the edge.

End-group effects are completely avoided when we investigate closed (cyclic) conjugated molecules, that is, rings instead of chains. For an infinite long system, its properties should not depend on the boundary conditions. The question is what happens with the BLA for finite molecules. This is especially interesting in the case of sp^2 hydrocarbons. Benzene (C_6H_6) is a peculiar system. It is an aromatic molecule with D_{6h} symmetry, and hence, all six bonds are perfectly identical in length (140 pm). Our aim is to gradually increase the size of the ring in order to find the critical size where the bond alternation appears. However, this is not so straightforward as one would naïvely think it is.

First of all, we restrict ourselves to $C_{4n+2}H_{4n+2}$ monocyclic, unsaturated hydrocarbon molecules with $n = 1$ to

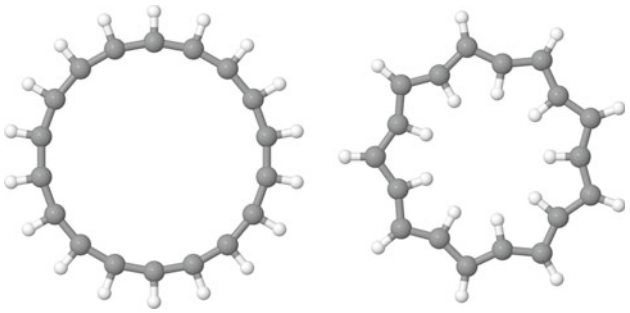

Fig. 2 [18]Annulene planar *all-cis* geometry (*left*) and [18]annulene planar *all-trans* geometry (*right*)

8 and 16. In other words, we consider annulenes, those ones which obey the Hückel's rule. Otherwise, the molecule cannot be aromatic, so there is ab ovo a bond length alternation. The next question is whether these molecules are planar or not. For the LHS model, this does not matter. In Hückel-type calculations, only the bond lengths play a role. However, for more sophisticated methods we need to know the precise spatial structure in three dimensions (3D). Therefore, we consider several possible configurations which correspond to local energy minima. Note that the structure of annulenes has been the subject of extensive research, see. for example, Refs. [21, 22].

The simplest case is the planar configuration, similar to the structure of benzene (see Fig. 2 left side). We call this *all-cis* structure. However, there are problems with the *all-cis* configuration. First, increasing the number of carbon atoms leads to an increasing deviation from the optimal 120° bond angle, that is, an increasing angular strain is induced. Second, the structure does not converge to that of the polyacetylene chain in the infinite case because all H atoms are on the same side of the carbon backbone. Even more, the *all-cis* structure is unstable in plane, as we will see later on.

Therefore, we consider the planar *all-trans* structures, as well (see Fig. 2 right side). Although this is very unfavourable for small rings (it is impossible, e.g. for benzene), it becomes, as opposed to the *all-cis* case, more and more favourable with increasing size, and, at the end, it converges to the structure of the *trans*-polyacetylene chain for the infinite case. Nevertheless, the *all-trans* structures are also unstable in a planar configuration, at least for not too large rings, as we will see later on.

We consider further structures as well. We optimize the geometry in 3D for [10]annulene (cyclodecapentaene = $C_{10}H_{10}$) and for [14]annulene (cyclotetradecaheptaene = $C_{14}H_{14}$). Figures 3 and 4 right side show that these molecules are indeed a non-planar structure in their relaxed geometries. It should be mentioned that these annulenes also have local energy minimum configuration where their

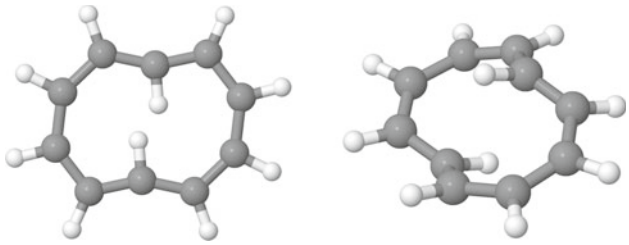

Fig. 3 [10]Annulene planar, optimized in two dimensions (2D) (*left*) and [10]annulene non-planar, optimized in 3D (*right*)

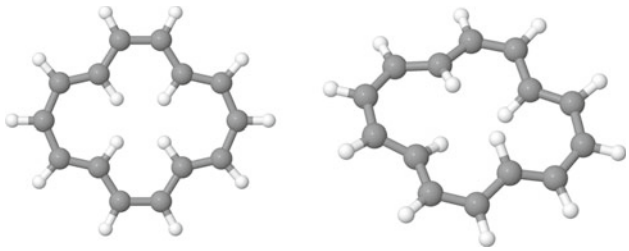

Fig. 4 [14]Annulene planar, optimized in 2D (*left*) and [14]annulene non-planar, optimized in 3D (*right*)

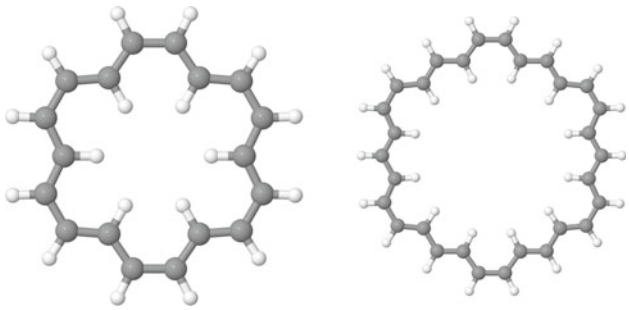

Fig. 5 Two annulenes with D_{6h} symmetry: [18]annulene-D_{6h} (*left*) and [30]annulene-D_{6h} (*right*)

structure is planar (see Figs. 3, 4 left side), but they are less favourable in energy than the non-planar ones in Figs. 3 and 4 right side.

The next annulene, [18]annulene (cyclooctadecanonaene = $C_{18}H_{18}$), is a special case. The most stable structure of this molecule is a planar aromatic structure with D_{6h} symmetry (see Fig. 5 left side). According to our geometry optimization, there are two slightly different carbon–carbon bond lengths: 140.0 pm (between carbons in *trans* position) and 141.6 pm (between carbons in *cis* position). In fact, according to Fig. 5 left side, one can define a whole family of rings. Introducing longer and longer *trans* segments between the six *cis* carbon pairs, the D_{6h} symmetry is retained. The $[6 + k \cdot 12]$annulenes belong to this family. Figure 5 right side shows, e.g. the [30]annulene molecule

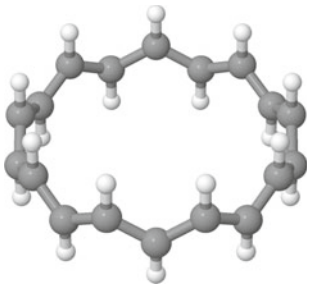

Fig. 6 [18]Annulene in nanoring form

with D_{6h} symmetry. Actually, with some indulgence, benzene can be regarded as the smallest molecule of this family, with no *trans* segments.

However, also the planar D_{6h} configurations are not without problems, because the bonds are symmetry inequivalent. The *cis* parts act as boundaries for the *trans* segments, so these molecules can be viewed as ones with internal delimiting effects, which can trigger the BLA even inside the *trans* segments. This leads us to consider *non-planar* hydrocarbon rings, with no end-group effects or internal delimitation (see Fig. 6 as an example). These $C_{4n+2}H_{4n+2}$ nanorings can be regarded as cut out appropriately from a $(4n+2, 0)$ zig-zag nanotube and hydrogenized. In other words, they can be viewed as a finite piece of *trans*-polyacetylene wrapped up *perpendicular* to the plane of the polymer. They are energetically unfavourable for short rings. However, they become more and more stable with increasing size as we will see, and they develop into *trans*-polyacetylene in the infinite limit. Their advantage is that they are the adequate molecules to investigate the length dependence of the Peierls transition. Before Peierls distortion switches on, the molecule has $D_{\tilde{n}d}$ symmetry (where $\tilde{n} = 2n + 1$) and all bonds are symmetry equivalent. The ground state is degenerated, and the BLA can appear only by symmetry breaking.

3 LHS results

The LHS model originates from an early work of Longuet-Higgins and Salem [7]. The model was further developed by Surján [11] and Kertész [23] and by Surján and Kürti [8, 20, 24, 25]. It is a Hückel-type method in essence but with two important extensions. First, the β parameter of the Hückel method is not constant but depends on the bond length:

$$\beta(r) = -A \cdot exp(-r/B). \tag{1}$$

Here the parameters A and B were optimized for carbon–carbon bonding so that the model can reproduce the BLA and the gap of *trans*-polyacetylene (see, e.g. in Ref. [8]).

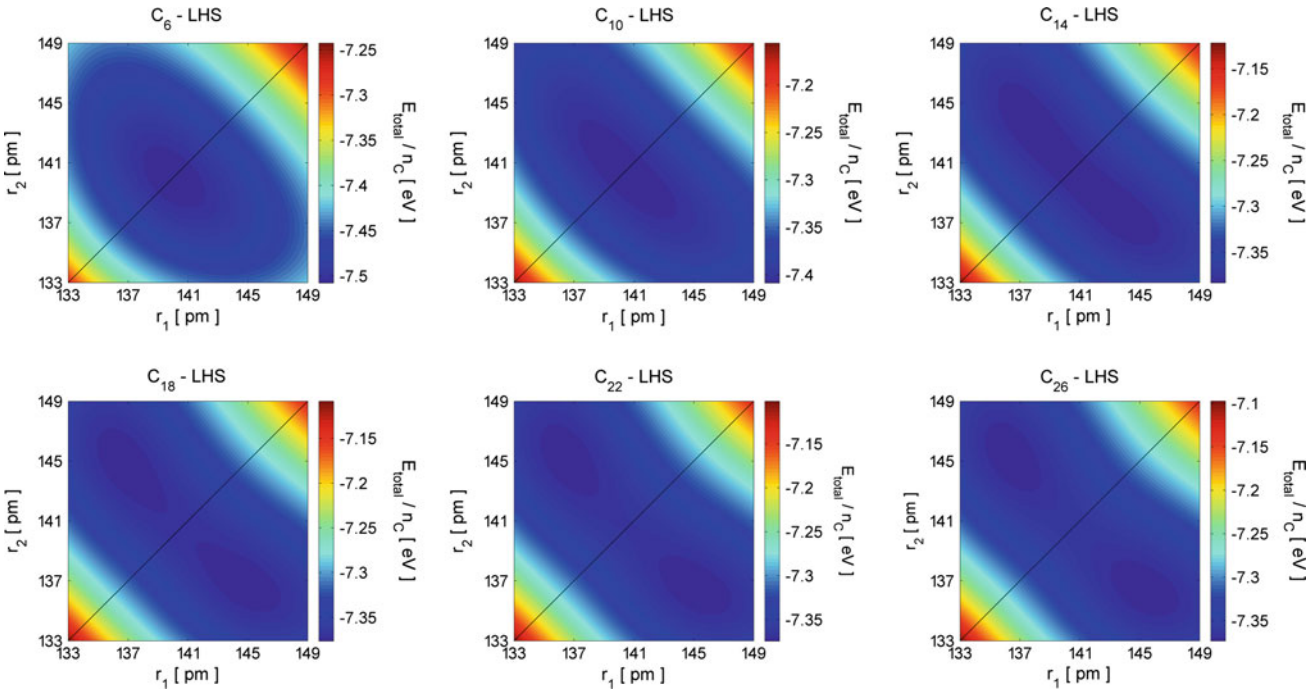

Fig. 7 Total energy per carbon atom contours for C_{4n+2} carbon rings as a function of the two consecutive bond lengths, according to the LHS model. The number of carbon atoms ($n_C = 4n + 2$) increases from 6 to 26 in steps of four atoms

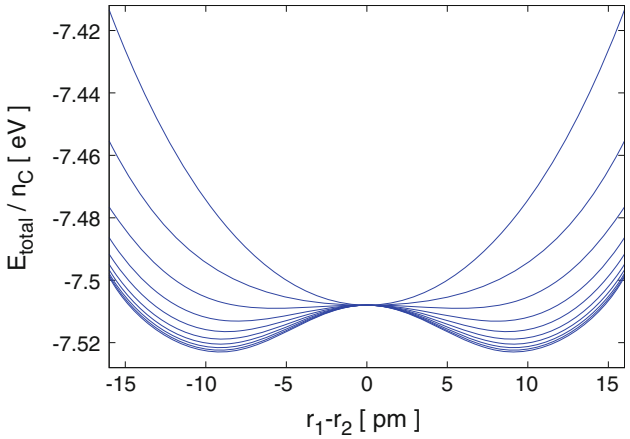

Fig. 8 Total energy per carbon atom for C_{4n+2} carbon rings versus bond length alternation, according to the LHS model. Increasing the number of carbon atoms ($n_C = 4n + 2$) from 6 to 42 in steps of four atoms results in a bifurcation. The BLA is initially zero and converges to $\approx \pm 9$ pm

The second important improvement is the explicit accounting for the σ-electrons by an empirical potential:

$$f_\sigma(r) = 2 \cdot \beta(r) \cdot (r - R_1 + B)/(R_1 - R_2), \tag{2}$$

where R_1 and R_2 are the lengths of the pure single and double bonds, respectively. This potential can be derived from, therefore is equivalent to, the empirical linear Coulson relation between bond length and (mobile) bond order [26]:

$$r = R_1 - (R_1 - R_2) \cdot p, \tag{3}$$

where p is the bond order for the π-electrons. The details of the model, together with some of its applications, can be found in the references mentioned above. We emphasize here only the most important property of the LHS method: as opposed to the usual Hückel theory, it allows the optimization of the bond lengths in a self-consistent manner by satisfying the Coulson relation, which at the same time minimizes the total ($\pi + \sigma$) energy. However, one has to keep in mind that the LHS model cannot handle the bond angles, only the bond lengths.

H atoms are neglected in this model. We used our LHS code to calculate the total energy of the C_{4n+2} rings, starting with $n_C = 4n + 2 = 6$ (benzene) until $n_C = 4n + 2 = 42$. We scanned the geometry according to dimerization, having only two independent bond lengths. The two consecutive bonds (r_1 and r_2) can be different, but all odd-numbered bonds are identical in length, as are all even-numbered bonds. Figure 7 shows the 2D total energy map, that is, the total energy per carbon atom contours as a function of the two neighbouring bond lengths, for rings C_6 to C_{26}. The maps are symmetric with respect to the $r_1 = r_2$ (BLA = 0) line.

The total energy has a stable minimum for C_6 and C_{10} at $r_1 = r_2 = 140$ pm. However, starting from C_{14} the minimum with BLA = 0 becomes a saddle point and a Peierls distortion appears. This can be seen more clearly in Fig. 8. These 1D curves show the total energy per carbon atom along the line which is perpendicular to the BLA = 0 line and goes through the minimum point for $n_C = 4n + 2 = 6$ and 10, or through the saddle point for $n_C = 4n + 2 \geq 14$. For the sake of clarity, the curves are shifted so that they all have the same energy value in the BLA = 0 point. For $n_C = 6$ the total energy has a relatively sharp minimum, and for $n_C = 10$ the minimum is already very flat. Starting from $n_C = 14$ a bifurcation occurs which becomes more and more pronounced converging to BLA $\approx \pm 9$ pm.

4 HF results

We already mentioned that the LHS model cannot handle either the H atoms or the bond angles. It takes into account only the topology of the C atoms. To check the reliability of the LHS results, we repeated the calculations on a higher level using the Hartree–Fock approximation. In this case, one has to know the true geometry of the molecule. We carried out the HF calculations for the planar *all-cis* configuration of the $C_{4n+2}H_{4n+2}$ molecules with $n_C = 4n + 2 = 6, 10$ and 14. We used the G09 code [27] to calculate the total energy of these molecules. We repeated the same procedure what was done with the LHS model. We scanned the geometry according to dimerization, having only two free parameters, lengths of the two independent consecutive carbon–carbon bonds (r_1 and r_2). The lengths and angles for the C–H bond were kept fixed. Figure 9 shows the 2D total energy map, that is, the total energy contours as a function of the two neighbouring bond lenghts, for $C_{4n+2}H_{4n+2}$ molecules with $n_C = 4n + 2 = 6$, 10 and 14. The energy values are defined as the total energy per carbon atom of the molecule minus the total energy per carbon atom for benzene. The maps are symmetric with respect to the $r_1 = r_2$ (BLA = 0) line.

The total energy has a stable minimum for C_6H_6 and $C_{10}H_{10}$ at $r_1 = r_2 = 139$ pm. However, for $C_{14}H_{14}$ the minimum with BLA = 0 becomes a saddle point and a Peierls distortion appears, with two different bond lengths of 137 and 146 pm (BLA = 9 pm), very similar to what was observed with LHS model.

5 DFT results

With the HF-method, we optimized only the positions of the carbon atoms. More reliable results can be obtained if one optimizes the structure by taking into account all geometrical degrees of freedom. This means not only the optimization of the positions of the H atoms but also allowing the molecule to distort out of plane. We

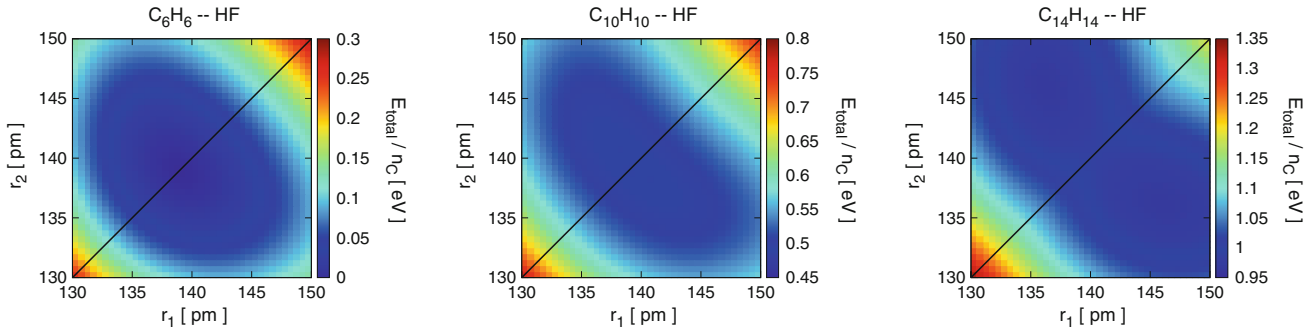

Fig. 9 Total energy per carbon atom contours for $C_{4n+2}H_{4n+2}$ planar *all-cis* rings as a function of the two consecutive bond lengths, according to the Hartree–Fock approximation. The number of carbon atoms ($n_C = 4n + 2$) increases from 6 to 14 in steps of four atoms

mentioned already earlier that in most cases the planar structure proved to be unstable. Our aim was to consider further ring configurations and to find possible structures in local energy minima. In order to do this, we have chosen density functional theory using the B3LYP/6-31G(d,p) functional of the G09 program package [27]. This *first principles* method already takes into account the correlation, but it is still manageable for molecules shown in Sect. 2.

We optimized the geometry with various constraints:

(a) The structure was relaxed in plane with *all-cis* geometry (see, e.g. Fig. 2 left part), for $n_C = 6, 10, \ldots 34$ and 66.
(b) The structure was relaxed in plane with *all-trans* geometry (see, e.g. Fig. 2 right part), for $n_C = 6, 10, \ldots 34$ and 66.
(c) The structure was relaxed in plane starting from the special sp^2 structure for $n_C = 10$ and 14 (see Figs. 3, 4 left parts).
(d) The structure was relaxed in 3D starting from the special sp^2 structure for $n_C = 10$ and 14 (see Figs. 3, 4 right parts).
(e) The structure was relaxed in plane starting from D_{6h} structure for $n_C = 18$, 30 and 66 (see Fig. 5 for $n_C = 18$ and 30).
(f) The structure was relaxed in 3D for nanorings with $n_C = 6, 10, \ldots 34$ and 66 (see, e.g. Fig. 6 for the case of $n_C = 18$).

As it was mentioned earlier, all molecules fulfil Hückel's rule: the number of C atoms is $n_C = 4n + 2$. Figure 10 shows the results for the calculated total energies per carbon atom. Benzene is the energetically most favourable structure, and its value was chosen as zero. Benzene belongs to two different families: it has an *all-cis* structure and D_{6h} symmetry at the same time. The energy of the *all-cis* series increases rapidly and starting from $n_C = 18$ they are the most unfavourable structures. Furthermore, they are unstable against

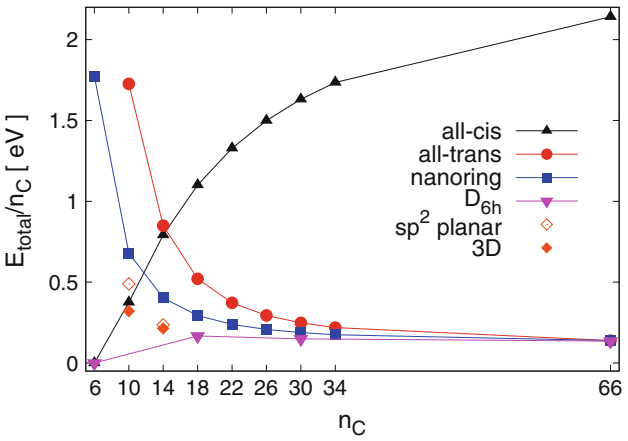

Fig. 10 Total energies per carbon atom obtained by B3LYP/6-31G(d,p) for various ring-type molecules shown in Figs. 2, 3, 4, 5 and 6. The obtained value for benzene was chosen as the reference point with zero energy. The *lines* are guides for the eye for the different families

out-of-plane distortions as it can be read out from the increasing number of imaginary frequencies in the vibrational analysis.

The behaviour of the *all-trans* series is reversed. It is very unfavourable in energy for small molecules, but its energy per carbon decreases with increasing n_C. Nevertheless, they are unstable against out-of-plane distortions. Interestingly, the *all-trans* structure will go over the nanoring structure for $n_C = 66$.

We investigated the special sp^2 structures, in planar as well as non-planar configuration, for $n_C = 10$ and 14. Their energies are quite favourable. Of course, the non-planar one is the most favourable structure, but the difference between the values for planar and non-planar case decreases when going from $n_C = 10$ to $n_C = 14$. For $n_C = 18$ they coincide and they are both identical with the D_{6h} structure. However, the bonds are symmetry inequivalent for these structures, even in the case of D_{6h} symmetry, with the only exception of

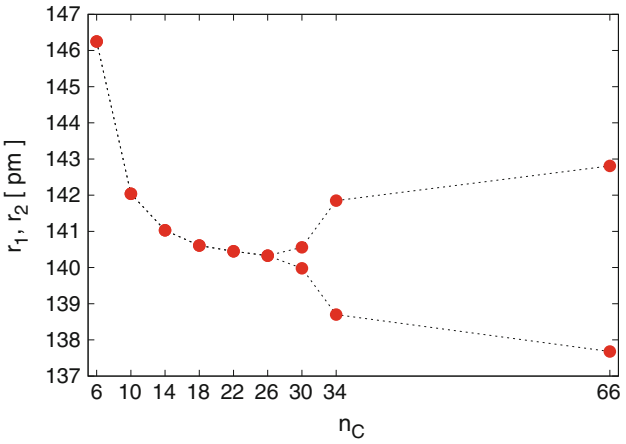

Fig. 11 Change of the bond lengths with increasing number of C atoms in the nanorings as obtained by B3LYP/6-31G(d,p). A bifurcation occurs at $n_C = 26$ and a finite BLA appears

benzene. Therefore, these molecules are not suitable for studying the appearance of Peierls distortion. (We mention that the D_{6h} symmetry lowers to D_{3h} symmetry for $n_C = 30$ and 66).

We arrive at the nanorings. As mentioned in Sect. 2, they are ring-like molecules with symmetry equivalent carbon–carbon bonds. The consecutive H atoms are all in *trans* position, and they lay not in the plane of the ring of C atoms, but perpendicular to this plane. The optimized geometry proves to be stable, without any imaginary frequency vibrational modes, until the largest nanoring we considered ($n_C = 66$). Due to the symmetry and the stability, the nanorings are the ideal systems to study the appearance of the bond length alternation. For small rings, until $n_C = 26$ there is no BLA in the molecule after geometry optimization. At $n_C = 30$ a bifurcation occurs and the BLA becomes finite. Figure 11 shows the evolution of the Peierls distortion in the finite system. The value of the BLA at $n_C = 66$ in the nanoring is 5 pm which is in very good agreement with the DFT calculated 5 pm BLA for infinite polyacetylene [12].

6 Summary

We investigated the appearance of bond length alternation (Peierls distortion in physical language, conjugation in chemical language) in closed sp^2 hydrocarbon molecules. For finite linear chains of the type $C_{2n}H_{2n+2}$ it is well known that short and long bonds alternate regularly (conjugated oligoenes). Although the BLA decreases with increasing chain length, it does not disappear but remains finite when the chain length goes to infinity. This means that there is no qualitative change in BLA when going from finite chains to the infinite chain. On the other hand, the situation is different for closed annulenes. Here, a qualitative change occurs. Benzene has no BLA, and all bonds have the same length. However, for long enough rings there should be a bond length alternation, because in the infinite limit the properties should not depend on the boundary conditions, that is, it should not matter whether the system is open (chain) or closed (ring). We investigated theoretically the transition from non-alternating rings to alternating ones, as a function of the number of carbon atoms in the ring for $C_{2n}H_{2n+2}$ molecules. Calculations have been done on different levels of theory. With the Longuet-Higgins–Salem and the Hartree–Fock methods, this transition occurs rather soon: as few as 14 carbon atoms are enough and the BLA becomes nonzero. According to our DFT results with B3LYP/6-31G(d,p) functional, the transition shifts to larger rings: the appearance of the BLA occurs at $C_{30}H_{30}$. This result was obtained for 'nanorings' which are slices from zig-zag nanotubes, saturated by H atoms, where the H–C bonds are parallel with the symmetry axis of the ring. We investigated many cyclic structures, planar and non-planar both. The planar *all-cis* and *all-trans* rings are either energetically unfavourable or unstable, with the only exception of benzene. The annulenes with D_{6h} symmetry are energetically favourable, but here and in some possible 3D cases the bonds are not symmetry equivalent. Therefore, the investigation of Peierls distortion is without meaning. The only cyclic hydrocarbon molecules are the $C_{2\tilde{n}}H_{2\tilde{n}}$ nanorings with $D_{\tilde{n}d}$ symmetry, which are energetically favourable and stable (except for the too small rings) and in which all carbon–carbon bonds are symmetry equivalent. The ground state is degenerate, and the BLA can appear only by symmetry breaking.

At the end, we mention that in the future there might be methods by which the planar structures, which are unstable in pristine state, can be stabilized by intercalation between the layers of 2D layered materials like boron nitride or transition metal dichalcogenide materials. Also the synthesis of hydrocarbon nanorings might be a challenge for preparative chemistry. Note that the synthesis of carbon picotubes [28] may be considered the first step in this direction.

Acknowledgments The authors acknowledge the financial support from OTKA in Hungary (Grant Number K108676). Je.K. acknowledges beneficial discussions with Sándor Pekker. The authors express their gratitude to Péter Surján on the occasion of Péter's 60th birthday. Jenő Kürti remembers with pleasure to the many joint works with Péter which resulted in more than ten joint publications, started from 1989.

References

1. Peierls RE, Peierls SRE (1955) Quantum theory of solids. Clarendon Press, Oxford
2. Roth S, Carroll D (2004) One-dimensional metals: conjugated polymers, organic crystals, carbon nanotubes. Wiley, London

3. Rusznyák Á, Zólyomi V, Kürti J, Yang S, Kertesz M (2005) Bond-length alternation and charge transfer in a linear carbon chain encapsulated within a single-walled carbon nanotube. Phys Rev B 72(15):155420(6)
4. Yang S, Kertesz M (2006) Bond length alternation and energy band gap of polyyne. J Phys Chem A 110(31):9771–9774
5. Körzdörfer T, Parrish RM, Sears JS, Sherrill CD, Brédas J-L (2012) On the relationship between bond-length alternation and many-electron self-interaction error. J Chem Phys 137(12):124305(8)
6. Al-Backri A, Zólyomi V, Lambert CJ (2014) Electronic properties of linear carbon chains: resolving the controversy. J Chem Phys 140(10):104306(4)
7. Longuet-Higgins HC, Salem L (1959) The alternation of bond lengths in long conjugated chain molecules. Proc R Soc Lond A Math Phys Eng Sci 251(1265):172–185
8. Kürti J, Surján PR (1992) Embedded units in conjugated polymers. J Math Chem 10(1):313–327
9. Su WP, Schrieffer JR, Heeger AJ (1980) Soliton excitations in polyacetylene. Phys Rev B 22(4):2099–2111
10. Heeger AJ, Kivelson S, Schrieffer JR, Su WP (1988) Solitons in conducting polymers. Rev Mod Phys 60:781–851
11. Surján PR, Kuzmany H (1986) Interruption of conjugations of polyacetylene chains. Phys Rev B 33(4):2615–2624
12. Sun G, Kürti J, Rajczy P, Kertesz M, Hafner J, Kresse G (2003) Performance of the Vienna ab initio simulation package (VASP) in chemical applications. J Mol Struct THEOCHEM 624(1–3):37–45
13. Chalifoux WA, Tykwinski RR (2010) Synthesis of polyynes to model the sp-carbon allotrope carbyne. Nat Chem 2(11):967–971
14. Kirby C, Kroto HW, Walton DRM (1980) The microwave spectrum of cyanohexatriyne, HCCCCCCCN. J Mol Spectrosc 83(2):261–265
15. Watts JD, Bartlett RJ (1992) A theoretical study of linear carbon cluster monoanions, C-n, and dianions, C2-n (n = 2–10). J Chem Phys 97(5):3445–3457
16. Monninger G, Förderer M, Gürtler P, Kalhofer S, Petersen S, Nemes L, Szalay PG, Krätschmer W (2002) Vacuum ultraviolet spectroscopy of the carbon molecule C3 in matrix isolated state: experiment and theory. J Phys Chem A 106(24):5779–5788
17. Zhao C, Kitaura R, Hara H, Irle S, Shinohara H (2011) Growth of linear carbon chains inside thin double-wall carbon nanotubes. J Phys Chem C 115(27):13,166–13,170
18. Kastner J, Kuzmany H, Kavan L, Dousek FP, Kürti J (1995) Reductive preparation of carbyne with high yield. An in situ Raman scattering study. Macromolecules 28(1):344–353
19. Heimann R, Evsyukov SE, Kavan L (2012) Carbyne and carbynoid structures. Springer, Berlin
20. Kürti J, Kuzmany H (1991) Resonance Raman scattering from finite and infinite polymer chains. Phys Rev B 44(2):597–613
21. Choi CH, Kertesz M (1998) Bond length alternation and aromaticity in large annulenes. J Chem Phys 108(16):6681–6688
22. Wannere CS, Sattelmeyer KW, Schaefer HF, Schleyer PvR (2004) Aromaticity: the alternating C–C bond length structures of [14]-, [18]-, and [22]annulene. Angew Chem Int Ed 43:4200–4206
23. Kertész M, Surján PR (1981) Trapping of phase kinks in polyacetylene. Solid State Commun 39(5):611–614
24. Kürti J, Kuzmany H (1987) Conjugation length and localization in conjugated polymers. In: Kuzmany PDH, Mehring PDM, Roth DS (eds) Springer series in solid-state sciences, vol 76., Electronic properties of conjugated polymersSpringer, Berlin, pp 43–47
25. Kürti J, Surján PR (1989) Quinoid-aromatic transition in polythiophene-like systems. In: Kuzmany H, Mehring M, Roth S (eds) Electronic properties of conjugated polymers III: basic models and applications: proceedings of an International Winter School, Kirchberg, Tirol, March 11-18, 1989, no. 91 in Springer series in solid-state sciences. Springer, Berlin, p 69
26. Coulson CA (1951) Bond lengths in conjugated molecules: the present position. Proc R Soc Lond A Math Phys Eng Sci 207(1088):91–100
27. Frisch MJ, Trucks GW, Schlegel HB, Scuseria GE, Robb MA, Cheeseman JR, Scalmani G, Barone V, Mennucci B, Petersson GA, Nakatsuji H, Caricato M, Li X, Hratchian HP, Izmaylov AF, Bloino J, Zheng G, Sonnenberg JL, Hada M, Ehara M, Toyota K, Fukuda R, Hasegawa J, Ishida M, Nakajima T, Honda Y, Kitao O, Nakai H, Vreven T, Montgomery Jr JA, Peralta JE, Ogliaro F, Bearpark M, Heyd JJ, Brothers E, Kudin KN, Staroverov VN, Kobayashi R, Normand J, Raghavachari K, Rendell A, Burant JC, Iyengar SS, Tomasi J, Cossi M, Rega N, Millam JM, Klene M, Knox JE, Cross JB, Bakken V, Adamo C, Jaramillo J, Gomperts R, Stratmann RE, Yazyev O, Austin AJ, Cammi R, Pomelli C, Ochterski JW, Martin RL, Morokuma K, Zakrzewski VG, Voth GA, Salvador P, Dannenberg JJ, Dapprich S, Daniels AD, Farkas Ö, Foresman JB, Ortiz JV, Cioslowski J, Fox DJ (2009) Gaussian 09, Revision B.01. Gaussian, Inc., Wallingford CT
28. Schaman C, Pfeiffer R, Zólyomi V, Kuzmany H, Ajami D, Herges R, Dubay O, Sloan J (2006) The transformation of open picotubes to a closed molecular configuration. Phys Status Solidi B 243:3151–3154

Theor Chem Acc (2015) 134:138
DOI 10.1007/s00214-015-1743-2

REGULAR ARTICLE

On the non-integer number of particles in molecular system domains: treatment and description

Roberto C. Bochicchio[1]

Received: 26 May 2015 / Accepted: 30 September 2015 / Published online: 23 October 2015

Abstract The energy of an atomic or molecular system undergoing Coulomb interactions is well known at the integer numbers of its neutral or ionic configurations. Nevertheless, the physical domains (atoms in molecules) inside the whole molecular system possess a non-integer number of particles due to the electron exchange with its surrounding. Hence, the dependence of the energy, the density matrix and their marginal distributions (reduced density matrices) with the number of particles become a problem of fundamental importance in the description of the electron distribution, its properties and transformations. In this work, we present a rigorous mathematical and physical basis for the treatment of this problem within the grand-canonical statistical distribution of few particles. In this context, the derivatives of the energy and the density referred as chemical descriptors (especially chemical potential and hardness) are analyzed in both cases, when the system is isolated and when it is subject to the interaction with an environment. The ground state energy convexity dependence with the number of particles of these systems simplifies the description.

Keywords Grand-canonical ensemble · Electronic structure · Density matrix · Descriptors

Published as part of the special collection of articles "Festschrift in honour of P. R. Surjan".

✉ Roberto C. Bochicchio
rboc@df.uba.ar

[1] Departamento de Física, Facultad de Ciencias Exactas y Naturales, Universidad de Buenos Aires and IFIBA (CONICET), Ciudad Universitaria, 1428 Buenos Aires, Argentina

1 Introduction

Generally, quantum chemical calculations of electronic structure take the number of electrons in the molecule as a fixed parameter which states for a closed system [1, 2], i.e., for its neutral state of N electrons or for any of their ionic configurations. This is usually the correct approach for a molecule in gas phase but not within the framework of a surrounding environment which may donate or accept electrons as for instance in the treatment of solvation phenomena, surface chemistry, or enzyme mechanisms, among others. Therefore, this scenario induces to describe these problems by means of fragments or physical domains as moieties like individual or group of atoms within the molecular structure. Thus, to associate non-integer charges to them is the main key to the understanding at atomic scale of complex processes of electron distributions undergoing charge flux transfer among subsystems of atoms and molecules under the influence of reactive interactions and/or external perturbations, conformational changes or interactions, related to chemical reactivity [3–5]. For such a goal, the fundamental magnitudes to be described are the energy, the electron density and their derivatives [3, 4, 6]. Therefore, an accurate quantum treatment which attempts to reach a complete and rigorous description of the electron distribution and of ulterior way the determination of the physicochemical properties, needs a precise definition of the system, its energy and state. These problems merit the introduction of the Atoms in Molecules (AIM) concept and the energy and state dependence with the number of particles in the system.

It has been a common trend in the literature to assume under certain success that the quadratic electrostatic interactions constitute a suitable approach of the energy dependence on fractional charge and independent of the

strength scale of the interaction [6–10]. Nevertheless, the inadequacy of this model has been noted, and a linear dependence within the density functional theory (DFT) and also for the state function approach was proposed as an attempt to obtain the right energy dependence for non-integral electron number $\mathcal{N}$ and its differentiability [4, 5, 11]. Recently, a general proof for that proposal going beyond the DFT and the pure state function approaches has been presented [12] under the hypothesis of the ground state energy convexity for atomic and molecular systems driven by Coulombic interactions [4, 5, 12, 13]. To understand the mechanism of charge transfer mentioned above, the fragments within the molecular structure or even a whole molecular system may be interpreted as open systems that exchange electrons and energy between them and/or with a reservoir [4, 14, 15]. Therefore, it follows that a non-integer electron number may arise as a time average caused by the fluctuating number of particles and thus the open system need to be described by a statistical mixture or ensemble of states with different number of particles [4, 6, 8, 12–14]. Regarding the dependence of each magnitude, i.e., energy and/or the density, with the number of particles, two kinds of descriptors arise from them. The zero-order descriptors are those which are integrated functions of the magnitudes itself such as those describing the electronic distribution from electron populations as atomic charges, covalent bond orders, valencies, free valencies among others [16, 17] or local indicators as those coming from the topological approach like critical points of the density, their ellipticity or the Laplacian functions of the density, among others [18, 19]. The other type are the so-called higher-order descriptors depending on the successive derivatives of these magnitudes as for instance, the chemical potential, the hardness, Fukui functions, etc. [3]. The behavior of the energy, density or other properties for ensemble [4, 12, 13] or even for pure states distributions [20, 21] is of fundamental importance for the latter type because of the discontinuities they undergo at integer numbers [4]. So that the system definition is supported on the AIM notion giving rise to atomistic models for molecules [18, 22, 23] which permits to determine the concept of net charge on an atom as the key variable for determining its energy [4, 9, 12]. The energy and the density matrices (DM) are piecewise-continuous linear functions of the number of particles $\mathcal{N}$ [4, 12], and consequently, its first derivatives are $\mathcal{N}$-staircase functions being undefined at the integers and constant in between [24]. So that, second derivatives vanish in between and are not defined at the integers. Hence, descriptors like hardness vanish [3]. This dependence has contradictory consequences as for instance, the violation of the electronegativity equalization principle [3, 6] closely related to reactivities and hardness [3].

In Ref. [24], it is clearly noted that the formal $\mathcal{N}$ piecewise-continuous linear dependence of the physical magnitudes with the number of particles contains the essence of the model for non-integer electron systems [4, 12]. Thus, admitting the onset of a more accurate reactivity theory going beyond the mentioned inconsistencies, it must be recognized that reactivity descriptors are chemical environment dependent and may not be defined for isolated species without considering a fragment and/or reservoir interaction, i.e., generally, system–reservoir (S–R) interactions from which the species exchanges or transfers electrons [24]. A formal approach which addresses the problem and proposed a formal solution at an ensemble level can found in Ref. [25].

The objective of this work is to introduce some recent rigorous developments about the structure of the density matrices (DM), i.e., the state of the system as an ensemble of pure states of different number of fixed particles M commonly called grand-canonical ensemble (GC), the calculation of the energy under the hypothesis of its convexity for ground state isolated molecular systems and their extensions to systems under the influence of an environment interaction, i.e., a fragment or a reservoir [14]. In this way, we attempt to obtain a solution based on the interaction between the subsystems (S–R) inducing a coherent DM distribution which overcomes the inconsistencies mentioned above. Hence, the solution lies within the formal structure of reactivity theory, and the second-type chemical descriptors (second derivatives) are obtained in the natural scenario of the GC [12, 13] and the chemical context in which the species exchanges or transfers electrons.

Finally, the marginal distributions of the GC DMs, i.e., p-RDMs of the non-coherent (isolated systems) [13] distributions of the molecular open systems, are calculated by means of the contraction mappings [13, 26] in order to evaluate the properties as averages of the associated quantum observable. As an example, an explicit derivation and generalization of the Fukui functions are shown as a first-order descriptor of the density from this formalism without using the finite difference methods. The article is organized as follows. Section 2 presents the theoretical aspects introducing the definition, characterization and features of the systems, the energy determination, their states (DM) and marginal distributions, i.e., the reduced density matrices p-RDMs in the GC ensemble. Also in this section, some important properties for the open systems are sketched. In Sect. 3, the chemical descriptors of interest and the solution for the quantum state of the system in the framework of the S–R interaction are presented to show the machinery in action. A final Section is dedicated to the concluding remarks.

2 Theoretical background

2.1 The system

The dissociation process of a molecule leads to separated atoms, i.e., physically isolated, which are neutral. This is an experimentally very well-supported result because the greatest electron affinity (EA) of all the neutral atoms is smaller than the least ionization potential (IP) [5, 6]. The inverse process of the dissociation is the formation of a stable structure by bonding interactions where their densities distort from the isolated ones and then polarize to produce a charge transfer as is also very well known by experimentalists [27]. Consequently, they become fractionally charged to form covalent, ionic or any other type of distribution [18, 19] regarding the linked atoms as open systems free to exchange electrons between them [4, 5] and no longer as isolated. Therefore, the notion of an atom in a molecule (AIM) as a physical domain within the physical space is needed for a theoretical determination of the transferred fraction of charge. For practical implementations, each physical magnitude may be decomposed for atoms or a group of them like moieties that can be for instance a functional group or a simple atom. Two equivalent methods but of different nature may be considered, the topological ones based on the physical partition of the real space by means of a rigorous methodology like the Bader's AIM [16–18, 28–30] or those supported by empirical parameters as the "fuzzy" atoms [22, 31, 32] while others, the fragment methods (FM) which are not of topological nature [23]. These ideas introduce the concept we will have in mind when we invoke the treatment of a non-integer domain population, i.e., they house a number of particles $\mathcal{N}$ with $\mathcal{N} \in \mathbb{R}$. In general, these systems can be considered a subsystem within a molecular framework or a whole molecule in contact with an electron reservoir so that both schemes admit the electron exchange [15].

2.2 Energy and states

To describe these systems, the physical extension of the ground energy level $\mathcal{E}_0^{\mathcal{N}}$ where $\mathcal{N}$ is the number of particles with $\mathcal{N} \in \mathbb{R}$, as well as their states as a function of a continuous number of particles is needed. The most general description of the state of a quantum system is the density matrix D [26, 33]. It describes the state of an isolated system as a non-coherent convex sum of the complete set of all accessible M-electron pure state density matrices [26, 33, 34]

$$ {}^{M}D_{\Phi_k^M} = |\Phi_k^M\rangle\langle\Phi_k^M| \tag{1} $$

in the mixture, where $|\Phi_k^M>$ is the kth quantum state function in the antisymmetric M-electron Hilbert space $\mathfrak{F}_M$ (Hamiltonian eigenstates) [34, 35]. Therefore, D is expressed by [34, 35]

$$ \begin{aligned} D &= \sum_M \sum_{\Phi_k^M} \omega_{\Phi_k^M} \, |\Phi_k^M\rangle\langle\Phi_k^M|; \\ &\sum_M \sum_{\Phi_k^M} \omega_{\Phi_k^M} = 1; \quad \omega_{\Phi_k^M} \geq 0 \end{aligned} \tag{2} $$

where $\omega_{\Phi_k^M}$ are the statistical weights, i.e., the probability of occurrence of the pure state $|\Phi_k^M\rangle$ in the mixture. The carrier space for this type of description is the entire Fock space $\mathfrak{F} = \bigoplus_{M=0}^{\infty} \mathfrak{F}_M$, where the symbol $\bigoplus$ indicates direct sum [35]. These states admit particle number fluctuation, and the number of particles is an average so that the system may posses a non-integer number of particles. We will refer to this state as the *grand-canonical* distribution (GC). The background of the GC formalism ideas to be used for systems with a few number of particles, like a molecule or an atom, is supported by the statistical interpretation of the DM and the existence of some physical criteria to determine the weights for the distribution, i.e., maximum entropy in statistical physics [6] or minimum energy in ground states of systems with a non-integer number of particles as shown in Ref. [12] on the mathematical basis of a finite subspace of the Fock space [36]. Hence, this representation admits the different number of particles M of the system, and therefore, their populations $\omega_{\Phi_k^M}$ are the variables defining any state DM [12, 13]. Note that it stands for a generalization of the PPLB [4] conjecture. D is an Hermitian, positive semi-definite (all eigenvalues are nonnegative or vanishing), bounded (the module of its elements are bounded) and finite trace (sum of the diagonal elements) matrix, and because of its probabilistic interpretation it may be normalized to unity, i.e., $\mathrm{Tr}(D) = \sum_M \sum_{\Phi_k^M} w_{\Phi_k^M} = 1$ [33, 34]. Let us mention that the well-known *canonical distribution* (C, all states in the mixture posses the same number of particles N), expressed by ${}^{N}D = \sum_{\Phi_k^N} \omega_{\Phi_k^N} |\Phi_k^N\rangle\langle\Phi_k^N|$, and the *microcanonical distribution* (MC, all weights vanish except one), i.e., pure states ${}^{N}D_{\Phi_k^N} = |\Phi_k^N\rangle\langle\Phi_k^N|$, are particular cases of the GC distribution.

The energy $\mathcal{E}$ is the average of the Hamiltonian over the distribution D and is defined by [33, 34]

$$ \mathcal{E} = \mathrm{Tr}(D\,\mathcal{H}) = \sum_M \sum_{\Phi_k^M} \omega_{\Phi_k^M} \mathrm{Tr}\left({}^{M}D_{\Phi_k^M}\,\mathcal{H}\right) \tag{3} $$

where $\mathcal{H}$ is the system Hamiltonian operator, and Tr means the mathematical trace operation. Let ${}^{M}D_0$ be a non-degenerate or removable degenerate ground pure state DM [37, 38] of the M-particle system and its associated energy given by

$$\mathcal{E}_0^M = \mathrm{Tr}\left({}^M D_0\, \mathcal{H}\right) \tag{4}$$

Introducing the notation, $\Delta^M = \mathcal{E}_0^{M-1} - \mathcal{E}_0^M$ as the energy difference convenient interval, i.e., the first ionization potential of the system, and the assumption that for $M > 1$, the $\Delta^M > \Delta^{M+1} > 0$ inequality holds [4–6, 24], then it results that the sequence $\left\{\mathcal{E}_0^M\right\}_{M\in\mathbb{N}}$ verifies the above inequality for arbitrary $N, M \in \mathbb{N}$ numbers, such that for $M \neq N, N+1$, it follows

$$\mathcal{E}_0^M \geq (N+1-M)\mathcal{E}_0^N + (M-N)\mathcal{E}_0^{N+1} \tag{5}$$

and the equality holds only for $M = N, N+1$ [12]. Equation (5) stands for the mathematical expression of the energy convexity for the ground state energies with respect to the number of particles. Let us introduce explicitly the non-integer number of electrons in the systems, $\mathcal{N} = N + \nu$ with $N \in \mathbb{N}$ and $\nu \in (0, 1)$, i.e., between the consecutive integer numbers, N and $N+1$, to extend the dependence of the energy between these numbers. The use of the variational principle for the energy in Eq. (3) with the statistical weights $\{\omega_{\Phi_k^M}\}$ as variational parameters and the constrain of the number of particles $\mathcal{N}$ leads to the solution for this problem in which D is unique and expressed by [12]

$$D = (1-\nu)\ {}^N D_0 + \nu\ {}^{N+1} D_0 \tag{6}$$

Consequently, the energy of the system with non-integer number of particles reads as [12]

$$\mathcal{E}_0^{N+\nu} = (1-\nu)\mathcal{E}_0^N + \nu\mathcal{E}_0^{N+1}. \tag{7}$$

which is the rigorous derivation of the PPLB proposal [4] and consequently for the corresponding DM structure of Eq. (6). Therefore, it follows that Eqs. (6) and (7) are valid for any type of state function, i.e., particle independent or correlated models [39]. At this stage, it is important to mention that all results are also valid for $N - \nu$, so we only refer to the $N + \nu$ case unless necessary for a clarifying need.

The fundamental chemical concepts derived from the physical properties and the chemical descriptors of a system are the summary of the physical information contained in the p-particle reduced density matrices ${}^p D$ (p-RDM) of an M-electron molecular system ($p < M$) which are derived by contraction operations from the DM and represent its marginal distributions [26]. Any property associated with a physical magnitude $\mathcal{A}$ is the average of the corresponding quantum observable A expressed by

$$\langle A \rangle = Tr(DA) \tag{8}$$

In general, the operators A are not a function of the coordinates of all particles in the system but only of a few of them, a subset p. They connect p-particles and are called p-particle operators noted by ${}^p A$, as for instance kinetic, nucleus–electron interaction potential or dipolar moment are 1-particle operators, ${}^1 A$; electron–electron interaction potential are 2-particle operators, ${}^2 A$ and so on [26, 40]. So that, the averages become [26, 40]

$$\langle {}^p A \rangle = Tr({}^p D\ {}^p A) \tag{9}$$

As said above, ${}^p D$ are the marginal distributions of the whole distribution D. To obtain them, the contraction mapping (CM) operation may be performed on D in order to reduce the number of variables from a fixed M number of particles to p, i.e., the order of contraction [26, 41]. In order to define this operation for the GC distribution which has no fixed number of particles, let us first sketch it for the MC and C distributions. For this goal, we introduce the p-RDMs in terms of the p-order replacement operators ${}^p E$ [42] in the second quantization formalism [43]

$${}^p E^{i_1,i_2,\ldots,i_p}_{j_1,j_2,\ldots,j_p} = c^+_{i_1} c^+_{i_2} \ldots c^+_{i_p} c_{j_p} \ldots c_{j_2} c_{j_1} \tag{10}$$

in which $i, j, k, l, \ldots$ indices denote spin orbitals of an orthogonal basis set, and c^+, c stand for the usual creation and annihilation fermion operators, respectively [43]. For a pure state ${}^M D$, the CM becomes defined by Eq. (11) as [26, 38]

$${}^p D^{i_1,i_2,\ldots,i_p}_{j_1,j_2,\ldots,j_p} = Tr({}^M D\ {}^p E^{i_1,i_2,\ldots,i_p}_{j_1,j_2,\ldots,j_p}) \tag{11}$$

The p-RDMs are hermitian, positive semi-definite and bounded [26] and obey the essential property of representability which states for the constraints that a given p-RDM must fulfill to be derivable from a DM [26, 44]. For both C and MC distributions in which the number of particles is fixed for all states in the distribution, any two of the reduced density matrices, say ${}^q D$ and ${}^p D$ ($q < p$), are related by a contraction operation [26, 41]. Equation (11) can be expressed in a more compact equivalent form by

$${}^p D = \binom{M}{p} \hat{L}^M_p \{{}^M D\} \tag{12}$$

where CM denoted by the symbol $\hat{L}^M_p$ is applied to ${}^M D$ and thus the p-RDM arise for both C or MC states [26, 41]. The binomial symbol $\binom{M}{p}$ is the Coleman's normalization factor or the number of the composed p-particles or p-ons [26]; $p = 1, 2, \ldots$ stand for the one-electron reduced density matrix ${}^1 D$ of M particles; the two-electron reduced density matrix ${}^2 D$ of $\binom{M}{2}$ pairs, and so on. More explicitly, it reads,

$${}^p D^{i_1,i_2,\ldots,i_p}_{j_1,j_2,\ldots,j_p} = \sum_{\Phi_k^M} \omega_{\Phi_k^M}\ {}^p D^{i_1,i_2,\ldots,i_p}_{j_1,j_2,\ldots,j_p}(\Phi_k^M) \tag{13}$$

where ${}^{p}D^{i_1,i_2,\ldots,i_p}_{j_1,j_2,\ldots,j_p}(\Phi^M_k) = \binom{M}{p}\hat{L}^M_p\{{}^{M}D_{\Phi^M_k}\}$ stands for the p-RDM associated with the $|\Phi^M_k\rangle$ kth accessible M-particle pure state of the system. The physical meaning of this operation is nothing but an *averaging* process over the remaining $M-p$ variables [45].

As stated above, any physical system featured by a non-integer number of particles $\mathcal{N}$ cannot be described by any other state than the GC. Therefore, a CM to take into account properly the M-particle different states in D defined by Eq. (2) in Fock space to calculate the p-RDMs marginal distributions may be introduced. This expression has been obtained recently [13] as

$$ {}^{p}D = \hat{L}_p\{D\} = \sum_{\{\Phi^M_k, M\geq p\}} \omega_{\Phi^M_k}\binom{M}{p}\hat{L}^M_p\{{}^{M}D_{\Phi^M_k}\} \tag{14}$$

Equation (14) is the definition for the GC CM $\hat{L}_p$ and permits to note that it involves several pure states ${}^{M}D_{\Phi^M_k}$ with the condition that the number of particles was $M \geq p$, i.e., the order of contraction p must be less than or equal to M and all states in the mixture not lying in this interval, i.e., $M < p$, will not contribute to the GC distribution, while for $M = p$, no action is needed [13]. These mathematical conditions are expressed by

$$\hat{L}^M_p\{{}^{M}D_{\Phi^M_k}\} = \mathbf{O} \quad M < p$$

and

$$\hat{L}^p_p\{{}^{p}D_{\Phi^p_k}\} = \mathcal{I}\,{}^{p}D_{\Phi^p_k} = {}^{p}D_{\Phi^p_k}$$

with $\mathcal{I}$ and $\mathbf{O}$, the identity and null superoperators, respectively [13]. These requirements complete the definition for the CM in Fock space, and the *p-RDM*s may be expressed by the expansion,

$$ {}^{p}D = \sum_{\{\Phi^M_k, M\geq p\}} \omega_{\Phi^M_k}\,{}^{p}D_{\Phi^M_k} \tag{15}$$

It is worthy to note that the trace operation calculated by $\mathrm{Tr}({}^{p}D) = \sum_{\{\Phi^M_k, M\geq p\}}\omega_{\Phi^M_k}\binom{M}{p} = \langle\binom{M}{p}\rangle$ is the number of p-ons number in the system as an average which is noted by the symbol $\langle\ldots\rangle$. In particular, for $p = 1$, $\mathrm{Tr}\left({}^{1}D\right) = \sum_{\{\Phi^M_k, M\geq 1\}}\omega_{\Phi^M_k} M = \langle M\rangle$, is the number of particles expressed by the non-integer number $\langle M\rangle = N + \nu$ mentioned above.

To finish this section, let us mention some important consequences coming from the marginal distributions in the GC structure of the density matrices which we will not treat in this work. As noted in this section, within the C and MC states, any ${}^{q}D$ may be obtained from other matrix ${}^{p}D$ with $q < p$ by a contraction operation [26]. The same is not true within the GC distribution [cf. Eq. (2)] without losing some information and hence any matrix may be only obtained directly by contraction of D [13]. Nevertheless, for the case of our interest in which the energy has a convex structure [cf. Eq. (6)], no information is lost, except for the case in which $q = N$ and $p = N + 1$ [13]. The other consequence we want to mention is that for a closed atomic and molecular systems, the energy is a functional of the second-order reduced density matrix as $\mathcal{E}^N_0 = \mathrm{Tr}\left({}^{2}D^{N}_{o}\,{}^{2}\mathcal{K}_N\right)$, where ${}^{2}\mathcal{K}_N$ stands for the Coleman reduced Hamiltonian, ${}^{2}D^{N}_{o}$ the ground state second-order reduced density matrix with a supra-index N which indicates that the 2-RDM comes from contraction of a N-particle DM [26, 38]. In contrast, for an open atomic or molecular system, the energy cannot be expressed similarly as a functional of the corresponding ${}^{2}D^{N+\nu}_{o}$ but as $\mathcal{E}^{N+\nu}_0 = \nu\mathrm{Tr}\left({}^{2}D^{N+1}_{o}\,{}^{2}\mathcal{K}_{N+1}\right) + (1-\nu)\,\mathrm{Tr}\left({}^{2}D^{N}_{o}\,{}^{2}\mathcal{K}_N\right)$, namely the energy is a functional $\mathbf{F}$ of ${}^{2}D^{N}_{o}, {}^{2}D^{N+1}_{o}$ and the fractional population number ν, i.e., $\mathcal{E}^{N+\nu}_0 = \mathbf{F}({}^{2}D^{N+1}_{o}, {}^{2}D^{N}_{o}, \nu)$ [13, 46].

3 Chemical descriptors: system–environment interactions and derivative discontinuities

The higher chemical descriptors are derivatives of the energy or of the electron density with respect of the number of particles $\mathcal{N}$ [3]. They are related to the concept of reactivity interpreted as a response function to proper chemical interactions [24]. Joint together with the zero-order descriptors, i.e., energy and functions of the density itself, provides the complete and detailed description of a molecular system and its intra- (with a solvent, a reservoir, etc.) and inner-interactions (between different fragments in the molecule). So that it imposes the knowledge of these magnitudes, $\mathcal{E}^{\mathcal{N}}_0$ and $\rho^{\mathcal{N}}$ (or more generally the associated DM from which $\rho^{\mathcal{N}}$ is obtained), dependence with $\mathcal{N}$ [5, 12, 13]. The common use of the method of finite differences with respect to integer number of the particles of isolated species to evaluate the derivatives [3] neglects their values at non-integer numbers [24] and consequently the true electron exchange between molecular subsystems which constitutes the onset of chemical behavior.

For ground states, the dependence of the energy $\mathcal{E}^{\mathcal{N}}_0$ and the DMs is a piecewise-continuous linear functions of $\mathcal{N}$ and only the closed systems with integers N and $N \pm 1$ enter in this ensemble as stated by Eqs. (6) and (7), respectively [12]. Hence, all ground state properties then have similar dependence, and the first derivatives of the energy and the density are staircase functions of $\mathcal{N}$, undefined at the integers and constant in between [24] leading to the second derivatives to vanish in between integers [4, 24]. The consequences of this dependence are nonphysical,

for example, the electronegativity equalization principle and the electronic principles based on hardness are senseless because they lose their foundations [3, 4, 24]. Let us show such dependence and make explicit the inconsistencies. The chemical potential is defined at constant external potential υ by [3, 6]

$$\mu = \left(\frac{\partial \mathcal{E}_o^{\mathcal{N}}}{\partial \mathcal{N}}\right)_{\upsilon} \tag{16}$$

which by explicit use of the ground state energy expression for open systems for both signs, i.e., $\pm\nu$ in Eq. (7) [4, 12]

$$\mathcal{E}_0^{N\pm\nu} = (1-\nu)\mathcal{E}_0^{N} + \nu\mathcal{E}_0^{N\pm 1}. \tag{17}$$

with $\mathcal{E}_0^{N\pm\nu}, \mathcal{E}_0^{N}$ and $\mathcal{E}_0^{N\pm 1}$ the energy of the systems with non-integer $N \pm \nu$, N and $N \pm 1$ number of electrons, respectively; then regarding $\partial\mathcal{N} = \pm\partial\nu (N = \text{constant})$, the derivative is

$$\mu^{\pm} = \pm\left(\frac{\partial \mathcal{E}_o^{\mathcal{N}}}{\partial \nu}\right)_{\upsilon} = \pm\left(\mathcal{E}_0^{N\pm 1} - \mathcal{E}_0^{N}\right) \tag{18}$$

yielding the two branches [4]

$$\mu^{+} = \mathcal{E}_0^{N+1} - \mathcal{E}_0^{N} = -EA, \quad \mu^{-} = \mathcal{E}_0^{N} - \mathcal{E}_0^{N-1} = -IP \tag{19}$$

with EA and IP the electron affinity and ionization potential energies, respectively [1, 2]. Hence, since both energies are different, the discontinuity becomes explicit. The other important first derivative is that of the electron density $\rho(\mathbf{r})$ at point $\mathbf{r}$ in space, at constant external field υ which is also expressed into two branches by

$$f^{\pm}(\mathbf{r}) = \left(\frac{\partial \rho(\mathbf{r})}{\partial \mathcal{N}}\right)_{\upsilon}^{\pm} = \pm\left(\frac{\partial \rho(\mathbf{r})}{\partial \nu}\right)_{\upsilon}^{\pm} \tag{20}$$

which stand for the well-known Fukui functions [3, 6, 47, 48]. The two derivatives appear by considering the cases in which $\mathcal{N}$ increases/decreases from N to $N \pm \nu$, respectively. This expression may be generalized to matrix form taking into account that $\rho(\mathbf{r})$ is the diagonal element of ${}^1D$ in the coordinate representation [26]. Therefore, application of the CM of Eq. (14) to D matrix of Eq. (6) and introducing the expression for ${}^1D^{N\pm\nu}$, where the supra-index indicates the matrix comes from the state of $N\pm\nu$ electrons, it results

$$F^{\pm}(\mathbf{r}|\mathbf{r}') = \pm\left({}^1D^{N\pm 1}(\mathbf{r}|\mathbf{r}') - {}^1D^{N}(\mathbf{r}|\mathbf{r}')\right) \tag{21}$$

It establishes a rigorous justification to the forms used to deal with accurate Fukui functions [3]. It is worthy to note Ref. [49] as a previous GC DFT formulation of the problem coincident with the determination performed by finite differences. For a complete description and properties of a matrix formulation of these magnitudes, see Refs. [50, 51]. Nevertheless, this magnitude has a different physical meaning than those coming from the energy, and it will not be subject of the present work.

The example of the chemical potential shows the nature of the discontinuities caused by the lack of terms depending on the charge transferred coupling the states of different number of particles. Hence, it does not enable the onset of nonvanishing higher-order derivatives. Let us deal with this lacking information and relate it to the interaction of the subsystem (fragment) within a molecular frame and/or the interaction of the whole molecule with an environment (reservoir) which permits electron exchange and so charge transfer. Some attempts based in the treatment of the energy dependence from the point of view of the state function approach have been reported in order to overcome these discontinuities and thus incorporate the information into the descriptors [5, 15, 52]. Nevertheless, as the theory indicates, a general statistical formulation is needed at the GC level of description to consider the interaction of the system with the environment, i.e., other subsystem and/or reservoir (S–R) interactions. Early attempts to implement such formulation within the DFT can be found in Ref. [25].

The remaining part of this report will be devoted to this topic in order to introduce such interactions within the DM structure [4, 12, 13] and thus calculate the expressions for the descriptors to shed some light into the essence of these reactivity indices.

In the previous section, it has been shown that the convex structure of D and the energy for ground states evolve into two branches, each one as a two-state level model of N and $N \pm 1$ Hilbert spaces as expressed in Eqs. (6) and (7) [4, 12, 13]. The corresponding pure ground state DMs in Dirac notation reads,

$${}^{N}D_0 = |\Phi_0^N\rangle\langle\Phi_0^N|$$

and

$${}^{N\pm 1}D_0 = |\Phi_0^{N\pm 1}\rangle\langle\Phi_0^{N\pm 1}|,$$

respectively. The interaction of the system (subsystem) with the environment may be described by means of a potential $\mathbf{U}_{\nu}$ which may have diverse nature regarding the type of interaction we are dealing with and depends on the electron fraction ν as indicated by the subscript. For instance, such potential may be considered as describing the interaction between subsystem fragments within the Atoms in Molecules (AIM) framework [11] or fragment methods [53], reservoir interactions effects [34], the influence of a solvent field on molecular systems (liquid phase)

[54, 55] or environmental effects [55] among others. Therefore, the Hamiltonian in the adiabatic approximation [56] for each of the two branches,

$$\mathbf{H} = \mathbf{H}_0 + \mathbf{U}_\nu \tag{22}$$

can be expressed in matrix form as

$$\begin{aligned}\mathcal{H} = \mathcal{E}_0^N |\Phi_0^N\rangle\langle\Phi_0^N| \; + \; \mathcal{E}_0^{N\pm1} |\Phi_0^{N\pm1}\rangle\langle\Phi_0^{N\pm1}| \\ + \; \mathcal{U}_\nu^{\pm} |\Phi_0^N\rangle\langle\Phi_0^{N\pm1}| \; + \; \mathcal{U}_\nu^{\pm *} |\Phi_0^{N\pm1}\rangle\langle\Phi_0^N|\end{aligned} \tag{23}$$

where $\mathbf{H}_0$ represents the isolated system Hamiltonian whose spectra and eigenstates are noted in Eq. (23) by the energies $\mathcal{E}_0^N$ and $\mathcal{E}_0^{N\pm1}$, and $|\Phi_0^N\rangle$ and $|\Phi_0^{N\pm1}\rangle$ for the neutral and the ionic states, respectively. $\mathbf{H}_0$ is diagonal at the basis set of its eigenstates as well as its density matrix D. The action of the interaction potential induces a new distribution $\tilde{D}$ which may describe the open system and reflects the coupling between both states, that of N with those of $N \pm 1$ [57, 58]. This equilibrium state may reach a permanent regime of electron exchange, i.e., the rate of electron exchange is constant in time. Therefore, the density matrix $\tilde{D}$ may exhibit a coherent structure (nondiagonal elements or coherences are no vanishing) due to the action of the interaction potential $\mathbf{U}_\nu$ [34], so that it will be expressed by

$$\tilde{D} \; = \; D \; + \; \Delta_\nu^{\pm} \, |\Phi_0^N\rangle\langle\Phi_0^{N\pm1}| \; + \; \Delta_\nu^{\pm *} \, |\Phi_0^{N\pm1}\rangle\langle\Phi_0^N| \tag{24}$$

where the first term stands for the isolated distribution of Eq. (6), i.e., corresponding to $\mathbf{H}_0$ [4, 12, 13], while the last two terms describe the coupling interaction of the $|\Phi_0^N\rangle$ and $|\Phi_0^{N\pm1}\rangle$ states. The coherences must obey the inequality related to its diagonal elements (or populations), $|\tilde{D}_{nm}|^2 \leq \tilde{D}_{nn}\tilde{D}_{mm}$ whose physical meaning is that there can be coherences only between states whose populations are not zero; in this case, $\left|\Delta_\nu^{\pm}\right|^2 \leq (1-\nu)\nu$ and if $\nu = 1, 0$, i.e., one of the states, that of N or $N \pm 1$ respectively, has no populations. Thus, the coherence between them vanishes, so that $\Delta_0^{\pm} = 0$ [59]. Then, the energy for the system interacting with the environment using Eq. (3) with $\tilde{D}$ distribution is expressed by

$$\tilde{\mathcal{E}}_0^{N\pm\nu} \; = \; Tr(\mathcal{H}\tilde{D}) \; = \; \mathcal{E}_0^{N\pm\nu} \; + \; 2\mathbb{R}e(\mathcal{U}_\nu^{\pm *}\Delta_\nu^{\pm}) \tag{25}$$

where the symbol $\mathbb{R}e$ indicates the real part of the complex number $\mathcal{U}_\nu^{\pm *}\Delta_\nu^{\pm}$. This term determines the interaction with the environment, and because the interaction potential must depend on the fraction ν to ensure the electron transfer, it introduces a ν-nonlinearity dependence for the energy and the DM. Thus, it enable us to perform the calculation of the chemical descriptors of arbitrary order avoiding the discontinuity problem. To show the machinery in action, let us write the descriptors defined above in order to clarify these ideas. The chemical potential of Eq. (16) becomes

$$\tilde{\mu}^{\pm} = \left(\frac{\partial \tilde{\mathcal{E}}_0^{\mathcal{N}}}{\partial \mathcal{N}}\right)_\upsilon = \pm\left(\frac{\partial \tilde{\mathcal{E}}_0^{N\pm\nu}}{\partial \nu}\right)_\upsilon \tag{26}$$

and then it results

$$\tilde{\mu}^{\pm} = \; \mu^{\pm} \pm \; 2\mathbb{R}e\left(\frac{\partial(\mathcal{U}_\nu^{\pm *}\Delta_\nu^{\pm})}{\partial \nu}\right)_\upsilon \tag{27}$$

The second term of the r.h.s of Eq. (27) permits to avoid the chemical potential discontinuity [4, 24], and thus the equalization principle can be fulfilled [3]. To understand it, let us consider two fragments Ω_A and Ω_B within a molecular framework which at equilibrium must obey the condition $\tilde{\mu}_{\Omega_A}^{+} = \tilde{\mu}_{\Omega_B}^{-}$, i.e., the chemical potential of the donor fragment must be equal to that of the acceptor fragment; it is the second term of the r.h.s. of Eq. (27) which enables this condition. Hence, the hardness which vanishes identically because of the chemical potential discontinuity for an isolated system, i.e., without interaction with an environment [24], becomes non-null due to the interaction and reads

$$\tilde{\eta}^{\pm} = \; \frac{1}{2}\left(\frac{\partial^2 \tilde{\mathcal{E}}_0^{\mathcal{N}}}{\partial^2 \mathcal{N}}\right)_\upsilon = \; \pm\mathbb{R}e\left(\frac{\partial^2(\mathcal{U}_\nu^{\pm *}\Delta_\nu^{\pm})}{\partial^2 \nu}\right)_\upsilon \tag{28}$$

showing the two signs as in the case of the chemical potential because of the openness of the systems.

4 Discussion and concluding remarks

The GC distribution has been used here avoiding the concept of temperature but explicitly based on the electronic information. This description has been recognized adequate to introduce the S–R interactions on the descriptors and permits by the means of a charge-dependent interaction potential to overcome the problem of the discontinuities in the derivatives of the energy. This treatment recovers the piecewise dependence when the interaction vanishes, i.e., $\mathbf{U}_\nu \to 0$, as expected. This formulation, as has been pointed out, is more realistic than evaluating the descriptors in isolated systems by finite difference methods. In conclusion, the GC distribution for open molecular domains enables to introduce statistical concepts to describe electron distributions in the molecular structure even they are few body systems.

It may be noted that for the present developments, the general structure of the DMs has been used, and hence, the results are valid at any level of approximation of the state functions, i.e., particle independent or correlated ones. Furthermore, it depends only of the model used for system–environment interaction.

Several topics deserve our attention as natural continuation of the present work to continue the understanding of the reactivity phenomena from a rigorous point of view and are being considered in our laboratory. Some of them are related to obtain an equation that preserves the constant rate of electron transfer between the open domains in the molecular structure and provides DM evolution within this context, the modeling of the interaction potential of different nature and the contraction mappings in Fock space for coherent density matrices, among others.

Acknowledgments This report has been financially supported by Projects 20020130100226BA (Universidad de Buenos Aires) and PIP No. 11220090100061 (Consejo Nacional de Investigaciones Científicas y Técnicas, República Argentina).

References

1. Szabo A, Ostlund NS (1989) Modern quantum chemistry. Introduction to advanced electronic structure theory. Dover Publications Inc, Mineloa, New York
2. Helgaker T, Jörgensen P, Olsen J (2000) Molecular electronic structure theory. Wiley Ltd, Chitester
3. Geerlings P, De Proft F, Langenaeker W (2003) Conceptual density functional theory. Chem Rev 103(5):1793–1873
4. Perdew JP, Parr RG, Levy M, Balduz J Jr (1982) Density-functional theory for fractional particle number: derivative discontinuities of the energy. Phys Rev Lett 49(23):1691–1694
5. Perdew JP (1985) In: Dreizler RM, da Providencia J (eds) Density functional theory methods in physics, NATO ASI series. Plenum, New York
6. Parr RG, Yang W (1989) Density-functional theory of atoms and molecules. Oxford Univesity Press, New York
7. Iczkowski RP, Margrave JL (1961) Electronegativity. J Am Chem Soc 83(17):3547–3551
8. Morales J, Martinez TJ (2001) Classical fluctuating charge theories: the maximum entropy valence bond formalism and relationships to previous models. J Phys Chem A 105(12):2842–2850
9. Ayers PW, Parr RG (2008) Local hardness equalization: exploiting the ambiguity. J Chem Phys 128(18):184108
10. Parr RG, Pariser R (2013) In: Ghosh SK, Chattaraj PK (eds) Concepts and methods in modern theoretical chemistry: electronic structure and reactivity. CRC Press, Boca Raton
11. Valone SM (2011) A concept of fragment hardness, independent of net charge, from a wave-function perspective. J Phys Chem Lett 2(20):2618–2622 and references
12. Bochicchio RC, Rial D (2012) Energy convexity and density matrices in molecular systems. J Chem Phys 137(22):226101
13. Bochicchio RC, Miranda-Quintana RA, Rial D (2013) Reduced density matrices in molecular systems: grand-canonical electron states. J Chem Phys 139(19):199101
14. Nalewajski RF (1998) Kohn–Sham description of equilibria and charge transfer in reactive systems. Int J Quant Chem 69(4):591–605
15. Valone SM, Atlas SR (2006) Energy dependence on fractional charge for strongly interacting subsystems. Phys Rev Lett 97(25):256402
16. Bochicchio RC, Lain L, Torre A (2003) Atomic valence in molecular systems. Chem Phys Lett 375(1–2):45–53 and references
17. Lain L, Torre A, Bochicchio RC (2004) Studies of population analysis at the correlated level: determination of three-center bond indices. J Phys Chem A 108(18):4132–4137 and references
18. Bader RFW (1994) Atoms in molecules: a quantum theory. Oxford University Press, Oxford
19. Popelier P (1999) Atoms in molecules: an introduction. Pearson Edu, London
20. Yang WT, Zhang YK, Ayers PW (2000) Degenerate ground states and fractional number of electrons in density and reduced density matrix functional theory. Phys Rev Lett 84(22):5172–5175
21. Ayers PW (2008) The continuity of the energy and other molecular properties with respect to the number of electrons. J Math Chem 43(1):285–303
22. Hirshfeld FL (1977) Bonded-atom fragments for describing molecular charge densities. Theor Chim Acta 44(2):129–138
23. Valone SM (2011) Quantum mechanical origins of the Iczkowski–Margrave model of chemical potential. J Chem Theory Comp 7(7):2253–2261
24. Cohen MH, Wasserman A (2007) On the foundations of chemical reactivity theory. J Chem Phys A 111(11):2229–2242
25. Ayers PW (2007) On the electronegativity nonlocality paradox. Theor Chem Acc 118(2):371–381
26. Coleman AJ, Yukalov VI (2000) Reduced density matrices: Coulson's challenge. Springer, New York
27. Gatti C, Macchi P (eds) (2012) Modern charge-density analysis. Springer, Dordrecht
28. Fradera X, Austen MA, Bader RFW (1999) The Lewis model and beyond. J Phys Chem A 103(2):304–314
29. Alcoba DR, Torre A, Lain L, Bochicchio RC (2005) Energy decompositions according to physical space partitioning schemes. J Chem Phys 122(7):074102
30. Alcoba DR, Lain L, Torre A, Bochicchio RC (2005) A study of the partitioning of the first-order reduced density matrix according to the theory of atoms in molecules. J Chem Phys 123(14):144113
31. Becke AD (1988) A multicenter numerical integration scheme for polyatomic molecules. J Chem Phys 88(4):2547–2553
32. Torre A, Alcoba DR, Lain L, Bochicchio RC (2005) Determination of three-center bond indices from population analysis: a fuzzy atom treatment. J Phys Chem A 109(29):6587–6591
33. Ter Haar D (1961) Theory and applications of the density matrix. Rep Prog Phys 24(1):304–362
34. Blum K (1981) Density matrix theory and applications. Plenum, New York
35. Emch GG (1972) Algebraic methods in statistical mechanics and quantum field theory. Wiley-Interscience, New York
36. Blaizot JP, Ripka G (2006) Quantum theory of finite systems. The MIT Press, Cambridge
37. Rosina M (2001) In: Cioslowsky J (ed) Many-electron densities and reduced density matrices. Kluwer, Dordrecht
38. Mazziotti DA (1998) Contracted Schrödinger equation: determining quantum energies and two-particle density matrices without wave functions. Phys Rev A 57(6):4219–4234
39. Hellgren M, Gross EKU (2012) Effect of discontinuities in Kohn–Sham-based chemical reactivity theory. J Chem Phys 136(11):114102
40. McWeeny R (2001) Methods of molecular quantum mechanics. Academic, San Diego
41. Kummer H (1967) n-Representability problem for reduced density matrices. J Math Phys 8(10):2063–2081
42. Paldus J (1976) In: Eyring H, Henderson DJ (eds) Theoretical chemistry: advances and perspectives, vol 2. Academic Press, New York
43. Surján PR (1989) Second quantized approach to quantum chemistry an elementary introduction. Springer-Verlag, Berlin

44. Mazziotti DA (ed) (2007) Reduced-Density-matrix mechanics: with application to many-electron atoms and molecules. Advances in chemical physics 134. Wiley
45. Valdemoro C (1996) Contracting and calculating traces over the N-electron space: two powerful tools for obtaining averages. Int J Quant Chem 60(1):131–139
46. Miranda-Quintana RA, Bochicchio RC (2014) Energy dependence with the number of particles: density and reduced density matrices functionals. Chem Phys Lett 593(1):35–39
47. Parr RG, Yang WT (1984) Density functional approach to the frontier-electron theory of chemical reactivity. J Am Chem Soc 106(14):4049–4050
48. Yang WT, Parr RG, Pucci R (1984) Electron density, Kohn–Sham frontier orbitals, and Fukui functions. J Chem Phys 81(6):2862–2863
49. Ayers P, Levy M (2000) Perspective on "Density functional approach to the frontier-electron theory of chemical reactivity". Theor Chem Acc 103(3–4):353–360
50. Bultinck P, Cardenas C, Fuentealba P, Johnson PA, Ayers PW (2014) How to compute the Fukui matrix and function for systems with (quasi-)degenerate states. J Chem Theory Comp 10(1):202–210
51. Bultinck P, Clarisse D, Ayers PW, Carbo-Dorca R (2011) The Fukui matrix: a simple approach to the analysis of the Fukui function and its positive character. Phys Chem Chem Phys 13(13):6110–6115
52. Cioslowski J, Stefanov BB (1993) Electron flow and electronegativity equalization in the process of bond formation. J Chem Phys 99(7):5151–5162
53. Parker SM, Shiozaki T (2014) Active space decomposition with multiple sites: density matrix renormalization group algorithm. J Chem Phys 141(21):211102 and references
54. Tapia O, Bertrán J (eds) (2003) Solvent effects in chemical reactivity. Kluwer, New York
55. Surján PR, Ángyán J (1983) Perturbation theory for nonlinear time-independent Schrödinger equations. Phys Rev A 28(1):45–48
56. Mead CA, Truhlar DG (1982) Conditions for the definition of a strictly diabatic electronic basis for molecular systems. J Chem Phys 77(12):6090–6098
57. Davies EB (1976) Quantum theory of open systems. Academic Press, London
58. Attal S, Joye A, Pillet CA (eds) (2006) Open quantum systems I. The Hamiltonian approach. In: Lecture Notes in Mathematics. Springer, Berlin
59. Cohen-Tannoudji C, Diu B, Laloë F (1991) Quantum mechanics, vol 1. Wiley, New York

Theor Chem Acc (2015) 134:148
DOI 10.1007/s00214-015-1751-2

REGULAR ARTICLE

Local random phase approximation with projected oscillator orbitals

Bastien Mussard[1,2,3] · **János G. Ángyán**[4,5]

Received: 31 July 2015 / Accepted: 22 October 2015 / Published online: 14 November 2015

Abstract An approximation to the many-body London dispersion energy in molecular systems is expressed as a functional of the occupied orbitals only. The method is based on the local-RPA theory. The occupied orbitals are localized molecular orbitals, and the virtual space is described by projected oscillator orbitals, i.e., functions obtained by multiplying occupied localized orbitals with solid spherical harmonic polynomials having their origin at the orbital centroids. Since we are interested in the long-range part of the correlation energy, responsible for dispersion forces, the electron repulsion is approximated by its multipolar expansion. This procedure leads to a fully non-empirical long-range correlation energy expression. Molecular dispersion coefficients calculated from determinant wave functions obtained by a range-separated hybrid method reproduce experimental values with <15 % error.

Keywords RPA · Oscillator orbitals · London dispersion energy · Dispersion coefficient · Local correlation method

Dedicated to Prof. Péter Surján on the occasion of his 60th birthday.

Published as part of the special collection of articles "Festschrift in honour of P. R. Surjan".

✉ János G. Ángyán
janos.angyan@univ-lorraine.fr

Bastien Mussard
bastien.mussard@upmc.fr

[1] Institut du Calcul et de la Simulation, Sorbonne Universités, UPMC Univ Paris 06, 75005 Paris, France

[2] UMR 7616, Laboratoire de Chimie Théorique, Sorbonne Universités, UPMC Univ Paris 06, 75005 Paris, France

[3] CNRS, UMR 7616, Laboratoire de Chimie Théorique, 75005 Paris, France

[4] Institut Jean Barriol, CRM2, UMR 7036, Université de Lorraine, 54506 Vandoeuvre-lès-Nancy, France

[5] CNRS, Institut Jean Barriol, CRM2, UMR 7036, 54506 Vandoeuvre-lès-Nancy, France

1 Introduction

According to the Perdew's popular classification of density functional approximations (DFA) [1], the random phase approximation (RPA) is situated on the highest, fifth rung of Jacob's ladder, which leads from the simplest Hartree level toward the "heaven" corresponding to the exact solution of the Schrödinger equation. When stepping upwards on Jacob's ladder, one uses more and more ingredients of the Kohn–Sham single determinant. Starting from the lowest rungs, the density, its gradient, the full set of occupied orbitals are successively necessary for the construction of the functional. At the highest rung DFA is usually based on many-body methods, which require the knowledge of the complete set of occupied and virtual orbitals. Such methods have the drawback that the size of the virtual orbital space can be very large even in a moderately sized atomic orbital basis. In the case of plane wave calculations, the virtual space can become even prohibitively large. One solution to keep the size of matrices in reasonable limits makes recourse to an auxiliary basis set to expand the occupied-virtual product functions. Such approaches are known in quantum chemistry as resolution of identity [2] or density-fitting [3, 4] methods. Similar advantages can be achieved by Cholesky decomposition [5] techniques. In plane wave calculations, the plane wave basis itself can be used to expand the product states [6]. Further gain can be achieved by projection methods, which avoid any explicit reference

to virtual orbitals. Such a technique, named projective dielectric eigenpotential (PDEP) method, has been successfully applied to construct the dielectric function in plane wave RPA calculations [7–9]. Recently, Rocca succeeded to reduce further the size of the problem by a prescreened set of virtuals [10].

The purpose of the present work is to demonstrate that an *approximate* variant of the RPA (and also of the MP2) correlation energy can be expressed by using quantities that are computable from occupied orbitals alone. In this context, one should mention the beautiful result, which has been obtained by Surján, who has shown that the MP2 correlation energy, exempt of any further approximation in a given basis set, can be reformulated as a functional of the Hartree-Fock density matrix, i.e., using exclusively the occupied orbitals [11]. Our main interest is not to reproduce the full correlation energy with high numerical precision, but we focus our attention to a well-defined part of it, namely on the long-range dynamical correlation energy, which is usually taken responsible for the London dispersion forces.

It is now well-documented that most of the conventional density functional calculations in the Kohn–Sham framework, unless special corrections are added to the total energy, are unable to grasp the physics of these long-range forces. Various fairly successful dispersion correction schemes are known, but although most of them were claimed to posses an essentially ab initio character, they use, without exception, some "external" data, like atomic polarizabilities, atomic radii, etc. [12–18]. Even if these quantities are usually not taken from experimental sources, and rather originate from ab initio computations, their presence deprives these theories of their self-contained character. Hence, although we do not pretend that the rather drastic approximations which are going to be implemented in the following allow us to achieve results of a quality comparable to the precision attained by carefully fine-tuned methodologies, we argue that the ingredients of the present approach originate from a controlled series of approximations and do not use any "external" inputs. Moreover, in contrast to the relatively costly and sophisticated methods, like RPA, we do not need virtual orbitals, i.e., we stay on the fourth rung of Jacob's ladder.

Our approach relies on the use of localized occupied molecular orbitals (LMOs) that can be obtained relatively easily by a unitary transformation in the subspace of occupied orbitals, according to either an external or an internal localization criterion [19]. The localization of virtual orbitals is much more difficult, since the usual localization criteria for the occupied orbitals lead often to divergent results. It is to be noted that recently a significant progress has been reported [20] for the efficient localization of virtual orbitals. However, we follow another strategy here and build excited determinants using localized functions which are able to span the essential part of the virtual space. One of the most popular local correlation approaches in this spirit consists in using the atomic orbital (AO) basis functions to represent the virtual space. They are made orthogonal to the occupied space by projection, leading to the projected AOs (PAOs) techniques [21–23]. The locality of these functions is guaranteed by construction, even if it may be somewhat deteriorated by the projection procedure.

In the present work we are going to revisit and explore a quite old idea of Foster and Boys from the early 60s [24–26]. The main concern of these authors was to construct a set of virtual orbitals directly from the set of occupied LMOs by multiplying them with solid spherical harmonic functions centered on the barycenter of the LMO. The orthogonality of these new functions can be ensured by a projection procedure. Boys and Foster called these new functions, obtained after multiplication, oscillator orbitals (OOs), and after removing the components of the OOs in the space of the occupied orbitals they may be called projected oscillator orbitals (POOs). Very few articles in the literature mention Boys' oscillator orbitals [27], probably because it had no particular numerical advantage in high-precision configuration interaction calculations and its practical implementation raised a number of complications which could be avoided by more straightforward algorithms, like the use of the full set of virtual molecular orbitals (VMOs). We have found only a single, very recent article, which referred to the notion of oscillator orbitals [28] as a useful concept, but not as a practical computational tool. To the best of our knowledge, the mathematical implications of using oscillator orbitals to define the virtual space has never been rigorously studied. Such an analysis is beyond the scope of the present study: it is going to be the subject of a forthcoming publication.

The POOs are non-orthogonal among each other, which is at the origin one of the complications mentioned above. This problem can be handled just like in the case of the PAOs; therefore, a theory of electron correlation based on POOs can follow a similar reasoning as local correlation methods using PAOs [29]. In particular, in this paper, the RPA method will be reformulated for a virtual space constructed from POOs.

It is worthwhile to mention that the projected oscillator orbitals bear some similarities to the trial perturbed wave function in the variation-perturbational technique associated with the names of Kirkwood [30], Pople and Schofield [31] (KPS), to calculate multipole molecular polarizabilities. The closely related Karplus–Kolker [32, 33] (KK) method and its variants [34, 35] use a similar *Ansatz* for the perturbed orbitals. In these latter methods, which were formulated originally as simplified perturbed Hartree–Fock theories, the first-order perturbed

wave function is a determinant with first-order orbitals $\psi_i^{(1)}$ which are taken in the following product form [36] $\psi_i^{(1)} = g_i\psi_i - \sum_k \langle\psi_k|g_i\psi_i\rangle\psi_k$, where g_i are linear combination of some analytically defined functions, like polynomials. As we shall see, the principal difference of this *Ansatz* and the POOs is that in the former case one multiplies the occupied canonical orbitals with the function g_i, while the oscillator orbitals are constructed from localized orbitals.

As mentioned previously, our main focus is the modeling of London dispersion forces. It has been demonstrated in our earlier works [37–39] that the essential physical ingredients of London dispersion forces are contained in the range-separated hybrid RPA method, where the short-range correlation effects are described within a DFA and the long-range exchange and correlation are handled at the long-range Hartree–Fock and long-range RPA levels, respectively. Among numerous possible formulations of the RPA [39, 40], we have chosen to adopt the variant based on the ring-diagram approximation to the coupled cluster doubles theory. The relevant amplitude equations will be rewritten with the help of POOs leading to simplified working equations, which do not refer to virtual orbitals explicitly. For the sake of comparison we are going to study the case where the POOs are expanded in the virtual orbital space. The long-range electron repulsion integrals, appearing in the range-separated correlation energy expression, can be reasonably approximated by a truncated multipole expansion. It means that in addition to the well-known improved convergence properties of the correlation energy with respect to the size of the basis set, one is able to control the convergence through the selection of the multipolar nature of the excitations, leading to a possibility of further computational gain.

The exploitation of localized orbitals for dispersion energy calculations has already been proposed since the early works on local correlation methods [41–45]. In classical and semiclassical models most often the atoms are selected as force centers; only a few works exploit the advantages related to the use of two-center localized orbitals and lone pairs. A notable exception is the recent work of Silvestrelli and coworkers [46–50], who adapted the Tkatchenko–Scheffler model [16] for maximally localized Wannier functions (MLWF), which are essentially Boys' localized orbitals for solids. It is worthwhile to mention that one of the very first use of the bond polarizabilities as interacting units for the description of London dispersion forces has been suggested as early as in 1969 by Claverie and Rein [51]; see also [52].

Our approach, at least in its simplest form, is situated somewhere between classical models and fully quantum local correlation methods and can be considered (practically in all its forms) as a coarse-grained nonlocal dispersion functional formulated exclusively on the basis of ground state densities and occupied orbitals. It will be shown how the various matrix elements can be expressed from occupied orbital quantities only. As a numerical illustration, molecular C_6 dispersion coefficients will be calculated from localized orbital contributions and compared to experimental reference data. The paper will be closed by a discussion of possible future developments.

2 Theory

2.1 Projected oscillator orbitals

The a posteriori localization of the subspace of the occupied orbitals is a relatively standard procedure, which can be achieved following a large variety of localization criteria (for a succinct overview, see Ref. [53]). In the context of correlation energy calculations, i.e., in various "local correlation approaches", the most widely used localization methods are based either on the criterion of Foster and Boys [24] or that proposed by Pipek and Mezey [54]. For reasons which become clearer below, in the present work we will use the Foster–Boys localization criterion, which can be expressed in various equivalent forms [26]. In its the most suggestive formulation, the Foster–Boys' localization procedure consists in the maximization of the squared distance between the centroids of the orbitals:

$$\max\left\{\sum_{i<j}^{\text{occ}} |\langle\phi_i|\hat{\mathbf{r}}|\phi_i\rangle - \langle\phi_j|\hat{\mathbf{r}}|\phi_j\rangle|^2\right\}. \tag{1}$$

Another form of the localization criterion, which is strictly equivalent to the previous one, corresponds to the minimization of the sum of quadratic orbital spreads

$$\min\left\{\sum_{i}^{\text{occ}} \langle\phi_i|\hat{\mathbf{r}}^2|\phi_i\rangle - |\langle\phi_i|\hat{\mathbf{r}}|\phi_i\rangle|^2\right\}. \tag{2}$$

As it has been demonstrated by Resta [55], the previous minimization implies that the sum of the spherically averaged squared off-diagonal matrix elements of the position operator is minimal too. This last property of the Boys' localized orbitals is going to be useful in the development of the present model.

Any set of localized orbitals obtained by a unitary transformation from a set of occupied orbitals spans the same invariant subspace as the generalized Kohn-Sham operator, $\hat{f}^\mu$, and satisfies the equation:

$$\hat{f}^\mu\phi_i^\mu = \sum_j^{\text{occ}} \varepsilon_{ij}^\mu\phi_j^\mu, \tag{3}$$

where $\hat{f}^{\mu}\phi_i = \hat{t} + \hat{v}_{\rm ne} + \hat{v}_{\rm H} + \hat{v}^{{\rm lr},\mu}_{x,{\rm HF}} + \hat{v}^{{\rm sr},\mu}_{xc,{\rm DFA}}$ is the range-separated hybrid operator. In this expression $\hat{t}$ is the kinetic energy, $\hat{v}_{\rm ne}$ is the nuclear attraction, $\hat{v}_{\rm H}$ is the full-range Hartree, $\hat{v}^{{\rm lr},\mu}_{x,{\rm HF}}$ is the long-range Hartree–Fock (non-local) exchange, and $\hat{v}^{{\rm sr},\mu}_{{\rm xc,DFA}}$ is the short-range exchange-correlation potential operator. The range-separation parameter, μ, defined below, cuts the electron repulsion terms to short- and long-range components. For $\mu = 0$ one recovers the full-range DFA, while for $\mu \to \infty$ one obtains the full-range Hartree–Fock theory.

As outlined in the introduction, inspired by the original idea suggested first by Foster and Boys [24] and refined later by Boys [26], we propose here to construct localized virtual orbitals by multiplying the localized occupied orbital $\phi_i(\mathbf{r})$ by solid spherical harmonics having their origin at the barycenter (centroid) of the localized occupied orbital. According to Boys [26], this definition can be made independent of the orientation of the coordinate system by choosing local coordinate axes which are parallel to the principal axes of the tensor of the moment of inertia of the charge distribution $\phi_i^*(\mathbf{r})\phi_i(\mathbf{r})$ (see Appendix 1).

In the following we are going to elaborate the theory for the simplest case, when these *oscillator orbitals* are generated by first-order solid spherical harmonic polynomials, i.e., the ith LMO is multiplied by $(\hat{r}_\alpha - D^i_\alpha)$, where $\hat{r}_\alpha$ is the $\alpha = x, y, z$ component of the position operator and D^i_α is a component of the position vector pointing to the centroid of the ith LMO, defined as $D^i_\alpha = \langle\phi_i|\hat{r}_\alpha|\phi_i\rangle$. It is possible to generate oscillator orbitals by higher order spherical harmonics too, which is left for forthcoming work. We denote the POO by $|\tilde{\phi}_{i_\alpha}\rangle$, where the index i_α refers to the fact that the OO has been generated from the ith LMO by using the $\hat{r}_\alpha$ function. For the sake of the simplicity of the formulae, the POOs will be expressed in the laboratory frame; the expressions for the dipolar POOs in a local frame are shown in the Appendix 1. The POO reads in the laboratory frame as

$$|\tilde{\phi}_{i_\alpha}\rangle = \left(\hat{I} - \sum_m^{\rm occ} |\phi_m\rangle\langle\phi_m|\right)\left(\hat{r}_\alpha - D^i_\alpha\right)|\phi_i\rangle = \hat{Q}\hat{r}_\alpha|\phi_i\rangle, \quad (4)$$

with $\hat{Q} = (\hat{I} - \sum_m^{\rm occ} |\phi_m\rangle\langle\phi_m|)$, the projector onto the virtual space.

In Eq. 4 the "pure" (OO) component of the POO is $\hat{r}_\alpha|\phi_i\rangle$, while the orthogonalization tails stem from the term $-\sum_{m\neq i}^{\rm occ} |\phi_m\rangle\langle\phi_m|\hat{r}_\alpha|\phi_i\rangle$. In this sense the "locality" of the OO is somewhat deteriorated, since we have contributions from each of the other LMOs. At this point the Boys localization criterion will be at our advantage, since it ensures that the sum of the off-diagonal elements of the x, y and z operators taken between the occupied orbitals, and appearing in the orthogonalization tails, be minimized [55]. In this sense, the Boys-localization scheme seems to be naturally adapted for the construction of dipolar oscillator orbitals.

To illustrate the concept of dipolar oscillator orbitals, two examples are taken from the oxygen lone pair and the C–H bonding orbitals of the formaldehyde molecule, described in the above-defined local frame. Figures 1 and 2 shows the localized orbitals and the three projected dipolar oscillator orbitals having a nodal surface intersecting the orbital centroid and oriented in the three Cartesian coordinate directions of the local coordinate system, x, y and z. It is quite clear that the node coincides with the region of the highest electron density of the orbital and thereby ensures an optimal description of the correlation. Higher order polynomials generate virtual orbitals with further nodes.

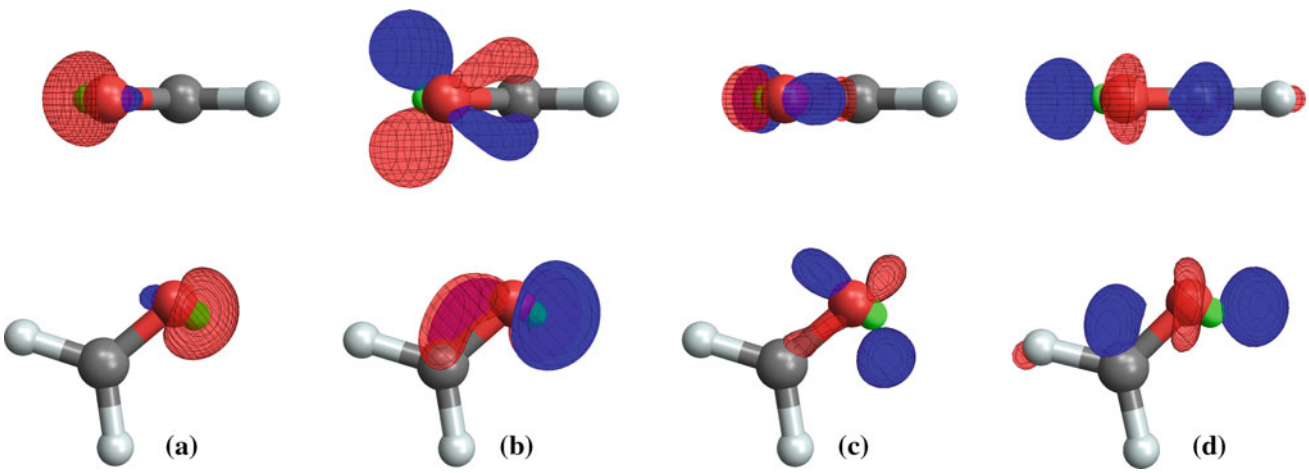

Fig. 1 Projected oscillator orbitals (**b–d**) generated by projection of the products of first-order *solid spherical* harmonics polynomials with the O lone pair orbital of $H_2C=O$ seen in **a**. The harmonics are aligned with the local frame axes, i.e., the principal axes of the tensor of the moment of inertia of the charge distribution of the oxygen lone pair orbital. The *green dot* indicates the position of the LMO centroid. **a** O lone pair $|i\rangle$, **b** $\hat{Q}\hat{r}_x|i\rangle$, **c** $\hat{Q}\hat{r}_y|i\rangle$, **d** $\hat{Q}\hat{r}_z|i\rangle$

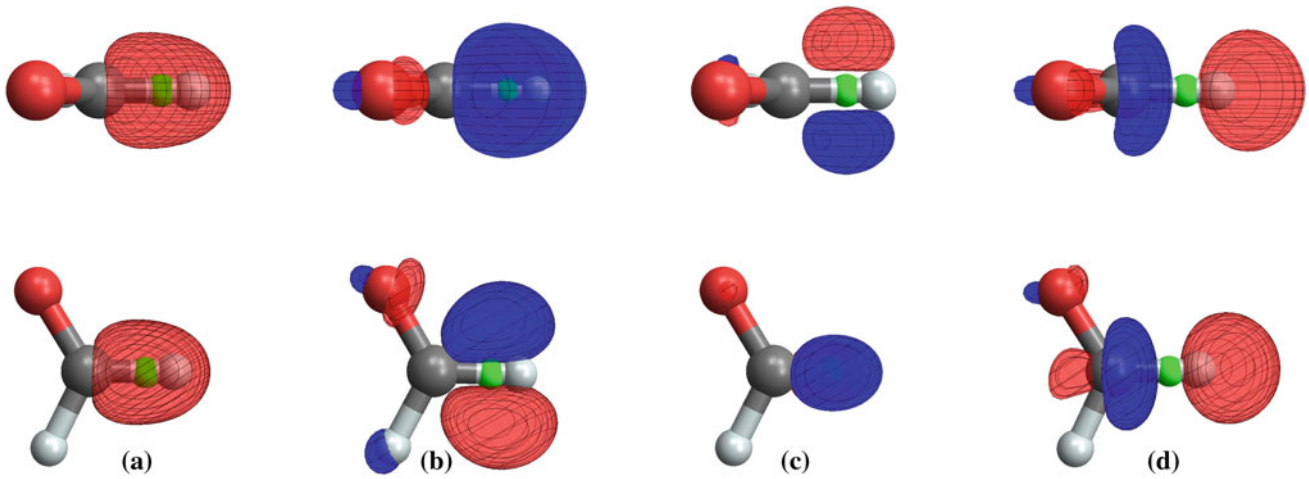

Fig. 2 Projected oscillator orbitals (**b**–**d**) generated by projection of the products of first-order *solid spherical* harmonics polynomials with the C–H bonding orbital of $H_2C=O$ (**a**). The harmonics are aligned with the local frame axes, i.e., the principal axes of the tensor of the moment of inertia of the charge distribution of the C–H bonding orbital. The *green dot* indicates the position of the LMO centroid. **a** C–H bonding orbital $|i\rangle$, **b** $\hat{Q}\hat{r}_x|i\rangle$, **c** $\hat{Q}\hat{r}_y|i\rangle$, **d** $\hat{Q}\hat{r}_z|i\rangle$

From now on, we will use the simplified notations $|\phi_i\rangle \equiv |i\rangle$ and $|\tilde{\phi}_{i_\alpha}\rangle \equiv |i_\alpha\rangle$, in other words the subscript α on the orbital index indicates that it is an oscillator orbital. We designate the occupied (canonical or localized) molecular orbitals as $i, j, k, \ldots$ and the canonical virtual molecular orbitals (VMOs) as $a, b, c, \ldots$.

The oscillator orbitals are non-orthogonal among each other; their overlap integral can be evaluated using the idempotency of the projectors:

$$S_{i_\alpha j_\beta} = \langle i_\alpha | j_\beta \rangle = \langle i | \hat{r}_\alpha \hat{r}_\beta | j \rangle - \sum_m^{\text{occ}} \langle i | \hat{r}_\alpha | m \rangle \langle m | \hat{r}_\beta | j \rangle. \tag{5}$$

Note that the overlap matrix $\mathbf{S}$ is of size $N_{\text{POO}} \times N_{\text{POO}}$, where N_{POO} is the number of projected oscillator orbitals.

The POOs can be expanded in terms of a set of orthonormalized virtual orbitals (e.g. the set of canonical virtuals). Although later we eliminate explicit reference to the set of virtual orbitals of the Fock/Kohn–Sham operator (i.e., everything will be written only in terms of the occupied orbitals or equivalently in terms of the corresponding density matrix), with the help of the resolution of identity, we give the explicit form of the coefficient matrix linking the POOs with the virtuals:

$$|i_\alpha\rangle = \left(\sum_p^{\text{all}} |p\rangle\langle p| \right) \hat{Q}\hat{r}_\alpha |i\rangle = \sum_a^{\text{virt}} |a\rangle \langle a | \hat{r}_\alpha | i \rangle = \sum_a^{\text{virt}} |a\rangle V_{ai_\alpha}. \tag{6}$$

The matrix $\mathbf{V}$ is constructed simply from the elements of the occupied/virtual block of the position operator, $V_{ai_\alpha} = \langle a | \hat{r}_\alpha | i \rangle$. The overlap matrix of the expanded POOs can be written in terms of the coefficient matrix $\mathbf{V}$:

$$S_{i_\alpha j_\beta} = \langle i_\alpha | j_\beta \rangle = \sum_{ab}^{\text{virt}} V^\dagger_{i_\alpha a} \langle a | b \rangle V_{bj_\beta} = \left(\mathbf{V}^\dagger \mathbf{V} \right)_{i_\alpha j_\beta}. \tag{7}$$

Higher order oscillator orbitals, not used in the present work, can be generated in an analogous manner, using higher order solid spherical harmonic functions.

2.2 Ring CCD-RPA equations with POOs

In the ring CCD (ring coupled cluster double excitations) formulation [39], the general RPA correlation energy (direct-RPA or RPA-exchange) is a sum of pair-contributions attributed to a pair of occupied (localized) orbitals:

$$E_c^{\text{RPA}} = \frac{1}{2} \sum_{ij}^{\text{occ}} \text{tr} \left\{ \mathbf{B}^{ij} \mathbf{T}^{ij} \right\}, \tag{8}$$

where the amplitudes $\mathbf{T}^{ij}$ satisfy the Riccati equations, which can be written in terms of orthogonalized occupied $i, j, k, \ldots$ and virtual $a, b, c, \ldots$ orbitals as:

$$\mathbf{R}^{ij} = \mathbf{B}^{ij} + ((\boldsymbol{\epsilon} + \mathbf{A})\mathbf{T})^{ij} + (\mathbf{T}(\mathbf{A} + \boldsymbol{\epsilon}))^{ij} + (\mathbf{TBT})^{ij} = \mathbf{0}, \tag{9}$$

with the matrix elements:

$$\begin{aligned} \epsilon^{ij}_{ab} &= \delta_{ij} f_{ab} - f_{ij} \delta_{ab} \\ A^{ij}_{ab} &= K^{ij}_{ab} - J^{ij}_{ab} = \langle aj | ib \rangle - \langle aj | bi \rangle \\ B^{ij}_{ab} &= K^{ij}_{ab} - K'^{ij}_{ab} = \langle ij | ab \rangle - \langle ij | ba \rangle, \end{aligned} \tag{10}$$

where $\mathbf{f}$ is the fock matrix of the fock operator $\hat{f}$ and with the two-electron integrals of spin-orbitals written with the physicists' notation:

$$\langle ij|ab\rangle = \int \phi_i^*(\mathbf{r})\phi_j^*(\mathbf{r}')w(\mathbf{r},\mathbf{r}')\phi_a(\mathbf{r})\phi_b(\mathbf{r}')\mathrm{d}\mathbf{r}\mathrm{d}\mathbf{r}', \quad (11)$$

where $w(\mathbf{r},\mathbf{r}') = |\mathbf{r}'-\mathbf{r}|^{-1}$ is the Coulomb electron repulsion interaction.

Note that the size of the matrices in Eqs. 8 and 9 is, for each pair $[ij]$, $N_{\mathrm{virt}} \times N_{\mathrm{virt}}$ and that in this notation the matrix multiplications are understood as, for example: $(\mathbf{T}(\mathbf{A}+\boldsymbol{\epsilon}))^{ij}_{ab} = \sum_{mc} T^{im}_{ac}A^{mj}_{cb} + T^{im}_{ac}\epsilon^{mj}_{cb}$.

Using the transformation rule between the amplitudes in the VMOs and in the POO basis, $\mathbf{T}^{ij} = \mathbf{V}\mathbf{T}^{ij}_{\mathrm{POO}}\mathbf{V}^\dagger$ (see Appendix 2), the Riccati equations can be recast in the POO basis as (again, see Appendix 2):

$$\begin{aligned}\mathbf{R}^{ij}_{\mathrm{POO}} = \mathbf{B}^{ij}_{\mathrm{POO}} &+ \left(\boldsymbol{\epsilon}_{\mathrm{POO}} + \mathbf{A}^{im}_{\mathrm{POO}}\right)\mathbf{T}^{mj}_{\mathrm{POO}}\mathbf{S}_{\mathrm{POO}} \\ &+ \mathbf{S}_{\mathrm{POO}}\mathbf{T}^{im}_{\mathrm{POO}}\left(\boldsymbol{\epsilon}_{\mathrm{POO}} + \mathbf{A}^{mj}_{\mathrm{POO}}\right) \\ &+ \mathbf{S}_{\mathrm{POO}}\mathbf{T}^{im}_{\mathrm{POO}}\mathbf{B}^{mn}_{\mathrm{POO}}\mathbf{T}^{nj}_{\mathrm{POO}}\mathbf{S}_{\mathrm{POO}} = \mathbf{0}. \end{aligned} \quad (12)$$

This corresponds to a local formulation of the ring CCD amplitudes equations, and the dimension of the matrices, emphasized by the subscript POO, is merely $N_{\mathrm{POO}} \times N_{\mathrm{POO}}$. As explained in Appendix 3, this type of Riccati equations can be solved iteratively in a pseudo-canonical basis.

2.3 Local excitation approximation

Since the excitations are limited to "pair-domains", the effective dimension of the equations for a pair is actually roughly independent from the size of the system, just like in any local correlation procedure.

As the simplest approximation, one can take only the three excitations to the dipolar POOs generated by a selected LMO, i.e., for each pair of LMOs $[ij]$ we have the local excitations $i \to i_\alpha$ and $j \to j_\beta$, leading to a 3×3 problem to solve and iterate on. Within this approximation, all matrices involved in the derivations can be fully characterized by two occupied LMO indices and two cartesian components, α and β (the subscript POO is omitted from now on):

$$\begin{aligned} &(\mathbf{A})^{ij}_{i_\alpha j_\beta} \equiv (\mathbf{A})^{ij}_{\alpha\beta} \quad \text{and} \quad (\mathbf{S})_{i_\alpha j_\beta} \equiv (\mathbf{S})^{ij}_{\alpha\beta} \\ &(\mathbf{B})^{ij}_{i_\alpha j_\beta} \equiv (\mathbf{B})^{ij}_{\alpha\beta} \qquad\quad (\mathbf{f})_{i_\alpha j_\beta} \equiv (\mathbf{f})^{ij}_{\alpha\beta} \\ &(\mathbf{T})^{ij}_{i_\alpha j_\beta} \equiv (\mathbf{T})^{ij}_{\alpha\beta} \end{aligned} \quad (13)$$

With this in mind, and with the additional approximation which consists in neglecting the overlap between POOs coming from different LMOs, i.e., $(\mathbf{S})^{ij}_{\alpha\beta} \approx \delta_{ij}(\mathbf{S})^{ii}_{\alpha\beta}$, the direct RPA Riccati equations of Eq. 12 become:

$$\begin{aligned}\mathbf{R}^{ij} = \mathbf{B}^{ij} &+ \mathbf{f}^{ii}\mathbf{T}^{ij}\mathbf{S}^{jj} - f_{ii}\mathbf{S}^{ii}\mathbf{T}^{ij}\mathbf{S}^{jj} + \mathbf{A}^{im}\mathbf{T}^{mj}\mathbf{S}^{jj} \\ &+ \mathbf{S}^{ii}\mathbf{T}^{ij}\mathbf{f}^{jj} - \mathbf{S}^{ii}\mathbf{T}^{ij}\mathbf{S}^{jj}f_{jj} + \mathbf{S}^{ii}\mathbf{T}^{im}\mathbf{A}^{mj} \\ &+ \mathbf{S}^{ii}\mathbf{T}^{im}\mathbf{B}^{mn}\mathbf{T}^{nj}\mathbf{S}^{jj} = \mathbf{0}. \end{aligned} \quad (14)$$

In the above equation, we have written explicitly the fock matrix contributions and used implicit summation conventions over m and n. A detailed derivation of Eq. 14 from Eq. 12 is shown in Appendix 4. These Riccati equations can be solved by a transformation to the pseudo-canonical basis, as described in Appendix 3.

2.4 Multipole approximation for the long-range two-electron integrals in the POO basis

In the context of range-separation, and in the spirit of constructing an *approximate* theory which takes advantage of the localized character of the occupied molecular orbitals, we are going to proceed via a multipole expansion of the long-range two-electron integrals.

The matrices $\mathbf{A}^{ij}_{\mathrm{POO}}$ and $\mathbf{B}^{ij}_{\mathrm{POO}}$ will be reinterpreted in terms of long-range two-electron integrals, i.e., $w(\mathbf{r},\mathbf{r}')$ will be replaced by $w_{\mathrm{lr}}(\mathbf{r},\mathbf{r}') = \mathrm{erf}(\mu|\mathbf{r}'-\mathbf{r}|)|\mathbf{r}'-\mathbf{r}|^{-1}$ in Eq. 11. They read respectively as (see Eq. 10 and the transformation described in Appendix 2):

$$K^{ij}_{m_\alpha n_\beta} - J^{ij}_{m_\alpha n_\beta} = \langle m_\alpha j|in_\beta\rangle_{\mathrm{lr}} - \langle m_\alpha j|n_\beta i\rangle_{\mathrm{lr}} \quad (15)$$

$$K^{ij}_{m_\alpha n_\beta} - K'^{ij}_{m_\alpha n_\beta} = \langle ij|m_\alpha n_\beta\rangle_{\mathrm{lr}} - \langle ij|n_\beta m_\alpha\rangle_{\mathrm{lr}}. \quad (16)$$

Note that these integrals could be calculated by using the POO to VMO transformation of Eq. 6. However, such an expression is not in harmony with our goal of getting rid of virtual orbitals, since it requires the full set of integrals transformed in occupied and canonical VMOs with an additional two-index transformation. We could formally eliminate virtual molecular orbitals by applying the resolution of identity, but in this case we would be faced with new type of two-electron integrals, in addition to the usual ones generated by the Coulomb interaction $|\mathbf{r}-\mathbf{r}'|^{-1}$, namely integrals generated by $\hat{r}_\alpha|\mathbf{r}-\mathbf{r}'|^{-1}$, $\hat{r}'_\beta|\mathbf{r}-\mathbf{r}'|^{-1}$ and $\hat{r}_\alpha\hat{r}'_\beta|\mathbf{r}-\mathbf{r}'|^{-1}$. Therefore we are going to proceed by a multipole expansion technique.

The expansion center for the multipole expansion will be chosen at the centroid of the LMOs, i.e., in this example at $\mathbf{D}^i$ and $\mathbf{D}^j$. Using the second-order long-range interaction tensor $\mathbf{L}^{ij}(\mathbf{D}^{ij})$, with $\mathbf{D}^{ij} = \mathbf{D}^i - \mathbf{D}^j$ (see Appendix 5), we have

$$\begin{aligned}K^{ij}_{m_\alpha n_\beta} = \langle m_\alpha j|in_\beta\rangle_{\mathrm{lr}} &\approx \sum_{\gamma\delta}\langle m_\alpha|\hat{r}_\gamma|i\rangle L^{ij}_{\gamma\delta}\langle j|\hat{r}_\delta|n_\beta\rangle \\ &+ \text{higher multipole terms.} \end{aligned} \quad (17)$$

A truly remarkable formal result emerging from the framework of oscillator orbitals is that the $\hat{r}_\gamma$ matrix element between the POO m_α and the LMO i that appears in the previous equation is nothing else but the overlap between the POOs m_α and i_γ (c.f. Eq. 5):

$$\langle m_\alpha|\hat{r}_\gamma|i\rangle = \langle m|\hat{r}_\alpha\hat{r}_\gamma|i\rangle - \sum_n^{\text{occ}}\langle m|\hat{r}_\alpha|n\rangle\langle n|\hat{r}_\gamma|i\rangle = S_{m_\alpha i_\gamma}, \quad (18)$$

so that the matrix element $K^{ij}_{m_\alpha n_\beta}$ simply reads:

$$K^{ij}_{m_\alpha n_\beta} = S_{m_\alpha i_\gamma} L^{ij}_{\gamma\delta} S_{j_\delta n_\beta}. \quad (19)$$

After applying the local excitation approximation, this bi-electronic integral becomes even simpler, according to the following expression:

$$\mathbf{K}^{ij} = \mathbf{S}^{ii}\mathbf{L}^{ij}\mathbf{S}^{jj}. \quad (20)$$

In the case of direct RPA, only the $\mathbf{K}^{ij}$ two-electron integrals are needed. For the more general exchange RPA (RPAx) case, most of the electron repulsion integrals, $\langle m_\alpha j|n_\beta i\rangle_{\text{lr}}$, can be neglected in the multipole approximation, since they correspond to the interaction of overlap charge densities formed by localized orbitals in different domains. Nevertheless, integrals of the type $\langle m_\alpha j|m_\beta j\rangle_{\text{lr}}$ should be kept: they describe the interaction of the overlap charge densities of the jth LMO and the m_α POO, which is a typical long-range Coulomb interaction. Similar considerations hold for the $\mathbf{K}'^{ij}$ matrix elements, which correspond to an exchange integral involving overlap charge densities of orbitals belonging to different domains and can be neglected at this point (a few integrals will however survive). The RPAx variant of the model will be considered in more details in forthcoming works.

2.5 Spherical average approximation

The previously discussed 3×3 matrices can be easily replaced by scalar quantities, if one considers a spherical average of the POO overlap and fock matrices:

$$S^{ii}_{\alpha\beta} \approx \tfrac{1}{3}s^i\delta_{\alpha\beta} \quad \text{with} \quad s^i = \sum_\alpha S^{ii}_{\alpha\alpha}, \quad (21)$$

and

$$f^{ii}_{\alpha\beta} \approx \tfrac{1}{3}f^i\delta_{\alpha\beta} \quad \text{with} \quad f^i = \sum_\alpha f^{ii}_{\alpha\alpha}. \quad (22)$$

In this diagonal approximation, and in the case of direct RPA where $\mathbf{A} = \mathbf{B} = \mathbf{K}$, the Riccati equations of Eq. 14 supposing implicit summations on m and n become:

$$\begin{aligned}\mathbf{R}^{ij} = {} & s^i s^j \mathbf{L}^{ij} + \left(f^i s^j - f_{ii}s^i s^j\right)\mathbf{T}^{ij} + \tfrac{1}{3}s^i s^m s^j \mathbf{L}^{im}\mathbf{T}^{mj} \\ & + \left(s^i f^j - s^i s^j f_{jj}\right)\mathbf{T}^{ij} + \tfrac{1}{3}s^i s^m s^j \mathbf{T}^{im}\mathbf{L}^{mj} \\ & + \tfrac{1}{3^2}s^i s^m s^n s^j \mathbf{T}^{im}\mathbf{L}^{mn}\mathbf{T}^{nj} = \mathbf{0}.\end{aligned} \quad (23)$$

This set of equations can be solved directly, i.e., without proceeding by the pseudo-canonical transformation described in Appendix 3 for the more general case. The only quantities needed are the spherically averaged s^i and f^i associated with localized orbitals and the long-range dipole-dipole tensors. The update formula to get the nth approximation to the amplitude matrix element is

$$T^{ij(n)}_{\alpha\beta} = \frac{s^i s^j L^{ij}_{\alpha\beta} + \Delta R^{ij}_{\alpha\beta}\left(\mathbf{T}^{(n-1)}\right)}{\Delta^i s^j + s^i \Delta^j}, \quad (24)$$

with

$$\Delta^i = f_{ii}s^i - f^i, \quad (25)$$

and

$$\begin{aligned}\Delta\mathbf{R}^{ij}(\mathbf{T}) = {} & \tfrac{1}{3}s^i s^m s^j \mathbf{L}^{im}\mathbf{T}^{mj} + \tfrac{1}{3}s^i s^m s^j \mathbf{T}^{im}\mathbf{L}^{mj} \\ & + \tfrac{1}{3^2}s^i s^m s^n s^j \mathbf{T}^{im}\mathbf{L}^{mn}\mathbf{T}^{nj}.\end{aligned} \quad (26)$$

Pursuing with the local excitation and the spherical average approximations, the long-range correlation energy is given by the following spin-adapted expression:

$$E_{\text{c}}^{\text{RPA,lr}} = \frac{4}{9}\sum_{ij}^{\text{occ}} s^i s^j \text{tr}\left\{\mathbf{L}^{ij}\mathbf{T}^{ij}\right\}. \quad (27)$$

2.6 Bond–bond C_6 coefficients

Using the first-order amplitudes, i.e., the amplitudes obtained in the first iteration step during the solution of Eq. 24:

$$\mathbf{T}^{ij(1)} = \frac{s^i s^j}{\Delta^i s^j + s^i \Delta^j}\mathbf{L}^{ij}, \quad (28)$$

the second-order long-range correlation energy becomes:

$$E_{\text{c}}^{(2),\text{lr}} = \frac{4}{9}\sum_{ij}^{\text{occ}} \frac{s^i s^j s^i s^j}{\Delta^i s^j + s^i \Delta^j}\text{tr}\left\{\mathbf{L}^{ij}\mathbf{L}^{ij}\right\}. \quad (29)$$

This expression describes the correlation energy as a pairwise additive quantity made up from bond–bond contributions. The summation over the components of the long-range interaction tensors gives (see Appendix 5):

$$\text{tr}\left\{\mathbf{L}^{ij}\mathbf{L}^{ij}\right\} = \frac{6}{\mathbf{D}^{ij6}}F^\mu_{\text{damp}}\left(\mathbf{D}^{ij}\right), \quad (30)$$

and allows us to cast the long-range correlation energy in a familiar form, as:

$$E_{\text{c}}^{(2),\text{lr}} = \sum_{ij}^{\text{occ}} \frac{C_6^{ij}}{\mathbf{D}^{ij6}}F^\mu_{\text{damp}}\left(\mathbf{D}^{ij}\right), \quad (31)$$

where C_6^{ij} is the dispersion coefficient between the i and j LMOs:

$$C_6^{ij} = \frac{8}{3}\frac{s^i s^j s^i s^j}{\Delta^i s^j + s^i \Delta^j}. \tag{32}$$

Note that the above dispersion coefficient corresponds to a single-term approximation to the bare (non-interacting) spherically averaged dipolar dynamic polarizability associated with the localized orbital i,

$$\overline{\alpha}_0^i(i\omega) \approx \frac{4}{3}\frac{\overline{\omega}_i}{\overline{\omega}_i^2 + \omega^2} s^i, \tag{33}$$

where $\overline{\omega}_i = \Delta^i / s^i$ is an effective energy denominator and the quantity s^i stands for the second cumulant moment (spread) of the localized orbital. Note that this possibility to approximate $\overline{\alpha}_0^i(i\omega)$ only as a function of objects like f^i and s^i is a direct consequence of the remarkable feature that the second moment between an LMO and a POO corresponds to an overlap between two POOs (see Eq. 18).

It is easy to verify that with the help of the Casimir–Polder formula

$$C_6^{ij} = \frac{3}{\pi}\int_0^\infty d\omega\, \overline{\alpha}_0^i(i\omega)\, \overline{\alpha}_0^j(i\omega), \tag{34}$$

that it is indeed the C_6^{ij} dispersion coefficient which is recovered from the polarizabilities defined in Eq. 33. This simple model for the dynamic polarizability associated to an LMO, deduced from first principles, can be the starting point of alternative dispersion energy expressions, e.g. based on the modeling of the dielectric matrix of the system or using the plasmonic energy expression.

3 Preliminary results: molecular C_6 coefficients

In order to have a broad idea about the appropriateness of this simple dispersion energy correction, we have calculated the molecular C_6 coefficients for a series of homodimers as the sum of the atom–atom dispersion coefficients given by Eq. 32.

The matrix elements between POOs, $S_{\alpha\beta}^{ii}$ and $f_{\alpha\beta}^{ii}$, which are needed to calculate the scalars s^i and f^i, can be obtained directly by manipulating the matrix representation of the operators. Such a procedure leads to what we will call the "matrix algebra" expressions (denoted by [M]), of the following form:

$$s^i_{[\mathrm{M}]} = \sum_\alpha \langle i|\hat{r}_\alpha \hat{Q} \hat{r}_\alpha|i\rangle = \sum_a^{\mathrm{virt}} |\langle i|\hat{\mathbf{r}}|a\rangle|^2, \tag{35}$$

and (see Appendix 6):

$$f^i_{[\mathrm{M}]} = \sum_{ab}^{\mathrm{virt}} \sum_\alpha \langle i|\hat{r}_\alpha|a\rangle f_{ab} \langle b|\hat{r}_\alpha|i\rangle. \tag{36}$$

Alternatively, these matrix elements can be obtained through the application of commutator relationships, therefore this latter option will be referred to as the "operator algebra" approach (denoted by [O]). They take the form:

$$s^i_{[\mathrm{O}]} = \sum_\alpha \langle i|\hat{r}_\alpha \hat{Q} \hat{r}_\alpha|i\rangle = \langle i|\hat{\mathbf{r}}^2|i\rangle - \sum_m^{\mathrm{occ}} |\langle i|\hat{\mathbf{r}}|m\rangle|^2, \tag{37}$$

and (again, see Appendix 6):

$$f^i_{[\mathrm{O}]} = \tfrac{3}{2} + \tfrac{1}{2}\sum_m^{\mathrm{occ}} \left(f_{im}\langle m|\hat{\mathbf{r}}^2|i\rangle + \langle i|\hat{\mathbf{r}}^2|m\rangle f_{mi} \right) - \sum_{mn}^{\mathrm{occ}} \sum_\alpha \langle i|\hat{r}_\alpha|m\rangle f_{mn} \langle n|\hat{r}_\alpha|i\rangle. \tag{38}$$

Four different Fock/Kohn-Sham operators have been applied to obtain the orbitals, which are subsequently localized by the standard Foster–Boys procedure. In addition to the local/semi-local functionals LDA and PBE, the range-separated hybrid RSHLDA [37, 56] with a range-separation parameter of $\mu = 0.5$ a.u. as well as the standard restricted Hartree–Fock (RHF) method were used. The notations LDA[M] and LDA[O] refer to the procedure applied to obtain the matrix elements: either by the matrix algebra [M] or by the operator algebra [O] method. All calculations were done with the aug-cc-pVTZ basis set, using the MOLPRO quantum chemical program package [57]. The matrix elements were obtained by the MATROP facility of MOLPRO [57]; the C_6 coefficients were calculated by Mathematica.

The results and their statistical analysis are collected in Table 1 for a set of small molecules taken from the database compiled by Tkatchenko and Scheffler [16], as used in [58]. The experimental dispersion coefficients have been determined from dipole oscillator strength distributions (DOSD) [59–71]. The percentage errors of some of the methods (LDA[M], PBE[M], RHF[M] and RSHLDA[M]) are shown in Fig. 3.

Besides Eq. 32, the C_6 coefficients were also calculated from an iterative procedure, where the amplitude matrices $\mathbf{T}^{ij}$ were updated according to the first two lines of Eq. 23. Such a procedure corresponds roughly to a local MP2 iteration, and the methods are labeled LDA2, PBE2, RHF2 and RSHLDA2. These results are summarized in Table 2, where a detailed statistical analysis is presented for all the computational results.

The dispersion coefficients obtained from LDA and PBE orbitals are strongly overestimated. It is not really surprising in view of the rather diffuse nature of DFA orbitals and their tendency to underestimate the occupied/virtual gap. Due to the fact that LDA and PBE lead to local potentials, the operator and matrix algebra results are very similar: their difference is smaller than the supposed experimental uncertainty of the DOSD dispersion coefficients (few

Table 1 Molecular C_6 coefficients from the dipolar oscillator orbital method, using LDA, PBE, RHF and sr-LDA/lr-RHF determinants in aug-cc-pVTZ basis set and Boys localized orbitals

Molecules	Ref.	LDA[M]	LDA[O]	PBE[M]	PBE[O]	RHF[M]	RHF[O]	RSHLDA[M]	RSHLDA[O]
H_2	12.1	18.4	18.4	17.2	17.2	9.6	16.2	**10.6**	16.9
HF	19.0	20.7	21.5	20.7	21.6	12.4	17.2	14.9	**19.3**
H_2O	45.3	55.6	56.5	55.1	56.1	31.9	**45.4**	36.4	48.9
N_2	73.3	118.3	118.8	117.6	118.0	**75.2**	109.0	81.1	110.9
CO	81.4	120.4	120.9	119.1	119.7	70.9	104.1	**79.1**	109.6
NH_3	89.0	118.8	119.9	116.7	117.8	66.3	**98.6**	72.6	102.0
CH_4	129.7	192.4	193.0	185.9	186.5	105.3	163.5	**114.5**	168.2
HCl	130.4	208.9	211.8	205.1	208.5	121.5	186.3	**126.7**	184.8
CO_2	158.7	234.9	237.0	233.2	235.4	130.9	184.0	**153.3**	202.8
H_2CO	165.2	205.7	207.2	202.8	204.3	115.2	**168.3**	129.4	178.4
N_2O	184.9	317.1	319.3	315.3	317.5	**178.9**	252.3	206.0	274.7
C_2H_2	204.1	343.5	345.2	340.4	342.2	**206.4**	316.1	209.7	306.5
HBr	216.6	303.3	325.9	302.5	325.4	**188.3**	293.5	188.2	282.7
H_2S	216.8	392.8	397.7	382.8	388.2	**213.0**	339.2	220.5	335.5
CH_3OH	222.0	303.8	305.3	297.0	298.5	166.8	**246.2**	187.2	260.2
SO_2	294.0	542.6	554.9	539.8	552.5	**284.9**	416.7	329.5	456.2
C_2H_4	300.2	466.1	467.8	456.7	458.4	266.3	406.4	**279.4**	405.8
CH_3NH_2	303.8	440.6	442.3	429.8	431.4	240.2	360.3	**263.2**	373.3
SiH_4	343.9	639.6	655.3	598.4	613.9	280.0	484.6	**310.9**	513.0
C_2H_6	381.9	579.2	580.9	560.9	562.5	313.5	480.9	**341.2**	495.5
Cl_2	389.2	727.4	735.4	714.3	723.7	**401.3**	607.5	424.3	612.2
CH_3CHO	401.7	627.5	630.4	613.3	616.0	333.2	493.6	**372.6**	521.7
COS	402.2	845.7	855.8	843.9	853.7	**456.3**	689.2	495.7	713.5
CH_3OCH_3	534.1	781.4	784.3	758.4	761.1	415.2	619.4	**464.8**	654.3
C_3H_6	662.1	1045.9	1049.4	1018.6	1021.8	571.2	868.2	**609.8**	881.2
CS_2	871.1	2099.4	2119.5	2073.4	2094.5	**1085.6**	1658.0	1144.0	1686.2
CCl_4	2024.1	3831.3	3861.0	3750.4	3784.0	**2004.8**	3007.0	2135.5	3051.9
MAD%E		59.84	61.69	56.71	58.62	15.22	33.75	11.84	37.60
STD%E		28.08	28.25	27.76	27.98	9.88	21.15	7.24	20.86
CSSD%E		67.14	68.92	64.11	65.97	18.39	40.37	14.07	43.62

The matrix elements are calculated with a matrix algebra [M] and operator algebra [O] approach, respectively. All results are in a.u.

Values highlighted as bold indicate the best agreement with experiment

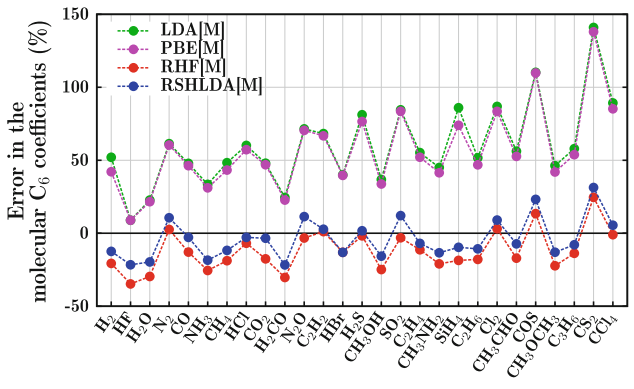

Fig. 3 Percentage errors in calculated molecular C_6 coefficients obtained with different methods using the matrix algebra approach

percent). It is quite clear from Fig. 3 that the errors for the molecules containing second-row elements are considerably higher than for most of the molecules composed of H, C, N, O and F atoms. Notable exceptions are the N_2 and N_2O molecules.

The performance of the method is significantly better for orbitals obtained by nonlocal exchange: RHF and RSHLDA. In the latter case the long-range exchange is nonlocal, and only the short-range exchange is described by a short-range functional. The best performance has been achieved by the RSHLDA[M] method. In contrast to the pure DFA calculations, the matrix and operator algebra methods differ for the RHF and RSH methods significantly: the mean absolute error and the standard deviation of the

Table 2 Detailed statistical analysis of the methods to obtain POO C_6 coefficients

	LDA[M]	PBE[M]	RHF[M]	RSHLDA[M]
MA%E	59.8	56.7	15.2	11.8
STD%E	28.1	27.8	9.9	7.2
CSSD%E	67.1	64.1	18.4	14.1
MED%E	55.3	52.1	17.1	11.4
MAX%E	141	138	24.6	31.3
MIN%E	9.1	8.8	−34.7	−21.7
	LDA2[M]	PBE2[M]	RHF2[M]	RSHLDA2[M]
MA%E	64.3	61	17.1	17.1
STD%E	35.7	35.3	12.3	12.3
CSSD%E	74.7	71.5	21.3	21.3
MED%E	53.5	50.6	15.3	15.3
MAX%E	142.1	148.7	54.3	54.3
MIN%E	−4.7	−5.1	−36.6	−36.6
	LDA[O]	PBE[O]	RHF[O]	RSHLDA[O]
MA%E	61.7	58.6	33.7	37.6
STD%E	28.3	28	21.2	20.9
CSSD%E	68.9	66	40.4	43.6
MED%E	55.8	52.7	34	34.6
MAX%E	143.3	140.4	90.3	93.6
MIN%E	13.4	13.4	−9.7	1.7
	LDA2[O]	PBE2[O]	RHF2[O]	RSHLDA2[O]
MA%E	65.9	62.7	51	51
STD%E	36.3	36.9	47.7	47.7
CSSD%E	76.3	73.8	70.5	70.5
MED%E	54.7	51.1	34	34
MAX%E	143.3	152.9	214.8	214.8
MIN%E	−1.1	−1.2	−10.6	−10.6

error is increased by a factor of 2 or 3. This deterioration of the quality of the results reflects the fact that in the operator algebra approach the commutator of the position and non-local exchange operators is neglected (see Appendix 6), while this effect is automatically taken into account in the matrix algebra calculations. In view of the simplicity of the model and of its fully ab initio character, the best ME%E of about 11 % seems to be very promising and indicates that further work in this direction is worthwhile.

4 Conclusions, perspectives

It has been shown that, using projected dipolar oscillator orbitals to represent the virtual space in a localized orbital context, the equations involved in long-range ring coupled cluster doubles type RPA calculations can be formulated without explicit knowledge of the virtual orbital set. The POO virtuals have been constructed directly from the localized occupied orbitals. The matrix elements and the electron repulsion integrals were evaluated using only the elements of the occupied block of the Fock/Kohn-Sham matrix in LMO basis and from simple multipole integrals between occupied LMOs. An interesting feature of the model is that, as far as one uses Boys localized orbitals and first-order dipolar oscillator orbitals, practically all the emerging quantities can be expressed by the overlap integral between two oscillator orbitals, which happens to be the matrix element of the dipole moment fluctuation operator. Various levels of approximations have been considered for the long-range RPA energy leading finally to a pairwise additive dispersion energy formula with a non-empirical expression for the bond–bond C_6 dispersion coefficient. At this simplest level a straightforward relationship has been unraveled between the ring coupled cluster and the dielectric matrix formulations of the long-range RPA correlation energy.

Our derivation, starting from the quantum chemical RPA correlation energy and pursuing a hierarchy of simplifying assumptions, has led us to a dispersion energy expression which is in a straightforward analogy with classical van der

Waals energy formulae. Our procedure produces an explicit model, derived from the wave function of the system, for the dynamical polarizabilities associated with the building blocks, which are bonds, lone pairs and in general localized electron pairs. Thus one arrives to the quantum chemical analogs of the "quantum harmonic oscillators" (QHO) appearing in the semiclassical theory of dispersion forces, elaborated within a RPA framework by Tkatchenko et al. [72, 73].

A promising perspective of the projected oscillator orbital approach concerns the description of dispersion forces in plane wave calculations for solids. Much effort has been spent recently in finding a compact representation of the dielectric matrix in plane wave calculations [10], but it still remains a bottleneck for a really fast non-empirical calculation of the long-range correlation energy. Projected oscillator orbitals may offer an opportunity to construct extremely compact representations of a part of the conduction band, which contributes the most to the local dipolar excitations at the origin of van der Waals forces. However, this approach is probably limited to relatively large gap semiconductors, where the construction of the MLWF [74, 75], which are the solid-state analogs of the Boys localized orbitals, is a convergent procedure. Such a methodology could become a fully non-empirical variant of Silvestrelli's extension of the Tkatchenko–Scheffler approach for MLWFs [46–50].

The main purpose of the present work has been to describe the principal features of the formalism, without extensive numerical applications. However, the first rudimentary numerical tests on the molecular C_6 coefficients have indicated that the results are quite plausible in spite of the simplifying approximations and it is reasonable to expect that more sophisticated variants of the method will improve the quality of the model. In view of the modest computational costs and the fully ab initio character of the projected oscillator orbital approach applied at various approximation levels of the RPA, which is able to describe dispersion forces even beyond a pairwise additive scheme, the full numerical implementation of the presently outlined methodology has certainly a great potential for the treatment of London dispersion forces in the context of density functional theory.

Acknowledgments J.G.A. thanks Prof. Péter Surján (Budapest), to whom this article is dedicated, the fruitful discussions during an early stage of this work.

Appendix 1: Dipolar oscillator orbitals in local frame

Let $\boldsymbol{\mathcal{R}}^i$ be the rotation matrix which transforms an arbitrary vector $\mathbf{v}$ from the laboratory frame to the vector $\mathbf{v}^{\mathrm{loc}}$ in the local frame defined as the principal axes of the second moment tensor of the charge distribution associated with a given localized occupied orbital i, $\boldsymbol{\mathcal{R}}^i \cdot \mathbf{v} = \mathbf{v}^{\mathrm{loc}}$. The expression in the local frame of a POO i_α constructed from the LMO i is then:

$$\begin{aligned} |i_\alpha^{\mathrm{loc}}\rangle &= \left(\hat{I} - \sum_m^{\mathrm{occ}} |m\rangle\langle m|\right)\left(\boldsymbol{\mathcal{R}}^i \cdot \left(\mathbf{r} - \mathbf{D}^i\right)\right)_\alpha |i\rangle \\ &= \left(\boldsymbol{\mathcal{R}}^i \cdot \mathbf{r}\right)_\alpha |i\rangle - \sum_m^{\mathrm{occ}} \left(\boldsymbol{\mathcal{R}}^i \cdot \langle m|\mathbf{r}|i\rangle\right)_\alpha |m\rangle \\ &= \sum_\beta \mathcal{R}^i_{\alpha\beta} r_\beta |i\rangle - \sum_m^{\mathrm{occ}} \sum_\beta \mathcal{R}^i_{\alpha\beta} \langle m|r_\beta|i\rangle |m\rangle \end{aligned} \tag{39}$$

Appendix 2: Riccati equations in POO basis

The first-order wave function $\Psi^{(1)}$ can be written in terms of Slater determinants $|\ldots ab\ldots|$ formed with LMOs and canonical virtual orbitals a and b on the one hand, and on the other hand in terms of Slater determinants $|\ldots m_\alpha n_\beta \ldots|$ formed with LMOs and POOs m_α and n_β. That is to say that:

$$\Psi^{(1)} = \sum_{ij}^{\mathrm{occ}} \sum_{ab}^{\mathrm{virt}} T^{ij}_{ab} |\ldots ab\ldots| \approx \sum_{ij}^{\mathrm{occ}} \sum_{m_\alpha n_\beta}^{\mathrm{POO}} T^{ij}_{m_\alpha n_\beta} |\ldots m_\alpha n_\beta \ldots|. \tag{40}$$

The canonical virtual orbitals and the POOs in question are related by (see Eq. 6):

$$|m_\alpha\rangle = \sum_a^{\mathrm{virt}} |a\rangle V_{am_\alpha} \quad \text{and} \quad |n_\beta\rangle = \sum_b^{\mathrm{virt}} |b\rangle V_{bn_\beta}. \tag{41}$$

This allows us to write:

$$\begin{aligned} \Psi^{(1)} &= \sum_{ij}^{\mathrm{occ}} \sum_{ab}^{\mathrm{virt}} T^{ij}_{ab} |\ldots ab\ldots| \\ &\approx \sum_{ij}^{\mathrm{occ}} \sum_{m_\alpha n_\beta}^{\mathrm{POO}} T^{ij}_{m_\alpha n_\beta} |\ldots m_\alpha n_\beta \ldots| \\ &= \sum_{ij}^{\mathrm{occ}} \sum_{m_\alpha n_\beta}^{\mathrm{POO}} \sum_{ab}^{\mathrm{virt}} V_{am_\alpha} T^{ij}_{m_\alpha n_\beta} V^\dagger_{n_\beta b} |\ldots ab\ldots|, \end{aligned} \tag{42}$$

and leads to the transformation rule between the amplitudes in the VMO and in the POO basis:

$$\mathbf{T}^{ij} = \mathbf{V}\mathbf{T}^{ij}_{\mathrm{POO}}\mathbf{V}^\dagger. \tag{43}$$

Multiplication of the Riccati equations of Eq. 9 by $\mathbf{V}^\dagger$ and $\mathbf{V}$ from the left and from the right, respectively, and expressing the amplitudes in POOs using Eq. 43 leads to:

$$\mathbf{V}^\dagger \mathbf{R}^{ij} \mathbf{V} = \mathbf{V}^\dagger \mathbf{B}^{ij} \mathbf{V} + \mathbf{V}^\dagger (\boldsymbol{\epsilon} + \mathbf{A})^{im} \left(\mathbf{V} \mathbf{T}^{mj}_{\mathrm{POO}} \mathbf{V}^\dagger \right) \mathbf{V} + \mathbf{V}^\dagger \left(\mathbf{V} \mathbf{T}^{im}_{\mathrm{POO}} \mathbf{V}^\dagger \right) (\boldsymbol{\epsilon} + \mathbf{A})^{mj} \mathbf{V} + \mathbf{V}^\dagger \left(\mathbf{V} \mathbf{T}^{im}_{\mathrm{POO}} \mathbf{V}^\dagger \right) \mathbf{B}^{mn} \left(\mathbf{V} \mathbf{T}^{nj}_{\mathrm{POO}} \mathbf{V}^\dagger \right) \mathbf{V} = \mathbf{0}, \quad (44)$$

where implicit summation conventions are supposed on m and n. Recognizing the expression for the overlap matrix, $\mathbf{S}_{\mathrm{POO}} = \mathbf{V}^\dagger \mathbf{V}$, we obtain:

$$\mathbf{R}^{ij}_{\mathrm{POO}} = \mathbf{B}^{ij}_{\mathrm{POO}} + (\boldsymbol{\epsilon}_{\mathrm{POO}} + \mathbf{A}_{\mathrm{POO}})^{im} \mathbf{T}^{mj}_{\mathrm{POO}} \mathbf{S}_{\mathrm{POO}} + \mathbf{S}_{\mathrm{POO}} \mathbf{T}^{im}_{\mathrm{POO}} (\boldsymbol{\epsilon}_{\mathrm{POO}} + \mathbf{A}_{\mathrm{POO}})^{mj} + \mathbf{S}_{\mathrm{POO}} \mathbf{T}^{im}_{\mathrm{POO}} \mathbf{B}^{mn}_{\mathrm{POO}} \mathbf{T}^{nj}_{\mathrm{POO}} \mathbf{S}_{\mathrm{POO}} = \mathbf{0}, \quad (45)$$

which defines $\mathbf{R}^{ij}_{\mathrm{POO}}$, $\boldsymbol{\epsilon}^{ij}_{\mathrm{POO}}$, $\mathbf{A}^{ij}_{\mathrm{POO}}$ and $\mathbf{B}^{ij}_{\mathrm{POO}}$ and which are the Riccati equations seen in Eq. 12.

Appendix 3: Solution of the Riccati equations in POO basis

To derive the iterative resolution of the Riccati equations seen in Eq. 12, we write explicitly the fock matrix contributions hidden in the matrix $\boldsymbol{\epsilon}$. The matrix elements in canonical virtual orbitals, ϵ^{ij}_{ab}, read:

$$\epsilon^{ij}_{ab} = \delta_{ij} f_{ab} - \delta_{ab} f_{ij}, \quad (46)$$

so that the matrix element in POOs is (we omit the "POO" indices):

$$\epsilon^{ij}_{m_\alpha n_\beta} = V^\dagger_{m_\alpha a} \epsilon^{ij}_{ab} V_{b n_\beta} = \delta_{ij} f_{m_\alpha n_\beta} - S_{m_\alpha n_\beta} f_{ij}. \quad (47)$$

The terms in the Riccati equations containing the matrix $\boldsymbol{\epsilon}$ then read (we use implicit summations over m and n):

$$\boldsymbol{\epsilon}^{im} \mathbf{T}^{mj} \mathbf{S} = \mathbf{f} \mathbf{T}^{ij} \mathbf{S} - f_{im} \mathbf{S} \mathbf{T}^{mj} \mathbf{S} \quad (48)$$

$$\mathbf{S} \mathbf{T}^{im} \boldsymbol{\epsilon}^{mj} = \mathbf{S} \mathbf{T}^{ij} \mathbf{f} - \mathbf{S} \mathbf{T}^{im} \mathbf{S} f_{mj}. \quad (49)$$

We this in mind, the Riccati equations of Eq. 12 yield:

$$\mathbf{R}^{ij} = \mathbf{B}^{ij} + (\mathbf{f} - f_{ii} \mathbf{S}) \mathbf{T}^{ij} \mathbf{S} + \mathbf{S} \mathbf{T}^{ij} (\mathbf{f} - \mathbf{S} f_{jj}) - \sum_{m \neq i} f_{im} \mathbf{S} \mathbf{T}^{mj} \mathbf{S} - \sum_{m \neq j} \mathbf{S} \mathbf{T}^{im} \mathbf{S} f_{mj} + \mathbf{A}^{im} \mathbf{T}^{mj} \mathbf{S} + \mathbf{S} \mathbf{T}^{im} \mathbf{A}^{mj} + \mathbf{S} \mathbf{T}^{im} \mathbf{B}^{mn} \mathbf{T}^{nj} \mathbf{S} = \mathbf{0}. \quad (50)$$

Remember that the matrices are of dimension $N_{\mathrm{POO}} \times N_{\mathrm{POO}}$. Due to the nonorthogonality of the POOs and the non diagonal structure of the fock matrix, the usual simple updating scheme for the solution of the Riccati equations should be modified in a similar fashion as in the local coupled cluster theory [29]. The fock matrix in the basis of the POOs will be diagonalized by the matrix $\mathbf{X}$ obtained from the solution of the generalized eigenvalue problem:

$$\mathbf{f} \mathbf{X} = \mathbf{S} \mathbf{X} \boldsymbol{\epsilon}. \quad (51)$$

Note that the transformation $\mathbf{X}^\dagger \mathbf{f} \mathbf{X}$ does not brings us back to the canonical virtual orbitals. We can write the transformation by the orthogonal matrix $\mathbf{X}$ as $X^\dagger_{\bar{a} i_\alpha} f_{i_\alpha j_\beta} X_{j_\beta \bar{b}} = \delta_{\bar{a}\bar{b}} \varepsilon_{\bar{b}}$, where $\bar{a}$ and $\bar{b}$ are pseudo-canonical virtual orbitals that diagonalize the fock matrix expressed in POOs. The Riccati equations of Eq. 50 are transformed separately for each pair $[ij]$ in the basis of the pseudo-canonical virtual orbitals that diagonalize $\mathbf{f}_{\mathrm{POO}}$:

$$\mathbf{X}^\dagger \mathbf{R}^{ij} \mathbf{X} = \mathbf{X}^\dagger \mathbf{B}^{ij} \mathbf{X} + \left(\mathbf{X}^\dagger \mathbf{f} - f_{ii} \mathbf{X}^\dagger \mathbf{S} \right) \mathbf{T}^{ij} \mathbf{S} \mathbf{X} + \mathbf{X}^\dagger \mathbf{S} \mathbf{T}^{ij} (\mathbf{f} \mathbf{X} - \mathbf{S} \mathbf{X} f_{jj}) - \sum_{m \neq i} f_{im} \mathbf{X}^\dagger \mathbf{S} \mathbf{T}^{mj} \mathbf{S} \mathbf{X} - \sum_{m \neq j} \mathbf{X}^\dagger \mathbf{S} \mathbf{T}^{im} \mathbf{S} \mathbf{X} f_{mj} + \mathbf{X}^\dagger \mathbf{A}^{im} \mathbf{T}^{mj} \mathbf{S} \mathbf{X} + \mathbf{X}^\dagger \mathbf{S} \mathbf{T}^{im} \mathbf{A}^{mj} \mathbf{X} + \mathbf{X}^\dagger \mathbf{S} \mathbf{T}^{im} \mathbf{B}^{mn} \mathbf{T}^{nj} \mathbf{S} \mathbf{X} = \mathbf{0}, \quad (52)$$

which can be simplified by the application of the generalized eigenvalue equation Eq. 51 and the use of the relationships $\mathbf{I} = \mathbf{S}\mathbf{X}\mathbf{X}^\dagger = \mathbf{X}\mathbf{X}^\dagger\mathbf{S}$:

$$\overline{\mathbf{R}}^{ij} = \overline{\mathbf{B}}^{ij} + (\boldsymbol{\epsilon} - f_{ii} \mathbf{I}) \overline{\mathbf{T}}^{ij} + \overline{\mathbf{T}}^{ij} (\boldsymbol{\epsilon} - f_{jj} \mathbf{I}) - \sum_{m \neq i} f_{im} \overline{\mathbf{T}}^{mj} - \sum_{m \neq j} \overline{\mathbf{T}}^{im} f_{mj} + \overline{\mathbf{A}}^{im} \overline{\mathbf{T}}^{mj} + \overline{\mathbf{T}}^{im} \overline{\mathbf{A}}^{mj} + \overline{\mathbf{T}}^{im} \overline{\mathbf{B}}^{mn} \overline{\mathbf{T}}^{nj} = \mathbf{0}, \quad (53)$$

with the notations:

$$\overline{\mathbf{R}}^{ij} = \mathbf{X}^\dagger \mathbf{R}^{ij} \mathbf{X}$$
$$\overline{\mathbf{A}}^{ij} = \mathbf{X}^\dagger \mathbf{A}^{ij} \mathbf{X}$$
$$\overline{\mathbf{B}}^{ij} = \mathbf{X}^\dagger \mathbf{B}^{ij} \mathbf{X}$$
$$\overline{\mathbf{T}}^{ij} = \mathbf{X}^\dagger \mathbf{S}\, \mathbf{T}^{ij} \mathbf{S}\, \mathbf{X}.$$

The new Riccati equations of Eq. 53 can be solved by the iteration formula:

$$\overline{T}^{ij(n)}_{\bar{a}\bar{b}} = - \frac{\overline{B}^{ij}_{\bar{a}\bar{b}} + \Delta \overline{R}^{ij}_{\bar{a}\bar{b}} \left(\overline{\mathbf{T}}^{(n-1)} \right)}{\varepsilon_{\bar{a}} - f_{ii} + \varepsilon_{\bar{b}} - f_{jj}}, \quad (54)$$

where $\Delta \overline{\mathbf{R}}^{ij} (\overline{\mathbf{T}})$ is

$$\Delta \overline{\mathbf{R}}^{ij} (\overline{\mathbf{T}}) = - \sum_{m \neq i} f_{im} \overline{\mathbf{T}}^{mj} - \sum_{m \neq j} \overline{\mathbf{T}}^{im} f_{mj} + \overline{\mathbf{A}}^{im} \overline{\mathbf{T}}^{mj} + \overline{\mathbf{T}}^{im} \overline{\mathbf{A}}^{mj} + \overline{\mathbf{T}}^{im} \overline{\mathbf{B}}^{mn} \overline{\mathbf{T}}^{nj}. \quad (55)$$

As presented here, the update of the "non-diagonal" part of the residue is done in the pseudo-canonical basis. After

convergence, we could transform the amplitudes back to the original POO basis according to:

$$\begin{aligned}\mathbf{T}^{ij} &= \left(\mathbf{X}^{\dagger}\mathbf{S}\right)^{-1}\overline{\mathbf{T}}^{ij}(\mathbf{S}\mathbf{X})^{-1}\\ &= \mathbf{S}^{-1}\left(\mathbf{X}^{\dagger}\right)^{-1}\overline{\mathbf{T}}^{ij}\mathbf{X}^{-1}\mathbf{S}^{-1}\\ &= \mathbf{X}\mathbf{X}^{\dagger}\left(\mathbf{X}^{\dagger}\right)^{-1}\overline{\mathbf{T}}^{ij}\mathbf{X}^{-1}\mathbf{X}\mathbf{X}^{\dagger}\\ &= \mathbf{X}\overline{\mathbf{T}}^{ij}\mathbf{X}^{\dagger}.\end{aligned} \tag{56}$$

However, this back-transformation is not necessary since the correlation energy can be obtained directly in the pseudo-canonical basis, as:

$$\begin{aligned}\sum_{ij}^{\mathrm{occ}}\mathrm{tr}\left\{\overline{\mathbf{B}}^{ij}\overline{\mathbf{T}}^{ij}\right\} &= \sum_{ij}^{\mathrm{occ}}\mathrm{tr}\left\{\mathbf{X}^{\dagger}\mathbf{B}^{ij}\mathbf{X}\mathbf{X}^{\dagger}\mathbf{S}\mathbf{T}^{ij}\mathbf{S}\mathbf{X}\right\}\\ &= \sum_{ij}^{\mathrm{occ}}\mathrm{tr}\left\{\mathbf{B}^{ij}\mathbf{T}^{ij}\mathbf{S}\mathbf{X}\mathbf{X}^{\dagger}\right\} = \sum_{ij}^{\mathrm{occ}}\mathrm{tr}\left\{\mathbf{B}^{ij}\mathbf{T}^{ij}\right\}.\end{aligned} \tag{57}$$

Appendix 4: Riccati equations in the local excitation approximation

The local excitation approximation imposes that in the matrices $\mathbf{R}$, $\boldsymbol{\epsilon}$, $\mathbf{A}$ and $\mathbf{B}$, the excitations remain on the same localized orbitals. In this approximation the Riccati equations of Eq. 12, with explicit virtual indexes, read:

$$\begin{aligned}R^{ij}_{i_\alpha j_\beta} &= B^{ij}_{i_\alpha j_\beta} + (\epsilon + A)^{im}_{i_\alpha m_\gamma}T^{mj}_{m_\gamma p_\delta}S_{p_\delta j_\beta}\\ &+ S_{i_\alpha p_\gamma}T^{im}_{p_\gamma m_\delta}(\epsilon + A)^{mj}_{m_\delta j_\beta}\\ &+ S_{i_\alpha p_\gamma}T^{im}_{p_\gamma m_\delta}B^{mn}_{m_\delta n_\tau}T^{nj}_{n_\tau q_\zeta}S_{q_\zeta j_\beta} = 0.\end{aligned} \tag{58}$$

In this context, the terms containing the matrix $\boldsymbol{\epsilon}$ are (with explicit POO indexes):

$$\epsilon^{im}_{i_\alpha m_\gamma}T^{mj}_{m_\gamma p_\delta}S_{p_\delta j_\beta} = f_{i_\alpha i_\gamma}T^{ij}_{i_\gamma p_\delta}S_{p_\delta j_\beta} - f_{im}S_{i_\alpha m_\gamma}T^{mj}_{m_\gamma p_\delta}S_{p_\delta j_\beta} \tag{59}$$

$$S_{i_\alpha p_\gamma}T^{im}_{p_\gamma m_\delta}\epsilon^{mj}_{m_\delta j_\beta} = S_{i_\alpha p_\gamma}T^{ij}_{p_\gamma j_\delta}f_{j_\delta j_\beta} - S_{i_\alpha p_\gamma}T^{im}_{p_\gamma m_\delta}S_{m_\delta j_\beta}f_{mj}. \tag{60}$$

Inserting this in Eq. 58 and using the shorthand notation $R^{ij}_{i_\alpha j_\beta} \equiv R^{ij}_{\alpha\beta}$, $B^{ij}_{i_\alpha j_\beta} \equiv B^{ij}_{\alpha\beta}$, $f_{i_\alpha j_\beta} \equiv f^{ij}_{\alpha\beta}$ and $S_{i_\alpha j_\beta} \equiv S^{ij}_{\alpha\beta}$, (note the matrix elements $T^{ij}_{i_\gamma p_\delta}$ cannot yet be translated to the shorthand notation) one obtains:

$$\begin{aligned}R^{ij}_{\alpha\beta} &= B^{ij}_{\alpha\beta} + f^{ii}_{\alpha\gamma}T^{ij}_{i_\gamma p_\delta}S^{pj}_{\delta\beta} - f_{im}S^{im}_{\alpha\gamma}T^{mj}_{m_\gamma p_\delta}S^{pj}_{\delta\beta} + A^{im}_{\alpha\gamma}T^{mj}_{m_\gamma p_\delta}S^{pj}_{\delta\beta}\\ &+ S^{ip}_{\alpha\gamma}T^{ij}_{p_\gamma j_\delta}f^{jj}_{\delta\beta} - S^{ip}_{\alpha\gamma}T^{im}_{p_\gamma m_\delta}S^{mj}_{\delta\beta}f_{mj} + S^{ip}_{\alpha\gamma}T^{im}_{p_\gamma m_\delta}A^{mj}_{\delta\beta}\\ &+ S^{ip}_{\alpha\gamma}T^{im}_{p_\gamma m_\delta}B^{mn}_{\delta\tau}T^{nj}_{n_\tau q_\zeta}S^{qj}_{\zeta\beta} = 0.\end{aligned} \tag{61}$$

It is then a further approximation to tell that the POOs coming from different LMOs have a negligible overlap, i.e., that $S^{ij}_{\alpha\beta} = \delta_{ij}S^{ii}_{\alpha\beta}$. The Riccati equations become:

$$\begin{aligned}R^{ij}_{\alpha\beta} &= B^{ij}_{\alpha\beta} + f^{ii}_{\alpha\gamma}T^{ij}_{i_\gamma j_\delta}S^{jj}_{\delta\beta} - f_{ii}S^{ii}_{\alpha\gamma}T^{ij}_{i_\gamma j_\delta}S^{jj}_{\delta\beta} + A^{im}_{\alpha\gamma}T^{mj}_{m_\gamma j_\delta}S^{jj}_{\delta\beta}\\ &+ S^{ii}_{\alpha\gamma}T^{ij}_{i_\gamma j_\delta}f^{jj}_{\delta\beta} - S^{ii}_{\alpha\gamma}T^{ij}_{i_\gamma j_\delta}S^{jj}_{\delta\beta}f_{jj} + S^{ii}_{\alpha\gamma}T^{im}_{i_\gamma m_\delta}A^{mj}_{\delta\beta}\\ &+ S^{ii}_{\alpha\gamma}T^{im}_{i_\gamma m_\delta}B^{mn}_{\delta\tau}T^{nj}_{n_\tau j_\zeta}S^{jj}_{\zeta\beta} = 0,\end{aligned} \tag{62}$$

which, in turn, allows us to use the shorthand notation $T_{i_\alpha j_\beta} \equiv T^{ij}_{\alpha\beta}$ to arrive at:

$$\begin{aligned}\mathbf{R}^{ij} &= \mathbf{B}^{ij} + \mathbf{f}^{ii}\mathbf{T}^{ij}\mathbf{S}^{jj} - f_{ii}\mathbf{S}^{ii}\mathbf{T}^{ij}\mathbf{S}^{jj} + \mathbf{A}^{im}\mathbf{T}^{mj}\mathbf{S}^{jj}\\ &+ \mathbf{S}^{ii}\mathbf{T}^{ij}\mathbf{f}^{jj} - \mathbf{S}^{ii}\mathbf{T}^{ij}\mathbf{S}^{jj}f_{jj} + \mathbf{S}^{ii}\mathbf{T}^{im}\mathbf{A}^{mj}\\ &+ \mathbf{S}^{ii}\mathbf{T}^{im}\mathbf{B}^{mn}\mathbf{T}^{nj}\mathbf{S}^{jj} = 0,\end{aligned} \tag{63}$$

Appendix 5: Screened dipole interaction tensor

Any interaction $L(\mathbf{r})$ can be expanded in multipole series using a double Taylor expansion around appropriately selected centers, here $\mathbf{D}^i$ and $\mathbf{D}^j$, such that, with $\mathbf{r} = \mathbf{r}^i - \mathbf{r}^j = (\mathbf{r}^i - \mathbf{D}^i) + \mathbf{D}^{ij} - (\mathbf{r}^j - \mathbf{D}^j)$ where $\mathbf{D}^{ij} = \mathbf{D}^i - \mathbf{D}^j$:

$$\begin{aligned}L(\mathbf{r}) = L^{ij}\left(\mathbf{D}^{ij}\right) &+ \sum_\alpha\left(\hat{r}^i_\alpha - D^i_\alpha\right)L^{ij}_\alpha\left(\mathbf{D}^{ij}\right) + \sum_\alpha\left(\hat{r}^j_\alpha - D^j_\alpha\right)L^{ij}_\alpha\left(\mathbf{D}^{ij}\right)\\ &+ \sum_{\alpha\beta}\left(\hat{r}^i_\alpha - D^i_\alpha\right)\left(\hat{r}^j_\beta - D^j_\beta\right)L^{ij}_{\alpha\beta}\left(\mathbf{D}^{ij}\right) + \cdots,\end{aligned} \tag{64}$$

where the definitions of $L^{ij}_\alpha(\mathbf{D}^{ij})$, $L^{ij}_{\alpha\beta}(\mathbf{D}^{ij})$ are obvious. For example, in the case of the long-range interaction, $L(\mathbf{r})$ will be defined according to the RSH theory as:

$$L(\mathbf{r}) = \frac{\mathrm{erf}(\mu r)}{r}, \tag{65}$$

with $r = |\mathbf{r}|$.

The multipolar expansion of the long-range interaction leads to the following first and second-order interaction tensors:

$$L^{ij}_\alpha\left(\mathbf{D}^{ij}\right) = -\frac{D^{ij}_\alpha}{D^{ij3}}\left(1 - \frac{2}{\sqrt{\pi}}D^{ij}\mu\mathrm{e}^{-\mu^2D^{ij2}} - \mathrm{erf}\left(\mu D^{ij}\right)\right) \tag{66}$$

$$\begin{aligned}L^{ij}_{\alpha\beta}\left(\mathbf{D}^{ij}\right) &= \frac{3D^{ij}_\alpha D^{ij}_\beta}{D^{ij5}}\left(\mathrm{erf}\left(\mu D^{ij}\right) - \frac{2}{3\sqrt{\pi}}D^{ij}\mu\mathrm{e}^{-\mu^2D^{ij2}}\left(3 + 2D^{ij2}\mu^2\right)\right)\\ &- \frac{\delta_{\alpha\beta}D^{ij2}}{D^{ij5}}\left(\mathrm{erf}\left(\mu D^{ij}\right) - \frac{2}{\sqrt{\pi}}D^{ij}\mu\mathrm{e}^{-\mu^2D^{ij2}}\right).\end{aligned} \tag{67}$$

Remembering that the full-range Coulomb interaction tensor reads $T^{ij}_{\alpha\beta}(\mathbf{D}^{ij}) = 3D^{ij}_{\alpha}D^{ij}_{\beta} - \delta_{\alpha\beta}D^{ij^2})D^{ij^{-5}}$, the long-range interaction tensor can be written in an alternate form which clearly shows the damped dipole–dipole interaction contribution:

$$L^{ij}_{\alpha\beta}\left(\mathbf{D}^{ij}\right) = T^{ij}_{\alpha\beta}\left(\mathbf{D}^{ij}\right)\left(\mathrm{erf}\left(\mu D^{ij}\right) - \frac{2}{3\sqrt{\pi}}D^{ij}\mu \mathrm{e}^{-\mu^2 D^{ij^2}}\left(3 + 2D^{ij^2}\mu^2\right)\right) - \delta_{\alpha\beta}\mathrm{e}^{-\mu^2 D^{ij^2}}\frac{4\mu^3}{3\sqrt{\pi}}. \tag{68}$$

The trace of the tensor product (used for the spherically averaged C_6) then reads:

$$\sum_{\alpha\beta} L^{ij}_{\alpha\beta}L^{ij}_{\alpha\beta} = \frac{6}{D^{ij6}}\left(4\mathrm{e}^{-2D^{ij^2}\mu^2}D^{ij}\mu\left(\frac{D^{ij}\mu\left(3 + 4D^{ij^2}\mu^2 + 2D^{ij^4}\mu^4\right)}{3\pi} - \frac{\left(3 + 2D^{ij^2}\mu^2\right)\mathrm{erf}\left(D^{ij}\mu\right)}{3\sqrt{\pi}}\right) + \mathrm{erf}\left(D^{ij}\mu\right)^2\right) = \frac{6}{D^{ij6}}F^{\mu}_{\mathrm{damp}}\left(D^{ij}\right). \tag{69}$$

Appendix 6: Fock matrix element in POO basis

The occupied–occupied block of the fock matrix, f_{ij}, is known. The POOs are orthogonal to the occupied subspace of the original basis set, they satisfy the local Brillouin theorem, i.e., the occupied-virtual block is zero. As a result, in the local excitation approximation, we need only to deal with the fock matrix elements $f^{ii}_{\alpha\beta}$:

$$f^{ii}_{\alpha\beta} = \langle i_\alpha|\hat{f}|i_\beta\rangle = \langle i|\hat{r}_\alpha\hat{Q}\hat{f}\hat{Q}\hat{r}_\beta|i\rangle, \tag{70}$$

from which we directly derive the quantity $f^{i}_{[}$M] of Eq. 36:

$$f^{i}_{[\mathrm{M}]} = \sum_{\alpha} f^{ii}_{\alpha\alpha} = \sum_{ab}^{\mathrm{virt}}\langle i|\hat{r}_\alpha|a\rangle f_{ab}\langle b|\hat{r}_\alpha|i\rangle. \tag{71}$$

Since we would like to express everything in occupied orbitals, we expand the projector $\hat{Q}$ and use that the occupied-virtual block of the fock matrix is zero to obtain the following expression:

$$f^{ii}_{\alpha\beta} = \langle i|\,\hat{r}_\alpha\hat{f}\hat{r}_\beta|i\rangle - \sum_{mn}^{\mathrm{occ}}\langle i|\hat{r}_\alpha|m\rangle f_{mn}\langle n|\hat{r}_\beta|i\rangle. \tag{72}$$

In order to transform the triple operator product, $\hat{r}_\alpha\hat{f}\hat{r}_\beta$, let us consider the following double commutator:

$$\left[\hat{r}_\alpha, \left[\hat{r}_\beta,\hat{f}\right]\right] = -\delta_{\alpha\beta}. \tag{73}$$

Note that this holds provided that the fockian contains only local potential terms, which commute with the coordinate operator: see later for the more general case. In this special case, the double commutator can be written as

$$\left[\hat{r}_\alpha, \left[\hat{r}_\beta,\hat{f}\right]\right] = \hat{r}_\alpha\hat{r}_\beta\hat{f} - \hat{r}_\alpha\hat{f}\hat{r}_\beta - \hat{r}_\beta\hat{f}\hat{r}_\alpha + \hat{f}\hat{r}_\beta\hat{r}_\alpha = -\delta_{\alpha\beta} \tag{74}$$

which allows us to express the two triple products:

$$\hat{r}_\alpha\hat{f}\hat{r}_\beta + \hat{r}_\beta\hat{f}\hat{r}_\alpha = \delta_{\alpha\beta} + \hat{r}_\alpha\hat{r}_\beta\hat{f} + \hat{f}\hat{r}_\beta\hat{r}_\alpha. \tag{75}$$

The diagonal matrix element of the triple operator product is then:

$$\langle i|\hat{r}_\alpha\hat{f}\hat{r}_\beta|i\rangle = \tfrac{1}{2}\delta_{\alpha\beta} + \tfrac{1}{2}\left(\langle i|\hat{r}_\alpha\hat{r}_\beta\hat{f}|i\rangle + \langle i|\hat{f}\hat{r}_\beta\hat{r}_\alpha|i\rangle\right) \tag{76}$$

Since the localized orbitals satisfy local Brillouin theorem, we finally obtain for the matrix elements of the fock operator with multiplicative potential (typically Kohn-Sham operator with local or semi-local functionals) between two oscillator orbitals:

$$f^{ii}_{\alpha\beta} = \tfrac{1}{2}\delta_{\alpha\beta} + \tfrac{1}{2}\sum_{m}^{\mathrm{occ}}\left(\langle i\,|\hat{r}_\alpha\hat{r}_\beta|m\rangle f_{mi} + f_{im}\langle m|\hat{r}_\alpha\hat{r}_\beta|i\rangle\right) - \sum_{mn}^{\mathrm{occ}}\langle i\,|\hat{r}_\alpha|m\rangle f_{mn}\langle n|\hat{r}_\beta|i\rangle. \tag{77}$$

From this, we obtain the quantity $f^{i}_{[\mathrm{O}]}$ of Eq. 38:

$$f^{i}_{[\mathrm{O}]} = \sum_{\alpha} f^{ii}_{\alpha\alpha} = \tfrac{3}{2} + \tfrac{1}{2}\sum_{m}^{\mathrm{occ}}\left(\langle i\,|\hat{\mathbf{r}}^2|m\rangle f_{mi} + f_{im}\langle m|\hat{\mathbf{r}}^2|i\rangle\right) - \sum_{mn}^{\mathrm{occ}}\sum_{\alpha}\langle i\,|\hat{r}_\alpha|m\rangle f_{mn}\langle n|\hat{r}_\alpha|i\rangle. \tag{78}$$

In the more general case, i.e., when the fockian contains a nonlocal exchange operator, like in hybrid DFT and in Hartree–Fock calculations, the relation seen Eq. 73 does not hold any more and the commutator of the position operator with the fockian contains an exchange contribution [76, 77], which gives rise to an additional term:

$$\left\langle i\left|\left[\hat{r}_\alpha, \left[\hat{r}_\beta, \hat{K}\right]\right]\right|i\right\rangle = \sum_{m}^{\mathrm{occ}}\left\langle im\right|(\hat{r}_\alpha - \hat{r}'_\alpha)w(\mathbf{r},\mathbf{r}')\left(\hat{r}_\beta - \hat{r}'_\beta\right)\left|mi\right\rangle, \tag{79}$$

where the nonlocal exchange operator is defined as

$$\hat{K} = \sum_{m}^{\mathrm{occ}}\int \mathrm{d}\mathbf{r}'\phi^{\dagger}_m(\mathbf{r}')w(\mathbf{r},\mathbf{r}')\hat{P}_{\mathbf{r}\mathbf{r}'}\phi_m(\mathbf{r}'), \tag{80}$$

where $\hat{P}_{\mathbf{r}\mathbf{r}'}$ is the permutation operator that changes the coordinates $\mathbf{r}'$ appearing after $\hat{K}$ to $\mathbf{r}$, and we recall that $w(\mathbf{r},\mathbf{r}')$ is the two-electron interaction. Hence, the diagonal blocks of the POO fockian in the general case can be written as:

$$\langle i_\alpha|\hat{f}|i_\beta\rangle = \tfrac{1}{2}\delta_{\alpha\beta} - \tfrac{1}{2}\sum_{m}^{\text{occ}}\langle im|\left(\hat{r}_\alpha - \hat{r}'_\alpha\right)w\left(\mathbf{r},\mathbf{r}'\right)\left(\hat{r}_\beta - \hat{r}'_\beta\right)|mi\rangle + \tfrac{1}{2}\sum_{m}^{\text{occ}}\left(\langle i|\hat{r}_\alpha\hat{r}_\beta|m\rangle f_{mi} + f_{im}\langle m|\hat{r}_\alpha\hat{r}_\beta|i\rangle\right) - \sum_{mn}^{\text{occ}}\langle i|\hat{r}_\alpha|m\rangle f_{mn}\langle n|\hat{r}_\beta|i\rangle. \quad (81)$$

In the present work, the exchange contribution, which is present only in the case of Hartree–Fock or hybrid density functional fockians and which would give rise to non-conventional two-electron integrals, is not treated explicitly. Possible approximate solutions for this problem will be discussed in forthcoming works. Although we do not use the elements of the off-diagonal ($i \neq j$) blocks of the POO fock operator, for the sake of completeness we give its expression:

$$\langle i_\alpha|\hat{f}|j_\beta\rangle = -\langle i\,|\hat{r}_\alpha\hat{\nabla}_\beta|j\rangle + \sum_{m}^{\text{occ}}\langle im|\hat{r}_\alpha w\left(\mathbf{r},\mathbf{r}'\right)\left(\hat{r}_\beta - \hat{r}'_\beta\right)|mj\rangle + \sum_{m}^{\text{occ}}\langle i\,|\hat{r}_\alpha\hat{r}_\beta|m\rangle\, f_{mi} - \sum_{mn}^{\text{occ}}\langle i\,|\hat{r}_\alpha|m\rangle\, f_{mn}\langle n|\hat{r}_\beta|i\rangle. \quad (82)$$

To derive this, instead of the double commutator of Eq. 73, one needs to consider the product of the commutator with a coordinate operator

$$\hat{r}_\alpha\left[\hat{r}_\beta,\hat{f}\right] = \hat{r}_\alpha\left[\hat{r}_\beta,\hat{T}\right] - \hat{r}_\alpha\left[\hat{r}_\beta,\hat{K}\right], \quad (83)$$

where $\hat{T}$ is the kinetic energy operator, and $[\hat{r}_\beta,\hat{T}] = \hat{\nabla}_\beta$.

References

1. Perdew JP, Schmidt K (2001) In: van Doren V, van Alsenoy K, Geerlings P (eds) AIP conference proceedings (AIP), pp 1–20
2. Eichkorn K, Treutler O, Ohm H, Haser M, Ahlrichs R (1995) Chem Phys Lett 240:283
3. Whitten JL (1973) J Chem Phys 58:4496
4. Roeggen I, Johansen T (2008) J Chem Phys 128:194107
5. Beebe NHF, Linderberg J (1977) Int J Quantum Chem 12:683
6. Harl J, Kresse G (2008) Phys Rev B 77:045136
7. Nguyen H-V, de Gironcoli S (2009) Phys Rev B 79:205114
8. Wilson HF, Lu D, Gygi F, Galli G (2009) Phys Rev B 79:245106
9. Wilson HF, Gygi F, Galli G (2008) Phys Rev B 78:113303
10. Rocca D (2014) J Chem Phys 140:18A501
11. Surján PR (2005) Chem Phys Lett 406:318
12. Johnson ER, Becke AD (2005) J Chem Phys 123:024101
13. Johnson ER, Mackie ID, DiLabio GA (2009) J Phys Org Chem 22:1127
14. Grimme S, Antony J, Ehrlich S, Krieg H (2010) J Chem Phys 132:154104
15. Grimme S (2011) Wires Comput Mol Sci 1:211
16. Tkatchenko A, Scheffler M (2009) Phys Rev Lett 102:073005
17. DiStasio RA Jr, Gobre VV, Tkatchenko A (2014) J Phys Condens Matter 26:213202
18. Reilly AM, Tkatchenko A (2015) Chem Sci 6:3289
19. Surján PR (1989) In: Maksic ZB (ed) Theoretical models of chemical bonding, vol 2. Springer, Heidelberg, pp 205–256
20. Høyvik I-M, Jansík B, Jørgensen P (2012) J Chem Phys 137:224114
21. Pulay P (1983) Chem Phys Lett 100:151
22. Pulay P, Saebø S (1986) Theor Chim Acta 69:357
23. Boughton JW, Pulay P (1993) J Comput Chem 14:736
24. Foster JM, Boys SF (1960a) Rev Mod Phys 32:300
25. Foster JM, Boys SF (1960b) Rev Mod Phys 32:303
26. Boys SF (1966) In: Löwdin PO (ed) Quantum theory of atoms, molecules, and the solid state, a tribute to John C. Slater. Academic Press, New York, pp 253–262
27. Alagona G, Tomasi J (1972) Theor Chem Acc 24:42
28. Santolini V, Malhado JP, Robb MA, Garavelli M, Bearpark MJ (2015) Mol Phys 113:1978
29. Knowles PJ, Schütz M, Werner H-J (2000) In: Grotendorst J (ed) Modern methods and algorithms of quantum chemistry, vol 3. John von Neumann Institute for Computing, NIC Series, Jülich, pp 97–179
30. Kirkwood JG (1932) Phys Z 33:57
31. Pople JA, Schofield P (1957) Philos Mag 2:591
32. Karplus M, Kolker HJ (1963a) J Chem Phys 39:1493
33. Karplus M, Kolker HJ (1963b) J Chem Phys 39:2997
34. Rivail J-L, Cartier A (1978) Mol Phys 36:1085
35. Rivail J-L, Cartier A (1979) Chem Phys Lett 61:469
36. Sadlej AJ, Jaszunski M (1971) Mol Phys 22:761
37. Toulouse J, Gerber IC, Jansen G, Savin A, Ángyán JG (2009) Phys Rev Lett 102:096404
38. Zhu W, Toulouse J, Savin A, Ángyán JG (2010) J Chem Phys 132:244108
39. Toulouse J, Zhu W, Savin A, Jansen G, Ángyán JG (2011) J Chem Phys 135:084119
40. Ángyán JG, Liu R-F, Toulouse J, Jansen G (2011) J Chem Theory Comput 7:3116
41. Kapuy E, Kozmutza C (1991) J Chem Phys 94:5565
42. Saebø S, Tong W, Pulay P (1993) J Chem Phys 98:2170
43. Hetzer G, Pulay P, Werner H-J (1998) Chem Phys Lett 290:143
44. Usvyat D, Maschio L, Manby FR, Casassa S, Schütz M, Pisani C (2007) Phys Rev B 76:075102
45. Chermak E, Mussard B, Ángyán JG, Reinhardt P (2012) Chem Phys Lett 550:162
46. Silvestrelli PL (2009) J Phys Chem A 113:5224
47. Silvestrelli PL, Benyahia K, Grubisic S, Ancilotto F, Toigo F (2009) J Chem Phys 130:074702
48. Ambrosetti A, Silvestrelli PL (2012) Phys Rev B 85:073101
49. Silvestrelli PL (2013) J Chem Phys 139:054106
50. Silvestrelli PL, Ambrosetti A (2014) J Chem Phys 140:124107
51. Claverie P, Rein R (1969) Int J Quantum Chem 3:537
52. Claverie P (1978) In: Pullman B (ed) Intermolecular interactions: from diatomics to biopolymers, vol 1, chap. 2. Wiley, New York, pp 69–305
53. Alcoba DR, Lain L, Torre A, Bochicchio RC (2006) J Comput Chem 27:596
54. Pipek J, Mezey PG (1989) J Chem Phys 90:4916
55. Resta R (2006) J Chem Phys 124:104104
56. Ángyán JG, Gerber IC, Savin A, Toulouse J (2005) Phys Rev A 72:012510
57. Werner H-J, Knowles PJ, Knizia G, Manby FR, Schütz M (2012) WIREs Comput Mol Sci 2:242–253. doi:10.1002/wcms.82
58. Toulouse J, Rebolini E, Gould T, Dobson JF, Seal P, Ángyán JG (2013) J Chem Phys 138:194106
59. Zeiss GD, Meath WJ, MacDonald J, Dawson DJ (1977) Can J Phys 55:2080

60. Margoliash DJ, Meath WJ (1978) J Chem Phys 68:1426
61. Kumar A, Meath WJ (2008) Mol Phys 106:1531
62. Kumar A, Jhanwar B, Meath W (2007) Can J Chem 85:724
63. Kumar A, Jhanwar B, Meath WJ (2005) Coll Czech Chem Commun 70:1196
64. Kumar A, Meath WJ (2004) J Comput Methods Sci Eng 4:307
65. Kumar A, Kumar M, Meath WJ (2003) Chem Phys 286:227
66. Kumar M, Kumar A, Meath WJ (2002) Mol Phys 100:3271
67. Kumar A, Meath WJ (1994) Chem Phys 189:467
68. Kumar A, Meath WJ (1992) Mol Phys 75:311
69. Meath WJ, Kumar A (1990) Int J Quantum Chem Symp 24:501
70. Kumar A, Fairley GRG, Meath WJ (1985) J Chem Phys 83:70
71. Kumar A, Meath WJ (1984) Chem Phys 91:411
72. Tkatchenko A, Ambrosetti A, DiStasio RA Jr (2013) J Chem Phys 138:074106
73. Ambrosetti A, Reilly AM, DiStasio RA Jr, Tkatchenko A (2014) J Chem Phys 140:18A508
74. Marzari N, Vanderbilt D (1997) Phys Rev B 56:12847
75. Marzari N, Mostofi AA, Yates JR, Souza I, Vanderbilt D (2012) Rev Mod Phys 84:1419
76. Starace AF (1971) Phys Rev A 3:1242
77. Harris RA (1969) J Chem Phys 50:3947

Theor Chem Acc (2015) 134:85
DOI 10.1007/s00214-015-1688-5

REGULAR ARTICLE

A study of the compactness of wave functions based on Shannon entropy indices: a seniority number approach

Luis Lain[1] · Alicia Torre[1] · Diego R. Alcoba[2,3] · Ofelia B. Oña[4] · Gustavo E. Massaccesi[5]

Received: 16 April 2015 / Accepted: 16 June 2015 / Published online: 4 July 2015

Abstract This work reports the formulation of Shannon entropy indices in terms of seniority numbers of the Slater determinants expanding an *N*-electron wave function. Numerical determinations of those indices prove that they provide a suitable quantitative procedure to evaluate compactness of wave functions and to describe their configurational structures. An analysis of the results, calculated for full configuration interaction wave functions in selected atomic and molecular systems, allows one to compare and to discuss the behavior of several types of molecular orbital basis sets in order to achieve more compact wave function expansions, and to study their multiconfigurational character.

Keywords Compactness of wave functions · Seniority number · Shannon entropy indices · Optimization of molecular orbital basis sets

Dedicated to Prof. P. R. Surjan on occasion of his 60th birthday.

Published as part of the special collection of articles "Festschrift in honour of P. R. Surjan."

✉ Luis Lain
qfplapel@lg.ehu.es

[1] Departamento de Química Física, Facultad de Ciencia y Tecnología, Universidad del País Vasco, Apdo. 644, 48080 Bilbao, Spain

[2] Departamento de Física, Facultad de Ciencias Exactas y Naturales, Universidad de Buenos Aires, Ciudad Universitaria, 1428 Buenos Aires, Argentina

[3] Instituto de Física de Buenos Aires, Consejo Nacional de Investigaciones Científicas y Técnicas, Ciudad Universitaria, 1428 Buenos Aires, Argentina

[4] Instituto de Investigaciones Fisicoquímicas Teóricas y Aplicadas, Universidad Nacional de la Plata, CCT La Plata, Consejo Nacional de Investigaciones Científicas y Técnicas, Diag. 113 y 64 (s/n), Sucursal 4, CC 16, 1900 La Plata, Argentina

[5] Departamento de Ciencias Exactas, Ciclo Básico Común, Universidad de Buenos Aires, Ciudad Universitaria, 1428 Buenos Aires, Argentina

1 Introduction

The configuration interaction (CI) methods have played an important role in describing *N*-electron systems, since they demand a lower computational cost than that required for determining the full configuration interaction (FCI) expansions which provide the exact descriptions for a given Hilbert space. Consequently, there has been a considerable interest in formulating *N*-electron wave functions in terms of CI expansions providing a rapid convergence to the FCI ones [1–4]. Traditionally, the CI wave functions have been expanded by means of *N*-electron Slater determinants selected according to their excitation degrees with respect to a given reference determinant. However, more recently, another selection criterion has also been proposed. This criterion is based on the seniority number of the Slater determinants used to construct the CI expansions [5–11]. Results arising from both excitation- and seniority number-based CI schemes show that the seniority number-based selection procedure is particularly suitable to describe systems exhibiting strong (static) correlation [5], what has increased the interest on this approach [9–11]. As is well known, the seniority number of a Slater determinant is defined as the number of singly occupied orbitals which possesses that determinant [12, 13]. The seniority number concept has been extended in Refs. [6, 9] to *N*-electron wave functions which describe electronic states of atomic and molecular systems,

as well as to N-electron spin-adapted Hilbert spaces. The expectation value of the seniority number operator with respect to an N-electron wave function is a weighted sum of the seniority numbers of all determinants involved in the expansion of that wave function. The weights that determine those expectation values depend on the molecular orbital basis set used to express the wave function, and consequently, this feature has been utilized to evaluate the compactness of the FCI and CI expansions in several molecular basis sets. Likewise, the seniority number value with respect to a wave function allows one to analyze the multiconfigurational character of the N-electron expansion, which is useful to describe the static and dynamic correlation of a determined state [14–17].

On the other hand, in Ref. [18], the extent of the multiconfigurational character of an N-electron wave function was evaluated by means of numerical determinations of an index set formulated within the Shannon information entropy approach [19–21]. This treatment provides a suitable information concerning the distribution of the wave function among different configurations characterized by the excitation degree of the Slater determinants. The aim of this work is to extend this methodology to the seniority-based CI scheme and to report the corresponding Shannon index numerical values in terms of the contributions of Slater determinants classified according to the seniority number criterion. More recently, in Ref. [6], we have proposed unitary transformations which lead to the construction of basis sets of molecular orbitals in which the expectation values of the seniority number operator with respect to N-electron wave functions reach minimum values. The results found using this type of molecular orbitals show that the wave function expansions present a more rapid convergence than those arising from the use of other molecular orbitals [9, 11]. Another aim of this work is to evaluate and compare quantitatively, by means of the proposed Shannon entropy indices, the compactness of wave functions expressed in canonical molecular orbital (CMO) basis sets, natural orbitals (NO), and those mentioned orbitals $M_{\min}$, which minimize the expectation value of the seniority number operator.

This article has been organized as follows. Section 2 summarizes the notation and formulation of the main concepts used in this work; it also reports the formulation of the Shannon entropy indices in terms of the seniority numbers of the Slater determinants. In Sect. 3, we present numerical values of those indices for wave functions of selected atomic and molecular systems; these values allow one to characterize the compactness of the wave function expansions. The calculation level and the computational details are also indicated in this section. An analysis and discussion of these results are reported in Sect. 4. Finally, in the last section, we highlight the main conclusions and perspectives of this work.

2 Theoretical framework

The K orbitals of an orthonormal basis set will be denoted by $i,j,k,l,\ldots$ and their corresponding spin-orbitals by $i^{\sigma}, j^{\sigma'}, \ldots$ (σ and σ' mean the spin coordinates α or β). The spin-free version of the N-electron seniority number operator $\hat{\Omega}$ has been formulated as [6, 9, 11]

$$\hat{\Omega} = \sum_{i=1}^{K} \left(\hat{E}_i^i - \hat{E}_{ii}^{ii} \right) \tag{1}$$

where $\hat{E}_i^i = \sum_{\sigma} a_{i^\sigma}^{\dagger} a_{i^\sigma}$ and $\hat{E}_{ii}^{ii} = \sum_{\sigma,\sigma'} a_{i^\sigma}^{\dagger} a_{i^{\sigma'}}^{\dagger} a_{i^{\sigma'}} a_{i^\sigma}$ are the spin-free first- and second-order replacement operators, respectively [22–25] and $a_{i^\sigma}^{\dagger}$ and a_{i^σ} are the usual creation and annihilation fermion operators [26].

Closing both sides of Eq. (1) by an N-electron Slater determinant Λ of S_z spin projection quantum number, one obtains

$$\Omega = \langle \Lambda | \hat{\Omega} | \Lambda \rangle \tag{2}$$

where, according to Eq. (1), the expectation value Ω is the difference $\sum_i \langle E_i^i \rangle - \sum_i \langle E_{ii}^{ii} \rangle$, which is the number of total electrons N minus the number of electrons corresponding to doubly occupied orbitals. The possible values for the Ω parameter are positive integers belonging to the sequence $\Omega = 2|S_z|, 2(|S_z|+1), \ldots, \Omega_{\max}$ (where $\Omega_{\max} = N$ if $K \geq N$ and $\Omega_{\max} = 2K - N$ if $K < N$); their meaning is the number of non-repeated orbitals in each determinant. That Ω parameter allows one to classify the Slater determinants Λ of S_z quantum number, according to the corresponding seniority level, and they will be denoted hereafter by $\Lambda(\Omega)$. Consequently, a FCI N-electron wave function with given spin quantum numbers S and S_z will be expressed by

$$|\Psi(N,S,S_z)> = \sum_{\Omega=2S}^{\Omega_{\max}} \sum_{\Lambda(\Omega)} C_{\Lambda(\Omega)} |\Lambda(\Omega)> \tag{3}$$

where $C_{\Lambda(\Omega)}$ stands for the coefficient corresponding to the Slater determinant $\Lambda(\Omega)$. Obviously, since there is no contribution of Slater determinants with $\Omega < 2S$ to spin-adapted N-electron wave functions ($\langle \Lambda(\Omega < 2S) | \Psi(N,S,S_z) \rangle = 0$), the lowest integer in the sum $\sum_{\Omega}$ is $2S$. If we truncate the series $\sum_{\Omega}$ in Eq. (3), we obtain CI(Ω) wave function expansions involving only Slater determinants belonging to the selected Ω levels.

According to Eqs. (1) and (3), the expectation value of the operator $\hat{\Omega}$ with respect to the FCI wave function $\Psi(N,S,S_z)$ is [6]

$$\langle \hat{\Omega} \rangle_{\Psi(N,S)} = N - \sum_{\Omega=2S}^{\Omega_{\max}} \sum_{\Lambda(\Omega)} \left| C_{\Lambda(\Omega)} \right|^2 \sum_{i}^{K} \langle \Lambda(\Omega) \left| \hat{E}_{ii}^{ii} \right| \Lambda(\Omega) \rangle \tag{4}$$

which is a spin-free quantity, independent of the S_z value, and consequently, we have dropped that quantum number. The coefficients $C_{\Lambda(\Omega)}$ and the $\langle\hat{\Omega}\rangle_{\Psi(N,S)}$ values are strongly dependent on the molecular orbital set utilized to formulate the Slater determinants $\Lambda(\Omega)$ in the expansion of the wave function expressed by Eq. (3). As mentioned in the Introduction, in Refs. [6, 9, 11], we have performed unitary transformations of the molecular orbitals, based on iterative procedures [27], which lead to the minimization of the $\langle\hat{\Omega}\rangle_{\Psi(N,S)}$ values; the resulting molecular orbital basis sets have been denominated $M_{\min}$. That minimization requires the search of molecular orbitals leading to high values for the coefficients $|C_{\Lambda(\Omega)}|$ corresponding to the determinants which possess greater doubly occupied orbital numbers, i.e., those providing higher values of the $\sum_i^K \langle\Lambda(\Omega)|\hat{E}_{ii}^{ii}|\Lambda(\Omega)\rangle$ quantities. Our results [6, 9, 11] have proven that the expansions for ground-state wave functions of atomic and molecular systems expressed in the molecular orbital basis sets $M_{\min}$ turn out to be more compact than those arising from the canonical molecular orbitals (CMO) or natural orbitals (NO).

Quantitative measures of the compactness of an N-electron wave function have been reported in Ref. [18] by means of the informational content (I_C (or Shannon entropy) within the traditional CI expansion method based on Slater determinants classified according to the excitation level with respect to a given reference determinant. Assuming that the N-electron wave function is normalized to unity ($\sum_\Omega \sum_{\Lambda(\Omega)} |C_{\Lambda(\Omega)}|^2 = 1$), the counterpart formulation of that index for the seniority-based CI approach is

$$I_C = -\sum_{\Omega} \sum_{\Lambda(\Omega)} \left|C_{\Lambda(\Omega)}\right|^2 \log_2 \left|C_{\Lambda(\Omega)}\right|^2, \quad C_{\Lambda(\Omega)} \neq 0 \tag{5}$$

in which the index Ω runs over all the values defining the chosen CI (Ω) expansion seniority levels. According to Eq. (5), the I_C index accounts for the wave function configurational distribution, having a minimum value in case of a single-determinant wave function.

The values of this I_C index quantify the multiconfigurational character of the CI wave function but do not report any detailed information on the contributions corresponding to different seniority subspaces. For CI (Ω) expansions involving several values of the Ω index, we can define a weight W_Ω which groups the contributions of all the Slater determinants with given seniority number Ω in that expansion

$$W_\Omega = \sum_{\Lambda(\Omega)} \left|C_{\Lambda(\Omega)}\right|^2 \tag{6}$$

These weights provide the definition of the cumulative index I_W, which in the seniority number approach is

$$I_W = -\sum_{\Omega} W_\Omega \log_2 W_\Omega, \quad W_\Omega \neq 0 \tag{7}$$

which evaluates that entropic quantity in terms of the weights corresponding to the seniority numbers Ω, providing a measure of the distribution of the wave function on different seniority subspaces.

One can also consider the distribution of each Ω subspace in terms of its corresponding Slater determinants and calculate its specific entropic index, which can be evaluated by means of the relationship

$$I_\Omega = -\sum_{\Lambda(\Omega)} \frac{\left|C_{\Lambda(\Omega)}\right|^2}{W_\Omega} \log_2 \frac{\left|C_{\Lambda(\Omega)}\right|^2}{W_\Omega}, \quad C_{\Lambda(\Omega)} \neq 0 \tag{8}$$

where the denominators W_Ω have been introduced for normalization requirements. Formula (8) accounts for the configuration distribution within a determined seniority number level.

As mentioned above, the multiconfigurational character of an N-electron wave function expanded in terms of Slater determinants allows one to distinguish between systems exhibiting static (strong) correlation (in which a suitable zeroth-order description requires several Slater determinants) and those possessing dynamic correlation (in which a single Slater determinant is a good zeroth-order wave function). In the next sections, we report numerical values of the I_C and I_W indices in selected atomic and molecular systems, in order to assess the ability of these devices to describe quantitatively both types of electronic correlation within the seniority number approach. Likewise, we present values of the I_Ω index which show the influence of the bond stretching on the configurational distribution within the seniority number subspaces. As these Shannon entropy indices and the seniority number quantity for a determined wave function are not invariant under a unitary single-particle transformation, it is possible to perform molecular basis set unitary transformations and to compare values of these entropic indices according to the different molecular basis sets utilized. In particular, we compare values of Shannon indices arising from the molecular basis sets $M_{\min}$ (in which the seniority number achieves their minimum values) with those provided by the CMO and NO sets.

3 Results

We have determined expansions of wave functions of several atomic and molecular systems in their ground states, at FCI level. These wave functions have been expressed in the three mentioned molecular basis sets CMO, NO, and $M_{\min}$, in order to study their compactness in different molecular orbital basis sets. Our aim is to analyze the structure and compactness of those expansions by means of the entropic indices proposed in Eqs. (5), (7), and (8) according to the seniority numbers. We have mainly chosen the systems of

Table 1 Calculated values of the I_C and I_W quantities (Eqs. (5) and (7)) for the ground states of atomic and molecular systems described by FCI expansions expressed in the canonical molecular orbitals (CMO), in the orbitals which minimize the seniority number $M_{\min}$ and in the natural orbitals (NO)

System	I_C			I_W		
	CMO	$M_{\min}$	NO	CMO	$M_{\min}$	NO
Be(STO-3G)	0.649	0.648	0.648	0.001	0.000	0.000
Be(cc-pVDZ)	0.737	0.602	0.602	0.181	0.001	0.001
Mg(6-31G)	0.648	0.521	0.522	0.184	0.007	0.007
LiH(R_e)	0.231	0.167	0.167	0.081	0.001	0.001
LiH(R_{st})	1.709	0.864	0.864	0.678	0.002	0.002
BeH^+(R_e)	0.222	0.164	0.164	0.073	0.001	0.001
BeH^+(R_{st})	1.767	0.990	0.990	0.733	0.001	0.001
Li_2(R_e)	0.664	0.598	0.598	0.078	0.003	0.003
Li_2(R_{st})	1.103	0.854	0.854	0.235	0.003	0.003
BH(R_e)	0.681	0.552	0.556	0.169	0.009	0.015
BH(R_{st})	0.979	0.802	1.005	0.224	0.026	0.028
BH_2^+(R_e)	0.301	0.299	0.298	0.074	0.064	0.071
BH_2^+(R_{st})	2.041	1.682	1.684	0.597	0.302	0.307
BeH_2(R_e)	0.282	0.265	0.278	0.080	0.049	0.077
BeH_2(R_{st})	2.695	1.883	1.892	0.875	0.275	0.293

Equilibrium distances (R_e) at experimental or optimized bond lengths and symmetrically stretched ones (R_{st}) at $R_{st} = 2.002\,R_e$ (for LiH), $R_{st} = 2.676\,R_e$ (for BeH^+), $R_{st} = 1.599\,R_e$ (for Li_2), $R_{st} = 1.487\,R_e$ (for BH), $R_{st} = 1.826\,R_e$ (for BH_2^+), $R_{st} = 2.066\,R_e$ (for BeH_2). Results for molecules correspond to standard STO-3G basis sets

four- and six-electron Be, LiH, BeH^+, Li_2, BH, BH_2^+, and BeH_2 and the basis sets STO-3G, in order to face up to an affordable computational cost. Moreover, we also report results corresponding to the Be atom in the cc-pVDZ basis set and the Mg one in the 6-31G basis sets, which are prototype examples of strongly correlated systems due to the near-degeneracies between it s and p shells. The molecular systems have been studied at equilibrium distances (R_e) and at stretched ones (R_{st}). The experimental geometrical distances have been used for the neutral species LiH, Li_2, BH, and BeH_2 [28]; in the molecular ion BeH^+, we have used the internuclear distance reported in Refs. [29] and [30], while in the system BH_2^+, the geometry was optimized with the GAUSSIAN package [31] at single and double excitations. The one- and two-electron integrals and the Hartree–Fock canonical molecular orbitals basis sets required for our calculations have been obtained from a modified version of the PSI 3.3 code [32]. We have constructed our own codes to determine the ground-state FCI wave functions for these systems expressed in the basis sets of CMO and NO; the orbitals minimizing the seniority number for a given wave function have been obtained from an iterative procedure reported in Ref. [27], using the CMO sets as initial bases of that iteration. The results found for the I_C and I_W quantities in those systems are gathered in Table 1, while Table 2 collects the I_Ω index values of each seniority number level in the corresponding wave function expansion.

4 Discussion

The numerical results reported in Tables 1 and 2 have been obtained from the FCI method which coincides with the CI ($\Omega = 0, 2, 4$) one, in the CI framework, for the 4-electron systems (Be, LiH, and BeH^+). Likewise, for the case of the 6-electron systems (Li_2, BH, BH_2^+, and BeH_2), the FCI and the CI($\Omega = 0, 2, 4, 6$) methods are identical. A survey of the results included in Table 1 shows that all described systems present low values for the I_W index, mainly at equilibrium geometries as well as at stretched ones in the NO and $M_{\min}$ molecular basis sets. It means that most of the Slater determinants involved in expansion (3) can be grouped into a weight W_Ω, constituting a narrow Ω-level distribution. In fact, the weights corresponding to $\Omega = 0$ for these closed-shell singlet ground states are close to unity ($W_{(\Omega=0)} \sim 1$) [6]. Consequently, the determinants $\Lambda(\Omega = 0)$ are quite dominant in those expansions, while the others $\Lambda(\Omega \neq 0)$ can be neglected. The CI ($\Omega = 0$) method has also been called doubly occupied configuration interaction (DOCI) [33], since their N-electron wave functions are expanded on all possible $\Lambda(\Omega = 0)$ determinants.

Table 2 Calculated values of the quantities I_Ω (Eq. 8) for the ground states of atomic and molecular systems described by FCI expansions expressed in the canonical molecular orbitals (CMO), in the orbitals which minimize the seniority number ($M_{\min}$) and in the natural orbitals (NO)

System	CMO				$M_{\min}$				NO			
	$I_{\Omega=0}$	$I_{\Omega=2}$	$I_{\Omega=4}$	$I_{\Omega=6}$	$I_{\Omega=0}$	$I_{\Omega=2}$	$I_{\Omega=4}$	$I_{\Omega=6}$	$I_{\Omega=0}$	$I_{\Omega=2}$	$I_{\Omega=4}$	$I_{\Omega=6}$
Be(STO-3G)	0.648	2.585	0.522	–	0.648	2.115	2.008	–	0.648	2.837	2.000	–
Be(cc-pVDZ)	0.493	2.772	4.794	–	0.601	4.517	4.634	–	0.601	4.503	4.633	–
Mg(6-31G)	0.399	2.710	6.400	8.462	0.511	3.807	6.843	8.110	0.511	4.982	7.134	8.430
LiH(R_e)	0.132	1.944	2.194	–	0.166	3.120	2.018	–	0.166	3.155	2.017	–
LiH(R_{st})	0.807	2.063	2.207	–	0.862	3.604	2.234	–	0.862	3.608	2.234	–
BeH^+(R_e)	0.132	1.956	2.124	–	0.163	3.405	2.007	–	0.163	3.414	2.007	–
BeH^+(R_{st})	0.986	1.221	2.210	–	0.989	3.596	2.181	–	0.989	3.603	2.181	–
Li_2(R_e)	0.572	2.109	5.328	5.059	0.594	4.262	5.091	5.664	0.594	4.249	5.098	5.663
Li_2(R_{st})	0.822	2.033	5.261	5.027	0.849	4.633	5.080	6.347	0.849	4.639	5.079	6.346
BH(R_e)	0.456	2.712	3.226	0.604	0.542	1.949	3.235	2.393	0.539	1.991	3.251	3.645
BH(R_{st})	0.672	2.971	3.020	1.650	0.771	2.638	3.001	3.355	0.631	2.563	3.006	3.073
BH_2^+(R_e)	0.210	3.977	2.160	2.923	2.213	3.259	2.383	1.856	0.210	3.493	2.168	2.665
BH_2^+(R_{st})	1.324	2.627	2.242	0.677	1.331	3.031	2.255	2.897	1.327	3.014	2.252	2.245
BeH_2(R_e)	0.183	3.571	2.063	3.760	0.199	3.571	2.353	1.860	0.183	3.578	2.072	2.704
BeH_2(R_e)	1.635	2.981	2.178	3.210	1.572	3.343	2.254	0.625	1.560	3.310	2.250	3.136

Equilibrium distances (R_e) at experimental or optimized bond lengths and symmetrically stretched ones (R_{st}) at $R_{st} = 2.002\,R_e$ (for LiH), $R_{st} = 2.676\,R_e$ (for BeH^+), $R_{st} = 1.599\,R_e$ (for Li_2), $R_{st} = 1.487\,R_e$ (for BH), $R_{st} = 1.826\,R_e$ (for BH_2^+), $R_{st} = 2.066\,R_e$ (for BeH_2). Results for molecules correspond to standard STO-3G basis sets

The low values found for the I_W index show that, in these FCI wave functions, the CI ($\Omega = 0$) or DOCI expansions are close to the FCI ones, which is in agreement with the conclusions reported in Ref. [34] where the DOCI method has been picked up as a valuable tool to describe a wide variety of systems possessing strong correlation. As shown in Table 1, the I_C values are higher than their counterpart I_W ones, indicating that the expansions (3) involve significant contributions of $\Lambda(\Omega = 0)$ Slater determinants other than the ground closed-shell ones, which are usually chosen as reference determinants within the traditional excitation CI approach. This result is confirmed by the values reported in Table 2, where the $I_{\Omega=0}$ indices show a configurational distribution that cannot be considered as narrow. The results for the Be and Mg atoms show that these general trends are kept when basis sets larger than minimal STO-3G ones are used. The presence of strong correlation in the Be atom is well known, and consequently, its wave functions possess a multiconfigurational character even at zeroth-order descriptions; identical behavior has been found in the Mg atom. Our results confirm this feature showing that in the three isoelectronic species Be, LiH(R_e), and BeH^+(R_e), the highest I_C index value corresponds to the Be atom (the widest multiconfigurational distribution), while the I_W index presents small values for that atomic system; its wave functions have a narrow distribution in terms of seniority levels, with low contribution of $\Lambda(\Omega \neq 0)$ determinants.

The results reported in Table 1 also allow one to compare, in terms of the values of the indices I_C and I_W, the expansions of the wave functions of these systems according to the molecular orbital basis sets in which they are expressed. As can be seen from that table, the values of both indices are considerably lower in the NO and $M_{\min}$ basis sets than in their CMO counterparts (except for the Be atom in the STO-3G basis set); the Be atom recovers the improvement in the $M_{\min}$ and NO molecular basis sets when the larger cc-pVDZ basis set is used. These results again confirm that the NO and $M_{\min}$ molecular basis sets lead to more compact wave functions, as has been reported in Refs. [6, 9, 11]. These values also point out that the I_C and I_W indices constitute suitable devices to describe quantitatively the compactness of a wave function. The high values found for the I_C indices in the Be and Mg atoms in the three molecular basis sets can be interpreted in terms of the strong correlation exhibited by those systems. The appropriate ground-state wave functions for these atoms require several dominant Slater determinants. The I_Ω values reported in Table 2 reflect that seniority levels with very low contribution to the wave functions can present a broad determinantal distribution, i.e., the Li_2 molecule exhibits $I_{\Omega=4} > 5$ values because its $W_{\Omega=4} = 10^{-4}$ weight is expanded on 7560 Slater determinants in the STO-3G basis set [6]. Moreover, the $I_{\Omega=0}$ index values reported in that table indicate that all systems possess a narrower

distribution at equilibrium distances in the three molecular basis sets. Likewise, the molecular system descriptions at the stretched geometries systematically present higher values for the I_C and I_W indices (Table 1) than their counterparts at the equilibrium distances. This effect is interpreted in the framework of the progressive openness of the chemical bonds until their complete dissociation, which is reflected in the values of both indices. However, the index I_C shows a more sensitive character than the I_W one, and consequently, its use must be favored in order to account for the influence of the bond stretching on the wave function features.

5 Concluding remarks and perspectives

In this work, we have extended the formulation of the Shannon entropy indices, informational content (I_C), cumulative (I_W), and specific Ω-subspace (I_Ω), within the framework of the seniority number criterion for constructing N-electron wave function expansions in terms of Slater determinants. The quantitative evaluation of these indices has allowed us to implement analyses of the wave function expansions, determining their compactness in the well-known canonical molecular orbital and natural orbital basis sets, as well as in the recently proposed molecular orbital basis set which minimizes the seniority number of a given wave function. The results obtained for several atomic and molecular systems described at the FCI level show the suitability of the seniority-based formulation of these indices to measure quantitatively the wave function expansion compactness, as well as to analyze their multiconfigurational structure. We have also studied the ability of these indices to provide information on the evolution of the wave functions according to the stretching of the chemical bondings. We are currently working in our laboratories on the formulation of unitary transformations of molecular basis sets leading to the minimization of the Shannon entropy indices, in order to achieve a higher improvement on the compactness of wave function expansions.

Acknowledgments This work has been financially supported by the Grant Nos. GIU12/09 and UFI11/07 (Universidad del Pais Vasco, Spain), UBACYT 20020100100197 (Universidad de Buenos Aires, Argentina), PIP No. 11220090100061, 11220090100369, 11220130100377CO, and 11220130100311CO (Consejo Nacional de Investigaciones Científicas y Técnicas, Argentina). We thank the Universidad del País Vasco for allocation of computational resources.

References

1. Shavitt I (1998) Mol Phys 94:3
2. Sherrill CD, Schaefer HF III (1999) Adv Quantum Chem 34:143 and references therein
3. Bytautas L, Ivanic J, Ruedenberg K (2003) J Chem Phys 119:8217
4. Giesbertz KJH (2014) Chem Phys Lett 591:220
5. Bytautas L, Henderson TM, Jiménez-Hoyos CA, Ellis JK, Scuseria GE (2011) J Chem Phys 135:044119
6. Alcoba DR, Torre A, Lain L, Massaccesi GE, Oña OB (2013) J Chem Phys 139:084103
7. Stein T, Henderson TM, Scuseria GE (2014) J Chem Phys 140:214113
8. Boguslawski K, Tecmer P, Limacher PA, Johnson PA, Ayers PW, Bultinck P, De Baerdemacker S, Van Neck D (2014) J Chem Phys 140:214114
9. Alcoba DR, Torre A, Lain L, Massaccesi GE, Oña OB (2014) J Chem Phys 140:234103
10. Limacher PA, Kim TD, Ayers PW, Johnson PA, De Baerdemacker S, Van Neck D, Bultinck P (2014) Mol Phys 5–6:853
11. Alcoba DR, Torre A, Lain L, Oña OB, Capuzzi P, Van Raemdonck M, Bultinck P, Van Neck D (2014) J Chem Phys 141:244118
12. Ring P, Schuck P (1980) The nuclear many-body problem. Springe, New York
13. Koltun DS, Eisenberg JM (1988) Quantum mechanics of many degrees of freedom. Wiley, New York
14. Garza AJ, Jiménez-Hoyos CA, Scuseria GE (2013) J Chem Phys 138:134102
15. Jiménez-Hoyos CA, Rodríguez-Guzmán R, Scuseria GE (2013) J Chem Phys 139:204102
16. Evangelista FA (2014) J Chem Phys 140:124114
17. Mentel LM, Van Meer R, Gritsenko OV, Baerends EJ (2014) J Chem Phys 140:214105
18. Ivanov VV, Lyakh DI, Adamowicz L (2005) Mol Phys 103:2131
19. Kullback S (1959) Information theory and statistics. Wiley, New York
20. Mathai AM, Tathie PN (1975) Basic concepts in information theory and statistics. Wiley, New York
21. Pfeiffer PE (1978) Concepts of probability theory. Dover, New York
22. Paldus J, Jeziorski B (1988) Theor Chim Acta 73:81
23. Lain L, Torre A, Karwowski J, Valdemoro C (1988) Phys Rev A 38:2721
24. Torre A, Lain L, Millan J (1993) Phys Rev A 47:923
25. Lain L, Torre A (1995) Phys Rev A 52:2446
26. Surjan PR (1989) Second quantized approach to quantum chemistry. Springer, Berlin
27. Subotnik JE, Shao Y, Liang W, Head-Gordon M (2004) J Chem Phys 121:9220
28. Jonhson RD III (ed) (2006) Computational chemistry comparison and benchmark database. NIST Standard reference database vol 101. http://www.srdata.nist.gov/cccbdb
29. Roos JB, Larson M, Larson A, Orel AE (2009) Phys Rev A 80:112501
30. Chakrabarti K, Tennyson J (2012) Eur Phys J 66:31
31. Frisch MJ, Trucks GW, Schlegel HB, Scuseria GE, Robb MA, Cheeseman JR, Scalmani G, Barone V, Mennucci B, Petersson GA, Nakatsuji H, Caricato M, Li X, Hratchian HP, Izmaylov AF, Bloino J, Zheng G, Sonnenberg JL, Hada M, Ehara M, Toyota K, Fukuda R, Hasegawa J, Ishida M, Nakajima T, Honda Y, Kitao O, Nakai H, Vreven T, Montgomery JA Jr, Peralta JE, Ogliaro F, Bearpark M, Heyd JJ, Brothers E, Kudin KN, Staroverov VN, Kobayashi R, Normand J, Raghavachari K, Rendell A, Burant JC, Iyengar SS, Tomasi J, Cossi M, Rega N, Millam MJ, Klene M, Knox JE, Cross JB, Bakken V, Adamo C, Jaramillo J, Gomperts R, Stratmann RE, Yazyev O, Austin AJ, Cammi R, Pomelli C, Ochterski JW, Martin RL, Morokuma K, Zakrzewski VG, Voth GA, Salvador P, Dannenberg JJ, Dapprich S, Daniels

AD, Farkas Ö, Foresman JB, Ortiz JV, Cioslowski J, Fox DJ (2009) Gaussian 09, Revision D.01. Gaussian Inc., Wallingford
32. Crawford TD, Sherrill CD, Valeev EF, Fermann JT, King RA, Leininger ML, Brown ST, Janssen CL, Seidl ET, Kenny JP, Allen WD (2007) J Comput Chem 28:1610
33. Weinhold F, Wilson EB (1967) J Chem Phys 46:2752
34. Henderson TM, Bulik IW, Stein T, Scuseria GE (2014) J Chem Phys 141:244104

Theor Chem Acc (2015) 134:116
DOI 10.1007/s00214-015-1719-2

REGULAR ARTICLE

Structural and spectral properties of tartrato complexes of vanadium(V) from quantum chemical calculations

Gabriela Orešková[1] · Lukáš Krivosudský[1] · Ján Šimunek[1] · Jozef Noga[1,2,3]

Received: 30 June 2015 / Accepted: 1 September 2015 / Published online: 16 September 2015

Abstract Structural and spectral properties of three complex anions of vanadium(V) with tartrato ligands were theoretically studied by all-electron DFT calculations employing various functionals, such as BP86, BLYP, B3LYP, BHHLYP, and the M06-family. Results were statistically evaluated, with the aim to find a reliable, fairly accurate, and yet computationally efficient combination of methods and basis sets to be used in computational chemistry of vanadium(V) complex anions at even larger scale. Subsequent vibrational analysis based upon BP86 and B3LYP data provided a fair agreement with the experimental vibrational spectra. Additionally, the absorption UV–Vis and the electronic circular dichroism spectra of studied compounds were simulated via time-dependent density functional theory calculations with the long-range corrected functionals (CAM-B3LYP, LC-ωPBE, and ωB97XD). Finally, the ^{51}V NMR chemical shifts were calculated using the GIAO approach at the B3PW91 level. The solvent effect was simulated within the PCM model. Where available, the calculated spectral properties were compared with experimental data.

Keywords Vanadium(V) complexes · Tartrato ligand · DFT calculations · Spectral properties · Chirality

1 Introduction

Transition metals complexes of tartaric acid have been the subject of research in all the main areas of practical applications of chirality: biochemistry and medicinal chemistry [1], asymmetric catalysis [2–4], and chiral separations [5–9]. It is not surprising that the rapid development of the chemistry of vanadium in recent decades smoothly covered all of these areas by itself. The main attention has been devoted to the insulin-mimetic activity of vanadium complexes of tartaric acid [10, 11]. Chirality of some insulinomimetic dinuclear vanadyl(IV)–tartrate complexes has been considered as well, resulting in an interesting finding that both the complexes of naturally occurring L-tartaric acid and racemic tartaric acid are highly active [12].

The catalytic activity of the VO(stearate)$_2$–L/D tartrate system with the suggested presence of a dinuclear oxidovanadium(IV) tartrato complex leads to an enantioselective oxidative coupling polymerization of 2,3-dihydroxynaphthalene [13]. Very recently, the second harmonic generation and spin-dimer behavior were observed for oxovanadium(IV) tartrates [14]. In addition, a study appeared on an interaction of tartratovanadates with chiral Fe(II) and Ni(II) tris(2,2′-bipyridine) complexes manifesting itself with the solid state by packing into homochiral layers in the crystal structure [15].

The following dinuclear and tetranuclear tartrato complexes of vanadium(V) previously isolated from

Published as part of the special collection of articles "Festschrift in honour of P. R. Surjan".

Electronic supplementary material The online version of this article (doi:10.1007/s00214-015-1719-2) contains supplementary material, which is available to authorized users.

✉ Jozef Noga
jozef.noga@fns.uniba.sk

[1] Department of Inorganic Chemistry, Faculty of Natural Sciences, Comenius University, Ilkovičova 6, 84215 Bratislava, Slovakia

[2] Institute of Inorganic Chemistry, Slovak Academy of Sciences, Dúbravská cesta 9, 84536 Bratislava, Slovakia

[3] Computing Centre, Slovak Academy of Sciences, Dúbravská cesta 9, 84535 Bratislava, Slovakia

aqueous-ethanolic solution and characterized by X-ray structure analysis and spectral methods (infrared (IR), Raman, UV–Vis, ^{51}V NMR) [16, 17] were included in our computational study:

$[V_2O_4((2R,3R) - H_2tart)_2]^{2-}$ (**1**)

$[V_2O_2((2R,3R) - tart)((2S,3S) - tart)]^{2-}$ (**2**)

$[V_4O_8((R,R) - tart)_2]^{4-}$ (**3**)

While the tetranuclear anion [17] always contains tartrato groups of the same enantiomeric form, formation of the dinuclear complexes is stereospecific [16]. Continuous effort to understand the stereospecific aspects of vanadium(V) tartrato complexes leads us to take a closer look at their spectral properties. Hence, this work is aimed to complement the aforementioned studies and provide deeper understanding of the experimental observations.

At present, the density functional theory (DFT) prevails in calculations of the structural and spectral parameters of transition metal complexes [18]. For this reason, and thanks to our previous positive experience with simulation and interpretation of the UV–Vis, IR, electronic and vibrational circular dichroism (ECD and VCD) spectra of chiral vanadium complexes [19], we decided to use the DFT methods as the main tool in the present work as well. We shall present the calculated molecular structures, vibrational and electronic spectra, as well as the ^{51}V chemical shifts of the chosen anions of the vanadium(V) tartrato complexes. Where applicable, results are confronted with the available experimental data, with the aim to assess the reliability of the individual methods for future calculations of a similar kind.

2 Experimental details

Absorption UV–Vis and ECD spectra were recorded on a JASCO J-815 CD spectrometer in CH_3CN and H_2O solutions with a 1-cm cell.

Experimentally observed IR and Raman fundamentals were extracted from the previously published spectra, and compounds were prepared based on established synthetic procedure [16, 17].

3 Computational details

The quantum chemistry calculations were carried out using Gaussian 09 software package [20]. For visualization of the molecular structures and assignments of the vibrational modes, the Molden program [21] was used.

Our largest complex anion includes 36 atoms and altogether 308 electrons, and the basis sets have been chosen accordingly. We have employed three basis sets: (a) Ahlrichs TZV set for all atoms (TZV) [22, 23]; (b) composite basis set (WI) consisting of Wachters+f set for the vanadium atom [24, 25] and 6-311G(d) sets for remaining atoms [26]; and (c) extended composite basis set (WII) where 6-311G(d) basis was replaced with the 6-311++G(d,p) basis set [26, 27]. Wachters+f set is frequently used for first-row transition metals. It proved to perform fairly well in calculations for complexes of vanadium, too [19, 28–30]. In order to improve the description of the donor–acceptor bond between the central and the donor atom, inclusion of *f* functions on the central atom is, however, fully appropriate. Smaller Ahlrichs TZV basis set was tested due to our growing interest in a larger polyoxovanadate clusters, where only small basis sets are applicable for geometry optimization. Geometries of the complexes were optimized using Hartree–Fock and DFT methods with gradient-corrected BP86 [31, 32], BLYP [31, 33], and hybrid functionals including B3LYP [33–35], BHHLYP [36], and the M06-class of meta-GGA functionals [37–40] applying tight convergence criteria and ultrafine integration grids. Vibrational frequencies, absorption intensities, and Raman activities were calculated accordingly at the same levels. Potential energy distribution (PED) analysis of calculated vibrational frequencies was evaluated using the Vibrational Energy Distribution Analysis (VEDA4) program [41]. The solvent effect was simulated using the polarizable continuum model (PCM) [42, 43] with default parameters (water as solvent for **1**, acetonitrile for **2** and **3**). Calculations for excited states in the UV–Vis region were performed within the TD-DFT approach [44, 45] employing the LC-ωPBE [46, 47], ωB97XD [48], and CAM-B3LYP [49] functionals using the optimized geometries determined at the BP86/WI level either in the gas phase or within PCM. Simulation of the UV–Vis and ECD spectra was carried out by the GaussSum software [50], including all calculated singlet electronic transitions and assuming Gaussian band shape with a 0.35 eV bandwidth. The ^{51}V NMR chemical shifts were calculated using the GIAO approach [51, 52] at the B3PW91 level [34, 53, 54] with the Wachters+f basis set for the vanadium atom and IGLO-II basis sets [55] for the remaining atoms (W-IGLO). All chemical shifts are given with respect to the $VOCl_3$ reference chemical shielding obtained at the same computational level.

4 Results and discussion

4.1 Molecular structures

Geometry optimizations always started from the available experimental data. All studied complexes are singlets in their electronic ground states. The molecular structures for

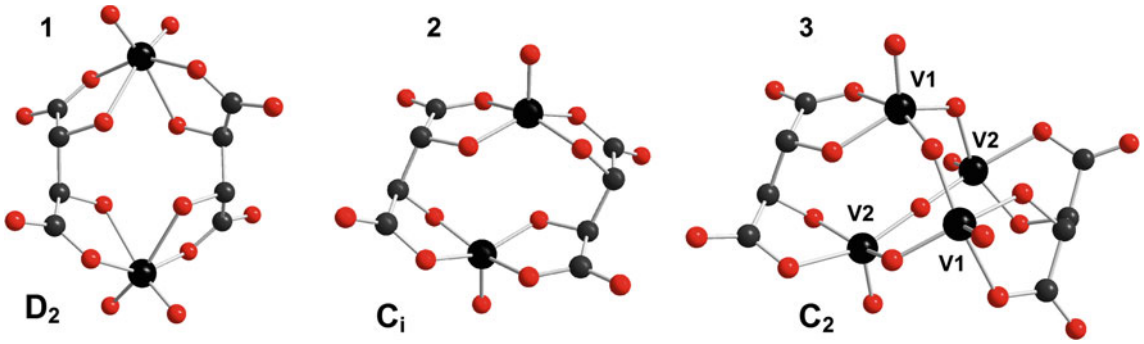

Fig. 1 Structures of the complex anions together with their point-group symbols. Hydrogen atoms are excluded for clarity. *Black*, *red*, and *gray colors* represent vanadium, oxygen, and carbon atoms, respectively

complexes **1**, **2**, and **3** are depicted in Fig. 1. This figure also serves to identify the corresponding atoms as given throughout the main text and the supplementary material.

4.1.1 Assessment of the geometry optimization schemes

As our complexes involve both weaker donor–acceptor and strong covalent bonds, for full geometry optimization a functional is wanted that describes both bonding situations. This was the reason, why we have still investigated a broader spectrum of 8 aforementioned DFT functionals. Here, we comment on the performance of the variety of different optimization schemes (method/basis set) from the statistical point of view as summarized in Table 1 and in Fig. 2. Selected bond lengths for all the three anions calculated with M06, BP86, and B3LYP functionals with WI basis together with experimental XRD crystal structure data [16, 17] are given in Table 2. Similar set for all investigated functionals can be found in Table S1 of the supplementary material. We have excluded the H-containing bonds, since the positions of the hydrogen atoms cannot be exactly determined from the XRD analysis.

Moreover, as seen from Table 2, gas-phase geometry optimization for **3** provided a C_2 symmetry, whereas bond lengths and/or bond angles that are equivalent in C_2 symmetry slightly differ in the experimental crystal structure that shows no symmetry (C_1). The same applies to the PCM calculations. These small differences are most probably due to the influence of crystal packing effects and impact of the surrounding cations on molecular structure of **3**.

Therefore, in Table 1 we show some statistical characteristics for the relative errors—with respect to the experiment—of the calculated bond lengths and bond angles just for complexes **1** and **2**. We have separately investigated ensembles of different bond types. First group involves bonding of the vanadium atom via donor–acceptor bonds with the ligands, in our case these are the V–O bonds. Second group comprises CC or CO bonds that are of covalent character. The third group (non-H) represents merging of the mentioned two, i.e., all bonds that do not involve hydrogen. Bond angles are treated in the same way.

Results reveal that there is essentially no gain in the accuracy of structural parameters when extending from WI to WII basis set and WI basis is superior in comparison with TZV due to the additional presence of polarization functions. In general, the bond lengths from the in vacuo optimization are in a very good agreement with the data obtained from the crystals by XRD analysis. Maximal discrepancies between the calculated and experimental data were within few hundredths of Å. The largest deviation of about 0.05–0.06 Å is observed for the V_2–O_c bonds for the complex **3**, causing a relative error of mere 2.8 %. The agreement with experiment is almost perfect for the complexes **1** and **2**, where both the theoretical model and experiment suggest symmetric structures. Nevertheless, only few of the investigated schemes provided mean error of the calculated bond lengths about 1 % for each of the selected groups.

Less accurate are the bond angles, as demonstrated in the second part of Table 1. For the bond angles involving a vanadium atom, the mean of the absolute values of the relative errors exceeds 1.5 % even for schemes with the closest agreement with experiment. In particular, the largest deviation is almost 10° for the O_c−V_1−O_c angles in **1**, corresponding to a relative error of almost 7 %.

Table 1 is complemented by Fig. 2 where normal distributions of the relative errors for the calculated bond lengths are depicted for selected computational schemes. As evident, M06-L that provides apparently smallest mean of absolute deviations at the same time unequally describes the V–O bonds and the C–C, C–O bonds. M06 and B3LYP with exact exchange are performing more uniformly for both groups of bonds and/or separately for bond angles. B3LYP gave rise to little overestimation for bond lengths and also for the angles. On the other hand, M06 provided a systematical underestimation of bond lengths and overestimation of bond angles.

Table 1 Maximal relative deviations (Δ_r^{max}), mean relative deviations ($\bar{\Delta}_r$), and mean of the absolute values of relative deviations ($\bar{\Delta}_r^{abs}$) of the calculated bond lengths and bond angles from the experimental data

Functional	Basis	VO bonds			CC, CO bonds			Non-H bonds	
		Δ_r^{max}	$\bar{\Delta}_r$	$\bar{\Delta}_r^{abs}$	Δ_r^{max}	$\bar{\Delta}_r$	$\bar{\Delta}_r^{abs}$	$\bar{\Delta}_r$	$\bar{\Delta}_r^{abs}$
M06-L	WI	1.91	0.85	0.85	−2.26	−0.23	0.65	0.13	0.72
M06	WI	−1.19	−0.18	0.80	−2.68	−0.56	0.71	−0.43	0.74
M06-2X	WI	−2.60	−0.55	1.32	−1.89	−0.33	0.63	−0.40	0.86
M06-HF	WI	−4.08	−1.31	1.76	−1.69	−0.47	0.73	−0.75	1.07
BP86	WI	2.17	1.23	1.23	1.91	0.80	1.05	0.94	1.11
BP86 PCM	WI	1.93	0.95	0.95	2.00	0.85	1.02	0.88	1.00
BLYP	WI	3.00	1.94	1.94	2.08	1.24	1.37	1.47	1.56
B3LYP	WI	1.52	0.37	0.71	−1.83	0.14	0.68	0.22	0.69
BHHLYP	WI	−2.58	−1.10	1.33	−2.54	−0.91	0.92	−0.97	1.06
HF	WI	−4.72	−1.84	1.98	−2.61	−1.18	1.24	−1.40	1.49
BP86	WII	2.43	1.24	1.24	2.24	0.89	1.13	1.00	1.17
B3LYP	WII	1.65	0.39	0.67	−1.72	0.21	0.72	0.27	0.70
BP86	TZV	2.48	1.87	1.87	4.16	2.11	2.11	2.03	2.03
BLYP	TZV	3.31	2.57	2.57	4.41	2.57	2.57	2.57	2.57
B3LYP	TZV	1.55	0.98	1.01	3.16	1.37	1.37	1.24	1.25
BHHLYP	TZV	−2.03	−0.57	0.62	1.91	0.24	0.60	−0.03	0.60
HF	TZV	−2.99	−1.45	1.45	1.16	−0.06	0.46	−0.52	0.79
Functional	Basis	∠OVO, ∠VOC			∠CCC, ∠CCO, ∠OCO			Non-H angles	
		Δ_r^{max}	$\bar{\Delta}_r$	$\bar{\Delta}_r^{abs}$	Δ_r^{max}	$\bar{\Delta}_r$	$\bar{\Delta}_r^{abs}$	$\bar{\Delta}_r$	$\bar{\Delta}_r^{abs}$
M06-L	WI	−6.92	0.44	1.84	1.83	0.35	0.92	0.40	1.36
M06	WI	−5.65	0.68	2.12	2.76	0.42	1.00	0.54	1.53
M06-2X	WI	−6.60	0.51	1.81	1.79	0.25	0.93	0.37	1.35
M06-HF	WI	−6.34	0.57	1.78	1.92	0.00	0.99	0.27	1.37
BP86	WI	−5.89	0.68	2.21	3.32	0.51	1.02	0.59	1.59
BP86 PCM	WI	−4.41	0.68	1.96	3.96	0.49	0.90	0.58	1.41
BLYP	WI	−6.04	0.82	2.52	3.73	0.59	1.10	0.70	1.78
B3LYP	WI	−6.51	0.85	2.54	3.28	0.52	1.14	0.68	1.81
BHHLYP	WI	−6.90	0.91	2.60	2.71	0.44	1.13	0.67	1.83
HF	WI	−8.22	1.25	3.18	2.72	0.44	1.15	0.83	2.12
BP86	WII	−5.80	0.76	2.29	3.06	0.50	0.96	0.63	1.60
B3LYP	WII	−6.82	0.96	2.68	3.03	0.51	1.10	0.72	1.85
BP86	TZV	−5.32	0.76	2.18	3.09	0.42	1.13	0.59	1.63
BLYP	TZV	−5.57	0.91	2.48	3.49	0.50	1.19	0.70	1.81
B3LYP	TZV	−6.06	1.03	2.71	3.29	0.42	1.24	0.71	1.94
BHHLYP	TZV	−6.74	1.22	3.49	3.35	0.32	1.28	0.75	2.34
HF	TZV	−8.31	1.60	4.07	3.00	0.28	1.33	0.91	2.64

Results (in %) are shown separately for ensembles of different bonds and angle types of the complex anions **1** and **2**

Finally, BP86 provided more uniform, though slightly larger, deviations from the crystal structure data. Simulating the environment by PCM resulted in an insignificant change in this picture. As seen, one can hardly suggest an optimal scheme from those investigated. Hence, in the following we shall selectively pick up results that fit best to the purpose of this paper, i.e., those that most closely mimic the available experimental data.

4.2 Spectral properties

4.2.1 Vibrational spectra

Table 3 contains assignments for selected parts of the vibrational spectra of **1**–**3**. Data for the whole pertinent frequency range are given in the supplementary material and complement the experimentally recorded IR and Raman spectra

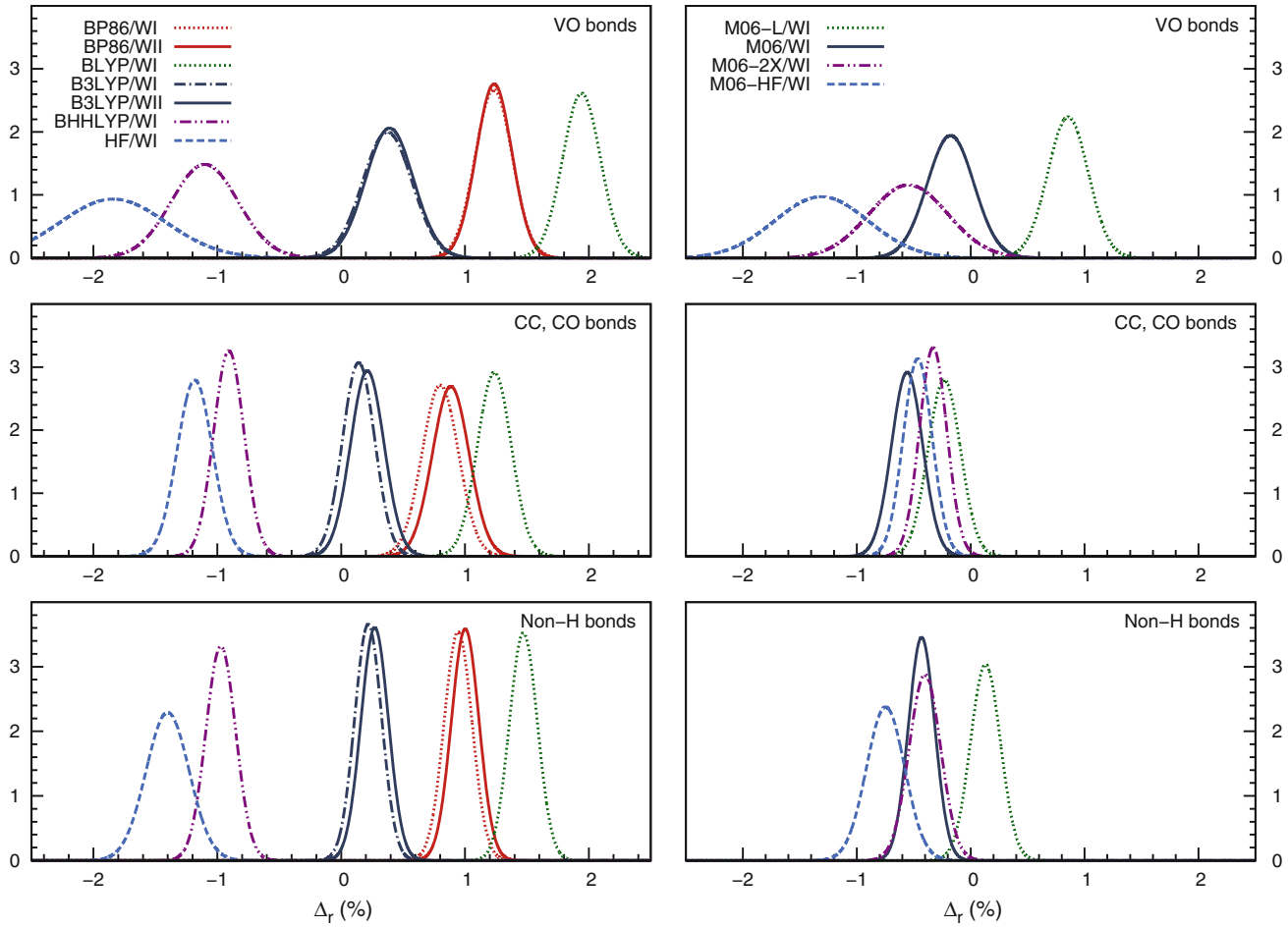

Fig. 2 Normal distributions of the relative errors Δ_r of the calculated bond lengths for the complex anions **1** and **2**. Errors are with respect to the experimental data

reported in [16, 17]. We show the calculated harmonic vibrational frequencies obtained with BP86 and B3LYP functionals in WI basis as fairly well coinciding with the measured spectra. Computed vibrational modes have been analyzed in terms of potential energy distribution (PED) contributions [41], as displayed together with the B3LYP values. Let us recall that the differences in the main features of the spectra recorded in solid state and/or solutions were rather small [16], which supports justification for confronting the solid-state experiment with the gas-phase data calculated here. Yet, one has to be aware of the fact that some discrepancies due to this fact are naturally inherent.

It is well known that the harmonic vibrational frequencies calculated by DFT methods are usually systematically overestimated with respect to experimental fundamentals, which was the case for most of our results, too. This systematic overestimation used to be corrected by rescaling the spectrum using scaling factors that are well tuned to specific functionals and basis sets. Such factors are available, e.g., for B3LYP/6-311G* [56]. For our schemes with combined basis sets, however, we have not found any suitable scaling factors. Hence, we display the unscaled values. Even in that case, the performance of BP86 is more than satisfactory, apparently due to a lucky cancellation of different biases. This fact has been stressed earlier and using the BP86 functional recommended as a pragmatic and cost-effective approach to calculating vibrational frequencies for large molecules [57, 58].

Involvement of the individual vibrations in different wave number ranges follows from the PED as given in Tables S2–S4 of the supplementary material, where contributions under 10 % are disregarded. From our point of view, the vibrations involving the vanadium atom are most relevant (Table 3), in particular those that distinguish the different coordination spheres. For **2**, the IR and Raman spectra are exclusively complementary for asymmetric and symmetric skeletal vibrations, respectively, due to its C_i symmetry. The stretching V–O_t vibrations are shifted to somewhat higher energies than in **1** or **3**. While in **2**, there is one active mode for this vibration in IR and one in the

Table 2 Selected bond lengths (Å) of the complex anions optimized at various levels of theory using composite WI basis set in vacuum

Bond[a]	Expt.[b]	M06	BP86	B3LYP
$[V_2O_4((2R,3R)-H_2tart)_2]^{2-}$ **(1)**				
VO_t	1.612(2)	1.599	1.626	1.606
VO_h	2.272(2)	2.319	2.353	2.366
VO_c	1.970(2)	1.990	2.009	2.000
CC	1.528(3)	1.517	1.537	1.532
CC_c	1.526(4)	1.530	1.546	1.541
CO_h	1.426(3)	1.409	1.429	1.419
CO_c	1.284(3)	1.280	1.301	1.289
CO_u	1.220(3)	1.222	1.240	1.229
$[V_2O_2((2R,3R)-tart)((2S,3S)-tart)]^{2-}$ **(2)**				
VO_t	1.590(1)	1.571	1.605	1.584
VO_h	1.834(1)	1.828	1.847	1.833
VO_h	1.815(2)	1.813	1.838	1.823
VO_c	1.970(2)	1.949	1.976	1.963
VO_c	1.933(1)	1.948	1.975	1.960
CC	1.530(2)	1.527	1.551	1.542
CC_c	1.538(3)	1.537	1.558	1.549
CC_c	1.545(3)	1.539	1.561	1.552
CO_h	1.419(3)	1.381	1.397	1.393
CO_h	1.409(3)	1.384	1.400	1.395
CO_c	1.311(2)	1.302	1.320	1.310
CO_c	1.323(3)	1.304	1.322	1.313
CO_u	1.217(3)	1.210	1.227	1.215
CO_u	1.203(3)	1.209	1.226	1.214
$[V_4O_8((R,R)-tart)_2]^{4-}$ **(3)**				
V_1O_t	1.618(4), 1.617(4)	1.592	1.625	1.603
V_2O_t	1.619(4), 1.603(4)	1.580	1.615	1.595
V_1O_h	1.964(4), 1.963(4)	1.907	1.917	1.896
V_2O_h	1.870(4), 1.883(4)	1.871	1.893	1.881
V_1O_c	2.070(4), 2.070(4)	2.086	2.115	2.107
V_2O_c	2.058(4), 2.069(4)	2.090	2.118	2.102
V_1O_{b2}	1.759(4), 1.784(4)	1.771	1.796	1.791
V_1O_{b1}	1.828(4), 1.823(4)	1.799	1.818	1.807
V_2O_{b2}	1.854(4), 1.838(4)	1.804	1.819	1.806
V_2O_{b1}	1.884(4), 1.889(4)	1.834	1.850	1.828
CC	1.538(8), 1.569(7)	1.538	1.564	1.555
CC_c	1.522(9), 1.554(9)	1.535	1.556	1.546
CC_c	1.564(8), 1.534(9)	1.532	1.552	1.544
CO_c	1.285(8), 1.308(7)	1.279	1.298	1.287
CO_c	1.270(8), 1.291(8)	1.277	1.296	1.285
CO_u	1.257(8), 1.225(7)	1.231	1.249	1.238
CO_u	1.245(7), 1.254(8)	1.231	1.250	1.238
CO_h	1.442(7), 1.397(7)	1.378	1.394	1.389
CO_h	1.401(7), 1.401(7)	1.375	1.391	1.386

[a] Subscripts definition: *h* hydroxylic, *c* coordinated and/or carboxylic, *u* uncoordinated carboxylic, *t* terminal, *bi* bridged to V_i

[b] Experimental crystal structure data from references [16, 17]

Raman spectrum, in **1**, the computations predict three relatively close levels in IR around ~955 cm^{-1} from which two are also active in the Raman spectrum. In addition, a single frequency in this region corresponding to the symmetric stretching of the VO_2 group appears in mere Raman spectrum. In **3**, the four V–O_t stretching modes should be active in both spectra, while the highest wave number (~978 cm^{-1}) is dominant in the Raman and the lower frequencies are dominated in IR spectra.

V–O_h stretchings have not appeared in the investigated range for **1** with pseudo-hexacoordinated vanadium atom, and the O_h–H stretching frequencies remain in their usual range. This behavior and the V–O_h bond length confirm a very weak bonding character for this bond. In **2**, the V–O_h stretchings dominantly contribute to IR bands around 660 cm^{-1} and in Raman spectrum around 625 cm^{-1}. In **3**, those stretchings contribute to frequencies around ~550–600 cm^{-1} together with the V–O_b stretchings and other skeletal bendings. IR bands at ~800 and ~770 cm^{-1} are mostly attributed to involvement of the V–O_b stretchings, as well as a medium intensity band in this region of the Raman spectrum.

4.2.2 UV–Vis and ECD spectra

In the range of 180–500 nm, there are about 90, 130, and 250 calculated singlet electronic transitions for **1**, **2**, and **3**, respectively. As these spectra are dominated by LMCT transitions (charge transfer from ligand to metal), in this case, we have used long-range corrected functionals [59] combined with BP86/WI-optimized geometries. We have checked the M06/WI-optimized structures, too, but the differences are negligible.

Our calculations and some new experimental data complement the UV–Vis spectra published in [16]. We are aware that the calculated values are still influenced by several approximations that might be quite crude but which are not easy to eliminate in a cost-effective way. First of all, the calculated spectra correspond to vertical transitions without vibronic couplings. Moreover, in order to simulate the environment we have used a standard PCM model, but for more accurate computations of excitation spectra the response of the environment to the excitation should be included either perturbatively, as, e.g., done within the corrected linear response (cLR) scheme [60, 61], or in a self-consistent manner within the state-specific (SS-PCM) scheme [62, 63].

Let us first discuss the complex **3**, for which we were able to measure the ECD (together with UV–Vis) spectra, as shown in Fig. 3. In Fig. 4, we display the simulated spectra using CAM-B3LYP and LC-ωPBE functionals with extended WII basis sets (see below a comment on the basis set effect). Here, we have skipped results obtained with

Table 3 Selected experimental vibrational wave numbers (cm^{-1}) for **1**–**3** compared with harmonic approximation values calculated using the composite WI basis set

Complex	Symmetry	Experimental[a]		BP86	B3LYP			
		IR	Raman	ν_i	ν_i	A_i^{IR}	I_i^{Raman}	PED (>10 %) and assignments
1	D_2^b $(NMe_4)_2[V_2O_4((2R,3R)-H_2tart)_2]\cdot 6H_2O$ [16]							
	A		938 vs	965	1021	0	102	97 $\nu(VO_t)$
	B_1	953 vs		960	1017	539	0	97 $\nu(VO_t)$
	B_2	929 vs		957	999	322	14	96 $\nu(VO_t)$
	B_3	910 vs	906 s	953	996	240	12	92 $\nu(VO_t)$
2	C_i^c $(NMe_4)_2[V_2O_2((2R,3R)-tart)((2S,3S)-tart)]$ Ref. [16]							
	A_g		995 vs	1009	1064	0	58	96 $\nu(VO_t)$
	A_u	993 vs		1004	1058	649	0	96 $\nu(VO_t)$
	...							
	A_u	665 s		644	673	227	0	40 $\nu(VO_h)$
	A_u	655 s		626	651	405	0	66 $\nu(VO_h)$
	A_g			622	647	0	3	35 $\nu(VO_h)$
	A_g		626 m	607	631	0	32	59 $\nu(VO_h)$
3	C_2^d , $(NEt_4)_4[V_4O_8((R,R)-tart)_2]\cdot 6H_2O$ Ref. [17]							
	A		977 vs	978	1034	63	125	82 $\nu(VO_t)$
	B			970	1023	227	16	96 $\nu(VO_t)$
	A	957 vs		957	1013	724	15	82 $\nu(VO_t)$
	B			952	1008	194	17	95 $\nu(VO_t)$
	...							
	B	800 m		805	850	1273	6	67 $\nu(VO_b)$
	...							
	B	770 b		738	765	1056	3	65 $\nu(VO_b)$
	...							
	A	667 s	672 m	696	724	329	16	42 $\nu(VO_b)$
	...							
	B		567 s	581	604	13	31	39 $\nu(VO_b)$
	A	592 m		580	593	52	0	18 $\nu(VO_h)$; 10 $\nu(VO_b)$
	B	547 b		551	575	339	1	29 $\nu(VO_h)$; 12 $\delta(CC_cO_c)$
	...							
	B	486 w		483	499	38	1	20 $\nu(VO_h)$
	A			482	495	0	2	19 $\nu(VO_h)$

Modes: ν stretching, δ in-plane bending

Absorption IR intensities (A^{IR}, km mol^{-1}), Raman activities (I^{Raman}, $Å^4$ amu^{-1}), and normal mode assignments are presented as well. Data for a wider frequency spectrum are given in the supplementary material

[a] Solid-state spectra

[b] Total of 96 normal modes $\Gamma_{vib} = 25A(Raman) + 23B_1(IR, Raman) + 24B_2(IR, Raman) + 24B_3(IR, Raman)$

[c] Total of 78 normal modes $\Gamma_{vib} = 39A_g(Raman) + 39A_u(IR)$

[d] Total of 102 normal modes $\Gamma_{vib} = 51A(IR, Raman) + 51B(IR, Raman)$

ωB97XD functional that practically copy the CAM-B3LYP spectra. One observes that the simulated UV–Vis spectra very well agree with the experimental recording. Except for a small range around the wavelength 200 nm, this statement is equally valid for the gas-phase and the PCM simulations. Yet, in the range toward the wavelength of about 200 nm the improving effect of PCM is visible. Generally, the simulated UV–Vis spectrum possesses all the features of the measured one in the CH_3CN solution, although the maxima are slightly shifted toward shorter wavelengths. The latter effect is somewhat stronger for the LC-ωPBE values.

Improving effect of the PCM is much more evident in the simulated ECD spectra. In particular, the positive sign wave in the 200–250 nm range failed to be well simulated in the mere gas-phase model. Indeed, also in experiment, the effect of the different environment in ECD spectrum

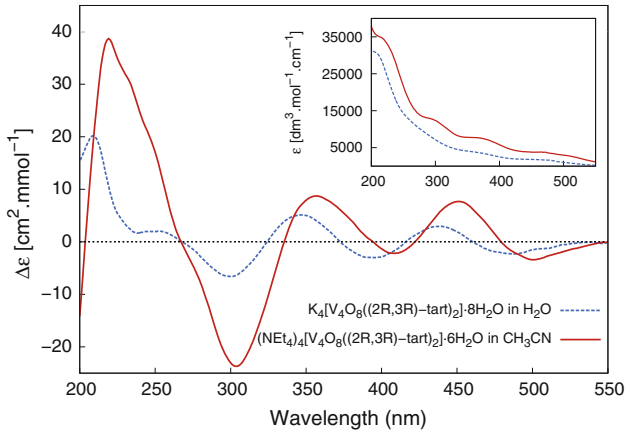

Fig. 3 Experimental absorption UV–Vis (*upper-right corner*) and ECD spectra of **3** in CH_3CN (5.012×10^{-5}) and in H_2O (5.020×10^{-5}) solution. Concentrations in mol dm^{-3}

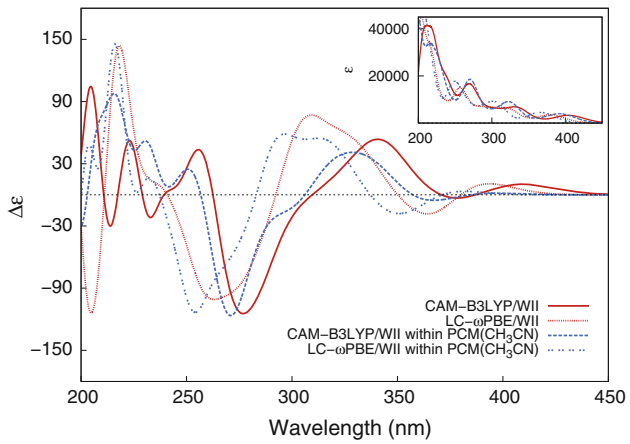

Fig. 4 Simulated UV–Vis (*upper-right corner*) and ECD spectra of **3**

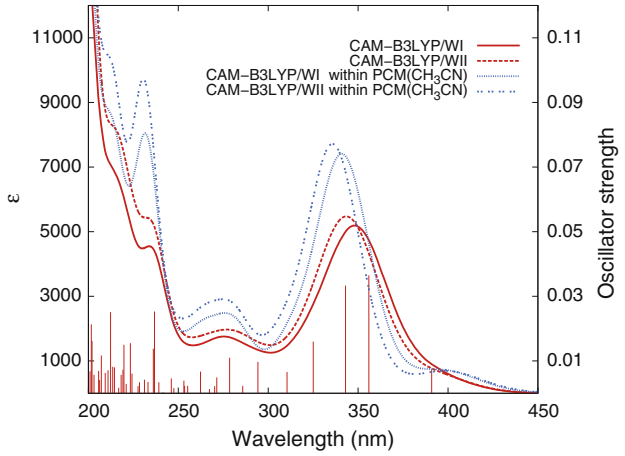

Fig. 5 Simulated UV–Vis spectra of **2**

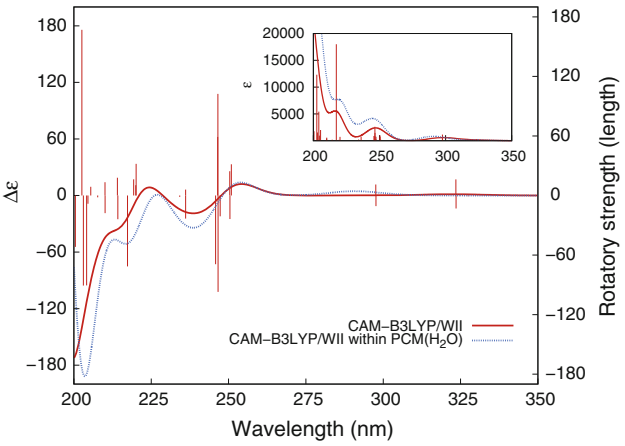

Fig. 6 Simulated UV–Vis (*upper-right corner*) and ECD spectra of **1**

is much more pronounced than for the UV–Vis. The basic features of the simulated ECD spectra reproduce the basic pattern of the experimental recording. Yet, amplitudes of the bands decrease too fast in the region of large wavelengths, and in accord with UV–Vis, the extremes are shifted toward shorter wavelengths. Though the overall performance of LC-ωPBE and CAM-B3LYP is not too different, CAM-B3LYP with PCM model seems to be preferable. Consequently, we shall use the latter to predict the ECD spectrum of complex **1**. Unfortunately, we were unable to reliably measure this spectrum due to its slow conversion to **3** in the water solution and its decomposition in CH_3CN [16].

In Fig. 5, the simulated UV–Vis spectra are shown for **2**, using CAM-B3LYP functional with both WI and WII basis sets. First, let us recall that the overall agreement with the experimental spectrum available beyond 300-nm range [16] is again very good. As expected, also here the simulated maximum at ~350 nm is slightly shifted toward shorter wavelength than in experiment (~400 nm). Evidently, extending the basis set from WI to WII has not caused a

Table 4 Comparison of experimental and calculated ^{51}V NMR isotropic chemical shifts (δ, relative to $VOCl_3$)

Geometry	GIAO-B3PW91/W-IGLO (in ppm)				
	σ_{ref}	δ			
Funct./basis	$VOCl_3$	**1**	**2**	**3**	
				V1	V2
BP86/WI	−2195	−620	−363	−523	−495
B3LYP/WI	−2107	−647	−402	−546	−501
M06L/WI	−2115	−609	−333	−508	−481
M06/WI	−2028	−625	−387	−531	−527
Exp. H_2O		−550	–	−522	
Exp. CH_3CN		–	−377	−495	

significant change in the overall pattern, i.e., also results with WI basis are fairly reliable. The PCM model slightly increased the calculated oscillator strengths, still preserving the overall shape of the spectrum as in the gas phase.

In Fig. 6, the predicted UV–Vis and ECD spectrum is shown for the complex **1**. It is worth noting that due to the mutual cancellation of rotatory strengths, the dichroism apparently disappears in the range beyond ~250 nm.

4.2.3 NMR spectra

Finally, let us briefly comment on the calculated isotropic NMR chemical shifts, as given in Table 4. The ^{51}V NMR chemical shifts were calculated using the GIAO approach with well-established B3PW91 functional and the W-IGLO basis set. These computations were performed employing optimized structures as defined in the first column of Table 4. All chemical shifts are given with respect to the $VOCl_3$ reference chemical shielding. Since PCM did not provide any improvement, we just show in vacuo values. A good agreement with experiment has been accomplished for **2** and also for **3**. In **3**, the calculated values for V_1 and V_2 are distinguished, unlike in experiment when a single peak was observed. A rather big discrepancy with experiment in the case of **1** indicates relatively large deviation of the calculated structure from the measured one in an aqueous solution. Similar differences were observed between computed and experimental values for $[VO_2(H_2O)_4]^+$ cation [28]. As for the performance of the employed geometries, even though the calculated chemical shifts vary within about 10 % of their values, this is still acceptable.

5 Concluding remarks

A number of DFT calculations investigating the performance of a variety of functionals were performed for three complex anions of vanadium(V) with tartrato ligands. As expected, one can hardly find a universal DFT method to equally well describe structures together with the spectral properties. Our further aim was to complement the experimentally available data for **1**, **2**, and **3** [16, 17]. Hence, we have confronted the results with those experiments. Structural parameters have been fairly well described using the BP86 functional which can be safely recommended for further computations of a similar kind as a good compromise between the cost-effectiveness and accuracy. Consequently, the vibrational energy distribution analysis confirmed and/or complemented the measured spectral data.

Since the LMCT electronic transitions are dominant in the electronic spectra, long-range corrected functionals have been employed in combination with the aforementioned optimized structures, CAM-B3LYP proving as a favorite one. Calculated UV–Vis and ECD spectra were confronted with the experimental recordings, performed in this work for **3**, as well. This confrontation allowed to reliably predict the pertinent spectra for **1**, where we were unable to obtain ECD spectrum experimentally. Calculated NMR chemical shifts were in good agreement with experiment for **2** and **3**, too.

Acknowledgments We thank Peter Schwendt for prompting this work. JN appreciates a long-term friendship with Péter Surján whom we dedicate this work on the occasion of his 60th birthday, and who started his scientific carrier by calculating the rotatory strengths [64]. This work has been supported by the Grant Agency of the Ministry of Education of the Slovak Republic and Slovak Academy of Sciences VEGA project no. 1/0336/13 as well as by the Slovak Research and Development Agency (APVV-0510-12). Calculations were performed in the Computing Center of the Slovak Academy of Sciences using the supercomputing infrastructure acquired in project ITMS 26230120002 and 26210120002 supported by the Research & Development Operational Programme funded by the ERDF.

Compliance with ethical standards

Conflict of interest The authors declare that they have no conflict of interest.

References

1. Blair GT, DeFraties JJ (2000) Hydroxy dicarboxylic acids, kirk othmer encyclopedia of chemical technology. Wiley, Hoboken, NJ
2. Williams ID, Pedersen SF, Sharpless KB, Lippard SJ (1984) J Am Chem Soc 106:6340
3. Bryliakov KP, Talsi EP (2008) Curr Org Chem 12:386
4. Gan CS (2008) Can J Chem 86:261
5. Molnár P, Thorey P, Bánsághi G, Székely E, Poppe L, Tomin A, Kemény EFS, Simándi B (2008) Tetrahedron Asymmetry 19:1587
6. Nakamura H, Fujii M, Sunatsuki Y, Kojima M, Matsumoto N (2008) Eur J Inorg Chem 8:1258
7. Tapscott ER, Belford RL, Paul IC (1969) Coord Chem Rev 4:323
8. Nakazawa H, Yoneda H (1978) J Cromatogr 160:89
9. Wijeratne AB, Spencer SE, Gracia J, Armstrong DW, Schug KA (2009) J Am Soc Mass Spectrom 20:2100
10. Sakurai H, Katoh A, Yoshikawa Y (2006) Bull Chem Soc Jpn 79:1645
11. Sakurai H, Kojima Y, Yoshikawa Y, Kawabe K, Yasui H (2002) Coord Chem Rev 226:187
12. Sakurai H, Funakoshi S, Adachi Y (2005) Pure Appl Chem 77:1629
13. Murakami S, Habane S, Higashimura H (2007) Polymer 48:6565
14. Cortese AJ, Wilkins B, Smith MD, Yeon J, Morrison G, Tran TT, Halasyamani PS, zur Loye HC (2015) Inorg Chem 54:4011
15. Antal P, Schwendt P, Tatiersky J, Gyepes R, Drábik M (2014) Trans Metal Chem 39:893
16. Gáliková J, Schwendt P, Tatiersky J, Tracey AS, Žák Z (2009) Inorg Chem 48:8423
17. Schwendt P, Tracey AS, Tatiersky J, Gáliková J, Žák Z (2007) Inorg Chem 46:3971
18. Koch W, Holthausen MC (2002) A chemist's guide to density functional theory. Viley-VCH, Weinheim
19. Krivosudský L, Schwendt P, Šimunek J, Gyepes R (2014) Chem Eur J 20:8872

20. Frisch MJ, Trucks GW, Schlegel HB, Scuseria GE, Robb MA, Cheeseman JR, Scalmani G, Barone V, Mennucci B, Petersson GA, Nakatsuji H, Caricato M, Li X, Hratchian HP, Izmaylov AF, Bloino J, Zheng G, Sonnenberg JL, Hada M, Ehara M, Toyota K, Fukuda R, Hasegawa J, Ishida M, Nakajima T, Honda Y, Kitao O, Nakai H, Vreven T, Montgomery JA, Peralta JE Jr, Ogliaro F, Bearpark M, Heyd JJ, Brothers E, Kudin KN, Staroverov VN, Kobayashi R, Normand J, Raghavachari K, Rendell A, Burant JC, Iyengar SS, Tomasi J, Cossi M, Rega N, Millam JM, Klene M, Knox JE, Cross JB, Bakken V, Adamo C, Jaramillo J, Gomperts R, Stratmann RE, Yazyev O, Austin AJ, Cammi R, Pomelli C, Ochterski JW, Martin RL, Morokuma K, Zakrzewski VG, Voth GA, Salvador P, Dannenberg JJ, Dapprich S, Daniels AD, Farkas Foresman JB, Ortiz JV, Cioslowski J, Fox DJ (2009) Gaussian09 Revision A.02. Gaussian Inc., Wallingford, CT
21. Schaftenaar G, Noordik JH (2000) J Comput Aided Mol Design 14:123
22. Schafer A, Horn H, Ahlrichs R (1992) J Chem Phys 97:2571
23. Schafer A, Huber C, Ahlrichs R (1994) J Chem Phys 100:5829
24. Wachters AJH (1970) J Chem Phys 52:1033
25. Bauschlicher CW, Langhoff SR, Barnes LA (1989) J Chem Phys 91:2399
26. Krishnan R, Binkley J, Seeger R, Pople J (1980) J Chem Phys 72:650
27. Clark T, Chandrasekhar J, Spitznagel GW, Schleyer P (1983) J Comput Chem 4:294
28. Bühl M, Parrinello M (2001) Chem Eur J 7:4487
29. Chrappová J, Schwendt P, Sivák M, Repiský M, Malkin VG, Marek J (2009) Dalton Trans 3:465
30. Orešková G, Chrappová J, Puškelová J, Šimunek J, Schwendt P, Noga J, Gyepes R (2015) Struct Chem. doi:10.1007/s11224-015-0593-9
31. Becke AD (1988) Phys Rev A 38:3098
32. Perdew JP (1986) Phys Rev B 33:8822
33. Lee C, Yang W, Parr RG (1988) Phys Rev B 37:785
34. Becke AD (1993) J Chem Phys 98:5648
35. Stephens PJ, Devlin FJ, Chabalowski CF, Frisch MJ (1994) J Phys Chem 98:11623
36. Becke AD (1993) J Chem Phys 98:1372
37. Zhao Y, Truhlar DG (2006) J Chem Phys 125:194101
38. Zhao Y, Truhlar DG (2008) Theor Chem Acc 120:215
39. Zhao Y, Truhlar DG (2006) J Phys Chem A 110:13126
40. Zhao Y, Truhlar DG (2008) Acc Chem Res 41:157
41. Jamróz MH (2013) Spectrochim Acta A 114:220
42. Pascual-Ahuir JL, Silla E, Tuñón I (1994) J Comput Chem 15:1127
43. Tomasi J, Mennucci B, Cancés E (1999) J Mol Struct 464:211
44. Runge E, Gross EKU (1984) Phys Rev Lett 52:997
45. Casida ME (1995) In: Chong DP (ed) Time-dependent density-functional response theory for molecules. World Scientific, Singapore
46. Vydrov OA, Scuseria GE (2006) J Chem Phys 125:234109
47. Vydrov OA, Heyd J, Krukau A, Scuseria GE (2006) J Chem Phys 125:074106
48. Chai JD, Head-Gordon M (2008) Phys Chem Chem Phys 10:6615
49. Yanai T, Tew D, Handy N (2004) Chem Phys Lett 393:5157
50. O'Boyle NM, Tenderholt AL, Langner KM (2008) J Comp Chem 29:839
51. Ditchfield R (1972) J Chem Phys 56:5688
52. Wolinski K, Hinton JF, Pulay P (1990) J Am Chem Soc 112:8251
53. Perdew JP (1991) Phys B 172:1
54. Perdew JP, Wang Y (1992) Phys Rev B 45:13244
55. Kutzelnigg W, Fleischer U, Schindler M (1991) In: Diehl P, Fluck E, Günther H, Kosfeld R, Seelig J (eds) NMR basic principles and progress. Springer, Berlin/Heidelberg
56. Scott AP, Radom L (1996) J Phys Chem 100:16502
57. Neugebauer J, Reiher M, Kind C, Hess BA (2002) J Comput Chem 23:895
58. Neugebauer J, Hess BA (2003) J Chem Phys 118:7215
59. Le Guennic B, Maury O, Jacquemin D (2012) Phys Chem Chem Phys 14:157
60. Cammi R, Corni S, Menuci B, Tomasi J (2005) J Chem Phys 122:104513
61. Caricato M, Menuci B, Tomasi J, Ingrosso F, Cammi R, Corni S, Scalmani G (2006) J Chem Phys 124:124520
62. Improta R, Barone V, Scalmani G, Frisch MJ (2006) J Chem Phys 125:054103
63. Improta R, Scalmani G, Frisch MJ, Barone V (2007) J Chem Phys 127:074504
64. Surján PR (1980) Theor Chim Acta 55:103

Theor Chem Acc (2015) 134:132
DOI 10.1007/s00214-015-1734-3

REGULAR ARTICLE

A QM/MM program using frozen localized orbitals and the Huzinaga equation

Bence Hégely[1] · Ferenc Bogár[2] · György G. Ferenczy[3] · Mihály Kállay[1]

Received: 23 July 2015 / Accepted: 15 September 2015 / Published online: 16 October 2015

Abstract A mixed QM/MM computer program coupling Amber and Mrcc is presented. This is the first implementation of the Huzinaga equation-based local self-consistent field (HLSCF) method that makes it possible to calculate ab initio wave functions without orthogonalizing the basis set to the frozen orbitals separating the QM and MM subsystems. A significant novelty of the program is that it includes an automatic generation of the frozen localized orbitals obtained from calculations performed for model molecules cut out of the system. The Amber–Mrcc code also allows the use of the link atom (LA) approach. Sample calculations were performed to check the performance of both the HLSCF and the LA approaches by describing the interactions between the QM and MM subsystems with electrostatic embedding. It was found that the conceptually appealing HLSCF method is a competitive alternative to the LA method.

Keywords Mixed quantum mechanics/molecular mechanics · Huzinaga equation-based local self-consistent field (HLSCF) · Frozen strictly localized molecular orbital · Link atom

1 Introduction

Mixed quantum mechanical/molecular mechanical (QM/MM) methods are multiscale modeling techniques that find widespread use in chemistry. The basic idea of QM/MM methods is that a localized event in a large molecular system is described by a sophisticated computational method applied explicitly to the central subsystem where the event takes place, while the effect of the further regions is taken into account in a more approximate way. Typical fields of application include reaction mechanisms, among them enzyme-catalyzed biochemical reactions, solvation, and spectroscopic properties. While QM methods are most often combined with MM methods, multiscale modeling also includes the combination of various level QM techniques. An early scheme developed by Náray-Szabó and Surján [1] calculates strictly localized molecular orbitals for the whole system followed by the release of localization for the central subsystem. This QM/QM scheme was originally developed at the CNDO/2 level and was later extended to the NDDO level [2]. A virtue of this method is that it offers a natural way to separate the central subsystem and the environment. A strictly localized orbital is the linear combination of hybrids centered on bound atoms and pointing toward one another. Then atoms at the boundary have hybrids pointing toward the strictly localized region on the

Published as part of the special collection of articles "Festschrift in honour of P. R. Surjan".

Electronic supplementary material The online version of this article (doi:10.1007/s00214-015-1734-3) contains supplementary material, which is available to authorized users.

✉ György G. Ferenczy
ferenczy.gyorgy@ttk.mta.hu

[1] MTA-BME Lendület Quantum Chemistry Research Group, Department of Physical Chemistry and Materials Science, Budapest University of Technology and Economics, P.O. Box 91, Budapest 1521, Hungary

[2] MTA-SZTE Supramolecular and Nanostructured Materials Research Group, University of Szeged, Dóm tér 8, Szeged 6720, Hungary

[3] Medicinal Chemistry Research Group, Research Centre for Natural Sciences, Hungarian Academy of Sciences, Magyar Tudósok Körútja 2, Budapest 1117, Hungary

one hand, and toward the delocalized region on the other hand. These latter hybrids contribute to the basis of the delocalized central subsystem. This computational scheme was shown to be appropriate to study various properties of extended systems like rotational barriers, protonation energies and conformational energy differences [1–3]. Furthermore, following the idea of Warshel and Levitt [4] strictly localized orbitals and predefined hybrids provided means for separating the covalently bound subsystems in several QM/MM schemes. In the local self-consistent field (LSCF) method [5] an atom on the boundary has a single hybrid orbital that forms a strictly localized molecular orbital with an atom in the QM subsystem, while other electrons of the atom are not treated explicitly; the interaction of this atom with atoms in the MM subsystem is described by a classical force field. The strictly localized molecular orbital is not included in the self-consistent field procedure, rather its coefficients are kept frozen at some predefined values. A similar separation with frozen localized orbitals but using a different orbital equation and specific parametrization is proposed by Friesner et al. [6, 7]. Another related approach, the generalized hybrid orbital (GHO) method [8, 9] puts hybrid orbitals on the QM boundary atom and includes the hybrid directed toward the QM subsystem in the SCF procedure, while other hybrids are kept fixed.

Other ways to separate covalently bound QM and MM subsystems have also been proposed, and most notable among them is the link atom approach. It cuts the bonds at the QM–MM interface and saturates the dangling bonds of the QM subsystem typically by hydrogen atoms. The principal advantage of the link atom approach is that its computational realization can be reduced to almost standard QM and MM calculations that greatly facilitates its implementation into existing codes. On the other hand, the link atom approach introduces extra atoms not present in the original system, and this creates artifacts that requires special considerations in the computation. Nevertheless, early comparisons of the link atom and the LSCF methods concluded that both can give valuable results when applied with precaution [10].

Early QM/MM methods were introduced at a semiempirical level, and later they were generalized to ab initio and DFT schemes. Such a generalization is typically straightforward for the link atom approach but poses difficulties for methods using frozen localized orbitals. The principal difficulty is that these methods assume orthogonality between the frozen and the optimized orbitals, and this is not automatically guaranteed at ab initio level. It is not straightforward to set up orbital equations that include the effect of frozen orbitals and give solutions that are orthogonal to these orbitals. A possible approach to circumvent this difficulty is to orthogonalize the basis functions of the orbitals to be optimized to the frozen orbitals [9, 11]. Alternative propositions include the neglect of the overlap between the frozen and optimized orbitals [9] or the explicit inclusion of the orbital overlap [12]. The orthogonality requirement can also be in included in the orbital equation. This was realized in Ref. [6] in the framework of a specific model with frozen localized orbitals. We have recently proposed [13] the application of the Huzinaga equation [14] to ensure the orthogonality of the optimized and frozen orbitals. Although the Huzinaga equation was originally proposed to calculate valence orbitals orthogonal to frozen core orbitals [15], it was shown [13] that the equation is well suited to calculate QM/MM wave functions with optimized orbitals orthogonal to the strictly localized frozen orbitals separating the covalently bound QM and MM subsystems. Having established the validity of this approach, it is highly desirable to implement it in a computer code that, first, extends its applicability with various techniques to a wide range of problems and, second, makes it conveniently available for the scientific community.

We selected the Amber [16, 17] molecular mechanics and the Mrcc [18] quantum chemical codes to develop a versatile and user-friendly QM/MM program which is freely available for academic purposes. The choice of Amber is motivated by its capabilities that include molecular mechanics, molecular dynamics, and techniques that allow the efficient calculation of free energies. Since the QM/MM program is organized in a way that the MM code drives the calculation and the input instructions are primarily based on the MM code, the widespread use of Amber ensures that the resulting QM/MM code can be used with reasonable extra effort for those familiar with Amber. It is also to be noted that although force fields in neither Amber, nor the Amber–Mrcc code restrict the use of force fields to the Amber force field, its application in a QM/MM code is expected to be advantageous owing to the charge derivation scheme that guaranties a sensible electrostatic potential in the QM region. The Mrcc code was selected for the QM region owing to its highly efficient implementation of local correlation techniques that are beneficial for calculating reaction mechanisms, a field with primary importance for QM/MM applications.

It has to be noted that the link atom method and the frozen localized orbital method require significantly different approaches in their implementation into existing computer codes. The link atom method basically performs standard MM and QM calculations, and it is the generation of the subsystems and the communication between the QM and MM programs that require special attention and coding. This is the reason, while interfaces connecting various MM and QM programs [19–24] can be developed, and only small modifications in the original codes are necessary to be introduced. The situation is different for the frozen localized orbital method where specific orbital equations

are to be used, and this requires more intensive modifications in the QM code. On the contrary, the adaptation of the MM code is more straightforward, and it is without the complications caused by the presence of extra atoms appearing in the link atom method.

In the forthcoming discussion, we present our results in the combination of the Amber and Mrcc codes. Both theoretical considerations and practical issues are discussed together with the results of test calculations.

2 Theory

Our QM/MM code uses frozen strictly localized orbitals to separate the covalently bound QM and MM subsystems. Since this method has been described in detail in Ref. [13], here only a summary of the most important features of the method are recapitulated.

The QM and MM regions are bound with a strictly localized molecular orbital (SLMO) (see Fig. 1). This is realized by defining an MM host (MMH) atom (which is also known as frontier atom in the literature) at the border of the QM and MM subsystems so that it is connected to an QM host (QMH) atom with a bond orbital whose basis functions are located exclusively on the two atoms. The QMH atom contributes to the SLMO with one electron, and its other electrons are part of the optimized wave function. The MMH atom of the SLMO also contributes with a single electron to the SLMO, while its other valence electrons are not treated explicitly.

The SLMO is not optimized, rather its coefficients are kept fixed at certain predefined values. These values are determined by calculations performed for model molecules that include a chemically similar bond to the SLMO (see later). Note that the core electrons of the MMH atom are also treated explicitly and their orbitals are taken from the calculations performed for deriving the valence SLMOs. MMH core orbitals can also be included in the set of orbitals to be optimized without significant effect on the calculated wave function and properties [13, 25]. The LSCF method allows the use of further molecular orbitals on the MMH atom, and it was demonstrated that the explicit treatment of the delocalized nitrogen lone pair of an amide bond makes it possible to separate the QM and MM subsystems along the amide bond and to produce good-quality potential energy surfaces [26, 27].

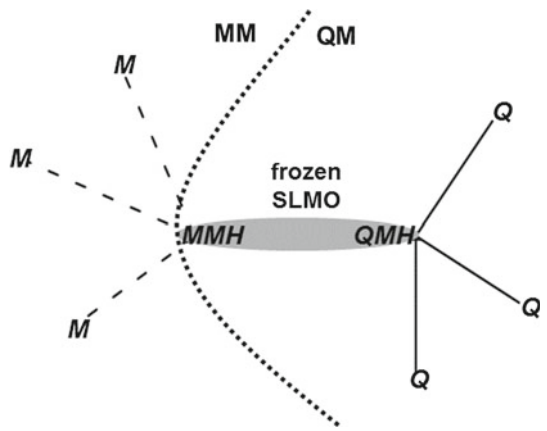

Fig. 1 Separation of the QM and MM subsystems by a frozen strictly localized molecular orbital (SLMO). QM and MM atoms are designated by **Q** and **M**, respectively. **QMH** is the QM host atom and **MMH** is the MM host atom, and the latter is also called frontier atom

It is convenient to use optimized orbitals that are orthogonal to the frozen SLMOs and this is achieved by calculating the optimized orbitals with the Huzinaga equation [14]. This can be written as

$$[\mathbf{F} - \mathbf{S}\mathbf{R}^{\mathrm{f}}\mathbf{F} - \mathbf{F}\mathbf{R}^{\mathrm{f}}\mathbf{S}]\mathbf{C}^{\mathrm{a}} = \mathbf{S}\mathbf{C}^{\mathrm{a}}\mathbf{E}^{\mathrm{a}}, \quad (1)$$

where **F** is the Fock matrix, **S** is the basis set overlap matrix, $\mathbf{C}^{\mathrm{a}}$ includes the coefficients of the orbitals to be optimized, $\mathbf{E}^{\mathrm{a}}$ is the diagonal matrix of the corresponding eigenvalues and $\mathbf{R}^{\mathrm{f}}$ projects onto the space of the frozen orbitals. Assuming orthonormal frozen orbitals $\mathbf{R}^{\mathrm{f}} = \mathbf{C}^{\mathrm{f}}(\mathbf{C}^{\mathrm{f}})^{\dagger}$, where $\mathbf{C}^{f}$ contains the coefficients of the frozen orbitals. The role of the last two terms on the left-hand side of Eq. (1) is to shift the eigenvalues of the frozen orbitals to positive values and to guaranty that the lowest eigenvalue orbitals, those that are used to construct the Fock matrix of the next iteration cycle, are orthogonal to the space spanned by the frozen orbitals. Three notes are appropriate here. First, the frozen orbitals are expected to appear with positive eigenvalues in Eq. (1) if they are reasonable approximations to the exact eigenfunctions of **F**. Second, the basis functions of the optimized orbitals have to include those of the SLMOs since this ensures that orthogonality between the optimized orbitals and the SLMOs could be achieved. Third, the subsystems can be connected by several SLMOs that are typically not orthogonal, and then the projector in Eq. (1) takes the form of $\mathbf{R}^{\mathrm{f}} = \mathbf{C}^{\mathrm{f}}(\sigma^{\mathrm{f}})^{-1}(\mathbf{C}^{\mathrm{f}})^{\dagger}$, where σ^{f} is the overlap matrix of the SLMOs.

It was found that the calculation of the optimized orbitals by Eq. (1) is advantageous when other valence electrons of the MMH atom are represented by point charges placed on the bonds connecting the MMH atom with MM atoms. In case of an sp3 carbon MMH atom, three negative charges, called bond charges, are placed on the three bonds connecting the MMH atom with three MM atoms, while the fourth valence electron is involved in the SLMO. The magnitude of the bond charges (q_{bond}) are determined so that

$$\sum q_{\mathrm{bond}} + q_{\mathrm{core}}^{\mathrm{MMH}} + (-3) = Q_{\mathrm{MM}}^{\mathrm{MMH}}, \quad (2)$$

where q_{core}^{MMH} is the MMH atom core charge, -3 accounts for the two core electrons and the single valence electron included in the SLMO, and Q_{MM}^{MMH} is the MM charge of the MMH atom. The magnitude of q_{core}^{MMH} is an adjustable parameter that determines q_{bond} via Eq. (2). Moreover, the position of the bond charges is, in principle, an additional parameter. These charges are placed at the midpoint of the bond formed by the MMH and the MM atom adjacent to the boundary to provide a sensible representation of the MMH valence electrons which are not accounted for quantum mechanically.

The MM parameters at the boundary are used similarly as they are implemented in AMBER for the link atom approach. Internal coordinate force field terms of bonds, angles, and dihedral angles are used if any MM or MMH atom is involved. Electrostatic and van der Waals (vdW) interactions are also calculated in accordance with the AMBER force field scheme [28]. Detailed description of the retained bonded and nonbonded terms, in particular the interactions with bond charges, is discussed in the following section.

3 Implementation

In this section, specific features of the QM/MM code obtained with the joint implementation of the molecular mechanics program Amber and the quantum mechanics program Mrcc are presented. The coupling of the two codes is mainly based on the interface of Walker et al. [23]; therefore, relevant parts of their work will be reviewed with special emphasis on the similarities and differences of the link atom and the frozen strictly localized molecular orbital approaches. In the Amber–Mrcc interface, as in most implementations of MM and QM program couplings [24], the necessary data exchange is realized by writing and reading of files. All tasks, except the solution of the QM orbital equations, are driven by Sander, the molecular dynamics engine program of Amber.

In order to preform a QM/MM calculation, the first step for the user is to prepare a parameter and topology file, a coordinate file, and a control file which are required for a regular molecular dynamics (MD) simulation. This procedure may not be straightforward in the case of QM/MM runs, because the QM subsystem may not be represented by classical chemical structures and corresponding force field parameters. Nevertheless, the construction of the topology file facilitates the QM/MM run since it allows the use of the MM program infrastructure with minimal modifications; moreover, it may support system preparations, for example, MM energy minimization or equilibration. It is worth also noting that the only consequence of the topology definition to the QM subsystem is the assignment of vdW parameters. Owing to the short-range nature of the vdW interactions, an appropriate choice of the QM subsystem can minimize the effect of potentially inconsistent parameters.

Changes in the control file with respect to a standard MM setup consist of marking the QM atoms, specifying the charge and multiplicity of the QM region as well as defining the theory and basis set. For compatibility reasons, only the most general Mrcc keywords can be denominated in the control file; however, the user can also set up the full range of options by referring in the control file to an MRCC template file. Having done these arrangements, all other procedures required for a simulation are automatically executed by Sander for the link atom (LA) approach and for the Huzinaga equation-based local self-consistent field (HLSCF) method, as well.

3.1 Link atom approach

In the case of link atom approach, the procedure for an AMBER-MRCC calculation closely follows that formerly implemented in Sander. Namely, it automatically determines the place where to cut bonds and also positions the hydrogen atoms as a function of the QMH and MMH positions to saturate the dangling bonds of the QM subsystem. (In the context of the link atom approach the MMH and QMH atoms are those whose bond is cut.) It is important to note that the LA method produces a good-quality wave function when an apolar bond (e.g., bond between two sp3 carbon atoms) is cut; moreover, link atoms connected to a common host atom is disadvantageous owing to their short spatial separation The latter criterion is checked by the program, and hence the user cannot mark arbitrary QM subsystems; furthermore, both criteria are applied in the rules of automatic selection of model molecules for the HLSCF method (see later). After the link atoms are defined, bonded terms in the QM region are removed, and in the case of electronic embedding, the point charges are zeroed on the QM atoms as well as, to avoid overpolarization, on the MMH atoms. In order to preserve the total charge of the system, residual charges are distributed among the nonzero charges of the MM region; however, there are several schemes for both charge distribution and bonded term removal which can be specified by the user. If the MM energy terms are defined, an input file will be written for Mrcc by the Amber–Mrcc interface in every simulation step, which consists of QM atom coordinates, atomic numbers, MM point charges and their coordinates, and the controlling keywords. Mrcc is then executed via a system call, and after a successful run, the energy of the QM region and forces acting on atoms are written into an output file

which is parsed by the interface. Here we note that LA calculations are performed during the preparation of a HLSCF run to generate SLMOs in model systems.

3.2 Huzinaga equation-based local self-consistent field approach

In the HLSCF method, just as in the LA approach, the communication between AMBER and MRCC is carried out by writing and reading files. The major difference between the two boundary methods as described earlier is that in the case of HLSCF, the QM and MM regions are connected by a frozen SLMO. The coefficients of a frozen SLMO are taken from a molecule containing a QMH–MMH bond preferably in a chemical environment similar to that in the system studied. Therefore, the first step in order to determine the SLMO coefficients of a QMH–MMH bond is to choose a suitable model system. Model systems are generated automatically in our implementation using selection rules (see Sect. 3.2.2), but the user can also select atoms for the model systems manually using the previously mentioned template file. After the model systems are set, the SLMOs are automatically calculated without any user intervention (see Sect. 3.2.1) for every QMH–MMH bond, and both the outputs of model calculations and the SLMO coefficients are saved in files. Following these procedures, bonded terms, which are defined only by QM atoms are removed, thus the following MM bonds, angles, and dihedrals are retained:

$$\text{Bonds} = \text{MM}{-}\text{MM}, \text{MM}{-}\text{MMH}, \text{MMH}{-}\text{QMH}$$

$$\text{Angles} = \text{MM}{-}\text{MM}{-}\text{MM}, \text{MM}{-}\text{MM}{-}\text{MMH},$$

$$\text{MM}{-}\text{MMH}{-}\text{QMH}, \text{MMH}{-}\text{QMH}{-}\text{QM}$$

$$\text{Dihedrals} = \text{MM}{-}\text{MM}{-}\text{MM}{-}\text{MM}, \text{MM}{-}\text{MM}{-}\text{MM}{-}\text{MMH},$$

$$\text{MM}{-}\text{MM}{-}\text{MMH}{-}\text{QMH}, \text{MM}{-}\text{MMH}{-}\text{QMH}{-}\text{QM},$$

$$\text{MMH}{-}\text{QMH}{-}\text{QM}{-}\text{QM},$$

where MM and QM are MM and QM atoms, respectively, while QMH is a QM host atom and MMH is an MM host atom. Note that the MMH atom, which is treated specially in the electrostatic terms is handled as any other MM atom in the bonded terms.

The vdW and electrostatic contributions of the nonbonded terms are calculated as in the LA approach; however, only those electrostatic point charges are zeroed which are defined on QM atoms, and furthermore, the charge of the full system is preserved by distributing the residual charges over all remaining point charges. Following this procedure, the charge of MMH atom is redistributed according to Eq. (2): the MMH point charge is replaced by the q_{core}^{MMH} core charge of the MMH atom and the q_{bond} charges are automatically positioned at the midpoint of the bonds formed between the MMH and the MM atom adjacent to the MMH atom. Interactions of the q_{core}^{MMH} and q_{bond} charges with MM atoms are calculated as in the AMBER force field [28]: q_{core}^{MMH} and q_{bond} interact neither with MM charges adjacent to MMH nor with MM atoms adjacent to these atoms (1–2, 1–3 interactions). Furthermore, interactions with three bonds away from MMH are divided by a factor of 1.2. It is important to mention that the interactions between q_{core}^{MMH} and q_{bond}, just as any interaction including these charges are computed only by direct summation, and hence, periodic boundary conditions cannot be handled at this stage of development.

When the setup of the MM energy terms completed, similarly to the LA approach, an input file is written for MRCC by the interface and MRCC is executed. In the case of HLSCF, host atoms are flagged in the input file. The aim of these flags is to assign the previously calculated SLMO coefficients to the proper host atoms and to build the $\mathbf{C}^{\mathrm{f}}$ matrix from the strictly localized molecular orbitals. Using these orbitals the overlap matrix of the frozen molecular orbitals are evaluated as $\sigma = (\mathbf{C}^{\mathrm{f}})^{\dagger}\mathbf{S}\mathbf{C}^{\mathrm{f}}$. The inverse square root of the orbital overlap matrix is used to calculate the projector $\mathbf{R}^{\mathrm{f}} = \mathbf{C}^{\mathrm{f}}(\sigma^{\mathrm{f}})^{-1}(\mathbf{C}^{\mathrm{f}})^{\dagger}$ and then in each iteration cycle the Fock matrix and the Huzinaga matrix $\mathbf{F} - \mathbf{S}\mathbf{R}^{\mathrm{f}}\mathbf{F} - \mathbf{F}\mathbf{R}^{\mathrm{f}}\mathbf{S}$ are built. The diagonalization of the Huzinaga matrix according to Eq. (1) produces orbitals orthogonal to the frozen orbitals. When self-consistency is reached the calculated SCF energy is written in an output file which is parsed by the interface. As to the force evaluation, note that the gradients derived in Ref. [13] for the QM atoms are implemented and tested in MRCC; however, the QM/MM gradients are not available at this stage of development.

3.2.1 Automatic generation of frozen strictly localized orbitals

The coefficients of the frozen SLMOs can be taken from model molecules that contain a chemical bond similar to that of the SLMO. The basic idea for the generation of the orbital coefficients is that after identifying a bond connecting the QM and MM subsystems, a molecular graph containing this bond is cut from the system, and a QM calculation is performed for the model molecule generated from the molecular graph using the link atom approach. The wave function of the model molecule is calculated by taking into account the electrostatic potential of the point charges of the whole system (all atoms except those included in the model molecule). Note that during the calculation of the model molecule bonded and vdW contributions are not calculated which is rationalized by the fact that the only aim is to determine the polarized wavefunction of the model molecule; nevertheless, charge neutrality is still assured by various charge distribution schemes set by the user. The orbitals obtained are Boys [29] or Pipek–Mezey

[30] localized which is followed by the Boughton–Pulay algorithm [31] to select those atoms on which the orbitals are localized.

The first step of the Boughton–Pulay algorithm is that for each localized orbital, the atoms are ranked according to their gross Mulliken population. Starting from the atom with the largest Mulliken population, subspaces of atoms are defined by adding atoms of smaller and smaller Mulliken populations. For each subspace, the localized molecular orbital is truncated to the subspace, and the norm of the square of the difference of the original and the truncated function is calculated. The procedure is terminated when the norm drops below a threshold ϵ; hence, the localized orbitals are assigned automatically to atoms whose basis functions span the best subspace for given localized orbital. In the implementation of the HLSCF method, a $1 - \epsilon = 0.985$ completeness criteria was chosen.

After assigning atoms to localized orbitals, the core orbitals of the MMH atom and the single valence orbital connecting the QMH and MMH atoms are selected. SLMOs are generated and saved from selected localized molecular orbitals by removing contributions from all atoms except the QMH and MMH atoms.

3.2.2 *Selection of the model molecule*

The model molecules are generated from the list of atom pairs defining those chemical bonds that connect the QM and MM subsystems. Our task is to select a molecular graph for every such atom pair and close their dangling bonds with hydrogens in a way to satisfy the considerations written in the Link atom approach section. Starting from a given atom pair, we use an incremental, step-by-step forwarding procedure to extend the initial model (graph) in both directions (see Fig. 2). In this procedure only the non-H atoms are used, and the H atoms are added to the model after the selection of heavy atoms is completed. For the easier formulation of the rules of extension, we introduce the following naming convention. At a certain step of the incremental procedure, the *base atoms* of the model molecule are those atoms that are connected to other atoms (*border atoms*) not included in the model. The basic idea of the model molecule selection is to find the smallest molecular subgraph every base atom of which is connected to the remaining part of the system by only one single bond. In the currently implemented algorithm, only single bonds can be cut to define the model molecule (*breakable bonds*), and all the other bond types are *non-breakable*. However, less restrictive definitions of the breakable bonds can also be applied.

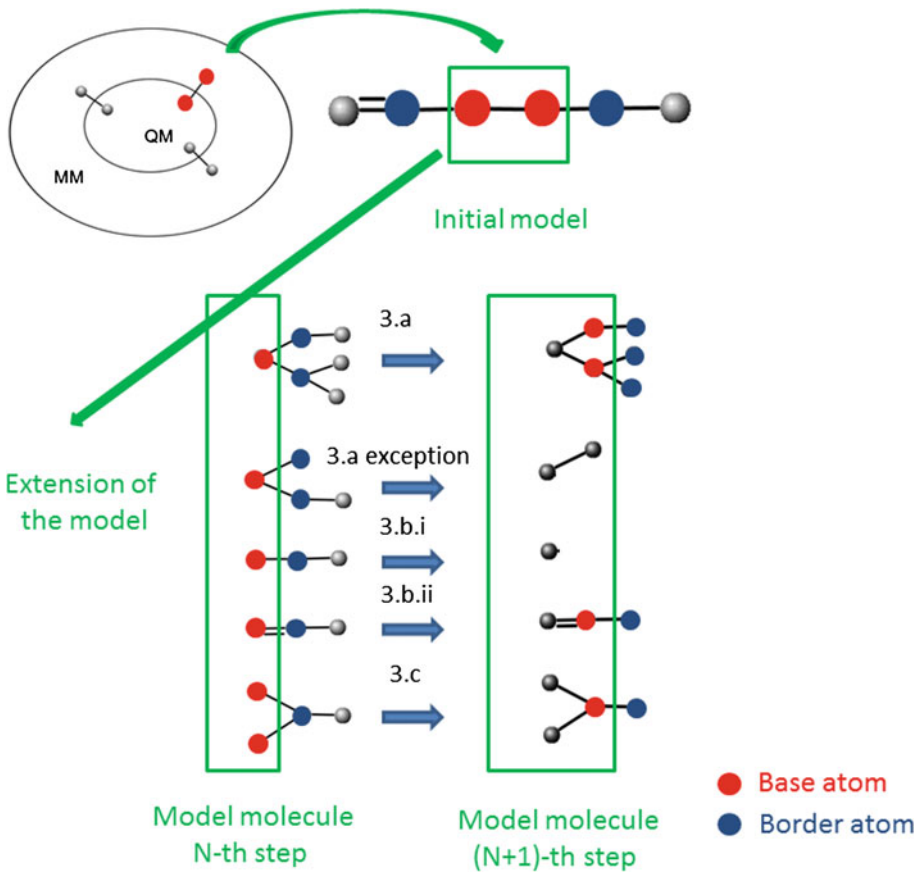

Fig. 2 Schematic representation of the incremental procedure used for the step-by-step extension of the model system. The rules applied in the *N*th step are also identified. See the text for the details

The main steps of the algorithm are demonstrated in Fig. 2 and can be summarized as follows.

1. Repeat the model molecule search below for every atom pairs defining single bonds between the QM and MM subsystems
2. Find the base atoms and the border atoms connected to them.
3. Extend the model molecule using the following rules

   (a) If more than one border atom is connected to a base atom, then all of them are attached to the model molecule, unless all but one base atom–border atom connections are terminal (the border atoms have no further bonds to heavy atoms not included in the model system). In this case, only the terminal atoms are added to the model system, and the remaining one bond is cut and it is not used in the subsequent base atom–border atom search.
   (b) If only one border atom is connected to a base atom and

(i) this bond is a breakable one, then terminate this extension path
(ii) this bond is a non-breakable one, then add its border atom to the model system.

   (c) If a border atom is connected to two different base atoms (crossing), then the common border atom is also attached to the model system.

4. If every base atom has at the most one non-terminal bond to the border atoms and this bond is breakable, and furthermore no crossings occur, then the model molecule is defined, otherwise go to step 2.
5. Add H atoms to terminate dangling bonds.

Examples indicating the selection of model molecules for several systems are presented as Supplementary Material. The described protocol was applied to generate model molecules in all calculation presented in the current contribution.

4 Sample calculations

In this section results obtained both with the widely used link atom approach and with the newly implemented Huzinaga equation-based local self-consistent field method are presented. Both QM/MM boundary methods were tested to model typical applications of hybrid methods. However, the systems selected are sufficiently small so that reference full QM calculations are feasible.

In all the calculations presented below, the wave function of the QM region was calculated with the Hartree–Fock–Roothaan equation for the LA approach and with the Huzinaga equation for the HLSCF approach. Pople-type Cartesian 6-31G* basis set [32] was used. The parameters defined in the ff14SB [28] and in the GAFF [33] force fields were used for peptide and hexanoic acid calculations, respectively, to evaluate the MM energy function. The MM parameters of the hexanoic acid were generated by the ANTECHAMBER program [34] using the AM1-BCC charge scheme [35, 36]. Input files were generated by using the Maestro [37] program and the TELEAP program which is part of the AMBERTOOLS package. Figures were prepared using Gnuplot [38] and Marvin [39].

As a first step, the full system was optimized at the HF/6-31G* level in all test cases, and then the obtained geometries were modified to perform single-point calculations along the defined reaction coordinates. The choice of the computational level for geometry calculations was motivated by generating reasonable geometries that are consistent with the calculations performed to test the QM/MM schemes. The tests were calculated in vacuum, without periodic boundary conditions and the cutoff for electrostatic and vdW terms was set to 999 Å. In the case of the link atom approach, the capping hydrogen atom was positioned 1.09 Å away from the QMH atom; furthermore, the residual charges, which were originated from the zeroing of the QM and MMH atoms, were distributed among all MM atoms. Those bonded terms which contained at least one MM or MMH atoms were retained. The SLMOs of the HLSCF method were only calculated for a single configuration, and these SLMO coefficients were used for all other configurations. This procedure was found to better reproduce reference results than the recalculation of the SLMOs for each individual configuration. We selected the configuration of the global potential minimum for calculating the SLMO coefficients. In this way, the SLMO coefficients are treated on an equal footing with the MM parameters in the sense that they both provide a constant environment for the rest of the QM subsystem. The SLMOs were generated with automatically selected model systems, using Boys localization and with the setup described for the link atom approach. The model systems utilized for the SLMO calculations are appended in the Supplementary information.

In all examples presented below, the effect of the QM subsystem size is investigated by varying the subsystem boundary. The boundary is defined by the bond cut by the subsystem separation. Note that "cut" in the LA approach indeed means bond cutting between the QM and MM subsystems and saturating the dangling bond of the QM

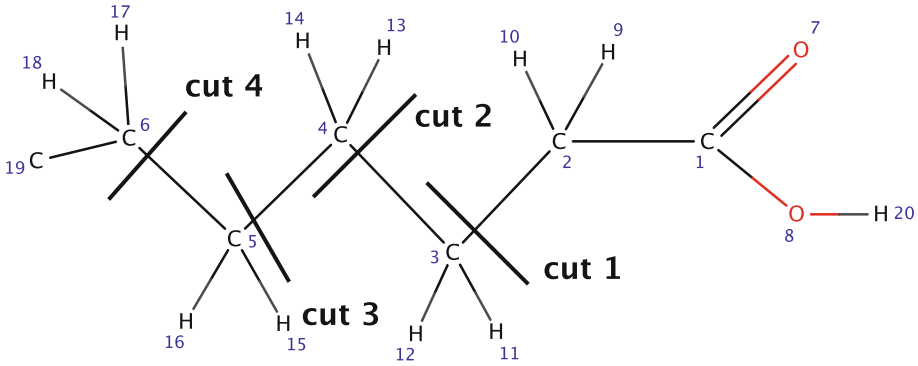

Fig. 3 System separation of the hexanoic acid

subsystem by a H atom. On the other hand, "cut" signifies a frozen SLMO in the HLSCF approach.

4.1 Deprotonation energy

The calculation of the deprotonation energy is a highly sensitive test for the HLSCF method since it requires the evaluation of the energy difference of differently charged systems. Therefore, the deprotonation energy of hexaonic acid was calculated both with the LA and the HLSCF approaches as a first test. Results were compared with the reference full QM calculations. As described above, the geometry of the natural hexaonic acid was first optimized using the reference method; however, the geometry of the deprotonated acid was obtained by simply removing the H_{20} hydrogen atom of the carboxyl group from the neutral form (see Fig. 3 for the numbering of atoms). Beside the same geometry of the two species, the MM subsystem and the SLMOs of the neutral hexanoic acid were also used for the deprotonated form to prevent the charge transfer between the QM and the MM subsystems.

The convergence of the QM/MM methods to the full QM calculations was investigated by gradually increasing the size of the QM subsystem. The various QM and MM subsystems are shown in Fig. 3. The core charge of Eq. 2 was determined in a trial-and-error procedure in which the absolute error belonging to largest QM subsystem, cut4 in Fig. 3, was minimized. It was found that the optimal core charge is +5.5, and this parameter was also used in the subsequent calculations.

The results of the LA and the HLSCF methods were compared with the reference, and the errors are presented in Table 1. The data show that the error decreases as the QM subsystem increases; hence, both QM/MM methods converge to the full QM calculation, and moreover, the errors are less than 0.1 kcal/mol if the largest QM subsystem (cut4) is used. For smaller QM subsystems the errors of the LA approach is smaller than those of the HLSCF approach. The larger HLSCF errors stem from the presence of a large positive MMH core charge and negative bond charges that have significant interactions with the site of deprotonation. It was found that the optimal charges depend on the subsystem separation and on the other parameters of the calculation. Optimal bond charges were found to depend also on whether vertical or adiabatic ionization energies are calculated and on whether the same or different SLBOs are used for the neutral and deprotonated species. It is expected that the force field and in particular the MM charges also affect the optimal choice of the bond charges. Results may benefit from the use of a polarizable force field, and polarization is expected to be increasingly important with the decrease in the QM subsystem. It is worth emphasizing that the sensitivity of the deprotonation energy on these parameters in the HLSCF approach is a consequence of calculating the energy difference of differently charged system. On the other hand, these parameters were found to have much less effect in typical QM/MM calculations where energies of systems with equal total charges are compared. This type of examples is presented in the forthcoming sections. In all these examples, an MMH core charge of 5.5 was used, but we note that this charge can also be treated as an adjustable parameter.

Table 1 QM/MM errors of deprotonation energies for the hexanoic acid molecule with various system separation (see Fig. 3)

System	LA (kcal/mol)	HLSCF (kcal/mol)
cut1	−1.65	−6.18
cut2	−0.62	−1.51
cut3	−0.19	−1.48
cut4	0.04	−0.02

4.2 Conformational energies

In the second test example, the rotation energy profile of the carboxyl group of hexaonic acid was investigated. Note that this is a challenging test because the energy change due to rotation is very small (only a few kcal/mol). Energies were calculated as a function of the C_3–C_2–C_1–O_7

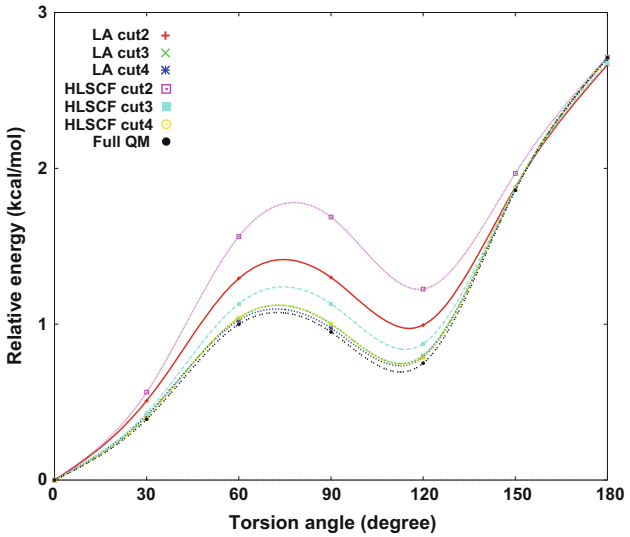

Fig. 4 Energy of the hexanoic acid molecule as a function of the rotation of carboxyl group

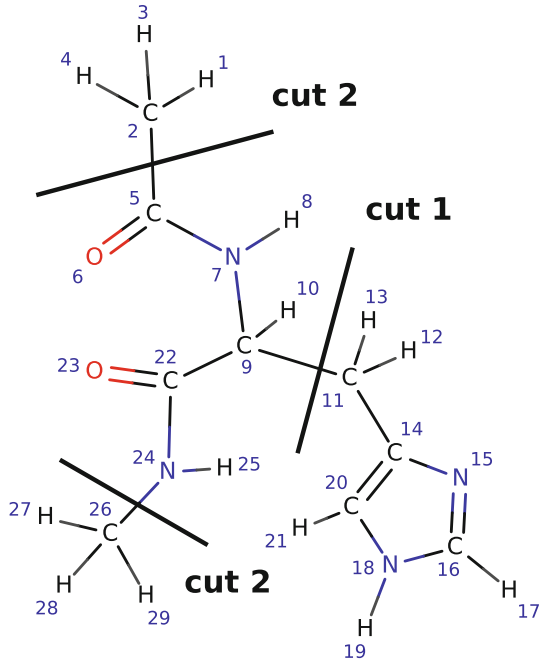

Fig. 5 System separation of the Ace–His–Nme system

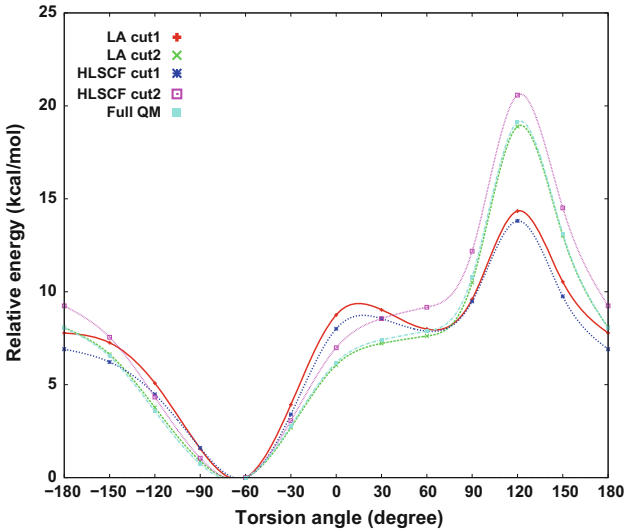

Fig. 6 Energy of the Ace–His–Nme molecule as a function of the rotation of the imidazole group

dihedral angle (see Fig. 3 for the atom numbering). Various system separations were applied in order to study the effect of QM subsystem size on the quality of the results.

Relative energies with respect of the lowest energy conformer as obtained with the LA, HLSCF and full QM calculations are presented in Fig. 4. The data show that both QM/MM methods reproduce the rotation energy curve of the reference method well; furthermore, as the QM subsystem increases, the absolute error decreases, and hence, the results of both approaches converge to that of the QM calculation. In the cases of cut3 and cut4, the estimation of the rotation energy profile is highly satisfactory since the largest absolute errors are within 0.1 kcal/mol. For the smallest QM subsystem (cut2) where the subsystem boundary is separated by a single bond from the rotating C–C bond, the maximum errors are few tenth of kcal/mol corresponding to 40–60 % relative errors and it larger for the HLSCF method. Summarizing the results, both approaches well reproduces the subtle energy changes of the reference calculations when the subsystem boundary is separated by more than a single bond from the rotating bond.

Another rotational energy curve calculation was performed for the Ace–His–Nme system by rotating the imidazol group. Single-point energy calculations were preformed varying the C_9–C_{11}–C_{14}–N_{15} dihedral angle (see Fig. 5 for the numbering of the atoms) by 30°. In order to test the effect of the QM subsystem size on the quality of the QM/MM results, calculations were performed with two QM–MM boundaries; a smaller (cut1) and a larger (cut2) QM region was chosen (Fig. 5). In the case of cut1, the boundary is at the bond between C_α (C_9) and C_β (C_{11}), while for cut2, only the methyl groups of the acetyl and *N*-methyl groups were included in the MM subsystem, and hence, the boundary is at the bonds between C_2–C_5 and N_{24}–C_{26}.

The relative energies with respect to the lowest energy conformer are shown for the LA, HLSCF, and reference full QM calculations in Fig. 6. (Tabulated data are available as Supplementary information.) The QM/MM methods well reproduce the shape of the energy profile of the reference for both system separations. Furthermore, the

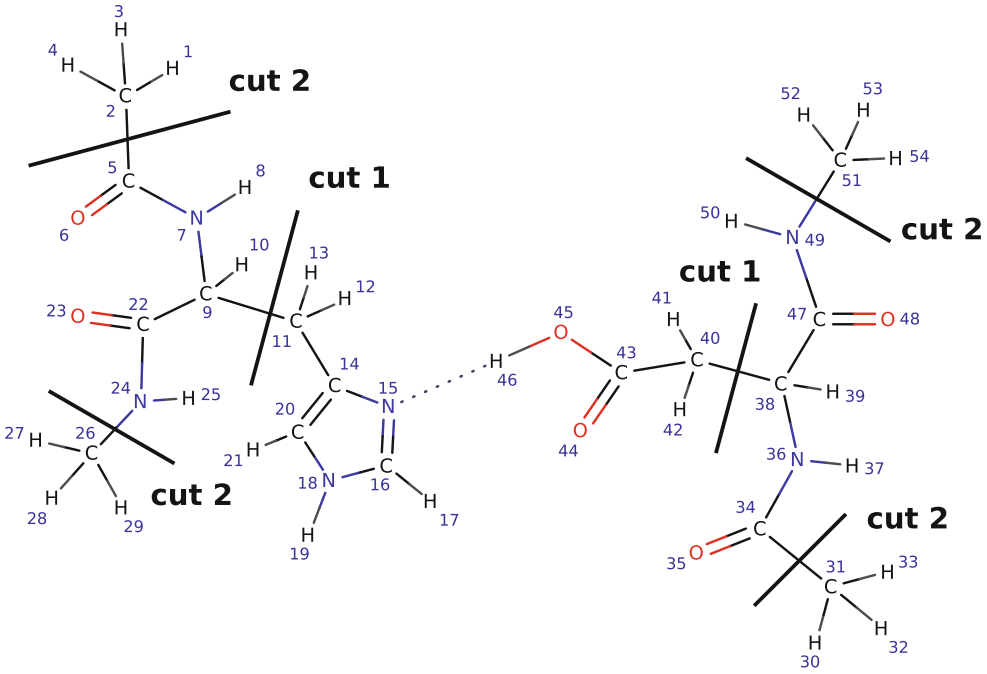

Fig. 7 System separation of the Ace–His–Nme and Ace–Asp–Nme system

results of both methods improve with larger QM subsystems. In the case of the smaller QM subsystem, cut1 in Fig. 6, the mean absolute error and the largest error are 1.5 and 4.8 kcal/mol, respectively, for the LA method, while they are 1.5 and 5.3 kcal/mol, respectively, for the HLSCF method. Note that MM dihedral parameters contribute to the obtained energies for this small QM subsystem. Increasing the size of the QM region decreases both the mean and the maximum error; 0.2 and 0.3 kcal/mol for the LA and 1.0 and 1.5 kcal/mol for the HLSCF method are obtained. In summary, it was found that both methods are able to reproduce the reference results for the rotation of the imidazole group within 5 % relative error when the amide bonds are included in the QM subsystems and thus the subsystem boundaries are separated from the rotating bond by 3 bonds.

4.3 Proton transfer energy curve

The fourth example comprises an Ace–His–Nme and a Ace–Asp–Nme peptide, where the proton transfer between the Asp and His residues was investigated. In this reaction, the oxygen(C_{45})–hydrogen(H_{46}) distance in the Asp residue was set as the reaction coordinate (see Fig. 7. for the numbering of the atoms). Single-point energy calculations were preformed as the starting oxygen–hydrogen distance (0.8 Å) was incremented by 0.1 Å. The relative energies with respect to the minimum of the potential energy surface are reported.

Just as in the third example, the effect of the QM subsystem size was investigated by choosing a smaller (cut1) and a larger (cut2) QM region. In the case of cut1, bonds between the C_α ($C_{9,His}$, $C_{38,Asp}$) and C_β ($C_{11,His}$, $C_{40,Asp}$) connect the QM and MM subsystems, while in cut2 only the methyl groups were included in the MM region; hence, the system was separated along the bonds $C_{2,His}$–$C_{5,His}$ and $N_{24,His}$–$C_{26,His}$, as well as $C_{31,Asp}$–$C_{34,Asp}$ and $N_{49,Asp}$–$C_{51,Asp}$ (Fig. 7).

Results of the LA and HLSCF approaches together with the reference full QM calculation are shown in Fig. 8. (Tabulated data are available as Supplementary information.)

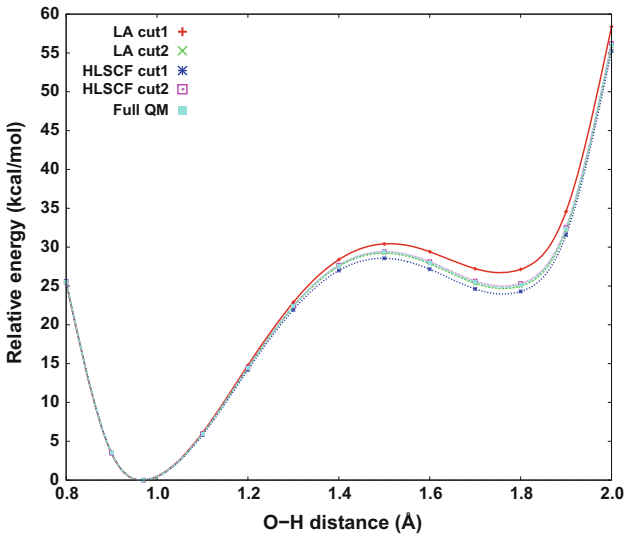

Fig. 8 Energy of the Ace–His–Nme and Ace–Asp–Nme system as a function of the proton from the oxygen of Asp

As in the previous test, both QM/MM boundary methods well approximate the reference; moreover, the quality of the energy curves also improves as the size of the QM subsystem increases. In the case of cut1, the mean absolute error and the error of barrier height at 1.5 Å are both 1.1 kcal/mol for the LA method, whereas these errors are 0.6 and 0.8 kcal/mol, respectively, for the HLSCF method. The positions of the two minima are also very well reproduced. Applying a larger QM region (cut2), both methods approximate the reference even better: For both methods, both the mean error and the error at the potential barrier are 0.1 kcal/mol (well below 1 %). Summarizing the results, it was found that the both methods perform well even with the smaller QM subsystem, and they reproduce both the positions and the relative heights of the reference minima extremely well with the larger QM subsystem.

5 Conclusions

A mixed QM/MM program is developed and tested with sample calculations. The coupling of the molecular mechanics program Amber and the quantum mechanics program Mrcc is based on the interface of Walker et al. [23]. Besides the traditional link atom approach, the Huzinaga equation-based local self-consistent field method was also implemented in the Amber–Mrcc code. In addition to the implementation of the Huzinaga equation, an automatic model system selector algorithm was also developed, which enables the automatic generation of the required strictly localized molecular orbital coefficients without any user intervention. This is an important step toward an effective and user-friendly QM/MM code since the necessity of the generation of system specific frozen SLMOs was considered as an obstacle that is eliminated by the proposed general method to derive the SLMOs.

The current implementation makes it possible to extensively test the HLSCF method, to analyze the effect of its parameters and to compare its results with those of the link atom and of the full QM calculations.

It was found from the deprotonation energy and from the rotational energy profile of the hexanoic acid that both boundary methods monotonously converge to the full QM calculations with increasing QM subsystem size. Calculations performed for peptides with various QM subsystem sizes also confirm this conclusion. The deprotonation energy was reproduced within a few tenth of kcal/mol by both boundary methods when the subsystem boundary is separated from the site of deprotonation by five bonds. The HLSCF results were found to be sensitive to the charge parameters at the boundary, and this sensitivity is attributed to the calculation of the energy difference of differently charged systems. The potential energy curves calculated by rotating the carboxyl group of the hexanoic acid in one example, and the imidazole group in the Ace–His–Nme peptide in the other example showed that the reference QM results are well reproduced by both methods with a maximal error not exceeding 5 % (1 kcal/mol and less then 0.1 kcal/mol in the two examples) when the rotating bond is separated from the QM–MM boundary by three bonds. The proton transfer energy curve between an Asp and His residues was very well reproduced considering both the positions and the energies of the minima. Even with a subsystem boundary separated by two bonds from the proton acceptors, the error is within 2 kcal/mol (7 %) and it reduces significantly, to less than 0.1 kcal/mol when the QM subsystem is further extended by three bonds.

The results obtained are in line with former studies [10] that compared the link atom and the LSCF approaches at semiempirical level and concluded that they give comparable results when applied cautiously. However, the LSCF approach is conceptually more appealing and its current Huzinaga equation-based implementation allows for the first time to perform calculations at the ab initio level without orthogonalizing the basis set to the frozen orbitals. Further developments, such as gradient calculations, inclusion of electron correlation effects from the QM side and the treatment of periodic boundary conditions and to perform molecular dynamics simulations on the MM side will be performed. These developments will allow a more thorough exploration of the optimal parameters of the HLSCF method with the aim of providing a versatile QM/MM tool to the community.

Acknowledgments This paper is dedicated to Professor Péter R. Surján on the happy occasion of his sixtieth birthday. M.K. expresses his gratitude to Professor Surján for mentoring him at the early stages of his career and for continuous support. G.G.F. is grateful to Professor Peter R. Surjan for his contribution to creating a highly motivating research atmosphere and for his friendly support the author enjoyed as a PhD student. The computing time granted on the Hungarian HPC Infrastructure at NIIF Institute is gratefully acknowledged. The research work has been accomplished in the framework of the "BME R+D+I project," supported by the grant TÁMOP 4.2.1/B-09/1/KMR-2010-0002. The authors are grateful for the financial support from the Hungarian Scientific Research Fund (OTKA, Grant No. K111862).

References

1. Náray-Szabó G, Surján P (1983) Chem Phys Lett 96:499–501
2. Ferenczy GG, Rivail JL, Surján PR, Náray-Szabó G (1992) J Comput Chem 13:830–837
3. Náray-Szabó G, Surján P (1985) Theochem 123:85–95
4. Warshel A, Levitt M (1976) J Mol Biol 103:227–249
5. Théry V, Rinaldi D, Rivail JL, Maigret B, Ferenczy GG (1994) J Comput Chem 14:269–282
6. Philipp DM, Friesner RA (1999) J Comput Chem 20:1468–1494
7. Murphy RB, Philipp DM, Friesner RA (2000) J Comput Chem 21:1442–1457

8. Gao J, Amara P, Alhambra C, Field MJ (1998) J Phys Chem A 102:4714–4721
9. Pu J, Gao J, Truhlar DG (2004) J Phys Chem A 108:632–650
10. Reuter N, Dejaegere A, Maigret B, Karplus M (2000) J Phys Chem A 104:1720–1735
11. Assfeld X, Rivail JL (1996) Chem Phys Lett 263:100–106
12. Ferenczy GG (2013) J Comput Chem 34:862–869
13. Ferenczy GG (2013) J Comput Chem 34:854–861
14. Huzinaga S, Cantu AA (1971) J Chem Phys 55:5543–5549
15. Huzinaga S (1995) Can J Chem 55:619–628
16. Case DA, Babin V, Berryman JT, Betz RM, Cai Q, Cerutti DS, Cheatham TE III, Darden TA, Duke RE, Gohlke H, Goetz AW, Gusarov S, Homeyer N, Janowski P, Kaus J, Kolossváry I, Kovalenko A, Lee TS, LeGrand S, Luchko T, Luo R, Madej B, Merz KM, Paesani F, Roe DR, Roitberg A, Sagui C, Salomon-Ferrer R, Seabra G, Simmerling CL, Smith W, Swails J, Walker RC, Wang J, Wolf RM, Wu X, Kollman PA (2014) AMBER 14. University of California, San Francisco
17. Salomon-Ferrer R, Case AA, Walker RC (2013) WIREs Comput Mol Sci 3:198–210
18. Mrcc, a quantum chemical program suite written by Kállay M, Rolik Z, Csontos J, Ladjánszki I, Szegedy L, Ladóczki B, Samu G See also Rolik Z, Szegedy L, Ladjánszki I, Ladóczki B, Kállay M (2013) J Chem Phys 139:094105, as well as: http://www.mrcc.hu
19. Woodcock HL, Hodosceck M, Gilbert ATB, Gill PMW, Schaefer HF, Brooks BR (2007) J Comput Chem 28:1485–1502
20. Torras J, Seabra GM, Deumens E, Trickey SB, Roitberg AE (2008) J Comput Chem 29:1564–1573
21. Hagiwara Y, Ohta T, Tateno M (2009) J Phys Condens Matter 21:064234
22. Metz S, Kästner J, Sokol AA, Keal TW, Sherwood P (2014) WIREs Comput Mol Sci 4:101–110
23. Götz W, Clark MA, Walker RC (2014) J Comput Chem 35:95–108
24. Riahi S, Rowley CN (2014) J Comput Chem 35:2076–2086
25. Loos P-F, Fornili A, Sironi M, Assfeld X (2007) Comput Lett 3:473–486
26. Monari A, Rivail J-L, Assfeld S (2013) Acc Chem Res 46:596–603
27. Monari A, Assfeld X (2001) In: Gorb L, Kuzmin V, Muratov E (eds) Application of computational techniques in pharmacy and medicine. Springer, New York
28. Cornell WD, Cieplak P, Bayly CI, Gould IR, Merz KM Jr, Ferguson DM, Spellmeyer DC, Fox T, Caldwell JW, Kollman PA (1995) J Am Chem Soc 117:5179–5197
29. Boys SF (1960) Rev Mod Phys 32:296–299
30. Pipek J, Mezey P (1989) J Chem Phys 90:4916–4926
31. Boughton JW, Pulay P (1993) J Comput Chem 14:736–740
32. Hehre WJ, Ditchfield R, Pople JA (1972) J Chem Phys 56:2257–2261
33. Wang J, Wolf RM, Caldwell JW, Kollman PA, Case DA (2004) J Comput Chem 25:1157–1174
34. Wang J, Wang W, Kollman PA, Case DA (2006) J Mol Graph Model 25:247–260
35. Jakalian A, Bush BL, Jack DB, Bayly CI (2000) J Comput Chem 21:132–146
36. Jakalian A, Jack DB, Bayly CI (2002) J Comput Chem 23:1623–1641
37. Schrödinger Release 2015–1: Maestro, version 10.1, Schrödinger, LLC, New York, NY, 2015
38. Williams T, Kelley C (2013) Gnuplot: an interactive plotting program. http://www.gnuplot.info. Last Accessed 10 Dec 13
39. Marvin was used for drawing and displaying chemical structures, Marvin 9.22.0, 2014, ChemAxon. http://www.chemaxon.com

Theor Chem Acc (2015) 134:149
DOI 10.1007/s00214-015-1747-y

REGULAR ARTICLE

The exchange coupling between the valence electrons of the fullerene cage and the electrons of the N atoms in $N@C_{60}^{-1,3}$

L. Udvardi[1]

Received: 15 June 2015 / Accepted: 19 October 2015 / Published online: 17 November 2015

Abstract MCSCF calculations are performed in order to determine the exchange coupling between the 2*p* electrons of the N atom and the LUMOs of the fullerene cage in the case of mono- and tri-anions of $N@C_{60}$. The exchange couplings provided our calculations are in the range of 1.5 meV which is large compared to the hyperfine interaction. The strong coupling can explain the missing EPR signal of the nitrogen in paramagnetic anions.

Keywords Fullerene · Exchange coupling

1 Introduction

Since the discovery of the first endohedral fullerene [1], the variety of endohedral structures has been extended tremendously [2]. Many metal atoms can be encapsulated by using discharge techniques or ion implantation. In all cases, the metal atom interacts strongly with the fullerene and acts as an electron donor occupying an 'off-centered' position inside the cage. In contrast, the nitrogen in $N@C_{60}$ is situated at the center of the molecule and retains its $S = 3/2$ spin quartet atomic state [3, 4]. This amazing property of the encapsulated N atom triggered several research on its possible application in quantum computing and spin labeling. Several publications [5–8] studied the promise and limitations of using endohedral fullerenes as quantum information carriers. Mehring et al. [9] pointed out experimentally the entanglement of the nuclear spin and the electronic spin of the encaged N atom. A detailed review of group V endohedral fullerenes can be found in Ref. [10].

The changes in the characteristic EPR signal of the quartet electronic spin of the N atom make it an ideal probe for monitoring chemical reactions of C_{60} [11]. During the last decades, a great deal of excitement has been brought by the discovery of the superconductivity of the alkali-doped fullerenes. In this type of fullerene compounds, the valence electrons of the ionized alkali atoms partially occupy the bands formed by the LUMOs of the C_{60} molecules. The applicability of the quartet atomic state of the N atom as a spin label depends on the strength of the interaction between the 2*p* electrons of the N atom and the valence electron of the fullerene cage. An interaction which is small compared to the hyperfine interaction results in a line width effect of the EPR signal, and the $N@C_{60}$ is a good candidate for a spin labeling agent. In the case of strong coupling, the EPR signal of the system is completely changed and the lines corresponding to the valence electrons of the N atom are hard to identify in the signal of the paramagnetic system.

The interaction between the 2*p* electrons of the N atom and the valence electrons of the C_{60} can be described by a Heisenberg-like effective Hamiltonian $H_{\text{int}} = J\mathbf{S}_{\text{N}}\mathbf{S}_{\text{C}_{60}}$ where $\mathbf{S}_{\text{N}}$ and $\mathbf{S}_{\text{C}_{60}}$ denote the spin operator for the valence electrons of the N atom and for the C_{60}, respectively, and J is the exchange coupling characterizing the strength of the interaction. The aim of the present paper is to determine theoretically the exchange coupling appearing in the effective Hamiltonian. The exchange coupling plays a role in the description of the transport through magnetic molecules [12, 13], which is particularly interesting from the point of

Published as part of the special collection of articles "Festschrift in honour of P. R. Surjan".

✉ L. Udvardi
udvardi@phy.bme.hu

[1] Department of Theoretical Physics, Budapest University of Technology and Economics, Budafoki út 8, Budapest 1111, Hungary

view of spintronics. Recent developments in nanotechnology permit the investigation of tunneling spectra of individual magnetic endofullerene molecules [14].

2 Computational details

The calculations have been performed using the Gamess quantum chemical program package [15]. The proper description of the open-shell $N@C_{60}^{-1}$ and $N@C_{60}^{-3}$ anions requires multi-determinant wave functions. The restricted open-shell (ROHF) calculations in the Gamess package are accessible via the generalized valence bond (GVB) or the multi-configurational self-consistent field (MCSCF) methods using an appropriate active space. The energy of the anions of $N@C_{60}$ with different multiplicity has been determined by means of CAS SCF calculations where the active space is confined to the $2p$ orbitals of the nitrogen atom and the threefold degenerate LUMOs of the fullerene molecule. In order to improve the convergence of the MCSCF orbitals, the excitations from the orbitals of the nitrogen to the LUMOs of the cage were excluded from the active space applying the occupation restricted multiple active space [16] technique, and vice versa. However, expanding the active space with charge transfer excitations changed the energy of the different states with a negligible amount. The MCSCF treatment of the open-shell systems using such a small active space is practically equivalent to the ROHF level of calculations. The calculation has been performed using split valence 631g basis on the carbon atoms. For the better description of the week interaction between the encapsulated atom and the fullerene molecule [17], the basis on the N atom is extended by additional diffuse p orbitals and two d polarization functions (631+g(dd)). The proper description of the electronic structure of negatively charged species requires application of diffuse basis functions. However, in the present case, the excess charge is distributed uniformly among the 60 carbon atoms, and the lack of diffuse basis on the carbon atoms does not affect dramatically our results. In order to check the sensitivity of the exchange coupling to the applied basis, the calculations have also been performed with the Dunning's double zeta [18] and the split valence 631+g basis sets on the carbon atoms. Although the $N@C_{60}^{-1}$ anion undergoes a Jahn-Teller distortion [19] in the present study, the I_h point group symmetry is kept during the optimization of the geometry by averaging the three degenerate states corresponding to $S = 2$. The same molecular structure has been used to find the energy of the $S = 1$ states. For the triple anion $N@C_{60}^{-3}$, the geometry has been optimized at ROHF level in the high spin $S = 3$ state and it is retained during the calculations of the energy of the systems with different $\mathbf{S}^2$ eigenstates.

Table 1 Energies of $N@C_{60}^{-1}$ and $N@C_{60}^{-3}$ with excess electron(s) occupying the $2p$ orbitals of the N atom (*a*) and the LUMOs of the C_{60} molecule (*b*)

	Configuration	E_{total}(Hartree)	Δ E (eV)	
$N@C_{60}^{-1}$	$N2p^4C_{60}8t_{1u}^0\ S=1$	−2325.30365		(*a*)
	$N2p^3C_{60}8t_{1u}^1\ S=1$	−2325.37155	−1.84	(*b*)
$N@C_{60}^{-3}$	$N2p^6C_{60}8t_{1u}^0\ S=0$	−2324.74514		(*a*)
	$N2p^3C_{60}8t_{1u}^3\ S=3$	−2325.10707	−9.84	(*b*)

3 Results and discussions

It has been shown experimentally that in the highly reduced states of the $N@C_{60}$ the excess electrons occupy the LUMOs of the fullerene and the N atom inside the cage remains in spin quartet state [20, 21]. In an EPR experiment, the $N@C_{60}$ was stepwise reduced with lithium. Among the spectra of the anions the well-known three-line signal characteristic for the nitrogen nuclear spin $I = 1$ appeared only for the hexa-anion, indicating that the excess charges occupy the threefold degenerate t_{1u} orbitals of the fullerene cage [10]. In order to check the consistency of our calculations to the experimental findings, we performed a set of ROHF calculations on the mono- and tri-anions populating at first the $2p$ orbitals of the nitrogen and then populating the LUMOs of the C_{60}. The results are summarized in Table 1. The valence electrons of the nitrogen referred as $N2p$ in Table 1 occupy the $7t_{1u}$ orbitals of the endohedral complex between the $6h_u$ HOMO and $8t_{1u}$ LUMO of the C_{60} in agreement with the result of ref [23]. Rather different value for the one-electron energy of the $N2p$ orbitals is reported by Greer [24]. This discrepancy is originated from the different treatment of the open-shell problem as it is discussed in Ref. [25]. In the case of the mono-anion, the energy of the two triplet states were compared, while in the case of the triply ionized molecule the energy of the singlet state with fully occupied valence orbitals of N was compared to the high spin state of the $N@C_{60}^{-3}$. For both ions, the system with intact N atom was energetically more favorable in agreement with the EPR measurements [20, 21].

The interaction between the electrons of the nitrogen atom and the valence electrons on the C_{60} anion is described by a Heisenberg-like effective Hamiltonian:

$$\mathrm{H}_{\text{int}} = J\mathbf{S}_{\mathrm{N}}\mathbf{S}_{\mathrm{c}_{60}} \tag{1}$$

where J is the coupling constant, $\mathbf{S}_{\mathrm{N}}$ and $\mathbf{S}_{\mathrm{c}_{60}}$ are the spin of the nitrogen atom and the C_{60} anion, respectively. The interaction Hamiltonian in Eq. 1 can describe only low-energy excitations of the system; however, they are relevant

in the explanation of EPR measurements. The square of the total spin operator $\mathbf{S}^2 = (\mathbf{S}_\mathrm{N} + \mathbf{S}_{c_{60}})^2$ commutes with the Hamiltonian of the full system $H = H_\mathrm{N} + H_{C_{60}} + H_\mathrm{int}$, and consequently, its eigenvalue is a good quantum number. Expressing the interaction in terms of the spin of the subsystems and the spin of the whole molecule:

$$H_\mathrm{int} = \frac{1}{2}J\left(\mathbf{S}^2 - \mathbf{S}_\mathrm{N}^2 - \mathbf{S}_{c_{60}}^2\right) \tag{2}$$

the energy can be simply given as:

$$E_S = E_0 + \frac{1}{2}JS(S+1), \tag{3}$$

where E_0 denotes the energy of the separated systems and the subscript S indicates the explicit dependence of the energy on the multiplicity.

In the case of $\mathrm{N@C}_{60}^{-1}$ $S_N = 3/2$ and $S_{C_{60}} = 1/2$ spanning an eight-dimensional direct product space. The total spin can have the values of $S = 1$ or $S = 2$ with the corresponding energies

$$E_{S=1} = E_0 + J, \quad E_{S=2} = E_0 + 3J. \tag{4}$$

Comparing the energy of the triplet and quintet states, one can easily extract the exchange coupling as:

$$J = \frac{1}{2}(E_{S=2} - E_{S=1}) \tag{5}$$

The results of the MCSCF calculations using 631g and DH basis are summarized in Table 2. Although the application of the double-zeta basis resulted in considerably deeper total energy, the deviation of the exchange couplings is small.

In the case of the triply ionized $\mathrm{N@C_{60}}$, the valence electrons form a $S_{C_{60}} = 3/2$ state on the LUMOs of the fullerene molecule according to the Hund's rule. From the two quartet states, $\mathbf{S}_N$, $\mathbf{S}_{C_{60}}$, four eigenstate of the $\mathbf{S}^2$ operator can be constructed with the spin of $S = 0, 1, 2, 3$, respectively. The corresponding energies as a function of S must be on a parabola according to Eq. 3. The results provided by the MCSCF calculations using three different basis sets are shown in Fig. 1. The energies can be fitted perfectly by the parabola given by Eq. 3. The exchange couplings obtained by using the split valence basis with and without diffuse p orbitals are practically the same. Although the magnitude of the exchange coupling corresponding to the double-zeta basis is somewhat smaller than that provided by the split valence basis, the agreement between them is satisfactory.

Ferromagnetic exchange couplings between the $2p$ orbitals of the N atom and the valence electrons of the fullerene molecule have been found in both anions. The exchange coupling of approximately 1.5 meV provided by our calculations for both systems is within the range of those found in organic ferromagnets [22]. This relatively strong coupling between the valence electrons of the nitrogen and the valence electrons of the fullerene cage could be responsible for the disappearance of the nitrogen lines in the spectrum of $\mathrm{N@C_{60}}$ anions with partially filled LUMOs [20, 21].

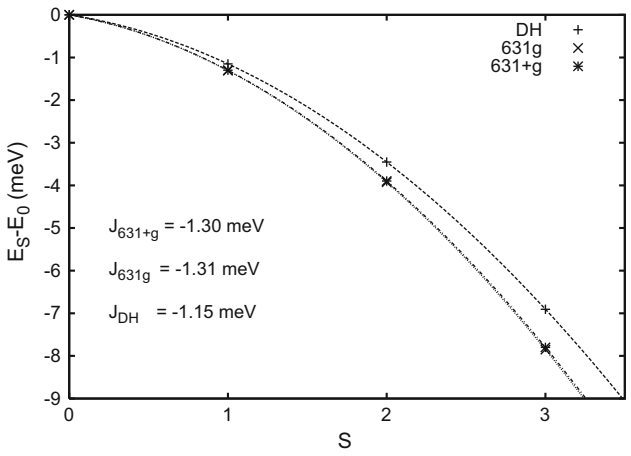

Fig. 1 Energies of $\mathrm{N@C}_{60}^{-3}$ corresponding to different multiplicity and the parabola fitted to the data points. The energy E_0 independent of spin is subtracted

Table 2 Energy of the $\mathrm{N@C}_{60}^{-1}$ resulted by MCSCF calculations using split valence (631g) and double-zeta (DH) basis on the carbon atoms and the exchange coupling extracted from the energies

Basis	$E_{S=1}$ (Hartree)	$E_{S=2}$ (Hartree)	J (meV)
631g	−2325.371558	−2325.371673	−1.56
DH	−2325.515025	−2325.515134	−1.49

4 Conclusions

ROHF and MCSF calculations have been performed on singly and triply ionized anions of $\mathrm{N@C_{60}}$ in order to determine the effective exchange coupling between the valence electrons of the encapsulated N atom and the fullerene cage. In agreement with experiments, we found that the excess electrons occupy the LUMOs of the fullerene molecule and the entrapped atom keeps its atomic character. The interaction between the valence electrons of the N atom and the LUMOs of the C_{60} can be well described by a Heisenberg-like Hamiltonian. The size of the exchange couplings obtained by our calculations is much larger than the hyperfine interaction and can explain the results of EPR measurements on radical anions of $\mathrm{N@C_{60}}$.

Acknowledgments This work is supported by the Hungarian National Science Foundation (contracts OTKA T115575).

References

1. Chai Y, Guo T, Jin C, Haufler RE, Chibante LPF, Fure J, Wang L, Alford JM, Smalley RE (1991) J Phys Chem 95:7564
2. Popov A, Yang S, Dunsch L (2013) Chem Rev 113:5989
3. Almeida Murphy T, Pawlik T, Weidinger A, Höhne M, Alcala R, Spaeth J-M (1996) Phys Rev Lett 77:1075
4. Pietzak B, Waiblinger M, Almeida Murphy T, Weidinger A, Höhne M, Dietel E, Hirsch A (1997) Chem Phys Lett 279:259
5. Harneit W (2002) Phys Rev A 65:032322
6. Suter D, Lim K (2002) Phys Rev A 65:052309
7. Twamley J (2003) Phys Rev A 67:052318
8. Feng M, Twamley J (2004) Phys Rev A 70:032318
9. Mehring M, Scherer W, Weidinger A (2004) Phys Rev Lett 93:206603
10. Pietzak B, Weidinger A, Dinse KP, Hirsch A (2002) In: Akasaka T, Nagase S (eds) Endofullerenes, a new family of carbon clusters. Kluwer Academic Publishers, Dordrecht, pp 13–66
11. Dietel E, Hirsch A, Pietzak B, Waiblinger M, Lips K, Weidinger A, Gruss A, Dinse KP (1999) J Am Chem Soc 121:2432
12. Elste F, Timm C (2005) Phys Rev B 71:155403
13. Yu Z, Chen J, Zhang L, Wang J (2013) J Phys Condens Matter 25:495302
14. Grose JE, Tam ES, Timm C, Scheloske M, Ulgut B, Parks JJ, Abrun HD, Harneit W, Ralph DC (2008) Nat Mater 7:884
15. Schmidt MW, Baldridge KK, Boatz JA, Elbert ST, Gordon MS, Jensen JH, Koseki S, Matsunaga N, Nguyen KA, Su SJ, Windus TL, Dupuis M, Montgomery JA (1993) J Comput Chem 14:1347–1363
16. Ivanic J (2003) J Chem Phys 119:9364,9377
17. Park JM, Tarakeshwar P, Kim KS (2002) J Chem Phys 116:10684
18. Dunning TH Jr, Hay PJ (1977) Chapter 1. In: Shaefer HF III (ed) Methods of electronic structure theory. Plenum Press, New York, pp 1–27
19. Udvardi L (2000) In: Kuzmany H, Fink J, Mehring M, Roth S (eds) Electronic properties of novel materialsMolecular nanostructures 187190. AIP, New York
20. Dinse KP, Godde B, Jakes P, Waiblinger M, Weidinger A, Hirsch A (2001) Abstr Pap Am Chem Soc 221st IEC-199. CODEN, ACSRAL ISSN: 0065–7727
21. Jakes P, Godde B, Waiblinger M, Weiden N, Dinse KP, Weidinger A (2000) AIP Conf Proc 544:174
22. Shultz DA, Vostrikova KE, Bodnar SH, Koo H-J, Whangbo M-H, Kirk ML, Depperman EC, Kampf JW (2003) J Am Chem Soc 125:1607
23. Lu J, Zhang X, Zhao X (1999) Chem Phys Lett 312:85
24. Greer JC (2000) Chem Phys Lett 326:567
25. Plakhutin BN, Breslavskaya NN, Gorelik EV, Arbuznikov AV (2005) J Mol Struct (Thoechem) 727:149

Theor Chem Acc (2015) 134:113
DOI 10.1007/s00214-015-1705-8

REGULAR ARTICLE

Partial-wave decomposition of the ground-state wavefunction of the two-electron harmonium atom

Jerzy Cioslowski[1]

Received: 3 May 2015 / Accepted: 17 July 2015 / Published online: 5 September 2015

Abstract An exact formula for the collective occupancy of natural orbitals with an angular momentum l is derived for the ground state of the two-electron harmonium atom. For confinement strengths ω that correspond to polynomial correlation factors as well as at the weak ($\omega \to \infty$) and strong ($\omega \to 0$) correlations limits, it reduces to closed-form expressions. At the former limit, a similar result obtains for the partial-wave contributions to the ground-state energy. Slow convergence of the collective occupancies to their leading large-l asymptotics provided by Hill's formula is uncovered. As the rate of convergence decreases strongly with ω, a complete breakdown of Hill's formula ensues upon the confinement strength becoming infinitesimally small. The relevance of these findings to the performance of the extrapolation schemes for the estimation of the complete-basis-set limits of quantum-mechanical observables is discussed.

Keywords Partial-wave decomposition · Two-electron harmonium atom · Electron correlation

1 Introduction

The vast majority of modern quantum-chemical calculations rely on approximating electronic wavefunctions (or their equivalents) with linear combinations of basis functions. The choice of these functions is dictated by computational expedience and usually does not reflect singularities present in the potential energy. Thus, at the one-electron level, the commonly employed Gaussian-type basis functions do not possess cusps at nuclei, and at the many-electron level, the Slater determinants do not reproduce the electron–electron coalescence cusps.

The failure to properly reproduce the particle–particle coalescence asymptotics bears upon the rates of convergence of the computed energies and other observables to their complete-basis-set (CBS) limits [1]. Whereas in practice this convergence is sufficiently rapid for the solutions of the Hartree–Fock equations [2, 3], obtaining accurate approximations to correlated electronic wavefunctions is much more difficult [4, 5]. In order to alleviate this problem, two distinct strategies have been developed, namely inclusion of a correlation factor in the trial function [6–8] and extrapolation to the CBS limit [9, 10]. Successful implementations of the latter approach hinge upon understanding how the approximate wavefunction approaches its exact counterpart as the size of the basis set increases.

In a seminal paper [4], Hill carefully analyzed this asymptotic behavior for singlet ground states of two-electron systems. Results of that investigation, subsequently rederived [11] and generalized to excited states [5] and explicitly correlated basis functions [12], have opened an avenue to a plethora of extrapolation formulae that furnish approximate CBS limits for the total energy in terms of the energies computed with sequences of basis sets truncated at particular values of angular momenta [9, 10].

Among Hill's results, the large-l asymptotics [4]

$$\lim_{l\to\infty} \left(l+\frac{1}{2}\right)^6 \nu_l = \frac{5\pi}{4} \int |\Psi(\vec{r},\vec{r})|^2 \, r^5 \, \mathrm{d}\vec{r}, \tag{1}$$

Published as part of the special collection of articles "Festschrift in honour of P. R. Surjan."

✉ Jerzy Cioslowski
jerzy@wmf.univ.szczecin.pl

[1] Institute of Physics, University of Szczecin, Wielkopolska 15, 70-451 Szczecin, Poland

which relates the rate of decay of the collective occupancy (per spin) ν_l of the natural orbitals (NOs) with the angular momentum l to the spatial part $\Psi(\vec{r}_1, \vec{r}_2)$ of the underlying electronic wavefunction, is of particular interest. Unfortunately, rigorous analysis of deviations of the collective occupancies from their asymptotic estimates given by Eq. (1), which would certainly aid in the development in more accurate extrapolation formulae, has not been carried out thus far. As demonstrated in the present paper, such an analysis, which is quite difficult (if not outright impossible) for fully Coulombic systems (i.e., the helium-like species) due to the unavailability of an explicit expression for ν_l, becomes facile upon replacing the external Coulombic potential with the harmonic one.

2 Theory

The two-electron harmonium atom, described by the nonrelativistic Hamiltonian [13, 14]

$$\hat{H} = -\frac{1}{2}\,(\hat{\nabla}_1^2 + \hat{\nabla}_2^2) + \frac{1}{2}\,\omega^2\,(r_1^2 + r_2^2) + \frac{1}{r_{12}}, \tag{2}$$

is an archetype of quasi-solvable systems of relevance to electronic structure theory. As such, it has been repeatedly employed in calibration and benchmarking of approximate electron correlation methods, especially in the context of the density functional theory [15–20]. Its three- and four-electron counterparts have also been extensively studied [21–25].

The spatial part of the $^1S_+$ ground-state wavefunction $\Psi(\omega; \vec{r}_1, \vec{r}_2)$ of the two-electron harmonium atom is given by the expression [13, 14]

$$\Psi(\omega; \vec{r}_1, \vec{r}_2) = \exp\left[-\frac{\omega}{2}\,(r_1^2 + r_2^2)\right] g(\omega; |\vec{r}_1 - \vec{r}_2|), \tag{3}$$

where the correlation factor $g(\omega; r)$ (inclusive of the normalization constant) has the power series representation

$$g(\omega; r) = \sum_{j=0}^{\infty} C_j(\omega)\, r^j. \tag{4}$$

It is worth noting that, since the ratio $C_1(\omega)/C_0(\omega)$ is fixed at $\frac{1}{2}$ by the electron–electron coalescence cusp condition, setting $\vec{r}_1 = \vec{r}_2 = 0$ in Eq. (3) yields $C_0(\omega) = \Psi(\omega; \vec{0}, \vec{0})$ and $C_1(\omega) = \frac{1}{2}\,\Psi(\omega; \vec{0}, \vec{0})$. For certain values of $\omega \in \{\omega_K\}$, the series (4) terminates at the Kth power of r ($K \geq 1$). The first four elements of the set $\{\omega_K\}$ are $\omega_1 = \frac{1}{2}$, $\omega_2 = \frac{1}{10}$, $\omega_3 = \frac{5-\sqrt{17}}{24}$, and $\omega_4 = \frac{35-3\sqrt{57}}{712}$ [13, 14].

Because to its spherical symmetry, $\Psi(\omega; \vec{r}_1, \vec{r}_2)$ can be partitioned into contributions $\Psi_l(\omega; r_1, r_2)$ due to individual angular momenta l,

$$\Psi(\omega; \vec{r}_1, \vec{r}_2) = \sum_{l=0}^{\infty} \Psi_l(\omega; r_1, r_2)\, P_l(\cos\theta_{12}), \tag{5}$$

where $P_l(t)$ is the lth Legendre polynomial and θ_{12} is the angle between the vectors $\vec{r}_1$ and $\vec{r}_2$. The norm $(2l+1)^{-1}\,\langle \Psi_l(\omega; r_1, r_2)\,|\,\Psi_l(\omega; r_1, r_2)\rangle$ equals $\nu_l(\omega)$ that according to Eq. (1) has the large-l asymptotics of

$$\begin{aligned}\lim_{l\to\infty} \left(l + \frac{1}{2}\right)^6 \nu_l(\omega) &= \frac{5\,\pi}{4}\,|g(\omega; 0)|^2 \int \exp(-2\,\omega\, r^2)\, r^5\, \mathrm{d}\vec{r} \\ &= \frac{15\,\pi^2}{16}\,\omega^{-4}\,|\Psi(\omega; \vec{0}, \vec{0})|^2.\end{aligned} \tag{6}$$

Computations of the partial-wave contributions commence with application of the identities [26]

$$\begin{aligned}|\vec{r}_1 - \vec{r}_2|^{2j} &= (r_1^2 + r_2^2 - 2\,r_1\,r_2\,\cos\theta_{12})^j \\ &= \sum_{l=0}^{j} \sum_{k=0}^{j-l} A_{jlk}\,(r_1\,r_2)^{l+2k}\,(r_1^2 + r_2^2)^{j-l-2k}\,P_l(\cos\theta_{12})\end{aligned} \tag{7}$$

and

$$\begin{aligned}|\vec{r}_1 - \vec{r}_2|^{2j-1} &= (r_1^2 + r_2^2 - 2\,r_1\,r_2\,\cos\theta_{12})^{(j-1/2)} \\ &= \sum_{l=0}^{\infty} \sum_{p=0}^{\min(j,l)} \sum_{q=p}^{j} \sum_{k=0}^{j-q} B_{jlpqk}\; r_<^{l+2k-2p+2q}\; r_>^{-l+2k+2p-1} (r_1^2 + r_2^2)^{j-q-2k}\, P_l(\cos\theta_{12}),\end{aligned} \tag{8}$$

where $r_< = \min(r_1, r_2)$, $r_> = \max(r_1, r_2)$,

$$A_{jlk} = (-1)^l\,(2l+1)\,\frac{2^{l+k}\,j!}{(j-l-2k)!\,(2l+2k+1)!!\,k!}, \tag{9}$$

and

$$B_{jlpqk} = (-1)^q\,(2l+1)\,\frac{2^{k+q}\,(2q+1)}{2l-2p+2q+1}\,\frac{j!}{k!\,(j-2k-q)!\,(2k+2q+1)!!}\binom{2p}{p}\binom{2l-2p}{l-p}\binom{2q-2p}{q-p}\binom{2l-2p+2q}{l-p+q}^{-1}. \tag{10}$$

Combining Eqs. (3), (4), and (5) with Eqs. (7)–(10) produces

$$\Psi_l(\omega; r_1, r_2) = \Psi_l^+(\omega; r_1, r_2) + \Psi_l^-(\omega; r_1, r_2), \tag{11}$$

where the contributions due to the terms with even and odd powers of r in the expansion (4) read

$$\Psi_l^+(\omega; r_1, r_2) = \exp\left[-\frac{\omega}{2}\,(r_1^2 + r_2^2)\right] \sum_{j=l}^{\infty} C_{2j}(\omega) \times \left[\sum_{k=0}^{j-l} A_{jlk}\,(r_1\, r_2)^{l+2k}\,(r_1^2 + r_2^2)^{j-l-2k}\right] \tag{12}$$

and

$$\Psi_l^-(\omega; r_1, r_2) = \exp\left[-\frac{\omega}{2}\,(r_1^2 + r_2^2)\right] \sum_{j=1}^{\infty} C_{2j-1}(\omega) \times \left[\sum_{p=0}^{\min(j,l)} \sum_{q=p}^{j} \sum_{k=0}^{j-q} B_{jlpqk}\; r_<^{l+2k-2p+2q} \times r_>^{-l+2k+2p-1}\,(r_1^2 + r_2^2)^{j-q-2k}\right], \tag{13}$$

respectively.

When employed in conjunction with the identity

$$\int_0^{\infty}\int_0^{\infty} r_<^{\alpha}\, r_>^{\alpha'}\,(r_1^2 + r_2^2)^{\beta} \exp\left[-\omega\,(r_1^2 + r_2^2)\right] r_1^2\, r_2^2\, \mathrm{d}r_1\, \mathrm{d}r_2 = \frac{2^{-(\alpha+\alpha'+4)/2}\;\omega^{-(\alpha+\alpha'+2\beta+6)/2}}{\alpha+3} \times \Gamma\left(\frac{\alpha+\alpha'+2\beta+6}{2}\right)\, {}_2F_1\left(\begin{matrix}1, -\frac{\alpha'+1}{2} \\ \frac{\alpha+5}{2}\end{matrix}\,\middle|\, -1\right) \tag{14}$$

where $\Gamma(t)$ and ${}_2F_1\left(\begin{matrix}a_1, a2 \\ b_1\end{matrix}\,\middle|\, t\right)$ are the pertinent gamma and hypergeometric functions, respectively, Eqs. (12) and (13) yield

$$\nu_l(\omega) = \sum_{j=l}^{\infty}\sum_{j'=l}^{\infty} \frac{C_{2j}(\omega)\, C_{2j'}(\omega)}{\omega^{j+j'+3}}\, D_{ljj'}^{++} + 2\sum_{j=1}^{\infty}\sum_{j'=l}^{\infty} \frac{C_{2j-1}(\omega)\, C_{2j'}(\omega)}{\omega^{j+j'+5/2}}\, D_{ljj'}^{-+} + \sum_{j=1}^{\infty}\sum_{j'=1}^{\infty} \frac{C_{2j-1}(\omega)\, C_{2j'-1}(\omega)}{\omega^{j+j'+2}}\, D_{ljj'}^{--}, \tag{15}$$

where

$$D_{ljj'}^{++} = \frac{\pi^3}{2l+1}\,(j+j'+2)! \sum_{k=0}^{j-l}\sum_{k'=0}^{j'-l} 2^{-4(l+k+k'+1/2)} \binom{2l+2k+2k'+2}{l+k+k'+1} A_{jlk}\, A_{j'lk'}, \tag{16}$$

$$D_{ljj'}^{-+} = \frac{\pi^2}{2l+1}\,\Gamma\left(j+j'+\frac{5}{2}\right) \sum_{p=0}^{\min(j,l)} \sum_{q=p}^{j} \sum_{k=0}^{j-q} \sum_{k'=0}^{j'-l} \frac{2^{-(l+2k+2k'+q-5/2)}}{2l+2k+2k'-2p+2q+3} \times\; {}_2F_1\left(\begin{matrix}1, -(k+k'+p) \\ l+k+k'-p+q+\frac{5}{2}\end{matrix}\,\middle|\, -1\right) A_{j'lk'}\, B_{jlpqk}, \tag{17}$$

and

$$D_{ljj'}^{--} = \frac{\pi^2}{2l+1}\,(j+j'+1)! \sum_{p=0}^{\min(j,l)} \sum_{q=p}^{j} \sum_{k=0}^{j-q} \sum_{p'=0}^{\min(j',l)} \sum_{q'=p'}^{j'} \sum_{k'=0}^{j'-q'} \frac{2^{-(2k+2k'+q+q'-3)}}{2(l+k+k'-p-p'+q+q')+3} \times\; {}_2F_1\left(\begin{matrix}1, l-(k+k'+p+p')+\frac{1}{2} \\ l+k+k'-p-p'+q+q'+\frac{5}{2}\end{matrix}\,\middle|\, -1\right) B_{jlpqk}\, B_{j'lp'q'k'}. \tag{18}$$

Although it is unlikely that in general the sums that enter Eqs. (16)–(18) are reducible to simple analytical expressions, they permit rapid computations of the collective occupancies for arbitrary angular momenta.

2.1 The case of a polynomial correlation factor

When $\omega = \omega_K$, the wavefunction (3) can be written in a closed form as the correlation factor $g(\omega; r)$ is a polynomial of degree K in the interelectron distance r. Accordingly, the even/even and odd/even terms in the rhs of Eq. (15) contribute only to the collective occupancies of NOs with $l \leq 2\left[\frac{K-1}{2}\right]$. In contrast, the odd/odd terms do not vanish for any value of the angular momentum, giving rise to the large-l asymptotics of $\nu_l(\omega)$. For individual (j, j') combinations, the summations in Eq. (18) can be carried out explicitly, producing expressions involving the digamma function $\gamma(t)$, e.g.,

$$D^{--}_{l11} = 2\pi^2\,(2l+1)\,\frac{(2l-3)!!}{(2l+3)!!}\Bigg(4\,(-16\,l^5-48\,l^4-32\,l^3-4\,l^2-23\,l+36)\,\frac{(2l-5)!!}{(2l+3)!!} + (-4\,l^2-4\,l+5)\left[\gamma\left(\frac{2l-3}{4}\right)-\gamma\left(\frac{2l-1}{4}\right)\right]\Bigg), \tag{19}$$

$$D^{--}_{l12} = 6\pi^2\,(2l+1)\,\frac{(2l-3)!!}{(2l+3)!!}\Big(4\left(64\,l^7+256\,l^6+80\,l^5-432\,l^4+380\,l^3+1424\,l^2+667\,l-1485\right)\,\frac{(2l-7)!!}{(2l+5)!!} + \left(4\,l^2+4\,l-7\right)\left[\gamma\left(\frac{2l-5}{4}\right)-\gamma\left(\frac{2l-3}{4}\right)\right]\Big), \tag{20}$$

$$D^{--}_{l22} = 18\pi^2\,(2l+1)\,\frac{(2l-5)!!}{(2l+5)!!}\Big(4\,(-512\,l^{10}-1280\,l^9+5888\,l^8+11136\,l^7-35712\,l^6-49344\,l^5 + 76112\,l^4+50312\,l^3-54758\,l^2+183873\,l-225540)\,\frac{(2l-9)!!}{(2l+5)!!}+(-16\,l^4-32\,l^3+88\,l^2+104\,l-189) \times\left[\gamma\left(\frac{2l-7}{4}\right)-\gamma\left(\frac{2l-5}{4}\right)\right]\Big), \tag{21}$$

etc. These expressions have the large-l asymptotics of

$$\lim_{l\to\infty}\left(l+\frac{1}{2}\right)^{2(j+j'+1)} D^{--}_{ljj'} = \mathcal{D}^{--}_{jj'}, \tag{22}$$

where $\mathcal{D}^{--}_{11} = \frac{15}{4}\pi^2$, $\mathcal{D}^{--}_{12} = -\frac{315}{4}\pi^2$, $\mathcal{D}^{--}_{22} = \frac{8505}{4}\pi^2$, etc. Consequently, the leading large-l asymptotics of $\nu_l(\omega)$ reads [compare Eqs. (15) and (22)]

$$\lim_{l\to\infty}\left(l+\frac{1}{2}\right)^{6}\nu_l(\omega) = \frac{15\pi^2}{4}\,\omega^{-4}\,[C_1(\omega)]^2 = \frac{15\pi^2}{16}\,\omega^{-4}\,|\Psi(\omega;\vec{0},\vec{0})|^2, \tag{23}$$

in agreement with the corollary (6) of Hill's formula. Equation (19) reproduces the collective occupancies produced by the previously published expressions valid for $K = 1$ [27, 28] and $K = 2$ [28].

2.2 The weak-correlation limit

At the weak-correlation limit of $\omega \to \infty$, closed-form expressions for the collective occupancies are readily obtainable. The wavefunctions $\{\Phi_{nlm}(\omega; \vec{r})\}$ of a three-dimensional harmonic oscillator with the circular frequency ω,

$$\Phi_{nlm}(\omega;\vec{r}) = 2\left(\frac{\omega^3}{\pi}\right)^{1/4}\left[\frac{(2n)!!}{(2n+2l+1)!!}\right]^{1/2} \times L_n^{l+1/2}\left(\omega\,r^2\right)\left(2\,\omega\,r^2\right)^{l/2}\exp\left(-\frac{\omega}{2}\,r^2\right)\,Y_l^m(\theta,\varphi)\quad, \tag{24}$$

provide a suitable basis set for such calculations thanks to the simple form of the respective two-electron integral

$$V_{lnn'}(\omega) = \left\langle \Phi_{nlm}(\omega;\vec{r}_1)\,\Phi_{000}(\omega;\vec{r}_2)\,|\frac{1}{r_{12}}|\,\Phi_{000}(\omega;\vec{r}_1)\,\Phi_{n'lm}(\omega;\vec{r}_2)\right\rangle = \left(\frac{8\,\omega}{\pi}\right)^{1/2} 2^{-(2n+2n'+l)}\,\frac{(2n+2n'+2l-1)!}{(n+n'+l-1)!} \times\left[\frac{(n+l)!\,(n'+l)!}{n!\,(2n+2l+1)!\,n'!\,(2n'+2l+1)!}\right]^{1/2}, \tag{25}$$

which facilitates explicit evaluation of the sums that enter the expressions

$$\tilde{\nu}_l(\omega) = (2l+1)\sum_{n,n'=0}^{\infty}\left[\frac{V_{lnn'}}{2\,\omega\,(n+n'+l)}\right]^2 \tag{26}$$

and

$$E_l^{(2)} = -(2l+1)\sum_{n,n'=0}^{\infty}\frac{V_{lnn'}^2}{2\,\omega\,(n+n'+l)}, \tag{27}$$

Table 1 The collective occupancies of NOs at the four largest values of ω that correspond to polynomial correlation factors

l	$\nu_l(\omega_K)$			
	$K=1$	$K=2$	$K=3$	$K=4$
0	9.755557×10^{-1}	9.146744×10^{-1}	8.392861×10^{-1}	7.637280×10^{-1}
1	2.375865×10^{-2}	8.478905×10^{-2}	1.606437×10^{-1}	2.344602×10^{-1}
2	5.910989×10^{-4}	4.626236×10^{-4}	5.577958×10^{-5}	1.809789×10^{-3}
3	7.141400×10^{-5}	5.589217×10^{-5}	9.702106×10^{-6}	1.412707×10^{-6}
4	1.539745×10^{-5}	1.205081×10^{-5}	2.993862×10^{-6}	2.857688×10^{-7}
5	4.574478×10^{-6}	3.580215×10^{-6}	1.016854×10^{-6}	1.383782×10^{-7}
6	1.671905×10^{-6}	1.308516×10^{-6}	3.973200×10^{-7}	6.519386×10^{-8}
7	7.070209×10^{-7}	5.533500×10^{-7}	1.746623×10^{-7}	3.183796×10^{-8}
8	3.332811×10^{-7}	2.608425×10^{-7}	8.439335×10^{-8}	1.641902×10^{-8}
9	1.708878×10^{-7}	1.337453×10^{-7}	4.400492×10^{-8}	8.940612×10^{-9}
10	9.370289×10^{-8}	7.333657×10^{-8}	2.441966×10^{-8}	5.114637×10^{-9}
20	1.690606×10^{-9}	1.323153×10^{-9}	4.578093×10^{-10}	1.054168×10^{-10}
50	7.564718×10^{-12}	5.920527×10^{-12}	2.071120×10^{-12}	4.896421×10^{-13}
100	1.217710×10^{-13}	9.530410×10^{-14}	3.339285×10^{-14}	7.924784×10^{-15}

where $E_l^{(2)}$ is the incremental contribution to the second-order energy $E^{(2)}$ [and also to its correlation component $E_{corr}^{(2)}$ for $l \neq 0$] arising from $\Psi_l(\omega; r_1, r_2)$. Application of well-known algebraic techniques [29] to these expressions, which follow for $l \neq 0$ from straightforward arguments based upon perturbation theory [30], produces

$$E_l^{(2)} = -\frac{4^{-l}}{\pi\,(2l+1)\,l}\;{}_3F_2\left(\left.\begin{matrix} l,\, l+\frac{1}{2},\, l+\frac{1}{2} \\ l+\frac{3}{2},\, 2l+2 \end{matrix}\right| 1\right) \tag{28}$$

and

$$\tilde{\nu}_l(\omega) = \left[\frac{4^{-l}}{2\,\pi\,l^2}\;{}_3F_2\left(\left.\begin{matrix} l,\, l,\, l+\frac{1}{2} \\ l+1,\, 2l+2 \end{matrix}\right| 1\right) + E_l^{(2)}\right]\omega^{-1}. \tag{29}$$

In Eqs. (24), (28), and (29), $L_n^{l+1/2}(t)$, $Y_l^m(\theta,\varphi)$, and ${}_3F_2\left(\left.\begin{matrix} a_1,\, a_2,\, a_3 \\ b_1,\, b_2 \end{matrix}\right| t\right)$ are the pertinent generalized Laguerre polynomial, spherical harmonic, and generalized hypergeometric function, respectively. Equation (29) yields the leading asymptotics $\{\tilde{\nu}_l(\omega)\}$ of the collective occupancies at the limit of $\omega \to \infty$ that, in excellent agreement with the previously published results of numerical calculations [14], equal $\frac{127-48\pi+36\ln 2}{24\pi}\,\omega^{-1} \approx 1.534\,321\,462 \cdot 10^{-2}\,\omega^{-1}$ for $l=1$ and $\frac{-2053+720\pi-300\ln 2}{360\pi}\,\omega^{-1} \approx 8.864\,544\,969 \cdot 10^{-4}\,\omega^{-1}$ for $l=2$.

2.3 The strong-correlation limit

At the strong-correlation limit of $\omega \to 0$, the wavefunction (3) is given by its asymptotic expression [13, 14]

$$\begin{aligned}\Psi(\omega;\vec{r}_1,\vec{r}_2) &\approx \tilde{\Psi}(\omega;\vec{r}_1,\vec{r}_2) \\ &= \frac{3^{1/8}}{2^{5/6}\,\pi^{3/2}}\,\omega^{5/3}\,\exp\left[-\frac{\omega}{4}\,(\vec{r}_1+\vec{r}_2)^2\right] \\ &\quad\times \exp\left[-\frac{\sqrt{3}}{4}\,\omega\,(|\vec{r}_1-\vec{r}_2|-r_0)^2\right],\end{aligned} \tag{30}$$

where $r_0 = (\frac{2}{\omega^2})^{1/3}$. The corresponding leading asymptotics $\{\tilde{\nu}_l(\omega)\}$ of the collective occupancies is given by

$$\begin{aligned}\tilde{\nu}_l(\omega) = \frac{16\,\pi^2}{2l+1}\,\frac{3^{1/4}}{2^{5/3}\,\pi^3}\,\omega^{10/3}\int_0^\infty\int_0^\infty\left(\frac{2l+1}{2}\int_0^\pi \exp\left[-\frac{\omega}{4}\,(r_1^2+r_2^2+2\,r_1\,r_2\,\cos\theta_{12})\right]\right. \\ \left.\times\;\exp\left[-\frac{\sqrt{3}}{4}\,\omega\left(\sqrt{r_1^2+r_2^2-2\,r_1\,r_2\,\cos\theta_{12}}-r_0\right)^2\right]\right. P_l(\cos\theta_{12})\,\sin\theta_{12}\,\mathrm{d}\theta_{12})^2\,r_1^2\,r_2^2\,\mathrm{d}r_1\,\mathrm{d}r_2.\end{aligned} \tag{31}$$

Table 2 Ratios of the collective occupancies of NOs to the respective asymptotic estimates [Eq. (23)] at the four largest values of ω that correspond to polynomial correlation factors

l	$\frac{16}{15}\,\pi^{-2}\,\omega_K^4\,\lvert\Psi(\omega_K;\vec{0},\vec{0})\rvert^{-2}\left(l+\frac{1}{2}\right)^6\nu_l(\omega_K)$			
	$K=1$	$K=2$	$K=3$	$K=4$
0	0.121488	0.145539	0.380930	1.458749
1	2.156895	9.835114	53.152806	326.466459
2	1.150164	1.150164	0.395576	54.011954
3	1.046288	1.046288	0.518071	0.317455
4	1.019022	1.019022	0.722141	0.290076
5	1.009200	1.009200	0.817617	0.468237
6	1.004966	1.004966	0.870434	0.601047
7	1.002904	1.002904	0.902988	0.692683
8	1.001807	1.001807	0.924564	0.756977
9	1.001180	1.001180	0.939632	0.803398
10	1.000803	1.000803	0.950584	0.837862
20	1.000058	1.000058	0.987013	0.956434
50	1.000002	1.000002	0.997857	0.992771
100	1.000000	1.000000	0.999459	0.998173

The integrals that enter Eq. (31) can be evaluated (in the asymptotic sense) with Laplace's method, yielding [22]

$$\tilde{\nu}_l(\omega) = 2^{7/3}\,(2l+1)\,\omega^{1/3}\,\exp\left[-(2\,\omega)^{1/3}\,(2l+1)^2\right]. \quad (32)$$

These collective occupancies properly sum to the number of electrons,

$$\lim_{\omega\to 0}\sum_{l=0}^{\infty}\tilde{\nu}_l(\omega) = \lim_{\omega\to 0}\int_0^{\infty}\tilde{\nu}_l(\omega)\,\mathrm{d}l = 1 \quad (33)$$

but obviously do not conform to Hill's asymptotic formula

$$\lim_{l\to\infty}\left(l+\frac{1}{2}\right)^6\tilde{\nu}_l(\omega) = \frac{5\,3^{5/4}}{2^{17/3}\,\pi}\,\omega^{-2/3}\,\exp\left(-\frac{3^{1/2}}{2^{1/3}\,\omega^{1/3}}\right). \quad (34)$$

3 Discussion and conclusions

The collective occupancies of natural orbitals pertaining to ground states of two-electron harmonium atoms with the four largest confinement strengths that give rise to polynomial correlation factors are listed in Table 1. As expected, the values of $\nu_0(\omega_K)$ gradually decrease with K as weakening of the confinement (note that $\forall_K\ \omega_{K+1} < \omega_K$) gives rise to stronger electron correlation. Interestingly, this depopulation of the s-type orbitals does not translate into uniform increases in the collective occupancies of NOs with nonzero angular momenta l. The key to understanding of this phenomenon lies in the behavior of the even/even, odd/even, and odd/odd terms in Eq. (15), namely the vanishing of the first two types of contributions for $l > 2\left[\frac{K-1}{2}\right]$. Thus, at least for $\omega \in \{\omega_K\}$, decreasing ω results in predominant enhancement of the collective occupancies of NOs with low values of l. The range of the angular momenta at which this mechanism is operative steadily increases with the extent of electron correlation.

In light of this observation, one anticipates large deviations of the collective occupancies from their asymptotic counterparts given by Hill's formula. Indeed, inspection of Table 2, in which the ratios of the computed data from Table 1 to those obtained from Eq. (23) are compiled, reveals dramatic failures of the asymptotic predictions for small angular momenta, attainment of the asymptotic convergence requiring larger and larger values of l as the electrons become more correlated. Consequently, the complete breakdown of Hill's asymptotics at the strong-correlation limit of $\omega \to 0$ comes as no surprise.

It is instructive to compare the exact expressions (28) and (29) with the asymptotic ones, i.e.,

$$\lim_{l\to\infty}\left(l+\frac{1}{2}\right)^6\tilde{\nu}_l(\omega) = \frac{15}{16\,\pi}\,\omega^{-1} \quad (35)$$

and

$$\lim_{l\to\infty}\left(l+\frac{1}{2}\right)^4 E_l^{(2)} = -\frac{3}{4\,\pi}. \quad (36)$$

The convergence of the exact collective occupancies and energy increments to their asymptotic counterparts is found to be rather slow, the differences at $l = 5$ amounting to 9.3 and 3.6 %, respectively, and decreasing to 3.0 and 1.1 % at $l = 10$. Thus, even at the weak-correlation limit of $\omega \to \infty$, significant deviations from the leading asymptotic terms of Hill's formulae are observed.

The results of the present study have direct relevance to construction of approximate extrapolation schemes that aim at estimation of the CBS limits. Relying on the dominance of the leading large-l asymptotic terms in the partial-wave expansions, these schemes are commonly employed in electronic structure calculations on systems with small to moderate electron correlation. As clearly demonstrated by the aforediscussed data, such extrapolations are bound to fail for strongly correlated species, especially when the nondynamical correlation effects are significant.

In addition to providing benchmarks for extrapolation schemes, Eqs. (28) and (29) give rise to some new identities of mathematical interest. First, combining Eq. (28) with the known asymptotic expansions for the total energy and its $l = 0$ component at the limit of $\omega \to \infty$ [31] yields the identity

$$\sum_{l=1}^{\infty} \frac{4^{-l}}{(2l+1)\,l}\,{}_3F_2\left(\left.\begin{matrix} l,\, l+\frac{1}{2},\, l+\frac{1}{2} \\ l+\frac{3}{2},\, 2l+2 \end{matrix}\right| 1\right) = \pi - 3. \tag{37}$$

In turn, employing this result in conjunction with Eqs. (29) and the known expression for $\tilde{\nu}_0(\omega)$ [31], one arrives at

$$\sum_{l=1}^{\infty} \frac{4^{-l}}{l^2}\,{}_3F_2\left(\left.\begin{matrix} l,\, l,\, l+\frac{1}{2} \\ l+1,\, 2l+2 \end{matrix}\right| 1\right) = 2\ln 2 - 1. \tag{38}$$

To author's best knowledge, the identities (37) and (38), which can also be derived from the integral representation of the generalized hypergeometric function, have not been previously published.

Acknowledgments The research described in this publication has been funded by NCN (Poland) under grant DEC-2012/07/B/ST4/00553.

References

1. Klahn B, Morgan JD III (1984) J Chem Phys 81:410
2. Kutzelnigg W (2013) Int J Quantum Chem 113:203
3. Kutzelnigg W (2012) AIP Conf Proc 1504:15
4. Hill RN (1985) J Chem Phys 83:1173
5. Kutzelnigg W, Morgan JD III (1992) J Chem Phys 96:4484
6. Hättig Ch, Klopper W, Köhn A, Tew DP (2012) Chem Rev 112:4 and the references cited therein
7. Mitroy J, Bubin S, Horiuchi W, Suzuki Y, Adamowicz L, Cencek W, Szalewicz K, Komasa J, Blume D, Varga K (2013) Rev Mod Phys 85:693 and the references cited therein
8. Ten-no S (2012) Theor Chem Acc 131:1070 and the references cited therein
9. Feller D, Peterson KA, Hill JG (2011) J Chem Phys 135:044102 and the references cited therein
10. Feller D (2013) J Chem Phys 138:074103 and the references cited therein
11. Goddard BD (2009) SIAM J Math Anal 41:77
12. Wang C (2013) Phys Rev A 88:032511
13. Taut M (1993) Phys Rev A 48:3561
14. Cioslowski J, Pernal K (2000) J Chem Phys 113:8434 and the references cited therein
15. Sahni V (2010) Quantal density functional theory II: approximation methods and applications. Springer, Berlin
16. Gori-Giorgi P, Savin A (2009) Int J Quantum Chem 109:2410
17. Zhu WM, Trickey SB (2006) J Chem Phys 125:094317
18. Elward JM, Hoffman J, Chakraborty A (2012) Chem Phys Lett 535:182
19. Elward JM, Thallinger B, Chakraborty A (2012) J Chem Phys 136:124105
20. Glover WJ, Larsen RE, Schwartz BJ (2010) J Chem Phys 132:144101
21. Cioslowski J (2015) J Chem Phys 142:114105
22. Cioslowski J (2015) J Chem Phys 142:114104
23. Cioslowski J (2013) J Chem Phys 139:224108
24. Cioslowski J, Strasburger K, Matito E (2014) J Chem Phys 141:044128
25. Cioslowski J, Strasburger K, Matito E (2012) J Chem Phys 136:194112
26. The first of these identities follows from the binomial theorem and elementary properties of the Legendre polynomials. In turn, when combined with the generating function of the Legendre polynomials, it yields the second identity upon application of the pertinent product formula
27. King HF (1996) Theor Chim Acta 94:345
28. Cioslowski J, Buchowiecki M (2005) J Chem Phys 122:084102
29. Petkovsek M, Wilf HS, Zeilberger D (1996) A=B. AK Peters, Wellesley
30. Kutzelnigg W (1963) Theor Chim Acta 1:327
31. White RJ, Byers Brown W (1970) J Chem Phys 53:3869

Theor Chem Acc (2015) 134:115
DOI 10.1007/s00214-015-1720-9

REGULAR ARTICLE

Benchmarks of graph invariants for hydrogen-bond networks in water clusters of different topology

Andrey M. Tokmachev[1] · Andrei L. Tchougréeff[2,3,4] · Richard Dronskowski[4]

Received: 18 July 2015 / Accepted: 1 September 2015 / Published online: 11 September 2015

Abstract The diversity of the various forms of water stems from systems of hydrogen bonds. Cooperative behaviour of hydrogen-bond networks gives rise to unique properties of water systems. A number of approaches to understand and model the collective behaviour of hydrogen bonds and predict their properties on the basis of a small number of calculations have been put forward. Among them, the concept of graph invariants provides most general descriptors for hydrogen-bond networks, which are routinely used to predict properties of water systems. In the present work, we examine the formalism of graph invariants and propose its modification which may be beneficial for water structures with defects. To benchmark graph invariants, we carried out quantum-chemical calculations of more than 10^7 water clusters with different hydrogen-bond configurations. The quality of the approximation is studied as a function of the type of graph invariant and its order. The results demonstrate that the method is applicable only to cage-like structures without significant strains.

Keywords Water clusters · Hydrogen bonds · Graphs · Invariants · APSG

Published as part of the special collection of articles "Festschrift in honour of P. R. Surjan".

✉ Andrei L. Tchougréeff
andrei.tchougreeff@ac.rwth-aachen.de

[1] NBICS Centre, NRC Kurchatov Institute, Kurchatov Sq. 1, Moscow 123182, Russia

[2] Moscow Center for Continuous Mathematical Education, Bol'shoy Vlas'evskiy 11, Moscow 119002, Russia

[3] Department of Chemistry, Moscow State University, Vorob'evy Gory 1, Build. 3, Moscow 119992, Russia

[4] Institut für Anorganische Chemie, RWTH Aachen University, Landoltweg 1, 52056 Aachen, Germany

1 Introduction

Water in all its forms constitutes the basis of our existence. The properties of water are unique and its beauty is limitless. Aggregates of water molecules are among the most studied chemical systems, but despite the intensive concerted efforts, water is still far from being understood. The reason behind is the set of hydrogen (H–) bonds keeping water molecules together. Networks of hydrogen bonds exhibit complex behaviour manifested as cooperative contributions to properties of water systems. The enormity of these contributions gives impetus to studies of the collective structure of H-bond networks. Among the most recent successes in electronic-structure theory devoted to H-bonded systems, we mention density-functional studies on carefully quantifying H-bonds in molecular crystals [1, 2] and in assessing the amount of covalency involved [3].

Water systems allow for numerous H-bond configurations even when the morphology of the system (adjacency matrix) is fixed and the restrictions of the ice rules (basically requiring the absence of ionized individual water molecules in a water system) [4] are imposed. The number of these configurations grows exponentially with the size of the system. Simple gas hydrate shells are a perfect illustration: the 5^{12} D-cage $(H_2O)_{20}$ allows for 30,026 symmetry independent configurations, the numbers for the larger $5^{12}6^2$ T-cage $(H_2O)_{24}$ and the $5^{12}6^4$ H-cage $(H_2O)_{28}$ are 3,043,836 and 61,753,344, respectively [5]. Clearly, not all of them are important, but information extracted from studies of the minimal energy configuration (which is commonly the only subject of the investigation) is often

insufficient. Any reasonable prediction of properties of such systems would require a thorough analysis of H-bond configurations because a significant part of them can be thermally populated.

Construction of a predictive model correlating the energy and other properties with the H-bond network structure is a long-standing problem. A number of approaches have been put forward, mostly for water clusters. A most straightforward approach is based on classification of all H-bonds in a cluster according to their local environment with subsequent counting the numbers of bonds of different types. The required classification can rely upon notions of weak and strong H-bonds (which are often associated with cis and trans H-bonds)—now so easily quantified by DFT [3]—or it can take into account the first neighbours of H-bonds leading to two types of trans-bonds and three types of cis-bonds [6]. Similar ideas underline the so-called Strong–Weak-Effective-Bond model for polyhedral water clusters which is based on estimating the effective pair interactions between nearest neighbours [7]. An alternative model, especially suited to water cages, classifies bonds according to the state of oxygen atoms (having a dangling O–H bond or a lone pair) [8], but it leads to the same five types of H-bonds. Our own calculations of all H-bond isomers of dodecahedral water cluster $(H_2O)_{20}$ indicate that there exists a correlation between the cluster energy and the number of trans or cis H-bonds or the number of pairs of dangling O–H bonds in vicinal positions, but it is not strong enough to build a predictive model [9].

A viable alternative to this approach is given by a general set of entities called graph invariants [10]. Those are automatically generated descriptors of the H-bond structure taking into account the symmetry of the system. The energy and other properties can be approximated as linear combinations of graph invariants. This approach seems very promising because it employs only the adjacency matrix, does not rely on special physical insight, and encompasses a hierarchy of approximations. Incidentally, other common descriptors of H-bond networks (such as numbers of H-bonds of different types, see above) emerge as particular cases of graph invariants. Moreover, the concept is highly useful for generation or enumeration of symmetry-distinct H-bond networks reducing N^2 scaling of these procedures to $N \log N$, where N is the total number of configurations.

The method has originally been developed for finite clusters, but its generalization to periodic systems [11] has been no less successful. Graph invariant descriptors provide a simple algorithm to extrapolate from a handful of expensive quantum-mechanical calculations to a larger set of H-bond configurations. Similarly, they can be used to extrapolate from calculations for smaller unit cells to statistical mechanical simulations employing larger unit cells. The method is routinely applied in studies of H-bond topology and proton-ordering transitions for different phases of ice [12–16]. At the same time, its applicability is not thoroughly tested in different aspects. First, only second-order invariants are used in all numerical applications. Second, only water systems without significant strains and any defects are studied. Third, all the applications correspond to a very small number of actually calculated H-bond isomers with the only exception provided by the 30,026 isomers of the dodecahedral water cluster $(H_2O)_{20}$, where the graph invariant approximation is compared with the exhaustive force field OSS2 calculations [10].

In the present paper, graph invariants are benchmarked against results of quantum-chemical calculations. Exhaustive calculations of all H-bond networks for water clusters of 24 different morphologies provide reference values of the energy. A series of tests attempting to approximate the energy by a linear combination of graph invariant descriptors reveals limits for applicability of the method.

2 Computational details

Benchmarking requires calculations for a number of water clusters, each providing a set of H-bond networks, large enough to be studied with graph invariants. To be representative, the set of water clusters should include clusters of different size, symmetry and strains. Most of the

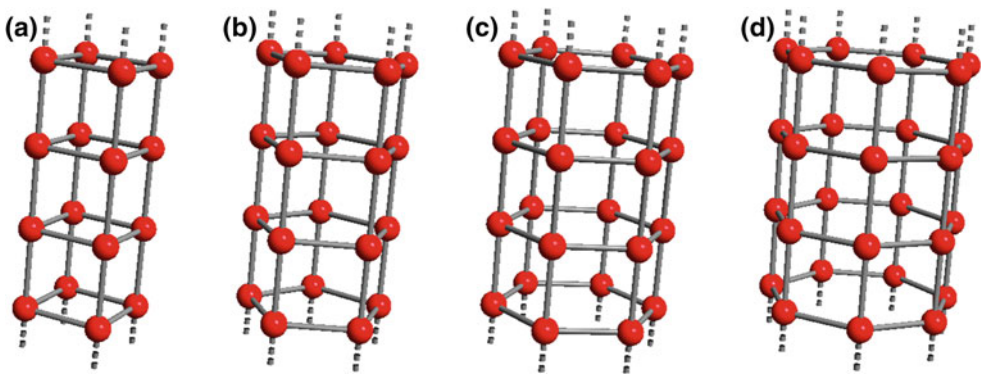

Fig. 1 Structures of ice nanotubes formed by rings of **a** 4; **b** 5; **c** 6 and **d** 7 water molecules

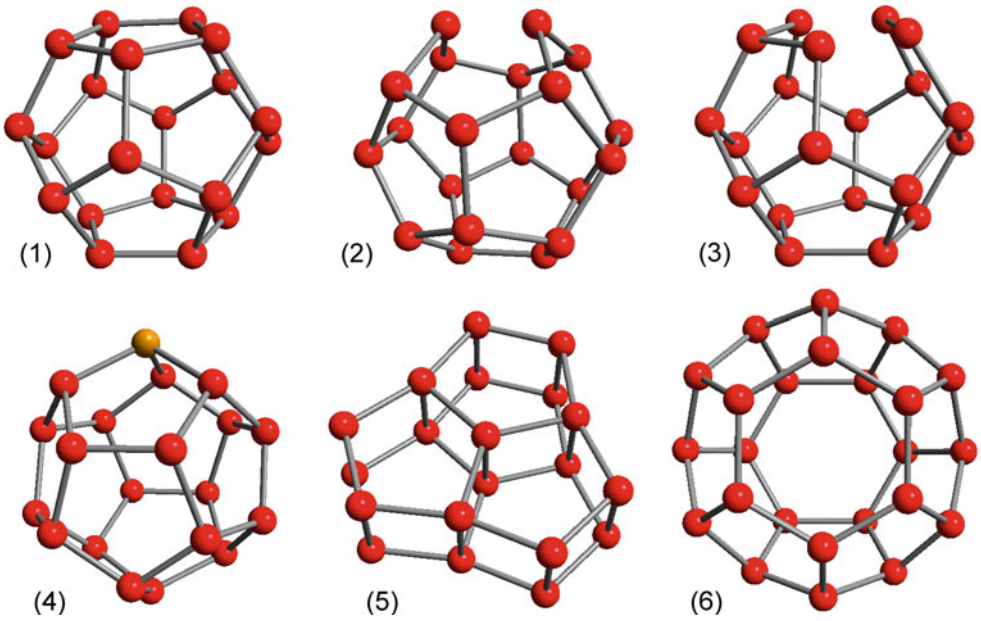

Fig. 2 Water clusters: **1** dodecahedral cage; **2** dodecahedral cage with one H-bond broken; **3** dodecahedral cage with two H-bonds broken; **4** dodecahedral cage with one water molecule replaced by HF; **5** edge-sharing pentagonal prisms; **6** tetrakaidecahedral cage

structures considered in the paper are finite fragments of experimentally known ice nanotubes (see Fig. 1), which can be viewed as stacks of n-membered rings (or rolled square-net sheets) with n being from 4 to 7. The fragments are denoted as INT_n^m where m is the number of n-membered layers. We studied structures with sufficient but not exceedingly large number of H-bond configurations, namely INT_4^m with $m = 3 \div 8$, INT_5^m with $m = 2 \div 6$, INT_6^m with $m = 2 \div 5$, and INT_7^m with $m = 2 \div 4$ [17]. The other clusters studied are shown in Fig. 2. They are the 5^{12} D-cage $(H_2O)_{20}$ (1); the same cage but having a single defect due to one H-bond broken (2) or two defects due to a couple of H-bonds broken (3); the same cage with one water molecule replaced by hydrogen fluoride HF (4); the isomer of the D-cage with the structure of edge-sharing pentagonal prisms (5); and the $5^{12}6^2$ T-cage $(H_2O)_{24}$ (6). The total number of configurations in the water clusters mentioned above is 10,366,824.

Quantum-chemical calculations on such a grand scale pose special requirements to the computational scheme. Clearly, the task is far beyond the scope of sophisticated ab initio methods of quantum chemistry. To solve the problem, we devised a specialized semiempirical method dubbed strictly local geminals (SLG) [18–21]. The method is based on geminals [22]—two-electron wave functions enabling construction of efficient methods for large molecular systems [23]. The water molecule is represented by an antisymmetrized product of four geminals—two describing the chemical bonds O–H and two describing the electron lone pairs. Interaction between molecules represented by geminal wave functions can be accounted for perturbatively [24], but we employ a different scheme. The H-bonds are represented by three-orbital four-electron wave functions. The resulting wave function combines geminals with other strictly local electron groups [25]. An important characteristic of the method is that it is ultra-fast but still highly reliable with respect to energy calculations for many classes of molecules. A modified PM3 parameterization is specially devised to describe water systems with this method [21]. The resulting binding energies are similar to MP2 and DFT benchmarks. The method is successfully applied to a number of water clusters [9, 17].

The present analysis requires the energy for each of H-bond networks under consideration. The simplest way to proceed is to build an idealized O frame for each water cluster morphology, fixed H atom positions being determined separately for each H-bond network. Energy calculations for such idealized structures may already give some impression of the usefulness of graph invariants. However, many water clusters are strained and the calculations without optimization of atomic positions would lead to a distorted picture. Therefore, we optimized the spatial structures of clusters for each H-bond network. It is important that the optimization does not change the topology of the H-bond network because the latter is explicitly incorporated into the structure of the wave function used. It should be stressed that the difference between the optimized and the idealized structures strongly depends on the H-bond pattern. In particular, the H-bond network structure determines the H–O–H angle in the idealized structure and thus determines the local distortion of the structure after optimization.

3 Results and discussion

Graph invariants are described in detail in Ref. [10], but it is instructive to recall their definition. H-bonds between water molecules are directional: the H atom is closer to one of O atoms participating in the bond. Therefore, any H-bond network can be represented as an oriented graph. Each water system (such as 24 structures mentioned above) defines the adjacency graph but not orientations of individual edges. In general, the graph can generate 2^l oriented graphs, where l is the number of edges, but only a small part of them satisfies the ice rules. In addition, the system may have a non-trivial symmetry and some of the oriented graphs become identical. It further reduces the number of the oriented graphs allowed. Thus, each water cluster (morphology) M generates a set of N^M_{conf} H-bond networks (oriented graphs) $\{X^M_k\}$, where $k = 1 \div N^M_{\text{conf}}$. The aim is to find descriptors distinguishing between networks X^M_k for different k and allowing for predictions of physical properties.

First, one introduces a set of functions b^M_{ij} with i and j denoting vertices of the adjacency graph for morphology M (it is assumed that $i < j$ to avoid duplication): $b^M_{ij} = 1$ if the edge between i and j is oriented towards j; $b^M_{ij} = -1$ if the same edge is oriented towards i; $b^M_{ij} = 0$ if i and j are not connected. The arguments of functions b^M_r (r here is a complex index denoting a pair of vertices) are H-bond networks X^M_k. Values of $b^M_r(X^M_k)$, $[b_r b_s](X^M_k)$, $[b_r b_s b_t](X^M_k)$, etc. are general descriptors of H-bond networks determining the direction of H-bonds, their pair correlations, triple correlations etc. Nevertheless, direct application of such descriptors is not generally recommended because most of the known water systems have that or another symmetry: physical entities such as energy are invariant with respect to symmetry operations, and this fundamental property should be reflected in the definition of H-bond topology descriptors.

The symmetry meant is not the spatial symmetry of an actual water cluster. Instead, symmetry operations are permutations of graph vertices preserving the adjacency matrix. The resulting symmetry group G often corresponds to the spatial symmetry group of the ideal framework of O atoms. Permutations of vertices induce transformations of bond functions b_r. Symmetry-invariant descriptors for H-bond networks are generated by projecting on the totally symmetric representation of group G. The first-order invariants (up to normalization constant) are given as:

$$I^M_r = \sum_{\alpha=1}^{n_G} g_\alpha \left(b^M_r \right), \tag{1}$$

where g_α are symmetry operations and the summation is over all n_G elements of the symmetry group. In full analogy, the second-order invariants are defined as:

$$I^M_{rs} = \sum_{\alpha=1}^{n_G} g_\alpha \left(b^M_r b^M_s \right), \tag{2}$$

where the group elements act upon products of bond variables. The generalization to higher orders is straightforward. Not all generated invariants are independent: some invariants are zero, while some other coincide.

To illustrate the definitions, we consider a model case of four-membered cyclic clusters with low symmetry group C_4. The idealized O framework is formed by a square of atoms A, B, C, and D. H-bonds 1–4 are between A and B, B and C, C and D, D and A, respectively. The only first-order invariant for such a system is simply the sum of all bond functions:

$$I^M_1 = b_1 + b_2 + b_3 + b_4. \tag{3}$$

Three independent second-order invariants can be constructed:

$$\begin{aligned} I^M_{11} &= b_1^2 + b_2^2 + b_3^2 + b_4^2; \\ I^M_{12} &= b_1 b_2 + b_2 b_3 + b_3 b_4 + b_4 b_1; \\ I^M_{13} &= 2(b_1 b_3 + b_2 b_4). \end{aligned} \tag{4}$$

If one considers the network of H-bonds directed from A to B, from B to C, from C to D, and from D to A, then all variables b are equal to 1 and all the above invariants are equal to 4. Another network of H-bonds directed from A to B, from C to B, from C to D, and from A to D is characterized by $b_1 = b_3 = 1$ and $b_2 = b_4 = -1$ leading to the following values for the invariants: $I^M_1 = 0$, $I^M_{11} = I^M_{13} = 4$, $I^M_{12} = -4$.

One can notice that the definition of graph invariants strongly depends on the definition of bond functions. We employ this degree of freedom and propose an alternative definition of graph invariants based on the occupation numbers. Instead of functions b^M_{ij} with $i < j$, we introduce twice as many functions d^M_{ij} defined for $i \neq j$: $d^M_{ij} = 1$ if the edge between i and j is oriented towards j and $d^M_{ij} = 0$ otherwise. That means, for example, that each existing H-bond is represented by two bond functions (d^M_{ij} and d^M_{ji}), one of them produces 1, while the other 0. The obvious advantage of this alternative scheme is that dangling O–H bonds can be naturally incorporated into the definition and used for generating the graph invariants. Graph invariants from functions d are formed using the same projection operation as before (Eqs. 1, 2). At the same time, the set of graph invariants for systems of H-bonds without defects remains unchanged: both schemes lead to the same linearly independent graph invariants because for each existing H-bond $b^M_{ij} = 2d^M_{ij} - 1$ and the other bond function $d^M_{ji} = 1 - d^M_{ij}$

Table 1 Number of invariants of different orders for H-bond networks in ice nanotubes

System	1-st order	2-nd order	3-rd order	4-th order	5-th order
INT_3^2	1	7	10	52	94
INT_3^3	1	15	56	279	963
INT_3^4	1	26	140	928	4374
INT_3^5	2	40	303	2350	14,138
INT_3^6	2	57	534	5004	36,204
INT_3^7	3	77	886	9457	80,171
INT_3^8	3	100	1336	16,384	158,692
INT_3^9	4	126	1949	26,568	289,818
INT_4^3	1	24	91	644	2606
INT_4^4	1	42	236	2172	12,372
INT_4^5	2	65	513	5540	40,828
INT_4^6	2	93	916	11,848	106,300
INT_4^7	3	126	1523	22,456	237,790
INT_4^8	3	164	2312	38,984	474,744
INT_5^3	1	24	144	1083	5,931
INT_5^4	1	42	374	3797	28,641
INT_5^5	2	65	806	9896	95,302
INT_5^6	2	93	1441	21,455	249,987
INT_5^7	3	126	2388	41,049	561,823
INT_5^8	3	164	3628	71,753	1,126,283
INT_6^3	1	33	202	1857	11,529
INT_6^4	1	58	529	6540	56,735
INT_6^5	2	90	1141	17,082	190,510
INT_6^6	2	129	2048	37,081	503,133
INT_6^7	3	175	3396	71,003	1,135,599

becomes redundant. The schemes are different only when the system of H-bonds allows for defects like broken H-bonds.

Before we start our analysis of the quality of the energy approximation by graph invariants, it is reasonable to look at their total numbers for different systems. Table 1 shows these numbers for some ice nanotubes INT_n^m. In particular, the dependence of the numbers of distinct graph invariants on the order of the invariant and the indices m and n is revealed. The values in the table can be found numerically by applying the graph invariant definition to a specific water cluster. Alternatively, one can determine these numbers analytically on the basis of symmetry considerations. Transformation of bond variables defines a (reducible) representation T of the symmetry group G of the cluster. The number of the kth order invariants is simply the number of the totally symmetric representations in the kth symmetric power of T. Thus, only characters of T are necessary to determine numbers in Table 1.

One can notice that the numbers of graph invariants grow very fast with their order. The number of fifth-order invariants is comparable and sometimes even exceeds the total number of H-bond configurations making their use unjustified. Even in the case of the highly symmetric 5^{12} D-cage, the total number of fifth-order invariants is 2286, which is only one order of magnitude smaller than the total number of configurations. At the same time, such unfavourable ratio of the numbers of H-bond configurations and high-order graph invariants is caused by the exclusion of configurations with defects. Moreover, many of the graph invariants are linearly dependent when they are computed for the given set of H-bond networks.

We carried out calculation of standard second-order graph invariants for all the systems mentioned above. The calculations correspond to two cases: one takes into account only H-bonds, while the other is based on dangling O–H bonds. Table 2 presents the results of our calculations for all 24 water clusters. The first column shows numbers of H-bond configurations N_{conf}^M satisfying the ice rules. When a graph invariant I_α^M is applied to the set of H-bond configurations $\{X_k^M\}$, it produces a vector of dimension N_{conf}^M comprising numbers $I_\alpha^M(X_k^M)$. Some of these vectors are linearly dependent. The next two columns of Table 2 present numbers of linearly independent second-order graph invariants (determined for both systems of bonds mentioned above) with respect to H-bond configurations satisfying the ice rules.

The calculated energies of H-bond networks also constitute vectors E_k^M of dimension N_{conf}^M. The linear predictive model approximates the energies by linear combinations of graph invariant descriptors:

$$E_k^M = \sum_\alpha C_\alpha^M I_\alpha^M\left(X_k^M\right). \tag{5}$$

The coefficients C_α^M are determined by the method of least squares for all 24 clusters. The quality of the approximation is characterized by R^2, a coefficient of determination routinely used in statistics. The remaining two columns of Table 2 show R^2 as determined for the same two systems of graph invariants (H-bonds and O–H bonds). The quality of the approximation turns out to be strongly dependent on the type of the cluster. In particular, energies of clusters with a cage structure are well described by linear combinations of graph invariant descriptors. The invariants defined for H-bonds provide slightly better results than those defined for O–H bonds, but both approximations are highly accurate. Quite expectedly, the system of O–H bonds is not sufficient to describe a defect in a system of H-bonds. Therefore, energies of clusters with defects (2) and (3) are reasonably well described only with graph invariants for systems of H-bonds.

Table 2 Description of H-bond networks in water clusters by second-order invariants: number of H-bond configurations N^M_{conf}; number of linearly independent second-order invariants for dangling O–H bonds and H-bonds (N^M_{inv}(O–H) and N^M_{inv}(H-bond)); the quality of the approximations (R-squared)

System	N^M_{conf}	N^M_{inv}(O–H)	N^M_{inv}(H-bond)	R^2(O–H)	R^2(H-bond)
INT^3_4	178	5	14	0.15332	0.47787
INT^4_4	978	5	21	0.26268	0.71627
INT^5_4	5588	5	29	0.04810	0.44210
INT^6_4	33,073	5	39	0.07379	0.49441
INT^7_4	198,706	5	50	0.06196	0.46588
INT^8_4	1,210,106	5	63	0.06761	0.54263
INT^2_5	102	5	9	0.98234	0.99138
INT^3_5	860	5	14	0.19914	0.57754
INT^4_5	7480	5	21	0.39873	0.83217
INT^5_5	66,160	5	29	0.10688	0.52272
INT^6_5	591,328	5	39	0.12638	0.56749
INT^2_6	408	7	13	0.96178	0.98239
INT^3_6	4962	7	20	0.19364	0.48253
INT^4_6	64,835	7	30	0.46010	0.85003
INT^5_6	865,243	7	41	0.11721	0.55329
INT^2_7	1474	7	13	0.94966	0.96614
INT^3_7	28,896	7	20	0.35136	0.38212
INT^4_7	580,200	7	30	0.35224	0.66997
(1)	30,026	5	7	0.96378	0.96403
(2)	443,112	5	8	0.46732	0.97290
(3)	2,772,313	5	8	0.24939	0.93086
(4)	394,000	39	78	0.99290	0.99345
(5)	22,960	9	36	0.41787	0.63397
(6)	3,043,836	19	35	0.98046	0.98140

The quality of the approximation deteriorates when significant strains are present in the structure (like those in ice nanotubes). Figure 3 shows the correlation between the calculated energy and its graph invariant approximation for clusters (1) and (5). The former is not strained, while the latter has mild strains. In line with this observation, the quality of the approximation is better for stable INT^m_5 and INT^m_6 than for strained INT^m_4 and INT^m_7. As for the indices m, the value of R^2 depends on its parity: R^2 is larger for even m than for odd m. Taking into account that the number of dangling O–H bonds does not depend on the size parameter m of INT^m_n, it is not surprising that the quality of the energy approximation by graph invariants for O–H bonds is inadequate for large m. All these conclusions are valid only for calculations with the optimized spatial structure. If we consider idealized structures of ice nanotubes, the value of R^2 becomes close to 1 because the energy of H-bond configurations becomes largely determined by the number of strained water molecules with both O–H bonds placed along the nanotube axis, and this parameter is expressible via second-order graph invariant descriptors.

There are different possibilities to improve the description based on increasing the number of graph invariants in play. One of them is to take a larger set of variables combining both H-bonds and dangling O–H bonds. This approach slightly increases the value of R^2: for example, in the case of cluster (2) it increases from 0.97290 to 0.97716, while in the case of cluster (3) it changes from 0.93086 to 0.93906. In the case of ice nanotubes, the effect of adding dangling O–H bonds to the set of variables is very small. Another obvious option is to increase the order of the invariants and this, indeed, increases the quality of the approximation, but

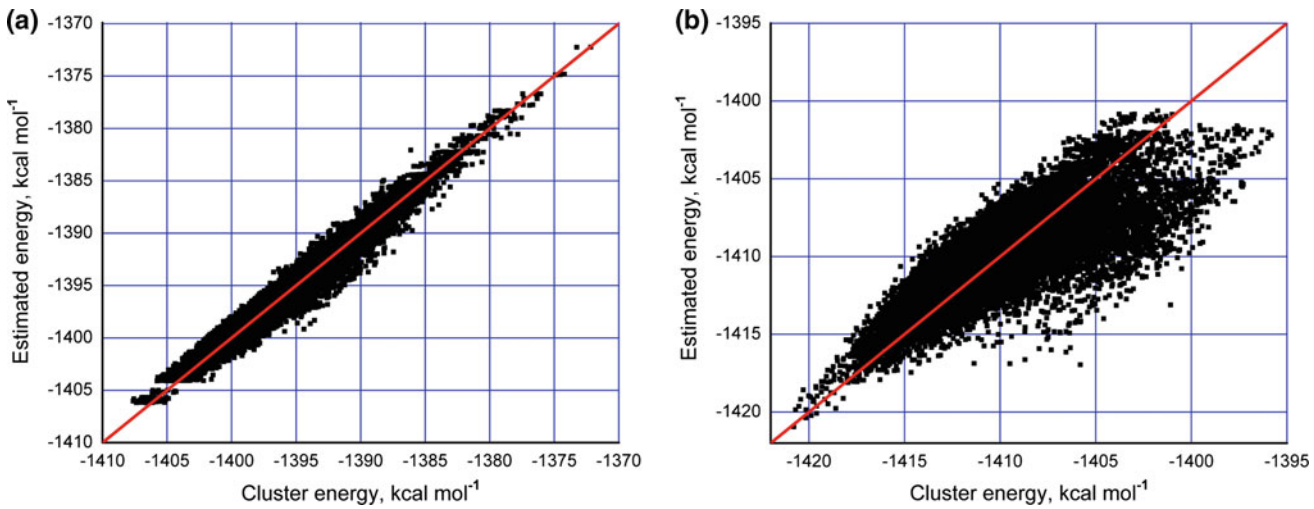

Fig. 3 Correlation between the calculated energy and its graph invariant approximation for clusters (1) and (5)

it is necessary to bear in mind that it comes with a significant increase in the number of graph invariants. For example, in the case of INT_4^4 the number of independent invariants increases from 21 to 57 and R^2 changes from 0.71627 to 0.74785 when the second-order graph invariants for H-bonds are replaced by third-order ones. The increase in R^2 is smaller when invariants for dangling O–H bonds are considered (for example, R^2 changes from 0.26268 to 0.27331 when the second-order invariants are replaced by fourth-order invariants for the same ice nanotube INT_4^4). Even a significant increase in the number of graph invariants doesn't necessarily bring serious improvement of the approximation. For example, in the case of graph invariants defined for dangling O–H bonds of water cage (1), the number of invariants increases from 5 to 58 when the order of invariants changes from 2 to 4, but the value of R^2 is improved only marginally (from 0.96378 to 0.96907).

Some systems allow for specific approaches. In the case of mixed cluster (4), it is possible to separately consider the configurations with a dangling F–H bond and those with the H-bond F–H$\cdots$O. It turns out that the value of R^2 is smaller for the first set (0.98550) than for the other (0.99435). Approaches employing graph invariants based on bond functions *b* and *d* are different in the case of clusters with broken H-bonds. Our calculations show that the change of the definition of the graph invariants does not bring significant improvements in terms of the quality of the approximation: the values of R^2 for two schemes are relatively close (larger for that based on bond functions *d*) and are equal to 0.97290 and 0.97763 for cluster (2) and 0.93086 and 0.94077 for cluster (3), respectively.

Finally, we provide a few thoughts about the general idea of graph invariants as given by totally symmetric projectors of the products of bond variables. Sometimes other representations of the symmetry group may be useful. An example is provided by ice nanotubes. They are thought to possess ferroelectric order with a net polarization when *n* is odd and to be "anti-ferroelectric" when *n* is even [26, 27]. This prediction is based on a simple model discarding most of the H-bond configurations. Alternatively, we can consider an idealized structure of ice nanotubes. In this case, the polarization parallel to the INT axis is proportional to the difference of the numbers of dangling O–H bonds on the INT ends, thereby confirming the original predictions. This parameter should also play a significant role for relaxed structures, but it corresponds to the representation A_1'' for INT_n^m with an odd *n* and to the representation A_{1u} for INT_n^m with an even *n*. Therefore, analysis of properties like polarization may require specialized graph descriptors based on the symmetry of the system.

4 Conclusion

In summary, a very large database of the energies of H-bond networks in water clusters is constructed with the help of an ultra-fast semiempirical method based on strictly local electron groups. It includes water clusters of different symmetry and morphology, clusters with ideal and defected structures, systems where one water molecule is replaced with hydrogen fluoride. Two varieties of graph invariant descriptors are benchmarked against quantum-chemical calculations, one of them being proposed in the present paper. Both types of descriptors lead to identical results when applied to ideal networks satisfying ice rules but differ for structures with defects. We established that the use of high-order invariants is not justified unless H-bond networks significantly deviating from ice rules are taken into consideration. Approximation of the water cluster energies by linear combinations of second-order graph invariants shows that this approach gives surprisingly good results for clusters without significant strains (including those with defects) but fails when four-membered water rings are present in the structure.

Acknowledgments This work is partially supported by National Research Center "Kurchatov Institute", Russian Science Foundation (Grant 14-19-00662), and Russian Foundation for Basic Research (Grants 13-07-00095 and 14-03-00867).

References

1. Hoepfner V, Deringer VL, Dronskowski R (2012) Accurate hydrogen positions in organic crystals: assessing a quantum-chemical aide. Cryst Growth Des 12:1014–1021
2. Hoepfner V, Deringer VL, Dronskowski R (2012) Hydrogen-bonding networks from first principles: exploring the guanidine crystal. J Phys Chem A 116:4551–4559
3. Deringer VL, Englert U, Dronskowski R (2014) Covalency of hydrogen bonds in solids revisited. Chem Commun 50:11547–11549
4. Bernal JD, Fowler RH (1933) A theory of water and ionic solution, with particular reference to hydrogen and hydroxyl ions. J Chem Phys 1:515–548
5. Yoo S, Kirov MV, Xantheas SS (2009) Low-energy networks of the T-cage $(H_2O)_{24}$ cluster and their use in constructing periodic unit cells of the structure I (sI) hydrate lattice. J Am Chem Soc 131:7564–7566
6. Chihaia V, Adams S, Kuhs WF (2004) Influence of water molecules arrangement on structure and stability of 5^{12} and $5^{12}6^2$ buckyball water clusters. A theoretical study. Chem Phys 297:271–287
7. Kirov MV, Fanourgakis GS, Xantheas SS (2008) Identifying the most stable networks in polyhedral water clusters. Chem Phys Lett 461:180–188
8. Anick DJ (2003) Application of database methods to the prediction of B3LYP-optimized polyhedral water cluster geometries and electronic energies. J Chem Phys 119:12442–12456

9. Tokmachev AM, Tchougréeff AL, Dronskowski R (2010) Hydrogen-bond networks in water clusters ($H_2O)_{20}$: an exhaustive quantum-chemical analysis. ChemPhysChem 11:384–388
10. Kuo J-L, Coe JV, Singer SJ, Band YB, Ojamäe L (2001) On the use of graph invariants for efficiently generating hydrogen bond topologies and predicting physical properties of water clusters and ice. J Chem Phys 114:2527–2540
11. Kuo J-L, Singer SJ (2003) Graph invariants for periodic systems: towards predicting physical properties from the hydrogen bond topology of ice. Phys Rev E 67:016114
12. Singer SJ, Kuo J-L, Hirsch TK, Knight C, Ojamäe L, Klein ML (2005) Hydrogen-bond topology and the ice VII/VIII and ice Ih/XI proton-ordering phase transitions. Phys Rev Lett 94:135701
13. Knight C, Singer SJ, Kuo J-L, Hirsch TK, Ojamäe L, Klein ML (2006) Hydrogen bond topology and the ice VII/VIII and ice Ih/XI proton ordering phase transitions. Phys Rev E 73:056113
14. Knight C, Singer SJ (2006) A reexamination of the ice III/IX hydrogen bond ordering phase transition. J Chem Phys 125:064506
15. Knight C, Singer SJ (2008) Hydrogen bond ordering in ice V and the transition to ice XIII. J Chem Phys 129:164513
16. Knight C, Singer SJ (2009) Site disorder in ice VII arising from hydrogen bond fluctuations. J Phys Chem A 113:12433–12438
17. Tokmachev AM, Dronskowski R (2011) Hydrogen-bond networks in finite ice nanotubes. J Comp Chem 32:99–105
18. Tokmachev AM, Tchougréeff AL (2001) Semiempirical implementation of strictly localized geminals for analysis of molecular electronic structure. J Comp Chem 22:752–764
19. Tokmachev AM, Tchougréeff AL (2003) Fast NDDO method for molecular structure calculations based on strictly localized geminals. J Phys Chem A 107:358–365
20. Tokmachev AM, Tchougréeff AL (2005) Efficient multipole model and linear scaling of NDDO-based methods. J Phys Chem A 109:7613–7620
21. Tchougréeff AL, Tokmachev AM, Dronskowski R (2009) Multipole model for the electron group function method. J Phys Chem A 113:11406–11415
22. Surján PR (1999) An introduction to the theory of geminals. Top Curr Chem 203:63–88
23. Tokmachev AM (2015) Perspectives of geminal methods for large molecular systems. Int J Quantum Chem. doi:10.1002/qua.24963
24. Jeszenszki P, Nagy PR, Zoboki T, Szabados Á, Surján PR (2014) Perspectives of APSG-based multireference perturbation theories. Int J Quantum Chem 114:1048–1052
25. Tokmachev AM, Tchougréeff AL (2006) Group functions approach based on the combination of strictly local geminals and molecular orbitals. Int J Quantum Chem 106:571–587
26. Luo C, Fa W, Zhou J, Dong J, Zeng XC (2008) Ferroelectric ordering in ice nanotubes confined in carbon nanotubes. Nano Lett 8:2607–2612
27. Mikami F, Matsuda K, Kataura H, Maniwa Y (2009) Dielectric properties of water inside single-walled carbon nanotubes. ACS Nano 3:1279–1287

Theor Chem Acc (2015) 134:128
DOI 10.1007/s00214-015-1745-0

REGULAR ARTICLE

Photodissociation dynamics of the D_2^+ ion initiated by several different laser pulses

Gábor J. Halász[1] · András Csehi[2] · Ágnes Vibók[2,3]

Received: 13 June 2015 / Accepted: 5 October 2015 / Published online: 14 October 2015

Abstract Nonadiabatic effects are ubiquitous in physics and chemistry. They are associated with conical intersections (CIs) which are degeneracies between electronic states of polyatomic molecules. Recently, it has been recognized that so-called light-induced conical intersections (LICIs) can be formed both by standing or by running laser waves even in diatomics. Owing to the strong nonadiabatic couplings, the appearance of such laser-induced conical intersections (LICIs) may significantly change the dynamical properties of a molecular system. In the present paper we investigate the photodissociation dynamics of D_2^+ ion initiating the nuclear dynamics from the superposition of all the vibrational states produced by ionizing D_2. The kinetic energy release and the angular distribution of the photodissociation products are computed with and without LICI for the several different values of the laser parameters. We performed both one- and two-dimensional calculations, as well. In the first scheme the molecules were rotationally frozen, whereas in the latter one, the molecular rotation is included as a full additional dynamic variable. The results obtained undoubtedly demonstrate that the impact of the LICI on the dissociation dynamics of the D_2^+ molecule strongly depend upon the laser parameters applied.

Keywords Photodissociation · Nonadiabatic effect · Laser-induced conical intersection · Diatomic molecule · Pulse length

1 Introduction

By separating the motion of the fast-moving electrons and the slow nuclei in a molecular system the Born–Oppenheimer (BO) approximation [1] usually can treat the dynamical process in a molecule after absorbing a photon. In this picture the nuclei move over a potential energy surface (PES) obtained from the electronic (adiabatic) eigenstates and therefore electrons and nuclei do not easily exchange energy. Although several chemical and physical dynamical processes can be described on a single Born – Oppenheimer PES, yet, in many important cases like radiationless relaxation of excited electronic states, dissociation, proton transfer or isomerization processes of polyatomic molecules etc. this approximation breaks down. The nuclear and electronic motion then couple and so-called conical intersection (CI) arises [2–11]. In this situation the energy exchange between the electrons and nuclei can become important. It is widely recognized today these conical intersections are very important in the nonadiabatic processes which are ubiquitous in photophysics and photochemistry.

For diatomic systems that have only one degree of freedom, it is not possible for two electronic states of the same symmetry to become degenerate and as a consequence of the well-known noncrossing rule an avoided crossing results. However, it stands only in field-free space. It was pointed out

Published as part of the special collection of articles "Festschrift in honour of P. R. Surjan".

✉ Ágnes Vibók
vibok@phys.unideb.hu

[1] Department of Information Technology, University of Debrecen, PO Box 12, 4010 Debrecen, Hungary

[2] Department of Theoretical Physics, University of Debrecen, PO Box 5, 4010 Debrecen, Hungary

[3] ELI-ALPS, ELI-HU Non-Profit Ltd, Dugonics tér 13, 6720 Szeged, Hungary

in previous works that conical intersections can be formed in a molecular system both by running or by standing laser waves even in diatomics [12, 13]. In this case the laser-light couples either the center of the mass motion with the internal rovibrational degrees of freedom (in case of standing laser field) or the vibrational motion with the emerged rotational degree of freedom (in the case of running laser field) and so-called light-induced conical intersection (LICI) arises. In contrast to field-free polyatomic molecules where the CI is given by nature, the energetic position of the LICI is determined by the laser frequency and the strength of its nonadiabatic coupling is controlled by the laser intensity.

A few years ago, we have started a systematic study of the nonadiabatic effect induced by laser waves in molecular systems. It has been demonstrated that the light-induced conical intersections have very significant impact on several different dynamical properties (like molecular spectra, molecular alignment or photodissociation probability etc….) of diatomic molecules [14–20]. Additionally, in a very recent paper [21] by studying carefully the dissociation process of the D_2^+ molecule we could provide the first "direct observable and measurable signature" of the light-induced conical intersections. It was also found that resonant laser pulses of high carrier frequency may induce an analogue of conical intersections of the complex potential energy surfaces of the ground and field-dressed resonant states [22–24]. This analogue of a conical intersection in the continuum states forms also in nature [25, 26]. In 2013 Cederbaum and his colleague published the first theoretical results on polyatomic system in the optical regime [27]. Besides these theoretical studies some important experimental papers have also been published recently. The first experimental observation of light-induced conical intersections in diatomic molecules is provided by Bucksbaum, and his co-workers [28]. In another works the experimental outcomes of the laser-induced isomerization and photodissociation processes of polyatomic molecules were qualitatively interpreted using the concept of the LICIs [29–32].

In the present article we focus on the photodissociation process of the D_2^+ molecule. This system and this process have extensively been studied in the last decades [33–57], but there are still many unclarified issues. Moreover, as the D_2^+ ion is a fairly simple system, the light-induced nonadiabatic phenomena can be investigated separately from other processes. By solving the time-dependent nuclear Schrödinger equation, we calculate the kinetic energy release (KER) spectra and the angular distribution of the photodissociated fragments with and without LICIs for several different values of the laser intensity and laser pulse length. We perform one (1d)- and two (2d)-dimensional calculations as well. In the first case the molecular rotational angle is only a parameter, while in the 2d situation the rotational angle is taken into account in the numerical simulations as a dynamic variable fully including the light-induced nonadiabatic phenomena. We will discuss in detail how the different laser intensities and pulse lengths influence the effect of the light-induced conical intersection for the investigated dynamical properties of the D_2^+ ion. This work can be considered as an extension of our previous work [18]. In that paper [18] the alignment dependence of the dissociated photofragments of the D_2^+ molecular ion has been studied, in the present work we focus on describing properly the pulse length dependence of these photoproducts. Results obtained by using an initial wave packet starting from one of the vibrational eigenstates can be more easily interpreted. Initiating the dynamics from a Franck–Condon distribution, we have a mixture of the eigenstates and it makes it more complicated to analyze the obtained results. However, from an experimental point of view it is easier to create a FC distribution for the initial wave packet by simply photoionizing the D_2 molecule, than to create a well defined eigenstate of the ion.

The article is structured as follows. In the next section, we provide the background required for our theoretical study. The applied methods and the calculated dynamical quantities are briefly summarized. In the third section, we present and discuss the numerical results for the values of several different laser parameters. In the last section, we summarize the conclusions.

2 Methods and details of the calculations

To study the dissociation dynamics, we consider the ground state of the D_2 molecule ($X^1\sum_g^+$) and the first two electronic states ($V_1 = 1s\sigma_g$ and $V_2 = 2p\sigma_u$) of the D_2^+ ion (Fig. 1). At first the D_2 molecule is in its ground ($X^1\sum_g^+$) electronic state and after ionization the vibrational wave packet is launched to the $1s\sigma_g$ state of D_2^+ in the Franck–Condon region. In the next step, the D_2^+ ion is excited from the $1s\sigma_g$ state by a laser pulse to the dissociative $2p\sigma_u$ state. The radiative interaction mediated by the non-vanishing electronic dipole moment between the $1s\sigma_g$ and $2p\sigma_u$ electronic states is responsible for the light-induced electronic transitions. In these two electronic states the time-dependent Hamiltonian can be written for the rovibronic nuclear motions as:

$$\hat{H} = \begin{pmatrix} -\frac{1}{2\mu}\frac{\partial^2}{\partial R^2} + \frac{L^2_{\theta\varphi}}{2\mu R^2} & 0 \\ 0 & -\frac{1}{2\mu}\frac{\partial^2}{\partial R^2} + \frac{L^2_{\theta\varphi}}{2\mu R^2} \end{pmatrix} + \begin{pmatrix} V_1(R) & -\epsilon_0 f(t) d(R)\cos\theta\cos\omega_L t \\ -\epsilon_0 f(t) d(R)\cos\theta\cos\omega_L t & V_2(R) \end{pmatrix}. \quad (1)$$

Here, R and (θ, φ) are the molecular vibrational and rotational coordinates, respectively, μ denotes the reduced mass, and $L_{\theta\varphi}$ is the angular momentum operator of the nuclei. θ is the angle between the polarization direction

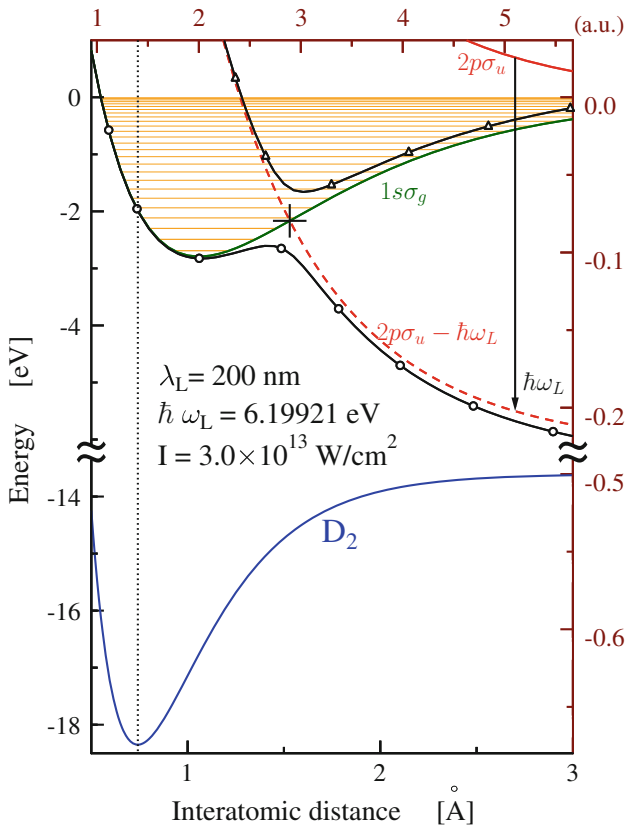

Fig. 1 Potential energy curves. Shown are the curves for the ground state ($X^1\sum_g^+$) of D_2, and for the ground ($1s\sigma_g$), first excited ($2p\sigma_u$) and field dressed ($2p\sigma_u - \hbar\omega$) states of the D_2^+ ion. The first laser pulse ionizes the D_2 molecule to create a vibrational wave packet on the $1s\sigma_g$ surface of D_2^+. The *solid green* and *red lines* show the field-free energies of the ground and first excited states of the ion, respectively, which are the diabatic energies when the field is on. The energy of the field-dressed excited state ($2p\sigma_u - \hbar\omega_L$; *dashed red line*) crosses the energy of the ionic ground state at the point where the light-induced conical intersection (LICI) of these two states is formed. These curves can also be viewed as cuts through the adiabatic surfaces at $\theta = \pi/2$ where the interaction between the states via the field vanishes. For further visualization, cuts of the adiabatic surfaces at $\theta = 0$ (parallel to the field polarization) are shown for a field intensity of $3 \times 10^{13}\,\mathrm{W\,cm^{-2}}$. The cuts through the lower and upper adiabatic surfaces are depicted by *solid black lines marked with circles and triangles*, respectively. The position of the LICI ($R_{\mathrm{LICI}} = 1.53$ Å $= 2.891$a.u. and $E_{\mathrm{LICI}} = -2.16611$ eV) is marked with a cross (figure is taken from Ref. [18])

and the direction of the transition dipole and thus one of the angles of rotation of the molecule. $V_1(R)$ ($1s\sigma_g$) and $V_2(R)$ ($2p\sigma_u$) are the bare potential curves of the two electronic states coupled by the laser (whose frequency is ω_L and maximal amplitude is ϵ_0), $f(t)$ is the envelop function and $d(R)(= -\langle\psi_1^e|\sum_j r_j|\psi_2^e\rangle)$ is the transition dipole matrix element ($e = m_e = \hbar = 1$; atomic units are used throughout the article). The potential energies $V_1(R)$ and $V_2(R)$ and the transition dipole moment were borrowed from [58, 59].

The Floquet representation is very illustrative and helps to understand the essence of the light-induced nonadiabatic phenomena. In this picture the Floquet curves are replicas of the field-free molecular potential curves that are shifted in energy due to the interaction with the laser field. The energy shift is given by the net number of photons the molecule absorbs from the field and a crossing between the diabatic ground and the diabatic shifted excited potential energy curves is formed. New field-induced states are obtained by diagonalizing the diabatic potential energy matrix. This gives rise to laser-induced V_{lower} and V_{upper} adiabatic molecular potentials and to a conical intersection as well, whenever the two conditions $\cos\theta = 0$ ($\theta = \pi/2$) and $V_1(R) = V_2(R) - \hbar\omega_L$ are simultaneously fulfilled.

The characteristic features of the light-induced conical intersection can be modified by changing the frequency and intensity of the laser field. In sharp contrast to field-free polyatomic molecules where the conical intersection is given by nature, the energetic position of the light-induced conical intersection can be controlled by the laser frequency and the strength of its nonadiabatic coupling [2–7, 10, 11] by the laser intensity.

To discuss the impact of the light-induced conical intersection on the photodissociation dynamics, we have to solve the time-dependent nuclear Schrödinger equation (TDSE) with the Hamiltonian $\hat{H}$ given by Eq. (1). One of the most efficient procedure for solving the time-dependent nuclear Schrödinger equation is the MCTDH (multi configuration time-dependent Hartree) approach [60–64]. To describe the vibrational degree of freedom we have applied FFT-DVR (Fast Fourier Transformation-Discrete Variable Representation) with N_R basis elements distributed on the range from 0.1 to 80 a.u. for the internuclear separation. The rotational degree of freedom was constructed by the Legendre polynomials $\{P_J(\cos\theta)\}_{j=0,1,2,\ldots,N_\theta}$. These so-called primitive basis sets (χ) were used to represent the single particle functions (ϕ) which in turn were applied to represent the wavefunction:

$$\begin{aligned}\phi_{j_q}^{(q)}(q,t) &= \sum_{l=1}^{N_q} c_{j_q l}^{(q)}(t)\;\chi_l^{(q)}(q) \qquad q = R,\,\theta \\ \psi(R,\theta,t) &= \sum_{j_R=1}^{n_R}\sum_{j_\theta=1}^{n_\theta} A_{j_R,j_\theta}(t)\phi_{j_R}^{(R)}(R,t)\phi_{j_\theta}^{(\theta)}(\theta,t).\end{aligned} \tag{2}$$

During the numerical simulations $N_R = 2048$ and, depending on the field intensity, $N_\theta = 6,\ldots,70$ have been used. To construct the nuclear wave packet of the system on both diabatic surfaces and for both degrees of freedom a set of $n_R = n_\theta = 3,\ldots,25$ single particle functions were applied. (The actual value of N_θ and $n_R = n_\theta$ was chosen depending on the peak field intensity I_0.) All the calculations were properly converged with these

Table 1 Total dissociation probability as a function of intensity and pulse duration

t_{pulse} (fs)	$I_0 = 1 \times 10^{12}\ W\,\text{cm}^{-2}$		$I_0 = 1 \times 10^{14}\ W\,\text{cm}^{-2}$	
	2d	1d	2d	1d
10	0.0539	0.0538	0.6885	0.6834
20	0.0712	0.0712	0.7803	0.7512
30	0.0862	0.0861	0.8466	0.7711
40	0.1009	0.1006	0.8850	0.7848
50	0.1144	0.1139	0.9107	0.7950

The columns labeled as 2d and 1d correspond to the full two-dimensional and the one-dimensional (no LICI situation) calculations, respectively

parameters. Because of the cylindrical symmetry of the problem, $L_\varphi = m$ is a good quantum number and we have only concentrated on discussing the $m = 0$ case.

Applying the nuclear wave function the kinetic energy release (KER) and the angular distribution of the photofragments [62] are defined as:

$$P_{\text{KER}}(E) = \int_0^\infty \mathrm{d}t \int_0^\infty \mathrm{d}t' \langle \psi(t)|W|\psi(t')\rangle e^{-iE(t-t')} \tag{3}$$

where $-iW$ is the complex absorbing potential (CAP) used at the last 10 a.u. of the grid related to the vibrational degree of freedom ($W = 0.00005 \cdot (r-70)^3$, if $r > 70$ a.u. on the $1s\sigma_g$ surface and $W = 0.00236 \cdot (r-75)^3$, if $r > 75$ a.u. on the $2p\sigma_u$ surface), and

$$P(\theta_j) = \frac{1}{w_j} \int_0^\infty \mathrm{d}t \langle \psi(t)|W_{\theta_j}|\psi(t)\rangle \tag{4}$$

where $-iW_{\theta_j}$ is the projection of the CAP to a specific direction of the angular grid ($j = 0, \ldots N_\theta$), and w_j is the weight related to this grid point according to the applied DVR.

To stress the impact of the laser-induced conical intersection on the dissociation process of D_2^+, we compare the results obtained from the full two-dimensional (2d) model in which both the rotational and vibrational coordinates are accounted as dynamical variables with one-dimensional (1d) calculations where the rotational degree of freedom and accordingly the LICI is not considered. In the 1d situation the molecule's initial orientation is not changing during the dissociation and the "effective field strength" in the Hamiltonian Eq. (1) was the projection of the real field to the axis of the molecule: $\varepsilon_0^{\text{eff}} = \varepsilon_0 \cos\theta$ ($I_0^{\text{eff}} = I_0 \cos^2\theta$). This restriction implies that the molecular rotation is frozen and therefore the orientation of the molecular axis relative to the polarization of the laser field does not change during the whole process.

3 Results and discussion

We used linearly polarized Gaussian laser pulses centered around $t = 12.3$ fs in the calculations. This is the value of the delay time when the mean of the internuclear distance of the ground state wave packet vertically transferred to the ground state of the ion reaches its maximal value in the field-free case. The center wavelength is 200 nm and the two employed laser field intensity values are ($1 \times 10^{12}\,\text{W cm}^{-2}$, $1 \times 10^{14}\,\text{W cm}^{-2}$). Several different pulse lengths given by their full width at half-maximum (FWHM) ($t_{\text{pulse}} = 10, 20, 30, 40$ and 50 fs) have been applied.

The initial wave packet is provided by a vertical transfer of the vibrational ground state of the neutral molecule to the potential energy curve of the ground electronic state of the D_2^+. This Franck–Condon distribution of the vibrational states of the ion has been employed. To obtain back the vibrational ground state of the neutral molecule one has to assume the initial wave packet on the $1s\sigma_g$ curve as the superposition of all the vibrational states of the D_2^+ ion.

No preliminary alignments have been considered for the molecules. We applied isotropic initial distributions in the numerical simulations (with the rotational quantum number of $J = 0$).

The total dissociation probabilities for the different applied laser pulses are collected in Table 1. Comparison of the results of the one-dimensional calculations with the full two-dimensional ones shows that rotation plays a role in the dissociation dynamics only at large field intensity combined with long pulse length.

3.1 Kinetic energy release (KER)

Results for the kinetic energy release spectra (KER) of the photofragments are displayed in Fig. 2. The longer the pulse, the more structured the spectrum (see on Fig. 2). According to the Heisenberg's uncertainty principle, the pulse length of 10 fs is too short to resolve the energy difference of the neighboring levels. For this pulse length the spectrum is rather wide and does not contain information about the vibrational structure of the ground electronic state of the D_2^+ ion. For the longer pulses the partial waves dissociating at different times can create an interference pattern related to the vibrational states of the system. This effect is even more pronounced at the lower ($1 \times 10^{12}\,\text{W cm}^{-2}$) intensity value. At the intensity of $1 \times 10^{14}\,\text{W cm}^{-2}$ even a such short as 10 fs pulse duration is enough to provide nearly 70 % dissociation probability. It means that even for longer pulse this large amount of the wave packet dissociates immediately at the first time it reaches the large internuclear distance region just after a half vibrational

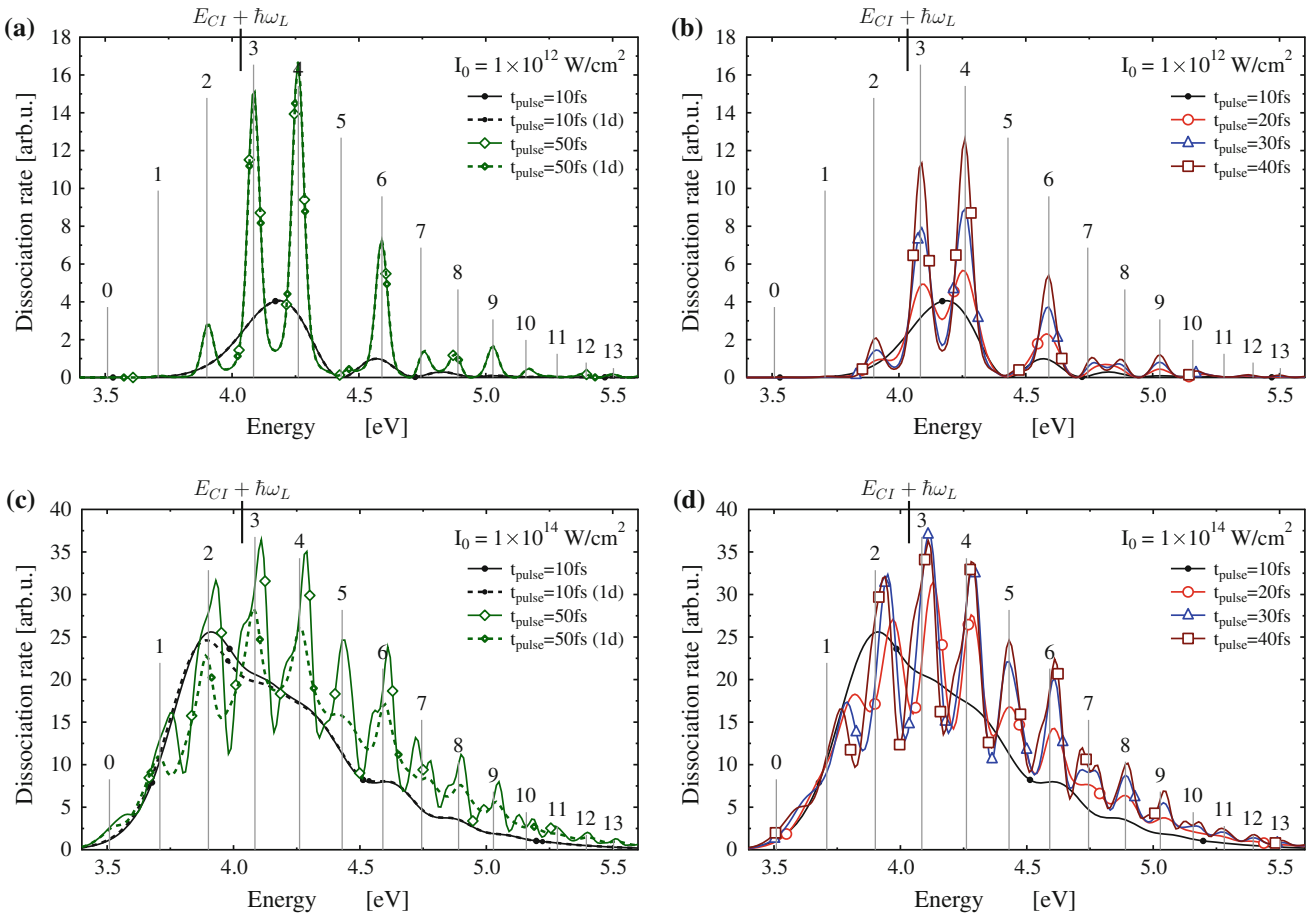

Fig. 2 Kinetic energy release (KER) spectra of the D_2^+ photofragments at 1×10^{12} (**a**, **b**) and 1×10^{14} W/cm^2 (**c**, **d**) intensities for five different (10, 20, 30, 40 and 50 fs) pulse lengths. The *dashed* (1d) and *solid curves* correspond to the one-dimensional (no LICI situation) and the full two-dimensional calculations, respectively. *Vertical lines* denote the different vibrational levels of the D_2^+ molecule in the field-free case shifted by the photon energy ($\hbar\omega_L$). The height of these lines is proportional to the population of the vibrational levels in the initial wave packet (Franck–Condon principle)

period. This part of the dissociated particles hardly collects any information about the ground electronic PES of the ion. The interference patterns observed in the KER spectra for the longer pulses are related to the excess dissociation taking place after some initial vibrations. Increasing the pulse length from 20 to 50 fs, the peaks of the spectra are continuously increasing for both intensities. According to Table 1 for the longest studied pulse (50 fs) this excess dissociation amount relative to the dissociation rate at 10 fs pulse is about 32 % for the intensity of 1×10^{14} W cm^{-2}, while it is approximately 110 % for the lower intensity (1×10^{12} W cm^{-2}). This is the reason why one can recognize much more characteristic fingerprint of the vibrational levels of the D_2^+ ion on the KER spectra at lower intensity.

Another important finding is that—similarly to the total dissociation rates—there is no noticeable difference between the 1d and 2d KERs at low intensities or at short pulses. We know from preliminary studies that at low intensities the effect of the laser-induced conical intersections are not so significant, and moreover, if the pulse length is not long enough substantial. rotation cannot emerge. For the case of the lower field intensity, the KERs from the 1d and the full calculations are indistinguishable (see. panel A on Fig. 2). The situation is quite different in the case of the higher field intensity. Even for the shortest pulse length there is a slight difference between the 1d and 2d results in the spectra around the photon energy shifted position of the LICI. Increasing the pulse length the differences become more pronounced. Not only the total dissociation rate reduces in the 1d model, (as we see in Table 1) but the interference peaks are also less characteristic. The peaks have smaller heights, and the minima between the peaks are not so deep as in the full 2d calculations. Moreover, there is a noticeable difference in the position of the peaks as well. In the 1d situation, similarly to the case of lower intensity the peaks are centered around the shifted

energies of the vibrational levels, while in the full calculations they are slightly shifted away from these values. The reason of this shift has already been discussed in [18].

Again, we find that at low (1×10^{12} W cm^{-2}) intensity the dissociation probability of the vibrational level $\nu = 5$ is practically zero (see panel A and B on Fig. 2). This finding has already been discussed by us. Namely, in a very special situation when one of the eigenvalues of the upper adiabatic potential [20] matches to the energy level of a certain vibrational eigenstate on the diabatic surface, the nuclear wave packet can spend a non-negligible amount of time in the upper adiabatic potential before reaching the dissociation region. The system somehow is being trapped for a certain time and as a result of it molecular fragments from this vibrational eigenstate are missing from the spectra. Nevertheless this phenomenon disappears at greater (1×10^{14} W cm^{-2}) intensity (see panel C and D on Fig. 2), because of the shift of the eigenvalues of the upper adiabatic potential due to the modification of its shape caused by the increased intensity.

3.2 Angular distribution and wave packet density

Figure 3 illustrates the results for the angular distribution of the photofragments. When the laser intensity is low the curves are smooth for each pulses. As in the case of the total dissociation yield or the KER spectra the 1d model also provides good description of the angular distribution. Noticeable differences appear only for the case of the longest laser pulse at the region of the small angles where the 1d model slightly underestimates the dissociation rate. At higher intensity, however, the situation changes significantly. In this case, for all the applied pulses, the 1d and 2d results strongly differ from each other. In fact, the 1d curves almost go together everywhere. One can observe small deviation between the curves only above 65 degrees. The strong field intensity rotates the molecules toward the direction of the external electric field and therefore more molecules appear parallel to the field direction than that would result from the isotopic distribution. This is the reason why the dissociation flux is much greater than 1 in the full two-dimensional calculations. The 1d model, however, cannot account for the rotation; therefore, in this model the dissociation rate is close to its largest possible value (1) at small angles, for which the effective field intensity ($I_0^{\text{eff}} = I_0 * \cos^2\theta$) is large enough to induce almost total dissociation.

At the larger intensity, except for the shortest pulse (10 fs) some modulations in the structure of the curves appear. We know from our earlier studies that these humps on the curves are the direct consequences of the rotation or the presence of the laser-induced conical intersection [19]. In the 1d calculations these modulations never appear. To

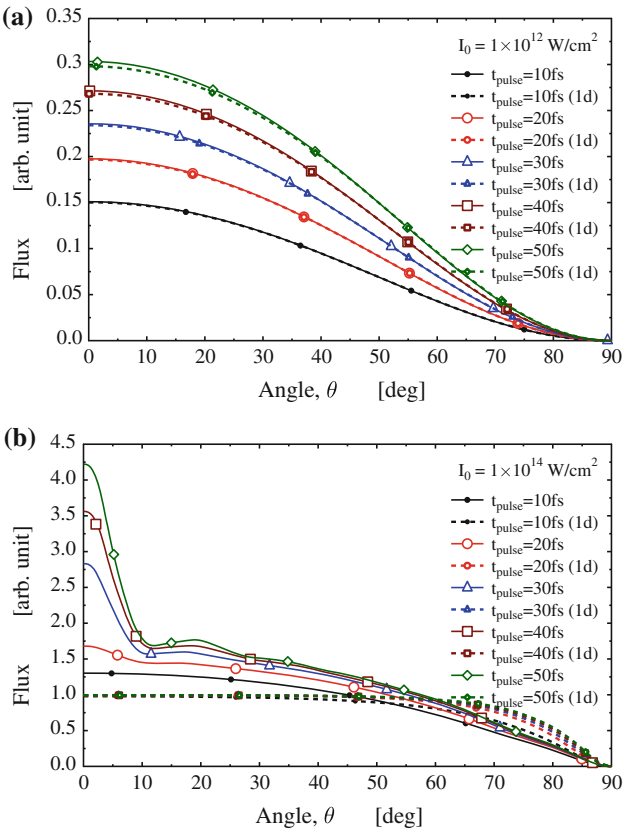

Fig. 3 Angular distributions of the D_2^+ photofragments at 1×10^{12} (**a**) and 1×10^{14} W/cm^2 (**b**) intensities for five different (10, 20, 30, 40 and 50 fs) pulse lengths. The *dashed* (1d) and *solid curves* correspond to the one-dimensional (no LICI situation) and the full two-dimensional calculations, respectively

see the clear signature of the LICI on the angular distribution of the photofragments, one needs large enough intensity and long enough pulse. The LICI exerts a strong nonadiabatic coupling via mixing the vibrational and rotational motions on both electronic surfaces. Rotational nodes are formed due to the high intensity. Applying longer pulses, higher rotational quantum numbers J are appearing.

To understand more deeply the role of the pulse lengths for the dynamics, we calculated and analyzed the nuclear density function $|\psi(R,\theta,t)|^2 (= |\psi^{1s\sigma_g}(R,\theta,t)|^2 + |\psi^{2p\sigma_u}(R,\theta,t)|^2)$. Obtained results are displayed in Figs. 4 and 5. In the absence of the laser field, the wave packet exhibits a periodic motion with an approximate time period of 24 fs. The first maximum of the average internuclear distance happens at 12.3 fs. This is the reason we have centered the applied laser pulse around this time delay after the ionization. As a consequence, in the presence of external electric field we can expect that the dissociation events occur around 12, 36, 60 fs and so on time delays after ionization. On the other hand, the minima of the average internuclear distance are

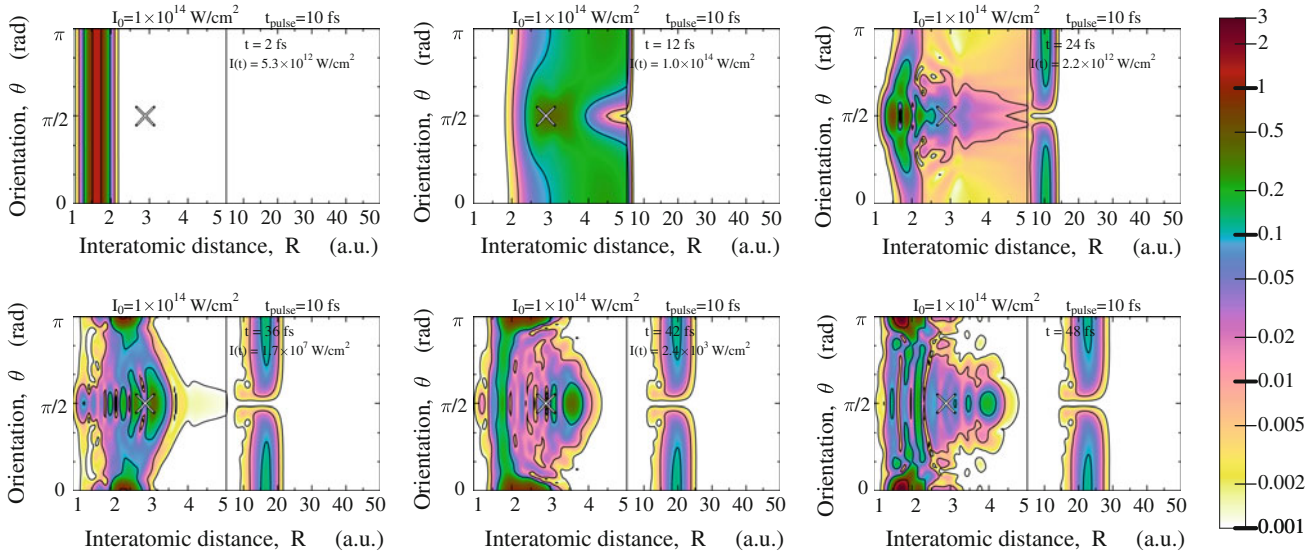

Fig. 4 Snapshots from the real-time evolution of the nuclear density of the D_2^+ due to a Gaussian laser pulse of peak intensity $1 \times 10^{14}\,\mathrm{W/cm^2}$ and 10 fs duration. The nuclear density exhibits interference effects and splits at larger distances around $\theta = \pi/2$. The instantaneous intensity is shown in the individual snapshots. The *yellow cross* denotes the position of the LICI. *All panels* show the results of the full 2d calculation. Note the jump in the interatomic scale

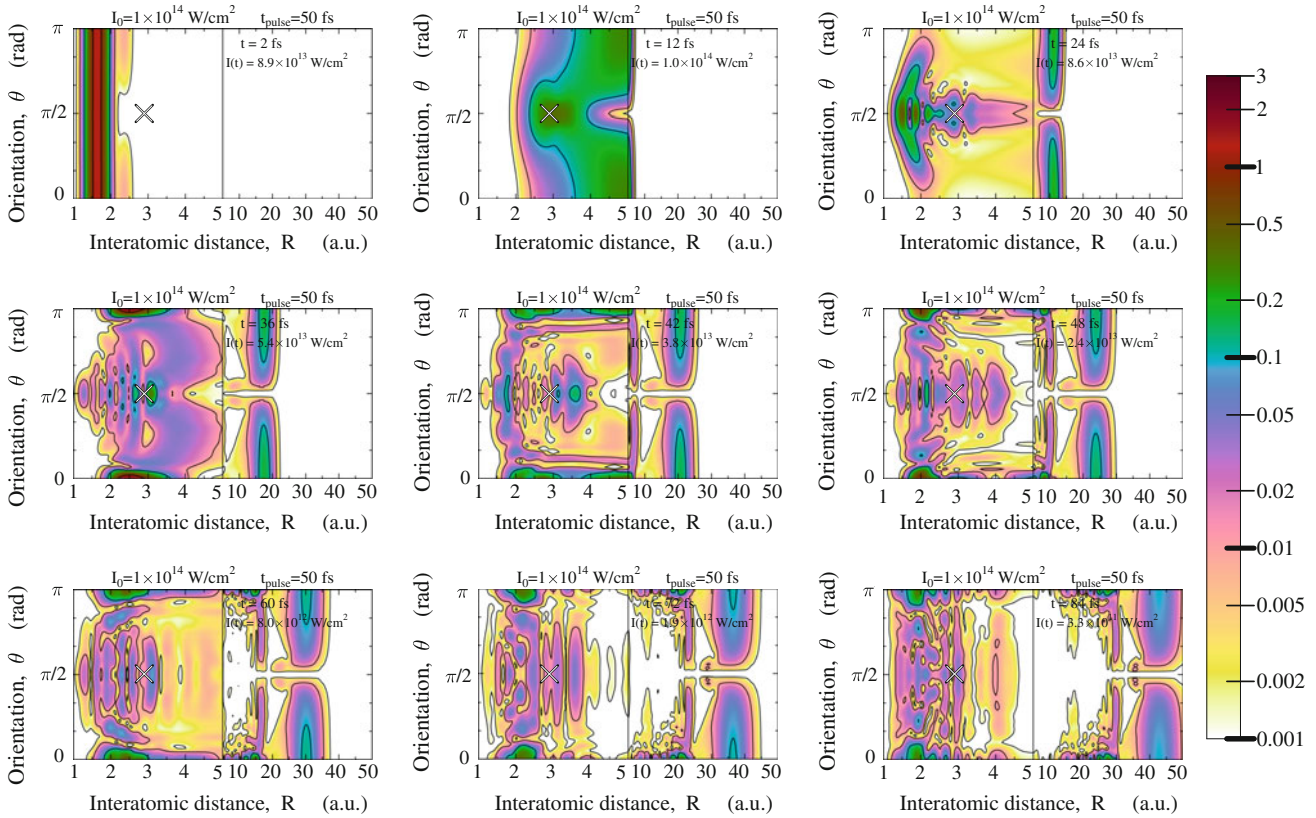

Fig. 5 Snapshots from the real-time evolution of the nuclear density of the D_2^+ due to a Gaussian laser pulse of peak intensity $1 \times 10^{14}\,\mathrm{W/cm^2}$ and 50 fs duration. The nuclear density exhibits severe interference effects and splits at larger distances around $\theta = \pi/2$. The instantaneous intensity is shown in the individual snapshots. The *yellow cross* denotes the position of the LICI. *All panels* show the results of the full 2d calculation. Note the jump in the interatomic scale

around 24, 48 fs and so on time delays. In the presence of external field as a first crude approximation, we can expect that the non-dissociated part of the wave packet also exhibits a similar periodic motion. The individual panels of the Figs. 4 and 5 are snapshots of the nuclear density function at the special times mentioned above and also at time 42 fs which is half way between the two neighboring ones. Applying 10 fs pulse length the external field has non-vanishing value only at the first interesting time interval with large internuclear distances. The whole dissociation process is practically completed when the nuclear wave packet is at first time in the large internuclear distance region. Then the remaining part of the wave packet oscillates back and force in the adiabatic lower surface exhibiting interference picture is the bound region. The nuclear wave packet will be again at the same position after another 24 fs, but because the intensity is very low further dissociation is no longer going to happen (see on Fig. 4; $t = 36$ fs). On the right sides of the panels (on Fig. 4), the time evolution of the dissociated part of the wave packet is illustrated using different scaling for the internuclear distance.

On Fig. 5 results are collected by using longer laser pulse (50 fs). For this pulse length a completely different situation applies. The dissociation takes place in several steps since the laser pulse is long enough. Then the direct consequence of this process is, that on the right hand side of the panels (on Fig. 5) the pictures of the time evolution of the dissociated part of the nuclear wave packet are more structured. Similarly, the interference pictures on the bounded region of these panels also show rich patterns. This behavior is the direct consequence of the laser field-induced rotational nodes, which are formed due to applying long pulses. The nuclear wave packet density is close to zero at the rotational nodes. But above and below these nodes, the value of the wave packet density is markedly different from zero and so-called quantum interference picture occurs. These quantum interference effects are then the sources of the modulations on the angular distribution curves of the photofragments. Applying short laser pulses, such interference patterns do not appear as rotational nodes are not formed.

4 Conclusions

We present results for the kinetic energy (KER) spectra and for the angular distribution of the photofragments of the D_2^+ ion. By means of two-dimensional quantum dynamical calculations, we have demonstrated that the impact of the laser-induced conical intersection for these dynamical quantities is the largest possible, if one uses high field intensity and long pulses together. Such a laser field can rotate the molecules significantly, which is the heart of the LICI in diatomic systems. Moreover, we have analyzed the time evolution of the nuclear wave packet density, which visualizes the occurring quantum interference effect during the dissociation due to the very strong nonadiabatic coupling between the electronic, vibrational and rotational motions.

Acknowledgments The authors acknowledge the financial support by the Deutsche Forschungsgemeinschaft (Project ID CE10/50-2). Á.V. acknowledges the OTKA Grant No. NN103251. The authors thank Lorenz Cederbaum for many fruitful discussions.

References

1. Born M, Oppenheimer JR (1927) Ann Phys 84:457
2. Köppel H, Domcke W, Cederbaum LS (1984) Adv Chem Phys 57:59–246
3. Baer M (2002) Phys Rep 358:75–142
4. Worth GA, Cederbaum LS (2004) Annu Rev Phys Chem 55:127–158
5. Domcke W, Yarkony DR, Köppel H (2004) Conical intersections: electronic structure, dynamics and spectroscopy. World Scientific, Singapore
6. Baer M (2006) Beyond born oppenheimer: electronic non-adiabatic coupling terms and conical intersections. Wiley, New York
7. Matsika S (2007) Rev Comput Chem 23:83–124
8. Althorpe SC, Stecher T, Bouakline FJ (2008) Chem Phys 129:214117
9. Bouakline F (2014) Chem Phys 442:31–40
10. Truhlar DG, Mead A (2003) Phys Rev A 68:032501
11. Tishchenko O, Li R, Truhlar DG (2010) PNAS 107:19139–19145
12. Moiseyev N, Sindelka M, Cederbaum LS (2008) J Phys B 41:221001–221006
13. Sindelka M, Moiseyev N, Cederbaum LS (2011) J Phys B 44:045603–045606
14. Halász GJ, Vibók Á, Sindelka M, Moiseyev N, Cederbaum LS (2011) J Phys B 44:175102–175112
15. Halász GJ, Sindelka M, Moiseyev N, Cederbaum LS, Vibók Á (2012) J Phys Chem A 116:2636–2643
16. Halász GJ, Vibók Á, Sindelka M, Cederbaum LS, Moiseyev N (2012) Chem Phys 399:146–150
17. Halász GJ, Vibók Á, Moiseyev N, Cederbaum LS (2012) J Phys B 45:135101–135110
18. Halász GJ, Vibók Á, Meyer HD, Cederbaum LS (2013) J Phys Chem A 117:8528–8535
19. Halász GJ, Vibók Á, Moiseyev N, Cederbaum LS (2013) Phys Rev A 88:043413-6
20. Halász GJ, Csehi A, Vibók Á, Cederbaum LS (2014) J Phys Chem A 118:11908–11915
21. Halász GJ, Vibók Á, Cederbaum LS (2015) J Phys Chem Lett 6:348–354
22. Cederbaum LS, Chiang YC, Demekhin PV, Moiseyev N (2011) Phys Rev Lett 106:123001–123005
23. Demekhin PV, Chiang YC, Cederbaum LS (2011) Phys Rev A 84:033417
24. Demekhin PV, Cederbaum LS (2013) J Phys B 46:164008
25. Estrada H, Cederbaum LS, Domcke W (1986) J Chem Phys 84:152
26. Feuerbacher S, Sommerfeld T, Cederbaum LS (2004) J Chem Phys 120:3201
27. Demekhin PV, Cederbaum LS (2013) J Chem Phys 139:154314–154315
28. Natan A, Ware MR, Bucksbaum PH (2015) Book of ultrafast phenomena XIX Springer proceedings in physics, vol 162, pp 122–125

29. Kim J, Tao H, White JL, Petrović VS, Martinez TJ, Bucksbaum PH (2012) J Phys Chem A 116:2758–2763
30. Kim J, Tao H, Martinez TJ, Bucksbaum PH (2015) J Phys B 48:164003–164010
31. Corrales ME, González-Vázquez J, Balerdi G, Solá IR, de Nalda R, Bañares L (2014) Nat Chem 6:785–790
32. Sola IR, González-Vázquez J, de Nalda R, Bañares L (2015) Phys Chem Chem Phys 17:13183–13200
33. Zavriyev A, Bucksbaum PH, Muller HG, Schumacher DV (1990) Phys Rev A 42:5500–5513
34. Bandrauk AD, Sink M (1978) Chem Phys Lett 57:569–572
35. Bandrauk AD, Sink M (1981) J Chem Phys 74:1110–1117
36. Aubanel EE, Gauthier JM, Bandrauk AD (1993) Phys Rev A 48:2145–2152
37. Charron E, Giusti-Suzor A, Mies FH (1994) Phys Rev A 49:R641–R644
38. Chelkowski S, Zuo T, Atabek O, Bandrauk AD (1995) Phys Rev A 52:2977–2983
39. Giusti-Suzor A, Mies FH, DiMauro LF, Charron E, Yang B (1995) J Phys B 28:309–339
40. Numico R, Keller A, Atabek O (1995) Phys Rev A 52:1298–1309
41. Sandig K, Figger H, Hansch TV (2000) Phys Rev Lett 85:4876–4879
42. Serov VN, Keller A, Atabek O, Billy N (2003) Phys Rev A 68:053401-16
43. Posthumus JH (2004) Rep Prog Phys 67:623–665
44. Serov VN, Keller A, Atabek O, Figger H, Pavidic D (2005) Phys Rev A 72:033413-21
45. Uhlmann M, Kunert T, Schmidt R (2005) Phys Rev A 72:045402-5
46. Wang PQ et al (2006) Phys Rev A 74:043411-21
47. Anis F, Esry BD (2008) Phys Rev A 77:033416-11
48. Anis F, Cackowski T, Esry BD (2009) J Phys B Fast Track Com 42:091001-6
49. Hua JJ, Esry BD (2009) Phys Rev A 80:013413-19
50. Adhikari S et al (2009) J Phys Chem A 113:7331–7337
51. Paul AK, Adhikari S, Baer M (2010) Baer R 81:013412-10
52. Thumm U, Niederhausen T, Feuerstein B (2008) Phys Rev A 77:063401-12
53. Fischer M et al (2011) New J Phys 13:053019-14
54. Fischer M, Lorenz U, Schmidt B, Schmidt R (2011) Phys Rev A 84:033422-5
55. McKenna J, Anis F, Sayler AM, Gaire B, Johnson NG, Parke E, Carnes KD, Esry BD, Ben-Itzhak I (2012) Phys Rev A 85:023405-15
56. He HX, Lu RF, Zhang PY, Han KL, He GZ (2012) J Chem Phys 136:024311-6
57. Furukawa Y, Nabekawa Y, Okino T, Eilanlou AA, Takahashi EJ, Lan P, Ishikawa KL, Sato T, Yamanouchi K, Midorikawa K (2012) Opt Lett 37:2922–2924
58. Bunkin FV, Tugov II (1973) Phys Rev A 8:601–612
59. Chu SI, Laughlin C, Datta K (1983) Chem Phys Lett 98:476–481
60. Meyer HD, Manthe U, Cederbaum LS (1990) Chem Phys Lett 165:73–78
61. Manthe U, Meyer HD, Cederbaum LS (1992) J Chem Phys 97:3199–3213
62. Beck MH, Jäckle A, Worth GA, Meyer HD (2000) Phys Rep 324:1–105
63. Worth GA et al. The MCTDH package, version 8.2; University of Heidelberg: Heidelberg, Germany, 2000. H. D. Meyer et al. The MCTDH package, versions 8.3 and 8.4; University of Heidelberg, Germany, 2002 and 2007. http://mctdh.uni-hd.de/
64. Meyer HD, Gatti F, Worth GA (2009) Multidimensional quantum dynamics: MCTDH theory and applications. Wiley, Weinheim

Theor Chem Acc (2015) 134:125
DOI 10.1007/s00214-015-1731-6

REGULAR ARTICLE

Spin contamination and noncollinearity in general complex Hartree–Fock wave functions

Patrick Cassam-Chenaï[1]

Received: 1 June 2015 / Accepted: 13 September 2015 / Published online: 12 October 2015

Abstract An expression for the square of the spin operator expectation value, $\langle S^2 \rangle$, is obtained for a general complex Hartree–Fock wave function and decomposed into four contributions: the main one whose expression is formally identical to the restricted (open-shell) Hartree–Fock expression. A spin contamination one formally analogous to that found for spin unrestricted Hartree–Fock wave functions. A noncollinearity contribution related to the fact that the wave function is not an eigenfunction of the spin-S_z operator. A perpendicularity contribution related to the fact that the spin density is not constrained to be zero in the xy-plane. All these contributions are evaluated and compared for the H_2O^+ system. The optimization of the collinearity axis is also considered.

Keywords Spin contamination · Collinearity · General complex Hartree–Fock

1 Introduction

Particle-independent models based on single Slater determinant wave functions have enjoyed considerable interest in quantum chemistry, since the pioneering works of Hartree, Slater and Fock [1–3].

When a quantum system is described by a spin-free Hamiltonian, which obviously commutes with the spin operators S_z and S^2, a spin-symmetry respectful way of using the Hartree–Fock method consists in:

(1) Using spin-orbitals of pure α- or β-spin, so that the HF optimized Slater determinant is an eigenfunction of S_z;
(2) Imposing the spin-equivalence restriction [4], which means that paired α- and β-spin-orbitals are formed from the same set of linearly independent orbitals. We have proved mathematically [5–7] that this additional constraint is a necessary and sufficient condition to insure that a Slater determinantal wave function is an eigenfunction of the spin operator S^2. In other words, we have shown that relaxing the S^2-symmetry constraint exactly amounts to allow different "paired orbitals," in the sense of Refs. [8, 9], to have different spins. This equivalence enabled us to characterize the variational space explored by the restricted open-shell Hartree–Fock (ROHF) method [10], which precisely consists in optimizing a Slater determinant subject to constraints (1) and (2) (plus spatial-symmetry constraints if any) [11]. The equivalence was also discovered independently [12] by optimizing a Slater determinant with a Lagrange multiplier, enforcing $\langle S^2 \rangle$ to be arbitrarily close to the ROHF value, instead of applying the spin-equivalence restriction. Not surprisingly, the determinant was approaching the ROHF solution.

Similar to the spin-free case is the "complex-free" one: when a quantum system is described by a real Hamiltonian, which obviously commutes with complex conjugation, one can restrict oneself to the calculation of real eigenfunctions. Then, it is also possible to employ only real spin-orbitals to construct the HF Slater determinant [13] (however, difficulties may occur when the symmetry group of the molecule cannot be represented over real numbers, and

Published as part of the special collection of articles "Festschrift in honour of P. R. Surjan".

✉ Patrick Cassam-Chenaï
cassam@unice.fr

[1] CNRS, LJAD, UMR 7351, University of Nice Sophia Antipolis, 06100 Nice, France

nonetheless, one wishes the spin-orbitals to be adapted to spatial symmetry).

However, it has been proposed by various authors to relax some or all of the above-mentioned constraints, to gain variational freedom. For example, the different orbitals for different spins method (DODS) of Refs. [14, 15] (which is usually just called "unrestricted Hartree–Fock" (UHF), but in this paper we use "DODS" to avoid confusions) relax the spin-equivalence restriction, and hence, the HF solution is no longer an eigenfunction of S^2. Other authors [16–18] have advocated the use of general spin-orbitals, mixing α-spin and β-spin parts, in conjunction with the use of projectors [19].

Along the same line of thought, the use of complex spin-orbitals has been proposed [17, 20] to increase variational freedom in the case of real Hamiltonian. Prat and Lefebvre went a step further with the so-called hypercomplex spin-orbitals to construct Slater determinants of arbitrary accuracy [21]. However, the coefficients of their spin-orbitals were elements of a Clifford algebra of dimension 2^{2n}, that was not a normed division algebra, also known as Cayley algebra, for arbitrary values of n. This was unfortunate, since such a structure appears to be a minimal requirement for a quantum formalism, if, for example, Born's interpretation of the wave function is to hold firmly. For $n = 1$, the Clifford algebra of Prat et al. was actually the noncommutative field of quaternions, therefore, a fortiori, a normed division algebra. The only larger normed division algebra is the octonion algebra. It is a Clifford algebra of dimension 8, which has also been proposed in a quantum mechanical context [22], but this algebra is neither commutative nor associative. The lack of these properties rises difficulties for its use for multipartite quantum systems; nevertheless, these difficulties can be overcome by keeping the product of octonion coefficients in the form of a tensor product. So, octonion-unrestricted HF appears to be the largest Cilfford algebra-unrestricted single determinantal method that can be considered in the spirit of Prat and Lefebvre's proposal. However, octonions seem incompatible with the desirable requirement that the algebra of quantum observables be what is now called a formally real Jordan algebra [23] acting on a vector space of arbitrarily large dimension. Octonions are also ruled out by the requirement of orthomodularity in infinite dimension according to Solèr's theorem [24, 25], which restricts quantum Hilbert spaces to be real, complex or at most quaternionic.

The first HF molecular calculations with general complex spin-orbitals, without projecting out the symmetry-breaking part of the wave function, are maybe those of Ref. [26]. It was found on the BH molecule around its equilibrium geometry that the general complex Hartree–Fock (GCHF) energy was indeed lower than the DODS one, which itself was lower than the restricted Hartree–Fock (RHF) solution. So necessarily, the corresponding GCHF wave functions had S^2-spin contamination and S_z-spin contamination, that is to say, the expectation values of these operators were different from 0, the value expected for a singlet ground state (it is not clear whether complex numbers were used for this molecule, but the authors did mention that they performed complex calculations for two-electron systems).

Relaxing the "S_z-constraint" hence the "collinearity constraint" becomes perfectly legitimate when hyperfine or spin–orbit couplings are considered, since the operator S_z no longer commutes with the Hamiltonian. As a matter of fact, real physical systems do exhibit either light [27, 28] or strong [29, 30] noncollinearity of their spin densities. Similarly, the use of complex spin-orbitals is natural, when considering relativistic corrections resulting in a complex Hamiltonian operator. So, in such a context, one should use no less than general complex spin-orbitals in HF calculations [31]. The "spin-same-orbit" coupling term used in these calculations does not commute with the S^2-operator. Therefore, one cannot strictly speak of "S^2-spin contamination" in relativistic GCHF wave functions. However, calculating the expectation value of S^2, a bona fide quantum observable, can still provide valuable physical information about the system.

A general expression for the expectation value of S^2 has been obtained in the DODS case [8] and has served as a measure of S^2-spin contamination. However, as far as we are aware, no such formula has been published in the case of a GCHF wave function. This gap will be filled in the next section.

Studying departure from collinearity is more difficult because of arbitrariness in the quantification axis. One possible way to overcome the difficulty would be to apply an external magnetic field to fix the z-axis but small enough not to perturb the GCHF solution. However, an elegant alternative has been proposed recently by Small et al. [32]. It is based on studying the lowest eigenvalue of a (3×3) -matrix built from expectation values of spin operator components and their products. In the GCHF case, the authors provided the expressions required to compute the matrix elements in a compact form. In the third section, we give a more extended formula in terms of molecular orbital overlap matrix elements. We also illustrate the connections between spin contamination, noncollinearity and its correlative: "perpendicularity" on the H_2O^+ cation example. We sum up our conclusions in the last section.

2 Spin contamination in GCHF

A general complex Hartree–Fock (GCHF) wave function,

$$\Phi_{\mathrm{GCHF}} = \phi_1 \wedge \cdots \wedge \phi_{N_e}, \tag{1}$$

is the antisymmetrized product (or wedge product, denoted by $\wedge$) of orthonormal spin-orbitals, or "two-component spinors,"

$$\phi_i = \begin{pmatrix} \phi_{i\alpha} \\ \phi_{i\beta} \end{pmatrix}, \tag{2}$$

$$\langle \phi_i | \phi_j \rangle = \delta_{i,j}, \tag{3}$$

where the scalar product $\langle \cdot | \cdot \rangle$ means integration over space variables and summation (i.e., taking the trace) over spin variables: $\langle \phi_i | \phi_j \rangle = \langle \phi_{i\alpha} | \phi_{j\alpha} \rangle + \langle \phi_{i\beta} | \phi_{j\beta} \rangle$, (where the same bracket symbol is used for the scalar product between orbital parts). We define the "number of α-spin electrons" (respectively, "number of β-spin electrons") as $N_\alpha := \sum_{i=1}^{N_e} \langle \phi_{i\alpha} | \phi_{i\alpha} \rangle$ (respectively, $N_\beta := \sum_{i=1}^{N_e} \langle \phi_{i\beta} | \phi_{i\beta} \rangle$). It is the expectation value of the projection operator on the α- (respectively, β-) one-electron Hilbert subspace (more rigorously speaking, the operator induced onto the n-electron Hilbert space by this one-electron projection operator). Note that these two numbers need not be integer numbers; however, their sum is an integer: $N_\alpha + N_\beta = N_e$.

Let us work out the expectation value of the spin operator,

$$S^2 = S_z^2 + \frac{1}{2}(S^+ S^- + S^- S^+), \tag{4}$$

on a general GCHF wave function.

The action of S_z is given by,

$$S_z \Phi_{\mathrm{GCHF}} = \frac{1}{2} \sum_{i=1}^{N_e} \hat{\Phi}^i_{\mathrm{GCHF}}, \tag{5}$$

where,

$$\hat{\Phi}^i_{\mathrm{GCHF}} = \phi_1 \wedge \cdots \wedge \phi_{i-1} \wedge \hat{\phi}_i \wedge \phi_{i+1} \wedge \cdots \wedge \phi_{N_e}, \tag{6}$$

and,

$$\hat{\phi}_i = \begin{pmatrix} +\phi_{i\alpha} \\ -\phi_{i\beta} \end{pmatrix}. \tag{7}$$

Note that,

$$\langle \hat{\phi}_i | \hat{\phi}_j \rangle = \langle \phi_i | \phi_j \rangle = \delta_{i,j}. \tag{8}$$

So, the expectation value of S_z is

$$\begin{aligned} \langle \Phi_{\mathrm{GCHF}} | S_z | \Phi_{\mathrm{GCHF}} \rangle &= \frac{1}{2} \sum_{i=1}^{N_e} \left\langle \Phi_{\mathrm{GCHF}} | \hat{\Phi}^i_{\mathrm{GCHF}} \right\rangle = \frac{1}{2} \sum_{i=1}^{N_e} \left\langle \phi_i | \hat{\phi}_i \right\rangle \\ &= \frac{1}{2} \sum_{i=1}^{N_e} \left(\langle \phi_{i\alpha} | \phi_{i\alpha} \rangle - \langle \phi_{i\beta} | \phi_{i\beta} \rangle \right) = \frac{N_\alpha - N_\beta}{2}, \end{aligned} \tag{9}$$

and that of S_z^2:

$$\begin{aligned} &\langle \Phi_{\mathrm{GCHF}} | S_z^2 | \Phi_{\mathrm{GCHF}} \rangle = \langle S_z \Phi_{\mathrm{GCHF}} | S_z \Phi_{\mathrm{GCHF}} \rangle \\ &= \frac{1}{4} \sum_{i,j=1}^{N_e} \left\langle \hat{\Phi}^i_{\mathrm{GCHF}} | \hat{\Phi}^j_{\mathrm{GCHF}} \right\rangle \\ &= \frac{1}{4} \left(\sum_{i=1}^{N_e} \left\langle \hat{\Phi}^i_{\mathrm{GCHF}} | \hat{\Phi}^i_{\mathrm{GCHF}} \right\rangle + \sum_{\substack{i,j=1 \\ i \neq j}}^{N_e} \left\langle \hat{\Phi}^i_{\mathrm{GCHF}} | \hat{\Phi}^j_{\mathrm{GCHF}} \right\rangle \right) \\ &= \frac{1}{4} \sum_{i=1}^{N_e} \left(\left\langle \hat{\phi}_i | \hat{\phi}_i \right\rangle + \sum_{\substack{j=1 \\ j \neq i}}^{N_e} (-1) \, |\langle \hat{\phi}_i | \phi_j \rangle|^2 + \langle \hat{\phi}_i | \phi_i \rangle \langle \phi_j | \hat{\phi}_j \rangle \right) \\ &= \frac{1}{4} \left(N_e + \sum_{\substack{i,j=1 \\ i \neq j}}^{N_e} (-1) \, |\langle \phi_{i\alpha} | \phi_{j\alpha} \rangle - \langle \phi_{i\beta} | \phi_{j\beta} \rangle|^2 \right. \\ &\quad \left. + \left(\langle \phi_{i\alpha} | \phi_{i\alpha} \rangle - \langle \phi_{i\beta} | \phi_{i\beta} \rangle \right) \left(\langle \phi_{j\alpha} | \phi_{j\alpha} \rangle - \langle \phi_{j\beta} | \phi_{j\beta} \rangle \right) \right) \\ &= \frac{1}{4} \left(N_e + \sum_{i,j=1}^{N_e} \left(\langle \phi_{i\alpha} | \phi_{i\alpha} \rangle - \langle \phi_{i\beta} | \phi_{i\beta} \rangle \right) \left(\langle \phi_{j\alpha} | \phi_{j\alpha} \rangle - \langle \phi_{j\beta} | \phi_{j\beta} \rangle \right) \right. \\ &\quad \left. - |\langle \phi_{i\alpha} | \phi_{j\alpha} \rangle - \langle \phi_{i\beta} | \phi_{j\beta} \rangle|^2 \right) \\ &= \left(\frac{N_\alpha}{2} - \frac{N_\beta}{2} \right)^2 + \frac{1}{4} \left(N_e - \sum_{i,j=1}^{N_e} |\langle \phi_{i\alpha} | \phi_{j\alpha} \rangle - \langle \phi_{i\beta} | \phi_{j\beta} \rangle|^2 \right). \end{aligned} \tag{10}$$

This equation reduces to $\left(\frac{N_\alpha}{2} - \frac{N_\beta}{2} \right)^2$ in the case of a DODS wave function. So, the second term on the right-hand side (rhs), which is $(\langle \Phi_{\mathrm{GCHF}} | S_z^2 | \Phi_{\mathrm{GCHF}} \rangle - \langle \Phi_{\mathrm{GCHF}} | S_z | \Phi_{\mathrm{GCHF}} \rangle^2)$, is directly related to relaxation of the S_z-constraint and will be called the "z-noncollinearity" contribution. Note, however, that for a GCHF wave function, the first term on the RHS does not necessarily correspond to an eigenvalue of S_z^2, according to the definition of N_α and N_β.

The action of S^+ is given by,

$$S^+ \Phi_{\mathrm{GCHF}} = \sum_{i=1}^{N_e} \acute{\Phi}^i_{\mathrm{GCHF}}, \tag{11}$$

where,

$$\acute{\Phi}^i_{\mathrm{GCHF}} = \phi_1 \wedge \cdots \wedge \phi_{i-1} \wedge \acute{\phi}_i \wedge \phi_{i+1} \wedge \cdots \wedge \phi_{N_e}, \tag{12}$$

and,

$$\acute{\phi}_i = \begin{pmatrix} +\phi_{i\beta} \\ 0 \end{pmatrix}. \tag{13}$$

Similarly, the action of S^- is given by,

$$S^- \Phi_{\mathrm{GCHF}} = \sum_{i=1}^{N_e} \grave{\Phi}^i_{\mathrm{GCHF}}, \tag{14}$$

where,

$$\grave{\Phi}^i_{\mathrm{GCHF}} = \phi_1 \wedge \cdots \wedge \phi_{i-1} \wedge \grave{\phi}_i \wedge \phi_{i+1} \wedge \cdots \wedge \phi_{N_e}, \tag{15}$$

and,

$$\grave{\phi}_i = \begin{pmatrix} 0 \\ +\phi_{i\alpha} \end{pmatrix}. \tag{16}$$

So, the expectation value of $S^- S^+$ is,

$$\begin{aligned}
\langle \Phi_{\mathrm{GCHF}} | S^- S^+ | \Phi_{\mathrm{GCHF}} \rangle &= \left\langle S^+ \Phi_{\mathrm{GCHF}} | S^+ \Phi_{\mathrm{GCHF}} \right\rangle \\
&= \sum_{i,j=1}^{N_e} \left\langle \acute{\Phi}^i_{\mathrm{GCHF}} | \acute{\Phi}^j_{\mathrm{GCHF}} \right\rangle \\
&= \sum_{i=1}^{N_e} \left\langle \acute{\Phi}^i_{\mathrm{GCHF}} | \acute{\Phi}^i_{\mathrm{GCHF}} \right\rangle + \sum_{\substack{i,j=1 \\ i \neq j}}^{N_e} \left\langle \acute{\Phi}^i_{\mathrm{GCHF}} | \acute{\Phi}^j_{\mathrm{GCHF}} \right\rangle \\
&= \sum_{i=1}^{N_e} \left(\left\langle \acute{\phi}_i | \acute{\phi}_i \right\rangle + \sum_{\substack{j=1 \\ j \neq i}}^{N_e} (-1) \left| \left\langle \acute{\phi}_i | \phi_j \right\rangle \right|^2 + \left\langle \acute{\phi}_i | \phi_i \right\rangle \langle \phi_j | \acute{\phi}_j \rangle \right) \\
&= \sum_{i=1}^{N_e} \left(\langle \phi_{i\beta} | \phi_{i\beta} \rangle + \sum_{\substack{j=1 \\ j \neq i}}^{N_e} (-1) \left| \langle \phi_{i\beta} | \phi_{j\alpha} \rangle \right|^2 + \langle \phi_{i\beta} | \phi_{i\alpha} \rangle \langle \phi_{j\alpha} | \phi_{j\beta} \rangle \right) \\
&= N_\beta + \sum_{i,j=1}^{N_e} \langle \phi_{i\beta} | \phi_{i\alpha} \rangle \langle \phi_{j\alpha} | \phi_{j\beta} \rangle - \langle \phi_{i\beta} | \phi_{j\alpha} \rangle \langle \phi_{j\alpha} | \phi_{i\beta} \rangle.
\end{aligned} \tag{17}$$

Similarly, the expectation value of $S^+ S^-$ is,

$$\begin{aligned}
\langle \Phi_{\mathrm{GCHF}} | S^+ S^- | \Phi_{\mathrm{GCHF}} \rangle &= \langle S^- \Phi_{\mathrm{GCHF}} | S^- \Phi_{\mathrm{GCHF}} \rangle \\
&= \sum_{i=1}^{N_e} \left(\langle \grave{\phi}_i | \grave{\phi}_i \rangle + \sum_{\substack{j=1 \\ j \neq i}}^{N_e} (-1) \left| \langle \grave{\phi}_i | \phi_j \rangle \right|^2 + \langle \grave{\phi}_i | \phi_i \rangle \langle \phi_j | \grave{\phi}_j \rangle \right) \\
&= \sum_{i=1}^{N_e} \left(\langle \phi_{i\alpha} | \phi_{i\alpha} \rangle + \sum_{\substack{j=1 \\ j \neq i}}^{N_e} (-1) \left| \langle \phi_{i\alpha} | \phi_{j\beta} \rangle \right|^2 + \langle \phi_{i\alpha} | \phi_{i\beta} \rangle \langle \phi_{j\beta} | \phi_{j\alpha} \rangle \right) \\
&= N_\alpha + \sum_{i,j=1}^{N_e} \langle \phi_{i\alpha} | \phi_{i\beta} \rangle \langle \phi_{j\beta} | \phi_{j\alpha} \rangle - \langle \phi_{i\alpha} | \phi_{j\beta} \rangle \langle \phi_{j\beta} | \phi_{i\alpha} \rangle.
\end{aligned} \tag{18}$$

Using Eq.(4) and putting together Eqs. (10), (17) and (18), one obtains the expectation value of S^2,

$$\begin{aligned}
\langle \Phi_{\mathrm{GCHF}} | S^2 | \Phi_{\mathrm{GCHF}} \rangle &= \left(\frac{N_\alpha}{2} - \frac{N_\beta}{2} \right)^2 + \frac{N_\alpha}{2} + \frac{N_\beta}{2} \\
&+ \frac{1}{4} \left(N_e - \sum_{i,j=1}^{N_e} \left| \langle \phi_{i\alpha} | \phi_{j\alpha} \rangle - \langle \phi_{i\beta} | \phi_{j\beta} \rangle \right|^2 \right) \\
&+ \sum_{i,j=1}^{N_e} \langle \phi_{i\alpha} | \phi_{i\beta} \rangle \langle \phi_{j\beta} | \phi_{j\alpha} \rangle - \langle \phi_{i\alpha} | \phi_{j\beta} \rangle \langle \phi_{j\beta} | \phi_{i\alpha} \rangle.
\end{aligned} \tag{19}$$

The expression reduces to the known formula in the case of a DODS wave function. Assuming, without loss of generality, that $N_\alpha \geq N_\beta$, we rewrite Eq. (19) as,

$$\begin{aligned}
\langle \Phi_{\mathrm{GCHF}} | S^2 | \Phi_{\mathrm{GCHF}} \rangle &= \left(\frac{N_\alpha}{2} - \frac{N_\beta}{2} \right) \left(\frac{N_\alpha}{2} - \frac{N_\beta}{2} + 1 \right) \\
&+ \frac{1}{4} \left(N_e - \sum_{i,j=1}^{N_e} \left| \langle \phi_{i\alpha} | \phi_{j\alpha} \rangle - \langle \phi_{i\beta} | \phi_{j\beta} \rangle \right|^2 \right) \\
&+ \left(N_\beta - \sum_{i,j=1}^{N_e} \langle \phi_{i\alpha} | \phi_{j\beta} \rangle \langle \phi_{j\beta} | \phi_{i\alpha} \rangle \right) \\
&+ \left| \sum_{i=1}^{N_e} \langle \phi_{i\beta} | \phi_{i\alpha} \rangle \right|^2.
\end{aligned} \tag{20}$$

In this formula, we identify four contributions: The first term is formally identical to the ROHF expression also found in the DODS case. However, care must be taken that it is actually different, because the numbers of α- and β-electrons are not good quantum numbers in the GCHF case. The second term is the "z-noncollinearity" contribution. The third term is formally analogous to the "spin contamination" of a DODS wave function as defined in [7, 8]. Finally, the last term is the square of the expectation value of the lowering or raising operator:

$$\left| \sum_{i=1}^{N_e} \langle \phi_{i\beta} | \phi_{i\alpha} \rangle \right|^2 = |\langle \Phi_{\mathrm{GCHF}} | S^+ | \Phi_{\mathrm{GCHF}} \rangle|^2 = |\langle \Phi_{\mathrm{GCHF}} | S^- | \Phi_{\mathrm{GCHF}} \rangle|^2. \tag{21}$$

A nonzero contribution of this term can only arise from the release of the S_z-constraint, which allows for the α- and β-components of a given, general spin-orbital to be both nonzero. But it originates from S^+S^- and S^-S^+ and is maximal when $\phi_{i\beta} = \exp(\imath\theta)\phi_{i\alpha}$ for all i, that is to say when the ϕ_i's are eigenfunctions of $\cos\theta\, S_x + \sin\theta\, S_y$ for some angle θ. It is related to the emergence of a nonzero spin density in the xy-plane, correlatively to the loss of z-collinearity. We tentatively call this term the "x, y-perpendicularity" contribution.

The present formulas have been implemented in the code TONTO [33] and applied in a recent article (third column of Tab. 4 in [34]). Let us discuss further the different contributions to S^2 for a H_2O^+ GCHF calculation similar to that reported in [34]. The z-quantization axis was the axis perpendicular to the plane of the molecule. The results, see Table 1, show that the main contribution to $\langle \Phi_{\mathrm{GCHF}} | S^2 | \Phi_{\mathrm{GCHF}} \rangle$ beside the reference expression (first term on the right-hand side of Eq. 20) is the so-called spin contamination contribution (we set $\hbar = 1$ throughout the paper). The x, y-perpendicularity and z-noncollinearity contributions are of the same order of magnitude and more than one order of magnitude smaller. Added

Table 1 Expectation value of $\langle S^2\rangle$ and related quantities for an H_2O^+ GCHF optimized wave function

N_α	+4.999546
N_β	+4.000454
$\left(\frac{N_\alpha}{2}-\frac{N_\beta}{2}\right)\left(\frac{N_\alpha}{2}-\frac{N_\beta}{2}+1\right)$	+0.749091
z-noncollinearity	+0.000461
x, y-nonperpendicularity	+0.000427
Spin contamination	+0.007033
$\langle S^2\rangle$	+0.757013

The geometry parameters were $r_{OH} = 0.99192$ Å, $\widehat{\mathrm{HOH}} = 101.411°$. The basis set consisted of the primitives Gaussian functions left uncontracted of Dunning's cc-pVDZ hydrogen and oxygen basis sets [35]. The infinite-order two-component (IOTC) relativistic Hamiltonian of Barysz and Sadlej [36] was employed

to $\left(\frac{N_\alpha}{2}-\frac{N_\beta}{2}\right)\left(\frac{N_\alpha}{2}-\frac{N_\beta}{2}+1\right)$, they almost make up the reference value of +0.75. So, the spin contamination value of 0.007033 amounts almost exactly to the difference between the exact expectation value $\langle\Phi_{\mathrm{GCHF}}|S^2|\Phi_{\mathrm{GCHF}}\rangle$ and this reference "ROHF value." This demonstrates that, in Table 4 of Ref. [34], the equality of the entries in column 2 (reference ROHF value plus spin contamination term) and column 4 (our $\langle\Phi_{\mathrm{GCHF}}|S^2|\Phi_{\mathrm{GCHF}}\rangle$ value) does not imply no noncollinearity. In contrast, if for a given line of the table, these two quantities differ, then necessarily there will be some noncollinearity in the corresponding GCHF wave function. This can be shown *reductio ad absurdum*. Suppose that the z-collinearity constraint is fulfilled, then N_α and N_β will be good quantum numbers and the first term in our expression of $\langle\Phi_{\mathrm{GCHF}}|S^2|\Phi_{\mathrm{GCHF}}\rangle$ will be equal to the ROHF reference value. The spin contamination contribution being included in both quantities, the difference between them must arise from the x, y-perpendicularity and z-noncollinearity contributions. One at least of the contributions arising from the release of the collinearity constraint must be nonzero, hence a contradiction. This hints that the following systems Cl, HCl^+, Fe, Cu, Cu^{2+} and $[OsCl_5(Hpz)]^-$ reported in Table 4 of Ref.[34] would present stronger noncollinearity than H_2O^+.

3 Collinearity in GCHF

In the previous section, we have encountered a z-(non)collinearity measure, $\mathrm{col}_z := (\langle S_z^2\rangle - \langle S_z\rangle^2)$. This quantity can be generalized to an arbitrary quantization direction defined by a unit vector $\mathbf{u} = \begin{pmatrix} u_x \\ u_y \\ u_z \end{pmatrix}$ of the unit sphere $\mathcal{S}^2$ of $\mathbb{R}^3$ by replacing S_z by $\mathbf{u}\cdot\mathbf{S} = \sum_{\mu\in\{x,y,z\}} u_\mu S_\mu$. Then, $\mathbf{u}$-(non)collinearity is measured by:

$$\mathrm{col}(\mathbf{u}) := \sum_{\mu,\nu\in\{x,y,z\}} u_\mu u_\nu(\langle S_\mu S_\nu\rangle - \langle S_\mu\rangle\langle S_\nu\rangle). \tag{22}$$

Small et al. [32] defined a (non)collinearity measure by:

$$\mathrm{col} := \min_{\mathbf{u}\in\mathcal{S}^2} \mathrm{col}(\mathbf{u}), \tag{23}$$

which corresponds to the lowest eigenvalue of the matrix A whose elements are given by,

$$A_{\mu\nu} = \Re(\langle S_\mu S_\nu\rangle) - \langle S_\mu\rangle\langle S_\nu\rangle, \tag{24}$$

where $\Re(z)$ is the real part of z. The associated eigenvector gives the optimal collinearity direction. Setting ${}^x\tilde{\phi} = \frac{1}{2}(\acute{\phi}+\grave{\phi})$, ${}^y\tilde{\phi} = \frac{-\imath}{2}(\acute{\phi}-\grave{\phi})$ and ${}^z\tilde{\phi} = \hat{\phi}$, we have in this notation,

$$\forall\mu,\nu\in\{x,y,z\} \qquad A_{\mu\nu} = \delta_{\mu\nu}\frac{N_e}{4} - \sum_{i,j=1}^{N_e}\langle{}^\mu\tilde{\phi}_i|\phi_j\rangle\langle\phi_j|{}^\nu\tilde{\phi}_i\rangle, \tag{25}$$

where $\delta_{\mu\nu}$ is the Krönecker symbol.

Returning to the H_2O^+ example and applying these formulae, we obtain

$$A = \begin{pmatrix} +0.253128 & +0.000145 & -0.009774 \\ +0.000145 & +0.253451 & +0.003745 \\ -0.009774 & +0.003745 & +0.000461 \end{pmatrix} \tag{26}$$

The diagonalization of the A-matrix gives the optimal collinear direction:

$$\mathbf{u}_0^t = (+0.0385908, \quad -0.014789, \quad +0.999146), \tag{27}$$

which is only slightly tilted with respect to the z-direction, and the system is quasi-collinear in this direction since $\mathrm{col} = 0.000028$ is very close to zero. This shows that the noncollinearity contribution to $\langle\Phi_{\mathrm{GCHF}}|S^2|\Phi_{\mathrm{GCHF}}\rangle$ could be further reduced by more than one order of magnitude by selecting the optimal quantization axis corresponding to $\mathbf{u}_0$ instead of the spatial z-axis. The perpendicularity contribution would decrease accordingly.

4 Conclusion

We have decomposed the expectation value of the spin operator S^2 into (1) a term formally identical to its expression for a ROHF reference wave function, (2) a term called "spin contamination" because it is formally analogous to that derived by Amos and Hall [8] for DODS wave functions, (3) a noncollinear contribution which can be minimized by following a procedure recently introduced [32], (4) a term called the "perpendicularity contribution" which arises from the release of the z-collinearity constraint but which should rather be regarded as arising from the release of the "nonperpendicularity constraint" on the spin density. The collinearity and nonperpendicularity constraints are correlatives.

We have evaluated these four different contributions for a GCHF calculation on the H_2O^+ cation. Note that we used the IOTC relativistic Hamiltonian [36] so that the term "spin contamination" is not really appropriate in this context, departure from the ROHF reference value being legitimate. However, the so-called spin contamination contribution has been found to dominate the noncollinearity and perpendicularity ones. This could be made even more so, by tilting the quantization axis to the optimal collinearity direction.

Acknowledgments We acknowledge Dr. Lukáš Bučinský for drawing our attention to the problem of the derivation of GCHF spin contamination, and to the fact that S^2 does not commutes with the "spin-same-orbit" coupling term, usually used in quantum chemistry. The referees and the editor are acknowledged for suggesting many improvements to the manuscript. This article is a tribute to Prof. P. Surjàn and is also dedicated to the memory of the late Prof. Gaston Berthier, who introduced to the author in the course of vivid discussions, many of the references listed below.

References

1. Hartree DR (1928) Proc Camb Philos Soc 24:89
2. Slater JC (1929) Phys Rev 34:1293
3. Fock V (1930) Physik 61:126
4. Berthier G (1964) In: Löwdin PO, Pullman B (eds) Molecular orbitals in chemistry, physics and biology. Academic Press, New York, p 57
5. Cassam-Chenaï P (1992) Algèbre fermionique et chimie quantique, Ph.D thesis, Université de Paris 6
6. Cassam-Chenaï P, Chandler GS (1992) Sur les fonctions de Hartree–Fock sans contrainte. Comptes-rendus de l'académie des sciences série II 314:755–757
7. Cassam-Chenaï P, Chandler GS (1993) Int J Quantum Chem 46:593–607
8. Amos AT, Hall GG (1961) Proc R Soc A 263:483
9. Löwdin PO (1962) J Appl Phys 33:251
10. Cassam-Chenaï P (1994) J Math Chem 15:303
11. Roothaan CCJ (1960) Rev Mod Phys 32:179
12. Andrews JS, Jayatilaka D, Bone RGA, Handy NC, Amos RD (1991) Chem Phys Lett 183:423
13. Brändas E (1968) J Mol Spectrosc 27:236
14. Berthier G (1954) Comptes-Rendus de l'Acadmie des Sciences 238:91–93
15. Pople JA, Nesbet RK (1954) J Chem Phys 22:571
16. Bunge C (1967) Phys Rev 154:70
17. Lefebvre R, Smyers YG (1967) Int J Quantum Chem 1:403
18. Lunell S (1972) Chem Phys Lett 13:93
19. Löwdin PO (1955) Phys Rev 97:509
20. Hendeković J (1974) Int J Quantum Chem 8:799
21. Prat RE, Lefebvre R (1969) Int J Quantum Chem 3:503
22. Penney R (1968) Am J Phys 36:871
23. Jordan P, Neumann JV, Wigner E (1934) Ann Math 35:29–64
24. Solèr MP (1995) Commun Algebra 23:219
25. Holland SS (1995) Bull Am Math Soc 32:205
26. Mayer I, Löwdin PO (1993) Chem Phys Lett 202:1
27. Cassam-Chenaï P (2002) J Chem Phys 116:8677–8690
28. Cassam-Chenaï P, Jayatilaka D (2012) Chem Phys 137:064107 (**And supplementary material**)
29. Coey JMD (1987) Revue canadienne de physique 65:1210
30. Libby E, McCusker JK, Schmitt EA, Folting K, Hendrickson DN, Christou G (1991) Inorg Chem 30:3486
31. Jayatilaka D (1998) J Chem Phys 108:7587
32. Small DW, Sundstrom EJ, Head-Gordon M (2015) J Chem Phys 142:094112
33. Jayatilaka D, Grimwood DJ (2003) In: Sloot P, Abramson D, Bogdanov A, Gorbachev Y, Dongarra J, Zomaya A (eds) Computational Science–ICCS 2003. Lectures notes in computer sciences, vol 2660. Springer, Berlin, pp 142–151
34. Bučinský L, Malček M, Biskupič S, Jayatilaka D, Vl Büchel GE, Arion B (2015) Comput Theor Chem 1065:27
35. Dunning TH (1989) J Chem Phys 90:1007
36. Barysz M, Sadlej AJ (2001) J Mol Struct (THEOCHEM) 573:181

Theor Chem Acc (2015) 134:151
DOI 10.1007/s00214-015-1756-x

REGULAR ARTICLE

PNOF5 calculations based on the "thermodynamic fragment energy method": C_nH_{2n+2} ($n = 1, 10$) and $(FH)_n$ ($n = 1, 8$) as test cases

Xabier Lopez[1,2] · **Mario Piris**[1,2,3]

Received: 28 April 2015 / Accepted: 30 October 2015 / Published online: 20 November 2015

Abstract The performance of the "thermodynamic fragment energy method" (FEM) in the context of natural orbital functional theory (NOFT) in its PNOF5 implementation is assessed. Two test cases are considered: the linear chains C_nH_{2n+2} ($n = 1, 10$) and the hydrogen-bonded $(FH)_n$ ($n = 1, 8$) clusters. Calculations show a fast convergence of the PNOF5-FEM method, which allows the treatment of extended system at a fractional cost of the whole calculation. We show that this type of methodologies could expand the range of systems achievable by NOFT due to the significant reduction in the computational cost.

Keywords Natural orbital functional theory · Fragment energy method · APSG wavefunction

1 Introduction

In the last decade, a series of functionals has been developed [1, 2] using a reconstruction proposed by Piris [3] of the two-particle reduced density matrix (2-RDM) in terms of the one-particle RDM (1-RDM). In particular, the Piris natural orbital functional 5 (PNOF5) [4, 5] has proved to be comparable to accurate quantum chemistry methods in many cases [4–18]. So far this is the only natural orbital functional (NOF) that has been obtained by top-down and bottom-up methods [19]. In the bottom-up method, the functional was generated by progressive inclusion of known necessary *N*-representability conditions on the 2-RDM, whereas the top-down method was used through reducing the energy expression generated from an *N*-particle wavefunction to a functional of the occupation numbers and natural orbitals [5]. In the case of PNOF5, this wavefunction is an antisymmetrized product of strongly orthogonal geminals (APSGs), with the expansion coefficients explicitly expressed by the occupation numbers [20, 21].

The idea of a function of this type dates back to the early fifties [22, 23] and is inspired by the valence bond theory [24, 25]; in fact, PNOF5 can also be considered as a type of GVB-PP method with fixed signs for the expansion coefficients of the corresponding determinants. Many scientists have worked actively in the field of strongly orthogonal geminals, and one of them is Professor Péter R. Surján to whom is dedicated this Festschrift. Indeed, an excellent review summarizing the evolution of the geminal theory up to 1999 can be found at his work [26]. An overview of geminal-based perturbative techniques for describing electron correlation was given recently [27].

Consequently, PNOF5 is an orbital-pairing approach that takes into account most of the non-dynamical effects, but also an important part of the dynamical electron correlation corresponding to the intrapair (intrageminal) interactions. The existence of a generating wavefunction confirms that PNOF5 is strictly *N*-representable, i.e., the 2-RDM is derived from a function that is antisymmetric in *N*-particles [28]. Moreover, it demonstrates the size extensivity and size consistency of PNOF5, which is an inherent property to the generating singlet-type APSG wavefunction [29, 30].

Published as part of the special collection of articles "Festschrift in honour of P. R. Surjan".

✉ Xabier Lopez
xabier.lopez@ehu.es

[1] Kimika Fakultatea, Euskal Herriko Unibertsitatea UPV/EHU, 1072, 20080 Donostia, Euskadi, Spain

[2] Donostia International Physics Center (DIPC), 20018 Donostia, Euskadi, Spain

[3] IKERBASQUE, Basque Foundation for Science, 48013 Bilbao, Euskadi, Spain

In NOF theory [31], the solution is established optimizing the energy functional with respect to the occupation numbers and to the natural orbitals, separately. If PNOF5 is employed, the occupancies can be expressed through auxiliary variables in order to enforce automatically the *N*-representability bounds on the 1-RDM, so the variation can be performed without constraints. A self-consistent procedure proposed in Ref. [32] yields the natural orbitals. This scheme requires computational times that scale as n^4, n being the number of basis functions, like in the Hartree–Fock (HF) approximation. However, our implementation in the molecular basis set requires also four-index transformation of the electron repulsion integrals, which is the time-consuming step though a parallel implementation of this part of the code has substantially improved the performance of our program. Besides the matrix scaling carried out in [32], the direct inversion in the iterative subspace (DIIS) method has recently been implemented in our code, but new techniques should be considered to reduce the number of iterations required to achieve the convergence.

In spite of its promising performance, the computational cost of PNOF5 calculations prevents them for a wider use. In this sense, any strategy to reduce calculation times is highly interesting, as it would expand the range of applicability of NOF theory. The fragmentation technique has allowed to span the range of systems attainable by wave-function-based and density-functional theories, by means of a dividing approach that allows the calculation of the whole system fragmented in subsystems. In the present paper, we use such an approach, the so-called thermodynamic fragment energy method (FEM) [33], to assess the performance of PNOF5 in the context of fragment energy calculations.

The aim of this work is to determine how PNOF5-FEM energies converge to the exact PNOF5 values for selected oligomers, namely the polyalkene chains C_nH_{2n+2} and planar zigzag $(FH)_n$ clusters. The size-consistency property, and the fact that the functional tends to localize spatially the natural orbitals, makes this functional an exceptional candidate for fragment calculations. We demonstrate that the convergence of fragment energy calculations is very fast, especially in those cases where the interaction between fragments is small.

2 Methods

2.1 The functional

At the beginning [4], PNOF5 was formulated as an orbital-pairing approach that involves coupling each orbital g, below the Fermi level ($g \leq F = N/2$), with only one orbital above F ($N_g = 1$). This model was further improved by a better description of the electron pair in the so-called extended PNOF5 [5], in which each orbital g was coupled with $N_g > 1$ orbitals above F. This pairing condition is reflected in the following sum rule for the occupation numbers:

$$\sum_{p\in\Omega_g} n_p = 1; \quad g = \overline{1,F} \tag{1}$$

where p is the running index referring to the spatial part of natural spin orbitals and n_p their occupation numbers. Notice that for spin-compensated systems the spatial part of α and β natural spin orbitals are the same, so that the total occupation number for a given natural spatial orbital is $n_p^{occ} = n_p^{\alpha} + n_p^{\beta} = 2 \times n_p$ and therefore can take values between [0, 2].

In Eq. (1), Ω_g is the subspace containing the orbital g and its N_g coupled orbitals. It is worth to note that these subspaces are mutually disjoint $\left(\Omega_{g_1} \cap \Omega_{g_2} = \varnothing\right)$, i.e., each orbital belongs only to one subspace Ω_g. The PNOF5 energy for a singlet state of an N-electron system can be cast as

$$E = \sum_{g=1}^{F} E_g + \sum_{g_1\neq g_2}^{F} \sum_{p\in\Omega_{g_1}} \sum_{q\in\Omega_{g_2}} E_{pq}^{int} \tag{2}$$

The first term of the energy (2) draws the system as independent F electron pairs described by

$$E_g = \sum_{p\in\Omega_g} n_p\left(2\mathcal{H}_{pp} + \mathcal{J}_{pp}\right) + \sum_{p,q\in\Omega_g, p\neq q} \Pi\left(n_p, n_q\right)\mathcal{L}_{qp} \tag{3}$$

$$\Pi\left(n_p, n_q\right) = \begin{cases} -\sqrt{n_p n_q}, & p = g \text{ or } q = g \\ \sqrt{n_p n_q}, & p, q > F \end{cases} \tag{4}$$

where $\mathcal{H}_{pp}$ denotes for the one-particle matrix elements of the core Hamiltonian. $\mathcal{J}_{pq} = \langle pq|pq\rangle$ and $\mathcal{K}_{pq} = \langle pq|qp\rangle$ are the usual direct and exchange integrals, respectively. $\mathcal{L}_{pq} = \langle pp|qq\rangle$ is the exchange and time-inversion integral [34], which only differs in phases of the natural orbitals with respect to the exchange integrals, so $\mathcal{L}_{pq} = \mathcal{K}_{pq}$ for real orbitals. The interaction energy E_{pq}^{int} is given by

$$E_{pq}^{int} = n_q n_p\left(2\mathcal{J}_{pq} - \mathcal{K}_{pq}\right) \tag{5}$$

Accordingly, the last term of Eq. (2) contains the contribution to the HF mean field of the electrons belonging to different pairs. It is clear that the weaknesses of this Ansatz is the absence of the interpair electron correlation. Recently [35], a new functional PNOF6, which includes interpair correlations, has been developed. The latter is able to treat orbital delocalization in aromatic systems such as in benzene, a key aspect in radical stabilization. In this work, we study systems in which such effects are not present, so it seems proper to use the PNOF5 approach. Moreover, we

will limit ourselves to the simplest formulation of the functional, i.e., we consider $N_g = 1$. Besides, in the present paper we will fix the n associated with core orbitals to 1.

2.2 The "fragment energy method" (FEM)

We follow the "fragment energy method" (FEM) proposed by Suárez et al. [33], in which the total energy of a molecule **P** composed by a linear chain of M interconnected fragments A_i ($A_1 - A_2 -_{...} - A_M$) is estimated as the sum of the energy of the fragments. Thus,

$$E(\mathbf{P}) = E_R^F(\mathbf{P}) + \delta E \tag{6}$$

where δE is the error committed by the approximation.

The fragment energy $E_R^F(\mathbf{P})$ is defined according to

$$E_R^F(\mathbf{P}) = E\left(A_1 - B_1^R\right) - \sum_{i=1}^{M-1} E\left(Y_i - B_i^R\right) + \sum_{i=2}^{M-1} E\left(Y_{i-1} - A_i - B_i^R\right) + E(Y_{M-1} - A_M) \tag{7}$$

where B_i^R are buffer regions that include a number of atoms around the fragments according to a well-defined R-dependent criterium (i.e., a distance and a number of monomer units), and Y_i are atoms or functional groups introduced to cap the boundaries upon fragmentation of covalent bonds. For details, we refer to the work of Suarez et al. [33]. The evaluation of fragment energies is less demanding computationally than the evaluation of the energy of the whole molecule. As the size of the buffer region increases, more accurate calculations are performed and smaller δE errors are obtained, but at higher computational cost. We have to take into account that PNOF5 scales as $f(m) \times N^4$ (where $f(m)$ is a prefactor related to the m number of iterations), due to the required four-index transformation of the J and K integrals in the molecular orbital basis (N^4 scaling). At present, the code is time-consuming since the required consistency on the minimization over occupations and coefficients of the natural orbital lead to the need of performing several cycles (large m). Moreover, this scaling prefactor increases with the size of the system. Therefore, there is a big advantage of using fragment energies. The aim of this work is to analyze the convergence of these errors with the fragment sizes for PNOF5 method.

3 Results and discussion

Geometries were optimized at the B3LYP/6-31+G(d) [36] level of theory using the GAUSSIAN09 program package [37]. For the $(FH)_n$ clusters, we first optimized the $(FH)_8$ cluster, and the rest of geometries were taken by deleting FH units, to prevent the collapse of the cluster of lower size to geometries other than zigzag ones. All PNOF5 calculations have been carried out using our computational code DoNOF with the 6-31G and 6-31G(d,p) basis set [38] and the correlation-consistent valence double-ζ (cc-pVDZ) developed by Dunning et al. [39]. The matrix element of the kinetic energy and nuclear attraction terms, as well as the electron repulsion integrals, are inputs to our computational code. In the current implementation, we have used the GAMESS program [40, 41] for this task. The convergence criteria applied for PNOF solutions is 10^{-8} a.u. in the energy and 10^{-5} for the tolerance of the hermiticity of the matrix of Lagrange multipliers λ (see reference [32] for details on the iterative diagonalization procedure).

3.1 Polyalkene chain C_nH_{2n+2}

PNOF5/6-31G energies for oligomers of size $n = 1$, 10 and PNOF5/cc-pVDZ energies for $n = 1$, 8 can be found in Table 1. In order to calculate fragment energies, we will particularize Eq. (7) for the C_nH_{2n+2} oligomers. In this case, the fragments are constituted by $A_i = -(CH_2)_i-$ units and the terminal $-CH_3$. H atoms are used to cap the boundaries upon fragmentation ($Y_i = H$). Finally, the buffer region is constituted by a number of $-CH_2-$ units, namely $B_i^R = -(CH_2)_R - H$. For this particular case, Eq. (7) can be cast as

$$E_R^F(\mathbf{P}_n) = E(\mathbf{P}_{R+1}) + (n - R - 1)\left[E(\mathbf{P}_R) - E(\mathbf{P}_{R-1})\right] \tag{8}$$

where n is the order of the oligomer. Equation (8) implies that the evaluation of fragment energy of a n-size oligomer with a R-buffer region requires the calculation of three oligomers of size $R + 1$, R and $R - 1$. Therefore, the size of the buffer region determines the size of the largest oligomer in the fragment energy calculation. Obviously, the larger the R-size, the more accurate the results, but also the higher computational cost. The formula above can be further simplified by taking into account that $E(P_R) - E(P_{R-1})$ is a measure of the bond energy between fragments, and this bond energy can also be estimated more accurately by $E(P_{R+1}) - E(P_R)$. Hence,

$$E_R^F(\mathbf{P}_n) = (n - R)E(\mathbf{P}_{R+1}) - (n - R - 1)E(\mathbf{P}_R) \tag{9}$$

For convenience, we will use the index l for the largest oligomer size in fragment calculations, namely

$$E_l^F(\mathbf{P}_n) = (n - l + 1)E(\mathbf{P}_l) - (n - l)E(\mathbf{P}_{l-1}) \tag{10}$$

In summary, the evaluation of a fragment energy requires the evaluation of the energy for two oligomers of size l and $l - 1$. The size of the largest oligomer in the fragment calculations is determined by the size of the buffer region according to $l = R + 1$.

Table 1 PNOF5/6-31G energies $E(P_n)$ and fragment energies $E_l^F(P_n)$ (Eq. 10), in a.u., for the C_nH_{2n+2} oligomers, and the corresponding error, δE, in kcal/mol

6-31G				cc-pVDZ				6-31G(d,p)			
n	$E(P_n)$ (a.u.)	l	$\delta E/n$ (kcal/mol)	n	$E(P_n)$ (a.u.)	l	$\delta E/n$ (kcal/mol)	n	$E(P_n)$ (a.u.)	l	$\delta E/n$ (kcal/mol)
1	−40.24169045			1	−40.25889725			1	−40.262046		
2	−79.30382845			2	−79.34030290			2	−79.344005		
3	−118.367272	2	−0.273	3	−118.422678	2	−0.203	3	−118.426983	2	−0.213
4	−157.430646	2	−0.399	4	−157.505028	2	−0.300	4	157.509836	2	−0.300
		3	0.011	4		3	0.004			3	0.020
5	−196.493955	2	−0.466	5	−196.587301	2	−0.349	5	−196.592634	2	−0.345
		3	0.026			3	0.016			3	0.038
		4	0.008			4	0.010			4	0.007
6	−235.557275	2	−0.512	6	−235.669573	2	−0.382	6	−235.675439	2	−0.376
		3	0.034			3	0.024			3	0.050
		4	0.012			4	0.016			4	0.011
		5	−0.001			5	0.000			5	0.000
7	−274.620592	2	−0.545	7	−274.751846	2	−0.405				
		3	0.041			3	0.030				
		4	0.016			4	0.021				
		5	−0.002			5	0.000				
		6	0.000			6	0.000				
8	−313.683917	2	−0.570	8	−313.834122	2	−0.422				
		3	0.045			3	0.034				
		4	0.018			4	0.024				
		5	−0.003			5	0.000				
		6	0.000			6	0.000				
		7	−0.001			7	0.000				
9	−352.747238	2	−0.589								
		3	0.048								
		4	0.019								
		5	−0.003								
		6	0.000								
		7	−0.001								
		8	0.000								
10	−391.810562	2	−0.604								
		3	0.051								
		4	0.021								
		5	−0.004								
		6	0.000								
		7	−0.001								
		8	0.000								
		9	0.000								

Geometries were optimized at the B3LYP/6-31+G(d) level of theory

As mentioned above, the aim of this work is to determine how fragment energies converge to the exact PNOF5 energy for a given size of the oligomer as function of l. Fragment energies, $E_l^F(\mathbf{P}_n)$, for the oligomers of size ($n = 3, 10$) calculated with the 6-31G basis set can be found in Table 1, along with the difference between the two energies per oligomer unit, $\delta E/n$, in kcal/mol. In Fig. 1, we represent $\delta E/n$ as a function of the largest oligomer size (l) used in the fragment calculation. Calculations were repeated with the cc-pVDZ basis set for $n = (3, 8)$ and 6-31G(d,p) basis set

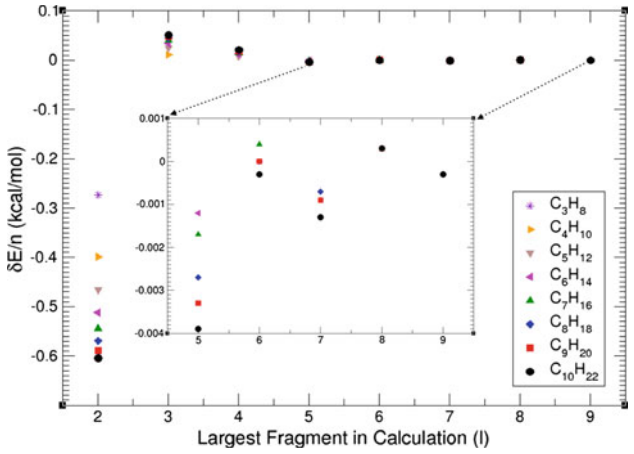

Fig. 1 Difference in energy between oligomer energy ($E(\mathbf{P}_n)$) and fragment energies ($E_l^F(\mathbf{P}_n)$) per oligomer size, namely $\delta E/n = \left[E(\mathbf{P}_n) - E_l^F(\mathbf{P}_n)\right]/n$, in kcal/mol. Calculations done at the PNOF5/6-31G level of theory for oligomers of size $n = 1, 10$

for ($n = 3, 6$), obtaining similar results. Therefore, we will analyze the PNOF5/6-31G results for which a larger dataset of oligomers was calculated.

There is a very good convergence of the fragment calculations for any of the oligomer size. It is remarkable, that in all cases, we are within chemical accuracy (as defined by an error of <1 kcal/mol per oligomer unit) for any oligomer and fragment size calculation. For instance, if we consider the largest oligomer, namely $C_{10}H_{22}$, the $\delta E/n$ error of the fragment energies for $l = 2, 9$ is -0.604, 0.051, 0.021, -0.004, 0.000, -0.001, 0.000, 0.000 kcal/mol, respectively. Thus, the errors in the energy converge very fast and gradually between $l = 2$ to $l = 6$. For higher fragment sizes, we can say that the results are converged within the accuracy of the method.

As expected for a given l, the errors get bigger as the size of the oligomer increases, but it is very relevant that these increases are very low. For instance, if we consider the smallest fragment calculation ($l = 2$), the error obtained for the different oligomer sizes is all within the same order of magnitude. Thus, for $l = 2$, we obtain a $\delta E/n$ of only -0.273 kcal/mol (C_3H_8), -0.399 (C_4H_{10}), -0.466 (C_5H_{12}), -0.512 (C_6H_{14}), -0.545 (C_7H_{16}), -0.570 (C_9H_{20}), -0.589, -0.604 ($C_{10}H_{22}$).

As one can see from Table 1, the improvement on the basis set implies no dramatic changes, even an slight amelioration of the convergence is observed in fragment energies. There is a very fast and good convergence of PNOF5 fragment energies with fragment size. In all cases when considering $l \approx n/2$, results are very accurate with errors within the chemical accuracy.

It is clear that linear C_nH_{2n+2} oligomers are a very favorable case for fragment energy calculations. This is not surprising due to the nonpolar nature of the bonds between fragments, and the small interaction expected among the monomers of the chain. Therefore, we decided to investigate a less favorable case: a chain of hydrogen bonds among units with polar bonds: $(FH)_n$.

3.2 Hydrogen-bonded chain $(FH)_n$

This case is a prototypical system bound by a chain of hydrogen bonds. We have constructed a planar zigzag $(FH)_8$ cluster and employed only the cc-pVDZ basis set. The incremental energies per cluster unit are depicted in Fig. 2. As the size of the cluster increases, the energy per FH unit decreases indicating some cooperativity among the whole hydrogen-bonded chain in the hydrogen bond interaction between two neighbor FH units. Notice that as the size of the clusters increases, one should reach a limiting value, still not attained by the size of the clusters of the present work.

Contrary to the alkane series, in this case, the higher the cluster size, the lower the energy per cluster unit. This is expected for a system bound by hydrogen bonds, due to the cooperative nature of the hydrogen bonding network. As the cluster size increases, the increments in energy per cluster unit tend to increase linearly. For instance, at $n = 2$, we obtain a value of 1.9 kcal/mol, and at $n = 8$, a value of 4.9 kcal/mol, at the PNOF5/cc-pVDZ level of theory. Remind that these structures are frozen.

Note that in this case there is no need to introduce cap atoms, since the fragments are constituted by each FH unit. The buffer region will be formed of R-number of FHs. It is straightforward to demonstrate that the fragment energies can be calculated according to a formula analogous to the one used in the previous section, namely

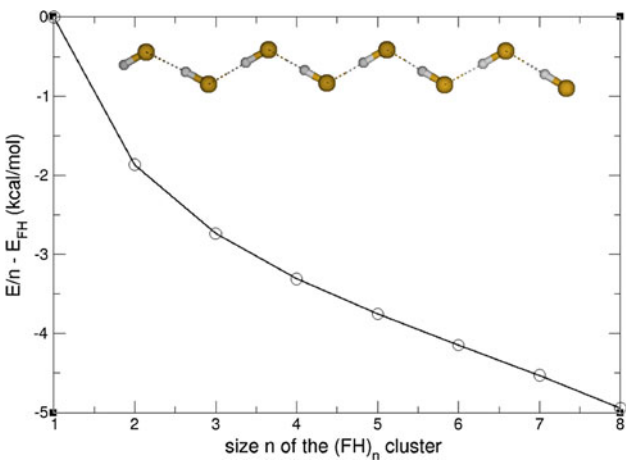

Fig. 2 Energy per oligomer unit (E/n) of the $(FH)_n$ clusters with respect to the energy of the hydrogen fluoride (E_{FH}). Calculations done at the PNOF5/cc-pVDZ level of theory

Table 2 PNOF5/cc-pVDZ energies, $E(P_n)$ and fragment energies $E_l^F(P_n)$ (Eq. 11), in a.u., for the $(FH)_n$ clusters, and the corresponding error divided by the number of FH units, $\delta E/N_{FH}$, in kcal/mol

n	$E(P_n)$ (a.u.)	1	$\delta E/N_{FH}$ (kcal/mol)
1	−100.076915		
2	−200.159778		
3	−300.243820	2	−0.247
4	−400.328752	2	−0.510
		3	−0.140
5	−500.414457	2	−0.764
		3	−0.320
		4	−0.097
6	−600.501109	2	−1.033
		3	−0.540
		4	−0.261
		5	−0.099
7	−700.588907	2	−1.328
		3	−0.799
		4	−0.480
		5	−0.273
		6	−0.103
8	−800.678348	2	−1.678
		3	−1.123
		4	−0.774
		5	−0.532
		6	−0.309
		7	−0.129

Geometries were optimized at the B3LYP/6-31+G(d) level of theory

$$E_l^F(P_n) = (n-l+1)E(l) - (n-l)E(l-1) \quad (11)$$

with $l = R + 1$. Results can be found in Table 2 and Fig. 3. The first aspect to remark is that the errors in fragment energies are bigger than for the alkane series. For instance, the error $\delta E/n$ for the $(FH)_8$ cluster with $l = 4$ is −0.7739 kcal/mol, whereas for C_8H_{16} is one order of magnitude less, 0.0239 kcal/mol. The convergence of fragment energies with l is significantly slower than in the case of C_nH_{2n+2}. The decay in $\delta E/n$ for $(FH)_8$ with $l = \overline{2,7}$ is −1.678, −1.229, −0.774, −0.532, −0.309, −0.129 kcal/mol, respectively. This is a significant reduction in error but at a much lower rate than for C_nH_{2n+2} system. On the other hand, notice that these errors show a systematic behavior, approaching the total energy of the cluster from above, due to the gradual recovery of the cooperative effects in the hydrogen bonding network as the size of the fragments increases and approaches the total size of the cluster. For a given size l, the errors also increase when the cluster grows at a higher rate than in the alkane series; for instance, for $l = 2$ the error in evaluating the energy for $(FH)_n$ increases

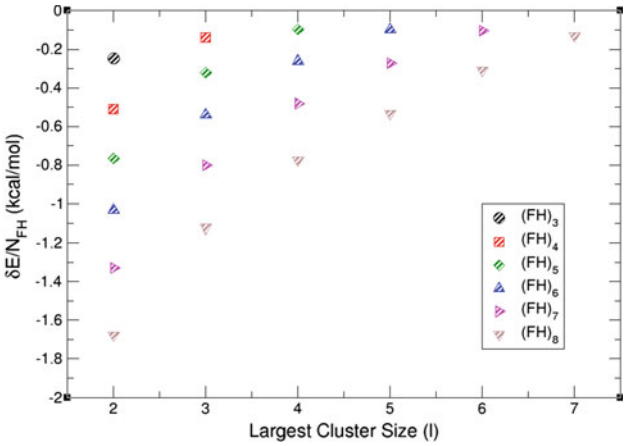

Fig. 3 Error in PNOF5/cc-pVDZ fragment energies, $E_l^F(P_n)$, with respect to the energy of the cluster $E(P_n)$ for the $(FH)_n$ clusters, divided by the number of FH units in the cluster, $\delta E/N_{FH}$, in kcal/mol

with the value of $n = \overline{3,8}$ as −0.247, −0.510, −0.764, −1.033, −1.328, −1.678 kcal/mol, respectively.

The origin of the worst performance of fragment energies for $(FH)_n$ cluster is the interaction between fragments. The interaction between hydrogen-bonded species is of long range type. Accordingly, the interaction is extended over large number of clusters and gives rise to cooperative effects among the hydrogen bonding network. The use of fragment energies will therefore have a sizable effect. However, in the case of alkane, even though we fragment the molecule through covalent bonds, the apolar nature of the fragments makes them more amenable for fragment calculations. However, one has to highlight that the convergence is still quite good, and considering fragment calculations of size $l \approx n/2$, chemical accuracy is obtained for all the clusters.

4 Conclusions

We can conclude that the size-consistent and localized orbital nature of PNOF5 allows for a good performance of fragment calculations. For fragment calculations of size $l \approx n/2$, the chemical accuracy is obtained for all the clusters, even in the case of hydrogen bond interactions between the units. This leads to very significant computational gains, at least of one order of magnitude. Therefore, the PNOF5-FEM method could be a promising tool to extend the size of systems amenable for PNOF-type calculations.

Acknowledgments Financial support comes from Eusko Jaurlaritza (Ref. IT588-13) and Ministerio de Economía y Competitividad (Refs. CTQ2012-38496-C05-01, CTQ2012-38496-C05-04). The SGI/

IZO–SGIker UPV/EHU is gratefully acknowledged for generous allocation of computational resources.

References

1. Piris M (2013) Int J Quantum Chem 113:620–630
2. Piris M, Ugalde JM (2014) Int J Quantum Chem 114:1169–1175
3. Piris M (2006) Int J Quantum Chem 106:1093–1104
4. Piris M, Lopez X, Ruipérez F, Matxain JM, Ugalde JM (2011) J Chem Phys 134:164102
5. Piris M, Matxain JM, Lopez X (2013) J Chem Phys 139(23):234109
6. Matxain JM, Piris M, Ruipérez F, Lopez X, Ugalde JM (2011) Phys Chem Chem Phys 13:20129–20135
7. Matxain JM, Piris M, Mercero JM, Lopez X, Ugalde JM (2012) Chem Phys Lett 531:272–274
8. Matxain JM, Piris M, Uranga J, Lopez X, Merino G, Ugalde JM (2012) ChemPhysChem 13:2297–2303
9. Piris M, Matxain JM, Lopez X, Ugalde JM (2012) J Chem Phys 136:174116
10. Lopez X, Ruipérez F, Piris M, Matxain JM, Matito E, Ugalde JM (2012) J Chem Theory Comput 8:2646–2652
11. Piris M, Matxain JM, Lopez X, Ugalde JM (2013) Theor Chem Acc 132:1298
12. Ruipérez F, Piris M, Ugalde JM, Matxain JM (2013) Phys Chem Chem Phys 15:2055–2062
13. Matxain JM, Ruipérez F, Infante I, Lopez X, Ugalde JM, Merino G, Piris M (2013) J Chem Phys 138:151102
14. Piris M (1003) Comput Theor Chem 2013:123–126
15. Lopez X, Piris M, Nakano M, Champagne B (2014) J Phys B Atomic Mol Opt Phys 47:015101
16. Piris M, March NH (2014) Phys Chem Liq 52:804–814
17. Ramos-Cordoba E, Salvador P, Piris M, Matito E (2014) J Chem Phys 141:234101
18. Piris M, March NH (2015) Phys Chem Liq. doi:10.1080/00319104.2015.1029478
19. Ludeña EV, Torres FJ, Costa C (2013) J Mod Phys 04:391–400
20. Pernal K (1003) Comput Theor Chem 2013:127–129
21. Piris M (2013) J Chem Phys 139:064111
22. Fock FA (1950) Dokl Akad Nauk USSR 73:735
23. Hurley AC, Lennard-Jones J, Pople JA (1953) Proc R Soc Lond A 220:446–455
24. Heitler W, London F (1927) Z Phys 44:455
25. Shaik S, Hiberty PC (2008) A chemist's guide to valence bond theory. Wiley, London
26. Surjan PR (1999) Topics in current chemistry, vol 203. Springer, Berlin
27. Jeszenszki P, Nagy PR, Zoboki T, Szabados A, Surjan PR (2014) Int J Quantum Chem 114:1048–1052
28. Coleman AJ (1963) Rev Mod Phys 35:668–687
29. Rassolov VA (2002) J Chem Phys 117:5978
30. Rassolov VA, Xu F (2007) J Chem Phys 127:044104
31. Piris M (2007) In: Mazziotti DA (ed) Reduced-density-matrix mechanics: with applications to many-electron atoms and molecules. Wiley, Hoboken, pp 387–427 chapter 14
32. Piris M, Ugalde JM (2009) J Comput Chem 30:2078–2086
33. Suárez E, Díaz N, Suárez D (2009) J Chem Theory Comput 1667–1679
34. Piris M (1999) J Math Chem 25:47–54
35. Piris M (2014) J Chem Phys 141:044107
36. Zhao Y, Truhlar DG (2008) Theor Chem Acc 120:215–241
37. Gaussian 09, Revision D.01, Frisch MJ, Trucks GW, Schlegel HB, Scuseria GE, Robb MA, Cheeseman JR, Scalmani G, Barone V, Mennucci B, Petersson GA, Nakatsuji H, Caricato M, Li X, Hratchian HP, Izmaylov AF, Bloino J, Zheng G, Sonnenberg JL, Hada M, Ehara M, Toyota K, Fukuda R, Hasegawa J, Ishida M, Nakajima T, Honda Y, Kitao O, Nakai H, Vreven T, Montgomery Jr JA, Peralta JE, Ogliaro F, Bearpark M, Heyd JJ, Brothers E, Kudin KN, Staroverov VN, Kobayashi R, Normand J, Raghavachari K, Rendell A, Burant JC, Iyengar SS, Tomasi J, Cossi M, Rega N, Millam JM, Klene M, Knox JE, Cross JB, Bakken V, Adamo C, Jaramillo J, Gomperts R, Stratmann RE, Yazyev O, Austin AJ, Cammi R, Pomelli C, Ochterski JW, Martin RL, Morokuma K, Zakrzewski VG, Voth GA, Salvador P, Dannenberg JJ, Dapprich S, Daniels AD, Farkas Ö, Foresman JB, Ortiz JV, Cioslowski J, Fox DJ, Gaussian, Inc., Wallingford CT, 2009
38. Hehre WJ, Ditchfield R, Pople JA (1972) J Chem Phys 56:2257–2261
39. Dunning TH, Dunning TH Jr (1989) J Chem Phys 90:1007–1023
40. Schmidt MW, Baldridge KK, Boatz JA, Elbert ST, Gordon MS, Jensen JH, Koseki S, Matsunaga N, Nguyen KA, Shyjun SU, Dupuis M, Montgomery JA (1993) J Comput Chem 14:1347–1363
41. Gordon MS, Schmidt MW (2005) Theory and applications of computational chemistry. Elsevier, Philadelphia

Theor Chem Acc (2016) 135:3
DOI 10.1007/s00214-015-1759-7

REGULAR ARTICLE

Orthogonality-constrained Hartree–Fock and perturbation theory for high-spin open-shell excited states

V. N. Glushkov[1] · **X. Assfeld**[2]

Received: 12 June 2015 / Accepted: 7 November 2015 / Published online: 10 December 2015

Abstract We present the orthogonality-constrained Hartree–Fock (HF) method for excited states in a combination with the Møller–Plesset-like perturbation theory for the correlation energy. This developed "HF + MP2" formalism for excited states allows for the treatment of both ground and excited states in a balanced manner. Unlike a previous work (Glushkov in Chem Phys Lett 287:189, 1998), our interest has shifted toward highly doubly excited states of atoms and doubly ionized core hole molecular states which are attractive from the experimental point of view. The accuracy of the method is demonstrated by calculations of more than 30 highly excited states of the He and Li atoms and about 10 doubly excited core hole states of some diatomic molecules (CO, NO and LiF).

Keywords Excited states · Constrained Hartree–Fock · Perturbation theory · Double core hole states · Frozen orbitals

Published as part of the special collection of articles "Festschrift in honour of P. R. Surjan."

✉ X. Assfeld
xavier.assfeld@univ-lorraine.fr

[1] Department of Physics, Electronics and Computer Systems, Oles Gonchar Dnipropetrovsk National University, Dnipropetrovsk, Ukraine

[2] Université de Lorraine Nancy, CNRS, Théorie-Modélisation-Simulation, SRSMC, Boulevard des Aiguillettes, 54506 Vandoeuvre-lès-Nancy, France

1 Introduction

It is well known that Hartree–Fock (HF) theory not only has been proven to be quite suitable for calculations of ground state (GS) properties of electronic systems, but has also served as a starting point to develop many-particle approaches which deal with electronic correlation, like perturbation theory, configuration interaction methods and so on (see e.g., [1]). Therefore, a large number of sophisticated computational approaches have been developed for the description of the ground states based on the HF approximation. One of the most popular computational tools in quantum chemistry for GS calculations is based on the effectiveness of the HF approximation and the computational advantages of the widely used many-body Møller–Plesset perturbation theory (MPPT) for correlation effects. We designate this scheme as "HF + MPPT," here after denoted "HF + MP2."

There is far less reported experience for the HF studies of electronic excited states (ESs). Especially, highly, doubly and core hole excited (ionized) states are not often studied. It is clear that existing ground state self-consistent field (SCF) methods cannot be directly applied to excited states of the same symmetry or of the same spin multiplicity as a lower state because of the so-called variational collapse i.e., the optimization procedure will find only the lowest solution of a given symmetry or a given spin multiplicity. Therefore, such calculations for ES cannot be considered as routine. The most powerful scheme for accurate treatment of ESs is based on multireference methods [2–8]. They typically provide an accuracy of about 0.1 eV but require the expense of much computational cost. Thus, it can be quite difficult to carry out the corresponding calculations. Such methods are, however, indispensable to study systems where

single-configuration methods cannot be applied. However, in cases where a multireference approach is necessary, it is clear that the orbitals of a single configuration, together with a basis set that has been specifically optimized for a given excited state, will prove more appropriate for the development of many-body correlation methods than orbitals expanded in a basis set constructed for the ground state. Furthermore, it would be very useful to have an analogue of the "HF + MP2" formalism for the description of excited states which can be adequately described by a single Slater determinant. In doing so, we should take into account that the basis functions that are used to construct molecular orbitals are typically optimized to describe the ground states of atoms. Remembering that the ground and excited states are often of quite different character, it is desirable to use different basis sets for different states. "The desirability of using different basis sets for different states" was already pointed out by Shull and Löwdin [9] in 1958. It is especially important for highly excited states. We shall show that our methodology allows a basis set to be optimized for the excited state under consideration with essentially the same computational efforts as for the ground state. Such an approach provides a compact and accurate representation of excited state wave functions. On the other hand, finding a method that offers a well-balanced treatment of both states is often problematic. Accounting for electron correlation in excited states is not as straightforward as in the ground state.

In this contribution, we further develop the "HF + MP2" formalism for excited states focusing our attention on calculations of the ground state and excited state energies in a balanced manner, i.e.,

1. Reference configurations are constructed by employing the same computational scheme. For example, the ground and excited SCF functions are constructed using the Hartree–Fock equations, whose solutions are approximated in one particle basis sets optimized specifically to the state under consideration.
2. Correlation effects are taken into account using comparable schemes for the ground and excited states using, for example, many-body Møller–Plesset-like perturbation theory.

Some preliminary results in this direction were reported in papers [10, 11]. Here, we extend the theory and practical calculations to highly doubly excited states and doubly ionized core hole states. A simple and easily implemented asymptotic projection (AP) method for taking orthogonality constraints into account, which has been proposed earlier [12–14], allows one to perform the "HF + MP2" scheme for the ground and excited states with essentially the same computational costs. The AP method is based on the properties of self-conjugate operators. It is general and applicable to any problem that can be cast in the form of an eigenvalue equation with some orthogonality constraints imposed on the eigenvectors.

The present work is arranged as follows: in Sect. 2, orthogonality constraints for single determinantal wave functions and some existing methods to prevent "variational collapse" are briefly discussed. Our orthogonality-constrained HF method for excited states is presented in Sect. 3. Unlike existing self-consistent field (SCF) techniques based on the Roothaan open-shell theory [15], it does not involve off-diagonal Lagrange multipliers. Additionally, equations for basis set optimization are also derived. The well-defined Møller–Plesset-like perturbation theory based on optimal excited orbitals generated by the proposed HF method is the subject of Sect. 4. In addition single excitations do not contribute because the excited state orbitals, like the ground state orbitals, satisfy the generalized Brillouin theorem. In Sect. 5, we apply the formalism to highly doubly excited states of atoms as well as to doubly ionized core hole states of diatomic molecules.

2 Specific features of SCF excited states calculations

Quantum mechanics requires *exact* wave functions to be orthogonal, but it makes no such demand on SCF functions. Indeed, consider the orthogonality condition for the *exact* many-electron wave functions describing the ground state, Ψ_0, and the first excited state Ψ_1, i.e., (see also [11])

$$\langle \Psi_0 \mid \Psi_1 \rangle = 0 \tag{1}$$

The exact ground state wave function, Ψ_0, can be written

$$\Psi_0 = \Phi_0 + \chi_0 \tag{2}$$

where Φ_0 is the many-electron ground state SCF wave function and χ_0 is the correlation correction. Without loss of generality, we can require

$$\langle \Phi_0 \mid \chi_0 \rangle = 0 \tag{3}$$

Similarly, the exact excited state wave function, Ψ_1, can be written

$$\Psi_1 = \Phi_1 + \chi_1 \tag{4}$$

where Φ_1 is the many-electron excited state SCF wave function and χ_1 is the corresponding correlation correction. Again, without loss of generality, we can require

$$\langle \Phi_1 \mid \chi_1 \rangle = 0 \tag{5}$$

Substituting (2) and (4) into (1), we have

$$\begin{aligned} \langle \Psi_0 \mid \Psi_1 \rangle = {} & \langle \Phi_0 \mid \Phi_1 \rangle + \langle \Phi_0 \mid \chi_1 \rangle \\ & + \langle \chi_0 \mid \Phi_1 \rangle + \langle \chi_0 \mid \chi_1 \rangle = 0 \end{aligned} \tag{6}$$

or

$$\langle \Phi_0 \mid \Phi_1 \rangle = -[\langle \Phi_0 \mid \chi_1 \rangle + \langle \chi_0 \mid \Phi_1 \rangle + \langle \chi_0 \mid \chi_1 \rangle] \quad (7)$$

Thus we see that the SCF wave functions do not, in general, satisfy orthogonality constraints analogous to those obeyed by the exact wave functions.

It is worth also noting that the imposition of the orthogonality constraint on an approximate lower state wave function, such as the Hartree–Fock function, does not, in general, yield an excited state energy which is an upper bound to the exact excited state energy. An upper bound to the excited state energy is obtained if we impose the additional constraint

$$\langle \Phi_0 | H | \Phi_1 \rangle = 0$$

which is much more difficult to implement. In practice, if the lower state energy and the corresponding wave function are known accurately, then the coupling matrix element $\langle \Phi_0 | H | \Phi_1 \rangle$ is expected to be small.

Several useful methods have been proposed to overcome the "variational collapse" problem, and a number of different schemes have been proposed for obtaining SCF wave functions for excited states [10, 16–26]. In recent years, there has been renewed interest in the orthogonality-constrained methods [14, 27] as well as in the SCF theory for excited states [28–32]. It is clear that an experience accumulated for the HF excited state calculations can be useful to develop similar methods within density functional theory [33–36]. Some of these approaches [10, 18, 19, 23, 24, 26, 30–35] explicitly introduce orthogonality constraints to lower states. Other methods [21, 22, 25] either use this restriction implicitly or locate excited states as higher solutions of nonlinear SCF equations [29]. In latter type of scheme, the excited state SCF wave functions of interest are not *necessarily* orthogonal to the best SCF functions for a lower state or states of the same symmetry.

In our methodology we impose a constraint upon the SCF excited state function so that

$$\langle \Phi_0 \mid \Phi_1 \rangle = 0, \quad (8)$$

i.e., we explicitly introduce the orthogonality constraint on Φ_1 to the best SCF ground state function Φ_0. On the one hand, the restriction (8) limits slightly the variational degrees of freedom, but, on the other hand, the imposition of the constraint (8) has some advantages:

1. it preserves the important orthogonality property of exact eigenstates;
2. any lack of orthogonality of the SCF wave functions may lead to excited state energies lying below the corresponding exact energies (For example, Cohen and Kelly [37] found for the *He* atom the first singlet excited state energy $E_1 = -2.16984$ hartree, whereas the observed energy $E_1^{\text{extract}} = -2.14598$ hartree (See also the work of Tatewaki et al. [38]).);
3. it allows the study of properties which depend on the wave functions of different states, e.g., in the evaluation of transition properties (see also [23, 24]);
4. it facilitates the development of a simple perturbation theory expansion for correlation effects in excited states [10] (see also Sect. 4).

We shall be concerned with ground and excited electronic states which can be adequately described by a single determinantal wave function. For simplicity, we consider singly excited states and show how our formalism can be applied to highly and doubly excited states.

Let Φ_0 be the ground state *unrestricted* Slater determinant constructed from a set of spin orbitals consisting of spatial part $|\varphi_{0i}^{\alpha}\rangle, (i^{\alpha} = 1, 2, \ldots, n^{\alpha})$ associated with α spin functions and orbitals $|\varphi_{0i}^{\beta}\rangle, (i^{\beta} = 1, 2, \ldots, n^{\beta})$ associated with β spin functions, i.e.,

$$\Phi_0 = (N!)^{-1/2} \det \left| \varphi_{01}^{\alpha}\alpha, \ldots, \varphi_{0n}^{\alpha}\alpha; \varphi_{01}^{\beta}\beta, \ldots, \varphi_{0n}^{\beta}\beta \right| \quad (9)$$

without loss of generality, we define $n^{\alpha} > n^{\beta}, n^{\alpha} + n^{\beta} = N$, where N is a number of electrons and $S = S_z = (n^{\alpha} - n^{\beta})/2$ is the total spin. Similarly, Φ_1 is a single *unrestricted* determinant wave function for the first excited state:

$$\Phi_1 = (N!)^{-1/2} \det \left| \varphi_{11}^{\alpha}\alpha, \ldots, \varphi_{1n}^{\alpha}\alpha; \varphi_{11}^{\beta}\beta, \ldots, \varphi_{1n}^{\beta}\beta \right| \quad (10)$$

Then, one can show [10, 11] that the orthogonality condition (8) is fulfilled if

$$\left\langle u \,\middle|\, \varphi_{1j}^{\alpha} \right\rangle = 0, \quad j = 1, 2, \ldots, n^{\alpha} \quad (11)$$

where $|u\rangle = \sum_i^{n^{\alpha}} b_i |\varphi_{0i}^{\alpha}\rangle$. Eq. (11) requires the orthogonality of all occupied excited state orbital associated with α spin functions to the arbitrary vector $|u\rangle$, from the subspace of the occupied ground state orbitals associated with α spin functions. In other words the vector $|u\rangle$ is orthogonal to the subspace defined by occupied excited state $\alpha-$ orbitals. A similar condition was also used in Refs. [23, 24, 35]. However, our practical implementation differs essentially from these works. In general, the coefficients b_i can be determined by minimizing the excited state Hartree–Fock energy, i.e., the complete variational space can be used instead of simply $|u\rangle = |\varphi_{0n}^{\alpha}\rangle$, where φ_{0n}^{α} is the highest occupied molecular orbital. However, our computational experience showed that such a choice is a good approximation for $|u\rangle$ and provides very simple implementation during SCF iteration procedure. Using a orthoprojector

$$P_u^{\alpha} = |\varphi_{0n}^{\alpha}\rangle\langle\varphi_{0n}^{\alpha}|$$

the requirement (11) can be rewritten in a symmetrical form, which is useful when deriving the excited state Hartree–Fock equations for orbitals, as follows:

$$\sum_{j}^{n^\alpha} \left\langle \varphi_{1j}^\alpha | P_u^\alpha | \varphi_{1j}^\alpha \right\rangle = 0, \tag{12}$$

This result can be easily extended to higher energy levels. For example, for the second excited state the operator P_u^α should be substituted by the orthoprojector

$$P_u^\alpha = \left| \varphi_{0n}^\alpha \right\rangle \left\langle \varphi_{0n}^\alpha \right| + \left| \varphi_{1n}^\alpha \right\rangle \left\langle \varphi_{1n}^\alpha \right| \equiv P_{u,0}^\alpha + P_{u,1}^\alpha \text{etc.}$$

It is clear, for arbitrary K^{th} singly excited state we have

$$P_u^\alpha = \sum_{k=0}^{K-1} P_{u,k}^\alpha, \quad \text{with } P_{u,k}^\alpha = \left| \varphi_{kn}^\alpha \right\rangle \left\langle \varphi_{kn}^\alpha \right|.$$

Furthermore, this idea can be extended to doubly, triply etc. excited states. In contrast to existing SCF methods for hole states, we achieve the effect of the excitation (or ionization) of electrons by using orthogonality constraints imposed on the orbitals of the doubly excited state's Slater determinant. For example, for description of excitations from φ_{0k}^α and φ_{0l}^β ground state orbitals, we require a fulfillment of conditions

$$\sum_{j}^{n^\alpha} \left\langle \varphi_{1j}^\alpha | P_k^\alpha | \varphi_{1j}^\alpha \right\rangle = 0, \tag{13}$$

and

$$\sum_{j}^{n^\beta} \left\langle \varphi_{1j}^\beta | P_l^\beta | \varphi_{1j}^\beta \right\rangle = 0, \tag{14}$$

where $P_k^\alpha = \left| \varphi_{0k}^\alpha \right\rangle \left\langle \varphi_{0k}^\alpha \right|$ and $P_l^\beta = |\varphi_{0l}^\beta\rangle\langle\varphi_{0l}^\beta|$.

At the HF level of theory, we call this method constrained self-consistent field (CSCF).

3 Hartree–Fock and basis set optimization equations for excited states

We shall follow the unrestricted Hartree–Fock (UHF) formalism for obtaining the restricted open-shell HF (ROHF) functions to derive the Hartree–Fock equations for excited states. For the sake of simplicity, we restrict our attention to the first excited state. The problem can be described as:

$$E_1^{\text{UHF}} = \min \langle \Phi_1 | H | \Phi_1 \rangle / \langle \Phi_1 | \Phi_1 \rangle \tag{15}$$

provided that

$$\langle \Phi_0 | \Phi_1 \rangle = 0, \tag{16}$$

$$\left\langle \Phi_1 \middle| \left\{ \hat{S}^2 - S(S+1) \right\} \middle| \Phi_1 \right\rangle = 0. \tag{17}$$

Equations (16) and (17) can be written in terms of one-particle orbitals:

1. Orbitals must satisfy the restrictions (12) which ensure the orthogonality of Slater determinants (16);
2. Equation (17) means that the excited Slater determinant must be an eigenvector of the $\mathbf{S}^2$ operator. As shown by Fock [39], the condition (17) is fulfilled if the set of orbitals associated with the β spin functions lies completely within the space defined by the set associated with the α spin functions. This condition eliminates spin contamination and can be written as the orthogonality constraint [40]:

$$\sum_{j}^{n^\beta} \left\langle \varphi_{1j}^\beta | Q_1^\alpha | \varphi_{1j}^\beta \right\rangle = 0, \tag{18}$$

$Q_1^\alpha = I - P_1^\alpha$ is the orthoprojector on the subspace of the virtual α spin orbitals and

$$P_1^\alpha = \sum_{i=1}^{n^\alpha} \left| \varphi_{1i}^\alpha \right\rangle \left\langle \varphi_{1i}^\alpha \right|$$

In order to obtain equations for optimal orbitals for the first excited state, we use the stationary condition

$$\delta L = \delta \left\{ E_1^{\text{UHF}} + \lambda_s \sum_{i=1}^{n^\beta} \left\langle \varphi_{1i}^\beta | Q_1^\alpha | \varphi_{1i}^\beta \right\rangle + \lambda_o \sum_{i=1}^{n^\alpha} \langle \varphi_{1i}^\alpha | P_u^\alpha | \varphi_{1i}^\alpha \rangle \right\} \tag{19}$$

Lagrange multipliers λ_o and λ_s are determined by the asymptotic projection methodology [10, 11, 40]. In practical applications, we invariably invoke the algebraic approximation by parameterizing the orbitals in a finite basis set. This approximation may be written

$$|\varphi_{1i}\rangle = P_1 |\varphi_{1i}\rangle \tag{20}$$

where P_1 is an orthoprojector defined by a chosen basis set for the first excited state.

Then the variations in orbitals can be divided into the following independent parts, e.g., for the α set

$$\left| \delta \varphi_{1i}^\alpha \right\rangle = P_1^\alpha \left| \delta \varphi_{1i}^\alpha \right\rangle + (P_1 - P_1^\alpha) \left| \delta \varphi_{1i}^\alpha \right\rangle + \sum_a (\partial_a P_1) \left| \varphi_{1i}^\alpha \right\rangle \delta \mu_a, \tag{21}$$

where μ_a, $a = 1, 2, \ldots, A$, represents the basis set parameters (i.e., the exponents and the positions) and $\partial_a P_1 = \partial P_1 / \partial \mu_a$. The first term in Eq. (21) does not lead to changes in the total energy because it is invariant to any orthogonal transformation of the orbitals of any spin among themselves. The energetically significant variations are described by the second and third terms. The second term corresponds to variations

within the finite-dimensional subspace spanned by the chosen basis set. The last term allows this subspace to be rotated within the Hilbert space of one-particle states to attain the deeper minimum with respect to the total energy.

Substituting Eq. (21) into Eq. (19) and taking into account the independence of the variations and their arbitrariness, we obtain the following equations for orbitals (see [10, 11] for more details):

$$P_1\left(F^\alpha - \lambda_s P_1^\beta + \lambda_o P_u^\alpha - \epsilon_i^\alpha\right)P_1\left|\varphi_{1i}^\alpha\right\rangle = 0\,,\ \lambda_s, \lambda_o \to \infty$$

$$P_1\left(F^\beta + \lambda_s Q_1^\alpha - \epsilon_i^\beta\right)P_1\left|\varphi_{1i}^\beta\right\rangle = 0, \qquad i = 1, 2, \ldots, M \tag{22}$$

and equations for basis set optimization

$$\sum_i^{n^\alpha}\left\langle\varphi_{1i}^\alpha\right|(\partial_a P_1)F^\alpha\left|\varphi_{1i}^\alpha\right\rangle + \sum_i^{n^\beta}\left\langle\varphi_{1i}^\beta\right|(\partial_a P_1)F^\beta\left|\varphi_{1i}^\beta\right\rangle = 0, \quad a = 1, 2, \ldots A \tag{23}$$

If the *K*th excited state is considered then, as mentioned, the projector P_u^α takes the following form $P_u^\alpha = \sum_{k=0}^{K-1}\left|\varphi_{kn}^\alpha\right\rangle\left\langle\varphi_{kn}^\alpha\right|$. Equations (22) represent the orthogonality-constrained HF method in its general form. According to the AP methodology, the orthogonality constraint of Eqs. (12) and (18) is satisfied in the limit $\lambda_o \to \infty$ and $\lambda_s \to \infty$„ respectively. By setting $\lambda_s = 0$, we can relax the spin-purity constraint (18) and go back from ROHF to UHF solutions. By setting $\lambda_o = 0$, we fall back to the ground state. The corresponding orbitals form an optimal set which satisfy the generalized Brillouin's theorem (see [40] for more details) and lead to the same total energy that the one obtained by the Roothaan procedure. In our method, the only additional computation required, beyond that arising in the standard UHF scheme, is the evaluation of the overlap matrix element $\langle\varphi_{0n}|\varphi_{kn}\rangle$.

Left side of Eq. (23) represent a gradient of the total energy with respect to nonlinear basis set parameters $\{\mu_a\}$. This expression allows these parameters to be determined *variationally* and can be also used to construct an algorithm for optimization based on the gradient-like methods.

Since neither λ_s nor λ_o can be infinity in practical calculations, one has to settle on some large finite values. The recommended values are $\lambda_s = 100$ hartrees for the spin-purity constraint and $\lambda_o = 1000$ hartrees for the orthogonality constraint. They provide target accuracy close to 10^{-6}.

In concluding this section, it is also worth noting that in our method all excited configurations based on the excited Slater determinant Φ_1, viz., Φ_i^a, Φ_{ij}^{ab} etc., where *i* and *j* refer to occupied orbitals and *a* and *b* to virtual ones, are orthogonal both to Φ_0 and among themselves. Therefore, these functions form the orthonormal basis set in the many-body space and can be used, unlike other SCF methods which do not satisfy the orthogonality of states in the explicit form, to develop many-body methods incorporating the correlation effects, in particular, a many-body Møller–Plesset-like perturbation theory (see next Section).

4 Second-order correction to the energy for excited states

It is known that within the framework of the Roothaan coupling operator approach, there is no unique way of choosing a reference Hamiltonian, $H^{(0)}$, with respect to which a perturbation expansion for correlation effects can be developed. Several proposals have been made for open-shell many-body perturbation theory expansions based on a reference from the ROHF formalism [41, 42] or the unrestricted Hartree–Fock formalism [43, 44]. We follow our papers [10, 45] where an alternative technique for the open-shell systems has been developed. In our method, the second-order correction to the ground state energy can be presented by [45]:

$$E_0^{(2)} = \sum_{i>j}^{\text{occ}}\sum_{a>b}^{\text{virt}}\frac{\left|\left(\varphi_{0a}\varphi_{0i}|\varphi_{0b}\varphi_{0j}\right) - \left(\varphi_{0a}\varphi_{0j}|\varphi_{0b}\varphi_{0i}\right)\right|^2}{\epsilon_{0i} + \epsilon_{0j} - \epsilon_{0a} - \epsilon_{0b}} \tag{24}$$

The summations are over spin-orbitals. Subscripts *i*, *j* and *a*, *b* correspond to occupied and virtual orbitals of the ground state determinant, respectively. Unlike the formalism developed in Refs. [43, 44], single excitations do not contribute because our orbitals satisfy the generalized Brillouin theorem.

An optimum set of MOs obtained by means of Eq. (22) allows us to construct a well-defined open-shell perturbation theory for excited states which is a natural extension of the popular closed-shell MP2. For example, the zeroth-order Hamiltonian for the first excited state is as follows:

$$H^{(0)} = \sum_{m=\text{electrons}}^{n^\alpha} F^\alpha(m) + \sum_{m=\text{electrons}}^{n^\beta} F^\beta(m)$$

with Fockians

$$F^\sigma = \sum_i^{M-1}\left|\varphi_i^\sigma\right\rangle\epsilon_i^\sigma\left\langle\varphi_i^\sigma\right|, \quad \sigma = \alpha, \beta$$

The summation up to $M - 1$ means that the vector $|\varphi_{0n}^\alpha$ is excluded from the subspace of virtual orbitals. Remind *M* is the dimension of the basis set for the first ES. We

Table 1 Constrained self-consistent (E^{CSCF}) Hartree–Fock energies (in hartrees) of triplet $1s\,ns$ ($n = 2, 3, \ldots, 10$) states of the He atom and energy difference between the MOM method (E^{MOM}) and the one proposed here (E), $\Delta^{\mathrm{HF}} = E^{\mathrm{CSCF}} - E^{\mathrm{MOM}}$ (μhartrees)

State	E^{CSCF} (this paper)	E^{MOM} [46]	Δ^{HF}
$1s2s\ ^3S$	−2.174 250 72	−2.174 250 78	0.06
$1s3s\ ^3S$	−2.068 484 88	−2.068 484 95	0.07
$1s4s\ ^3S$	−2.036 436 35	−2.036 436 42	0.07
$1s5s\ ^3S$	−2.022 582 55	−2.022 582 62	0.07
$1s6s\ ^3S$	−2.015 357 22	−2.015 357 34	0.12
$1s7s\ ^3S$	−2.011 117 33	−2.011 117 58	0.25
$1s8s\ ^3S$	−2.008 418 90	−2.008 419 01	0.11
$1s9s\ ^3S$	−2.006 595 66	−2.006 595 90	0.24
$1s10s\ ^3S$	−2.005 306 45	−2.005 306 75	0.30

shall also omit the subscript "1" for a given ES and $\Phi_1 \equiv \Phi^{(0)}, \quad \Phi_0 \equiv \Phi_0^{(0)}$.

In contrast to the ground state case, for the excited state it is necessary to take into consideration the orthogonality constraints. For the first-order correction to the excited state reference function, $\Phi^{(1)}$, these constraints have the form

$$\left\langle \Phi^{(0)} | \Phi^{(1)} \right\rangle = 0,$$

and the constraints determined by the orthogonality condition for the states in the first-order perturbation theory leads to equation

$$P_0^{(0)} \left| \Phi^{(0)} \right\rangle + P_0^{(1)} \left| \Phi^{(1)} \right\rangle = 0$$

where $P_0^{(0)} = |\Phi_0^{(0)}\rangle\langle\Phi_0^{(0)}|$ and $P_0^{(1)} = |\Phi_0^{(0)}\rangle\langle\Phi_0^{(1)}| + |\Phi_0^{(1)}\rangle\langle\Phi_0^{(0)}|$. Then one can show that the Rayleigh–Schrödinger perturbation theory leads to the following expression for the second-order correction to the ES energy [10]:

$$E^{(2)} = \sum_{i>j}^{\mathrm{occ}} \sum_{a>b}^{\mathrm{virt}} \frac{\left|\left(\varphi_a\varphi_i|\varphi_b\varphi_j\right) - \left(\varphi_a\varphi_j|\varphi_b\varphi_i\right)\right|^2}{\epsilon_i + \epsilon_j - \epsilon_a - \epsilon_b} - \left\langle \Phi^{(0)}|H|\Phi_0^{(0)} \right\rangle \left\langle \Phi_0^{(1)}|\Phi^{(0)} \right\rangle \tag{25}$$

Here subscripts "*i*" and "*j*" are occupied and "*a*," "*b*" are virtual orbitals in $\Phi^{(0)}$.

The first term in Eq. (25) is immediately recognized as the second-order perturbation theory expression for the ground state energy [*cf.* with (24)]. The second term in Eq. (25) appears because the Hartree–Fock ground and excited state functions are not eigenfunctions of the Hamiltonian H. In practice, if the ground state and excited state energies and the corresponding wave functions are known accurately then the coupling matrix element $\langle\Phi^{(0)}|H|\Phi_0^{(0)}\rangle$ is expected to be small (see also [14], Sect. 3.1). Furthermore, as the overlap element $\langle\Phi_0^{(1)}|\Phi^{(0)}\rangle < 1$, the last term in Eq. (25) may be neglected during the first stage of calculations. We used this approximation here.

Thus, we obtain comparable perturbation schemes for the ground and excited state energies. Use of the asymptotic projection technique ensures that calculations for excited states require practically the same computational time as those for the ground state.

5 Results and discussion

At present, there are only very few published finite basis set calculations for excited states (especially for Rydberg states [46]) having the same symmetry as the ground state which are based on existing Hartree–Fock methods. In this section we demonstrate the potential of our methodology by means of the HF calculations for highly doubly excited ^3S states of the He atom ($2s\,ns$, $n = 3, 4, \ldots, 10$ and $3s\,ns$, $n = 4, 5, \ldots, 11$), highly excited $1s^2\,ns$ ($n = 3, \ldots, 9$) states of the Li atom and of the doubly ionized core hole states for some diatomic molecules (CO, NO, LiF) computed at the HF + MP2 level of theory.

5.1 Atoms

For atoms, basis sets of 42*s*-gaussians were constructed according to the even-tempered prescription i.e., the exponents, ζ_p, were defined by the geometric series:

$$\zeta_p = \alpha\beta^p, \quad p = 1, 2, \ldots, M$$

The parameters α and β were optimized for each atom and a given excited state. Information of the even-tempered basis sets for low-lying states of the He and Li atom can be found in Ref. [47]. More information for highly excited state basis sets is available from authors on request.

As a first test for orthogonality-constrained HF method, hereafter denoted CSCF for constrained self-consistent field, the energies of triplet singly excited $1s\,ns$ ($n = 2$, 3, …, 10) states of the He atom were computed and compared with the HF energies obtained with the maximum overlap method (MOM) [46] which does not use orthogonality restrictions. The calculations in [46] were carried out using 70*s* even-tempered Slater-type basis functions. The results of [46] can be considered as benchmark data. These authors used the extended precision in the Mathematica package to avoid problems with almost linearly dependent basis set. Unlike Ref. [46], our calculations were restricted to nine states (up to $1s\ 10s$) because for $n > 10$ we observed that the corresponding basis sets present some linear dependencies and the iterative SCF procedure does not converge. We used double precision. The corresponding results are listed

Table 2 Doubly excited energies (hartrees) computed at the constrained self-consistent Hartree–Fock level (method proposed in this paper) and their comparison with "exact" values for the $2s\,ns$ ($n = 3$, 4, …, 10) states of He

State	E^{CSCF} (this work)	E^{exact} [48][a]	$E^{\mathrm{CSCF}} - E^{\mathrm{exact}}$
$2s3s\ ^3S$	−0.584 843 21	−0.602 577 51	0.017 734 30
$2s4s\ ^3S$	−0.541 993 88	−0.548 840 86	0.006 846 98
$2s5s\ ^3S$	−0.525 150 96	−0.528 413 97	0.003 263 01
$2s6s\ ^3S$	−0.516 757 01	−0.518 546 37	0.001 789 36
$2s7s\ ^3S$	−0.511 964 04	−0.513 046 50	0.001 789 36
$2s8s\ ^3S$	−0.508 969 03	−0.509 672 80	0.001 082 46
$2s9s\ ^3S$	−0.506 966 91	−0.507 456 06	0.000 489 15
$2s10s\ ^3S$	−0.505 538 99	−0.505 922 15	0.000 383 16

[a] Configuration interaction method with the Hylleraas basis set functions

Table 3 Doubly excited energies (hartrees) computed at the constrained self-consistent Hartree–Fock level and their comparison with "exact" values for the $3s\,ns$ ($n = 4$, 5, …, 11) states of He

State	E^{CSCF} (this work)	E^{exact} [48][a]	$E^{\mathrm{CSCF}} - E^{\mathrm{exact}}$
$3s4s\ ^3S$	−0.272 245 05	−0.287 277 14	0.015 032 09
$3s5s\ ^3S$	−0.250 554 08	−0.258 133 98	0.007 579 90
$3s6s\ ^3S$	−0.240 598 58	−0.244 807 49	0.004 208 91
$3s7s\ ^3S$	−0.235 129 72	−0.237 672 21	0.002 542 49
$3s8s\ ^3S$	−0.231 791 54	−0.233 433 33	0.001 641 79
$3s9s\ ^3S$	−0.229 600 06	−0.230 719 09	0.001 119 03
$3s10s\ ^3S$	−0.228 079 97	−0.228 880 00	0.000 800 03
$3s11s\ ^3S$	−0.226 915 03	−0.227 577 80	0.000 662 77

[a] Configuration interaction method with the Hylleraas basis set functions

in Table 1. One can see that the largest deviation from benchmark results is only 0.30 μhartrees.

In Tables 2 and 3, triplet doubly excited energies of $2s\,ns$ ($n = 3$, 4, …, 10) states and $3s\,ns$ ($n = 4$, 5, …, 11) states of He, computed at the CSCF level, are presented. Calculations of Ref. [46] were restricted to only singly excited states. Therefore, we compare our CSCF calculations with accurate theoretical calculations based on a configuration interaction approach with the explicitly correlated Hylleraas basis set functions [48]. One can see that the accuracy of the CSCF calculations is improved when n increases. This observation is in agreement with Ref. [46]. whose authors pointed out that "In those states where $n \gg 1$, the electrons are spatially well separated and one might anticipate intuitively that they will be weakly correlated and that the Hartree–Fock method, which neglects such effects, may be an excellent approximation."

In Table 4, we compare our CSCF excited doublet $1s^2\,ns$ ($n = 3$, …, 9) energies and excitation energies of the

Table 4 Excited doublet $1s^2ns$ ($n = 3$, 4, …, 9) energies (hartrees) and excitation energies ΔE (eV) computed at the constrained self-consistent Hartree–Fock level with respect to the $1s^23s$ state and their comparison to "exact" [49] values for Li atom

State	E^{CSCF} (this work)	E^{exact} [49][a]	ΔE (eV)	
			CSCF	«Exact» [49][a]
$1s^23s\ ^2S$	−7.310 207 76	−7.354 098 42	0	0
$1s^24s\ ^2S$	−7.274 883 90	−7.318 530 85	0.961	0.968
$1s^25s\ ^2S$	−7.259 978 78	−7.303 551 58	1.367	1.375
$1s^26s\ ^2S$	−7.252 316 91	−7.295 859 51	1.575	1.585
$1s^27s\ ^2S$	−7.247 864 34	−7.291 392 27	1.696	1.706
$1s^28s\ ^2S$	−7.245 049 87	−7.288 569 83	1.773	1.783
$1s^29s\ ^2S$	−7.243 155 19	−7.286 673 59	1.825	1.835

[a] Configuration interaction method with the Hylleraas basis set functions

Table 5 Total energies (hartree) for the ground (GS) and doubly ionized states (DIS) calculated at different levels of approximation, namely at the constrained self-consistent Hartree–Fock level and at the HF + MP2 level

Molecule	Core level[a]	CSCF	HF + MP2
CO	GS	−112.776 750	−113.103 104
	DIS		
	$C1s^{-2}$	−88.253 476	−88.694 091
	$O1s^{-2}$	−69.636 053	−69.866 416
	$C1s^{-1}\,O1s^{-1}$, S	−81.367 221	−81.666 059
	$C1s^{-1}O1s^{-1}$, T	−81.367 167	−81.665 687
NO	GS	−129.264 594	−129.623 929
	DIS		
	$O1s^{-2}$, D	−86.091 825	−86.341 259
	$N1s^{-2}$, D	−96.024 538	−96.399 098
LiF	GS	−106.988 804	−107.245 424
	DIS		
	$F1s^{-2}$	−52.645 367	−52.816 963
	$Li1s^{-1}\,F1s^{-1}$, S	−79.049 260	−79.232 405
	$Li1s^{-1}F1s^{-1}$, T	−79.049 465	−79.232 198

T, D and S refer to triplet, doublet and singlet of two holes created on different atomic sites, respectively

[a] Core level notations of Ref. [51] are used, for example, core level $C1s^{-1}\ O1s^{-1}$ means double core hole state obtained by removing electrons from the 1s carbon core orbital and from the 1s oxygen core orbital

Li atom to the "exact" energies obtained with the most accurate configuration interaction wave function using the Hylleraas basis set [49]. The calculations show that the correlation energies $E^{\mathrm{exact}} - E^{\mathrm{CSCF}}$ for different excited states are very similar, since they mainly arise from the 1s–1s correlation. As a result, excitation energies based on the

Table 6 Double core hole ionization potentials (eV) calculated at different levels of approximation

Molecule	Core level	CSCF (this work)	SCF [51]	HF + MP2 (this work)	CASSCF [51]
CO[a]	$C1s^{-2}$, S	667.32	667.90	664.22	664.42
	$O1s^{-2}$, S	1173.93	1175.38	1176.55	1176.56
	$C1s^{-1}\,O1s^{-1}$, S	854.71	857.07	855.47	854.74
	$C1s^{-1}O1s^{-1}$, T	854.71	857.07	855.48	855.20
NO[b]	$O1s^{-2}$, D	1174.80	1176.43	1177.79	1177.70
	$N1s^{-2}$, D	904.51	904.85	904.10	902.95
LiF	$F1s^{-2}$, S	1478.77	1480.42	1481.09	1481.49
	$Li1s^{-1}\,F1s^{-1}$, S	760.28	763.45	762.28	763.21
	$Li1s^{-1}\,F1s^{-1}$, T	760.28	763.44	762.28	763.28

T, D and S refer, respectively, to triplet, doublet and singlet spin couplings of two holes created on different atomic sites

[a] Experimental values Ref. [53]: $C1s^{-2}$: 667.9 eV; $C1s^{-1}\,O1s^{-1}$: 855.3 eV

[b] SCF and CASSCF values are taken from Ref. [52]

CSCF method are in good agreement with those computed with highly correlated methods.

5.2 Molecules

In this subsection, we apply our HF + MP2 methodology on doubly ionized core hole states. It is known that double core ionization potentials are more sensitive to changes in the molecular environment [50]. It is worth also noting that there exist very few reported applications for double core hole (DCH) states, especially of open-shell molecules [51, 52]. For molecules under consideration (CO, NO, LiF), basis sets consisting of 30*s*9*p* distributed Gaussians were used. The exponents and positions of functions were determined by minimizing the HF energy for each individual state. Each *p*-functions were presented as a linear combination of two *s*-functions (so-called lobe representation). In Table 5, we present total energies for the ground (GS) and doubly ionized states (DIS) calculated at different levels of approximation (CSCF and HF + MP2). Using these data, double core hole ionization potentials were calculated (see Table 6) and compared for the NO molecule with results of Ref. [52] and for closed-shell molecules with results of Ref. [51] and available experiment [53]. In Refs. [51, 52], the corresponding calculations were carried out at the self-consistent field (SCF) level of theory and using the complete active space self-consistent field (CASSCF) method. It is worth noting that the SCF and CASSCF calculations in these works were performed using a large cc-pVTZ basis set.

One can see that our results at the CSCF and HF + MP2 level of approximation are in acceptable agreement with experiment and other calculations performed at the corresponding level of approximation.

We conclude that the developed constrained HF + MP2 formalism can be applied to both atoms and molecules and to a wide class of physically different states, including highly excited states and core excited states, with a reasonable accuracy. However, it is also worth noting that the proposed approach cannot be directly applied to important class of singlet excited states which are usually described in terms of two open-shell determinants. Preliminary applications of our modified methodology to this problem can be found in Ref. [54] where a partially restricted Hartree–Fock wave function for singlet excited states is introduced.

Acknowledgments With this manuscript, the authors want to thank Professor Peter Surjan for his tremendous contribution to quantum theory, especially on constrained (localized) wave functions and on the development of post-Hartree–Fock methods.

References

1. Gidopoulos NI, Papaconstantinou PG, Gross EKU (2002) Phys Rev Lett 88:33003
2. Chattopadhyay S, Mahapatra US, Chaudhuri RK (2012) Theor Chem Acc 131:1213
3. Roos BO (2005) In: Dykstra CE, Frenking G, Kim KS, Scuseria GE (eds) Theory and applications of computational chemistry: the first 40 years. Elsevier, Amsterdam, pp 725–764
4. Pahari D, Chattopadhyay S, Das S, Mukherjee D, Mahapatra US (2005) In: Dykstra CE, Frenking G, Kim KS, Scuseria GE (eds) Theory and applications of computational chemistry: the first 40 years. Elsevier, Amsterdam, pp 581–633
5. Piecuch P, Kowalski K (2002) Int J Mol Sci 3:676
6. Lyakh DI, Musial M, Lotrich VF, Bartlett RJ (2012) Chem Rev 112:182
7. Hoffmann MR, Datta D, Das S, Mukherjee D, Szabados A, Rolik Z, Surjan PR (2009) J Chem Phys 131:204104
8. Kobayashi M, Szabados A, Nakai H, Surjan PR (2010) J Chem Theory Comput 6:2024
9. Shull H, Löwdin P-O (1958) Phys Rev 110:1466
10. Glushkov VN (1998) Chem Phys Lett 1998(287):189
11. Glushkov VN, Gidopoulos N, Wilson S (2008) In: Wilson S, Grout PJ, Delgado-Barrio G, Maruani J, Piecuch P (eds) Frontiers in quantum systems in chemistry and physics. Progress in

theoretical chemistry and physics, Pt. 2. Springer, Dordrecht, p 451
12. Glushkov VN (2002) J Math Chem 31:91
13. Glushkov VN (2002) Opt Spectrosc 93:11
14. Glushkov VN, Gidopoulos N, Wilson S (2008) In: Wilson S, Grout PJ, Delgado-Barrio G, Maruani J, Piecuch P (eds) Frontiers in quantum systems in chemistry and physics. Progress in theoretical chemistry and physics, Pt. I. Springer, Dordrecht, p 429
15. Roothaan CCJ (1960) Rev Mod Phys 32:179
16. Hunt WJ, Goddard WA (1969) Chem Phys Lett 3:414
17. Huzinaga S, Arnau C (1971) J Chem Phys 54:1948
18. Morokuma K, Iwata S (1972) Chem Phys Lett 16:192
19. Mrozek J, Golebiewski A (1977) Int J Quantum Chem 12:207
20. Firsht D, McWeeny R (1976) Mol Phys 32:1637
21. Davidson ER, Stenkamp LZ (1976) Int J Quantum Chem Symp 10:21
22. Davidson ER, McMurchie EL (1985) Excit States 5:1
23. Colle R, Fortunelli A, Salvetti O (1987) Theor Chim Acta 71:467
24. Colle R, Fortunelli A, Salvetti O (1989) Theor Chim Acta 75:323
25. Gidopoulos N, Theophilou A (1994) Phil Mag 69:1067
26. Assfeld X, Rivail J-L (1996) Chem Phys Lett 263:100
27. Surjan PR (2000) Chem Phys Lett 325:120
28. Ferre N, Assfeld X (2002) J Chem Phys 117:4119
29. Gilbert ATB, Besley NA, Gill PMW (2008) J Phys Chem A 112:13164
30. Tassi M, Theophilou I, Thanos S (2013) Int J Quantum Chem 113:690
31. Richings GW, Karadakov PB (2007) Mol Phys 105:2363
32. Richings GW, Karadakov PB (2013) Theor Chem Acc 132:1400
33. Glushkov VN, Levy M (2007) J Chem Phys 126:174106
34. Staroverov VN, Glushkov VN (2010) J Chem Phys 133:244104
35. Evangelista FA, Shushkov R, Tully JC (2013) J Phys Chem A 113:690
36. Cullen J, Krykunov M, Ziegler T (2011) Chem Phys 391:11
37. Cohen M, Kelly PS (1965) Can J Phys 43:1867
38. Tatewaki H, Koga T, Sakai Y, Thakkar AJ (1994) J Chem Phys 101:4945
39. Fock VA (1940) Z Exp Teor Fiz 10:961
40. Glushkov VN (1997) Chem Phys Lett 273:122
41. Lauderdale WJ, Stanton JF, Gauss J, Watts JD, Bartlett RJ (1991) Chem Phys Lett 187:21
42. Murray C, Davidson ER (1991) Chem Phys Lett 187:451
43. Andrews JS, Jayatilaka D, Bone RGA, Handy NC, Amos RD (1991) Chem Phys Lett 183:423
44. Knowles PJ, Andrews JS, Amos RD, Handy NC, Pople JA (1991) Chem Phys Lett 186:130
45. Glushkov VN (2004) Int J Quantum Chem 99:236
46. Deng J, Gilbert ATB, Gill PMW (2009) Int J Quantum Chem 109:1915
47. Glushkov VN, Wilson S (2006) In: Julien J-P, Maruani J, Mayou D, Wilson S, Delgado-Barrio G (eds) Progress in theoretical chemistry and physics. Recent advances in the theory of chemical and physical systems. Springer, Dordrecht, p 107
48. Burgers A, Wintgen D, Rost J-M (1995) J Phys B: At Mol Opt Phys 28:3163
49. Puchalski M, Kedziera D, Pachucki K (2010) Phys Rev A 28:062509
50. Cederbaum LS, Tarantelli F, Sgamellotti A, Schrimer J (1986) J Chem Phys 85:6513
51. Tashiro M, Ehara M, Fukuzawa H, Ueda K, Buth C, Kryzhevoi NV, Cederbaum LS (2010) J Chem Phys 132:184302
52. Tashiro M, Ehara M, Ueda K (2010) Chem Phys Lett 496:217
53. Berrah N, Fang L, Murphy B, Osipov T, Ueda K, Kukk E, Feifel R, van der Meulen P, Salen P, Schmidt HT, Thomas RD, Larsson M, Richter R, Prince KC, Bozek JD, Bostedt C, Wada S, Piancastelli MN, Tashiro M, Ehara M (2011) Proc Natl Acad Sci 108:16912
54. Glushkov VN (2007) Comput Lett 3:65

Theor Chem Acc (2015) 134:109
DOI 10.1007/s00214-015-1704-9

REGULAR ARTICLE

Metallic and semiconducting 1D conjugated polymers based on –S–C≡C– repeating units in poly(sulfur acetylide)

Károly Németh[1]

Received: 20 May 2015 / Accepted: 17 July 2015 / Published online: 22 August 2015

Abstract The existence and the properties of a new 1D conjugated polymer, poly(sulfur acetylide), with –S–C≡C– repeating unit are predicted on the basis of density functional theory calculations. Depending on the conformation of the polymer, specifically on the C–S–C angles, the corresponding material is either a metallic conductor (C–S–C near linear) or a semiconductor (C–S–C not linear). It is a semiconductor with 1.6 eV band gap in the minimum energy conformation bent geometry. The polymer can be stretched out at a relatively large and impractical energy cost of 2.6 eV per –S–C≡C– unit upon which it becomes a metallic conductor. However, this semiconductor–metal transition appears to be unique in as much as it happens along a bending mode of the polymeric backbone. This new material appears to be easy to synthesize and is expected to be stable under normal conditions. Despite its simplicity and close relation to other well-known 1D conjugated polymers, such as poly(sulfur nitride) $(SN)_x$, polyacetylene $(CH)_x$ or polyyne $(–C≡C–)_x$, poly(sulfur acetylide) still remains to be explored.

Keywords Poly(sulfur acetylide) · Conjugated polymer · Organic semiconductor · Band structure design

Electronic supplementary material The online version of this article (doi:10.1007/s00214-015-1704-9) contains supplementary material, which is available to authorized users.

Published as part of the special collection of articles "Festschrift in honour of P. R. Surjan".

✉ Károly Németh
nemeth@agni.phys.iit.edu

[1] Physics Department, Illinois Institute of Technology, Chicago, IL 60616, USA

1 Introduction

Synthetic metals and semiconductors are an important field of materials chemistry and physics. These materials are based on conjugated π-electron systems. On the one hand, the various options of synthetic chemistry to link numerous possible pieces of conjugated π-electron systems together allow for tuning the properties of these materials. On the other hand, band structure calculations allow for the theoretical design of conjugated π-electron systems with specific predefined properties [1–8]. Poly(sulfur nitride), $(SN)_x$, has been the earliest example of a synthetic metal based on a 1D conjugated π-electron system [9]. It has first been synthesized [10] in 1910, but its conductivity has been measured only in 1973 [11], and its superconductivity at 0.26 K has been discovered in 1975 [12]. Another significant advance in the field of quasi 1D (semi)conductors was the synthesis and characterization of polyacetylene $(CH)_x$ by Heeger, MacDiarmid, Shirakawa and coworkers [13–15] in 1977. While $(SN)_x$ is a metal without doping, $(CH)_x$ is a semiconductor with a 1.4 eV band gap [16]. Despite decades of work on conjugated polymers, $(SN)_x$ remains the sole polymer that is metallic without doping. $(CH)_x$ and other known conjugated polymers become metallic only when doped, e.g., by iodine [16].

Peierls' instability theorem from 1955 predicts [17] that an equidistantly placed (quasi) 1D chain of identical atoms with a single electron per atomic site is unstable and undergoes geometric rearrangements, such as bond-length alternation in a unit cell containing two atoms instead of one, to stabilize itself. In fact, Peierls' instability theorem is a special case of the well-known Jahn–Teller distortion [18] which states that a molecule with a degenerate ground state is unstable and undergoes a geometric distortion until its ground state becomes non-degenerate. Peierls' instability

theorem has later been extended to any (quasi) 1D crystals containing multiple types of atoms and more than one electron per atomic site, for reviews see Refs. [19, 20]. The distortion toward the stabilized structure may also be based on charge or spin density waves with a doubled periodicity as compared to the geometric periodicity of the system.

In reality, 1D polymers form bunches and interact with each other. The strength of this interaction also has an effect on the applicability of Peierls' instability theorem. $(CH)_x$ appears to be a classic example of the original form of Peierls' instability theorem, as in reality the unit cell consists of two CH units and alternating shorter and longer C–C bonds are present along the polymeric backbone [21]. Bond-length alternation is present in $(SN)_x$ as well [22]; however, it is believed that the intermolecular interaction in $(SN)_x$ is strong enough to suppress Peierls' instability and forces $(SN)_x$ to take up a specific geometry in which each strand becomes a metal instead of a semiconductor [3, 19, 23–26]. Therefore, the origin of metallicity in $(SN)_x$ is a 3D effect of interchain interactions, and $(SN)_x$ is generally considered a 3D system instead of a loose set of 1D polymers.

Our recent work in the field of ternary acetylides-based semiconductors [8, 27] directed the attention of the present author toward acetylenic polymers with –M–C≡C– repeating units, where M may be a transition metal or a metalloid element, such as Te or Se, or sulfur. Several such polymers exist in an alkali-doped form in ternary acetylides [28]. While the doped forms are mechanically stable, the undoped ones are explosive. On the other hand, stable organic compounds with –C≡C–(Te/Se/S)–C≡C– structural units have been known for decades [29, 30]. The generalization of such chemical bonding systems into the corresponding polymers appears reasonable, but has not been carried out yet. While the corresponding polymers with Te or Se may be explosive, similar to transition metal acetylides, the one with sulfur, $(–S–C≡C–)_x$, is potentially stable at least to the degree of stability of $(SN)_x$, which is known to be explosive when heated to 240 °C [31]. The explosivity of transition metal acetylides also varies, for example, CuC_2 is a well-known explosive, while stable forms of Cu_2C_2 have been produced [32, 33].

The investigation of the –S–C≡C– polymer is attractive also because its synthesis should be straightforward, based on existing synthesis methods on –C≡C–S–C≡C– compounds (see, e.g., Ref. [30] and reviews Refs. [34–36]). Following these recipes, the reaction of dialkali acetylides with sulfur dichloride is expected to result in the desired polymer, according to

$$xA_2C_2 + xSCl_2 \rightarrow (-S-C\equiv C-)_x + 2xACl, \quad (1)$$

where A is conveniently Li or Na. Furthermore, this proposed polymer is also related to polyyne (carbyne), $(–C≡C–)_x$, the one-dimensional carbon-only chain with alternating single and triple bonds. While polyyne is very unstable and the longest synthesized species contain only about one hundred acetylenic units [37–41], embedding S atoms between the –C≡C– units may be a way to create long stable polymers, with attractive materials properties. Ladder-type copolymers with acetylenic linking units between main strands have been proposed by Kertesz et al. [6] as a way of reducing the band gap of conjugated polymers, primarily that of $(CH)_x$. Poly(para-phenylene sulfide) (PPS, [42]) is a similar polymer to the proposed $(–S–C≡C–)_x$ one, in as much as the sulfur atoms link para-phenylene groups (a benzene ring with two external links on inversionally symmetric carbon sites) instead of acetylenic –C≡C– units. PPS is an industrially produced material, and it is synthesized by a polycondensation reaction analogous to Eq. 1 with NaCl by-product. Recently, Duan et al. developed a composite material consisting of polyyne cross-polymerized with polysulfur links performing well as cathode material in Li ion batteries [43]. The present study focuses on predicting a few basic properties of the proposed $(–S–C≡C–)_x$ polymer, poly(sulfur acetylide).

2 Results and discussion

Density functional theory calculations using the Quantum Espresso program package [44] have been carried out using the PBEsol [45] exchange–correlation functional with ultrasoft pseudopotentials as provided with the program package. Eighty Rydbergs wavefunction cutoff has been applied. Structural optimization has been carried out until the residual forces became smaller than 0.0001 Rydberg/bohr and the residual pressure on the cell was smaller than 1 kbar. Three different conformers and crystal packings of the $(–S–C≡C–)_x$ polymer have been explored. The one with I4/mmm space group contains straight polymeric strands of $(–S–C≡C–)_x$, the one with P4/mma space group has polymers with armchair conformation, and the one with C2/m space group has polymers in zig–zag conformation. Figure 1 depicts the conformers, while Fig. 2 shows the associated band structures. The band structure of the I4/mmm crystal has been calculated for a unit cell containing a single –S–C≡C– unit, using a $10 \times 10 \times 10$ k-space grid. The band structure of the P4/mma crystal has been calculated in a unit cell containing four –S–C≡C– units, using a $4 \times 6 \times 10$ k-space grid. The band structure calculation of the C2/m crystal used a cell with two –S–C≡C– units and a $5 \times 6 \times 10$ k-space grid. The geometries of the given structures have been relaxed using the above defined k-space grids.

The band structures in Fig. 2 indicate that the straight polymers (space group I4/mmm) are metallic, while the zig–zag (C2/m) and armchair (P4/mma) ones are

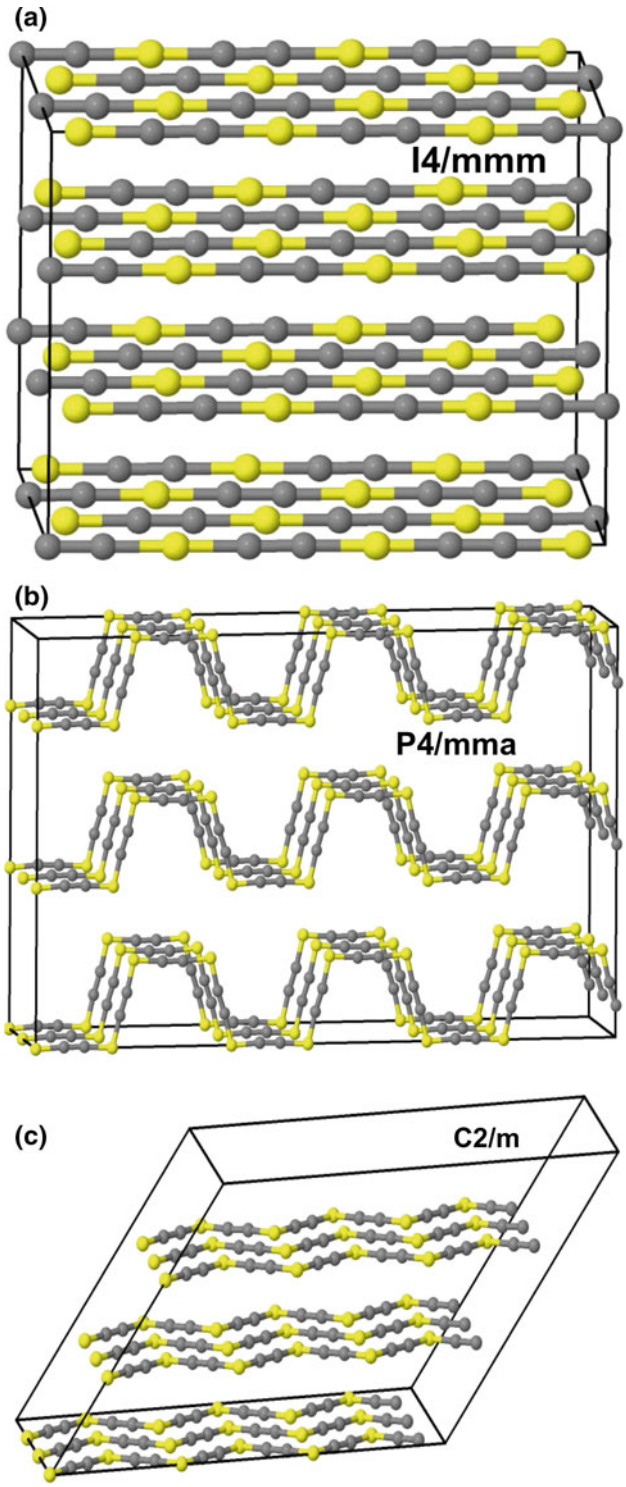

Fig. 1 Supercells of three different conformers of the (–S–C≡C–) polymer as obtained from geometry optimization using density functional theory: the linear polymer in a crystal of I4/mmm space group symmetry (**a**), the armchair conformer in a crystal of P4/mma space group symmetry (**b**) and the zig–zag conformer in a crystal of C2/m space group symmetry (**c**). Colors: S—*yellow*, C—*gray*

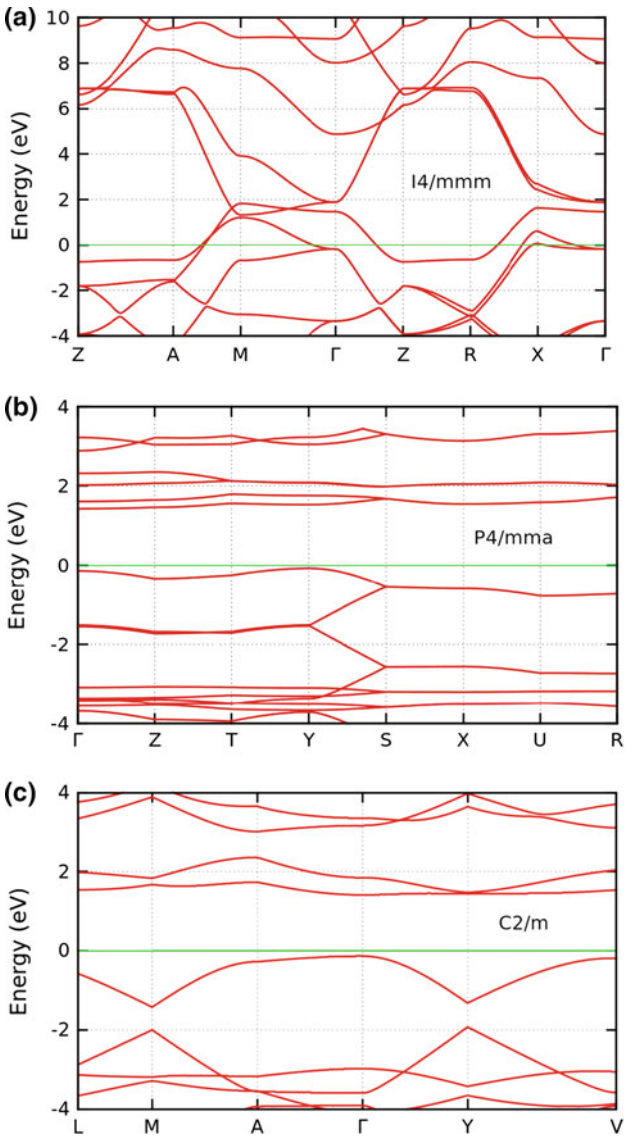

Fig. 2 Band structures of three different conformers of the (–S–C≡C–) polymer. The one crystallizing in space group I4/mmm (linear conformer, panel **a**) is a metal, while the other two ones with space groups P4/mma ("armchair" conformation, panel **b**) and C2/m ("zig–zag" conformation, panel **c**) are semiconductors, both with ≈ 1.6 eV band gaps. The origin of the energy scale is the Fermi energy in each case. For paths expansions, see, e.g., Ref. [58]. For space group I4/mmm (main axis c is parallel with the chains), the directions Z–A, M–Γ, Z–R and X–Γ are perpendicular to the chains, while A–M, Γ–Z and R–X are parallel with the linear chains. For the space group C2/m (zig–zag geometry, unique axis is b, the direction of the chains), the direction A-Γ is parallel with the chains, while Γ–Y is perpendicular, the rest of the directions close a non-rectangular angle with the chains. For space group P4/mma (*c* axis is perpendicular to plane of arm-chairs, a axis is parallel with chains), the direction Y-S is parallel with the chains, while the rest of the directions are perpendicular

Table 1 Geometric parameters and relative electronic energies per formula unit ($E(SC_2)$) of the three different crystalline conformers of the (S–C≡C) polymer and those of an isolated linear strand

	I4/mmm (linear)	P4/mma (armchair)	C2/m (zig–zag)	Isolated linear
a	4.011	11.637	7.243	(10.0)
b	4.011	8.084	4.389	(10.0)
c	4.011	4.136	5.556	5.928
α	109.5	90.0	67.9	90.0
β	109.5	90.0	49.4	90.0
γ	109.5	90.0	90.0	90.0
C≡C	1.277	1.221	1.224	1.281
S–C	1.692	1.675	1.677	1.683
C–S–C	180.0	101.2	101.4	180.0
$E(SC_2)$	2.610	0.029	0.0	2.600

Lattice parameters refer to simulation cells. Lengths (a, b, c, C≡C, S–C) are given in Å, angles (α, β, γ, C–S–C) are given in degrees, energies in eV per formula unit

semiconductors with ≈ 1.6 eV band gaps. Furthermore, the bands of the I4/mmm packed linear polymers cross the Fermi level in intervals that are directions parallel to the chains and close to boundaries of intervals that are directions perpendicular to the chains, also indicating that metallicity is primarily an intrinsic property of the linear polymers, instead of being due to interchain interactions.

Geometric parameters of the relaxed structures are given in Table 1. In the optimum geometry, layers of the zig–zag conformers are shifted relative to each other approximately by and along a full S–C≡C–S unit, the distance of the layers is 3.663 Å. The armchair conformers form planes with no phase shift between the polymeric strands, and the planes are replicated along the surface normal (*c* axis) at a distance of 4.136 Å. Nearest neighbor straight polymer strands in the I4/mmm packing are translated relative to each other such that the S atoms will be located closest to the center of the C≡C bond of the nearest strands, and –S–C≡C– chains are parallel with the longest body diagonal of the primitive cell.

The S–C bond lengths are symmetric at each S atom in all conformers and slightly longer, by 0.006–0.017 Å, for the straight polymers than for the bent ones. The C≡C bond lengths are significantly longer, by ≈0.06 Å, for the straight polymers than for the bent ones, while they are only slightly longer, by ≈0.02 Å in the bent ones than in acetylene gas (1.203 Å). The C–S–C angle was 101.4° in the zig–zag conformer and 101.2° in the armchair one, being very close to that in dimethyl sulfide (observed [46]: 99.0°, calculated by the present DFT technique: 100.7°). Also note that the electronic energy of the straight C–S–C conformer of dimethyl sulfide is higher by about 3.1 eV per molecule than that of the bent one. This is very similar to the energetics of the $(–S–C≡C–)_x$ polymers where the electronic energy of the straight conformers is greater by about 2.6 eV per repeating unit, indicating the energy cost of straightening the C–S–C angle. As the energy cost of straightening the polymeric chains is in the range of the energy of visible photons, the polymers may become straightened out in the excited states upon illumination with visible light.

In order to investigate the effect of intermolecular interaction on the metallicity and bond lengths of the linear –S–C≡C– chains, additional band structure calculations have been carried out on strands of $(–S–C≡C–)_x$ isolated by 10 Å distance from each other. Lattice and atomic position relaxations were allowed only along the chains, not for the interchain distances, in a rectangular cell with a single strand modeled with a double –S–C≡C– unit to allow for charge/spin density waves as well. The polymeric chains have been constrained to linearity. The results indicate that the intermolecular interaction does not have significant effect on the bond lengths, and the isolated linear strands are also metallic. Allowing for deviation from linearity leads to lower-energy bent polymers indicating that the linear optima are saddle points.

In the straight conformers, there is apparently some degree of π-electron back-donation from the p_x and p_y orbitals of sulfur to the antibonding orbitals of the C≡C unit, this makes the C≡C bond-length longer by about 0.06 Å which is approximately the same value as what was observed for the bond-length alternation in $(CH)_x$ (0.08 Å, [21]).

Also note that the interchain interactions are poorly described in the present model for the lack of explicit van der Waals terms. The focus here is on the properties of the individual chains rather than their interactions. The I4/mmm crystal packing of the linear polymers has been motivated by analogous linear transition metal acetylenic polymers in crystals of ternary acetylides [28]. As both isolated and I4/mmm packed linear polymers are metallic, it is reasonable to assume that the metallicity of the linear polymers is an intrinsic property of the linear $(SC_2)_x$ and is not a result of van der Waals interactions, while the enforcement of the linear conformation by external pressure would likely lead to significant energetic contributions from van der Waals interactions.

While the S atom has a Löwdin charge of +0.49 and 0.47 in the armchair and zig–zag conformers, in the straight polymer it is +0.52, while the corresponding carbon charges are −0.12, −0.13 and −0.15, respectively, indicating a slightly greater polarization in the linear chains as compared to the zig–zag and armchair ones. Note that the Löwdin charges do not sum up to zero in any of the molecules, as the projection of electron density from plane wave basis to atomic orbitals is incomplete.

In general, anything is a Peierls' distortion that moves an unstable (quasi) 1D system of atoms from a metallic ground state to a semiconductor one. The application of the term "Peierls distortion" is favored here by the present author, because—unexpectedly—the linear structure is metallic. Would the linear structure be nonmetallic, the term "Peierls distortion" could not be used and the distortion should be explained simply by the favored hybridization of the sulfur atom in the given bonding system. While linear H_2S or HC≡C–S–C≡CH has degenerate ground states, such ground states cannot be called metallic for the lack of band structure in isolated molecules, and therefore, they can be associated neither with Peierls distortion, nor with Jahn–Teller distortion, the latter of which does not apply for linear molecules at all. All previously known cases of Peierls' distortion happened along normal modes involving bond lengths only, or by charge/spin density waves. In the present case, Peierls' distortion happens along a different type of normal mode that involves only bond angles.

It is clear from the above analysis that Peierls' distortion is realized through C–S–C angle bending in the $(–S–C≡C–)_x$ polymer. This is not surprising as the S atom is known to strongly prefer taking up two, four or six valences, and in the present situation, it could take up more than two valences only if at least one of its neighboring –C≡C– units would convert to cumulenic =C=C= structure instead of the acetylenic –C≡C– one. The feasibility of such a conversion typically depends on the end units of the –C≡C– chain and is energetically unfavorable in the present situation when the end units are sp^3 hybridized S atoms. While in $(SN)_x$ the N strongly prefers to have three valences and thus can to some degree force the sulfur to take up three or four valences in some of the possible resonance structures [47], the –C≡C– unit is much less able to enforce more than two valences on sulfur in the present situation, as mentioned above. This also implies that there is virtually no opportunity for S–C bond-length alternation in $(–S–C≡C–)_x$.

In the straight polymer, the hybridization of S changes to sp^1 establishing a continuous conjugation of carbon and sulfur p_x and p_y orbitals and some of sulfur's d orbitals allowing for significant π-electron donation from sulfur to antibonding orbitals of the C≡C bond, as mentioned also above. This conjugation is also present at the bent C–S–C angles though to a lesser degree, through hyperconjugation of carbon π-orbitals and sulfur sp^3 lone pairs and d orbitals. Even though charge or spin density wave would theoretically be possible as an alternative of C–S–C angle bending for Peierls' distortion, it is not realized in the conformers studied here.

Methods to enforce the metallic straight conformation may involve external pressure or strain, transition metal (M) salts that complex and cross-link the –S–C≡C– polymers through S–M–S bridges, substrates that favor $(–S–C≡C–)_x$ crystallization in the straight conformers, e.g., surfaces of transition metal compounds with suitable lattice parameters. Even though the energy required to straighten the C–S–C angles (2.6 eV per repeating unit) is high as compared to thermal energy at room temperature, it is still relatively low to the energy of phase transitions accessible in diamond anvil cells. Such phase transitions involve the compression of oxygen to a metallic solid [48] or the compression of carbon dioxide to a quartz like crystal [49]. To the best of the knowledge of the present author, there is no other conjugated polymer that would become metallic from semiconductor by a moderately energetic stretching as in the case of the present $(–S–C≡C–)_x$ polymer.

Chemical doping of $(–S–C≡C–)_x$ is also possible to control its conductivity, similar to other conjugated polymers. Controlled distribution of the torsional angles around the polymeric backbone may also be possible, similar to $(CH)_x$ which was shown to crystallize in helical conformations in the presence of chiral nematic liquid crystals [50]. A particularly interesting helical conformer would consist of helical turns composed of approximately four –S–C≡C– units as the equilibrium bent C–S–C angle is only slightly larger than 90°. Similar to the composite polyyne-sulfur materials recently proposed by Duan et al. [43], mentioned above, the presently proposed $(–S–C≡C–)_x$ polymer may also find application as electroactive material in batteries, and this potential will be analyzed in a forthcoming paper.

3 Summary and conclusions

A simple new conjugated polymer, poly(sulfur acetylide) with –S–C≡C– repeating units, has been proposed on the basis of density functional theory calculations. The new polymer is predicted to be metallic in a straight conformation, while it is a semiconductor with ≈1.6 eV band gap when bent at the C–S–C angles. It appears to be unique among conjugated polymers by its ability to become metallic when straightened out along a bending coordinate on the polymeric backbone, albeit the process requires a relatively large, 2.6 eV energy per repeating unit. Owing to its relative simplicity, potentially easy synthesis through polycondensation and close relationship to other fundamentally important conjugated polymers, such as $(SN)_x$, $(CH)_x$ and $(–C≡C–)_x$, and to the great variety of synthetic opportunities and materials properties that can be associated with it, the experimental exploration of this new polymer is proposed.

Acknowledgments The author of the present study gratefully acknowledges countless valuable discussions and an enduring support and mentorship to Professor Péter Surján, to whose 60th birthday this Festschrift is dedicated. Károly Németh started research on the field of theoretical design of small band gap conjugated polymers in 1990

as an undergraduate student in a collaborative research involving Professors Péter Surján and Jenő Kürti at Eötvös University, Budapest, Hungary [5]. This research has later been extended to various other topics of conjugated π-electron systems during the doctoral student period of the present author under the supervision of Professor Péter Surján, between 1992 and 1996 [51–54]. Recently, the present author's research is centered around the theoretical design of functional materials for efficient electrochemical energy storage devices (batteries), especially those derived from conjugated π-electron systems, such as functionalized boron nitrides [55–57], still benefitting from the conjugated π-electron system studies conducted two decades ago with Professor Péter Surján. The author also thanks Prof. J. Kürti (Eötvös University, Budapest, Hungary) for helpful discussions in the subject of the present work and NERSC (U.S. DOE DE-AC02-05CH11231) for the use of computational resources.

References

1. André J, Delhalle J, Brédas J (1991) Quantum chemistry aided design of organic polymers: an introduction to the quantum chemistry of polymers and its applications. Lecture and course notes in chemistry series. World Scientific, ISBN 9789810200046
2. Leclerc M, Morin J (2010) Design and synthesis of conjugated polymers. Wiley, ISBN 9783527629794
3. Nalwa H (2000) Handbook of advanced electronic and photonic materials and devices. Academic Press, ISBN 9780125137454
4. Kürti J, Surján P, Kertész M, Frapper G (1993) Synth Met 57:4338
5. Surján PR, Németh K (1993) Synth Met 57:4260
6. Yang S, Kertesz M (2007) Macromolecules 40:6740
7. Kertesz M, Cui C (1992) In: Electronic properties of polymers. Springer, New York, pp 397–400
8. Terdik JZ, Németh K, Harkay KC, Terry JH Jr, Spentzouris L, Velázquez D, Rosenberg R, Srajer G (2012) Phys Rev B 86:035142
9. Pintschovius L (1978) Colloid Polym Sci 256:883
10. Burt FP (1910) J Chem Soc Trans 97:1171
11. Walatka V, Labes M, Perlstein JH (1973) Phys Rev Lett 31:1139
12. Greene R, Street GB, Suter L (1975) Phys Rev Lett 34:577
13. Chiang C, Fincher C, Park Y, Heeger A, Shirakawa H, Louis E, Gau S, MacDiarmid AG (1977) Phys Rev Lett 39:1098
14. Chiang C, Druy M, Gau S, Heeger A, Louis E, MacDiarmid AG, Park Y, Shirakawa H (1978) J Am Chem Soc 100:1013
15. Shirakawa H, Louis EJ, MacDiarmid AG, Chiang CK, Heeger AJ (1977) J Chem Soc Chem Commun 16:578–580
16. Fincher C Jr, Ozaki M, Tanaka M, Peebles D, Lauchlan L, Heeger A, MacDiarmid A (1979) Phys Rev B 20:1589
17. Peierls R (1955) Quantum theory of solids. International series of monographs on physics. Clarendon Press, Oxford
18. Jahn HA, Teller E (1937) Proceedings of the Royal Society of London. Series A, mathematical and physical sciences, pp 220–235
19. Toombs GA (1978) Phys Rep 40:181
20. Aissing G, Monkhorst HJ, Hu C (1993) Int J Quantum Chem 48:245
21. Yannoni C, Clarke T (1983) Phys Rev Lett 51:1191
22. Müller H, Svensson S, Birch J, Kvick Å (1997) Inorg Chem 36:1488
23. Keller H (1977) Chemistry and physics of one-dimensional metals, NATO ASI series. Series B: physics. Springer, ISBN 9780306357251
24. Kertész M, Koller J, Ažman A, Suhai S (1975) Phys Lett A 55:107
25. Dovesi R, Pisani C, Roetti C, Saunders V (1984) J Chem Phys 81:2839
26. Causa M, Dovesi R, Pisani C, Roetti C, Saunders V (1988) J Chem Phys 88:3196
27. Németh K, Unni AK, Kalnmals C, Segre CU, Kaduk J, Bloom ID, Maroni VA (2015) RSC Adv 5:55986
28. Ruschewitz U (2006) Zeitschrift für anorganische und allgemeine Chemie 632:705
29. Radchenko S, Petrov A (1989) Russ Chem Rev 58:948
30. Gedridge RW Jr, Brandsma L, Nissan RA, Verkruijsse HD, Harder S, De Jong RL, O'Connor CJ (1992) Organometallics 11:418
31. Wiberg E, Wiberg N (2001) Inorganic chemistry. Academic Press, ISBN 9780123526519
32. Balamurugan B, Mehta B, Shivaprasad S (2003) Appl Phys Lett 82:115
33. Judai K, Nishijo J, Nishi N (2006) Adv Mater 18:2842
34. Brandsma L, Heus-Kloos Y, van der Heiden R, Verkruijsse H (1988) Preparative acetylenic chemistry. Elsevier, ISBN 9780444429605
35. Brandsma L (2003) Best synthetic methods: acetylenes, allenes and cumulenes: acetylenes, allenes and cumulenes. Best synthetic methods. Elsevier Science, ISBN 9780080542201
36. Stang P, Diederich F (2008) Modern acetylene chemistry. Wiley, ISBN 9783527615261
37. Hlavatỳ J, Kavan L (1998) Die Angewandte Makromolekulare Chemie 254:75
38. Cataldo F (1997) Polym Int 44:191
39. Cataldo F (1998) Eur J Solid State Inorg Chem 35:293
40. Cataldo F, Capitani D (1999) Mater Chem Phys 59:225
41. Cataldo F (2005) Polyynes: synthesis, properties, and applications. Taylor & Francis, ISBN 9781420027587
42. Campbell RW (1975) P-phenylene sulfide polymers. US patent 3,919,177
43. Duan B, Wang W, Wang A, Yuan K, Yu Z, Zhao H, Qiu J, Yang Y (2013) J Mater Chem A 1:13261
44. Giannozzi P, Baroni S, Bonini N, Calandra M, Car R, Cavazzoni C, Ceresoli D, Chiarotti GL, Cococcioni M, Dabo I et al (2009) J Phys Condens Matter 21:395502 (19pp). http://www.quantum-espresso.org
45. Perdew JP, Ruzsinszky A, Csonka GI, Vydrov OA, Scuseria GE, Constantin LA, Zhou X, Burke K (2008) Phys Rev Lett 100:136406
46. Sim G, Sutton L (1975) Molecular structure by diffraction methods. Nuclear magnetic resonance. Royal Society of Chemistry, ISBN 9780851865270
47. Okada M, Tanaka K, Takata A, Yamabe T (1993) Synth Metals 59:223
48. Akahama Y, Kawamura H, Häusermann D, Hanfland M, Shimomura O (1995) Phys Rev Lett 74:4690
49. Iota V, Yoo C, Cynn H (1999) Science 283:1510
50. Goh M, Matsushita S, Akagi K (2010) Chem Soc Rev 39:2466
51. Surján PR, Udvardi L, Németh K (1994) J Mol Struct (Thoechem) 311:55
52. Surján P, Németh K (1994) Solid State Commun 92:407
53. Surján P, Németh K, Bennati M, Grupp A, Mehring M (1996) Chem Phys Lett 251:115
54. Bennati M, Németh K, Surján P, Mehring M (1996) J Chem Phys 105:4441
55. Németh K (2014a) Int J Quantum Chem 114:1031
56. Németh K (2014b) J Chem Phys 141:054711
57. Nemeth K (2015) Functionalized boron nitride materials as electroactive species in electrochemical energy storage devices, patent pending, WO/2015/006161
58. Setyawan W, Curtarolo S (2010) Comput Mater Sci 49:299

Theor Chem Acc (2015) 134:74
DOI 10.1007/s00214-015-1670-2

REGULAR ARTICLE

Unconventional bond functions for quantum chemical calculations

Dávid Mester[1] · **József Csontos**[1] · **Mihály Kállay**[1]

Received: 30 March 2015 / Accepted: 16 April 2015 / Published online: 15 May 2015

Abstract New types of bond function (BF) basis sets are proposed and tested for quantum chemical applications. First, BF basis sets constituted of conventional Gaussian-type orbitals (GTO) are considered. Both the exponents and the positions of the BFs are optimized, but, in contrast to previous studies, the position of each BF shell is varied separately. Second, new types of basis functions, the general ellipsoidal Gaussian-type orbitals (EGTOs), are proposed for quantum chemical applications. The EGTOs are distorted spherical GTOs and, as such, are expected to be well suited for describing the polarized charge densities in molecular environments. EGTOs can be used either as atom-centered (AC) basis functions or as BFs. In this study, the latter possibility is explored, and BF basis sets including EGTOs are optimized and compared to those containing only conventional GTO BFs. The performance of the developed GTO and EGTO BF basis sets is assessed for Hartree–Fock and density functional calculations against conventional AC GTO basis sets. Our results show that using GTO BF basis sets, the results are significantly improved, while the number of the basis functions can be decreased by about 10 %, which is not dramatic; however, the average angular momentum quantum number in the BF sets is significantly lower. The accuracy of the computed energies can be further increased by about 15 % if EGTO BFs are used.

Keywords Bond functions · Ellipsoidal Gaussian functions · Polarization functions · Unconventional basis functions

1 Introduction

In quantum chemistry, the computational cost of a theoretical investigation is substantially influenced by the size of the basis set selected. On the other hand, the "goodness" of the basis set for a given property can decide about the quality of the work. The most frequently used basis sets, such as those developed by Pople et al. [1–6], Ahlrichs et al. [7–9], and Dunning et al. [10–13], consist of atom-centered (AC) Gaussian-type orbitals (GTO), which were proposed by Boys [14]. Polarization functions first have been introduced to help in describing the non-spherical symmetry of the atoms in the molecular environment [15]. However, beside characterizing molecular polarization effects, their use is also inevitable in the accurate treatment of the electron correlation problem [16, 17]. Nevertheless, their addition to the basis set, due to their higher angular momentum, considerably increases the number and the computational complexity of the evaluation of molecular integrals. It is reasonable to assume that the substitution of AC polarization functions with bond-centered (BC) *s*- and *p*-type Gaussians (bond functions, BFs) may provide a more natural account of the polarized molecular environment, and less BC than AC functions are needed to achieve the same effect.

Several studies with BF basis sets have been reported about replacing the polarization basis functions with BC

Published as part of the special collection of articles "Festschrift in honour of P. R. Surjan."

This paper is dedicated to Professor Péter R. Surján on the happy occasion of his 60th birthday.

✉ Mihály Kállay
kallay@mail.bme.hu

[1] MTA-BME Lendület Quantum Chemistry Research Group, Department of Physical Chemistry and Materials Science, Budapest University of Technology and Economics, P.O. Box 91, Budapest 1521, Hungary

functions. Frost and Preuss were among the first in the 1960s who pioneered the use of BFs [18, 19]. Preuss [18] studied the electron correlation problem in the H_3^+ ion with *s*-type GTOs positioned at the atomic nuclei and the three bond centers as well as the centroid of the equilateral triangle structure. Frost described a simple floating spherical Gaussian orbital model (FSGO) and applied it to the LiH molecule [19]. His model can be used for the qualitative description of singlet ground states; each pair of electrons is modeled by an FSGO, the centers and exponents of which are determined to satisfy the variational principle.

The *floating orbital* geometry optimization (FOGO) procedure was developed by Huber [20], and its feasibility was demonstrated in subsequent papers [21–23]. In the FOGO procedure, the energy gradient and the Hellmann–Feynman force are simultaneously minimized letting the nuclei and orbitals move independently. It is worth noting that the additional calculation of the Hellmann–Feynman force does not cause any serious computational overhead because it does not require the calculation of the two-electron derivatives. The agreement between the experimental and FOGO geometries and dipole moments was found to be excellent [22]. Furthermore, rotational barriers obtained in FOGO using a double-ζ basis set without polarization functions were in line with those calculated using energy gradient optimization and basis sets including polarization functions [23].

Helgaker and Almlöf [24] studied the first- and second-order molecular properties of small molecules at the Hartree–Fock (HF) level using double-ζ quality basis sets including floating GTOs. They found that although the electronic energies were only slightly better in comparison with the results obtained with the large 6-311++G(3df,3pd) basis set, the accuracy of calculated properties greatly improved in many cases.

Rothenberg and Schaefer [25] investigated the effectiveness of various polarization schemes including BFs and concluded that "bond functions provide a reasonable alternative to the more conventional type of polarization function."

The first thorough studies about BFs were conducted by Neisius and Verhaegen [26, 27]. First, BF parameters, positions and exponents, were determined for the C–C and C–H bonds as well as carbon lone pairs [26]. Later, they extended their basis set work for molecules containing C, N, O, and H atoms [27]. In both studies, the *s*- and *p*-type functions were restricted to be centered at the same position, had identical exponents, and were optimized to be used with the 6-31G basis set. Their results showed that for less computational cost, the 6-31G basis set with additional BFs provided on average as accurate energies as the 6-31G* basis set.

The first extensive BF study with correlation methods was performed by Martin et al. [28]. The total and dissociation energies of first-row hydrides were calculated using fourth-order Møller–Plesset perturbation theory with hybrid bond/polarization basis sets. Their hybrid basis sets based on the 6-31G basis set and contained both higher angular momentum functions and BFs. The results obtained with the hybrid basis sets were competitive with those calculated using considerably larger polarization-only basis sets. Furthermore, the computational savings gained were also substantial, and the cost of the calculations was reduced by a factor of 4–20.

Bauschlicher and Partridge [29] investigated the bond energies of eight diatomics using a series of correlation consistent basis sets with and without BFs. They concluded that although the addition of BFs to a given basis set always improved the bond energies, the use of BFs does not offer any advantages over AC basis sets when the results were extrapolated to the basis set limit. Nevertheless, for the double- and triple-ζ basis sets, they reported a sizable improvement in the bond energetics due to the incorporation of BFs.

Jensen et al. [30] examined the basis set convergence properties of BFs in density functional theory (DFT) calculations using the H_2, N_2, and N_4 species as test systems. They compared the convergence patterns of basis sets consisting of BFs only, AC polarization functions only, and a mixture of BFs and AC polarization functions. They showed that the BFs only basis sets yield the slowest convergence toward the basis set limit. The convergence behavior of the other two basis set types was faster and similar. Some of their results also indicated that optimal BFs might have fairly high angular momentum. It was concluded that although the use of low angular momentum BFs can reduce the number of high angular momentum AC polarization functions, BFs do not provide any computational advantage over pure AC basis functions.

Styszyński et al. [31] studied the performance of BFs in relativistic HF and non-relativistic and relativistic electron correlation calculations for the BF, AlF, and GaF molecules. It was found that at both the non-relativistic and relativistic HF levels, the diffuse and polarization functions of an AC basis set can be effectively substituted by BFs unless the calculations with the AC basis itself yield near-HF-limit energies. However, in correlation calculations, the benefits of BFs were not obvious because when many BFs were used, the rate of convergence was usually ruined. Nevertheless, when the number of BFs was relatively small, a considerable improvement could be observed in the correlation energy at practically no additional computational cost.

Besides BFs, there have been numerous attempts made to introduce unconventional AC basis functions which improve upon conventional GTOs. Nearly a decade after Boys' [14] paper on GTOs, the mathematical background of the application of special ellipsoidal (elliptical)

Gaussian-type orbitals (EGTOs) was laid down in a report by Browne and Poshusta [32]. They introduced the following class of functions:

$$\chi = x^i y^j z^k \exp\left[-\left(\alpha_1 x^2 + \alpha_2 y^2 + \alpha_3 z^2\right)\right], \quad (1)$$

and the corresponding molecular integrals were also derived and presented. It is easy to recognize that when $\alpha_1 = \alpha_2 = \alpha_3$, the ellipsoidal case simplifies to a conventional GTO. They expected that the allowance for asymmetry in the exponents will improve the description of electron distribution.

The analytical formulas for the integrals of generalized Hermite Gaussian functions were presented by Katriel [33] and Katriel and Adam [34]. They also investigated the effects of these basis functions for H_2 and He_2^{2+} test systems. A serious drawback of their approach is its coordinate dependence.

Bishop and Leclerc [35] investigated several unconventional basis functions including EGTOs, generalized Slater–Gauss-type, non-integer n Slater, rational, Hulthén, and Bessel functions and found that the non-integer n Slater basis performed best. However, the scope of their study was fairly limited; only one system, the H_2 molecule, was probed.

More detailed studies dealing with EGTOs were conducted by Cohen and Basch [36, 37]. In their first paper [36], new, efficient analytic integral evaluation formulas were developed and tested for the calculation of the total energies of HF and CO_2. In their work, two single-ζ basis sets ($3s1p/1s$), a spherical and an ellipsoidal one, were generated and compared with a double-ζ basis set ($4s2p/2s$) for HF calculations. In the single-ζ sets, both the spherical and ellipsoidal exponents were optimized for the valence orbitals of the atoms. They found that the optimized ellipsoidal single-ζ basis set results approached the double-ζ values and also performed better than the optimized spherical single-ζ basis set. In the second report [37], further molecular systems were investigated using the methodology developed in their first study [36]. However, beside the total energy, several one-electron properties were also examined and compared to the double-ζ basis set results. Based on the one-electron properties, they concluded that the ellipsoidal valence orbitals in the single-ζ basis set were too rigid to represent simultaneously both the spherical atomic and the ellipsoidal bonding regions of the molecules and exaggerate the transfer of charge density from the atomic regions to the bonding regions of the molecules. They suggested that a more selective use of ellipsoidal basis functions will yield better results.

To describe the polarization caused by the molecular environment, Szalay and Surján [38] considered AC Slater-type orbitals whose exponents depended on the polar angles. For the two-center one-electron problem, H_2^+, they presented the necessary molecular integrals and demonstrated that the potential curve of H_2^+ obtained with these distorted s functions in the minimal basis agrees well with the exact curve.

Here, we also refer to some other studies that are less directly related to our present work. Gaussian Lobe Functions were introduced by Preuss [39]. In this representation, the higher angular momentum functions are constructed as a linear combination of usually two or more s-type GTOs located on different centers. The study of Tasi and Császár [40] is also notable. In their work, in addition to the molecular orbital coefficients, both the position and the exponents of the GTOs were treated as variational parameters during the solution of the HF equations. They were able to obtain HF-limit energies for small atomic and molecular systems with the help of a few dozen s-type GTOs.

The purpose of this study is twofold. First, we develop new types of BF basis sets constituted of conventional GTOs. We optimize both the exponents and the positions of the BFs, but, in contrast to previous studies, the position of each BF shell is optimized separately. Second, we propose new types of basis functions for quantum chemical calculations, the general EGTOs. To ensure the coordinate-system invariance of the results, the EGTOs are also used as BFs, and BF basis sets including EGTOs are optimized and compared to those containing only conventional GTO BFs. In both cases, we assess the performance of the developed BF basis sets for HF and DFT calculations against conventional AC GTO basis sets including polarization functions.

2 Bond-centered spherical Gaussian functions

Our first aim was to study and compare the effects of spherical BC GTOs with those of AC higher angular momentum functions. In the following, the optimization of the GTO parameters is described and the results obtained with the application of BC GTOs are discussed in light of the data calculated with conventional polarization basis sets.

2.1 Optimization of function parameters

Basis sets most frequently used in quantum chemistry made up of contracted GTOs which are by definition linear combinations of the

$$\chi(\mathbf{r}, \mathbf{A}, \mathbf{l}, \alpha) = (x - A_x)^i \left(y - A_y\right)^j (z - A_z)^k \mathrm{e}^{-\alpha(\mathbf{r}-\mathbf{A})^2} \quad (2)$$

Cartesian GTOs. In the above expression, $\mathbf{r} = (x, y, z)$ designates the electron's coordinates, $\mathbf{A} = (A_x, A_y, A_z)$ contains the coordinates of the function's center, and $\mathbf{l} = (i, j, k)$ determines the function's type, for example, in the case of

Table 1 Total HF energies in E_h calculated with the original and optimized basis sets

Molecule	Basis set	Hartree–Fock energy		Number of functions
		Original	Optimized	
Methane	6-31G	−40.18051		17
C–H	6-31G*	−40.19482		22
	6-31G**	−40.20166	−40.20578	34
	6-31G–2*s* BF		−40.20676	25
	6-31G–3*s* BF		−40.20781	29
	6-31G–4*s* BF		−40.20819	33
Ethane	6-31G	−79.15410		30
C–C	6-31G*	−79.22261		40
	6-31G**	−79.23780	−79.24383	58
	6-31G–2*s* BF		−79.24446	44
	6-31G–3*s* BF		−79.24655	51
	6-31G–4*s* BF		−79.24777	58
Ethene	6-31G	−78.00357		26
C=C	6-31G*	−78.03040		36
	6-31G**	−78.03779	−78.02809	48
	6-31G–1*s*1*p* BF		−78.03662	42
	6-31G–2*s*1*p* BF		−78.04077	43
Ethyne	6-31G	−76.79244		22
C≡C	6-31G*	−76.81660		32
	6-31G**	−76.82102	−76.80603	38
	6-31G–1*s*2*p* BF		−76.83781	35
Ammonia	6-31G	−56.16199		15
N–H	6-31G*	−56.18282		20
	6-31G**	−56.19445	−56.19813	29
	6-31G–2*s* BF		−56.18796	21
	6-31G–3*s* BF		−56.19556	24
	6-31G–4*s* BF		−56.20233	27
	6-31G–1*s*1*p* BF		−56.20629	27
Water	6-31G	−75.98399		13
O–H	6-31G*	−76.00913		18
	6-31G**	−76.02264	−76.02861	24
	6-31G–2*s* BF		−76.01125	17
	6-31G–3*s* BF		−76.01679	19
	6-31G–4*s* BF		−76.01726	21
	6-31G–1*s*1*p* BF		−76.04319	21
Methylamine	6-31G	−95.16441		28
N–C	6-31G*	−95.20423		38
	6-31G**	−95.21675	−95.22251	53
	6-31G–1*s*1*p* BF		−95.23022	49
Methanol	6-31G	−114.98356		26
O–C	6-31G*	−115.03095		36
	6-31G**	−115.04296	−115.04931	48
	6-31G–1*s*1*p* BF		−115.06603	43
Methanimine	6-31G	−93.97984		24
N=C	6-31G*	−94.02656		34
	6-31G**	−94.03403	−94.03705	43
	6-31G–1*s*1*p* BF		−94.03843	38
Hydrogen cyanide	6-31G	−92.82786		20

Table 1 continued

Molecule	Basis set	Hartree–Fock energy		Number of functions
		Original	Optimized	
N≡C	6-31G*	−92.87303		30
	6-31G**	−92.87519	−92.87899	33
	6-31G–1*s*2*p* BF		−92.88782	28
Formaldehyde	6-31G	−113.78464		22
O=C	6-31G*	−113.85103		32
	6-31G**	−113.85462	−113.86307	38
	6-31G–1*s*1*p* BF		−113.86341	32
	6-31G–2*s*1*p* BF		−113.87019	33

The leftmost column shows the name of the molecule used in the optimizations and the bond type whose BFs were optimized

Table 2 B3LYP total energies in E_h for saturated hydrocarbons as a function of the number of BFs

Molecule	Basis set				
	6-31G**	r6-31G**	6-31G–2*s* BF	6-31G–3*s* BF	6-31G–4*s* BF
Propane	−119.05848	−119.06998	−119.06897	−119.07312	−119.07482
Butane	−158.34503	−158.36037	−158.35976	−158.36377	−158.36659
Isobutane	−158.34583	−158.36191	−158.36127	−158.36557	−158.36771
Pentane	−197.63154	−197.65064	−197.64815	−197.65485	−197.65789
Isopentane	−197.63085	−197.65049	−197.64890	−197.65469	−197.65777
Neopentane	−197.63282	−197.65440	−197.65338	−197.65901	−197.66116
Cyclopentane	−196.42107	−196.43789	−196.43371	−196.43912	−196.44255

an *s*-type function ($l = i + j + k = 0$), while for a *p*-type ($l = i + j + k = 1$), the orbital exponent is labeled by α.

In this study, the 6-31G basis set [3] was augmented with *s*- and *p*-type BFs. The BFs were optimized for most common organic bond types including C–H, C–C, C=C, C≡C, N–H, O–H, C–N, C–O, C=N, C=O, and C≡N. In contrast to previous investigations, both the positions and the exponents of the BFs were simultaneously optimized. However, to keep our method coordinate-system independent, the positions of the BFs were constrained to stay in the bond lines. In the optimization process, the molecular symmetries were also exploited. Optimal values of the parameters were obtained by the downhill simplex algorithm of Nelder and Mead [41]. During the optimization, the objective was to locate the minimum of the HF total energy. The algorithm was programmed using the FORTRAN language and implemented in our MRCC [42][1] suite of quantum chemistry programs. To avoid being trapped in local minima in each case, the optimization process was repeated about 100 times using different initial parameter sets. The parameters for a given BF were determined using the smallest molecular entities containing the corresponding bond; the geometries of the molecules were extracted from accurate literature data [43–48].

[1] See also Ref. [56] as well as http://www.mrcc.hu/.

We note here that AC GTOs are also called atomic orbitals (AOs) and the two terms will be used interchangeably in the current text. In the following, 6-31G–*XY* refers to a basis set whose 6-31G GTOs are centered on the atomic nucleus, while *Y* denotes the BC *Y*-type function and *X* gives the number of such BC functions. For example, in the case of methane, 6-31G–3*s* means 6-31G AO basis on atoms H and C, and three *s*-type BFs on each C–H bond, or in the case of a C=C bond, the 6-31G–1*s*1*p* basis set indicates 6-31G AO basis on the C atoms and additional BFs, one *s* and one *p* shell between the carbons.

2.2 Numerical results and discussion

2.2.1 *Saturated hydrocarbons*

For modeling the chemical bonds in saturated hydrocarbons, first, we considered methane [43] and optimized the positions and exponents of *s*-type BFs for the C–H bonds together with the exponents and contraction coefficients of the AO basis functions centered on the carbon and hydrogen atoms. For consistency and fair comparison, the conventional 6-31G** basis set was also reoptimized; the r6-31G** notation will be used hereafter for the basis set obtained in this way. The results are compiled in Table 1.

It can be observed that for methane, the energy obtained with the r6-31G** basis set can be recovered by two *s*-type BFs placed on the C–H bonds, while the number of basis functions is only 25 instead of 34. In the next step, using the C–H BFs and the C and H AO basis sets optimized for methane, the positions and exponents of BFs placed on the C–C bond were determined for the ethane molecule [43]. For consistency, for the optimization of the C–C BFs, we always chose the basis set optimized for methane that includes the same number of BFs on the C–H bonds. Inspecting the corresponding block in Table 1, we can conclude that two *s*-type BFs are also sufficient for ethane to reach the accuracy of the r6-31G** basis set, while the number of basis functions is lower by 14, though the energy difference at the HF level with respect to the r6-31G** results is somewhat smaller than for methane.

In order to select the final basis set augmented with BFs for the description of saturated hydrocarbons, further test calculations were carried out for linear, branched, and cyclic hydrocarbons at the DFT level using the B3LYP (Becke's three-parameter hybrid functional including the correlation functional of Lee, Yang, and Parr) functional [49, 50]. For each species, the most stable conformer was considered. The geometries of the test molecules were optimized with the M06-2X hybrid functional of Truhlar et al. [51] with the cc-pVDZ basis set [52] using the

Table 3 Number of basis functions for saturated hydrocarbons

Molecule	Basis set			
	6-31G**	6-31G–2*s* BF	6-31G–3*s* BF	6-31G–4*s* BF
Propane	82	63	73	83
Butane	106	82	95	108
Isobutane	106	82	95	108
Pentane	130	101	117	133
Isopentane	130	101	117	133
Neopentane	130	101	117	133
Cyclopentane	120	95	110	125

Table 4 B3LYP total energies in E_h for unsaturated hydrocarbons with various basis sets

Molecule	Basis set			
	6-31G**	r6-31G**	6-31G-BF	cc-pVTZ
2,3-Dimethylbuta-1,3-diene	−234.46392	−234.46842	−234.49145	−234.54413
2-Methylbut-1-ene	−196.40363	−196.41235	−196.42748	−196.46967
2-Methylprop-1-ene	−157.11878	−157.12350	−157.13945	−157.17302
3-Methylbuta-1,2-diene	−195.16249	−195.16412	−195.18604	−195.23082
Benzene	−232.09867	−232.09475	−232.12102	−232.17872
But-1-en-3-yne	−154.63399	−154.62281	−154.65758	−154.69479
But-1-yne	−155.86263	−155.85995	−155.88784	−155.92111
Naphthalene	−385.64628	−385.64313	−385.67152	−385.77458
Prop-1-ene	−117.82646	−117.82633	−117.84181	−117.86918
Mean absolute error	0.071	0.071	0.048	

Table 5 Number of basis functions for unsaturated hydrocarbons

Molecule	Basis set		
	6-31G**	6-31G–BF	cc-pVTZ
2,3-Dimethylbuta-1,3-diene	134 (0, 30, 66, 38)	125 (0, 0, 45, 80)	320 (42, 110, 114, 54)
2-Methylbut-1-ene	120 (0, 25, 60, 35)	109 (0, 0, 33, 76)	290 (35, 100, 105, 50)
2-Methylprop-1-ene	96 (0, 20, 48, 28)	87 (0, 0, 27, 50)	232 (28, 90, 84, 40)
3-Methylbuta-1,2-diene	110 (0, 25, 54, 31)	101 (0, 0, 36, 65)	262 (35, 90, 93, 44)
Benzene	114 (0, 30, 54, 30)	114 (0, 0, 18, 96)	264 (42, 90, 90, 42)
But-1-en-3-yne	76 (0, 20, 36, 20)	71 (0, 0, 33, 38)	176 (28, 60, 60, 38)
But-1-yne	86 (0, 20, 42, 24)	79 (0, 0, 30, 49)	204 (28, 60, 82, 34)
Naphthalene	180 (0, 30, 84, 46)	185 (0, 0, 93, 92)	412 (70, 140, 138, 64)
Prop-1-ene	72 (0, 15, 36, 21)	65 (0, 0, 21, 44)	174 (21, 60, 63, 30)

In parenthesis, the number of functions is given for each angular momentum quantum number from *f* to *s*

Gaussian 09 suite [53]. The computed total energies are displayed in Table 2, while the number of basis functions is collected in Table 3.

Our results show that increasing the size of the system, two *s*-type BFs are not sufficient any more at the B3LYP level to obtain energies of quality similar to that of r6-31G**. However, with three BFs, the calculated total energies are lower by 1.2–4.6 mE_h than the corresponding values obtained with r6-31G**. If four BFs are employed, even the smallest difference is 4.7 mE_h„ but in this case, the number of functions in the BF basis is somewhat larger. Taking into account these observations in the further calculations, the basis sets optimized with three *s*-type BFs were used for the C–H and C–C bonds.

2.2.2 *Unsaturated hydrocarbons*

In the next step, we constructed BF basis sets for the double and triple bonds present in unsaturated hydrocarbons. The AO basis sets optimized for the C and H atoms as well as the three *s*-type BFs selected for the saturated molecules were placed on the ethene [44] and ethine [44] molecules, and the parameters for the BFs of C=C and C≡C bonds were optimized. To be consistent with the chemical picture, *p*-type BFs were used for the description of π bonds; thus, at least one and two *p* functions were used for the double and triple bonds, respectively. Inspecting the results in Table 1, we can conclude that the 6-31G** AO basis sets reoptimized for methane perform less well for ethene and ethine than the original Pople basis sets; therefore, the performance of the basis sets including BFs was compared to the latter. For ethene, an additional *s* function is required beside the 1*s* 2*p* minimal BF set for an accurate energy, while for ethine, one *s* and two *p* functions are sufficient.

To assess the performance of the optimized basis sets for unsaturated hydrocarbons, test calculations were carried out at the DFT level. For reference, the energies obtained with Dunning's cc-pVTZ basis set were used. The energies are collected in Table 4, while the number of functions in the various basis sets is presented in Table 5.

As can be seen, the mean absolute error with respect to the reference value is smaller by 33 % with the basis set augmented with the selected BFs (6-31G–BF) than with the reoptimized Pople basis set containing polarization functions, while the total number of functions is lower by 6 %. It means that the decrease in the size of the basis set is not dramatic; however, in the BF basis sets, there are no *d* functions at all, while there are, in average, 24 ones in the 6-31G** basis sets for the considered molecules, as well as the number of *p* functions also decreases by about 32 %. In turn, the number of *s* functions is significantly higher; however, the evaluation of two-electron integrals over *s* functions is substantially faster than that for basis functions of higher angular momenta.

2.2.3 *Heteroatom-containing hydrocarbons*

Of the heteroatom-containing organic compounds, the nitrogen- and oxygen-substituted ones were considered. As for the BFs of hydrocarbons, the BFs for a particular bond type were optimized for the smallest molecule in which the bond of that type can be found. In this case, only the AO basis functions centered on the N and O atoms were reoptimized, and for the H and C atoms, just as for the C–H and C–C bonds, the basis functions were taken over from the 6-31G–BF basis optimized for the hydrocarbons and were not varied. First, for the description of the O–H and N–H bonds, we considered the water [43] and ammonia

Table 6 B3LYP total energies in E_h for heteroorganic molecules with various basis sets

Molecule	Basis set			
	6-31G**	r6-31G**	6-31G–BF	cc-pVTZ
2-Aminopropan-1-ol	−249.55731	−249.57884	−249.60150	−364.17802
But-3-en-2-imine	−211.22286	−211.23126	−211.25137	−211.29976
But-3-en-2-one	−231.09874	−231.10993	−231.13414	−231.18563
Dimethylacetamide	−287.65991	−287.68500	−287.70126	−287.76399
Dimethylamine	−135.07599	−135.08945	−135.09761	−135.12468
Dimethyl ether	−154.93346	−154.94772	−154.96355	−154.99341
Ethanol	−154.94764	−154.96156	−154.97903	−155.01009
Ethyl cyanate	−247.12216	−247.14223	−247.16181	−247.21739
Ethyl methyl carbonate	−381.49093	−381.50859	−381.55443	−381.64087
Methyl propanoate	−307.53089	−307.55567	−307.58037	−307.64626
Propan-1-amine	−174.37198	−174.38821	−174.39859	−174.43428
Propanoic acid	−267.02444	−267.03636	−267.07153	−267.13211
Mean absolute error	0.089	0.072	0.050	

Table 7 Number of basis functions for heteroorganic molecules

Molecule	Basis set		
	6-31G**	6-31G–BF	cc-pVTZ
2-Aminopropan-1-ol	115 (0, 25, 57, 33)	107 (0, 0, 45, 62)	276 (35, 95, 99, 47)
But-3-en-2-imine	105 (0, 25, 51, 29)	98 (0, 0, 42, 56)	248 (35, 85, 87, 41)
But-3-en-2-one	100 (0, 25, 48, 27)	93 (0, 0, 39, 54)	234 (35, 80, 81, 38)
Dimethylacetamide	129 (0, 30, 54, 30)	119 (0, 0, 48, 71)	306 (42, 105, 138, 51)
Dimethylamine	77 (0, 15, 39, 23)	71 (0, 0, 27, 44)	188 (21, 65, 69, 33)
Dimethyl ether	72 (0, 15, 36, 21)	65 (0, 0, 24, 41)	174 (21, 60, 63, 30)
Ethanol	72 (0, 15, 36, 21)	65 (0, 0, 24, 41)	174 (21, 60, 63, 30)
Ethyl cyanate	95 (0, 25, 45, 25)	88 (0, 0, 42, 46)	220 (35, 75, 75, 35)
Ethyl methyl carbonate	128 (0, 35, 60, 33)	113 (0, 0, 45, 68)	294 (49, 100, 99, 46)
Methyl propanoate	124 (0, 30, 60, 34)	119 (0, 0, 60, 59)	292 (42, 100, 102, 48)
Propan-1-amine	101 (0, 20, 51, 30)	93 (0, 0, 33, 60)	246 (28, 85, 90, 43)
Propanoic acid	90 (0, 25, 42, 23)	83 (0, 0, 42, 41)	206 (35, 70, 69, 32)

In parenthesis, the number of functions is given for each angular momentum quantum number from *f* to *s*

[43] molecules and monitored the change of total energy increasing the number of basis functions and optimizing their parameters. Based on Table 1, we find that polarization functions decrease the energy of water and ammonia, respectively, by 38.7 and 32.5 mE_h, while for methane, this number is 21.1 mE_h. As expected, the more electrons build up an atom or the more a bond is polarized, the better description is achieved by the use of BFs. In these cases, *s*-type BFs seem to be insufficient for the replacement of polarization functions, but using *p*-type ones, the energy is considerably lower than with basis sets including polarization functions. We note that the *p*-type BFs are always located closer to the nitrogen and oxygen atoms improving also the description of atoms, while the *s*-type functions are farther from the heavy atoms contributing primarily to the description of bonds. Evaluating the results, we selected the 6-31G–1*s*1*p* BF basis set for both bond types for further calculations.

The next step is to study single bonds between heteroatoms and the carbon atom. We chose methylamine [45] and methanol [46] and optimized the BFs for the N–C and O–C bonds using the AO and BF basis sets optimized previously for the atoms and other bonds. As we have seen, for accurate energies, the N–H and O–H bonds require *p*-type BFs, which improve the quality of the description of both the atoms and the bonds. Since it is likely to be the case for the N–C and O–C bonds, we also considered BF sets including *p* functions for the latter bonds. This turned out to be especially important for molecules which include N–C and O–C bonds but no O–H and N–H bonds, such as ethers, because for those systems, the *p*-type functions improving the atoms would be missing. Performing the optimizations, we again observe that the *p* functions are closer to the heavy atom of higher electronegativity. Considering the results (see Table 1), we can conclude that the performance of the BF basis sets is superior to that for the conventional AO basis sets including polarization functions.

Double and triple bonds between heteroatoms and the carbon atom (N=C, N≡C, O=C) were treated similar to the carbon–carbon multiple bonds: A set of *p* functions was placed on each π-bond. The model systems include methanimine [47], hydrogen cyanide [44], and formaldehyde [48]; the results of the optimizations are presented in Table 1. As can be seen, if the heteroatom is nitrogen, even one *s*-type function is sufficient in addition to the *p* functions used for the π-bonds to achieve the accuracy of the reoptimized AO basis set. For oxygen, two *s* functions are desirable since the energies obtained with the 1*s*1*p* BF set are only slightly better than those computed with the r6-31G** basis, and, as we have seen for hydrocarbons, if the BF basis sets optimized for the small molecules are used for bigger systems, their performance with respect to the original AO bases is relatively worse.

With the BF basis sets optimized for the bonds including heteroatoms, we performed benchmark calculations for a test set of 12 molecules including alcohol, ketone, carbonic acid, carbonate, ester, ether, primary and secondary amine, imine, amide, and nitrile. As reference, the cc-pVTZ basis set was employed again. The numerical results are summarized in Table 6, while the number of functions in the various basis sets is collected in Table 7.

Using the 6-31G–BF basis set, the energy decreases by 21.6–63.5 mE_h relative to the original 6-31G** basis, while this interval is 8.1–45.8 mE_h with respect to the reoptimized AO basis sets. The average error against the cc-pVTZ reference decreases by 43 and 30 %, respectively, if BFs are used. The total number of basis functions is lower by 9 %, but as for the hydrocarbons, the angular

momentum quantum number of the functions is in average significantly lower: There is no *d* function in the basis sets, and the number of *p* functions is also considerably lower.

3 Bond-centered general ellipsoidal Gaussian functions

In this section, we study an extension of the BF approach. Only BF basis sets including *s*-type functions will be considered, but instead of the conventional, spherical Gaussians BC ellipsoidal Gaussians of general form will be employed. Since such functions, to the best of our knowledge, have not yet been considered in quantum chemistry, first, we briefly discuss how the integrals over ellipsoidal Gaussians can be evaluated and what modifications in a quantum chemistry program are required to process such functions. Second, we will examine to what extent the additional flexibility of ellipsoidal functions with respect to conventional Gaussians improves the calculated energies.

The ellipsoidal Gaussians that we propose here to be used as basis functions can be written in the

$$\chi(\mathbf{r},\mathbf{A},\mathbf{l},\boldsymbol{\alpha}) = (x-A_x)^i\left(y-A_y\right)^j(z-A_z)^k \mathrm{e}^{-(\mathbf{r}-\mathbf{A})^\dagger\boldsymbol{\alpha}(\mathbf{r}-\mathbf{A})} \quad (3)$$

form, where $\boldsymbol{\alpha}$ is 3×3, symmetric, positive definite matrix. It can be easily seen that the above functions are distorted Cartesian Gaussians, which reduce to the latter if matrix $\boldsymbol{\alpha}$ is diagonal with all elements equal to α. As such, ellipsoidal Gaussians are expected to be particularly well suited for describing the polarized charge densities in molecular environments.

The use of special ellipsoidal Gaussians including diagonal $\boldsymbol{\alpha}$ matrices as atom-centered basis functions in electronic structure calculations was already proposed more than 50 years ago [32]; however, these functions did not gain acceptance, probably because of the coordinate-system-dependent results and the difficulties in the evaluation of the corresponding integrals. To cope with the first problem, we propose to use "adaptive" EGTO BFs (EBFs for short), for which the elements of matrix $\boldsymbol{\alpha}$ are chosen so that the resulting ellipsoidal Gaussian will be stretched in the direction of the bond. With an appropriate choice of the exponent matrix, not only basis functions "polarized" in the direction of chemical bonds are obtained, but also the coordinate-system invariance of the results is guaranteed.

3.1 Evaluation of molecular integrals

Since the purpose of this initial study is to evaluate the potential of ellipsoidal Gaussian basis functions, we did not endeavor to develop a highly efficient integral code. The one-electron integrals were simply computed on a grid used for DFT calculations. The grid construction follows the design principles of Becke [54], the angular grids are Lebedev quadratures, while the radial grid is that of Gauss and Chebyshev. The accuracy of the integrals was tested for conventional basis sets for various molecules. We found that using a 302-point Lebedev quadrature and about 40 radial quadrature points, the integrals are accurate to 7–8 decimals, which is already sufficient for our purposes, but the numerically exact value can also be reproduced if at least 1730-point angular quadrature is applied. The two-electron integrals, of course, cannot be evaluated on a grid even for the smallest systems, and we had to develop a more sophisticated algorithm for that purpose based on analytical formulas. Supposing only *s*-type functions, a general two-electron Coulomb integral,

$$\left\langle \chi_\mu\chi_\nu\left|\frac{1}{\mathbf{r}_{12}}\right|\chi_\lambda\chi_\sigma\right\rangle = \iint \chi_\mu(\mathbf{r}_1)\chi_\nu(\mathbf{r}_1)\frac{1}{\mathbf{r}_{12}}\chi_\lambda(\mathbf{r}_2)\chi_\sigma(\mathbf{r}_2)\mathrm{d}\mathbf{r}_1\mathrm{d}\mathbf{r}_2, \quad (4)$$

where $\mathbf{r}_{12}=\mathbf{r}_1-\mathbf{r}_2$, can be reexpressed using Eq. (3) as

$$\iint \mathrm{e}^{-(\mathbf{r}_1-\mathbf{A})^\dagger\boldsymbol{\alpha}(\mathbf{r}_1-\mathbf{A})}\mathrm{e}^{-(\mathbf{r}_1-\mathbf{B})^\dagger\boldsymbol{\beta}(\mathbf{r}_1-\mathbf{B})}\frac{1}{\mathbf{r}_{12}}\mathrm{e}^{-(\mathbf{r}_2-\mathbf{C})^\dagger\boldsymbol{\gamma}(\mathbf{r}_2-\mathbf{C})} \times \mathrm{e}^{-(\mathbf{r}_2-\mathbf{D})^\dagger\boldsymbol{\delta}(\mathbf{r}_2-\mathbf{D})}\mathrm{d}\mathbf{r}_1\mathrm{d}\mathbf{r}_2. \quad (5)$$

Rewriting the product of the four exponential factors as one exponential function and performing the algebraic operations in its exponent, the latter can be expressed as

$$\begin{aligned}&-\mathbf{r}_1^\dagger\boldsymbol{\alpha}\mathbf{r}_1+2\mathbf{A}^\dagger\boldsymbol{\alpha}\mathbf{r}_1-\mathbf{A}^\dagger\boldsymbol{\alpha}\mathbf{A}-\mathbf{r}_1^\dagger\boldsymbol{\beta}\mathbf{r}_1+2\mathbf{B}^\dagger\boldsymbol{\beta}\mathbf{r}_1-\mathbf{B}^\dagger\boldsymbol{\beta}\mathbf{B}\\&-\mathbf{r}_2^\dagger\boldsymbol{\gamma}\mathbf{r}_2+2\mathbf{C}^\dagger\boldsymbol{\gamma}\mathbf{r}_2-\mathbf{C}^\dagger\boldsymbol{\gamma}\mathbf{C}-\mathbf{r}_2^\dagger\boldsymbol{\delta}\mathbf{r}_2+2\mathbf{D}^\dagger\boldsymbol{\delta}\mathbf{r}_2-\mathbf{D}^\dagger\boldsymbol{\delta}\mathbf{D}.\end{aligned} \quad (6)$$

To further simplify the expression, we introduce the $\mathbf{r}=(\mathbf{r}_1,\mathbf{r}_2)$ six-component vector containing the electronic coordinates. The terms that are quadratic in $\mathbf{r}$ can be expressed with the aid of a 6×6 matrix

$$\boldsymbol{\Gamma} = \begin{pmatrix}\boldsymbol{\alpha}+\boldsymbol{\beta} & 0\\ 0 & \boldsymbol{\gamma}+\boldsymbol{\delta}\end{pmatrix}_{6\times 6} \quad (7)$$

as $\mathbf{r}^\dagger\boldsymbol{\Gamma}\mathbf{r}$; the linear terms can be rewritten as $\mathbf{J}^\dagger\mathbf{r}$, where

$$\mathbf{J} = 2\begin{pmatrix}\left(\mathbf{A}^\dagger\boldsymbol{\alpha}\right)_1+\left(\mathbf{B}^\dagger\boldsymbol{\beta}\right)_1\\ \left(\mathbf{A}^\dagger\boldsymbol{\alpha}\right)_2+\left(\mathbf{B}^\dagger\boldsymbol{\beta}\right)_2\\ \left(\mathbf{A}^\dagger\boldsymbol{\alpha}\right)_3+\left(\mathbf{B}^\dagger\boldsymbol{\beta}\right)_3\\ \left(\mathbf{C}^\dagger\boldsymbol{\gamma}\right)_1+\left(\mathbf{D}^\dagger\boldsymbol{\delta}\right)_1\\ \left(\mathbf{C}^\dagger\boldsymbol{\gamma}\right)_2+\left(\mathbf{D}^\dagger\boldsymbol{\delta}\right)_2\\ \left(\mathbf{C}^\dagger\boldsymbol{\gamma}\right)_3+\left(\mathbf{D}^\dagger\boldsymbol{\delta}\right)_3\end{pmatrix} = \begin{pmatrix}J_1\\J_2\\J_3\\J_4\\J_5\\J_6\end{pmatrix}; \quad (8)$$

while the coordinate-independent terms can be regrouped in constant

$$c = \mathbf{A}^\dagger\boldsymbol{\alpha}\mathbf{A}+\mathbf{B}^\dagger\boldsymbol{\beta}\mathbf{B}+\mathbf{C}^\dagger\boldsymbol{\gamma}\mathbf{C}+\mathbf{D}^\dagger\boldsymbol{\delta}\mathbf{D}. \quad (9)$$

Exploiting these definitions, Eq. (5) can be recast as

$$\iint \mathrm{e}^{-(\mathbf{r}^\dagger \boldsymbol{\Gamma} \mathbf{r} - \mathbf{J}^\dagger \mathbf{r}) - c} \frac{1}{\mathbf{r}_{12}} \mathrm{d}\mathbf{r}_1 \mathrm{d}\mathbf{r}_2. \tag{10}$$

To get rid of the $\mathbf{r}_{12}^{-1}$ factors, they were approximated by the

$$\frac{1}{\mathbf{r}_{12}} = \sum_{n=1}^{m} \omega_n \mathrm{e}^{-\kappa_n \mathbf{r}_{12}^2} \tag{11}$$

expansion proposed by Hackbusch et al. [55], where ω_n and κ_n are, respectively, the weight and exponent of the nth exponential term in the expansion, and m is the number of terms. The exponentials in the above expansion can also be regarded as ellipsoidal Gaussians, that is, if the

$$\boldsymbol{\Lambda}_n = \begin{pmatrix} \kappa_n & 0 & 0 & -\kappa_n & 0 & 0 \\ 0 & \kappa_n & 0 & 0 & -\kappa_n & 0 \\ 0 & 0 & \kappa_n & 0 & 0 & -\kappa_n \\ -\kappa_n & 0 & 0 & \kappa_n & 0 & 0 \\ 0 & -\kappa_n & 0 & 0 & \kappa_n & 0 \\ 0 & 0 & -\kappa_n & 0 & 0 & \kappa_n \end{pmatrix} \tag{12}$$

6×6 matrix is introduced, the exponent of the nth exponential function can be expressed as $-\mathbf{r}^\dagger \boldsymbol{\Lambda}_n \mathbf{r}$, and finally operator $\mathbf{r}_{12}^{-1}$ is approximated as

$$\frac{1}{\mathbf{r}_{12}} = \sum_{n=1}^{m} \omega_n \mathrm{e}^{-\mathbf{r}^\dagger \boldsymbol{\Lambda}_n \mathbf{r}}. \tag{13}$$

Substituting this into Eq. (10), utilizing the properties of the exponential function, an $(ss|ss)$-type integral can be calculated using the

$$\sum_{n=1}^{m} \omega_n \int \mathrm{e}^{-(\mathbf{r}^\dagger \boldsymbol{\Omega}_n \mathbf{r} - \mathbf{J}^\dagger \mathbf{r}) - c} \mathrm{d}\mathbf{r} = \sum_{n=1}^{m} \omega_n S_n \tag{14}$$

formula, where $\boldsymbol{\Omega}_n = \boldsymbol{\Lambda}_n + \boldsymbol{\Gamma}$, and the S_n integrals are evaluated according to the

$$S_n = \int \mathrm{e}^{-(\mathbf{r}^\dagger \boldsymbol{\Omega}_n \mathbf{r} - \mathbf{J}^\dagger \mathbf{r}) - c} \mathrm{d}\mathbf{r} = \sqrt{\frac{\pi^6}{\det \boldsymbol{\Omega}_n}} \mathrm{e}^{\frac{1}{4} \mathbf{J}^\dagger \boldsymbol{\Omega}_n^{-1} \mathbf{J} - c} \tag{15}$$

analytic expression.

Two-electron integrals including functions of higher angular momentum quantum numbers can be derived by differentiating Eq. (15) with respect to the components of vector $\mathbf{J}$. Taking into account Eq. (3) and the above derivation a $(p_z s|ss)$, two-electron integral can be calculated as

$$(p_z s|ss) = \sum_{n=1}^{m} \omega_n \int (z_1 - A_z) \mathrm{e}^{-(\mathbf{r}^\dagger \boldsymbol{\Omega}_n \mathbf{r} - \mathbf{J}^\dagger \mathbf{r}) - c} \mathrm{d}\mathbf{r}. \tag{16}$$

If we differentiate the corresponding $(ss|ss)$ integral with respect to J_3, we arrive at the

$$\begin{aligned} \frac{\partial S_n}{\partial J_3} = \int z_1 \mathrm{e}^{-(\mathbf{r}^\dagger \boldsymbol{\Omega}_n \mathbf{r} - \mathbf{J}^\dagger \mathbf{r}) - c} \mathrm{d}\mathbf{r} = \frac{1}{2} \Big[&\left(\boldsymbol{\Omega}^{-1}\right)_{13} J_1 + \left(\boldsymbol{\Omega}^{-1}\right)_{23} J_2 \\ + &\left(\boldsymbol{\Omega}^{-1}\right)_{33} J_3 + \left(\boldsymbol{\Omega}^{-1}\right)_{34} J_4 + \left(\boldsymbol{\Omega}^{-1}\right)_{35} J_5 \\ + &\left(\boldsymbol{\Omega}^{-1}\right)_{36} J_6 \Big] S_n = S_n^{z_1} \end{aligned} \tag{17}$$

expression, where $(\boldsymbol{\Omega}^{-1})_{ij}$ is the corresponding element of the inverse of matrix $\boldsymbol{\Omega}$, and obviously the integrals in the above expansion can be evaluated as

$$\begin{aligned} \int (z_1 - A_z) \mathrm{e}^{-(\mathbf{r}^\dagger \boldsymbol{\Omega}_n \mathbf{r} - \mathbf{J}^\dagger \mathbf{r}) - c} \mathrm{d}\mathbf{r} &= \left(\frac{\partial}{\partial J_3} - A_z \right) S_n \\ &= S_n^{z_1} - A_z S_n. \end{aligned} \tag{18}$$

It is easy to see that similar expressions apply to the $(p_x s|ss)$ and $(p_y s|ss)$ integrals which can be derived by the differentiation of the $(ss|ss)$ integral with respect to J_1 and J_2, respectively.

Following this procedure, expressions can be derived for integrals with more p functions and also for higher angular momentum functions. For instance, to derive working equations for the evaluation of the $(p_z p_z|ss)$ integrals, the second derivative of S_n is calculated with respect to J_3 as

$$\begin{aligned} \frac{\partial^2 S_n}{\partial J_3^2} = \frac{\partial S_n^{z_1}}{\partial J_3} &= \int z_1^2 \mathrm{e}^{-(\mathbf{r}^\dagger \boldsymbol{\Omega}_n \mathbf{r} - \mathbf{J}^\dagger \mathbf{r}) - c} \mathrm{d}\mathbf{r} \\ &= \frac{1}{2} \left(\boldsymbol{\Omega}^{-1}\right)_{33} S_n + S_n^{z_1 z_1}. \end{aligned} \tag{19}$$

Utilizing this, the $(p_z p_z|ss)$ integral can be evaluated via the

$$\begin{aligned} (p_z p_z|ss) &= \left(\frac{\partial}{\partial J_3} - A_z \right) \left(\frac{\partial}{\partial J_3} - B_z \right) S_n \\ &= S_n^{z_1 z_1} - S_n^{z_1} A_z S_n - S_n^{z_1} B_z S_n + A_z B_z S_n \end{aligned} \tag{20}$$

Table 8 Total HF energies in E_h calculated with the optimized BF basis sets

Molecule (bond)	Basis set		
	6-31G–BF(p)	6-31G–BF(s)	6-31G–EBF(s)
Methane (C–H)		−40.20781	−40.20865
Ethane (C–C)		−79.24655	−79.24929
Ammonia (N–H)	−56.20630	−56.20239	−56.20503
Water (O–H)	−76.04319	−76.01726	−76.01928
Methylamine (N–C)	−95.23023	−95.22698	−95.22693
Methanol (O–C)	−115.06603	−115.04191	−115.04721

The leftmost column shows the name of the molecule used in the optimizations and the bond type whose BFs were optimized for the molecule

Table 9 HF total energies in E_h for various organic molecules using BF basis sets

Molecule	Basis set			
	6-31G–BF(*p*)	6-31G–BF(*s*)	6-31G–EBF(*s*)	cc-pVTZ
2-Aminoethanol	−170.10944	−170.08562	−170.08956	−170.14462
4-Aminobutan-2-ol	−287.23088	−287.20761	−287.21697	−287.28420
Cyclopentane		−195.19168	−195.19690	−195.22775
Ethane-1,2-diamine	−189.30786	−189.30331	−189.31327	−189.34628
Ethanol	−154.11357	−154.09108	−154.09459	−154.14173
Ethyldimethylamine	−212.33961	−212.18074	−212.23173	−212.37917
Methoxyethane	−193.14374	−193.12196	−193.11781	−193.17841
Pentane		−196.36954	−196.37901	−196.40166
Propane-1,2-diol	−268.02891	−267.98610	−267.98956	−268.07842
Propane-2-amine	−173.32185	−173.31926	−173.32636	−173.35336
Mean absolute error	0.039	0.068	0.058	

expression. Analogously, for integrals $(p_z s|p_z s)$, $(p_z p_z|p_z s)$, and $(p_z p_z|p_z p_z)$, we arrive at the

$$(p_z s|p_z s) = \left(\frac{\partial}{\partial J_3} - A_z\right)\left(\frac{\partial}{\partial J_6} - C_z\right) S_n \tag{21}$$

$$(p_z p_z|p_z s) = \left(\frac{\partial}{\partial J_3} - A_z\right)\left(\frac{\partial}{\partial J_3} - B_z\right)\left(\frac{\partial}{\partial J_6} - C_z\right) S_n \tag{22}$$

$$(p_z p_z|p_z p_z) = \left(\frac{\partial}{\partial J_3} - A_z\right)\left(\frac{\partial}{\partial J_3} - B_z\right)\left(\frac{\partial}{\partial J_6} - C_z\right)\left(\frac{\partial}{\partial J_6} - D_z\right) S_n \tag{23}$$

formulas. For other Cartesian components, the corresponding components of vector **J** and the appropriate nuclear centers should be considered.

We have derived and coded the analytical formulas for the $(ss|ss)$, $(ps|ss)$, $(ps|ps)$, $(pp|ss)$, $(pp|ps)$, and $(pp|pp)$ integrals. For the approximation of $\mathbf{r}_{12}^{-1}$, simply the largest expansion with $m = 51$ proposed by Hackbusch and co-workers was taken. Probably this expansion is far too long for our purposes, but no attempt has been made to find the optimal expansion and to increase the efficiency of the integral calculation. As we tested for integrals over conventional Gaussians, the error in the final total energies introduced by this approximation is negligible. We also note that the above algorithm is only executed if at least one of the four functions in the integral is an ellipsoidal Gaussian. Other integrals are still evaluated with the conventional algorithms.

3.2 Determination of the exponent matrix

The processing of conventional Gaussian BFs is trivial, however, that for the EBFs is a bit more complicated. In addition to the molecular integrals, the determination of exponent matrix $\boldsymbol{\alpha}$ also requires special treatment. In order to avoid the coordinate-system dependence and to be consistent with the chemical picture, the ellipsoidal Gaussians must be stretched in the direction of the chemical bond. The corresponding exponent matrix can be constructed as follows.

A specific coordinate system is defined for each ellipsoidal Gaussian. Its origin is the center of the Gaussian, hereafter denoted by **E**, while its z-axis points in the direction of the bond. In the bond-specific coordinate system, the exponent matrix denoted by $\overline{\boldsymbol{\alpha}}$ takes the

$$\overline{\boldsymbol{\alpha}} = \begin{pmatrix} \alpha & 0 & 0 \\ 0 & \alpha & 0 \\ 0 & 0 & \alpha\varepsilon \end{pmatrix} \tag{24}$$

form, where α will be referred to as the exponent and ε is the stretch factor. Thus, in these coordinate systems, the general ellipsoidal Gaussian is equivalent to a diagonal one, that is, reduces to Eq. (1) with $\alpha_1 = \alpha_2 = \alpha$ and $\alpha_3 = \alpha\varepsilon$. To obtain the parameters of the ellipsoidal Gaussian in laboratory coordinate system, the

$$\mathrm{e}^{-\overline{\mathbf{r}}^\dagger \overline{\boldsymbol{\alpha}} \overline{\mathbf{r}}} \rightarrow \mathrm{e}^{-(\mathbf{r}-\mathbf{E})^\dagger \boldsymbol{\alpha} (\mathbf{r}-\mathbf{E})} \tag{25}$$

transformation is required, where $\overline{\mathbf{r}}$ is a vector in the bond-specific coordinate systems. **If U** is the rotation matrix transforming the coordinate systems into each other, the final exponent matrix is calculated as $\boldsymbol{\alpha} = \mathbf{U}^\dagger \overline{\boldsymbol{\alpha}} \mathbf{U}$.

In contrast to simple Gaussian BFs, which have two parameters, the exponent and the position, in the case of EBFs, there are three adjustable parameters: the exponent, the position, and the stretch factor. These parameters were varied in the basis set optimizations.

3.3 Numerical results and discussion

In this initial study, only s-type EBFs were considered, and the EBF basis sets were optimized for single bonds. We

sought to answer two questions: (1) To what extent does the energy decrease if the conventional BFs are replaced by EBFs, and (2) can conventional *p*-type BFs be replaced by *s*-type EBFs, e.g., for heteroatom–carbon bonds, in order to further reduce the average angular momentum quantum number of the basis functions? To that end, for conventional BF basis sets containing only *s* functions, EBF sets with the same number of *s*-type EBFs were optimized. For the BF bases including also *p* functions, in the corresponding EBF basis set, each *p* shell was replaced by three *s*-type EBFs. For comparison, in the latter case, we also constructed a GTO BF basis with the same number of *s*-type BFs. The parameters of the functions were optimized as described in Sect. 2.

The results of the optimizations are summarized in Table 8, where 6-31G–BF(*p*) refers to the original BF basis sets containing *p* functions, if any, under 6-31G–BF(*s*), the results obtained with BF basis sets including exclusively *s*-type GTO BFs (the original BF basis if it does not contain *p* functions, and the new GTO BF basis optimized for this purpose otherwise) are presented, whereas 6-31G–EBF(*s*) stands for the EBF basis sets. As can be seen from the table, due to the variation of the additional parameter of the EGTOs, the stretch factor, for molecules where all the parameters of the basis sets are optimized at a time (methane, ammonia, and water), the energy computed with the EBF sets is lower by less than a mE_h per bond with respect to that obtained with the corresponding BF basis set including only *s* functions. For the remaining molecules, such as ethane, methylamine, and methanol, where only the EBFs of the C–C, N–C, and O–C bonds are optimized, respectively, and other EBFs, just as the AO basis, are taken from methane, ammonia, and water, the energy either decreases (ethane and methanol) or practically does not change (methylamine). Concerning the difference with respect to the basis sets including *p* functions, the results suggest that the accuracy of the latter cannot be approached if the *p* functions are replaced by the EGTOs.

To further study the performance of the various BF basis sets, we compiled a test set of ten molecules including hydrocarbons, alcohols, ethers, and various amines. The results are presented in Table 9, where the cc-pVTZ energies are used again as reference values, and the same notations are employed as in Table 8.

The trends are similar to those we observed for the molecules used in the basis set optimizations. In average, EBFs decrease the energy by 10 mE_h, and thus, the error by 15 % with respect to purely *s*-type GTO BF basis sets, which correspond to sub-mE_h decrease per bond. The energy decrease is consistent, and the only exception is methoxyethane, where a slight increase can be noticed. Compared to the BF sets including *p* functions, the EBF bases are still not flexible enough to defeat them, but the error is considerably smaller than with the simple GTO BF bases. Nevertheless, these results prove the potential of EGTOs and also suggest that it is worthwhile testing the performance of *p*-type EBFs in future.

4 Conclusions and outlook

In this paper, new types of BF basis sets have been tested. First, we considered conventional GTO BFs, but optimized the center of each BF shell separately. Our results show that using these BF sets, HF and DFT energies of similar quality can be achieved as with conventional AO basis sets including polarization functions, while the number of basis functions is somewhat smaller and the angular momentum quantum numbers of the basis functions are in average significantly lower resulting in less expensive molecular integrals. Second, we tested ellipsoidal GTO BFs. The results show that *s*-type EBFs decrease the error by about 15 % with respect to basis sets with simple GTO BFs. All in all, for total energies, the performance of the new types of BF basis sets proposed here is encouraging, and further studies will be required to test them for other types of chemical bonds and with larger AO basis sets.

Further investigations are also desirable to test the performance of our approach for energy differences, such as reaction energies or barrier heights. However, here we must also tackle with the general problems of the BF methodology. Though the proposed scheme for the positioning of the BFs guarantees smooth potential energy surfaces (PESs) and unbiased results for the energies of most reactions, for particular reactions and transition states, the situation is ambiguous. The simplest example is probably the ring opening of cyclopropane to form propane, where we have three C–C bonds in the educt, while only two ones in the product. If the entire PES along the reaction coordinate is computed, the BFs originally located on the splitting bond will migrate close to the middle carbon atom of propane. This is not elegant, but more importantly, the reaction energy will be different as if it was directly calculated from the total energies of the reactant and the product. A possible alternative approach, which resolves this problem but partly retains the advantages of BFs, is to use atom-centered ellipsoidal Gaussian functions stretched in the direction of the bonds with geometry-dependent stretch factors. If the latter are determined by an algorithm which guarantees that they converge to unity upon bond dissociation, the ellipsoidal Gaussians will reduce to simple atom-centered spherical Gaussians. The calculation of energy differences and the development of atom-centered ellipsoidal Gaussian basis sets will be the subject of subsequent papers.

Acknowledgments M.K. expresses his gratitude to Professor Surján for mentoring him at the early stages of his career and for continuous support. J.C. acknowledges the financial support of the János Bolyai fellowship of the Hungarian Academy of Sciences. The authors gratefully acknowledge the computing time granted on the Hungarian HPC Infrastructure at NIIF Institute, Hungary.

References

1. Hariharan PC, Pople JA (1973) Theor Chim Acta 28:213
2. Krishnan R, Binkley JS, Seeger R, Pople JA (1980) J Chem Phys 72:650
3. Hehre WJ, Ditchfield R, Pople JA (1972) J Chem Phys 56:2257
4. Dill JD, Pople JA (1975) J Chem Phys 62:2921
5. Francl MM, Petro WJ, Hehre WJ, Binkley JS, Gordon MS, DeFrees DJ, Pople JA (1982) J Chem Phys 77:3654
6. Binkley JS, Pople JA, Hehre WJ (1980) J Am Chem Soc 102:939
7. Schäfer A, Horn H, Ahlrichs R (1992) J Chem Phys 97:2571
8. Schäfer A, Huber C, Ahlrichs R (1994) J Chem Phys 100:5829
9. Weigend F, Ahlrichs R (2005) Phys Chem Chem Phys 7:3297
10. Dunning TH Jr (1989) J Chem Phys 90:1007
11. Kendall RA, Dunning TH Jr, Harrison RJ (1992) J Chem Phys 96:6796
12. Woon DE, Dunning TH Jr (1993) J Chem Phys 98:1358
13. Peterson KA, Dunning TH Jr (2002) J Chem Phys 117:10548
14. Boys SF (1950) Proc R Soc Lond Ser A 200:542
15. Davidson ER, Feller D (1986) Chem Rev 86:681
16. Dunning TH, Peterson KA, Woon DE (1998) In: Schleyer PR, Jorgensen WL, Schaefer III HF, Schreiner PR, Thiel W (eds) Encyclopedia of computational chemistry. Wiley, New York, p 88
17. Jensen F (2013) Wiley Interdiscip Rev Comput Mol Sci 3:273
18. Preuss H (1965) Z Naturforsch A 20:21
19. Frost AA (1967) J Chem Phys 47:3707
20. Huber H (1979) Chem Phys Lett 62:95
21. Huber H (1980) Chem Phys Lett 70:353
22. Huber H (1980) Theor Chim Acta 55:117
23. Huber H (1981) J Mol Struct (Theochem) 76:277
24. Helgaker T, Almlöf J (1988) J Chem Phys 89:4889
25. Rothenberg S, Schaefer HF III (1971) J Chem Phys 54:2764
26. Neisius D, Verhaegen G (1979) Chem Phys Lett 66:358
27. Neisius D, Verhaegen G (1981) Chem Phys Lett 78:147
28. Martin JML, Francois JP, Gijbels R (1989) J Comput Chem 10:152
29. Bauschlicher CW Jr, Partridge H (1998) J Chem Phys 109:4707
30. Bruun J, Helgaker T, Jensen F (2004) Mol Phys 102:2559
31. Matio E, Kobus J, Styszyński J (2006) Chem Phys 321:277
32. Browne JC, Poshusta RD (1962) J Chem Phys 36:1933
33. Katriel J (1969) Chem Phys Lett 3:624
34. Katriel J, Adam G (1970) J Chem Phys 53:302
35. Bishop DM, Leclerc JC (1972) Mol Phys 24:979
36. Cohen D, Basch H (1976) Theor Chim Acta 42:199
37. Cohen D, Basch H (1978) Theor Chim Acta 50:263
38. Szalay Z, Surján PR (2008) J Math Chem 43:227
39. Preuss VH (1956) Z Naturforsch 11:823
40. Tasi G, Császár AG (2007) Chem Phys Lett 438:139
41. Nelder JA, Mead R (1965) Comput J 7:308
42. Kállay M, Rolik Z, Csontos J, Ladjánszki I, Szegedy L, Ladóczki B, Samu G MRCC, a quantum chemical program suite
43. Helgaker T, Gauss J, Jørgensen P, Olsen J (1997) J Chem Phys 106:6430
44. Huber KP, Herzberg G (1979) Molecular spectra and molecular structure. IV. Constants of diatomic molecules. Van Nostrand Reinhold, New York
45. Iijima T, Jimbo H, Taguchi M (1986) J Mol Struct 144:381
46. Lees RM, Baker JG (1968) J Phys Chem 48:5299
47. Harmony MD, Laurie VW, Kuczkowski RL, Schwendeman RH, Ramsay DA, Lovas FJ, Lafferty WJ, Maki AG (1979) J Phys Chem Ref Data 8:619
48. Gurvich LV, Veyts IV, Alock CB (1992) Thermodynamic properties of individual substances, 4th edn. Hemisphere, New York
49. Becke AD (1993) J Chem Phys 98:5648
50. Lee C, Yang W, Parr RG (1988) Phys Rev B 37:785
51. Zhao Y, Truhlar DG (2006) Theor Chem Acc 120:215
52. Dunning TH Jr (1970) J Chem Phys 53:2829
53. Frisch MJ, Trucks GW, Schlegel HB, Scuseria GE, Robb MA, Cheeseman JR, Scalmani G, Barone V, Mennucci B, Petersson GA, Nakatsuji H, Caricato M, Li X, Hratchian HP, Izmaylov AF, Bloino J, Zheng G, Sonnenberg JL, Hada M, Ehara M, Toyota K, Fukuda R, Hasegawa J, Ishida M, Nakajima T, Honda Y, Kitao O, Nakai H, Vreven T, Montgomery JA Jr, Peralta JE, Ogliaro F, Bearpark M, Heyd JJ, Brothers E, Kudin KN, Staroverov VN, Keith T, Kobayashi R, Normand J, Raghavachari K, Rendell A, Burant JC, Iyengar SS, Tomasi J, Cossi M, Rega N, Millam JM, Klene M, Knox JE, Cross JB, Bakken V, Adamo C, Jaramillo J, Gomperts R, Stratmann RE, Yazyev O, Austin AJ, Cammi R, Pomelli C, Ochterski JW, Martin RL, Morokuma K, Zakrzewski VG, Voth GA, Salvador P, Dannenberg JJ, Dapprich S, Daniels AD, Farkas O, Foresman JB, Ortiz JV, Cioslowski J, Fox DJ (2010) Gaussian 09, revision B.01. Gaussian, Wallingford
54. Becke AD (1988) J Chem Phys 88:2547
55. Takatsuka A, Ten-no S, Hackbusch W (2008) J Chem Phys 129:044112
56. Rolik Z, Szegedy L, Ladjánszki I, Ladóczki B, Kállay M (2013) J Chem Phys 139:094105

Theor Chem Acc (2015) 134:118
DOI 10.1007/s00214-015-1718-3

REGULAR ARTICLE

Excitation energies from time-dependent generalized valence bond method

Koushik Chatterjee[1] · **Katarzyna Pernal**[2]

Received: 1 July 2015 / Accepted: 1 September 2015 / Published online: 18 September 2015

Abstract A generalized valence bond perfect-pairing (GVB-PP) wavefunction has been extensively used in computational chemistry methods due to its multiconfigurational character, which captures in an inexpensive way static electron correlation. GVB-PP has been mostly applied to ground states and not much is known about its performance in predicting electronic spectra of molecules. Here, we present the formalism based on the time-dependent linear response theory which provides excitation energies from the GVB-PP ground-state wavefunction. The accuracy of the excitation energy dissociation curves parallels that of the TD-HF method around ground-state equilibrium geometries of the investigated molecules. For stretched-bond molecules, when TD-HF breaks down, the proposed TD-GVB method remains reliable. TD-GVB may therefore serve as a useful and inexpensive tool for exploring potential energy surfaces of excited states of molecules.

Keywords Generalized valence bond · Time-dependent linear response · Excitation energy

1 Introduction

Valence bond (VB) theory has been developed since the early days of quantum chemistry in parallel with molecular orbital theory [1]. The VB is particularly well suited for describing bond breaking or forming processes since the valence bond wavefunction has a proper form in the dissociation limit [2]. Generalized valence bond (GVB) method is a variational counterpart to VB in which orbitals are optimized self-consistently [3–6]. In the GVB, wavefunction orbitals comprising a breaking bond form a GVB pair

$$\psi_{\text{pair}}^{\text{GVB}} = [\phi_1(1)\phi_2(2) + \phi_2(1)\phi_1(2)](\alpha\beta - \beta\alpha), \tag{1}$$

where the orbitals ϕ_a and ϕ_b are overlapping. The remaining electrons are treated at the Hartree–Fock (HF) level. A special case of the GVB wavefunction is obtained if all electron pairs in a molecule are described by distinct, strongly orthogonal GVB functions formed from the (orthogonal) natural orbitals [6, 7]

$$\psi_{\text{pair}}^{\text{GVB-PP}} = \left[c_1\,\varphi_1(1)\varphi_1(2) + c_2\,\varphi_2(1)\varphi_2(2)\right](\alpha\beta - \beta\alpha). \tag{2}$$

A method based on the ansatz for the wavefunction comprised of the antisymmetrized product of the GVB pairs (2) is known as perfect-pairing GVB (GVB-PP) [3, 6]. Unlike in the full GVB wavefunction, which allows all possible spin couplings of different orbitals, GVB-PP is more restrictive, allowing only perfect-pairing (singlet) coupling of the spins. The immediate advantage of this restriction is a gain in computational efficiency of the GVB-PP optimization compared to the full GVB ansatz. The GVB-PP wavefunction retains a desired property of the GVB approximation, namely it accounts for a left–right correlation between electrons in each pair and allows for bond breaking.

The GVB-PP wavefunction can also be derived from of the strongly orthogonal geminals theory as a special case of the APSG (antisymmetrized product of strongly orthogonal geminal) ansatz [7–10] if each APSG geminal is restricted to be expanded in a two-dimensional subset of orbitals.

Published as part of the special collection of articles "Festschrift in honour of P. R. Surjan".

✉ Katarzyna Pernal
pernalk@gmail.com

[1] Faculty of Chemistry, Lodz University of Technology, ul. Zeromskiego 116, 90-924 Lodz, Poland

[2] Institute of Physics, Lodz University of Technology, ul. Wolczanska 219, 90-924 Lodz, Poland

Interestingly, recently the GVB-PP approximation has been reinvented within the natural orbital functional theory [11, 12]. Namely, one of the recently proposed natural orbital functionals—PNOF5 [13]—obtained by reconstructing two-electron reduced density matrix in terms of the one-electron reduced density matrix, has been shown to be equivalent to the GVB-PP approximation [14]. Fully variational PNOF5 calculations have proved usefulness of the method in predicting ground-state energies of molecules of diverse and challenging electronic structures [13, 15].

GVB or GVB-PP approximations have been mostly employed to describe ground states of molecules. However, since the methods are variational and they are based on a wavefunction ansatz, then excited states calculations should be also possible in a similar fashion as it is done for the multiconfiguration self-consistent field methods. However, application of the GVB-PP method to excited states either by performing variational calculations or by employing the time-dependent linear response formalism has not been explored so far. The aim of this paper is to fill this gap. We present a linear response GVB-PP formalism leading to obtaining singlet excitation energies and discuss its performance by presenting excitation energy curves for a few small molecules.

2 Theory

The reference GVB perfect-pairing (GVB-PP) wavefunction can be seen as a special case of the antisymmetrized product of strongly orthogonal geminal (APSG) ansatz if each geminal is given by only two orbitals [14]. For a closed-shell N-electron system, the GVB-PP wavefunction is therefore given by the antisymmetrized product of $N/2$ geminals:

$$\Psi^{\mathrm{GVB-PP}}(\mathbf{x}_1,\ldots,\mathbf{x}_N) = \hat{A}\prod_{P=1}^{N/2}\psi_P(\mathbf{x}_{2P-1},\mathbf{x}_{2P}), \tag{3}$$

where each electron pair is singlet spin coupled and each geminal ψ_P is restricted to be given in terms of two orbitals only, i.e.,

$$\begin{aligned}\forall_{P\le N/2}\quad \psi_P^{\mathrm{GVB-PP}}(\mathbf{x}_1,\mathbf{x}_2) = 2^{-1/2}[&c_{P_1}\,\varphi_{P_1}(\mathbf{r}_1)\varphi_{P_1}(\mathbf{r}_2)\\ &+ c_{P_2}\,\varphi_{P_2}(\mathbf{r}_1)\varphi_{P_2}(\mathbf{r}_2)]\\ &\times[\alpha(1)\beta(2)-\beta(1)\alpha(2)].\end{aligned} \tag{4}$$

In the expression above, the orbitals $\{\varphi_p(\mathbf{r})\}$ are the natural orbitals associated with the wavefunction (3), i.e., they diagonalize a corresponding one-electron reduced density matrix (1-RDM) γ

$$\gamma(\mathbf{x},\mathbf{x}') = \sum_p n_p\,\varphi_p(\mathbf{r}')^*\varphi_p(\mathbf{r})\,[\alpha(1')^*\alpha(1)+\beta(1')^*\beta(1)], \tag{5}$$

so they are orthonormal. Squares of the coefficients $\{c_p\}$ are equal to the pertinent natural spinorbital occupation numbers $\{n_p\}$

$$\forall_p\quad n_p = c_p^2 \tag{6}$$

$$\forall_p\quad 0\le n_p\le 1. \tag{7}$$

Geminals in the GVB-PP theory are restricted to be strongly orthogonal

$$\forall_{P\neq Q},\ \forall_{\mathbf{x}_1,\mathbf{x}_1'}\quad \int \psi_P^{\mathrm{GVB-PP}}(\mathbf{x}_1,\mathbf{x}_2)\psi_Q^{\mathrm{GVB-PP}}(\mathbf{x}_1',\mathbf{x}_2)\,\mathrm{d}\mathbf{x}_2 = 0, \tag{8}$$

which implies that sets of orbitals belonging to individual geminals are disjoint, i.e., each orbital belongs to only one geminal [16]. Normalization of each geminal implies that two occupation numbers, Eq. (6), of orbitals belonging to a given geminal sum up to one

$$\forall_{P\le N/2}\quad (c_{P_1})^2 + (c_{P_2})^2 = 1. \tag{9}$$

The GVB-PP wavefunction is the simplest wavefunction of the multiconfigurational character, which is capable of describing bond dissociation, but by construction it misses a large part of the dynamic correlation. Consequently, unlike a more general APSG ansatz, GVB-PP is not exact (not equivalent to the full CI wavefunction) even for the simplest case of two-electron systems unless one goes to the strong correlation limit. For example, for the hydrogen molecule the APSG and GVB-PP wavefunctions become identical in the dissociation limit (we will come back to this issue when discussing the results for H_2).

The ground-state GVB-PP energy follows from the optimization of the simple expression reading [9, 14]

$$\begin{aligned}E^{\mathrm{GVB-PP}} = 2\sum_P^{N/2}\sum_{p\in P}c_p^2 h_{pp} &+ \sum_P^{N/2}\sum_{p,q\in P}c_p c_q\langle\varphi_p\varphi_p|\varphi_q\varphi_q\rangle\\ &+\sum_{P\neq Q}^{N/2}\sum_{p\in P,q\in Q}c_p^2 c_q^2\langle\varphi_p\varphi_q||\varphi_p\varphi_q\rangle,\end{aligned} \tag{10}$$

where $\{h_{pp}\}$ are matrix elements of the one-electron Hamiltonian in the natural orbital representation, and two-electron integrals are defined as

$$\langle\varphi_p\varphi_q|\varphi_r\varphi_s\rangle = \int\int \varphi_p(\mathbf{r}_1)^*\varphi_q(\mathbf{r}_2)^*|\mathbf{r}_1-\mathbf{r}_2|^{-1}\varphi_r(\mathbf{r}_1)\varphi_s(\mathbf{r}_2)\,\mathrm{d}\mathbf{r}_1\mathrm{d}\mathbf{r}_2 \tag{11}$$

and

$$\langle\varphi_p\varphi_q||\varphi_p\varphi_q\rangle = 2\langle\varphi_p\varphi_q|\varphi_p\varphi_q\rangle - \langle\varphi_p\varphi_q|\varphi_q\varphi_p\rangle. \tag{12}$$

A notation "$p\in P$" adopted in Eq. (10) and below means that a natural orbital φ_p is assigned to a Pth geminal, which

in turn implies that the corresponding coefficient c_p is, in general, greater than zero. At first sight, the expression for the energy (10) looks identical to its APSG counterpart, but one should keep in mind that orbitals in GVB-PP are paired [cf. Eq. (4)] and the set of conditions given in Eq. (9) must be imposed while optimizing the functional (10). Clearly therefore, the APSG energy is a lower bound to the GVB-PP energy and both are bounded from below by the exact ground-state value,

$$E_0^{\text{exact}} \leq E_0^{\text{APSG}} \leq E_0^{\text{GVB-PP}}. \tag{13}$$

There is one significant computational advantage of optimizing the GVB-PP energy functional rather than that of the APSG. In the latter, all natural orbitals have nonzero occupation numbers, whereas in the former, only N orbitals are fractionally occupied and the rest of orbitals forms a set of virtual (unoccupied) orbitals. A need to optimize all (often very weakly occupied) orbitals in the APSG approach leads to a slowly converging optimization problem. Optimization of the GVB-PP energy, on the other hand, is much more efficient (orbitals which are very weakly occupied in APSG are virtual orbitals in GVB and have no contribution to the energy).

GVB-PP method has been applied mostly to description of ground states of molecules although, in principle, one can also converge the GVB-PP energy to a selected excited state. A time-dependent linear response theory approach, which allows one to find a number of excitation energies in a single calculation, has not been exploited in the context of the GVB-PP so far. Recently, we have derived time-dependent linear response equations for the APSG wavefunction and applied the resulting method to computing APSG excitation energies [17, 18]. Similar equations can be immediately written for the GVB-PP ansatz by repeating derivation presented in Ref. [18]. The derivation starts by writing the quantum action integral, A, for the time-dependent GVB-PP wavefunction [Eq. (3)]

$$\begin{aligned} A &= \int_0^T \left\langle \Psi^{\text{GVB-PP}}(t) | \hat{H}(t) - i\frac{\partial}{\partial t} | \Psi^{\text{GVB-PP}}(t) \right\rangle \mathrm{d}t \\ &= 2\sum_{P=1}^{N/2}\sum_{p\in P}\int_0^T c_p(t)^* c_p(t) h_{pp}(t)\mathrm{d}t \\ &\quad + \sum_{P=1}^{N/2}\sum_{p,q\in P}\int_0^T c_p(t)^* c_q(t)\, \langle \varphi_p(t)\varphi_p(t)|\varphi_q(t)\varphi_q(t)\rangle \mathrm{d}t \\ &\quad + \sum_{P\neq Q}^{N/2}\sum_{p\in P,q\in Q}\int_0^T |c_p(t)|^2 |c_q(t)|^2 \, \langle \varphi_p(t)\varphi_q(t)||\varphi_p(t)\varphi_q(t)\rangle \mathrm{d}t \\ &\quad - i\sum_{P=1}^{N/2}\sum_{p\in P}\int_0^T \left[c_p(t)^* \frac{\partial c_p(t)}{\partial t} + 2c_p(t)^* c_p(t) \left\langle \varphi_p(t) \frac{\partial \varphi_p(t)}{\partial t} \right\rangle \right] \mathrm{d}t, \end{aligned} \tag{14}$$

and assuming that a Hamiltonian $\hat{H}(t)$ is composed of the time-independent part and a time-dependent perturbation, namely $\hat{H}(t) = \hat{T} + \hat{V}_{\text{ee}} + \hat{V}_{\text{ext}} + \delta\hat{V}(t)$. Employing stationarity of the action to variations of the coefficients and orbitals leads to the following time-dependent equations

$$\frac{\delta A}{\delta c_p(t)} = 0, \tag{15}$$

$$\frac{\delta A}{\delta c_p(t)^*} = 0, \tag{16}$$

$$\left\langle \frac{\delta\left[A - \int_0^T \sum_{rs} \lambda_{rs}(t)\langle\varphi_r(t)|\varphi_s(t)\rangle\right]}{\delta\varphi_p(t)^*} \varphi_q(t)^* \right\rangle = 0, \tag{17}$$

$$\left\langle \frac{\delta\left[A - \int_0^T \sum_{rs} \lambda_{rs}(t)\langle\varphi_r(t)|\varphi_s(t)\rangle\right]}{\delta\varphi_p(t)} \varphi_q(t) \right\rangle = 0, \tag{18}$$

where the time-dependent Lagrange coefficients $\{\lambda_{rs}(t)\}$ have been introduced to keep the orbitals orthogonal. Equations. (15)–(18) are nonperturbative time-dependent equations for the expansion coefficients $\{c_p(t)\}$, the natural orbitals $\{\varphi_p(\mathbf{r},t)\}$ and their complex conjugates. Upon applying the standard linear response theory, the following eigenequation is obtained for the excitation energies $\{\omega_\nu\}$ (cf. Eq. (34) in Ref. [18])

$$\begin{pmatrix} \mathbf{A}^+\mathbf{A}^- + 2\mathbf{D}^+(\mathbf{D}^-)^T & \mathbf{A}^+\mathbf{D}^- + \mathbf{D}^+\mathbf{E}^- \\ 2\left[(\mathbf{D}^+)^T\mathbf{A}^- + \mathbf{E}^+(\mathbf{D}^-)^T\right] & 2(\mathbf{D}^+)^T\mathbf{D}^- + \mathbf{E}^+\mathbf{E}^- \end{pmatrix} \begin{pmatrix} \tilde{\mathbf{Y}} \\ \tilde{\mathbf{W}} \end{pmatrix}_\nu = \omega_\nu^2 \begin{pmatrix} \tilde{\mathbf{Y}} \\ \tilde{\mathbf{W}} \end{pmatrix}_\nu. \tag{19}$$

Elements of the matrices $\mathbf{A}^+, \mathbf{A}^-, \mathbf{D}^+, \mathbf{D}^-, \mathbf{E}^+, \mathbf{E}^-$ are given in terms of the stationary orbitals $\{\varphi_p(\mathbf{r})\}$ and the coefficients $\{c_p\}$ obtained by minimizing the GVB-PP energy expression given in Eq. (10). Definitions of the aforementioned matrices are provided in Refs. [18, 19], but for the convenience of the reader, we repeat them in the "Appendix."

By analogy with the TD-APSG method proposed in Ref. [18], we call the method for calculating GVB-PP excitation energies based on solving eigenequation (19) TD-GVB. From now on, it is assumed that stationary orbitals are in a descending order with respect to their occupancies. The first N orbitals are therefore occupied (assigned to N / 2 geminals) and starting from the index $N+1$ the orbitals are virtual ($\forall_{p>N} \quad c_p = 0$). In the linear response equations, only responses of the N coefficients and orbitals are considered. First-order perturbations of the orbitals have been expanded in the whole set of the

stationary orbitals (including both occupied and virtual orbitals), namely

$$\forall_{p\leq N} \quad \varphi_p^{(1)}(\mathbf{r},t) = \sum_q \delta U_{pq}(t)\varphi_q(\mathbf{r}). \tag{20}$$

In the TD-GVB equations, the elements of the vector $\tilde{\mathbf{Y}}$ are linked to perturbations $\delta U_{pq}(t)$ and the range of indices of the $\tilde{Y}_{pq}$ elements is as follows

$$^{\text{TD-GVB}}\tilde{Y}_{pq} \,:\, p = q+1,\ldots,M_{\text{basis}} \text{ and } q = 1,\ldots,N, \tag{21}$$

where M_{basis} stands for a number of basis set functions employed in calculations. The value of the $\tilde{Y}_{pq}$ element can be interpreted as a contribution to a given excitation from a transition either between two occupied orbitals ($p \leq N$) or between occupied and virtual orbitals ($p > N$) [20, 21]. Notice at this point that the dimensions of the analogous $\tilde{Y}$ vectors present in the TD-APSG and TD-HF equations are, respectively, higher and lower. The indices of the respective vectors change as follows

$$^{\text{TD-APSG}}\tilde{Y}_{pq} \,:\, p = q+1,\ldots,M_{\text{basis}} \text{ and } q = 1,\ldots,M_{\text{basis}}, \tag{22}$$

$$^{\text{TD-HF}}\tilde{Y}_{pq} \,:\, p = N/2+1,\ldots,M_{\text{basis}} \text{ and } q = 1,\ldots,N/2, \tag{23}$$

Thus, in TD-HF there are only occupied–virtual transitions, while in TD-APSG, all combinations are possible (also transitions between weakly occupied orbitals). The $\tilde{\mathbf{W}}$ component of the eigenvector in Eq. (19) comprises only N elements

$$^{\text{TD-GVB}}\tilde{W}_p \,:\, p = 1,\ldots,N, \tag{24}$$

and is related to responses of the coefficients $\{c_p\}$. In the TD-APSG method, on the other hand, the $\tilde{\mathbf{W}}$ vector is longer since it is composed of M_{basis} elements (also responses of the c_p coefficients pertaining to weakly occupied orbitals are taken into account)

$$^{\text{TD-APSG}}\tilde{W}_p \,:\, p = 1,\ldots,M_{\text{basis}}. \tag{25}$$

Since all orbitals in the HF approximation are either fully occupied ($n_p = 1$) or virtual ($n_p = 0$) the first-order responses of the occupation numbers are zero and eigenvectors in the TD-HF equations comprise only $\tilde{Y}$ components. It has been discussed in Ref. [18] that $\tilde{\mathbf{W}}$ in TD-APSG is nonzero only for excitations to totally symmetric states. Nonzero contributions from $\tilde{W}_p$ elements or $\tilde{Y}_{pq}$ when both $p,q > N/2$ (transition between two weakly occupied orbitals) indicates a double character of a given excitation [18, 22, 23].

It is worth mentioning that excitation energies can be also obtained from the GVB-PP ground-state wavefunction by employing the extended random phase approximation (ERPA) in the framework of the Rowe's equations of motion formalism [24] by [17]. ERPA equations are of the form

$$\mathbf{A}^+\mathbf{A}^-\,\tilde{\mathbf{Y}} = \omega^2\,\tilde{\mathbf{Y}}, \tag{26}$$

where the matrices $\mathbf{A}^+, \mathbf{A}^-$ are identical to the pertinent matrices present in the TD-GVB Equations (19). ERPA excitations are only different from their TD-GVB counterparts if the excitation in question is totally symmetric. For other symmetries, ERPA and TD-GVB solutions coincide by construction.

Finally, we want to point out to the connection of the TD-GVB equations with the recently formulated TD-PINO (time-dependent phase including natural orbital) formalism [25–27]. TD-PINO is an extension of the TD-RDMFT (time-dependent reduced density matrix functional theory) formalism to functionals depending not only on the natural occupation numbers and the natural spinorbitals but also on the phases of the latter. The phases are not generic features of the natural spinorbitals, i.e., they cannot be recovered from diagonalization of the one-electron density matrix. Rather they should be seen as additional variational parameters of the functional. Since it has been shown that the GVB-PP energy function (10) is identical to PNOF5—one of the phase including natural orbital functionals [14]—then, from the perspective of the natural orbital functional theory, the TD-GVB equations (19) can be seen as TD-PINO equations [18, 26] applied to the PNOF5 functional. In other words, the results discussed in the next section can be viewed as the TD-PINO (in the adiabatic approximation) excitation energies obtained by employing the PNOF5 functional.

3 Results

The results presented in this section have been obtained in symmetry adapted orbital basis sets. To stabilize the TD-APSG and TD-GVB equations and avoid obtaining occasionally spurious excitation energies (cf. a discussion in Ref. [18]), we have assumed the lower and upper cutoffs for sums of pairs of occupation numbers that are included in calculations for LiH and H_2O molecules. In other words, the accepted elements $\tilde{Y}_{pq}$ of the eigenvectors are such that $\forall_{p>q}\, 1\times 10^{-4} < n_p + n_q < 1.98$ .The matrices $\mathbf{A}^+, \mathbf{A}^-, \mathbf{D}^+, \mathbf{D}^-$ are truncated accordingly.

We begin with the $^1\Sigma_g^+$ and $^1\Sigma_u^+$ excitation energy curves for the hydrogen molecule presented in Figs. 1 and 2. They have been obtained by employing the TD-APSG, TD-GVB, and TD-HF methods in the aug-cc-pVTZ basis set [28]. The TD-APSG approach yields exact (in a given basis set) excitation energies since it is equivalent to the FCI method [22, 23] for two-electron systems. In the

dissociation limit ($R \to \infty$) the natural occupation numbers of the two occupied orbitals predicted by the GVB-PP method achieve the value 1/2. In this limit, all but two APSG orbitals become virtual (their occupation numbers go to zero). Thus, asymptotically the GVB-PP and APSG methods become equivalent, yielding the same ground-state density matrices and ground-state energies. In the TD-APSG, eigenequations contributions to a given excitation energy from transitions between virtual orbitals and from the elements of the $\tilde{\mathbf{W}}$ vector corresponding to virtual orbitals vanish. Consequently, in the dissociation limit one expects that excitation energies predicted by the TD-GVB and TD-APSG methods become equal, which is numerically confirmed by the results presented in Figs. 1 and 2. For shorter interatomic distances R, the TD-GVB curves also follow rather closely the exact TD-APSG curves. Around $R = 3.5$ a.u. the first $^1\Sigma_g^+$ excitation acquires a double character, which is manifested by large values of the $\tilde{W}_{11}$, $\tilde{W}_{22}$ elements in both TD-GVB and TD-APSG equations. The TD-HF excitation energies are very close to the exact values around the ground-state equilibrium geometry ($R = 1.4$ a.u.), but they deteriorate rapidly when the bond is stretched. This is mainly due to the erroneous one- and two-electron density matrices produced by the HF approach which miss static correlation. The first two HF orbitals are fully occupied instead of becoming half-occupied in the dissociation limit.

The conclusions drawn for the H_2 molecule can be extended to the lithium hydride molecule. In Figs. 3 and 4, we present $^1\Sigma^+$ and $^1\Pi$ excitation energy curves for this molecule obtained in the cc-pVTZ basis set [28]. The CCSD results delivered by the Dalton package [29] are used as references. The core electrons of the lithium atom do not play a role in low electronic excitations and LiH molecule can be considered a quasi two-electron system. Consequently, the TD-APSG excitations almost coincide with the reference CCSD values. In the dissociation limit, the bonding and antibonding natural orbitals, belonging to the same geminal, in both APSG and GVB-PP approaches are degenerated, i.e., their occupation numbers become equal. The other geminal includes a core orbital and it is localized on the lithium atom. The occupation numbers of the first two orbitals belonging to the core geminal are almost identical within the APSG and GVB-PP methods in the dissociation limit. For example at $R = 7$ a.u. the core geminal includes orbitals of the occupancies amounting to $n_1^{\text{core}} = 0.9986$ and $n_2^{\text{core}} = 1.356 \times 10^{-3}$ in GVB-PP and $n_1^{\text{core}} = 0.9986$ and $n_2^{\text{core}} = 1.360 \times 10^{-3}$ in APSG. Thus, in the dissociation limit, the one- and two-electron density matrices resulting from the APSG and GVB-PP wavefunctions possess the same structure and one expects that the

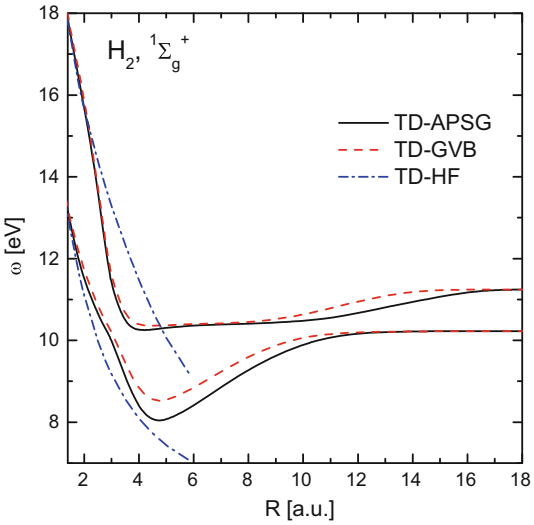

Fig. 1 Potential energy curves of the first two $^1\Sigma_g^+$ excited states for the dissociating H_2 molecule. *Solid lines*: TD-APSG, *dashed lines*: TD-GVB, and *dashed-dotted lines*: TD-HF results.

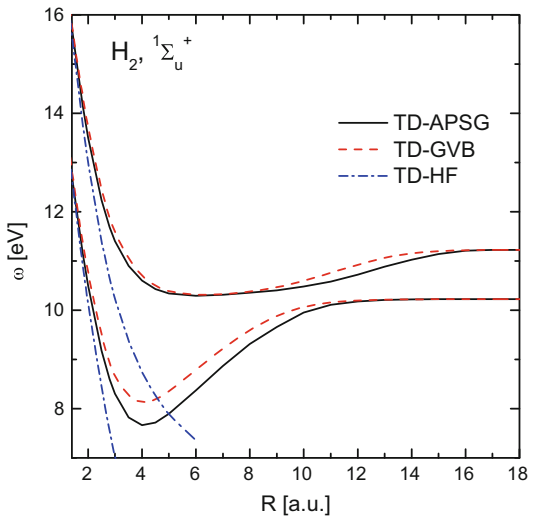

Fig. 2 Potential energy curves of the first two $^1\Sigma_u^+$ excited states for the dissociating H_2 molecule. *Solid lines*: TD-APSG, *dashed lines*: TD-GVB, and *dashed-dotted lines*: TD-HF results

corresponding time-dependent linear response equations would yield excitation energies of the similar accuracy. Figures 3 and 4 show that indeed for elongated bonds, the TD-GVB excitation energies tend to their TD-APSG counterparts. For shorter interatomic distances, the density matrices slightly differ and so do the excitation energies originating from the two methods. Deviations between the two methods stay within a few tenths of eV.

For water molecule, one observes qualitatively the same picture when comparing TD-GVB, TD-APSG,

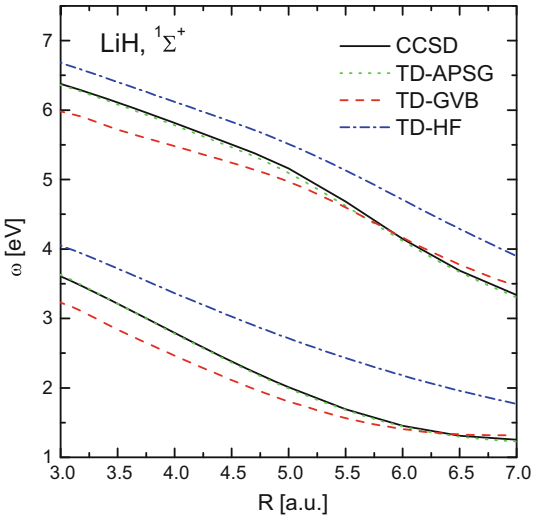

Fig. 3 Potential energy curves of the first two $^1\Sigma^+$ excited states for the dissociating LiH molecule. *Solid lines*: CCSD, *dotted lines*: TD-APSG, *dashed lines*: TD-GVB, and *dashed-dotted lines*: TD-HF results

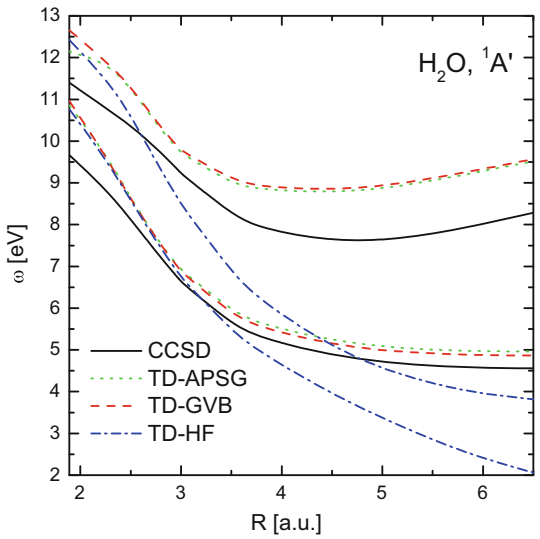

Fig. 5 Potential energy curves of the first two $^1A'$ excited states for H_2O molecule with one dissociating OH bond. *Solid lines*: CCSD, *dotted lines*: TD-APSG, *dashed lines*: TD-GVB, and *dashed-dotted lines*: TD-HF results

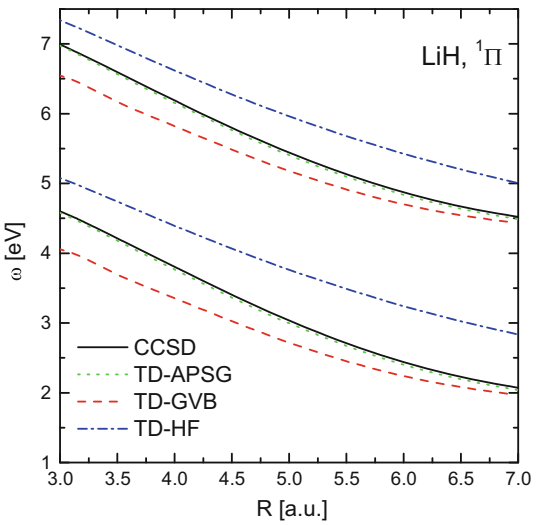

Fig. 4 Potential energy curves of the first two $^1\Pi$ excited states for the dissociating LiH molecule. Solid lines: CCSD, dotted lines: TD-APSG, dashed lines: TD-GVB, and dashed-dotted lines: TD-HF results

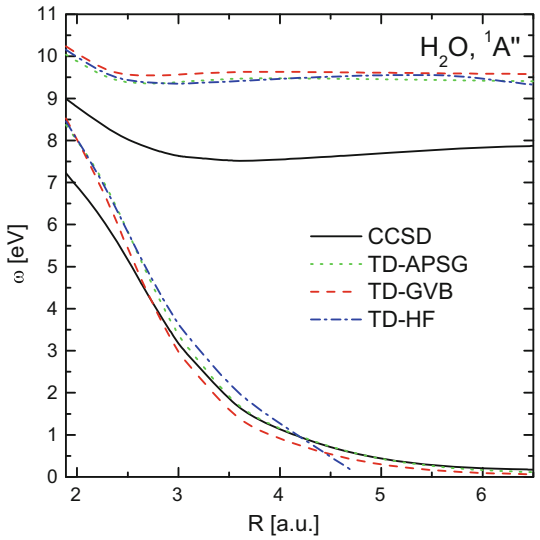

Fig. 6 Potential energy curves of the first two $^1A''$ excited states for H_2O molecule with one dissociating OH bond. *Solid lines*: CCSD, *dotted lines*: TD-APSG, *dashed lines*: TD-GVB, and *dashed-dotted lines*: TD-HF results

and TD-HF performance as for smaller molecules. Figures 5 and 6 present $^1A'$ and $^1A''$ excitation energies for H_2O (the basis set is taken from Ref. [30]) as functions of the length, R, of one of the OH bonds. Around the ground-state equilibrium geometry ($R = 1.8$ a.u.) all three linear response methods: TD-APSG, TD-GVB, and TD-HF yield similar values of excitation energies, which are in a substantial error (more than 1 eV) with respect to the CCSD counterparts. When the bond is stretched, the TD-APSG and TD-GVB approaches are more reliable than TD-HF in reproducing excitations which involve transitions from bonding or antibonding orbitals describing the breaking OH bond. This is understandable taking into account that both the APSG and GVB-PP methods are capable of describing bond

breaking so the ground state of the water molecule with the elongated bond is qualitatively correctly described unlike in the HF approximation. Thus, in the case of the first two $^1A'$ and the first $^1A''$ excitation energy the TD-HF curves break down when R increases, whereas the TD-GVB and TD-APSG curves stay together and they parallel the CCSD reference. The second $^1A''$ excitation, on the other hand, does not include contributions from the orbitals involved in bond breaking but from orbitals localized on the OH bond of a constant length. The TD-GVB method does not outperform the TD-HF approach for this excitation.

4 Conclusions

The purpose of this paper was to fill a gap and formulate time-dependent linear response equations for the GVB-PP wavefunction and to show performance of the resulting TD-GVB method in predicting excitation energies of molecules with stretched bonds. Although we have only investigated a few very small systems, the obtained results allow one to formulate general conclusions about quality of the TD-GVB excitations. Each geminal in the GVB-PP ansatz includes only two orbitals in its expansion as opposed to APSG geminals which comprise an unrestricted number of orbitals. Thus, the GVB-PP wavefunction (and the corresponding reduced density matrices) misses more dynamic correlation than its APSG counterpart. However, this seems to have little effect on the quality of excitation energies obtained from the linear response methods. Each excitation involves transitions from strongly occupied orbitals (bonding, antibonding, lone pairs) to weakly occupied orbitals (including antibonding orbitals). By confronting the structure of the eigenvectors in the TD-GVB equations [Eq. (21)] and in the TD-APSG [Eq. (22], it is clear that in both methods such transitions are accounted for. The main difference between the two approaches is that orbitals which are purely virtual in the GVB method (their occupation is exactly 0) are nearly virtual in APSG, i.e., the corresponding natural occupation numbers are greater than 0 (typically their values are of the order of 10^{-3} or less). Apparently, whether the orbital is exactly or nearly virtual affects the excitation energies to only a small extent and the accuracy of the TD-GVB, and TD-APSG excitations is observed to be comparable. Computationally, TD-GVB is more advantageous then the TD-APSG method due to the smaller computational effort in obtaining the GVB-PP ground state than that of the APSG and lower dimensionality of the TD-GVB eigenproblem comparing to TD-APSG. Unfortunately, when applied to molecules in ground-state equilibrium geometries, the TD-GVB does not lead to obtaining excitations of substantially better accuracy than the uncorrelated TD-HF method. When bonds are stretched, however, TD-GVB benefits from the correct description of a ground state and the method is much more reliable than TD-HF.

Taking into account that (1) solving the TD-GVB equations can be used to correct ground-state GVB-PP energies [31–33], (2) the TD-GVB equations lead to obtaining often reasonably accurate excitation energies, and finally that (3) the calculations can be done at modest computational cost, the TD-GVB approximation may be a useful tool in exploring potential energy surfaces of excited states of molecules.

Finally, we want to stress out that since the GVB-PP approximation is equivalent to PNOF5 [13, 14]—one of the natural orbital functionals—the results presented in this paper can be seen as examples of performance of the PNOF5 functional in the framework of the recently proposed TD-PINO theory [26].

Acknowledgments This work has been supported by the National Science Centre of Poland under grant DEC-2012/07/E/ST4/03023. K.C. acknowledges financial support under Grant DEC-2014/13/N/ST4/03990.

Appendix

The matrices $\mathbf{A}^+, \mathbf{A}^-, \mathbf{D}^+, \mathbf{D}^-$ and $\mathbf{E}^+, \mathbf{E}^-$ appearing in the TD-GVB Eq. (19) are determined by the optimal natural orbitals $\{\varphi_p(\mathbf{r})\}$ and the expansion coefficients $\{c_p\}$ resulting from the optimization of the GVB-PP energy expression, Eq. (10). Their elements read

$$\forall_{\substack{p>q \\ r>s}} \quad A^+_{pq,rs} = (c_p + c_q)^{-1}(A_{pq,rs} + B_{pq,rs})(c_r + c_s)^{-1}, \tag{27}$$

$$\forall_{\substack{p>q \\ r>s}} \quad A^-_{rs,pq} = (c_p - c_q)^{-1}(A_{pq,rs} - B_{pq,rs})(c_r - c_s)^{-1}, \tag{28}$$

$$\forall_{\substack{p>q \\ r}} \quad D^+_{pq,r} = \frac{B_{pq,rr}}{2(c_p + c_q)c_r}, \tag{29}$$

$$\forall_{pq} \quad E^+_{pq} = \frac{B_{pp,qq}}{4c_p c_q}, \tag{30}$$

where

$$\begin{aligned}
\forall_{\substack{p\neq q\\ r\neq s}}\quad & B_{pq,rs}=A_{pq,sr}=(n_p-n_q)(\delta_{ps}h_{qr}-\delta_{qr}h_{ps})\\
&+(c_pc_s\delta_{I_pI_s}+c_qc_r\delta_{I_qI_r})(\langle pq|rs\rangle+\langle pq|sr\rangle)\\
&+[n_pn_s(1-\delta_{I_pI_s})+n_qn_r(1-\delta_{I_qI_r})-n_pn_r(1-\delta_{I_pI_r})-n_qn_s(1-\delta_{I_qI_s})]\langle pr||qs\rangle\\
&-\delta_{qr}c_p\sum_t\delta_{I_pI_t}c_t\langle ps|tt\rangle-\delta_{ps}c_q\sum_t\delta_{I_qI_t}c_t\langle qr|tt\rangle-\delta_{pr}c_r\sum_t\delta_{I_rI_t}c_t\langle qs|tt\rangle\\
&-\delta_{qs}c_s\sum_t\delta_{I_sI_t}c_t\langle pr|tt\rangle+\delta_{ps}\sum_t n_t[n_p(1-\delta_{I_pI_t})-n_q(1-\delta_{I_qI_t})]\langle qt||rt\rangle\\
&-\delta_{qr}\sum_t n_t[n_p(1-\delta_{I_pI_t})-n_q(1-\delta_{I_qI_t})]\langle pt||st\rangle\,,
\end{aligned}\tag{31}$$

and

$$\forall_{p\neq q}\quad B_{pq,rr}=B_{rr,pq}=2c_r(c_q\delta_{I_rI_q}+c_p\delta_{I_rI_p})\langle rr|pq\rangle-2c_r(\delta_{rq}+\delta_{rp})\sum_s c_s\delta_{I_rI_s}\langle ss|pq\rangle,\tag{32}$$

$$\forall_{p,q}\quad B_{pp,qq}=4c_pc_q\left\{\delta_{I_qI_p}\langle qq|pp\rangle+\delta_{pq}\left[2\sum_r n_r(1-\delta_{I_qI_r})\langle qr||qr\rangle+2h_{qq}-\mu_{I_q}\right]\right\}.\tag{33}$$

Additionally, the matrices $\mathbf{D}^-$ and $\mathbf{E}^-$ are of the form

$$\begin{aligned}
\forall_{\substack{p>q\\ r}}\quad (c_p-c_q)D^-_{pq,r}=&\,2c_r(\delta_{rp}-\delta_{rq})h_{qp}+(\delta_{rp}-\delta_{rq})\sum_s c_s\delta_{I_rI_s}\langle ss|pq\rangle\\
&+(c_p\delta_{I_rI_p}-c_q\delta_{I_rI_q})\langle rr|pq\rangle\\
&+2(\delta_{rp}-\delta_{rq})c_r\sum_s(1-\delta_{I_rI_s})n_s\langle qs||ps\rangle\\
&+2c_r[n_p(1-\delta_{I_rI_p})-n_q(1-\delta_{I_rI_q})]\langle qr||pr\rangle,
\end{aligned}\tag{34}$$

$$\begin{aligned}
\forall_{pq}\quad E^-_{pq}=&\,\delta_{I_pI_q}\langle pp|qq\rangle+\delta_{pq}\left[2\sum_r n_r(1-\delta_{I_qI_r})\langle qr||qr\rangle+2h_{qq}-\mu_{I_q}\right]\\
&+4c_pc_q(1-\delta_{I_pI_q})\langle pq||pq\rangle.
\end{aligned}\tag{35}$$

The two-electron integrals $\langle pq|rs\rangle$ and $\langle pq||rs\rangle$ are in terms of the natural orbitals, and they are defined in Eqs. (11) and (12). The Lagrange multipliers $\{\mu_{I_p}\}$ are obtained from the stationary equations for the ground-state expansion coefficients $\forall_P\,\forall_{p\in P}\,\partial[E^{GVB-PP}-\mu_{I_p}\sum_{q\in P}c_q^2]/\partial c_p=0$ reading

$$\begin{aligned}
\forall_{P=1,\ldots,N/2}\quad \forall_{p\in P}\quad \mu_{I_p}c_p=&\,2c_ph_{pp}+\sum_q c_q\delta_{I_qI_p}\langle qq|pp\rangle\\
&+2c_p\sum_q(1-\delta_{I_pI_q})n_q\langle pq||pq\rangle.
\end{aligned}\tag{36}$$

Notice that the symbol I_p used in Eqs. (27)–(36) in the context of the GVB-PP for an N-electron system should be understood as follows: For an occupied orbital φ_p ($c_p\neq 0$) I_p is equal to an index of a geminal to which an orbital is assigned ($I_p=P$ if $p\in P$), for a virtual orbital ($c_p=0$) $I_p=N/2+1$—so there is an additional $(N/2+1)$ th geminal and it includes all the virtual orbitals.

References

1. Shaik S, Hiberty PC (2004) Valence bond theory, its history, fundamentals, and applications: a primer. Wiley, New York
2. Goddard WA III (1967) Phys Rev 157:81
3. Hunt WJ, Hay PJ, Goddard WA III (1972) J Chem Phys 57:738
4. Goddard WA III, Dunning TH Jr, Hunt WJ (1969) Chem Phys Lett 4:231
5. Hunt WJ, Dunning TH Jr, Goddard WA III (1969) Chem Phys Lett 3:606
6. Bobrowicz FW, Goddard WA (1977) In: Schaefer HF III (ed) Modern theoretical chemistry: methods of electronic structure theory. Plenum, New York, pp 79–127
7. Hurley AC, Lennard-Jones JE, Pople JA (1963) Proc R Soc A 220:446

8. Surján PR (1999) Topics in current chemistry, vol 203. Springer, Berlin, pp 63–88
9. Kutzelnigg W (1964) J Chem Phys 40:3640
10. Mehler EL, Ruedenberg K, Silver DM (1970) J Chem Phys 52:1181
11. Piris M, Ugalde JM (2014) Int J Quantum Chem 114:1169
12. Piris M (2007) In: Mazziotti DA (ed) Reduced-density-matrix mechanics: with applications to many-electron atoms and molecules. Wiley, Hoboken, NJ, pp 387–427
13. Piris M, Lopez X, Ruipèrez F, Matxain JM, Ugalde JM (2011) J Chem Phys 134:164102
14. Pernal K (2013) Comput Theor Chem 1003:127
15. Lopez X, Ruiperez F, Piris M, Matxain JM, Matito E, Ugalde JM (2012) J Chem Theor Comput 8:2646
16. Arai T (1960) J Chem Phys 33:95
17. Chatterjee K, Pernal K (2012) J Chem Phys 137:204109
18. Pernal K, Chatterjee K, Kowalski PH (2014) J Chem Phys 140:014101
19. Pernal K, Chatterjee K, Kowalski PH (2014) J Chem Phys 140:189901
20. Giesbertz KJH, Gritsenko OV, Baerends EJ (2012) J Chem Phys 136:094104
21. Pernal K (2012) J Chem Phys 136:184105
22. Giesbertz KJH, Baerends EJ, Gritsenko OV (2008) Phys Rev Lett 101:033004
23. Giesbertz KJH, Pernal K, Gritsenko OV, Baerends EJ (2009) J Chem Phys 130:114104
24. Rowe DJ (1968) Rev Mod Phys 40:153
25. Giesbertz KJH, Gritsenko OV, Baerends EJ (2010) Phys Rev Lett 105:013002
26. Giesbertz KJH, Gritsenko OV, Baerends EJ (2010) J Chem Phys 133:174119
27. van Meer R, Gritsenko OV, Giesbertz KJH, Baerends EJ (2013) J Chem Phys 138:094114
28. Dunning TH Jr (1989) J Chem Phys 90:1007
29. DALTON, a molecular electronic structure program, Release 2.0 (2005), see http://www.kjemi.uio.no/software/dalton/dalton.html
30. Christiansen O, Koch H, Jørgensen P, Olsen J (1996) Chem Phys Lett 256:185
31. Chatterjee K, Pernal K (in preparation)
32. Pastorczak E, Pernal K (2015) Phys Chem Chem Phys 17:8622
33. Pernal K (2014) J Chem Theor Comput 10:4332

Theor Chem Acc (2015) 134:100
DOI 10.1007/s00214-015-1703-x

REGULAR ARTICLE

Novel orthogonalization and biorthogonalization algorithms

Towards multistate multiconfiguration perturbation theory

Zsuzsanna Tóth[1] · Péter R. Nagy[2] · Péter Jeszenszki[1] · Ágnes Szabados[1]

Received: 27 May 2015 / Accepted: 15 July 2015 / Published online: 1 August 2015

Abstract Orthogonalization with the prerequisite of keeping several vectors fixed is examined. Explicit formulae are derived both for orthogonal and biorthogonal vector sets. Calculation of the inverse or square root of the entire overlap matrix is eliminated, allowing computational time reduction. In this special situation, it is found sufficient to evaluate the functions of matrices of the dimension matching the number of fixed vectors. The (bi)orthogonal sets find direct application in extending multiconfigurational perturbation theory to deal with multiple reference vectors.

Keywords Overlap · Orthogonalization · Biorthogonal sets · Multiconfiguration perturbation theory · Multistate theory

1 Introduction

There are two different, equivalent approaches for treating nonorthogonality of a nonredundant vector set in a linear algebraic problem. One way is creating biorthogonal vectors to the overlapping set, and the other more common way is orthogonalizing the basis set. Let us assume that $\{\mathbf{c}^i\}_{i=1}^N$ is a nonredundant, nonorthogonal set of N-dimensional vectors. Arranging vectors $\mathbf{c}^i$ as columns in matrix $\mathbf{C}$, the overlap matrix

$$\mathbf{S} = \mathbf{C}^\dagger\mathbf{C}$$

is a positive definite, nonunit matrix. Orthonormalization implies a linear transformation $\mathbf{B} = \mathbf{C}\mathbf{L}_\mathrm{o}$, obeying

$$\mathbf{B}^\dagger\mathbf{B} = \mathbf{L}_\mathrm{o}^\dagger\mathbf{S}\mathbf{L}_\mathrm{o} = \mathbf{I}\,. \tag{1}$$

Vector set $\{\widetilde{\mathbf{c}}^i\}_{i=1}^N$, biorthonormal to $\{\mathbf{c}^i\}_{i=1}^N$ is obtained by the transformation $\widetilde{\mathbf{C}} = \mathbf{C}\mathbf{L}_\mathrm{bo}$, fulfilling

$$\widetilde{\mathbf{C}}^\dagger\mathbf{C} = \mathbf{L}_\mathrm{bo}^\dagger\mathbf{S} = \mathbf{I}\,, \tag{2}$$

where $\widetilde{\mathbf{C}}$ contains vectors $\widetilde{\mathbf{c}}^i$ in columns. In contrast to orthonormalization, the task of biorthonormal or reciprocal set construction has the uniquely defined solution

$$\mathbf{L}_\mathrm{bo} = \mathbf{S}^{-1}$$

as a direct consequence of Eq. (2).

Of the possible orthonormalization procedures, Löwdin's symmetric scheme [1, 2], operating with $\mathbf{L}_\mathrm{o} = \mathbf{S}^{-1/2}$, is widely exploited in quantum chemistry. Gram–Schmidt orthogonalization is a popular, less costly alternative that lacks the symmetry conservation and resemblance [2–4] properties of Löwdin's symmetric treatment. Gram–Schmidt orthogonalization is known to depend on the ordering of vectors $\mathbf{c}^i$, which is not necessarily a shortcoming. It is a deliberate advantage, e.g., if one, selected vector is meant to be fixed.

This situation may be met when aiming to describe dynamic electron correlation starting from a single, multideterminantal reference vector. Correction schemes based on perturbation theory (PT) have been applying successive Gram–Schmidt orthogonalization in such circumstances [5–7], occasionally combined with Löwdin's symmetrical [8] or

Published as part of the special collection of articles "Festschrift in honour of P. R. Surjan."

✉ Ágnes Szabados
szabados@chem.elte.hu

[1] Laboratory of Theoretical Chemistry, Eötvös University, POB 32, Budapest 1518, Hungary

[2] MTA-BME Lendület Quantum Chemistry Research Group, Department of Physical Chemistry and Materials Science, Budapest University of Technology and Economics, POB 91, Budapest 1521, Hungary

canonical procedure [9, 10]. Biorthogonal treatment of the overlap when correcting a single, multideterminantal reference has been advocated and investigated extensively in the laboratory of Péter Surján [11–13]. The framework termed multiconfigurational PT (MCPT) collects several approaches differing in the treatment of overlap and choice for the zero-order Hamiltonian (see Ref. [14] for an elaboration on the perturbative partitioning). Focusing on the handling of overlap, options exploited so far, given a single reference vector are

1. orthogonal projection to the reference (first step of a Gram–Schmidt procedure)
   (a) biorthonormal set construction in the $(N-1)$ -dimensional space
   (b) Löwdin orthogonalization in the $(N-1)$-dimensional space
2. omit orthogonal projection to the reference
   (a) biorthonormal set construction in the N-dimensional space

A notable feature of all three strategies is that the (bi)orthonormal set can be given explicitly, eliminating the need of numerical overlap treatment. Option 2b is lucidly missing from the above list just for the reason that no close form of the underlying inverse square root of the overlap could be constructed. Notation 2a is hence somewhat superfluous, which we however keep to stress analogy with 1a. The procedure of option 1b is equivalent to the Jacobi rotations' inspired orthogonalization, designed by Mayer [15, 16]. For applications of the above (bi)orthogonal schemes in PT strategies alternative to MCPT, see Refs. [17, 18].

In the present work, we extend the above overlap treatments for the case of multiple reference vectors. This involves derivation of explicit formulae for the (bi)orthonormal sets in cases analogous to 1a, 1b, and 2a above, with reference vectors, $m > 1$ in number. Construction of $\mathbf{S}^{-1}$ and $\mathbf{S}^{-1/2}$ in case 1 for the $(N-m)\times(N-m)$ overlap matrix and $\mathbf{S}^{-1}$ in case 2 for the $N\times N$ overlap matrix is presented in Sect. 2. These results facilitate a multistate extension of the MCPT framework. The pertinent formulae are given in Sect. 3, followed by an illustrative numerical study in Sect. 4.

2 (Bi)orthogonal vector sets

Let $\{\mathbf{e}^i\}_{i=1}^N$ be the set of unit vectors, and let us replace the first m vectors with the orthonormal set[1] of vectors $\{\mathbf{c}^i\}_{i=1}^m$. The new N-dimensional set, $\{\mathbf{c}^i\}_{i=1}^m \cup \{\mathbf{e}^i\}_{i=m+1}^N$ is not orthogonal as its subsets $\{\mathbf{c}^i\}_{i=1}^m$ and $\{\mathbf{e}^i\}_{i=m+1}^N$ overlap.

Let us assume that coefficients C_{ji} of the expansion

$$\mathbf{c}^i = \sum_{j=1}^{N} \mathbf{e}^j\, C_{ji}$$

are arranged in matrix $\mathbf{C}$, of dimension $N\times m$. We now introduce notation $\mathbf{C}_1$ for the upper $m\times m$ block of $\mathbf{C}$, and $\mathbf{C}_2$ for the lower $(N-m)\times m$ block. This allows to write

$$\mathbf{C} = \begin{pmatrix} \mathbf{C}_1 \\ \mathbf{C}_2 \end{pmatrix}. \tag{3}$$

Orthonormality of vectors $\mathbf{c}^i$ is reflected by

$$\mathbf{I}_m = \mathbf{C}_1^\dagger \mathbf{C}_1 + \mathbf{C}_2^\dagger \mathbf{C}_2 = \mathbf{A} + \mathbf{C}_2^\dagger \mathbf{C}_2, \tag{4}$$

where $\mathbf{I}_m$ denotes the m-dimensional unit matrix, and shorthand $\mathbf{A}$ is introduced for subsequent use. We note here that the union of sets $\{\mathbf{c}^i\}_{i=1}^m$ and $\{\mathbf{e}^i\}_{i=m+1}^N$ being N-dimensional relies on the tacit assumption that matrix $\mathbf{A}$ is positive definite.

To extend option 1, projector $\mathbf{P}$ corresponding to the vector set $\{\mathbf{c}^\mathbf{i}\}_{i=1}^m$ is formulated as

$$\mathbf{P} = \mathbf{C}\mathbf{C}^\dagger = \left(\begin{array}{c|c} \mathbf{C}_1\mathbf{C}_1^\dagger & \mathbf{C}_1\mathbf{C}_2^\dagger \\ \hline \mathbf{C}_2\mathbf{C}_1^\dagger & \mathbf{C}_2\mathbf{C}_2^\dagger \end{array}\right).$$

As the next step, vectors $\{\mathbf{e}^\mathbf{i}\}_{i=m+1}^N$, arranged as the last $N-m$ columns of unit matrix $\mathbf{I}_N$, are projected orthogonal to $\{\mathbf{c}^\mathbf{i}\}_{i=1}^m$ to generate the set $\{\mathbf{e}^{i\prime}\}_{i=m+1}^N$. Denoting the corresponding matrix $\mathbf{D}'$, we get

$$\mathbf{D}' = (\mathbf{I}_N - \mathbf{P})\begin{pmatrix} 0 \\ \mathbf{I}_{N-m} \end{pmatrix} = \begin{pmatrix} -\mathbf{C}_1\mathbf{C}_2^\dagger \\ \mathbf{I}_{N-m} - \mathbf{C}_2\mathbf{C}_2^\dagger \end{pmatrix}, \tag{5}$$

with obvious notation for $\mathbf{I}_{N-m}$. Overlap of vectors $\mathbf{e}^{\mathbf{i}\prime}$ can be expressed as

$$\mathbf{D}'^\dagger\mathbf{D}' = I_{N-m} - \mathbf{C}_2\mathbf{C}_2^\dagger, \tag{6}$$

using Eqs. (4) and (5). Matrix $\mathbf{D}'^\dagger\mathbf{D}'$ represents the nontrivial part of the $N\times N$ overlap matrix

$$\mathbf{S} = \left(\begin{array}{c|c} \mathbf{I}_m & \\ \hline & \mathbf{D}'^\dagger\mathbf{D}' \end{array}\right) \tag{7}$$

of the set $\{\mathbf{c}^\mathbf{i}\}_{i=1}^m \cup \{\mathbf{e}^{\mathbf{i}\prime}\}_{i=m+1}^N$.

In the following paragraphs, the inverse and inverse square root of the overlap matrix of Eq. (7) is constructed. Clearly, it suffices to focus on $\mathbf{D}'^\dagger\mathbf{D}'$ of Eq. (6). We approach the problem in a general manner, by expressing any analytic function, $f:\ (0,1]\to\ \mathbb{R}$ of matrix $\mathbf{S}$. Matrix function $f(\mathbf{S})$ is defined via Taylor expansion, written as

$$f\left(\mathbf{I}_{N-m} - \mathbf{C}_2\mathbf{C}_2^\dagger\right) = \sum_{n=0}^{\infty} d_n \left(\mathbf{C}_2\mathbf{C}_2^\dagger\right)^n, \tag{8}$$

[1] Orthonormality of vectors $\mathbf{c}^i$ is assumed since orthonormalizing m vectors is relatively cheap for $m \ll N$.

with $d_n = (-1)^n f^{(n)}(1)/n!$. Since $||\mathbf{C}_2\mathbf{C}_2^\dagger|| < 1$ (taking, e.g., the 2-norm of the matrix), the Taylor series is convergent if the coefficients d_n are bounded. Explicit form of the Taylor coefficients d_n is not necessary for further derivation, all we need to know is that they are indeed bounded for the inverse and inverse square root function.

We now recognize the following recursion for the powers of $\mathbf{C}_2\mathbf{C}_2^\dagger$

$$\left(\mathbf{C}_2\mathbf{C}_2^\dagger\right)^n = \mathbf{C}_2(\mathbf{I}_m - \mathbf{A})^{n-1}\mathbf{C}_2^\dagger \tag{9}$$

that is easy to prove by induction. While the $n = 1$ case is trivial, case $n = 2$ is obtained as

$$\left(\mathbf{C}_2\mathbf{C}_2^\dagger\right)^2 = \mathbf{C}_2\mathbf{C}_2^\dagger\mathbf{C}_2\mathbf{C}_2^\dagger = \mathbf{C}_2(\mathbf{I}_m - \mathbf{A})\mathbf{C}_2^\dagger,$$

an obvious consequence of Eq. (4). To take the induction step, let us suppose that statement (9) holds for $n-1$ and examine the case $n > 2$. We find

$$\begin{aligned}\left(\mathbf{C}_2\mathbf{C}_2^\dagger\right)^n &= \mathbf{C}_2(\mathbf{I}_m - \mathbf{A})^{n-2}\mathbf{C}_2^\dagger\mathbf{C}_2\mathbf{C}_2^\dagger \\ &= \mathbf{C}_2(\mathbf{I}_m - \mathbf{A})^{n-2}(\mathbf{I}_m - \mathbf{A})\mathbf{C}_2^\dagger \\ &= \mathbf{C}_2(\mathbf{I}_m - \mathbf{A})^{n-1}\mathbf{C}_2^\dagger,\end{aligned}$$

which completes the proof.

Let us now substitute Eq. (9) into the Taylor expansion of Eq. (8) and utilize $d_0 = f(1)$. We obtain

$$\begin{aligned} & f\left(\mathbf{I}_{N-m} - \mathbf{C}_2\mathbf{C}_2^\dagger\right) \\ &= f(1)\mathbf{I}_{N-m} + \mathbf{C}_2\left[\sum_{n=1}^{\infty} d_n(\mathbf{I}_m - \mathbf{A})^n\right](\mathbf{I}_m - \mathbf{A})^{-1}\mathbf{C}_2^\dagger \\ &= f(1)\mathbf{I}_{N-m} + \mathbf{C}_2\left\{\left[\sum_{n=0}^{\infty} d_n(\mathbf{I}_m - \mathbf{A})^n\right] - f(1)\mathbf{I}_m\right\}(\mathbf{I}_m - \mathbf{A})^{-1}\mathbf{C}_2^\dagger \\ &= f(1)\mathbf{I}_{N-m} + \mathbf{C}_2(f(\mathbf{A}) - f(1)\mathbf{I}_m)(\mathbf{I}_m - \mathbf{A})^{-1}\mathbf{C}_2^\dagger . \end{aligned} \tag{10}$$

In the case $\mathbf{I}_m = \mathbf{A}$, the second term of the expression above is zero. The role of the analytical treatment can be clearly pointed out at this step. Instead of evaluating function f of an $(N-m)\times(N-m)$ matrix, it is sufficient to calculate the inverse and the same function f of $m \times m$ matrices. As long as $m \ll N$, much can be gained in computational time, the eventual speedup depending on the structure of $\mathbf{A}$ and the nature of f. As $m \to N$, the computational advantage evidently disappears.

2.1 Extended option 1a

Let us now work out the general formula of Eq. (10) for our two functions of interest. Starting with the inverse function, we obtain:

$$\left(\mathbf{I}_{N-m} - \mathbf{C}_2\mathbf{C}_2^\dagger\right)^{-1} = \mathbf{I}_{N-m} + \mathbf{C}_2\underbrace{\left(\mathbf{A}^{-1} - \mathbf{I}_m\right)(\mathbf{I}_m - \mathbf{A})^{-1}}_{\mathbf{A}^{-1}}\mathbf{C}_2^\dagger$$

The inverse of the overlap matrix of Eq. (7) therefore reads

$$\mathbf{S}^{-1} = \left(\begin{array}{c|c} \mathbf{I}_m & \\ \hline & \mathbf{I}_{N-m} + \mathbf{C}_2\left(\mathbf{C}_1^\dagger\mathbf{C}_1\right)^{-1}\mathbf{C}_2^\dagger \end{array}\right).$$

Evaluating the biorthogonal counterpart of vectors $\mathbf{e}^{i\prime}$, one obtains

$$\widetilde{\mathbf{D}}' = \mathbf{D}'\left(\mathbf{I}_{N-m} + \mathbf{C}_2\mathbf{A}^{-1}\mathbf{C}_2^\dagger\right) = \begin{pmatrix} -\mathbf{C}_1\mathbf{A}^{-1}\mathbf{C}_2^\dagger \\ \mathbf{I}_{N-m}\end{pmatrix},$$

having utilized Eqs. (4) and (5). Noting that $\mathbf{C}_1\mathbf{A}^{-1} = \mathbf{C}_1^{\dagger -1}$, the special case of $m = 1$ is recovered as

$$\widetilde{\mathbf{e}}^{i\prime} = \mathbf{e}^i - \frac{c_i^*}{c_1^*}\mathbf{e}^1\ , \quad i = 2,\ldots,N, \tag{11}$$

c_i denoting the components of the single column vector $\mathbf{C}$ of Eq. (3). While the biorthogonal vectors of Eq. (11) were introduced in Ref. [11], Eq. (3) of Ref. [12] allows for a more transparent comparison.

2.2 Extended option 1b

Let us step now to the inverse square root of Eq. (7). Based on the general result of Eq. (10), we obtain

$$\left(\mathbf{I}_{N-m} - \mathbf{C}_2\mathbf{C}_2^\dagger\right)^{-1/2} = \mathbf{I}_{N-m} + \mathbf{C}_2\underbrace{\left(\mathbf{A}^{-1/2} - \mathbf{I}_m\right)(\mathbf{I}_m - \mathbf{A})^{-1}}_{[(\mathbf{I}_m + \mathbf{A}^{1/2})\mathbf{A}^{1/2}]^{-1}}\mathbf{C}_2^\dagger. \tag{12}$$

The $-1/2$ power of the overlap matrix of Eq. (7) hence becomes

$$\mathbf{S}^{-1/2} = \left(\begin{array}{c|c} \mathbf{I}_m & \\ \hline & \mathbf{I}_{N-m} + \mathbf{C}_2\left[\left(\mathbf{I}_m + \left(\mathbf{C}_1^\dagger\mathbf{C}_1\right)^{1/2}\right)\left(\mathbf{C}_1^\dagger\mathbf{C}_1\right)^{1/2}\right]^{-1}\mathbf{C}_2^\dagger \end{array}\right).$$

The special case of $m = 1$, derived in Ref. [16], is obtained as

$$\left(S^{-\frac{1}{2}}\right)_{ij} = \delta_{ij} + \frac{c_i c_j^*}{|c_1|(1+|c_1|)}, \quad i,j > 1,$$

utilizing that $\mathbf{C}$ of Eq. (3) is composed of a single column.

Matrix $\mathbf{S}^{-1/2}$ above facilitates to construct the Löwdin-orthogonalized counterpart of vectors $\mathbf{e}^{i\prime}$ as

$$\begin{aligned}\mathbf{D}'^L &= \mathbf{D}'\left(\mathbf{I}_{N-m} + \mathbf{C}_2\left(\mathbf{A}^{-1/2} - \mathbf{I}_m\right)(\mathbf{I}_m - \mathbf{A})^{-1}\mathbf{C}_2^\dagger\right) \\ &= \begin{pmatrix} -\mathbf{C}_1\mathbf{A}^{-1/2}\mathbf{C}_2^\dagger \\ \mathbf{I}_{N-m} - \mathbf{C}_2\left(\mathbf{I}_m + \mathbf{A}^{1/2}\right)^{-1}\mathbf{C}_2^\dagger\end{pmatrix},\end{aligned}$$

having made use of Eqs. (4), (5), and (12).

2.3 Extended option 2a

Let us finally consider the almost trivial case of reciprocal set construction to the set $\{\mathbf{c^i}\}_{i=1}^{m} \cup \{\mathbf{e^i}\}_{i=m+1}^{N}$. Note that the orthogonal projection of Eq. (5) is now omitted. The $N \times N$ overlap matrix of this set reads

$$\mathbf{S} = \left(\begin{array}{c|c} \mathbf{I}_m & \mathbf{C}_2^\dagger \\ \hline \mathbf{C}_2 & \mathbf{I}_{N-m} \end{array}\right).$$

Partitioning $\mathbf{S}^{-1}$ into the same structure as $\mathbf{S}$ and solving for the individual blocks, the inverse overlap is readily found to be

$$\mathbf{S}^{-1} = \left(\begin{array}{c|c} \mathbf{A}^{-1} & -\mathbf{A}^{-1}\mathbf{C}_2^\dagger \\ \hline -\mathbf{C}_2\mathbf{A}^{-1} & \mathbf{I}_{N-m} + \mathbf{C}_2\mathbf{A}^{-1}\mathbf{C}_2^\dagger \end{array}\right). \tag{13}$$

The $N \times m$ matrix $\widetilde{\mathbf{C}}$ and $N \times (N-m)$ matrix $\widetilde{\mathbf{D}}$ collecting reciprocal column vectors are obtained as

$$\left(\widetilde{\mathbf{C}}\middle|\widetilde{\mathbf{D}}\right) = \left(\begin{array}{c|c} \mathbf{C}_1 & 0 \\ \hline \mathbf{C}_2 & \mathbf{I}_{N-m} \end{array}\right)\mathbf{S}^{-1},$$

their explicit form reading as

$$\widetilde{\mathbf{C}} = \begin{pmatrix} \mathbf{C}_1\mathbf{A}^{-1} \\ 0 \end{pmatrix},$$

and

$$\widetilde{\mathbf{D}} = \begin{pmatrix} -\mathbf{C}_1\mathbf{A}^{-1}\mathbf{C}_2^\dagger \\ \mathbf{I}_{N-m} \end{pmatrix}.$$

Similarly to Eq. (10), the most demanding computational task (inversion of $\mathbf{A}$) is connected to an $m \times m$ matrix, instead of the entire $N \times N$ overlap matrix.

It is interesting to observe that the reciprocal vectors $\widetilde{\mathbf{D}}'$ of extended option 1a and $\widetilde{\mathbf{D}}$ of extended option 2a match explicitly. In the special case of $m = 1$, the first reciprocal vector reads $\widetilde{\mathbf{e}}^1 = c_1^{*-1}\,\mathbf{e}^1$, while $\widetilde{\mathbf{e}}^i$ are the same as $\widetilde{\mathbf{e}}^{i\prime}$ of Eq. (11) for $i > 1$, in accordance with [12].

3 Multistate extension of MCPT

Electronic structure description often reaches its target in two successive steps. A first, qualitative approximation is corrected in a second shot to incorporate the so-called dynamic correlation. Situations where a single vector—even if multiconfigurational in character—does not represent an adequate first approximation call for two or more reference vectors. Targeting more states of the system at a time is another example where multiple reference vectors are necessary. Many correction schemes have a version designed for such situations, assuming multiple reference states that form a so-called model space (MS). Equations of Rayleigh–Schrödinger PT [19, 20] for instance can be regarded as a special case of the Bloch equation [21], corresponding to a one-dimensional model space.

Bloch-equation-based multistate PT formulations, termed quasidegenerate PT (QDPT) [22], largely assume an orthonormal set of vectors in the configuration interaction (CI) space that is partitioned for a model space and its complement. This restricts applicability to model spaces easily separable from the rest, e.g., formed by simple determinants. While determinants facilitate a transparent derivation of many-body QDPT formulae [23, 24], identifying the determinants that need to be included in the model space is not always trivial. Though complete active space (CAS) appears a simple way out, CAS-based QDPT is unfortunately prone to the so-called intruder problem, especially for large active spaces.

The idea of picking multiconfigurational vectors to span the model space is appealing for two reasons. On one hand, the dimension of the space is reduced as compared to the case of using determinants. On the other hand, it may have a beneficial effect on intruder sensitivity, due to the internally coupled nature of reference vectors. Such an approach is however hard to find for the simple reason that the orthogonal complement of multiple multiconfiguration vectors is not easy to construct. It is at this point where the overlap treatments elaborated in Sect. 2 can be relied upon. Detailed derivation of the multistate extension of the MCPT framework is out of the scope of the present report. In what follows we confine ourselves to the key formulae necessary for the illustrative application of Sect. 4.

Multiconfigurational reference functions, $m > 1$ in number, constitute the starting point of our approximation. Vectors $\{\mathbf{c}^i\}_{i=1}^{m}$ of Sect. 2 are associated with these reference functions, C_{ji} denoting the jth component in the determinantal expansion of reference $\mathbf{c}^i$. In accordance with the generally applicable philosophy of MCPT, we do not assume any special structure of the reference functions, apart from being orthonormal. Unit vectors $\{\mathbf{e}^i\}_{i=1}^{N}$ of Sect. 2 now represent determinants spanning the CI space. The first m among determinants, $\mathbf{e}^i$ are selected based on their projection to the model space. In particular, rows j for which $\sum_i C_{ji}^2$ are the largest, constitute $\mathbf{C}_1$.

The central quantity of PT approaches, the zero-order Hamiltonian, is formulated in MCPT via its spectral resolution. Extended overlap treatment options 1a and 2a both imply a nonsymmetrical operator, 1b works with a

Table 1 Zero-order eigenvalues within the Epstein–Nesbet partitioning in multistate MCPT variants

	MS-pMCPT	MS-pLMCPT	MS-uMCPT
$\mathbf{E}^{(0)}_{P,i}$	$\langle \mathbf{c}^i \vert H \vert \mathbf{c}^i \rangle$	$\langle \mathbf{c}^i \vert H \vert \mathbf{c}^i \rangle$	$\langle \widetilde{\mathbf{c}}^i \vert H \vert \mathbf{c}^i \rangle$
$\mathbf{E}^{(0)}_{P\perp,i}$	$\langle \widetilde{\mathbf{e}}^{i\prime} \vert H \vert \mathbf{e}^{i\prime} \rangle$	$\langle \mathbf{e}^{i\prime L} \vert H \vert \mathbf{e}^{i\prime L} \rangle$	$\langle \widetilde{\mathbf{e}}^i \vert H \vert \mathbf{e}^i \rangle$

Subscript P refers to the model space, $P\perp$ stands for the complementary space. See text for further notations

symmetrical expression. The zero-order Hamiltonian of option 1a, introduced in projected MCPT (pMCPT) [11, 13], can be extended as

$$\mathbf{H}^{(0)}_{\mathrm{MS-pMCPT}} = \mathbf{C}\,\mathbf{E}^{(0)}_P\,\mathbf{C}^\dagger + \mathbf{D}'\,\mathbf{E}^{(0)}_{P\perp}\,\widetilde{\mathbf{D}}'^\dagger,$$

MS standing for "multistate." Overlap treatment option 1b, applied, e.g., in Ref. [16], can be extended for multiple reference vectors as

$$\mathbf{H}^{(0)}_{\mathrm{MS-pLMCPT}} = \mathbf{C}\,\mathbf{E}^{(0)}_P\,\mathbf{C}^\dagger + \mathbf{D}'^L\,\mathbf{E}^{(0)}_{P\perp}\,\mathbf{D}'^{L\,\dagger}.$$

Finally, the complete biorthogonal treatment of option 2a, termed originally SC2-MCPT or unprojected MCPT (uMCPT) [12, 13], can be extended to the multistate case as

$$\mathbf{H}^{(0)}_{\mathrm{MS-uMCPT}} = \mathbf{C}\,\mathbf{E}^{(0)}_P\,\widetilde{\mathbf{C}}^\dagger \;+\; \mathbf{D}\,\mathbf{E}^{(0)}_{P\perp}\,\widetilde{\mathbf{D}}^\dagger.$$

Diagonal matrices $\mathbf{E}^{(0)}_P$ and $\mathbf{E}^{(0)}_{P\perp}$ above contain zero-order energies corresponding to the model space and its complement, respectively. Zero-order energies in the Epstein–Nesbet (EN) partitioning [25, 26] are collected in Table 1 for completeness.

Energy corrections are calculated in MS theories as eigenvalues of an effective Hamiltonian, obtained relying on the Bloch equation and the zero-order operator. Matrix elements for the MS-pLMCPT variant at order 2 read as

$$\left(\mathbf{H}^{\mathrm{eff}\,(2)}_{\mathrm{MS-pLMCPT}}\right)_{ij} = \delta_{ij}\mathbf{E}^{(0)}_{P,i} - \sum_{k=m+1}^{N} \frac{\langle \mathbf{c}^i \vert H \vert \mathbf{e}^{k\prime L} \rangle \langle \mathbf{e}^{k\prime L} \vert H \vert \mathbf{c}^j \rangle}{\mathbf{E}^{(0)}_{P\perp,k} - \mathbf{E}^{(0)}_{P,j}}. \quad (14)$$

Corrected energies, $E^{(2)}$ and reference functions, $\mathbf{c}^{i(2)}$ arise as

$$\sum_j \mathbf{H}^{\mathrm{eff}\,(2)}_{ij}\, d^{(2)}_{jk} = E^{(2)}_k\, d^{(2)}_{ik},$$

and

$$\mathbf{c}^{i(2)} = \sum_j \mathbf{c}^j d^{(2)}_{ji} \quad ,$$

respectively.

Closing this section, let us note that the MS-MCPT variants would merit a detailed formal and numerical examination respecting, e.g., size consistency, intruder sensitivity, or dependence on the zero-order eigenvalues. We intentionally withdraw from such a study presently, as MS-MCPT merely serves an illustration purpose here.

4 Numerical illustration

Choosing suitable reference function(s) is a persisting challenge for multireference theories. Geminal-based approaches, continuously cultivated by Péter Surján, are promising in this respect [27–29] as they are more economic than CAS, still they often reflect the multiconfigurational nature of the target function correctly. Obviously, geminal wavefunctions have their own shortcomings. We focus here on one of these, the process of switching between two Lewis structures of the same molecule. A simple case study is provided by the rectangular-to-square distortion of the H_4 system. Antisymmetrized product of strongly orthogonal geminals (APSG) produces a cusp on the energy curve of this system at square geometry, as reflected by Fig. 1. The problem is connected to the fact that geminals (assigned to bonds) are reordered at the switching point, thereby capturing the correct, dominant Lewis structure at both rectangular arrangements.

There exist solutions to this problem [30–32], APSG-based PT is however notably not among them, since a qualitative defect of the reference cannot be cured by PT. This is reflected by the MCPT curve in Fig. 1. If wishing to proceed by PT, it appears straightforward to construct two reference functions, corresponding to either of the Lewis structures, and follow a MS-MCPT strategy with two-dimensional model space. The energy profile obtained by such a procedure is shown for the MS-pLMCPT variant in Fig. 1. Multistate theory apparently results a smooth energy curve with a correct, zero derivative at 90°. One can also observe in Fig. 1 a characteristic overshooting of EN partitioning at order 2.

Due to the small system size, the example of Fig. 1 cannot illustrate the gain in computational time, brought about by the results of Sect. 2. To give an impression in this line, let us consider the ground state of p-benzyne. Description by a geminal-based MS-MCPT approach necessitates three reference vectors, corresponding to the three dominant Lewis structures. Value for N of Sect. 2 is given by the length of the determinantal expansion of the reference vectors. Depending on the geminal scheme chosen, N may range from a couple of hundreds (in case of a minimalistic APSG) to astronomical dimensions. The all pair coupled cluster doubles wavefunction, e.g., a geminal-type function [33], includes determinants on the order of 10^{16}, in a double zeta, polarized basis set, cores assumed frozen. Accordingly, analytic handling of

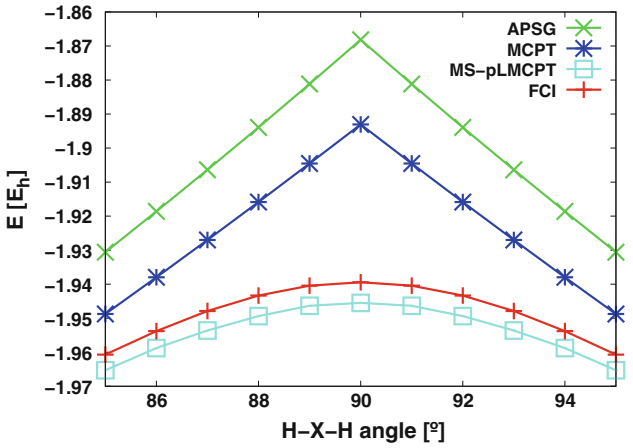

Fig. 1 Total energy for H_4, in STO-3G basis set. The four hydrogen atoms are confined to a circle with a radius of $\sqrt{2}$ bohr. Angle of two neighboring hydrogen atoms (H) and the center of mass (X) are labeled angle(H–X–H). The APSG wavefunction, involving two geminals, with two orbitals assigned to each represents one of the reference states. The other reference function is generated by (1) localizing orbitals to atoms within the Arai subspaces; (2) assigning these orbitals to geminals representing the longer HH bonds, instead of the shorter; (3) optimizing geminal coefficients but not the orbitals. The MS-pLMCPT energy is obtained as the lower lying root of the effective Hamiltonian of Eq. (14). The curve MCPT is obtained in EN partitioning following the APSG-based PT strategy of Ref. [11]. Full CI is shown for comparison

overlap allows for dealing with 3×3 matrices instead of the numerical treatment of the $N \times N$ overlap matrix, with the above values for N.

Acknowledgments The authors are indebted to a Referee who helped to significantly improve the manuscript. The work presented here is a direct continuation of the research being followed in the laboratory of Péter Surján. It is a delight for the authors—all of them students of prof. Surján for some time in their life—to congratulate him on the occasion of reaching 60 and express their gratitude to the outstanding scholar.

References

1. Löwdin PO (1950) J Chem Phys 18:365
2. Löwdin PO (1970) Adv Quantum Chem 5:185
3. Mayer I (2002) Int J Quantum Chem 90(1):63. doi:10.1002/qua.981
4. Mayer I (2003) Simple theorems, proofs, and derivations in quantum chemistry. Kluwer, New York
5. Wolinski K, Sellers H, Pulay P (1987) Chem Phys Lett 140:225
6. Wolinski K, Pulay P (1989) J Chem Phys 90:3647
7. van Dam HJJ, van Lenthe JH (1998) Mol Phys 93:431
8. Werner HJ (1996) Mol Phys 89:645
9. Andersson K, Malmqvist PÅ, Roos BO, Sadlej AJ, Wolinski K (1990) J Phys Chem 94:5483
10. Andersson K, Malmqvist PÅ, Roos BO (1992) J Chem Phys 96:1218
11. Rolik Z, Szabados Á, Surján PR (2003) J Chem Phys 119:1922
12. Szabados Á, Rolik Z, Tóth G, Surján PR (2005) J Chem Phys 122:114104
13. Kobayashi M, Szabados Á, Nakai H, Surján PR (2010) J Chem Theory Comput 6:2024
14. Surján P, Rolik Z, Szabados Á, Kőhalmi D (2004) Ann Phys (Leipzig) 13:223
15. Mayer I (2000) Theor Chim Acta 104:163
16. Nagy P, Surján P, Szabados Á (2012) Theor Chem Acc (Theoretica Chimica Acta) 131:1109. doi:10.1007/s00214-012-1109-y
17. Limacher PA, Ayers PW, Johnson PA, De Baerdemacker S, Neck DV, Bultinck P (2014) Phys Chem Chem Phys 16:5061
18. Nagy PR, Szabados Á (2012) Int J Quantum Chem 113:230
19. Rayleigh LJWS (1976) The theory of sound, vol 1. Dover, New York
20. Schrödinger E (1926) Ann Phys 80:437
21. Lindgren I, Morrison J (1986) Atomic many-body theory. Springer, Berlin
22. Shavitt I, Bartlett RJ (2009) Many-body methods in chemistry and physics. Cambridge University Press, Cambridge
23. Hose G, Kaldor U (1979) J Phys B 12:3827
24. Meissner L, Bartlett RJ (1989) J Chem Phys 91:4800
25. Epstein P (1926) Phys Rev 28:695
26. Nesbet R (1955) Proc R Soc (Lond) A230:312
27. Surján PR (1999) Top Curr Chem 203:63
28. Surján PR, Szabados Á, Jeszenszki P, Zoboki T (2012) J Math Chem 50:534
29. Jeszenszki P, Nagy PR, Zoboki T, Szabados Á, Surján PR (2014) Int J Quantum Chem 114:1048
30. Rassolov VA, Xu F (2007) J Chem Phys 127:044104
31. Small DW, Head-Gordon M (2009) J Chem Phys 130:084103
32. Jeszenszki P, Rassolov V, Surján PR, Szabados Á (2015) Mol Phys 113(3–4):249
33. Johnson PA, Ayers PW, Limacher PA, Baerdemacker SD, Neck DV, Bultinck P (2013) Comput Theor Chem 1003:101

Theor Chem Acc (2016) 135:13
DOI 10.1007/s00214-015-1768-6

REGULAR ARTICLE

Deviation from the anti-Markovnikov rule: a computational study of the regio- and stereoselectivity of diene hydroboration reactions

Laurence Hamdan[1] · Khaled Abdel-Maksoud[1] · Riya Radia[1] · Janine Boodram[1] · Kwan Y. Man[1] · Iain McGregor[1] · Catherine Munteanu[1] · Kishan Muthu[1] · Jannat Poddar[1] · Joanna Roberts[1] · Stephanie Sadler[1] · Nabeela Siddiqi[1] · Sianne Tam[1] · Anna Andreou[2] · Oren A. Scherman[2] · Edina Rosta[1]

Received: 17 August 2015 / Accepted: 20 November 2015 / Published online: 26 December 2015

Abstract Hydroboration and subsequent use of boron compounds in novel organic synthesis have been flourishing in recent years largely due to its amiability in producing asymmetric stereo- and regioselective products. Direct products of diene hydroboration, however, have received little attention, with most substrates being assumed to produce the anti-Markovnikov product expected from textbook organic chemistry understanding. Previous experimental studies have observed the presence of a plethora of hydroboration products, and a significant progress has been made in assigning species to experimental data—though often with contradicting results. This study has used a computational approach employing quantum chemical calculations to determine atomic charges of cyclic and acyclic dienes and correlate these with calculated activation energy barriers in order to predict the regio- and stereoselective outcome of hydroboration reactions. Results indicated a strong correlation between the most polarized atomic charges of double-bonded carbons and the lowest energy transition states as expected. Intriguingly, we identified 1,3-cyclohexadiene as the main example that does not follow the anti-Markovnikov rule. We proceed to show that in addition to the polarity of the double bonds within a molecule, in this case, the conjugation with the allyl double bond and the specific geometric features of the cyclohexane ring were key stabilizing factors for the unexpected transition state preference, resulting in a regioselectivity that is in quantitative agreement with previous experimental data. Our results further indicated that Re-face attacks and steric factors due to substituents of the substrate influenced mainly the stereoselective outcome of the reaction, also affecting the pathways available to proceed through to complete the hydroboration process.

Keywords Hydroboration · Anti-Markovnikov rule · Markovnikov rule · 11B NMR · Lewis acid–base · Frustrated Lewis pair

1 Introduction

Hydroboration is one of the most central reactions pertaining to boron chemistry, due to its involvement in a wide array of chemical synthesis applications [1–5]. Hydroboration of alkenes has great importance because of the wide variety of uses of the resulting organoboranes, such as in Suzuki cross-coupling reactions and aldol condensation reactions [6–8]. Compared with other intermediate compounds, organoboranes are readily prepared from alkenes and alkynes with various structures, giving them their great applicability in organic synthesis [6, 9–11]. Furthermore, the highly stereo- and regioselective nature of hydroboration products has lent themselves to applications in pharmaceuticals [12], as well in the reduction of environmental CO_2 [13] and in the polymerization of propylene into polypropylene [14]. Despite the relevance of the direct

Published as part of the special collection of articles "Festschrift in honour of P. R. Surjan".

Electronic supplementary material The online version of this article (doi:10.1007/s00214-015-1768-6) contains supplementary material, which is available to authorized users.

✉ Edina Rosta
edina.rosta@kcl.ac.uk

[1] Department of Chemistry, King's College London, London SE1 1DB, UK

[2] Melville Laboratory for Polymer Synthesis, Department of Chemistry, University of Cambridge, Lensfield Road, Cambridge CB2 1EW, UK

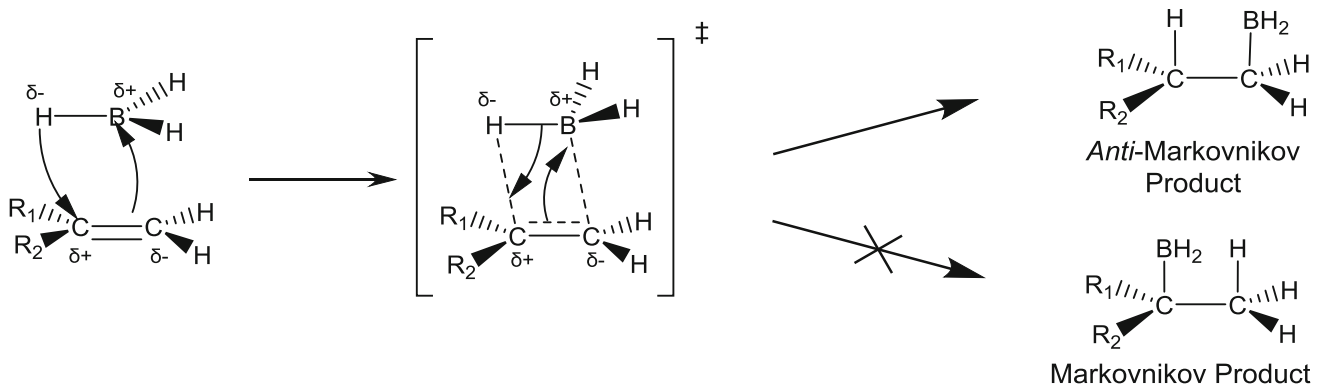

Scheme 1 General mechanism of hydroboration with the favored anti-Markovnikov product

hydroboration products in the final product specificity, previous studies have mainly focused on the subsequent reactions, such as their oxidation to form alcohols, and the direct unoxidized hydroboration products have until now received little attention [15–17].

Stereo- and regiospecificity of the final synthetic products depends on the specificity of the first hydroboration reaction steps. It is well established that hydroboration favors the anti-Markovnikov regiochemistry and *cis* stereochemistry (*syn*-addition, Scheme 1), hence highly useful in chemical synthesis where only one stereoisomer is desired. In hydrocarbons with complex substituents, and more than one double bond, the anti-Markovnikov rule is not directly applicable (i.e., the number of hydrogens at two non-equivalent carbon atoms of the same double bond can be equal), and determining the reaction specificity is not immediately obvious. Simplified explanations of hydroboration use the positions of resulting hydroxyl groups to assign the positions of boron attachment and infer the reaction mechanism. This, however, is known to be inaccurate, as an oxidized product can arise from several different organoboranes [17], and a mechanistic explanation is missing that describes the complete process, including the specific identity of the unoxidized compounds [17]. In addition, owing to the high reactivity and sensitivity of the direct hydroboration products to oxidation, their study using solely analytical techniques is highly challenging. Here we studied potential direct hydroboration reaction products focusing on possible pathways depicted in Scheme 2.

We characterized the specificity of the direct hydroboration reaction products of straight chain and cyclic dienes using computational methods. It was previously thought that only partial hydroboration takes place in dienes, resulting in unsaturated reaction products described by Brown and Bhat [18]. Our recent study [17] demonstrated that hydroboration was not limited to one of the double bonds, and that in fact polymers formed as a result of fully saturated, boron-containing hydrocarbons cross-linking together. We report here the results of quantum chemical calculations of hydroboration reactions, focusing on the regiospecificity of the obtained products. We compare reaction energy barriers and partial charges of carbon atoms to predict the most prevalent products. We validate our structural models by comparing calculated and experimental ^{11}B NMR chemical shifts.

2 Results and discussion

We focused primarily around the ten cyclic, and one non-cyclic dienes (Fig. 1), with experimental data available from previous work for eight [17]. Hydroboration of the initial substrates yields a monosubstituted species, which can further react to form various fully hydroborated products, depending on the ratio of the borane and the reactant diene [17]. The amount of diene available to react affects the ratios of the resulting products, and its excess might only allow the first step of the reaction to proceed and thus yield a monosubstituted olefin. This is well documented in the example of hydroboration of 1,3-cyclohexadiene [18, 19], when hydroboration proceeds only to the first step in Scheme 2, and both allyl (2-cyclohexene-1-ol) and homoallyl (3-cyclohexene-1-ol) species are formed, with the first one in excess (Fig. 2). Interestingly, up to 90 % regioselectivity was observed for the allyl product with specific hydroboration agents [18]. This unexpected regioselective outcome [19] posed an interesting case in our analysis and is discussed further in Sect. 2.1.

2.1 Monohydroboration products of dienes

In our first analysis step, we were interested in determining the regio- and stereoselectivity of the hydroboration reactions under reaction conditions where monohydroboration products are formed primarily. To analyze the selectivity of the reactions, we focused on the rate-determining step

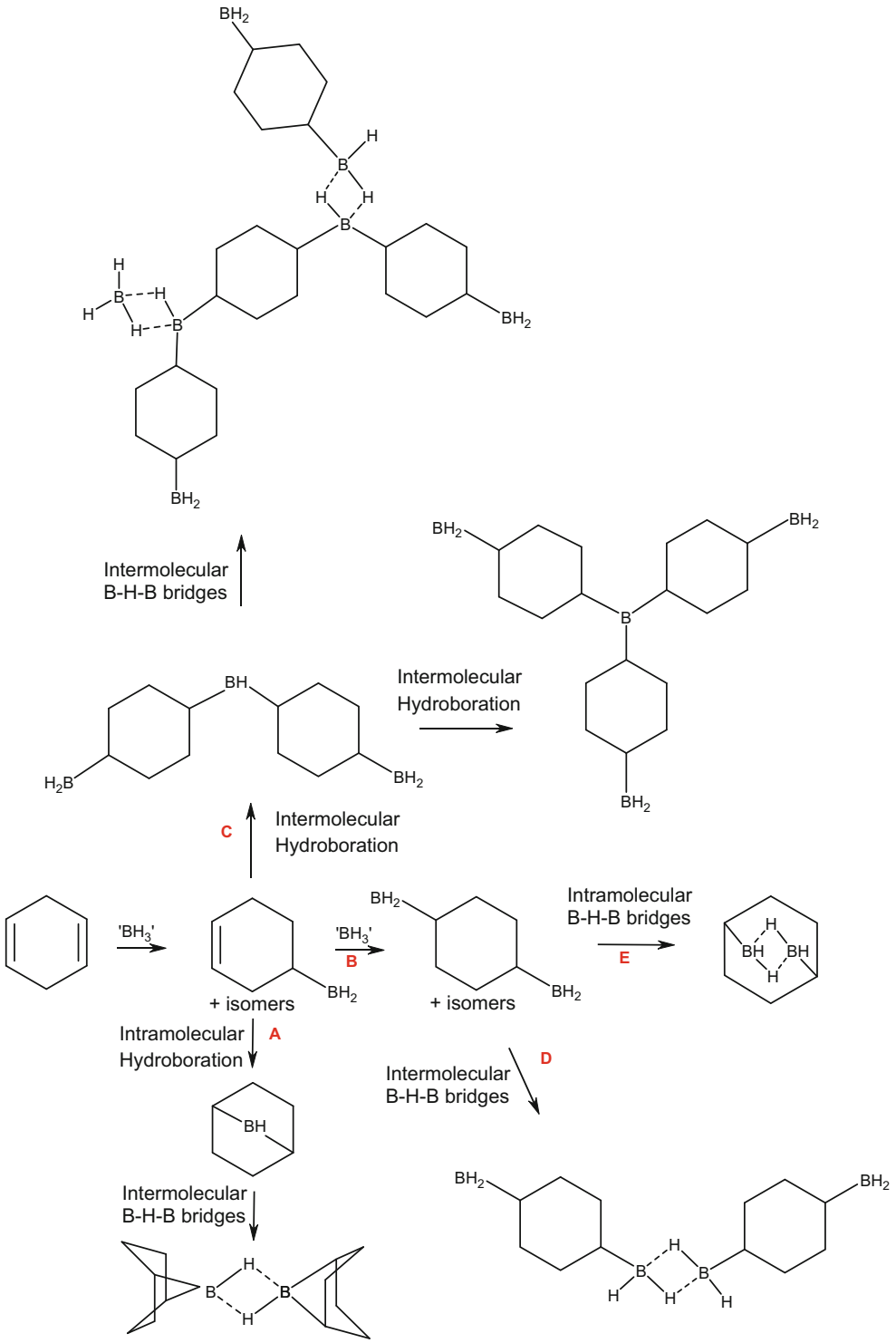

Scheme 2 Schematics of possible reaction intermediates and products in hydroboration reaction pathways utilizing hydroboration of C=C double bonds together with B–H–B bridge formation. Pathways A or B + E (*red*) lead to small-molecule products, whereas pathways C or B + D (*red*) can lead to the formation of polymers

using the high-energy BH_3-diene adducts as our starting reactant states [17]. We calculated the energies of geometry-optimized reactant and transition states corresponding to hydroboration on all possible sp^2 carbons of the 8 molecules with previously available experimental data [17] from Fig. 1. With the calculated transition state barriers,

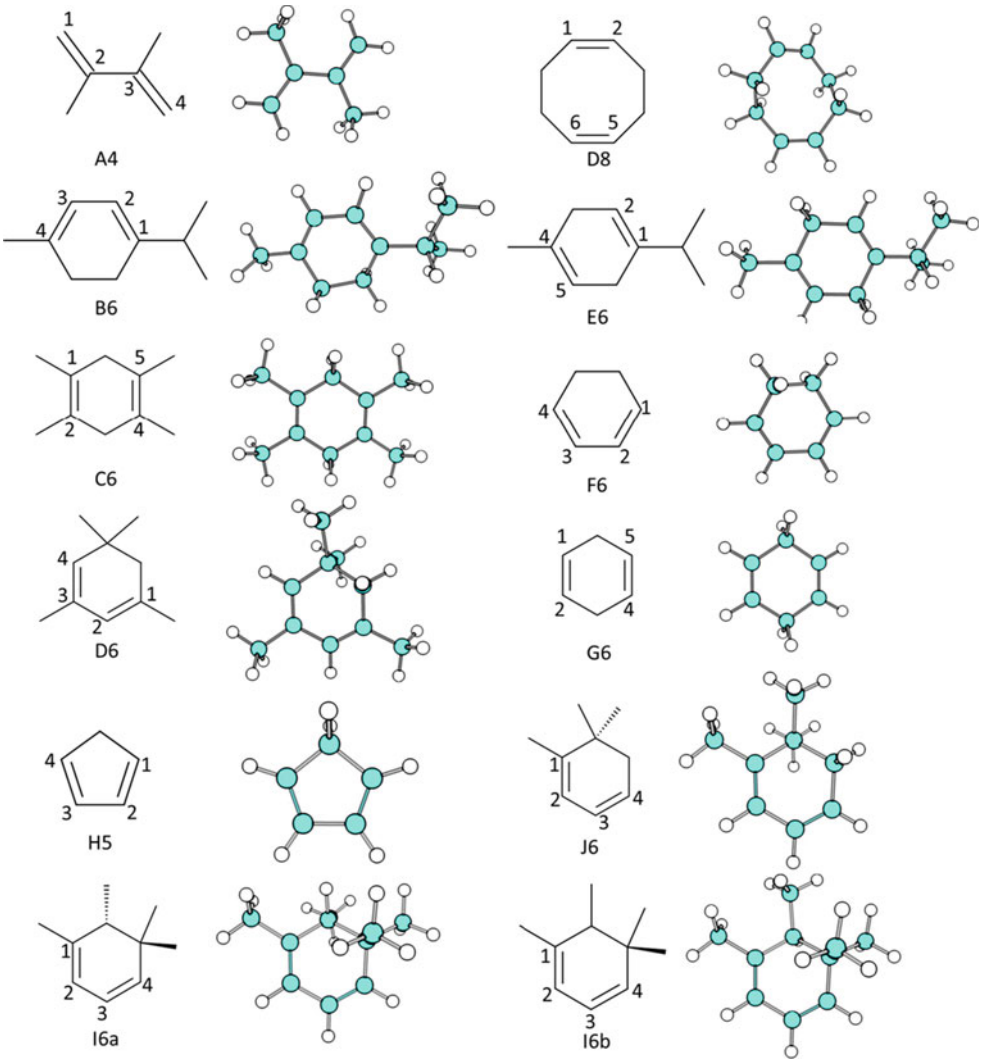

Fig. 1 Schematic and actual optimized molecular structures of the reactant diene molecules considered in this work: 2,3-dimethyl-1,3-butadiene (A4), α-terpinene (B6), 1,2,4,5-tetramethyl-1,4-cyclohexadiene (C6), 1,3,5,5-tetramethyl-1,3-cyclohexadiene (D6), 1,5-cyclooctadiene (D8), γ-terpinene (E6), 1,3-cyclohexadiene (F6), 1,4-cyclohexadiene (G6), 1,3-cyclopentadiene (H5), 1,5,5,6-tetramethyl-1,3-cyclohexadiene (I6a,b), 1,6,6-trimethyl-1,3-cyclohexadiene (J6)

and assuming a kinetically controlled mechanism, we can predict the most favorable isomers computationally [21, 22]. Previous computational studies have also pointed out the fact that the final thermodynamically favored products might not reflect the selectivity of the kinetically favored hydroboration reactions [23] and emphasized the importance of dynamical effects beyond transition state theory [24–26].

The regioselectivity of hydroboration reactions is generally dominated by the anti-Markovnikov product, where boron adds to the least substituted carbon. However, in cyclic dienes, especially those which are symmetrical, the regioselectivity is not immediately obvious owing to the equal number of hydrogens on both sides of the carbon–carbon double bond. A key relationship was previously highlighted between the reacting carbon atomic charge and the energy of the intermediates at the transition state [23]. Instead of analyzing the charge distribution of the intermediates, here we hypothesized that the charge density of the reacting dienes would mainly determine the product selectivity, corresponding to the reaction with the lowest transition state barrier. To test this, we calculated the atomic charges of the double-bonded carbon atoms (Figure S1) on the separate reacting molecules without BH_3 and compared these to the transition state barriers for each specific hydroboration reaction (Table 1). The calculated free energies using harmonic approximation are consistent with the obtained energy differences and are also reported in Table 1 (in parentheses). We analyzed the results focusing on both (1) the most negative carbons and the corresponding C–BH_2 bond formation and (2) the most positive carbons and the corresponding new C–H bond formation.

Our results, presented in Table 1, were generally consistent with the anti-Markovnikov rule, and the most negatively charged carbon atom afforded the lowest energy transition state (Fig. 3, left). Analogously, the most positive carbon had the lowest energy transition state corresponding to the formation of the new C–H bond on that carbon atom

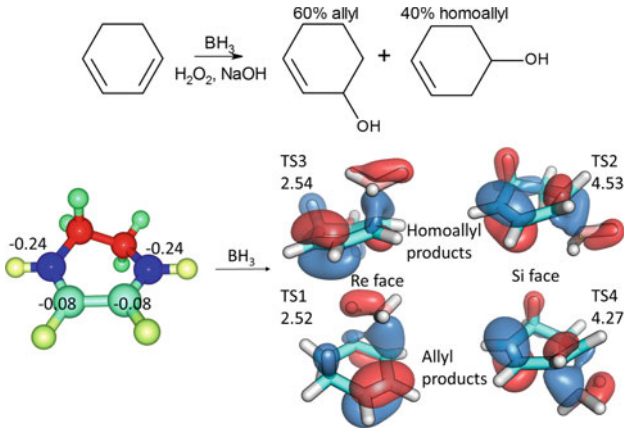

Fig. 2 *Top* reaction scheme for the hydroboration of 1,3-cyclohexadiene, giving rise to the allyl and homoallyl products. Yields are reported using B_2H_6 as the hydroboration agent in THF solvent [20]. *Bottom* optimized geometries of the F6 molecule and possible transition states leading to regio- and stereoselective monohydroboration intermediates. CHelpG atomic charges of the sp^2 carbons of the F6 molecule are shown (a.u., *color code* corresponds to atomic charges), and for each transition state, the HOMO orbitals are displayed together with the corresponding activation energies (kcal/mol)

(Fig. 3, right). Both focusing on the carbon with the C–BH_2 or on the one with the C–H bond, the corresponding correlations are very similar and they show a good agreement with the expected selectivity. It is worth noting that the CHelpG charge scheme [27] performs much more consistently than the Mulliken charge scheme, as expected. The seemingly contradicting atomic charge results between the two schemes can be attributed to the basis set size. CHelpG charges proved to be consistent across smaller (6-31G) and larger (cc-pVTZ) basis sets for F6 (data not shown). On the other hand, Mulliken charges fluctuated and showed great variations depending on basis set size. In particular, atomic charges of the carbons for A4 are unphysically polarized using diffuse orbitals with the 6-31+G or 6-31+G* basis sets, and the polarization of the BH_3 molecule is the opposite of the expected bond polarity using 6-31+G* or cc-pVTZ basis sets (Table S3). The low electronegativity of boron results in the attached hydrogens being more electronegative, allowing the boron to preferentially bond to the most negative conjugated carbon and the hydrogen to bond to the most positive carbon. Interestingly, slightly better correlation is found when considering the positivity of the carbon that forms the new C–H bond for B6 molecule (Fig. 3, right); however, the most reactive double bond is also the most polarized bond for all three asymmetric cases (B6, D6, and E6). The correlation with the reactant's atomic charges is less strong considering the prediction for the highest energy transition states, indicating that for the high-energy transition states additional contributing factors are present. None of the highest energy transition states corresponded to the least negative carbon (or least

Table 1 The activation energies (and free energies in parentheses) are given in kcal/mol units for the C–BH_2 bond formation for each non-equivalent carbon atom corresponding to the energy difference between the transition state (TS) and the most stable BH_3–diene adduct reactant state of the first eight molecules in Fig. 1

Molecule		Carbon number	Atomic charge		Activation energy (free energy)	
			CHelpG	Mulliken	Re face	Si face
A4	TS1	1	−0.479	−1.370	2.37 (2.96)	
	TS2	2	0.149	1.078	5.56 (6.77)	
B6	TS1	1	−0.167	0.027	7.60 (8.51)	7.77 (8.48)
	TS2	4	0.082	0.015	5.08 (5.92)	7.51 (8.14)
	TS3	2	−0.108	−0.150	5.89 (6.57)	4.88 (5.79)
	TS4	3	−0.249	−0.141	3.10 (3.94)	4.97 (5.63)
C6	TS1	1	−0.117	1.263	5.25 (6.26)	
D6	TS1	2	−0.354	−0.322	4.40 (5.28)	4.76 (5.85)
	TS2	1	0.125	0.911	7.97 (8.78)	8.78 (9.64)
	TS3	3	0.287	0.204	5.61 (6.31)	10.00 (10.94)
	TS4	4	−0.594	−0.758	2.12 (2.95)	7.70 (8.61)
E6	TS1	4	0.052	0.813	5.73 (6.47)	5.86 (6.20)
	TS2	5	−0.387	−0.190	3.25 (4.03)	3.30 (3.56)
	TS3	1	−0.175	0.186	7.96 (8.52)	6.23 (6.91)
	TS4	2	−0.302	0.398	3.87 (4.71)	4.37 (4.74)
F6	TS1	2	−0.083	−0.189	2.52 (3.39)	4.27 (4.98)
	TS2	1	−0.243	−0.007	2.54 (3.52)	4.53 (5.06)
G6	TS1	1	−0.256	0.093	3.25 (3.98)	

Atomic charges (in a.u.) are given for the reacting molecules without BH_3 (Figure S1) using both the CHelpG [27] and the Mulliken charge schemes. To assess potential stereospecificity, activation energies were also calculated from Si-face attack leading to enantiomers for B6, D6, E6, and F6

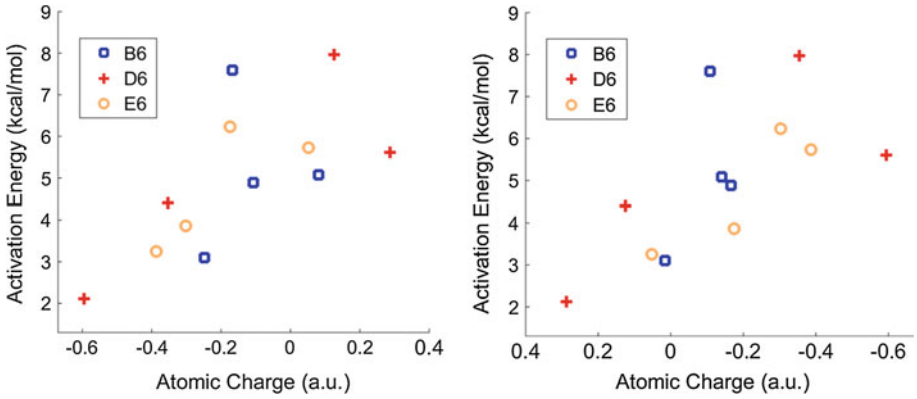

Fig. 3 Correlation between the carbon atomic charges (a.u.) and the activation energies (kcal/mol) corresponding to the C–BH_2 (*left*) and new C–H bond formation (*right*) for B6, D6, and E6 (the lower energy structures are chosen between the Re- and Si-face attack positions)

positive, if considering C–H bond formation), which might be explained by the more readily available polarization of the double bond with the most negative carbon, to accommodate the TS.

For our first set of 8 molecules corresponding to experimental data, in all but one case, the lowest energy transition state corresponded to the most polarized double bond with the expected selectivity for the hydroboration. Intriguingly, 1,3-cyclohexadiene (F6 molecule) was an exception, despite the strong polarization of the double bonds. The allyl and homoallyl products were approximately equally preferred, with the allyl TS lower in energy by 0.09 kcal/mol based on the larger cc-pVTZ basis set calculations. This agrees well with the experimentally observed slight preference for the allyl product (60–65 %) reported for this molecule using THF as solvent and B_2H_6 as hydroboration agent [20]. The experimental selectivity corresponds to a free energy difference of less than 0.4 kcal/mol, which is a difference well within the error of the calculations. Depending on the hydroboration agent, the allyl product can have even higher prevalence over the homoallyl product, with the more positive carbon forming the C–B bond, opposite to other known hydroboration selectivities that follow the anti-Markovnikov rule [19].

According to our calculated TS structures, there was also a strong stereoselectivity of the final products in the R configuration corresponding to the Re-face attack (Table 1) at both the allyl and homoallyl carbon positions. However, the observed products would be a mixture of enantiomers, as the cyclohexadiene ring would have an equivalent conformer, leading to the opposite selectivity with identical energies. Additional asymmetric substituents at the CH_2 groups would likely stabilize one of the two conformers of the ring, leading to stereospecific products.

To quantitatively analyze the energetic and structural reasons for the observed unexpected regioselectivity of F6, we performed separate QM calculations on the cyclohexadiene ring and the BH_3 molecules in their respective TS structures. We found that the structural differences were almost negligible for the BH_3 molecule and were very minor for the TSs corresponding to the Re-face (TS1 and TS3, RMSD = 0.062 Å) or the Si-face attacks (TS2 and TS4, RMSD = 0.045 Å). The main structural changes were due to slight movements of the CH_2 groups (Figure S2). The Re- and Si-face attacking direction naturally affects the hydrogen atoms already bonded to the carbons on the double bond, as these carbons move toward sp^3 hybridization. We compared the energy differences between the TS geometries and the fully optimized F6 geometry for each TS structure (Table S1; Fig. 4). In general, the allyl and the Re-face attack structures were lower in energy than the homoallyl and the Si-face attack structures, respectively. Consequently, TS1 has the lowest energy, while TS2 the highest. The difference in the relative energies between the Re- and the Si-face attack structures is likely due to the specific flexibility of the cyclohexadiene ring, with the TS1 and TS3 structures being visibly closer to a chair conformation, whereas TS2 and TS4 are closer to the boat conformation. Interestingly, these minor structural changes lead to significant polarization of the attacked carbon bonds 1 and 2, respectively. In case of TS1 and TS4, the BH_2 group attacks at carbon 1. This carbon also becomes more negative compared to F6, with partial atomic charges changing from −0.08 to −0.18 a.u., for example, for TS1. On the other hand, for TS2 and TS3, the carbon 2 atomic charges change from −0.24 to about −0.32 a.u. These results indicate that the structural changes observed between the allyl and homoallyl intermediates are consistent with the pre-polarization of the carbon to allow charge transfer to the positively charged boron at the TS structure. This is also suggested by the displayed HOMO orbitals that are delocalized to the B-H breaking bond in the allyl attack (Fig. 2). In this specific case, the adjacent Lewis base double bond is likely a contributing factor for the preference toward the allyl intermediate.

The paradoxical regioselectivity is often attributed to steric effects of the CH_2 groups in the literature [19]. To test whether steric effects might be responsible for the

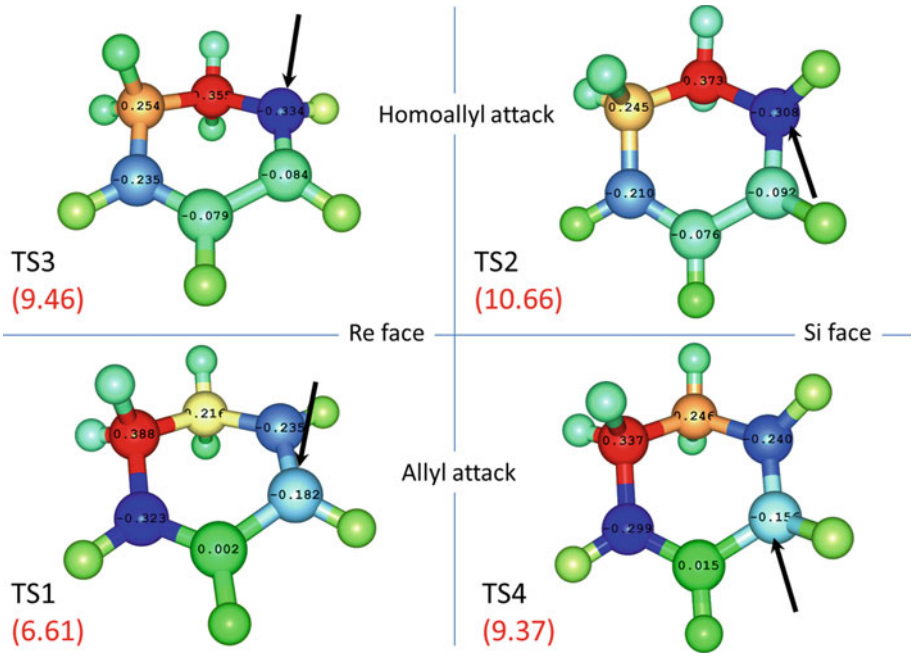

Fig. 4 Charge distribution and structures of the cyclohexadiene ring at the TS (color code corresponds to the atomic charges, from *blue negative* to *red positive*). The allyl attack conformations pre-polarize the allyl carbon from −0.08 a.u. to about −0.17 a.u., regardless of the attack orientation (Re or Si face). On the other hand, the conformations corresponding to the homoallyl attack pre-polarize the homoallyl carbon from −0.24 a.u. to about −0.32. Relative energies of the F6 molecules are shown in parenthesis (kcal/mol, *red*) compared to the optimized geometry, and *arrows* indicate the boron attack

observed energy differences, we analyzed the TS structures with respect to the closest CH_2–BH_3 distances (Figure S3). For TS2 and TS4, these distances are as short as 2.30 Å. However, there are no significant steric effects between TS1 and TS3 that could prompt the observed energy difference of the F6 geometries (6.61 vs. 9.46 kcal/mol). To test this, we reoptimized the TS1 transition state enforcing a fixed distance of 2.38 Å between two hydrogens as shown in Figure S3C, matching the shortest distance present in TS3. The increase in the energy was only 0.2 kcal/mol for the TS structure and 0.15 kcal/mol for only the F6 energy without BH_3, which does not explain the almost 3 kcal/mol energy difference between the altered F6 geometries of TS1 and TS3 (Fig. 4). Taken together, the data suggest that the main reason for the structural stabilization energy observed for the allyl attack F6 geometries is due to the differences in polarizability between the allyl and homoallyl positions. Interestingly, we previously reported that when the BH_2 substituent is in an axial position, the double bond delocalizes over to the boron dihydride substituent at the allyl position as seen by the HOMO [17] and by the atomic charges (Figure S4). This allyl borane–π bond interaction, reminiscent to that of frustrated Lewis pairs [28], imparts a degree of stability to the molecule, through increasing the electron density located at the boron, and contributes to lowering the activation energy of the corresponding transitions states.

To determine the electrostatic and polarization energies between the F6 and BH_3 molecules at the TS structures, we compared the energies of the fully interacting and non-interacting cyclohexadiene and BH_3 molecules (Table S1). The calculated interaction energies show an excellent correlation with the dipole–dipole interactions derived from the parallel B–H and C=C bonds at the TS (Figure S5). As expected based on the anti-Markovnikov rule, the homoallyl attack corresponds to significantly stronger electrostatic interactions due to the more favorable polarization of the double bond in F6 interacting with the dipole of the B-H bonds at TS3 and TS2.

To further explore examples where the deviation from the anti-Markovnikov rule might be present, we included three additional species in our analysis, described in previous experimental work [18, 29, 30]. Cyclopentadiene (H5) is known to follow the anti-Markovnikov rule, and our calculations also predicted the more favorable homoallyl product [18] both on the basis of the atomic charges of H5 and the calculated activation energies (Table S2). Previous experimental data suggested that 1,5,5,6-tetramethyl-1,3-cyclohexadiene (I6a,b), 1,6,6-trimethyl-1,3-cyclohexadiene (J6) can favor the allyl product under some conditions. For both of these molecules, the most polarized double bond corresponds to carbons 3 and 4, with carbons 1 and 3 being the most positively charged sp^2 carbons (Table S2). According to the anti-Markovnikov rule, we would expect the homoallyl carbon 4 to be most likely substituted by the BH_2 substituent after hydroboration. The activation energies suggest, however, that there is a nearly equal amount of allyl (I6a TS1 and I6b TS3 in total) and homoallyl (I6b TS4) products for I6 at carbons 3 and 4, respectively. Here, the unexpected preference for the positively charged carbon 3 is likely compensated for by the highly polarized double bond and by the conjugation also

observed in F6. In J6, the most preferred substitution corresponds to carbon 2 according to our calculations, favoring the allyl position, and the most negatively charged homoallyl carbon 4 is less preferred with a higher activation energy.

In summary, our results show that the regioselectivity can be attributed to the interplay between two main factors (1) the dipole–dipole interactions of the boron B-H bond with the double bond and (2) the allyl position of a second double bond providing favorable polarization in the six-membered ring. In addition, the stereoselectivity is largely controlled by the structural flexibility of the cyclohexene ring favoring the Re attack.

These results lend themselves to predicting the most likely product of hydroboration reactions, as the molecule with the lowest energy transition state should yield the kinetic product. These results are also in correlation with the anti-Markovnikov regioselectivity of the reaction: the electropositive boron within a hydrogen-boron bond of the borane electrostatically favors the most negatively charged sp^2 carbon within the molecule. Intriguingly, 1,3-cyclohexadiene presents an important exception to the anti-Markovnikov rule, whereas transition state theory continues to predict the selectivity of the reaction.

The observed product specificity does depend not only on the selectivity of the first hydroboration step leading to monosubstituted RBH_2 compounds, but also on subsequent hydroboration reactions as well. We showed previously that the RBH_2 products can be more reactive than the borane, and we expect rapid formation of R_2BH products [17]. We assumed here that the selectivity remains similar using RBH_2 for hydroboration; however, future studies aiming for fully quantitative results would need to take into account subsequent steps. Here we further analyzed the possible hydroboration products after the completion of the hydroboration reactions.

2.2 Full hydroboration products of dienes

To better understand the nature of final hydroboration products before subsequent oxidation, we considered competing pathways of hydroboration reactions (Scheme 2). The end product of the first hydroboration step using an activated 'BH_3' is a mixture of monosubstituted boranes with a single double bond. Further borane addition can take place in three different ways: by intermolecular hydroboration via the attached BH_2 substituent (pathway A in Scheme 2), by another activated 'BH_3' molecule (pathway B in Scheme 2), or by intramolecular hydroboration via another monosubstituted borane (pathway C in Scheme 2). Covalent polymers can thus form via pathway C [17], following the intermolecular hydroboration reaction pathway. In pathway C, subsequent hydroboration of R_2BH species can further occur to form trialkyl boranes. Accordingly, well-documented examples suggest that the corresponding species are often found as homologues of trialkylboranes (R_3B) [20, 31].

Immediately following the hydroboration reactions, the high-energy trigonal boron species are stabilized by forming intermolecular (e.g., via pathway D) or intramolecular (when possible, e.g., via pathway E) B–H–B bridges. Stabilization can also occur via adduct formation with the solvent or with BH_3. Trialkyl species are exceptions, in that they are generally stable trigonal boron species that do not form adducts [17].

In Scheme 2, dimeric or monomeric small-molecule compounds form via pathways A and B + E. On the other hand, polymers may form via pathways C or B + D. Here we aimed to compare the A and B + E pathways and to verify whether the species are also observed experimentally, and to infer their relative prevalence.

In hydroboration reactions described in our previous study [17], two possible products were observed depending on the nature of the reactant dienes and the reaction conditions: formation of cross-linked polymers, which precipitate out of solution, or formation of soluble, small-molecule products, which have been analyzed using ^{11}B NMR. Previous analysis [17] of the experimental NMR data (reproduced here as Figs. 5 and S6) suggested that a range of fully hydroborated product species were present. The substrates F6, 1,3-cycloheptadiene, 1,3-cyclooctadiene, G6, and E6 all yielded cross-linked polymers, whereas substrates D8, B6, C6, and the control A4 all yielded clear solutions. Interestingly, the excess equivalents of borane used in the reaction can also affect the outcome of the reaction products for certain molecules, such as in the example of 1,3,5,5-tetramethyl-1,3-cyclohexadiene (D6), which was seen to form a clear solution when only one equivalent of borane was used, but an insoluble precipitate was observed when two equivalents were used [17]. The clear solution of D6 eventually formed a precipitate after 2 h.

^{11}B NMR of the clear solutions of substrates reacted with two equivalents of borane resulted in spectra with many peaks, the origins of which were not all apparent. The presence of peaks at −10.4 and −29.1 ppm was attributed to the presence of impurities in the $BH_3{\cdot}SMe_2$ starting material, but were found not to participate in the hydroboration reaction. The presence of a quartet at −20.4 ppm was due to unreacted $BH_3{\cdot}SMe_2$. The main experimental peaks of the hydroboration products are listed in Table 2 together with initial assignment of the corresponding species [32]. In this work, we calculated theoretical chemical shifts for possible reaction products (Table S4) through the use of quantum chemical calculations, and their concordance with reported experimental data was compared.

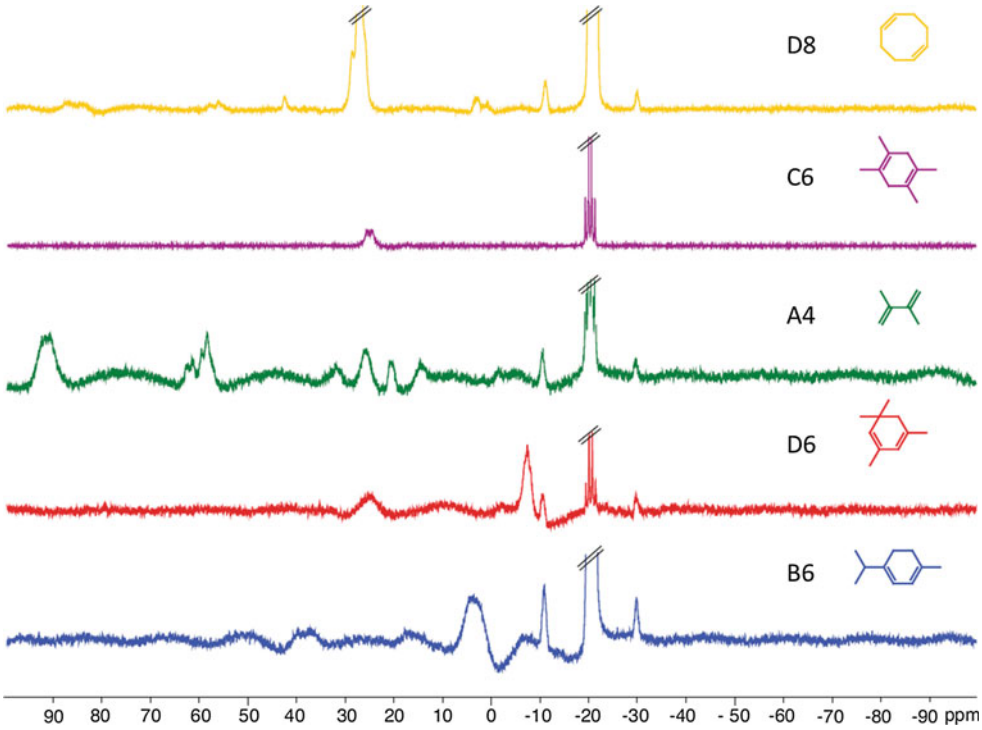

Fig. 5 ^{11}B NMR spectra at one equivalent $BH_3{\cdot}SMe_2$. The ^{11}B NMR spectra of the clear solutions after hydroboration of (from *bottom* to *top*) α-terpinene (B6), 1,3,5,5-tetramethyl-1,3-cyclohexadiene (D6), 2,3-dimethyl-1,3-butadiene (A4), 1,2,4,5-tetramethyl-1,4-cyclohexadiene (C6), and 1,5-cyclooctadiene (D8) in diglyme. Diagram adapted from Andreou et al. [17]

The competing reaction pathways during hydroboration have very different rates depending on the chemical structure of the diene, thus resulting in entirely different outcomes. Previous work by Brown and Bhat [18] suggested that monohydroboration was prevalent in six-membered rings, which were thought to be relatively inert to dihydroboration. Our recent work has shown that with sufficient excess borane using either B_2H_6 or $BH_3{\cdot}SMe_2$, all cyclic dienes undergo complete hydroboration of all double bonds [17].

As evident, a large number of ^{11}B NMR peaks in Table 2 for the first hydroboration products can be attributed to the formation of intermolecular B–H–B-bridged compounds, such as R_2BHBH_3. Interestingly, however, in the characterization of the direct products of diene hydroboration, the possibility of intermolecular hydroboration via RBH_2 species and the role of pathway C are often omitted in theoretical calculations. In Table 1, we also focused on the reactions with BH_3 as the hydroboration agent; however, we note that to quantitatively account for the selectivity, subsequent reactions also need to be taken into account where RBH_2 species serve as hydroboration agents. Toward this aim, here we investigate a second, intramolecular dihydroboration step of pathway A, leading to bridged bicyclic rings.

Pathway A with intramolecular hydroboration is favored for dienes where the double bonds are farther apart, hence the rapid dihydroboration of the 1,5-cyclooctadiene [19]. On the other hand, molecules such as 1,3-cyclooctadiene and 1,3-cycloheptadiene were seen to polymerize following pathway B or C, and only the 1,5-cyclooctadiene was observed to yield clear solution. Therefore, with six-membered or larger rings, the intramolecular hydroboration will occur dominantly when the double bonds are not in proximity to each another [18]; otherwise, steric constraints take precedence and the cyclic product does not rapidly form. With smaller rings, the energy barrier to form cyclic products is higher, and pathways A and B can be in competition with one another.

To better understand the structures and energetics of the mechanism for reaction pathway A, we performed initial reaction coordinate scanning using the B–C bond distance as the reaction coordinate with ORCA and calculated the energy profiles for A4 and D8 molecules (Figure S7, top). Subsequently, we optimized the TS geometries using Gaussian 09 (Fig. 6, and Figure S7, bottom). To ensure that the correct saddle point was identified, we calculated the minimum energy reaction pathway using the intrinsic reaction coordinate (IRC) [33] with Gaussian 09 (Fig. 6, left).

The calculated energy barrier starting with the monohydroborated D8 1,5-cyclooctadiene was 8.25 kcal/mol, which is easily overcome in room temperature, and therefore, a rapid reaction is expected. Note, however, that to determine the actual activation energies, the relative energy of the reactant states also needs to be accounted for, as B-H-B bridges are generally more stable than the interacting intramolecular π-bond–borane adduct [17]. We have not calculated this here, but estimate it to be below 7 kcal/

Table 2 Experimental ^{11}B NMR chemical shifts in THF and diglyme, their structural attributions, and calculated chemical shifts

Reactant molecule	Exp. ^{11}B NMR		Attribution
	THF	diglyme	
B6	**4.7**	**4.9**	R_2BHBH_3
	40.8	40.0	R_2BHBH_3
D6	**−6.9**	**−7.1**	$RBH_2{\cdot}SMe_2$
	26.0	**25.0**	$(RBH_2)_2$
A4	**14.7**	**14.9**	R_2BHBH_2R
	21.3	**21.1**	$(RBH_2)_2$
	26.6	**26.1**	$(R_2BH)_2$
	32.1	**32.4**	R_2BHBH_2R
	58.7	**58.8**	N/A
	60	60	N/A
	91.5	**91.2**	R_3B
C6	**24.8**	**26.0**	$(R_2BH)_2$
	17.8	**17.7**	
	−12.9		
D8	8.5	1.4	R_2BHBH_3
		3.7	
	18.5	13.4	N/A
	27.6	**27.6**	Cyclic $(R_2BH)_2$
		29.1	
	43.0	43.0	R_2BHBH_3
		56.7	
	84.8	88.3	R_3B
	87.6		R_3B

The chemical shifts of the most prominent peaks are highlighted in bold. Corresponding calculated potential structures are available in SI (Table S4)

mol based on calculations presented in Table S1 of Andreou et al. [17], resulting in an overall barrier below 15 kcal/mol. The dihydroborated D8 product species affords a bicyclic ring system consisting of two six-membered rings. Figure 6 illustrates that a stable reactant complex is formed via the intramolecular borane adduct formation, and the reaction proceeds via a relatively sharp transition state, corresponding likely to the simultaneous breaking and forming of rigid hydrogen bonds (B–H and C–H) at the TS. In a solution where borane is not readily available, this secondary intramolecular hydroboration step would be even faster due to the availability of the already activated RBH_2 species, in particular where BH_2 does not yet form stable B–H–B bridges, only adducts with the solvent.

In contrast to D8, the intramolecular dihydroboration step of monohydroborated A4 has an increased barrier of 15.04 kcal/mol. This is largely due to the steric strains due to the smaller alkyl chain, as seen from the unusual intramolecular adduct reactant state structure (A4 RS in Fig. 6). Cyclic dienes with 6-membered rings are expected to have further steric constraints to the barrier of the intramolecular dihydroboration. Accordingly, we obtained a 16.17 kcal/mol activation barrier for C6 (Figure S7), a slight increase from that of the A4 molecule. To consider entropic effects at the harmonic approximation, we also calculated the zero point energies and determined the corresponding activation free energies. Entropic effects generally render the barriers higher as shown also in Table 1. The difference is particularly significant for A4 (17.88 kcal/mol), whereas C6 (17.04 kcal/mol) and D8 (8.58 kcal/mol) have only a relatively small increase between activation energies and activation free energies.

Subsequently, we calculated the ^{11}B NMR chemical shifts both for the dimeric cyclic disubstituted boranes obtained via pathway A followed by dimerization and for the intramolecular B–H–B-bridging diborane compounds obtained via pathway B + E (Table 3). The calculated chemical shifts are listed alongside the experimental values in the range of +20 to +30 ppm (Table 3). The difficulties in assigning chemical shifts to specific species arose due to the ±2 ppm error margin of both theoretical and experimental data. Despite this, many peaks were possible to assign accurately. In the case of D8, the expected

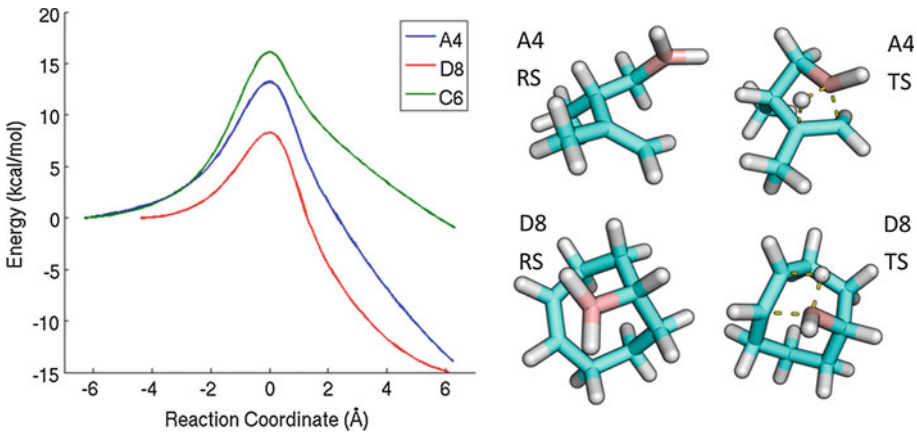

Fig. 6 Reactant intermediate and transition state species of A4 (*top right*) and D8 (*bottom right*) for intramolecular dihydroboration. Reaction energy profiles were determined by IRC calculations [33] for A4, D8, and C6 (*left*). Geometry-optimized reactant and product states provided activation (free) energies of 15.04 kcal/mol (17.88 kcal/mol) for A4, 8.25 kcal/mol (8.58 kcal/mol) for D8, and 16.17 kcal/mol (17.04 kcal/mol) for C6

Table 3 Calculated NMR chemical shifts (ppm) of dimeric cyclic boranes and intramolecular B–H–B-bridging diborane

	Cyclic $(R_2BH_2)_2$	Intramolecular $(RBH_2)_2$	Exp.
A4	28.7	19.5	21.3, 26.6
B6	23.6	25.2, 25.6	N/A
C6	26.5	23.8	25.0–26.0
D6	22.4	19.3, 24.0	25.0–26.0
D8	26.7	23.3	27.6

Experimentally observed peaks close to the calculated chemical shifts are also given

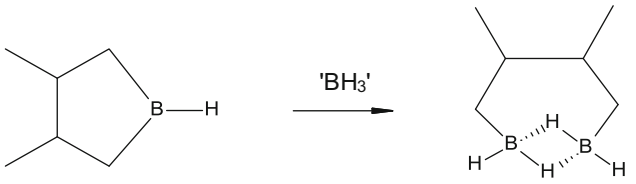

Scheme 3 Breaking of the borolane ring upon further addition of borane, BH_3, to form a diborane A4 species

cyclic products are formed at the calculated +26.7 ppm, and the diborane species are not observed. On the other hand, A4 appears to have both kinds of molecules. The diborane species at +19.5 ppm matches the experimental value of +21.3 ppm well. The assignment of the cyclic products at the calculated +28.7 ppm, however, is less certain considering other potential species that might account for the observed peak at +26.6 ppm. In general, the chemical shifts of the diborane and cyclic dimer species are very similar for B6, C6, and D6, and their assignment cannot be done without ambiguity. Interestingly, all molecules exhibit strong peaks at the +20 to +30 ppm region and likely contain at least one of the species considered in Table 3, except for B6. The NMR spectrum of B6 is significantly different from all other species, and the predicted R_2BH species in the R_2BHBH_3 remains elusive.

Experimentally, monosubstituted and *unbridged* disubstituted products are commonly accepted, and the formation of cyclic disubstituted products is thought to be more limited to larger cyclic dienes or longer alkyl chains [18]. The explanation underpinning this can be partly due to the strained geometries of the cyclic transition states, such as that for A4 (Fig. 6), and this can result in further ring-opening reactions with BH_3 as proposed earlier via a hydrogen–alkyl exchange mechanism (Scheme 3) [15, 34, 35]. Analogously, we found that the A4.6 (Table S3) species with +22.42 ppm calculated chemical shift has a lower energy by 4.85 kcal/mol compared with the A4.5 cyclic $(R_2BH_2)_2$ species and might correspond to the observed peak at +21.07 ppm. On the other hand, the corresponding cyclic diene derivatives were less energetically favorable for C6 (data not shown), D6 (D6.5 vs D6.4 in Table S3), and D8 (D8.2 vs D8.6 in Table S3).

Figure 5 and S6 of one and two equivalents of borane, respectively, show highly similar spectra for most molecules. The largest differences are observed in the case of A4, which showed products of the form $(RBH_2)_2$ and $(R_2BH)_2$ become the major products when two borane equivalents are used. This suggests that these peaks do not correspond to the cyclic $(R_2BH_2)_2$ species, as these would be expected to become less prominent when borane is in excess due to ring-opening reactions. Analogously, this decrease is observed for D8, where the borane excess enhances minor peaks, and the main peak is visibly reduced. Interestingly, precipitate formation was also observed for D8 almost instantly when two equivalents of borane were used, analogously to D6 [32]. The excess equivalents of borane via the ring-opening reactions thus might contribute to polymer formation.

3 Methodology

All calculations were performed and completed using the Gaussian 09 and ORCA suites of programs [36, 37]. Geometry optimizations of the reactant and transition states were done at the B3LYP level of theory with the 6-31+G(d,p) basis set [38] and the GD3 empirical dispersion correction [39] for each reported molecule using Gaussian 09. To determine the reaction profiles for intramolecular hydroboration, initial relaxed surface scans were performed with ORCA along the B–C bond distance of the A4, C6, and D8 molecules at 0.05 Å increments, using density functional theory methods as described above. The identified transition and product states were then fully optimized using Gaussian 09, and subsequent IRC calculations [33] were performed to confirm the RS and PS states corresponding to the TS structures identified. Vibrational frequencies were calculated for all optimized geometries to confirm the identity of each state using Gaussian 09.

The CHelpG population analysis method implemented in Gaussian 09 was used to calculate Merz–Kollman atomic charges [27, 40] for each atom within the optimized diene reactant states as described above.

Theoretical predictions for the NMR chemical shifts of the hydroboration products were done using optimized geometries obtained as described above. Single-point calculations were performed employing a larger basis set, 6-311+G(d,p), to determine the NMR shielding tensors using the Gaussian implementation of the gauge-independent atomic orbital (GIAO) method developed by Pulay et al. [41].

All previous experimental ^{11}B NMR work was carried out by Andreou et al. in both THF and bis(2-methoxyethyl)ether (diglyme) solvents [17, 32]. THF solvent was purchased from Acros, diglyme from Sigma-Aldrich, and deuterated NMR solvents from Euriso-top. ^{11}B NMR spectra were carried out using a Bruker Advance BB-ATM-500 MHz NMR spectrometer using $BF_3{\cdot}OEt_2$ as a reference.

Experimental work involved the following dienes: α-terpinene (0.12 mL, 0.7340 mmol), γ-terpinene (0.12 mL, 0.7340 mmol), 1,3-cyclohexadiene (0.07 mL, 0.7340 mmol), 1,3-cyclooctadiene (0.09 mL, 0.7340 mmol), 1,3,5,5-tetramethyl-1,3-cyclohexadiene (0.13 mL, 0.7340 mmol), 1,2,4,5-tetramethyl-1,4-cyclohexadiene (0.1 g, 0.7340 mmol), 1,5-cyclooctadiene (0.12 mL, 0.7340 mmol), 2,3-dimethyl-1,3-butadiene (0.09 mL, 0.7340 mmol).

In THF, the representative procedure for the hydroboration of dienes used $BH_3{\cdot}SMe_2$, utilizing the borane to diene addition mode: $BH_3{\cdot}SMe_2$ (0.14 mL, 1.4680 mmol) was added dropwise to a solution of a diene dissolved in THF (1 mL) pre-cooled to −40 °C. The reaction mixture was left to stir under nitrogen at 0 °C for 1 h to give a clear solution, which, depending on the diene used, contained a white precipitate.

In diglyme, the representative procedure for the hydroboration of dienes used $BH_3{\cdot}SMe_2$, utilizing the borane to diene addition mode: $BH_3{\cdot}SMe_2$ (0.07 mL, 0.7340 mmol or 0.14 mL, 1.4680 mmol) was added dropwise to a solution of a diene dissolved in diglyme (3.2 mL). The reaction mixture was left to stir under nitrogen at 0 °C for 1 h to give a clear solution, which, depending on the diene used, contained a white precipitate.

4 Conclusions

Hydroboration is one of the most valuable chemical synthesis methods, due to many reasons, including its highly specific regio- and stereoselectivity. However, in complex reagents, the identity of the preferred anti-Markovnikov product is not apparent at first glance. The use of electrostatic potential-based atomic charges has proved to be a useful tool in predicting the regioselectivity of hydroboration reactions. Here we studied 11 molecules, representing 10 cyclic dienes and a straight chain diene. In most examples, the regioselectivity for the preferred product was predicted both by the extended anti-Markovnikov rule, using the atomic charges of the reactants, and also by transition state theory—comparing the activation energies of all possible products. Here we identified the 1,3-cyclohexadiene molecule as a key exception to the anti-Markovnikov rule, which had an unforeseen preference toward the allyl product according to the transition state barrier heights. Our calculated activation energies accurately predicted the selectivity favoring almost equally the allyl products, in agreement with previous experimental studies [19], therefore validating our transition state theory-based calculation results. The unexpected selectivity was suggested to arise due to steric effects [19]. We found, however, that steric effects do not directly contribute to the observed selectivity, leading to a deviation from the anti-Markovnikov rule. Instead, the stability of the axial BH_2 group via conjugation with the allyl double bond is a more important stabilizing factor, which also relies on the unique structural properties of the cyclohexene ring as additional required factors for the paradoxical regioselectivity. We also introduced two additional derivatives (I6 and J6) and confirmed the similar selectivity rules favoring allyl positions for these molecules as well. These molecules lend themselves as additional examples with exceptional regioselectivity against the anti-Markovnikov rule.

As the anti-Markovnikov rule follows the same general principle as the Markovnikov rule [23] in terms of the most energetically favorable reaction pathway being determined by the attractive dipole–dipole interactions within a carbon–carbon double bond and the reacting X–H substituent, our results therefore provide an exception (on the basis of F6, I6, and J6) to these rules in general. We found that the Lewis acid borane, and the second remaining double bond with Lewis base properties, resembling frustrated Lewis pair-type moieties, worked synergistically to stabilize allyl–π bond interactions resulting in the unexpected selectivity. Using this as a design principle, molecules with similar electronic properties might provide an interesting avenue for the exploration of synthetically useful exceptions to the Markovnikov rule, resulting in novel chemical reactivity.

Although it is known that the process of hydroboration can occur fully at all unsaturated sites within an alkene, the precise nature of the unoxidized species formed after the completion of the reactions still remains within a gray area. ^{11}B NMR results show that several hydroboration reactions are possible, and that a variety of products may be formed.

Quantum chemical calculations together with NMR measurements can thus shed light on why a subset of reactants does not polymerize, while others do, and what the potential reaction pathways and stable products are. The observation of a plethora of products indicates that competing pathways concurrently take place within hydroboration reactions. It was concluded that the position of the double bonds, in relation to sterically demanding groups, was a strongly influencing factor in determining the structure of the product [17]. We have elucidated the mechanism for the formation of cyclic monohydroborated species, as well as specific diborane species. Our results are in very

good agreement with experimental ^{11}B chemical shifts; thus, computational methods can unveil detailed mechanistic hydroboration pathways and accurately predict the NMR peaks of specific products, verifying the reaction mechanism.

Studying the experimental conditions necessary to secure a specific product would prove to be an interesting avenue of research to pursue, as current procedures allow for the possibility of multiple product species, such as dimers, polymers, and oligomeric species. Quantum chemical calculations thus lend themselves as useful tools to help design novel enantio- and diastereoselective chemical synthesis strategies. They are also becoming easily available standard tools that are accessible in undergraduate education for computational laboratories.

Acknowledgments LH was supported by the King's Undergraduate Research Fellowships. ER gratefully acknowledges Péter Surján and the inspiration she received from the undergraduate research in his laboratory, leading to her first papers. Péter continues to inspire her work through research and teaching, including this study that was carried out together with undergraduate students at King's College, London.

References

1. Yang DT, Mellerup SK, Wang X, Lu JS, Wang SN (2015) Reversible 1,1-hydroboration: boryl Insertion into a C–N Bond and competitive elimination of HBR2 or R–H. Angew Chem Int Ed 54(18):5498–5501. doi:10.1002/anie.201500487
2. Fan XT, Zheng JH, Li ZH, Wang HD (2015) Organoborane catalyzed regioselective 1,4-hydroboration of pyridines. J Am Chem Soc 137(15):4916–4919. doi:10.1021/jacs.5b03147
3. Chong CC, Hirao H, Kinjo R (2015) Metal-free sigma-bond metathesis in 1,3,2-diazaphospholene-catalyzed hydroboration of carbonyl compounds. Angew Chem Int Ed 54(1):190–194. doi:10.1002/anie.201408760
4. Taniguchi T, Curran DP (2014) Hydroboration of arynes with N-heterocyclic carbene boranes. Angew Chem Int Ed 53(48):13150–13154. doi:10.1002/anie.201408345
5. Sztáray B, Rosta E, Böcskey Z, Szepes L (1999) Geometry and electronic structure of bis(tetrahydridoborato) bis(cyclopentadienyl)zirconium(IV). J Organomet Chem 582(2):267–272. doi:10.1016/S0022-328X(99)00062-5
6. Suzuki A (2010) Organoboranes in organic synthesis including suzuki coupling reactions. Jpn Inst Heterocycl Chem 80(1):15–43. doi:10.3987/COM-09-S(S)Summary
7. Allais C, Tsai AS, Nuhant P, Roush WR (2013) Highly diastereo- and enantioselective aldol reactions of stereochemically defined tetrasubstituted enolborinates generated by 1,4-hydroboration of α, β-unsaturated morpholine carboxamides with (diisopinocampheyl)borane. Angew Chem Int Ed Engl 52(49):12888–12891. doi:10.1002/anie.201307302
8. Dhillon RS (2007) Hydroboration and organic synthesis: 9-borabicyclo[3.3.1]nonane (9-BBN). doi:10.1007/978-3-540-49076-0
9. Hu NF, Zhao GQ, Zhang YY, Liu XQ, Li GY, Tang WJ (2015) Synthesis of chiral alpha-amino tertiary boronic esters by enantioselective hydroboration of alpha-arylenamides. J Am Chem Soc 137(21):6746–6749. doi:10.1021/jacs.5b03760
10. Obligacion JV, Neely JM, Yazdani AN, Pappas I, Chirik PJ (2015) Cobalt catalyzed Z-selective hydroboration of terminal alkynes and elucidation of the origin of selectivity. J Am Chem Soc 137(18):5855–5858. doi:10.1021/jacs.5b00936
11. Zhang L, Zuo ZQ, Wan XL, Huang Z (2014) Cobalt-catalyzed enantioselective hydroboration of 1,1-disubstituted aryl alkenes. J Am Chem Soc 136(44):15501–15504. doi:10.1021/ja5093908
12. Klotter F, Studer A (2015) Short and divergent total synthesis of (+)-machaeriol B, (+)-machaeriol D, (+)-delta(8)-THC, and analogues. Angew Chem Int Ed Engl 54(29):8547–8550. doi:10.1002/anie.201502595
13. Yang Y, Xu M, Song D (2015) Organocatalysts with carbon-centered activity for CO_2 reduction with boranes. Chem Commun (Camb UK) 51(56):11293–11296. doi:10.1039/c5cc04337a
14. Niu H, Dong J-Y (2015) Regio-chemistry control in propylene/isoprene copolymerization by metallocene catalysts. Polym Int 64(8):1023–1029. doi:10.1002/pi.4878
15. Brown HC, Negishi EI, Burke PL (1971) Organoboranes. 12. Hydroboration of 1,3-butadiene with borane in tetrahydrofuran in a ratio equal to or smaller than 1 1—interconversion between B-alkylborolanes and 1,2-tetramethylenediboranes. J Am Chem Soc 93(14):3400. doi:10.1021/ja00743a017
16. Brown HC, Negishi EI, Gupta SK (1970) Reaction of B-methoxydialkylboranes with lithium aluminum hydride in presence of olefins—a new and general synthesis of acyclic and cyclic mixed trialkylboranes and their conversion into corresponding trialkylcarbinols via carbonylation–oxidation. J Am Chem Soc 92(22):6648. doi:10.1021/ja00725a050
17. Andreou A, Leskes M, Jambrina PG, Tustin GJ, Grey CP, Rosta E, Scherman OA (2015) Divergence from the classical hydroboration reactivity; boron containing materials through a hydroboration cascade of small cyclic dienes. Chem Sci. doi:10.1039/C4SC02729A
18. Brown HC, Bhat KS (1986) Hydroboration 76. Hydroboration of cyclic dienes with representative hydroborating agents. J Org Chem 51(4):445–449. doi:10.1021/jo00354a005
19. Zweifel G, Nagase K, Brown HC (1962) Hydroboration. XIII. The hydroboration of dienes with disiamylborane. A convenient procedure for the conversion of selected dienes into unsaturated alcohols. J Am Chem Soc 84(2):190–195
20. Zweifel G, Nagase K, Brown HC (1962) Hydroboration. XII. The hydroboration of dienes with diborane. J Am Chem Soc 84(2):183–189. doi:10.1021/ja00861a012
21. Houk KN, Rondan NG, Wu Y-D, Metz JT, Paddon-Row MN (1984) Theoretical studies of stereoselective hydroborations. Tetrahedron 40(12):2257–2274. doi:10.1016/0040-4020(84)80009-5
22. Ess DH, Kister J, Chen M, Roush WR (2009) Quantum-mechanical study of 10-R-9-borabicyclo[3.3.2]decane alkene hydroboration. J Org Chem 74(22):8626–8637. doi:10.1021/jo901737d
23. Ilich P-P, Rickertsen LS, Becker E (2006) Polar addition to C=C group: why is anti-Markovnikov hydroboration–oxidation of alkenes not "anti-"? J Chem Educ 83(11):1681. doi:10.1021/ed083p1681
24. Oyola Y, Singleton DA (2009) Dynamics and the failure of transition state theory in alkene hydroboration. J Am Chem Soc 131(9):3130–3131. doi:10.1021/ja807666d

25. Zheng J, Papajak E, Truhlar DG (2009) Phase space prediction of product branching ratios: canonical competitive nonstatistical model. J Am Chem Soc 131(43):15754–15760. doi:10.1021/ja904405v
26. Glowacki DR, Liang CH, Marsden SP, Harvey JN, Pilling MJ (2010) Alkene hydroboration: hot intermediates that react while they are cooling. J Am Chem Soc 132(39):13621–13623. doi:10.1021/ja105100f
27. Breneman CM, Wiberg KB (1990) Determining atom-centered monopoles from molecular electrostatic potentials. The need for high sampling density in formamide conformational analysis. J Comput Chem 11(3):361–373. doi:10.1002/jcc.540110311
28. Stephan DW (2015) Frustrated Lewis pairs: from concept to catalysis. Acc Chem Res 48(2):306–316. doi:10.1021/ar500375j
29. Uzarewicz A (1964) Rocz Chem 38:599
30. Uzarewicz A (1964) Rocz Chem 38:385
31. Matsumi N, Chujo Y (1997) Synthesis of novel organoboron polymers by hydroboration polymerization of bisallene compounds. Polym Bull (Berl) 38(5):531–536. doi:10.1007/s002890050083
32. Andreou A (2013) Synthesis and reactivity of boron hydrides for the preparation of chiral diboranes and bis-phosphines. University of Cambridge, Cambridge
33. Fukui K (1981) The path of chemical reactions—the IRC approach. Acc Chem Res 14(12):363–368. doi:10.1021/ar00072a001
34. Brown HC, Negishi EI (1972) The cyclic hydroboration of dienes. A simple convenient route to heterocyclic organoboranes. Pure Appl Chem 29:527–545
35. Brown HC, Negishi E, Burke PL (1970) Facile opening of the borolane ring with borane. A simple entry into 1,2-tetramethylenediboranes. J Am Chem Soc 92(22):6649–6651. doi:10.1021/ja00725a051
36. Frisch MJ, Trucks GW, Schlegel HB, Scuseria GE, Robb MA, Cheeseman JR, Scalmani G, Barone V, Mennucci B, Petersson GA, Nakatsuji H, Caricato M, Li X, Hratchian HP, Izmaylov AF, Bloino J, Zheng G, Sonnenberg JL, Hada M, Ehara M, Toyota K, Fukuda R, Hasegawa J, Ishida M, Nakajima T, Honda Y, Kitao O, Nakai H, Vreven T, Montgomery JA Jr, Peralta JE, Ogliaro F, Bearpark MJ, Heyd J, Brothers EN, Kudin KN, Staroverov VN, Kobayashi R, Normand J, Raghavachari K, Rendell AP, Burant JC, Iyengar SS, Tomasi J, Cossi M, Rega N, Millam NJ, Klene M, Knox JE, Cross JB, Bakken V, Adamo C, Jaramillo J, Gomperts R, Stratmann RE, Yazyev O, Austin AJ, Cammi R, Pomelli C, Ochterski JW, Martin RL, Morokuma K, Zakrzewski VG, Voth GA, Salvador P, Dannenberg JJ, Dapprich S, Daniels AD, Farkas Ö, Foresman JB, Ortiz JV, Cioslowski J, Fox DJ (2009) Gaussian 09. Gaussian Inc, Wallingford
37. Neese F (2012) The ORCA program system. Wiley Interdiscip Rev Comput Mol Sci 2(1):73–78. doi:10.1002/wcms.81
38. Ditchfield R, Hehre WJ, Pople JA (1971) Self-consistent molecular-orbital methods. IX. An extended Gaussian-type basis for molecular-orbital studies of organic molecules. J Chem Phys 54(2):724–728
39. Grimme S, Antony J, Ehrlich S, Krieg H (2010) A consistent and accurate ab initio parameterization of density functional dispersion correction (DFT-D) for the 94 elements H–Pu. J Chem Phys 132:154104
40. Singh UC, Kollman PA (1984) An approach to computing electrostatic charges for molecules. J Comput Chem 5(2):129–145. doi:10.1002/jcc.540050204
41. Wolinski K, Hilton JF, Pulay P (1990) Efficient implementation of the gauge-independent atomic orbital method for NMR chemical shift calculations. J Am Chem Soc 112(23):8251–8260. doi:10.1021/ja00179a005

Theor Chem Acc (2015) 134:143
DOI 10.1007/s00214-015-1746-z

REGULAR ARTICLE

A second-order multi-reference quasiparticle-based perturbation theory

Zoltán Rolik[1] · **Mihály Kállay**[1]

Received: 5 September 2015 / Accepted: 14 October 2015 / Published online: 7 November 2015

Abstract The purpose of this paper is to introduce a second-order perturbation theory derived from the mathematical framework of the quasiparticle-based multi-reference coupled-cluster approach (Rolik and Kállay in J Chem Phys 141:134112, 2014). The quasiparticles are introduced via a unitary transformation which allows us to represent a complete active space reference function and other elements of an orthonormal multi-reference basis in a determinant-like form. The quasiparticle creation and annihilation operators satisfy the fermion anti-commutation relations. As the consequence of the many-particle nature of the applied unitary transformation these quasiparticles are also many-particle objects, and the Hamilton operator in the quasiparticle basis contains higher than two-body terms. The definition of the new theory strictly follows the form of the single-reference many-body perturbation theory and retains several of its beneficial properties like the extensivity. The efficient implementation of the method is briefly discussed, and test results are also presented.

Keywords Multi-reference · Perturbation theory · Quasiparticles

Published as part of the special collection of articles "Festschrift in honour of P. R. Surjan".

✉ Zoltán Rolik
rolik@mail.bme.hu

[1] MTA-BME "Lendület" Quantum Chemistry Research Group, Department of Physical Chemistry and Materials Science, Budapest University of Technology and Economics, H1521 Budapest, Hungary

1 Introduction

The adequate description of electron correlation for molecular systems with multi-reference (MR) character is still a challenge for the theory. Due to technical and theoretical difficulties—e.g., the polynomial scaling of computation cost, treatment of large complete active spaces (CAS), the question of extensivity—the applicability of existing multi-reference-based methods is limited to small systems. To extend the scope of MR-based theories, a large number of various formalisms emerged in this field aiming at a proper generalization for the successful single-reference-based perturbation (PT) [6, 28], coupled-cluster (CC) [9–11], and configuration interaction (CI) theories. An extensive review of the MR-based CI and PT methods can be found in the recent paper of Szalay et al. [42]. The authors of this paper have also contributed to the improvement in these MR methods [12, 13, 20–22, 38, 39, 41] in many cases in cooperation with Péter Surján or with his support.

Along this line, in a recent paper [37] we introduced the so-called quasiparticle-based MR CC method (QMRCC). The mathematical structure of QMRCC is more or less the same as that of the well-known SR CC theory, i.e., the reference function is a determinant, commuting cluster operators are applied, normal-ordering and diagram techniques can be used, the method is extensive, *etc.* The point where the MR description appears is the application of quasiparticle states instead of the ordinary molecular orbitals. These quasiparticles are second-quantized many-particle objects introduced by a unitary transformation which allows us to represent the reference CAS function in a determinant-like form. As it is shown in the cited paper, on one hand the QMRCC method has some advantages with respect to the closely related SR-based MR CC theory [22, 31, 34] (more

stable, faster convergence), but on the other hand it is more complex and still Fermi-vacuum dependent.

Recently Sokolov and Chan published a paper where another quasiparticle-based framework was outlined [40]. This approach has the enviable feature of Fermi-vacuum independence. In that paper the concept of a non-particle-number-conserving canonical transformation was introduced and, as a low-order approximation, the application of a Bogoliubov transformation in a second-order perturbation theory was investigated to describe MR situations. The presented results, as well as the intruder problem on the PES in the BeH_2 model, indicate that the applied approximation needs further improvements.

Although the original aim of our QMRCC project is to develop tools to serve high accuracy calculations, it is also worth investigating the possibility of a quasiparticle-based second-order perturbation theory as a low-cost alternative of the CC method. Development of such a perturbative approach would offer twofold benefits, namely it would provide a cheap and easy to modify tool which helps the development of the more complex CC approach (understanding difficulties, testing new ideas) and it can be an efficient alternative of the existing MR perturbation theories. The aim of this paper is to investigate this second point.

The early attempts to develop MR perturbation methods focused on the use of an effective Hamiltonian determined from the Bloch equation [7, 18, 24, 27]. The main drawback of these theories is the intruder state problem, i.e., the appearance of close to zero denominators which give nonphysical contribution to the effective Hamiltonian matrix elements, especially for large CAS spaces where the high lying model functions are energetically not separated from the outer space determinants. To tackle with this problem the application of incomplete model spaces [18, 27], various level shift-based techniques [14, 23, 30, 45] and the concept of intermediate Hamiltonian [26] were intensively studied, but the most common solution is to use a state-specific description, where only a single target state is described [3–5, 8, 16, 17, 29, 44].

Among the large set of various state-specific MR perturbation theories, we selected two popular methods to compare our QMBPT2 approach to. These are the second-order CAS-based PT (CASPT2) [2, 3, 8] method—which is undoubtedly the most popular MR approach—and the second-order n-electron-valence state PT (NEVPT2) [4, 5] method.

The zeroth-order Hamiltonian of the CASPT2 theory is a projected generalized Fock operator, and the orthogonal functions are internally contracted excitations. In this case the resolvent operator is not diagonal, and thus its inverse is determined in an iterative process. To be able to perform the inversion of the resolvent operator efficiently, the zero-order Hamiltonian has a block-diagonal structure. The well-known drawback of CASPT2 is the lack of size-consistency.

The NEVPT approach has a list of remarkable qualitative properties (size-consistency, invariance to the rotation of active orbitals, absence of intruder states, first-order correction to the wave function is a pure spin state) which indicates that this as a serious candidate when an MR problem should be solve. Although with all these properties the QMBPT2 method cannot compete (e.g., it is obviously not invariant to the rotation of active orbitals), the relative accuracy of these methods is still an interesting question.

The structure of the paper is as follows. In Sect. 2 the quasiparticle approach is briefly summarized, and the new perturbation theory is introduced. The efficient way of implementation and the scaling properties will be presented in Sect. 3. Some numerical results will be presented in Sect. 4 and the conclusions of this study are collected in Sect. 5.

2 Theory

The main idea behind the new approach is to extend the mathematical structure of the SR-based correlation methods to the MR case. To that end an orthonormal MR basis is defined where one element of this basis is the reference function which is supposed to a CAS wave function. We also suppose that these functions can be uniquely labeled by occupied and virtual one-particle indices as the ordinary determinants, where these indices indicate the type of excitations with respect to a given predefined principal determinant (PD) hereafter denoted by $|0\rangle$. In the notation of the MR functions,

$$\Phi_0, \Phi_I^A, \Phi_i^a, \Phi_i^A, \Phi_I^a, \ldots, \Phi_{ij}^{Ab}, \Phi_{Ij}^{ab}, etc. \tag{1}$$

$A, B, \ldots$ and $I, J, \ldots$ letters are used for active virtual and active occupied orbitals, respectively, while $a, b, \ldots$ and $i, j, \ldots$ stand for the inactive occupied and inactive virtual orbitals, finally Φ_0 is the reference CAS function.

Due to the one-particle labeling of these functions, we have a mapping between these functions and any set of determinants where a PD is defined and the excited determinants are labeled in a similar fashion. More precisely, this mapping is a unitary transformation, where the PD is transformed into the reference function $\Phi_0 = \hat{U}|0\rangle$, and

$$\begin{aligned} |\Phi_I^A\rangle = \hat{U}|_I^A\rangle, |\Phi_i^a\rangle = \hat{U}|_i^a\rangle, |\Phi_i^A\rangle = \hat{U}|_i^A\rangle, \ldots, |\Phi_{ij}^{Ab}\rangle \\ = \hat{U}|_{ij}^{Ab}\rangle, |\Phi_{Ij}^{ab}\rangle = \hat{U}|_{Ij}^{ab}\rangle, etc, \end{aligned} \tag{2}$$

where $|_I^A\rangle, |_i^a\rangle, \ldots$ are ordinary determinants excited with respect to the PD. Such a unitary transformation can be

parametrized in an exponential form, $\hat{U} = e^{\hat{S}}$, where $\hat{S}$ is an anti-hermitian operator, $\hat{S} = \hat{\chi} - \hat{\chi}^+$ containing not only one-body but also higher-body terms. To restrict the dimensionality of the unitary transformation, we suppose that it transforms exclusively the active part of the functions.

Before giving the definition of the unitary transformation we should fix the PD. A simple choice for this is to use the determinant which has the maximal overlap with the reference function Φ_0 as the PD. Optimizing the active orbitals accordingly will lead to the exact Brueckner orbitals in the active space [19, 33].

Once the reference function and the PD are determined, we can suppose that the unitary transformation satisfies the

$$|\Phi_0\rangle = e^{\hat{S}}|0\rangle, \tag{3}$$

relation. Generally, the condition at Eq. (3) is not enough to define the parameters of $\hat{S}$, but using a special, minimal parameterization,

$$\hat{\chi} = \sum_{A_1,I_1} \chi_{I_1}^{A_1} \hat{A}_1^+ \hat{I}_1^- + \sum_{A_1<A_2,I_1<I_2} \chi_{I_1\,I_2}^{A_1A_2} \hat{A}_1^+ \hat{A}_2^+ \hat{I}_2^- \hat{I}_1^- + \ldots + \sum_{\substack{A_1<A_2<\ldots<A_s \\ I_1<I_2<\cdots<I_s}} \chi_{I_1\,I_2\ldots\,I_s}^{A_1A_2\ldots A_s} \hat{A}_1^+ \hat{A}_2^+ \cdots \hat{A}_s^+ \hat{I}_s^- \cdots \hat{I}_2^- \hat{I}_1^- \tag{4}$$

where creation operators $\hat{A}_i^+$ are virtual, annihilation operators $\hat{I}_i^-$ are occupied orbitals, the unitary transformation can be uniquely defined. Equations (3) and (4) are basically the second-quantized parameterization of the multi-determinantal CAS function.

As a useful tool to describe the excitation process among the MR basis elements, we can introduce the quasiparticle creation and annihilation operators,

$$\hat{Q}_X^+ = \hat{U}\hat{X}^+\hat{U}^\dagger \tag{5}$$

$$\left(\hat{Q}_X^+\right)^\dagger = \hat{U}\hat{X}^-\hat{U}^\dagger = \hat{Q}_X^-, \tag{6}$$

where X is a general active orbital. One can also define the inactive quasiparticles. Since $\hat{U}$ keeps the inactive orbitals intact, $\hat{Q}_i^+ = \hat{U}\hat{i}^+\hat{U}^\dagger = \hat{i}^+$ and $\hat{Q}_a^+ = \hat{U}\hat{a}^+\hat{U}^\dagger = \hat{a}^+$. The quasiparticle creation and annihilation operators with arbitrary indices obviously satisfy the fermion anti-commutation relations,

$$\left\{\hat{Q}_p^+, \hat{Q}_q^-\right\} = \delta_{pq}, \quad \left\{\hat{Q}_p^-, \hat{Q}_q^-\right\} = 0. \tag{7}$$

Supposing that the second-quantized form of the PD is $|0\rangle = |I_{n_a} \ldots I_2 I_1 i_{n_c} \ldots i_1\rangle$, the reference CAS function reads as

$$|\Phi_0\rangle = \hat{Q}_{I_{n_a}}^+ \ldots \hat{Q}_{I_2}^+ \hat{Q}_{I_1}^+ \hat{Q}_{i_{n_c}}^+ \ldots \hat{Q}_{i_1}^+|\rangle, \tag{8}$$

where Eq. (3) and $\hat{U}^\dagger\hat{U} = \hat{I}$ are utilized, and n_a and n_c are the number of active and core orbitals, respectively, and $|\rangle$ is the physical vacuum. The form of the singly excited MR basis functions can be written as

$$\begin{aligned} |\Phi_{I_k}^{A_l}\rangle &= \hat{Q}_{A_l}^+\hat{Q}_{I_k}^-|\Phi_0\rangle = \hat{Q}_{A_l}^+\hat{Q}_{I_k}^-\hat{Q}_{I_{n_a}}^+ \ldots \hat{Q}_{I_2}^+\hat{Q}_{I_1}^+\hat{Q}_{i_{n_c}}^+ \ldots \hat{Q}_{i_1}^+|\rangle \\ &= |\ldots Q_{I_{k+1}} Q_{A_l} Q_{I_{k-1}} \ldots i_{n_c} \ldots i_1\rangle, \\ |\Phi_{i_k}^{a_l}\rangle &= \hat{a}_l^+\hat{i}_k^-|\Phi_0\rangle = |Q_{I_{n_a}} \ldots Q_{I_1} \ldots i_{k+1} a_l i_{k-1} \ldots\rangle, \end{aligned} \tag{9}$$

and

$$|\Phi_{i_k}^{A_l}\rangle = \hat{Q}_{A_l}^+\hat{i}_k^-|\Phi_0\rangle = |Q_{I_{n_a}} \ldots Q_{I_1} i_{n_c} \ldots i_{k+1} Q_{A_l} i_{k-1} \ldots\rangle, \tag{10}$$

where typical active–active, inactive–inactive and active–inactive single excitations are presented. The doubly, triply, etc., excited MR functions can be generated in a similar fashion resulting in the desired MR functions.

To be able to apply this quasiparticle framework we should derive the quasiparticle representation of the Hamiltonian. The first step along this line is to substitute the ordinary second-quantized operators by quasiparticles using the inverse of Eqs. (5) and (6) as

$$\begin{aligned} \hat{H} &= \sum_{pq} h_{pq}\hat{p}^+\hat{q}^- + \frac{1}{4}\sum_{pqrs}\langle pq||sr\rangle \hat{p}^+\hat{q}^+\hat{r}^-\hat{s}^- \\ &= \sum_{pq} h_{pq}\hat{U}^\dagger\hat{Q}_p^+\hat{Q}_q^-\hat{U} + \frac{1}{4}\sum_{pqrs}\langle pq||sr\rangle \hat{U}^\dagger\hat{Q}_p^+\hat{Q}_q^+\hat{Q}_r^-\hat{Q}_s^-\hat{U} \\ &= \hat{U}^\dagger\hat{\mathcal{H}}\hat{U}, \end{aligned} \tag{11}$$

where h_{pq} and $\langle pq||sr\rangle$ are one- and antisymmetrized two-particle integrals, respectively. The bare Hamiltonian $\hat{\mathcal{H}}$, implicitly defined by the second equation, can be written in normal-ordered form as

$$\hat{\mathcal{H}} = E_{\mathrm{HF}} + \sum_{pq} f_{pq}\left\{\hat{Q}_p^+\hat{Q}_q^-\right\}_{\mathrm{N}} + \frac{1}{4}\sum_{pqrs}\langle pq||sr\rangle\left\{\hat{Q}_p^+\hat{Q}_q^+\hat{Q}_r^-\hat{Q}_s^-\right\}_{\mathrm{N}}, \tag{12}$$

where the $\{\}_{\mathrm{N}}$ bracket denotes the normal-ordered operator product with respect to the CAS reference function Φ_0, while E_{HF} and f_{pq} are the energy and Fock matrix elements defined by the occupied subspace of the PD, respectively.

As a consequence of the many-body nature of the unitary transformation higher than two-body terms also appear in the Hamiltonian,

$$\hat{H} = E_{\mathrm{CAS}} + \sum_{pq}\overline{f}_q^p\left\{\hat{Q}_p^+\hat{Q}_q^-\right\}_{\mathrm{N}} + \frac{1}{4}\sum_{pqrs} v_{2\,sr}^{pq}\left\{\hat{Q}_p^+\hat{Q}_q^+\hat{Q}_r^-\hat{Q}_s^+\right\}_{\mathrm{N}} + \frac{1}{36}\sum_{pqrs} v_{3\,uvw}^{pqr}\left\{\hat{Q}_p^+\hat{Q}_q^+\hat{Q}_r^+\hat{Q}_w^-\hat{Q}_v^-\hat{Q}_u^-\right\}_{\mathrm{N}} + \cdots, \tag{13}$$

where the above expansion starts with the energy of the reference function and $\overline{f}^p_q$, $v_2{}^{pq}_{sr}$, $v_3{}^{pqr}_{uvw}$, etc., are the elements of the one-, two-, three- and higher-body antisymmetrized integral lists.

To emphasize the analogy with the single-reference case, the quasiparticle Fockian denomination will be used for the one-particle part of the above expansion. Using a proper unitary transformation of the ordinary molecular orbitals, the quasiparticle Fockian has a block-diagonal structure, i.e., (1) for a Φ_0 obtained as a solution of a CAS problem, its active–active block can be always kept diagonal; (2) using pseudo-canonical orbitals to expand the inactive occupied and inactive virtual subspaces, the inactive blocks of the quasiparticle Fockian are also diagonal

The first property can be easily understood by considering a general active–inactive matrix element of $\overline{f}^p_q$,

$$\overline{f}^A_I = \langle \Phi_0 | \hat{H} \left\{ \hat{Q}^+_A \hat{Q}^-_I \right\}_{\mathrm{N}} | \Phi_0 \rangle, \tag{14}$$

which is zero, as $\left\{ \hat{Q}^+_A \hat{Q}^-_I \right\}_{\mathrm{N}} | \Phi_0 \rangle$ is orthogonal to the reference state and lies completely in the CAS. As the f_{AB} and f_{IJ} off-diagonal elements can be eliminated by simple rotations of molecular orbitals, for which the reference function Φ_0 is invariant, the active–active block of the quasiparticle Fockian can be transformed into a diagonal form. Investigating the inactive virtual block of the quasiparticle Fockian would lead to similar conclusion.

To investigate the occupied inactive–inactive blocks of the quasiparticle Fockian we can start from the

$$\overline{f}^i_j = -\langle \Phi_0 | \hat{Q}^+_i \hat{H}_{\mathrm{N}} \hat{Q}^-_j | \Phi_0 \rangle \tag{15}$$

relation. After some straightforward manipulation, it leads to the $\overline{f}^i_j = h_{ij} + \sum_{pq} \langle ip||jq \rangle P_{pq} + \Delta E_{\mathrm{CAS}}\, \delta_{ij}$ expression, where the first and the second terms together at the left-hand side form the occupied block of the generalized Fock matrix and ΔE_{CAS} is the correlation energy of Φ_0. When pseudo-canonical orbitals are used, this block of the generalized Fockian is diagonal, and thus $\overline{f}^i_j$ is also diagonal. One can reach a similar conclusion for the virtual inactive block, where the matrix elements are defined by the

$$\overline{f}^a_b = \langle \Phi_0 | \hat{Q}^-_a \hat{H}_{\mathrm{N}} \hat{Q}^+_b | \Phi_0 \rangle \tag{16}$$

relation.

The presented quasiparticle framework offers a simple way to develop the MR versions of the single-reference-based correlation methods, such as the CI or the CC approaches [37]. To introduce the MR variant of the MBPT [6], first the Hamiltonian should be separated into a zeroth-oder and a perturbation part, $\hat{H} = \hat{H}^{(0)} + \hat{V}$. Following the MBPT, it seems to be a natural choice to use the diagonal part of the one-particle term from Eq. (13) as the zeroth-order Hamiltonian,

$$\hat{H}_0 = \sum_p \varepsilon_p \left\{ \hat{Q}^+_p \hat{Q}^-_p \right\}_{\mathrm{N}}, \tag{17}$$

where $\varepsilon_p = \overline{f}^p_p$. The zeroth- and the first-order perturbation energies together provide the CAS energy of the reference function, $E^{(0)} + E^{(1)} = \langle \Phi_0 | \hat{H}_0 + \hat{V} | \Phi_0 \rangle = E_{\mathrm{CAS}}$. In the basis of the functions introduced in Eqs. (8) and (9)—these are the zeroth-order functions—the zeroth-order Hamiltonian is diagonal,

$$\hat{H}_0 | \Phi_K \rangle = E_K | \Phi_K \rangle, \quad K = 0, 1, 2, \ldots, \tag{18}$$

where, for the sake of brevity, the MR basis elements are labeled by the serial numbers instead of the one-particle labels. The second-order energy correction according to the Rayleigh–Schrödinger PT reads as

$$E^{(2)} = \sum_{K, K \neq 0} \frac{\langle \Phi_0 | \hat{H} | \Phi_K \rangle \langle \Phi_K | \hat{H} | \Phi_0 \rangle}{E_0 - E_K}, \tag{19}$$

where we could replace $\hat{V}$ by $\hat{H}$ utilizing that $\langle \Phi_0 | \hat{H}_0 | \Phi_K \rangle$ is zero for any K.

The above $E^{(2)}$ energy correction directly provides an approximation to the dynamical electron correlation. For this correction only those Φ_K functions give contributions where at least one inactive excitation appears, otherwise $\langle \Phi_K | \hat{H} | \Phi_0 \rangle = 0$. It means that at least one inactive one-particle energy shows up in the denominator, which is a useful property, as it provides a certain amount of protection against the singular behavior of the perturbation denominator.

It can be easily seen that the above generalization of the MBPT2 keeps the size-consistency of the original theory. Supposing that we have two noninteracting subsystems, A and B, separately described by $\hat{H}_A$ and $\hat{H}_B$, and the reference function has a product form, $\Phi_0 = \Phi^A_0 \Phi^B_0$, where Φ^A_0 and Φ^B_0 are solutions of the CAS problems of the subsystems, and then the unitary transformation at Eq. (3) is also product separable, $\hat{U} = \hat{U}_A \hat{U}_B$. Considering the definition of quasiparticles at Eqs. (5) and (6) it is obvious now that these are localized either on subsystem A or on subsystem B, and the zeroth-order functions defined by the quasiparticles at Eq. (9) are product separable, i.e., $\Phi_K = \Phi_{K_A} \Phi_{K_B}$. Using these results the contribution of any Φ_K to the energy is a sum of the subsystem contributions,

$$\frac{\langle \Phi_0 | \hat{H}_A | \Phi^{a_A \ldots C_A \ldots}_{i_A \ldots J_A \ldots} \rangle \langle \Phi^{a_A \ldots C_A \ldots}_{i_A \ldots J_A \ldots} | \hat{H}_A | \Phi_0 \rangle}{\varepsilon_{i_A} + \cdots + \varepsilon_{J_A} + \cdots - \varepsilon_{a_A} - \cdots - \varepsilon_{C_A} - \cdots} + \frac{\langle \Phi_0 | \hat{H}_B | \Phi^{a_B \ldots C_B \ldots}_{i_B \ldots J_B \ldots} \rangle \langle \Phi^{a_B \ldots C_B \ldots}_{i_B \ldots J_B \ldots} | \hat{H}_B | \Phi_0 \rangle}{\varepsilon_{i_B} + \cdots + \varepsilon_{J_B} + \cdots - \varepsilon_{a_B} - \cdots - \varepsilon_{C_B} - \cdots}, \tag{20}$$

where $\Phi_K = \Phi^{a_A \ldots C_A \ldots a_B \ldots C_B \ldots}_{i_A \ldots J_A \ldots i_B \ldots J_B \ldots}$ and thus the QMBPT2 energy of the supersystem is the sum of the subsystem energies.

We can also check the extensivity of the method [36], i.e., the connectedness of the QMBPT2 energy. To that end it is practical to reformulate the matrix elements in the numerator of Eq. (19), $\langle \Phi_0 | \hat{H} | \Phi_K \rangle = \langle 0 | \hat{U}^\dagger \hat{H} \hat{U} | K \rangle$, where $|K\rangle$ is the determinant assigned to $|\Phi_K\rangle$. Using the exponential parameterization of $\hat{U}$ it is easy to show that $\hat{U}^\dagger \hat{H} \hat{U}$ is a connected quantity (see Ref. [37] for more details) and in this way the QMBPT2 energy is also connected.

3 Computational considerations

To investigate the scaling of the computation cost of QMBPT2, it is advantageous to use the orbital labeling instead of the composite label K in Eq. (19). For a small CAS problem the most expensive terms contain four inactive indices,

$$E^{(2)} = \sum_{abij} \frac{\langle \Phi_0 | \hat{H} | \Phi^{ab}_{ij} \rangle \langle \Phi^{ab}_{ij} | \hat{H} | \Phi_0 \rangle}{\varepsilon_i + \varepsilon_j - \varepsilon_a - \varepsilon_b} + \cdots, \tag{21}$$

where the above term has the same form that is known from the SR theory (see later) and its scaling is $n_v^2 n_c^2$, where n_v and n_c are the number of inactive virtual and inactive occupied orbitals, respectively. The most expensive contributions coming from the MR nature of QMBPT2 have three inactive indices,

$$E^{(2)} = \ldots + \sum_{abA \ldots CiJK \ldots L} \frac{\langle \Phi_0 | \hat{H} | \Phi^{abA \ldots C}_{iJK \ldots L} \rangle \langle \Phi^{abA \ldots C}_{iJK \ldots L} | \hat{H} | \Phi_0 \rangle}{\varepsilon_i + \varepsilon_J + \varepsilon_K + \ldots + \varepsilon_L - \varepsilon_a - \varepsilon_b - \varepsilon_A + \ldots + \varepsilon_B} \tag{22}$$

Supposing that the $\langle \Phi^{abA \ldots C}_{iJK \ldots L} | \hat{H} | \Phi_0 \rangle$ matrix element is given, the computation cost of this term scales as $n_v^2 n_c n_{ao} N_{\mathrm{act}}$, where n_{ao} is the number of active occupied orbitals and N_{act} is the number of active configurations.

There is another component of the calculations which has a significant cost, namely the evaluation of the $\langle \Phi^{abA \ldots C}_{iJK \ldots L} | \hat{H} | \Phi_0 \rangle$ type of matrix elements. As the efficient implementation of these terms are not that straightforward the rest of this section is dedicated to this problem.

The matrix element in Eq. (19) can be expanded in the basis of determinants,

$$\begin{aligned} \langle \Phi_K | \hat{H} | \Phi_0 \rangle &= \sum_{LM} [U_K]^L [U_0]^M \langle L | \hat{H} | M \rangle \\ &= \sum_{\mathcal{LM}} [U_\mathcal{K}]^\mathcal{L} [U_\mathcal{O}]^\mathcal{M} \langle \mathcal{L}, k | \hat{H} | \mathcal{M}, o \rangle, \end{aligned} \tag{23}$$

where in the last term we separated the active and inactive parts of the determinants. Here calligraphic letters are used for the active, and roman letters stand for the inactive part of the determinants, $|L\rangle = |\mathcal{L}, l\rangle$. As $\hat{U}$ transforms only the active labels, the coefficient matrix $[U_\mathcal{K}]^\mathcal{L}$ holds exclusively calligraphic letters.

Since the coefficient matrix belongs to a unitary transformation, those components of the above expression where no active orbitals appear in the Hamiltonian can be trivially calculated. For example,

$$\begin{aligned} \langle \Phi^{ab}_{ij} | \hat{H} | \Phi_0 \rangle &= \sum_{\mathcal{LM}} [U_\mathcal{K}]^\mathcal{L} [U_\mathcal{O}]^\mathcal{M} \\ &\times \sum_{pqrs} \frac{1}{4} \langle pq || rs \rangle \langle \mathcal{L}, o^{ab}_{ij} | \hat{p}^+ \hat{q}^+ \hat{s}^- \hat{r}^- | \mathcal{M}, o \rangle = \langle ab || ij \rangle, \end{aligned} \tag{24}$$

where o^{ab}_{ij} is a double inactive excitation with respect to the core part (o) of Φ_0. Those terms where the active part of the Hamiltonian is involved are more complex. The most time-consuming component from this class of terms is the one where one active occupied orbital appears,

$$\begin{aligned} &\langle \Phi^{abA \ldots C}_{iI \ldots K} | \hat{H} | \Phi_0 \rangle \\ &= \sum_{\mathcal{LM}} \left[U^{A \ldots C}_{I \ldots K} \right]^\mathcal{L} [U_\mathcal{O}]^\mathcal{M} \sum_{pqrs} \frac{1}{4} \langle pq || rs \rangle \\ &\quad \times \langle \mathcal{L}, o^{ab}_i | \hat{p}^+ \hat{q}^+ \hat{s}^- \hat{r}^- | \mathcal{M}, o \rangle \\ &= \sum_{\mathcal{M}} \sum_{J} \left[U^{A \ldots C}_{I \ldots K} \right]^{\mathcal{M}_J} [U_\mathcal{O}]^\mathcal{M} \langle ab || iJ \rangle \\ &\quad \times \langle \mathcal{M}_J, o^{ab}_i | \hat{b}^+ \hat{a}^+ \hat{i}^- \hat{J}^- | \mathcal{M}, o \rangle, \end{aligned} \tag{25}$$

where $\mathcal{M}_J$ is the inactive configuration obtained by eliminating J from configuration $\mathcal{M}$. According to the above expression the overall computation cost of these terms scales as $n_v^2 n_c n_{ao} N_{\mathrm{act}}^2$. To reduce the computation cost one can try to factorize this expression into active and inactive parts,

$$\begin{aligned} &\sum_J \langle ab || iJ \rangle \sum_{\mathcal{M}} \left[U^{A \ldots C}_{I \ldots K} \right]^{\mathcal{M}_J} [U_\mathcal{O}]^\mathcal{M} \\ &\quad \langle \mathcal{M}_J, o^{ab}_i | \hat{a}^+ \hat{b}^+ \hat{i}^- | \mathcal{M}_J, o \rangle \langle \mathcal{M}_J, o | \hat{J}^- | \mathcal{M}, o \rangle. \end{aligned} \tag{26}$$

At this point we can realize that though formally the matrix element containing the inactive second-quantized expression still $\mathcal{M}_J$ dependent, its value (1 or -1) is completely determined by the number of active electrons (N_{ae}) in $\mathcal{M}_J$, i.e.,

$$sign(a, b, i, N_{ae} - 1) = \langle \mathcal{M}_J, o^{ab}_i | \hat{a}^+ \hat{b}^+ \hat{i}^- | \mathcal{M}_J, o \rangle. \tag{27}$$

Eq. (26) can be reformulated accordingly,

$$\sum_J \langle ab||iJ\rangle sign(a,b,i,N_{ae}-1) \times \sum_{\mathcal{M}} \left[U^{A\ldots C}_{I\ldots K}\right]^{\mathcal{M}_J} [U_{\mathcal{O}}]^{\mathcal{M}} \langle \mathcal{M}_J, o|\hat{J}^-|\mathcal{M}, o\rangle = sign(a,b,i,N_{ae}-1) \sum_J \langle ab||iJ\rangle \left[W^{A\ldots C}_{I\ldots K}\right]_J, \quad (28)$$

where the

$$\left[W^{A\ldots C}_{I\ldots K}\right]_J = \sum_{\mathcal{M}} \left[U^{A\ldots C}_{I\ldots K}\right]^{\mathcal{M}_J} [U_{\mathcal{O}}]^{\mathcal{M}} \langle \mathcal{M}_J, o|\hat{J}^-|\mathcal{M}, o\rangle \quad (29)$$

intermediate quantity is introduced. The computation cost of these intermediates scales as $N^2_{\mathrm{act}} n_{oa}$ and independent of the number of inactive orbitals, while the overall scaling of Eq. (25) is reduced to $N^2_{\mathrm{act}} n_{oa} + n^2_v n_c n_{ao} N_{\mathrm{act}}$. It is clear now that using the above ideas we could significantly reduce the calculation cost, but we still have a component which scales quadratically with the CAS size which prevents the application of QMBPT2 for large CAS problems. At this point we can also mention that each contribution to Eq. (25) is multiplied by the same $sign(a,b,i,N_{ae}-1)$ factor and, for that reason, these factors can be completely eliminated as for the QMBPT2 energy only the square of Eq. (25) is needed.

Of course, $\left[W^{A\ldots C}_{I\ldots K}\right]_J$ can be used for the calculation of $\langle \Phi^{qA\ldots C}_{I\ldots K}|\hat{H}|\Phi_0\rangle$ terms as well, and similarly to Eq. (26) further intermediates can be introduced to calculate other types of matrix elements. Some typical intermediates are listed here:

$$\begin{aligned}
\left[W^{A\ldots C}_{I\ldots K}\right]^J &= \sum_{\mathcal{M}} \left[U^{A\ldots C}_{I\ldots K}\right]^{\mathcal{M}^J} [U_{\mathcal{O}}]^{\mathcal{M}} \langle \mathcal{M}^J, o|\hat{J}^+|\mathcal{M}, o\rangle \\
\left[W^{A\ldots C}_{I\ldots K}\right]_B &= \sum_{\mathcal{M}} \left[U^{A\ldots C}_{I\ldots K}\right]^{\mathcal{M}_B} [U_{\mathcal{O}}]^{\mathcal{M}} \langle \mathcal{M}_B, o|\hat{B}^-|\mathcal{M}, o\rangle \\
\left[W^{A\ldots C}_{I\ldots K}\right]^B &= \sum_{\mathcal{M}} \left[U^{A\ldots C}_{I\ldots K}\right]^{\mathcal{M}^B} [U_{\mathcal{O}}]^{\mathcal{M}} \langle \mathcal{M}^B, o|\hat{B}^+|\mathcal{M}, o\rangle \\
\left[W^{A\ldots C}_{I\ldots K}\right]^B_J &= \sum_{\mathcal{M}} \left[U^{A\ldots C}_{I\ldots K}\right]^{\mathcal{M}^B_J} [U_{\mathcal{O}}]^{\mathcal{M}} \langle \mathcal{M}^B_J, o|\hat{B}^+\hat{J}^-|\mathcal{M}, o\rangle \\
\left[W^{A\ldots C}_{I\ldots K}\right]^J_B &= \sum_{\mathcal{M}} \left[U^{A\ldots C}_{I\ldots K}\right]^{\mathcal{M}^J_B} [U_{\mathcal{O}}]^{\mathcal{M}} \langle \mathcal{M}^J_B, o|\hat{J}^+\hat{B}^-|\mathcal{M}, o\rangle \\
\left[W^{A\ldots C}_{I\ldots K}\right]^B_C &= \sum_{\mathcal{M}} \left[U^{A\ldots C}_{I\ldots K}\right]^{\mathcal{M}^B_C} [U_{\mathcal{O}}]^{\mathcal{M}} \langle \mathcal{M}^B_C, o|\hat{B}^+\hat{C}^-|\mathcal{M}, o\rangle \\
\left[W^{A\ldots C}_{I\ldots K}\right]^J_K &= \sum_{\mathcal{M}} \left[U^{A\ldots C}_{I\ldots K}\right]^{\mathcal{M}^J_K} [U_{\mathcal{O}}]^{\mathcal{M}} \langle \mathcal{M}^J_K, o|\hat{J}^+\hat{K}^-|\mathcal{M}, o\rangle \\
&\vdots
\end{aligned} \quad (30)$$

The above list can be easily completed as the derivation of the various classes of the $\langle \Phi_K|\hat{H}|\Phi_0\rangle$ matrix elements expressed by these intermediates is also rather straightforward, and thus for the sake a brevity these equations are not listed here.

4 Numerical results

To test the QMBPT approach, following the ideas discussed in Sect. 3, a FORTRAN code has been written. Using this implementation calculations were performed to describe the dissociation process of the HF molecule, the symmetric dissociation of the water molecule and the perpendicular insertion reaction of Be to H_2 to form the BeH_2 molecule. For these calculations cc-pVDZ basis set was applied, the core orbitals were kept frozen, and the inactive subspaces were described by pseudo-canonical orbitals. The results obtained by the new theory are compared against the FCI values which are calculated using our own implementation based on the string-based algorithm published by Olsen [32]. The quality of the QMBPT2 energies is also compared to the accuracy of NEVPT2 and CASPT2 results. For the CASPT2 calculations the version published by Celani and Werner [8] was used. The multi-configurational self-consistent field (MCSCF) reference functions, CASPT2, and NEVPT2 results together with the transformed molecular integrals are calculated with the Molpro program package [43]. The NEVPT2 calculations were performed with both the partially and the strongly contracted versions. As these methods provide similar results for the investigated examples only the strongly contracted NEVPT2 results are presented.

As it can be clearly seen in Fig. 1, for the dissociation of the HF molecule the CASPT2 calculations provide the most accurate results. The non-parallelity error (NEP) of the potential energy surface (PES) is an order of magnitude smaller than that for the other presented methods. The accuracy of the NEVPT2 and the QMBPT2 is comparable.

The next example is the symmetric dissociation process of the H_2O molecule. For this model the NEVPT2 method provides the most accurate PES. For the presented interval (see Fig. 2) the NEP for the NEVPT2 curve is roughly 4 mE_h, while for the CASPT2 and QMBPT2 it is about 6 mE_h. It is worth noting here that, since for the above dissociation problems closed-shell orbitals were used, the wave functions are not product separable at the dissociation limit; therefore, the QMBPT2 cannot provide size-consistent results.

The insertion reaction of the BeH_2 system is frequently used to demonstrate the capabilities of various MR methods [1, 15, 25, 30]. The reaction path is parametrized by the z distance of Be from the midpoint of the H_2 bond. The

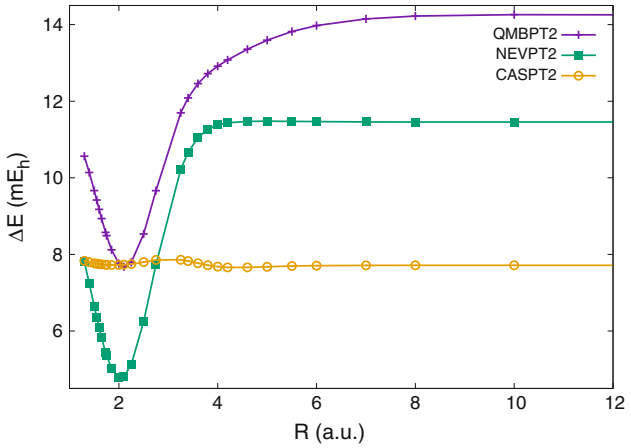

Fig. 1 Performance of the QMBPT method in comparison with that for the CASPT2 and NEVPT approaches for the dissociation of the HF molecule. Two-by-two CAS reference space, cc-pVDZ basis set. The errors of total energies with respect to the FCI are presented

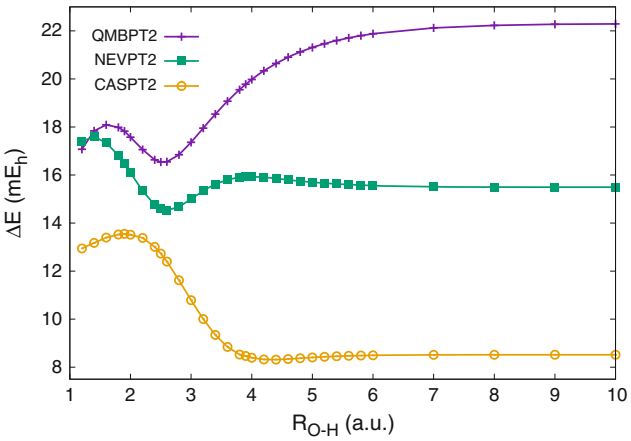

Fig. 2 Performance of the QMBPT method in comparison with that for the CASPT2 and NEVPT approaches for the symmetric dissociation of the water molecule. Four-by-four CAS reference space, cc-pVDZ basis set. The errors of total energies with respect to the FCI are presented

Be atom is fixed at the x = 0, y = 0, z = 0 point, while the positions of hydrogens are x = 0, y = ±(2.54 a.u. − 0.46*z) [35]. This process can be qualitatively described by a two-by-two CAS problem which contains two determinants $D_A = 1a_1^2 2a_1^2 1b_2^2$ and $D_B = 1a_1^2 2a_1^2 3a_1^2$, which give contribution to the ground state MCSCF wave function. The two determinants change role at the 2.875–2.9 a.u. interval, i.e., for z < 2.9 a.u. D_A is the leading determinant, while for the larger z values determinant D_B has the larger coefficient. To demonstrate the Fermi-vacuum dependence of the QMBPT2 method these calculations were performed for both possible PDs. The results of the BeH_2 calculations

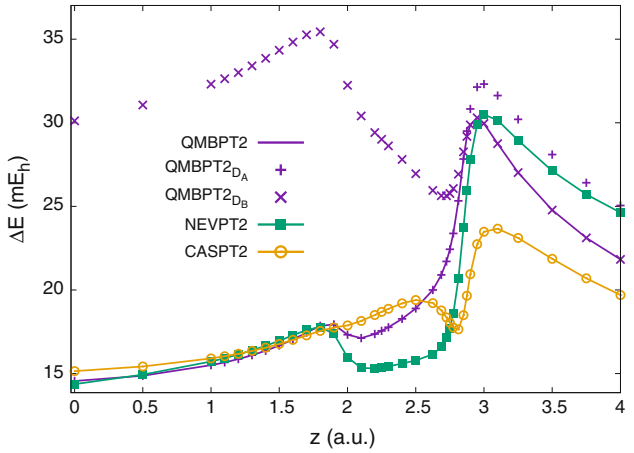

Fig. 3 Performance of the QMBPT method in comparison with that for the CASPT2 and NEVPT approaches for the dissociation of the BeH_2 molecule. The results obtained from the $D_A = 1a_1^2 2a_1^2 1b_2^2$ ($D_B = 1a_1^2 2a_1^2 3a_1^2$) PD are denoted by QMBPT2$_{D_A}$ (QMBPT2$_{D_B}$). Two-by-two CAS reference space, cc-pVDZ basis set. The errors of total energies with respect to the FCI are presented

are shown in Fig. 3, where the QMBPT2 curve is obtained by using D_A for z < 2.9 a.u. and D_B for larger z values. Results of the D_A- and D_B-based calculations for the complete reaction path are also shown in Fig. 3. Comparing the accuracy of these results one can see that the NEP of the QMBPT2 calculations is similar to that of the NEVPT2 curve, while the CASPT2 results are significantly better.

Finally, we can mention that using the QMBPT2 method we have not observed any singular behavior. Since the gap between the occupied and the virtual orbitals was large enough, there was no need to use level shift for the presented calculations.

5 Conclusions

In this paper a new perturbation approach has been introduced based on a quasiparticle framework where the quasiparticles are introduced by a many-particle unitary transformation. The new approach has some beneficial qualitative properties like the size-extensivity and robustness against the intruder problem. According to the presented test calculations its accuracy is comparable to that of the NEVPT approach. The main disadvantages of the quasiparticle-based MBPT are the lack of invariance to the rotation of active orbitals and the high calculation cost of intermediate quantities for large CAS problems.

Acknowledgments Financial support has been provided by the Hungarian Scientific Research Fund (OTKA), Grant No. PD108451.

References

1. Amor N, Maynau D (1998) Chem Phys Lett 286:211
2. Andersson K, Malmquist P, Roos BO (1992) J Chem Phys 96:1218
3. Andersson K, Malmquist P, Roos BO, Sadlej AJ, Wolinski K (1990) J Chem Phys 94:5483
4. Angeli C, Cimiraglia R, Evangelisti S, Leininger T, Malrieu JP (2001) J Chem Phys 114:10252
5. Angeli C, Cimiraglia R, Pastore M (2007) Theor Chim Acta 117:743
6. Bartlett RJ (1981) Annu Rev Phys Chem 32:359
7. Brandow BH (1967) Rev Mod Phys 39:771
8. Celani P, Werner HJ (2000) J Chem Phys 112:5546
9. Čížek J (1966) J Chem Phys 45:4256
10. Čížek J (1969) Adv Chem Phys 14:35
11. Čížek J, Paldus J (1971) Int J Quantum Chem 5:359
12. Das S, Kállay M, Mukherjee D (2010) J Chem Phys 133:234110
13. Das S, Mukherjee D, Kállay M (2010) J Chem Phys 132:074103
14. Finley JP (1998) J Chem Phys 108:1081
15. Füsti-Molnár L, Szalay P (1996) J Chem Phys 100:6288
16. Ghosh P, Chattopadhyay S, Jana D, Mukherjee D (2002) Int J Mol Sci 3:733
17. Hirao K (1993) Chem Phys Lett 201:59
18. Hose G, Kaldor U (1979) J Phys B 12:3827
19. Jankowski K, Rubiniec K, Sterna P (1998) Mol Phys 94:29
20. Kállay M, Surján PR (2000) J Chem Phys 113:1359
21. Kállay M, Surján PR (2001) J Chem Phys 115:2945
22. Kállay M, Szalay PG, Surján PR (2002) J Chem Phys 117:980
23. Kozlowski PM, Davidson ER (1994) Chem Phys Lett 222:615
24. Lindgren I (1974) J Phys B 7:2241
25. Mahapatra U, Datta B, Mukherjee D (1999) J Chem Phys 110:6171
26. Malrieu J, Durand P, Daudey JP (1985) J Phys A 18:809
27. Meissner L, Bartlett RJ (1989) J Chem Phys 91:4800
28. Møller C, Plesset M (1934) Phys Rev 46:618
29. Murphy RB, Messmer RP (1991) Chem Phys Lett 183:443
30. Nakano H (1993) J Chem Phys 99:7983
31. Oliphant N, Adamowicz L (1991) J Chem Phys 94:1229
32. Olsen J, Roos BO, Jørgensen P, Jensen HJA (1988) J Chem Phys 89:2185
33. Paldus J, Čížek J, Keating BA (1973) Phys Rev A 8:640
34. Piecuch P, Oliphant N, Adamowicz L (1993) J Chem Phys 99:1875
35. Purvis G, Shepard R, Brown F, Bartlett R (1983) Int J Quantum Chem 23:835
36. Purvis GD, Bartlett RJ (1978) Int J Quantum Chem 14:561
37. Rolik Z, Kállay M (2014) J Chem Phys 141:134112
38. Rolik Z, Szabados Á (2009) Int J Quantum Chem 109:2554
39. Rolik Z, Szabados Á, Surján PR (2003) J Chem Phys 119:1922
40. Sokolov AY, Chan GKL (2015) J Chem Phys 142:124107
41. Szabados A, Rolik Z, Tóth G, Surján PR (2005) J Chem Phys 122:114104
42. Szalay PG, Müller T, Gidofalvi G, Lischka H, Shepard R (2012) Chem Rev 112:108
43. Werner HJ, Knowles PJ, Knizia G, Manby FR, Schütz M, et al. (2012) Molpro, version 2012.1, a package of ab initio programs. See
44. Wolinski K, Pulay P (1989) J Chem Phys 90:3647
45. Zaitevskii A, Malrieu JP (1995) Chem Phys Lett 233:597

Theor Chem Acc (2015) 134:107
DOI 10.1007/s00214-015-1710-y

REGULAR ARTICLE

Second-order Møller–Plesset perturbation (MP2) theory at finite temperature: relation with Surján's density matrix MP2 and its application to linear-scaling divide-and-conquer method

Masato Kobayashi[1,2] · **Tetsuya Taketsugu**[1,2]

Received: 24 June 2015 / Accepted: 28 July 2015 / Published online: 15 August 2015

Abstract In 2005, Surján showed two explicit formulas for evaluating the second-order Møller–Plesset perturbation (MP2) energy as a functional of the Hartree–Fock density matrix $\boldsymbol{D}$ (Chem Phys Lett 406:318, 2005), which are referred to as the $\Delta E_{\mathrm{MP2}}[\boldsymbol{D}]$ functionals. In this paper, we present the finite-temperature (FT) MP2 energy functionals of the FT Hartree–Fock density matrix. There are also two formulas for the FT-MP2, namely the conventional and renormalized ones; the latter of which has recently been formulated by Hirata and He (J Chem Phys 138:204112, 2013). We proved that there exists one-to-one correspondence between the formulas of two FT-MP2 and the $\Delta E_{\mathrm{MP2}}[\boldsymbol{D}]$ functionals. This fact can explain the different behavior of two $\Delta E_{\mathrm{MP2}}[\boldsymbol{D}]$ functionals when an approximate Hartree–Fock density matrix is applied, which was previously investigated by Kobayashi and Nakai (Chem Phys Lett 420:250, 2006). We also applied the FT-MP2 formalisms to the linear-scaling divide-and-conquer method for improving the accuracy with tiny addition of the computational efforts.

Keywords Fractional occupation number · Many-body perturbation theory · Laplace-transformed Møller–Plesset perturbation · Linear-scaling electronic structure method

1 Introduction

The perturbation theory has widely been used in quantum chemistry to account for the dynamical electron correlation in single Slater [i.e., Hartree–Fock (HF)] and multideterminantal states [1]. Surján has worked on the perturbation theories for both HF and non-HF references. For non-HF reference functions, he and his coworkers proposed a series of multiconfiguration perturbation (MCPT) theories [2–6]. Because the MCPT theories are applicable to any reference functions, they have occasionally been applied to the antisymmetric product of strongly orthogonal geminals wave functions [7–9].

Although many of Surján's famous works are related to the multideterminantal framework, he has also worked on the Møller–Plesset perturbation (MP) theory [10, 11], where the HF wave function is adopted as the reference function. The importance of the MP theory, especially the second-order MP (MP2) method, remains unchanged as the simplest non-empirical way to consider the electron correlation, even though the practical density functional theory (DFT) is getting mature [12, 13]. The computational time for the canonical MP2 calculation, however, scales as $\mathcal{O}(N^5)$, where N is the number of basis functions, which is significantly longer than those for the DFT and HF calculations of $\mathcal{O}(N^3)$. There have been proposed several techniques to reduce the computational time for the MP2 calculation. Surján [14] proposed a method to evaluate the MP2 correlation energy as the functional of the HF density matrix (DM), $\boldsymbol{D}$, based on the Laplace-transformed MP2

Published as part of the special collection of articles "Festschrift in honour of P. R. Surjan".

✉ Masato Kobayashi
k-masato@mail.sci.hokudai.ac.jp

Tetsuya Taketsugu
take@sci.hokudai.ac.jp

[1] Department of Chemistry, Faculty of Science, Hokkaido University, Sapporo 060-0810, Japan

[2] Elements Strategy Initiative for Catalysts and Batteries (ESICB), Kyoto University, Kyoto 615-8245, Japan

formalism [15–17]. One of the authors (MK) followed this DM-MP2 or $\Delta E_{\mathrm{MP2}}[\boldsymbol{D}]$ functional [18]. Its extension to higher-order MP energies was also mentioned by Surján and Szabados [19].

Another simple but straightforward way of reducing the computational time of quantum chemical calculations is the fragmentation of the system under consideration. Kobayashi, Nakai, and coworkers have developed one of them, called the divide-and-conquer (DC) method [20–22], which was first proposed by Yang [23, 24] in the framework of the mean-field theories. The characteristic feature of the DC method, which allows the method to be applied to delocalized systems, is the use of the overlapped fragmentation that is managed by introducing the buffer region with the assistance of the finite-temperature (FT) HF formalism. They also proposed two types of the extension of the DC method to the post-HF correlation theories, including MP2. The first one, called the DC–DM MP2 method, applies the approximate HF density matrix obtained from the DC-HF calculation to the $\Delta E_{\mathrm{MP2}}[\boldsymbol{D}]$ functional [25]. In the other method, called the DC-MP2 method, the correlation energy corresponding to each subsystem is evaluated using the subsystem molecular orbitals (MOs) [26]. The latter one has also been applied to the cluster expansion theories [27–29]. Although it was practically found that the DC–DM MP2 energy often shows better agreement with the canonical MP2 energy than the DC-MP2 one, the DC-MP2 method is usually adopted because of its smaller computational cost. In the DC–DM MP2 method, the FT effect is considered to be included through the use of FT DC-HF density matrix. But in the DC-MP2 method, the subsystem MOs are clearly separated into occupied and virtual ones.

By the way, the MP2 theory was also extended to the FT ensemble [30, 31] based on the FT Green's function theory. Recently, Hirata and He [32] formulated a novel representation, called the *renormalized* formula, which is free from the so-called Kohn–Luttinger conundrum [33]. Kohn–Luttinger conundrum refers to the following inconsistency: taking the limit of $T \to 0$ for the conventional FT many-body perturbation formalism does not lead to the zero-temperature correspondence for metallic system because of the appearance of the *anomalous* diagram. In addition, the renormalized FT-MP2 method consistently connects the divergence rates of the zero-temperature MP2 energy for homogeneous electron gas system to the FT formalism. Their method is based on the FT normal ordering and thermal Wick's theorem [34, 35]. In this paper, we reveal the relation between two DM-MP2 and two FT-MP2 energy expressions. Then, we introduce the FT effect to the DC-MP2 correlation energy. The theoretical aspects of this paper are given in Sect. 2. It is followed by the numerical assessment in calculations of small benzene molecule and fairly large polyene system, $C_{60}H_{62}$.

2 Theory

2.1 Laplace-transformed MP2 and $\Delta E_{\mathrm{MP2}}[\boldsymbol{D}]$ functionals

The closed-shell pure state (i.e., zero temperature) MP2 correlation energy is expressed by [10, 11, 36]

$$\Delta E_{\mathrm{MP2}} = \sum_{ij}^{\mathrm{occ}} \sum_{ab}^{\mathrm{vir}} \langle ij|ab\rangle \left(2\tilde{t}_{ij,ab} - \tilde{t}_{ij,ba}\right), \tag{1}$$

with the following amplitude

$$\tilde{t}_{ij,ab} = -\frac{\langle ab|ij\rangle}{\varepsilon_a + \varepsilon_b - \varepsilon_i - \varepsilon_j}. \tag{2}$$

Through this paper, $\{i,j,\ldots\}$ and $\{a,b,\ldots\}$ refer to occupied and virtual MOs for pure HF state, respectively, and $\{p,q,\ldots\}$ to arbitrary MOs, which are constructed as the linear combination of atomic orbitals (AOs), $\{\phi_\mu\}$,

$$\psi_p = \sum_\mu C_{\mu p}\phi_\mu. \tag{3}$$

Here, $\mathbf{C}_p$ and ε_p are the coefficient vector and the energy of the MO p, obtained by solving the following Roothaan equation:

$$\boldsymbol{F}\mathbf{C}_p = \varepsilon_p \boldsymbol{S}\mathbf{C}_p. \tag{4}$$

$\boldsymbol{F}$ and $\boldsymbol{S}$ are the Fock and overlap matrices, respectively, of which the elements are expressed by

$$F_{\mu\nu} = H^{\mathrm{core}}_{\mu\nu} + \sum_{\lambda\sigma} D_{\lambda\sigma}\left[2\langle\mu\sigma|\nu\lambda\rangle - \langle\mu\sigma|\lambda\nu\rangle\right], \tag{5}$$

$$S_{\mu\nu} = \langle\phi_\mu|\phi_\nu\rangle, \tag{6}$$

$$H^{\mathrm{core}}_{\mu\nu} = \langle\phi_\mu|\hat{h}|\phi_\nu\rangle, \tag{7}$$

with the usual two-electron integral notation of $\langle\mu\sigma|\nu\lambda\rangle = \iint \phi_\mu(\mathbf{r}_1)\phi_\sigma(\mathbf{r}_2) r_{12}^{-1} \phi_\nu(\mathbf{r}_1)\phi_\lambda(\mathbf{r}_2) d\mathbf{r}_1 d\mathbf{r}_2$, the one-electron Hamiltonian of $\hat{h}$, and the HF density matrix $\boldsymbol{D}$ at zero temperature:

$$\boldsymbol{D} = \sum_i^{\mathrm{occ}} \mathbf{C}_i \mathbf{C}_i^{\mathrm{T}}. \tag{8}$$

Due to the existence of the denominator in Eq. (2), the straightforward computation of the MP2 energy with Eq. (1) requires $\mathcal{O}(N^5)$ time with the number of basis functions N. Almlöf [15] first used the Laplace transformation for evaluating the MP2 energy to remove the denominator:

$$\Delta E_{\mathrm{MP2}} = -\int_0^\infty e_2(t)dt. \tag{9}$$

The integrand in Eq. (9) is given in AO-based formalism by [16, 17]

$$e_2(t) = \sum_{\gamma\delta\kappa\varepsilon}\sum_{\mu\nu\lambda\sigma} X_{\mu\gamma}(t)Y_{\nu\delta}(t)X_{\lambda\kappa}(t)Y_{\sigma\varepsilon}(t) \langle\gamma\kappa|\delta\varepsilon\rangle[2\langle\nu\sigma|\mu\lambda\rangle - \langle\nu\sigma|\lambda\mu\rangle], \tag{10}$$

where $\boldsymbol{X}(t)$ and $\boldsymbol{Y}(t)$ are the energy-weighted density matrices of electron and hole given by

$$\boldsymbol{X}(t) = \sum_{i}^{\mathrm{occ}} e^{\varepsilon_i t}\mathbf{C}_i\mathbf{C}_i^{\mathrm{T}}, \tag{11}$$

$$\boldsymbol{Y}(t) = \sum_{a}^{\mathrm{vir}} e^{-\varepsilon_a t}\mathbf{C}_a\mathbf{C}_a^{\mathrm{T}}, \tag{12}$$

respectively. Because these matrices are sparse for large systems, the evaluation of the MP2 energy can be reduced to $\mathcal{O}(N^2)$ [16] or even $\mathcal{O}(N)$ [17].

Using this Laplace MP2 formalism, Surján [14] derived the explicit MP2 energy functional of the HF density matrix, while Ayala and Scuseria [17] suggested previously. Using the Roothaan Eq. (4), one can transform Eqs. (11) and (12) to

$$\boldsymbol{X}(t) = e^{t\boldsymbol{S}^{-1}\boldsymbol{F}}\boldsymbol{D}, \tag{13}$$

$$\boldsymbol{Y}(t) = e^{-t\boldsymbol{S}^{-1}\boldsymbol{F}}\bar{\boldsymbol{D}}, \tag{14}$$

where $\bar{\boldsymbol{D}}$ is the complement of the HF density matrix $\boldsymbol{D}$:

$$\bar{\boldsymbol{D}} = \sum_{a}^{\mathrm{vir}} \mathbf{C}_a\mathbf{C}_a^{\mathrm{T}} = \boldsymbol{S}^{-1} - \boldsymbol{D}. \tag{15}$$

Substituting Eqs. (13) and (14) for Eq. (10), the MP2 correlation energy can be obtained as a functional of the HF density matrix, which is referred to as $\Delta E_{\mathrm{MP2}}[\boldsymbol{D}]$ functional or DM-MP2 method in this paper. Hereafter, Eqs. (13) and (14) are referred to as the $\boldsymbol{S}^{-1}\boldsymbol{F}$ formulas. Furthermore, using the commutation relationship of $\boldsymbol{FDS} = \boldsymbol{SDF}$ and the idempotency of the density matrix, $(\boldsymbol{DS})^n = \boldsymbol{DS}$, one can further derive

$$\boldsymbol{X}(t) = e^{t\boldsymbol{DF}}\boldsymbol{D}, \tag{16}$$

$$\boldsymbol{Y}(t) = e^{-t\bar{\boldsymbol{D}}\boldsymbol{F}}\bar{\boldsymbol{D}}. \tag{17}$$

These equations, referred to as the $\boldsymbol{DF}$ formulas, can also be used instead of Eqs. (13) and (14).

This $\Delta E_{\mathrm{MP2}}[\boldsymbol{D}]$ functional can be used to obtain proper MP2 correlation energy from the non-canonical HF method that cannot yield MOs of the system. The performance of the DM-MP2 method for the use with approximate density matrix was numerically assessed by Kobayashi and Nakai [18]. As an example, the density matrix obtained from the DC-HF calculation was applied to this functional [25]. Although this scheme, called the DC-DM MP2 method, succeeded in accurately evaluating the MP2 correlation energy based on the DC method, the DC-MP2 method based on the subsystem MOs, explained in Sect. 2.3, has been used as the standard extension of the DC method to the MP2 theory.

2.2 Finite-temperature MP2 and Laplace-transformed formula

For the FT ensemble, the HF density matrix is expressed as [37, 38]

$$\boldsymbol{D} = \sum_{p} f_p\mathbf{C}_p\mathbf{C}_p^{\mathrm{T}}, \tag{18}$$

where f_p is the Fermi-distributed occupation number,

$$f_p = f_\beta\left(\varepsilon_{\mathrm{F}} - \varepsilon_p\right), \tag{19}$$

with Fermi level, ε_{F}, and Fermi distribution function $f_\beta(x) = [1 + \exp(-\beta x)]^{-1}$ for the inverse temperature $\beta = (k_{\mathrm{B}}T)^{-1}$. The electronic FT-HF energy is expressed by the usual formula as

$$E_{\mathrm{HF}} = \mathrm{Tr}[\boldsymbol{D}(\boldsymbol{H}^{\mathrm{core}} + \boldsymbol{F})], \tag{20}$$

with the FT density matrix of Eq. (18). Although the grand potential can also be evaluated with the entropy, obtained from the occupation numbers, and the Fermi level, we do not care about these terms in this study because they are not included in the DC formalism [20, 24].

The MP2 theory has also been generalized to the FT ensemble [31, 38, 39]. At finite temperature, the MP2 correlation energy is *conventionally* expressed as

$$\Delta E_{\mathrm{MP2}}^{\mathrm{C}} = \sum_{pqrs}\langle pq|rs\rangle\left(2\tilde{t}_{pq,rs}^{\mathrm{C}} - \tilde{t}_{pq,sr}^{\mathrm{C}}\right). \tag{21}$$

with the following amplitude

$$\tilde{t}_{pq,rs}^{\mathrm{C}} = -\frac{f_{pq,rs}\langle rs|pq\rangle}{\varepsilon_r + \varepsilon_s - \varepsilon_p - \varepsilon_q}. \tag{22}$$

Here, $f_{pq,rs}$ is obtained from the orbital occupation number of Eq. (19) and its complement,

$$\bar{f}_p = 1 - f_p, \tag{23}$$

by

$$f_{pq,rs} = f_p f_q \bar{f}_r \bar{f}_s. \tag{24}$$

The energy expression of Eq. (21) can be derived from the finite-temperature Green's function [40]. Obviously, Eq. (22) diverges at finite β (or nonzero temperature) for $p = r$ and $q = s$, for example. These divergent terms

should be neglected in practical calculations. Hirata and He [32] recently proposed the *renormalized* formalism for the FT many-body perturbation theory that changes the divergence rate to be consistent to the zero-temperature counterpart:

$$\Delta E^{\mathrm{R}}_{\mathrm{MP2}} = \sum_{pqrs} \langle pq|rs\rangle \left(2\tilde{t}^{\mathrm{R}}_{pq,rs} - \tilde{t}^{\mathrm{R}}_{pq,sr}\right), \tag{25}$$

$$\tilde{t}^{\mathrm{R}}_{pq,rs} = -\frac{f_{pq,rs}\langle rs|pq\rangle}{\bar{f}_r\varepsilon_r + \bar{f}_s\varepsilon_s - f_p\varepsilon_p - f_q\varepsilon_q}. \tag{26}$$

This formula comes from the thermal Wick's theorem [34, 35]. Note that this renormalized FT-MP2 energy as well as the conventional FT-MP2 energy diverges for metallic system. The conventional FT-MP2 energy, however, may diverge even for insulators. In this subsection, we clarify the correspondence of the above two formalisms with two $\Delta E_{\mathrm{MP2}}[\boldsymbol{D}]$ functionals.

According to the standard AO-based formalism [17], the Laplace transformation of $\Delta E^{\mathrm{C}}_{\mathrm{MP2}}$ and $\Delta E^{\mathrm{R}}_{\mathrm{MP2}}$ leads to

$$\Delta E^{\mathrm{C/R}}_{\mathrm{MP2}} = -\int_0^\infty e_2^{\mathrm{C/R}}(t)dt. \tag{27}$$

The integrand in Eq. (27) is given by

$$e_2^{\mathrm{C/R}}(t) = \sum_{\gamma\delta\kappa\varepsilon}\sum_{\mu\nu\lambda\sigma} X^{\mathrm{C/R}}_{\mu\gamma}(t)Y^{\mathrm{C/R}}_{\nu\delta}(t)X^{\mathrm{C/R}}_{\lambda\kappa}(t)Y^{\mathrm{C/R}}_{\sigma\varepsilon}(t) \langle\gamma\kappa|\delta\varepsilon\rangle[2\langle\nu\sigma|\mu\lambda\rangle - \langle\nu\sigma|\lambda\mu\rangle]. \tag{28}$$

For the conventional formalism, the energy-weighted density matrices are given by

$$\boldsymbol{X}^{\mathrm{C}}(t) = \sum_p e^{\varepsilon_p t} f_p \mathbf{C}_p\mathbf{C}_p^{\mathrm{T}}, \tag{29}$$

$$\boldsymbol{Y}^{\mathrm{C}}(t) = \sum_p e^{-\varepsilon_p t} \bar{f}_p \mathbf{C}_p\mathbf{C}_p^{\mathrm{T}}, \tag{30}$$

and for the renormalized formalism, they are

$$\boldsymbol{X}^{\mathrm{R}}(t) = \sum_p e^{\varepsilon_p f_p t} f_p \mathbf{C}_p\mathbf{C}_p^{\mathrm{T}}, \tag{31}$$

$$\boldsymbol{Y}^{\mathrm{R}}(t) = \sum_p e^{-\varepsilon_p \bar{f}_p t} \bar{f}_p \mathbf{C}_p\mathbf{C}_p^{\mathrm{T}}. \tag{32}$$

The expressions for the conventional formalism are different from Eqs. (11) and (12) only in the existence of the occupation number before $\mathbf{C}_p\mathbf{C}_p^{\mathrm{T}}$. For the renormalized formalism, the occupation number also appears on the exponential.

If the HF equation of Eq. (4) is satisfied, one can derive the following equation:

$$\boldsymbol{X}^{\mathrm{C}}(t) = e^{t\boldsymbol{S}^{-1}\boldsymbol{F}}\boldsymbol{D}, \tag{33}$$

$$\boldsymbol{Y}^{\mathrm{C}}(t) = e^{-t\boldsymbol{S}^{-1}\boldsymbol{F}}\bar{\boldsymbol{D}}, \tag{34}$$

where $\bar{\boldsymbol{D}}$ is the complement of the FT-HF density matrix,

$$\bar{\boldsymbol{D}} = \sum_p \bar{f}_p \mathbf{C}_p\mathbf{C}_p^{\mathrm{T}} = \boldsymbol{S}^{-1} - \boldsymbol{D}. \tag{35}$$

These are formally the same as the $\boldsymbol{S}^{-1}\boldsymbol{F}$ formulas of Eqs. (13) and (14). However, it cannot be further transformed to the $\boldsymbol{DF}$ formulas because the density matrix is no longer idempotent at finite temperature but has the following relationship:

$$(\boldsymbol{DS})^n = \sum_p f_p^n \mathbf{C}_p\mathbf{C}_p^{\mathrm{T}}\boldsymbol{S}. \tag{36}$$

As for the renormalized formulas, on the contrary, using the relationships of $\boldsymbol{FDS} = \boldsymbol{SDF}$ and Eq. (36) leads to

$$\boldsymbol{X}^{\mathrm{R}}(t) = e^{t\boldsymbol{DF}}\boldsymbol{D}, \tag{37}$$

$$\boldsymbol{Y}^{\mathrm{R}}(t) = e^{-t\bar{\boldsymbol{D}}\boldsymbol{F}}\bar{\boldsymbol{D}}. \tag{38}$$

These are formally the same as the $\boldsymbol{DF}$ formulas of Eqs. (16) and (17).

Here, we summarize the important point in this Section. As derived in the previous studies [14, 18], two DM-MP2 formalisms (i.e., the $\boldsymbol{S}^{-1}\boldsymbol{F}$ and $\boldsymbol{DF}$ formulas) are equivalent at zero temperature (see Eqs. 13 and 16, for example). At finite temperature, however, these two formulas are no longer equivalent and further coincide with the conventional and renormalized FT-MP2 formulas (see Eqs. 33 and 37, for example).

When Kobayashi and Nakai [18] calculated the MP2 correlation energy using Eq. (10) with the density matrix having random noise, they obtained a reasonable MP2 correlation energy with Eqs. (16) and (17), although they could not with Eqs. (13) and (14). The noise-introduced HF density matrix can be represented as Eq. (18) having noise in the occupation number, f_p, if the basis set spans the complete space. Therefore, this result can now be interpreted that the amplitude of Eq. (22) for $p = r$ and $q = s$, for instance, diverges when using a density matrix for a mixed state.

2.3 Finite-temperature DC-MP2 method

Kobayashi and coworkers [20, 21, 26, 41] have proposed a linear-scaling DC-MP2 method. This method utilizes MOs determined in the subsystem α, $\{\psi_p^\alpha\}$, which are constructed as

$$\psi_p^\alpha = \sum_{\mu\in\mathcal{L}(\alpha)} C^\alpha_{\mu p}\phi_\mu, \tag{39}$$

where the coefficient $C^{\alpha}_{\mu p}$ is obtained by solving the HF equation in subsystem α :

$$\boldsymbol{F}^{\alpha}\mathbf{C}^{\alpha}_{p} = \varepsilon^{\alpha}_{p}\boldsymbol{S}^{\alpha}\mathbf{C}^{\alpha}_{p}. \tag{40}$$

In Eq. (39), $\mathcal{L}(\alpha)$ is the set of AOs used in the expansion of MOs in subsystem α, which consists of two parts:

$$\mathcal{L}(\alpha) = \mathcal{S}(\alpha) \sqcup \mathcal{B}(\alpha). \tag{41}$$

$\mathcal{S}(\alpha)$ is the AOs corresponding to the *central region* of the subsystem α, which is mutually exclusive:

$$\mathcal{S}(\alpha) \cap \mathcal{S}(\beta) = \emptyset, \quad \forall \alpha \neq \beta, \tag{42}$$

and $\mathcal{B}(\alpha)$ is the AOs corresponding to the neighboring region of the central region of the subsystem α, called the *buffer region*. $\boldsymbol{F}^{\alpha}$ and $\boldsymbol{S}^{\alpha}$ are the subsystem Fock and overlap matrices, respectively, of which the elements are expressed by

$$F^{\alpha}_{\mu\nu} = H^{\mathrm{core}}_{\mu\nu} + \sum_{\lambda\sigma} D_{\lambda\sigma}[2\langle\mu\sigma|\nu\lambda\rangle - \langle\mu\sigma|\lambda\nu\rangle], \tag{43}$$

$$S^{\alpha}_{\mu\nu} = \langle\phi_{\mu}|\phi_{\nu}\rangle. \tag{44}$$

Obviously, the matrix elements of Eqs. (43) and (44) are the same as Eqs. (5) and (6). Here in Eq. (43), one can adopt any density matrix, $\boldsymbol{D}$, which is appropriately determined. A possible candidate is the DC-HF density matrix:

$$D^{\mathrm{DC}}_{\mu\nu} = \sum_{\alpha} P^{\alpha}_{\mu\nu} D^{\alpha}_{\mu\nu}, \tag{45}$$

where

$$\boldsymbol{D}^{\alpha} = \sum_{p}^{\mathrm{MO}(\alpha)} f^{\alpha}_{p}\mathbf{C}^{\alpha}_{p}\mathbf{C}^{\alpha\mathrm{T}}_{p}. \tag{46}$$

f^{α}_{p} is the Fermi-distributed occupation number:

$$f^{\alpha}_{p} = f_{\beta}(\varepsilon_{\mathrm{F}} - \varepsilon^{\alpha}_{p}), \tag{47}$$

and $\boldsymbol{P}$ is the partition matrix defined by

$$P^{\alpha}_{\mu\nu} = \begin{cases} 1 & (\mu \in \mathcal{S}(\alpha) \wedge \nu \in \mathcal{S}(\alpha)) \\ 1/2 & (\mu \in \mathcal{S}(\alpha) \wedge \nu \in \mathcal{B}(\alpha), \text{or } \textit{vice versa}) \\ 0 & (\text{otherwise}). \end{cases} \tag{48}$$

Fermi level, ε_{F}, in Eq. (47) is determined from the number of electrons in the entire system, n_{e}, by solving the following equation:

$$n_{\mathrm{e}} = \mathrm{tr}(\boldsymbol{D}^{\mathrm{DC}}\boldsymbol{S}). \tag{49}$$

As shown above, the Fermi level and the FT formalism are introduced in the DC-HF method. Recently, Yoshikawa and Nakai proposed an alternative DC procedure, where the number of electrons in each subsystem is fixed after a couple of iterations for improving the parallel efficiency of the DC-HF calculations [42]. The Fermi level is no longer constant through the entire system in this scheme, which is also related to the adjustable density matrix assembly method [43, 44].

In the DC-MP2 method, the total correlation energy is estimated by summing up the subsystem correlation energies:

$$\Delta E_{\text{DC-MP2}} = \sum_{\alpha} \Delta E^{\alpha}_{\mathrm{MP2}}. \tag{50}$$

The correlation energy of the subsystem α, $\Delta E^{\alpha}_{\mathrm{MP2}}$, has been estimated from the energy density analysis [45] with the subsystem MOs as follows:

$$\Delta E^{\alpha}_{\mathrm{MP2}} = \sum_{ij}^{\mathrm{occ}(\alpha)} \sum_{ab}^{\mathrm{vir}(\alpha)} \sum_{\mu\in\mathcal{S}(\alpha)} C^{\alpha}_{\mu i}\langle\mu j^{\alpha}|a^{\alpha}b^{\alpha}\rangle \times \left(2\tilde{t}^{\alpha}_{ij,ab} - \tilde{t}^{\alpha}_{ij,ba}\right). \tag{51}$$

$\tilde{t}^{\alpha}_{ij,ab}$ is the effective two-electron excitation amplitude for subsystem α, which is expressed in MP2 case with the subsystem MOs as follows:

$$\tilde{t}^{\alpha}_{ij,ab} = -\frac{\langle a^{\alpha}b^{\alpha}|i^{\alpha}j^{\alpha}\rangle}{\varepsilon^{\alpha}_{a} + \varepsilon^{\alpha}_{b} - \varepsilon^{\alpha}_{i} - \varepsilon^{\alpha}_{j}}. \tag{52}$$

In the previous DC-MP2 method with integer occupation numbers, the subsystem MOs should clearly be separated into occupied and virtual ones by the Fermi level. In the DC-HF method, however, fractional occupations of MOs are allowed around Fermi level because the FT ensemble is formally treated (see Eq. 46).

It is also possible to adopt the FT-MP2 formalisms of Eqs. (21) or (25) in the DC-MP2 method. On the analogy to Eq. (51), the subsystem correlation energy at finite temperature can be evaluated as

$$\Delta E^{\mathrm{C/R}\alpha}_{\mathrm{MP2}} = \sum_{pqrs}^{\mathrm{MO}(\alpha)} \sum_{\mu\in\mathcal{S}(\alpha)} C^{\alpha}_{\mu p}\langle\mu q^{\alpha}|r^{\alpha}s^{\alpha}\rangle \times \left(2\tilde{t}^{\mathrm{C/R}\alpha}_{pq,rs} - \tilde{t}^{\mathrm{C/R}\alpha}_{pq,rs}\right). \tag{53}$$

$\tilde{t}^{\mathrm{C/R}\alpha}_{pq,rs}$ is

$$\tilde{t}^{\mathrm{C}\alpha}_{pq,rs} = -\frac{f^{\alpha}_{pq,rs}\langle r^{\alpha}s^{\alpha}|p^{\alpha}q^{\alpha}\rangle}{\varepsilon^{\alpha}_{r} + \varepsilon^{\alpha}_{s} - \varepsilon^{\alpha}_{p} - \varepsilon^{\alpha}_{q}}, \tag{54}$$

or

$$\tilde{t}^{\mathrm{R}\alpha}_{pq,rs} = -\frac{f^{\alpha}_{pq,rs}\langle r^{\alpha}s^{\alpha}|p^{\alpha}q^{\alpha}\rangle}{\bar{f}^{\alpha}_{r}\varepsilon^{\alpha}_{r} + \bar{f}^{\alpha}_{s}\varepsilon^{\alpha}_{s} - f^{\alpha}_{p}\varepsilon^{\alpha}_{p} - f^{\alpha}_{q}\varepsilon^{\alpha}_{q}}, \tag{55}$$

where

$$\bar{f}^{\alpha}_{p} = 1 - f^{\alpha}_{p}, \tag{56}$$

$$f^{\alpha}_{pq,rs} = f^{\alpha}_{p} f^{\alpha}_{q} \bar{f}^{\alpha}_{r} \bar{f}^{\alpha}_{s}. \tag{57}$$

As mentioned in the previous DC-MP2 and DC coupled cluster papers [27, 28, 41, 46, 47], the buffer region used in the DC-MP2 method can be set to be smaller than that in the DC-HF method without significant loss of accuracy. When this dual-buffer DC-MP2 scheme was adopted, the Fermi level was used to be redetermined using the MOs constructed in the smaller subsystems. In the integer occupation DC-MP2 method, however, the use of the Fermi level obtained from the prior DC-HF calculation does not significantly change the results because the Fermi level is used only for separating the subsystem MOs into occupied and virtual ones. On the other hand, in the FT DC-MP2 method, the subsystem MP2 correlation energy of Eq. (53) may largely depend on the Fermi level due to the occupation numbers appearing in the coefficients of Eqs. (54) and (55). Because the reference state for the DC-MP2 method is the preceding DC-HF state, the authors decided to use the Fermi level determined in the DC-HF calculation throughout the DC-MP2 calculation. The dependence of the FT DC-MP2 energy on the Fermi level will also be assessed below.

Fundamentally, the difference between the implementations of the FT and integer occupation DC-MP2 methods is the summation lengths in Eqs. (51) and (53). Although the MO indices in Eq. (53) formally run over all subsystem orbitals, the MO p of subsystem α is regarded as to be doubly occupied or fully vacant if $f^{\alpha}_{p} > 1-\theta$ or $f^{\alpha}_{p} < \theta$, respectively (throughout this paper, the threshold of $\theta = 10^{-15}$ is adopted). Therefore, the computational costs for the MP2 calculation of subsystem α depend on the practical numbers of occupied and virtual MOs, which are defined with the numbers of all MOs (N^{α}), uncorrelated core MOs ($N^{\alpha}_{\mathrm{core}}$), doubly occupied MOs ($N^{\alpha}_{\mathrm{docc}}$, including $N^{\alpha}_{\mathrm{core}}$), and fully vacant MOs ($N^{\alpha}_{\mathrm{fvac}}$) by

$$N^{\alpha}_{\mathrm{occ}} = N^{\alpha} - N^{\alpha}_{\mathrm{fvac}} - N^{\alpha}_{\mathrm{core}} \tag{58}$$

and

$$N^{\alpha}_{\mathrm{vir}} = N^{\alpha} - N^{\alpha}_{\mathrm{docc}}, \tag{59}$$

respectively.

The above-mentioned methods were implemented into the development version of the GAMESS program [48, 49], which was used in calculations for the next Section.

3 Numerical assessments

3.1 DM-MP2 and FT-MP2 calculations of benzene

First, the relation between FT-MP2 and DM-MP2, derived in the previous Section, was numerically assessed in calculations of benzene molecule with 6-31G** basis set [50]. In DM-MP2 calculations, we applied the Chebyshev expansion for the evaluation of matrix exponential, which is implemented in the EXPOKIT library program [51]. For the numerical quadrature of the Laplace-transformed integrals of Eqs. (9) and (27), we used the τ-point Euler–Maclaurin (trapezoidal) quadrature

$$\begin{aligned}\int_0^{\infty} e_2(t)dt &= \int_0^1 f_2(r)dr \\ &\approx \frac{1}{\tau+1}\left[\sum_{k=1}^{\tau} f_2\left(\frac{k}{\tau+1}\right) + \frac{f_2(0)+f_2(1)}{2}\right]\end{aligned} \tag{60}$$

with

$$f_2(r) = e_2(t)\frac{dt}{dr} \tag{61}$$

and the following change in variable

$$t = \frac{r^3 - 0.9r^4}{(1-r)^2} + r^2 \tan\left(\frac{\pi r}{2}\right), \tag{62}$$

according to the previous assessment [18] (note that $f_2(0) = f_2(1) = 0$).

Figure 1 shows the inverse temperature (β) dependence of the FT-MP2 (Eqs. 21 and 25) and the DM-MP2 (Eq. 27) energies of a benzene molecule with C–C and C–H bond lengths of 140 and 109 pm. In the DM-MP2 calculations, the number of quadrature points was set to $\tau = 7$. The MP2 energy at zero temperature (−231.535 Hartree) is shown with dotted line. At low temperature ($\beta \geq 30$ a.u.), all the four MP2 energies shown in Fig. 1 coincide with the zero-temperature energy because the benzene molecule has large band gap. For $\beta \leq 20$ a.u., the energy gradually increases as β decreases, except for the DM-MP2 result with the $\boldsymbol{S}^{-1}\boldsymbol{F}$ formula. Even in this high-temperature region, the

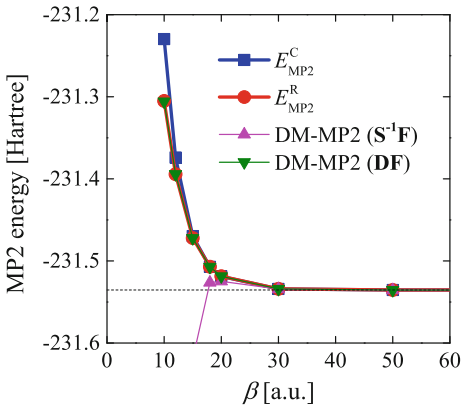

Fig. 1 Inverse temperature (β) dependence of the FT- and DM-MP2 energies of benzene

Table 1 The dependence of FT DM-MP2 energies (in Hartree) of benzene on the number of numerical quadrature points, τ

τ	$\boldsymbol{S}^{-1}\boldsymbol{F}$ formula		***DF*** formula	
	MP2 energy	Diff.	MP2 energy	Diff.
3	−231.499433	−0.029700	−231.479424	−0.007277
5	−231.516181	−0.046448	−231.471887	+0.000259
7	−231.619518	−0.149786	−231.472234	−0.000087
10	−231.863400	−0.393668	−231.472130	+0.000016
Ref.	−231.469733[a]		−231.472147[b]	

Inverse temperature was set to $\beta = 15$ a.u.

[a] Conventional FT-MP2 energy, Eq. (21)

[b] Renormalized FT-MP2 energy, Eq. (25)

DM-MP2 result with ***DF*** formula agrees well with the renormalized FT-MP2 one: The difference between these two results comes from the numerical quadrature error of Eq. (27). The DM-MP2 result with $\boldsymbol{S}^{-1}\boldsymbol{F}$ formula shows divergent behavior as β decreases due to the divergent terms of Eq. (22). As described in Sect. 2.2, these divergent terms are not taken into account in the conventional FT-MP2 calculations. Although the conventional FT-MP2 result shows good agreement with the renormalized FT-MP2 one up to $\beta = 15$ a.u., the difference between two FT-MP2 results increases as β decreases. In addition, this result numerically supports the reason for the divergence of DM-MP2 with $\boldsymbol{S}^{-1}\boldsymbol{F}$ formula when the density matrix is approximately obtained.

Table 1 shows the dependence of FT DM-MP2 energies of benzene on the number of numerical quadrature points, τ. Here, the results for $\beta = 15$ a.u., where two DM-MP2 energies in Fig. 1 show large discrepancy, are given. The energy with the ***DF*** formula smoothly converges to the renormalized FT-MP2 energy, $E^{\mathrm{R}}_{\mathrm{MP2}}$, as τ increases. The energy with $\tau = 7$, adopted in Fig. 1, only differs by 0.1 mHartree from the renormalized FT-MP2 energy. On the contrary, the result with the $\boldsymbol{S}^{-1}\boldsymbol{F}$ formula shows divergent behavior as τ increases. This divergence may be a correct behavior because the FT DM-MP2 energy with $\boldsymbol{S}^{-1}\boldsymbol{F}$ formula includes the divergent terms, which are avoided when evaluating $E^{\mathrm{C}}_{\mathrm{MP2}}$.

3.2 Polyene system with bond alternation

Next, we assessed the FT DC-MP2 method in calculations of polyene system, $C_{60}H_{62}$, with bond alternation, depicted in Fig. 2. ΔR_{BA} indicates the magnitude of bond alternation, i.e., larger ΔR_{BA} leads more single- and double-bond alternating picture, and $\Delta R_{\mathrm{BA}} = 0$ means fully delocalized structure. All the bond angles of ∠C-C-C and ∠C-C-H were set to be 120°. A HC=CH (or H_2C=CH for the edges)

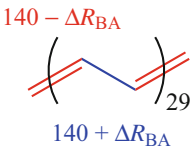

Fig. 2 Polyene system, $C_{60}H_{62}$, with bond alternation, ΔR_{BA}. Values in the figure are the bond lengths in pm

unit was adopted as the central region, and its adjacent n_b^{HF} and n_b^{MP2} units (on either side) were adopted as the buffer regions in DC-HF and DC-MP2 calculations, respectively.

Figure 3 shows the dependence of the DC-MP2 energy deviation of polyene system, $C_{60}H_{62}$, from the zero-temperature canonical MP2 energy on the bond alternation, ΔR_{BA}. Three DC-MP2 formalisms (I for integer occupation, C for conventional FT, and R for renormalized FT) were used. In the MP2 correlation calculation, the C 1s orbitals were frozen. We adopted two different inverse temperature parameters, i.e., (a) lower temperature ($\beta = 500$ a.u.) and (b) higher temperature ($\beta = 50$ a.u.). Here, the 6-31G** basis set [50] was used. The DC-HF buffer size used in these calculations was $n_b^{\mathrm{HF}} = 6$. The energy deviations with $n_b^{\mathrm{MP2}} = 6$ (solid lines) are always smaller than with $n_b^{\mathrm{MP2}} = 4$ (dashed lines). For large ΔR_{BA}, the difference between the conventional and renormalized FT DC-MP2 results is tiny: 0.14 mHartree or less for $\Delta R_{\mathrm{BA}} = 4$ pm. The difference between the integer occupation and FT-MP2 is also small for $\Delta R_{\mathrm{BA}} = 10$ pm, and the maximum differences are 0.06 and 0.22 mHartree with $\beta = 500$ and 50 a.u., respectively. As the bond alternation, ΔR_{BA}, decreases, the energy deviation gradually increases because more delocalized electronic structure makes the DC approximation worse. The difference between the integer occupation and FT-MP2 also increases: For $\Delta R_{\mathrm{BA}} = 4$ pm, the maximum differences are 0.7 and 1.5 mHartree with $\beta = 500$ and 50 a.u., respectively. For the same ΔR_{BA} and n_b^{MP2}, the energy deviations obtained by the FT DC-MP2 formulas are smaller than those by the integer occupation DC-MP2 one except for the renormalized FT-MP2 result with $\Delta R_{\mathrm{BA}} = 0$, $\beta = 50$ a.u., and $n_b^{\mathrm{MP2}} = 4$. Because the renormalized FT-MP2 energy also shows divergent behavior for small band gap systems, the conventional FT-MP2, in which the divergent terms are necessarily avoided, may be a better choice when the FT-MP2 formula is combined with the DC-MP2 method.

Table 2 summarizes the practical numbers of occupied and virtual MOs, defined by Eqs. (58) and (59), in the FT DC-MP2 calculations of $C_{60}H_{62}$ without bond alternation (i.e., $\Delta R_{\mathrm{BA}} = 0$). The data for two characteristic subsystems, namely the middle and edge subsystems, are provided in the table. The inverse temperature parameter, β, was varied from 50 to 500 a.u. The numbers for the integer

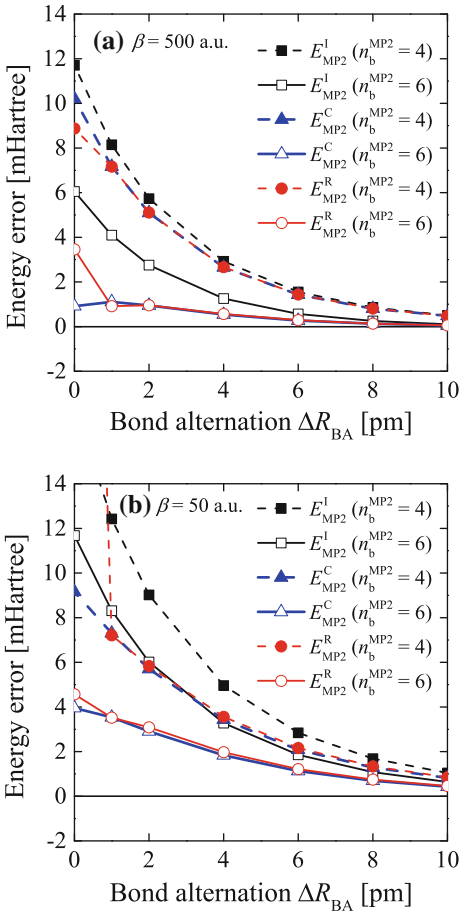

Fig. 3 Bond alternation (ΔR_{BA}) dependence of the DC-MP2 energy deviations of polyene system, $C_{60}H_{62}$, with integer occupation ($E^{\mathrm{I}}_{\mathrm{MP2}}$), conventional FT ($E^{\mathrm{C}}_{\mathrm{MP2}}$), and renormalized FT ($E^{\mathrm{R}}_{\mathrm{MP2}}$) formalisms for (a) $\beta = 500$ a.u. and (b) $\beta = 50$ a.u., where β is the inverse temperature parameter appeared in the occupation number

occupation DC-MP2 are given together for comparison. The buffer size was fixed to $n_b^{\mathrm{HF}} = n_b^{\mathrm{MP2}} = 6$. Even for this delocalized system, the numbers for $\beta \geq 200$ a.u. are close to those for the integer occupation DC-MP2 method. Therefore, in case of large β, the additional computational costs for the FT-MP2 treatment are tiny, although the energy improvement shown in Fig. 3 is considerable. $N^{\alpha}_{\mathrm{occ}}$ and $N^{\alpha}_{\mathrm{vir}}$ gradually increases as the temperature increases. It was concluded that the use of low temperature is important in DC-MP2 calculation not only to improve the accuracy but also to reduce the computational demands for the FT-MP2 treatment. Although the use of high temperature often improves the self-consistent field convergence in DC-HF calculation, so-called annealing technique can be adopted to lower the final temperature [52].

Up to this point, as discussed in Sect. 2.3, the Fermi level determined in the DC-HF calculation was also used for Eqs. (54) and (55). If the Fermi level is redetermined using the subsystem MOs constructed for the DC-MP2 calculation and is used for Eqs. (54) and (55), the result of Fig. 3 changes to be Fig. 4 for $\beta = 500$ a.u. Here, the data for $n_b^{\mathrm{MP2}} = 6$ are not given, because the result does not change for the case of $n_b^{\mathrm{HF}} = n_b^{\mathrm{MP2}}$. For the integer occupation DC-MP2 method, the results of Figs. 3a and 4 are the same. On the other hand, the results for the FT DC-MP2 calculations are considerably different between Figs. 3a and 4. For example, the differences between the integer occupation and the conventional FT DC-MP2 energies for $\Delta R_{\mathrm{BA}} = 0$ are 1.5 and 16.7 mHartree for Figs. 3a and 4, respectively. The renormalized FT DC-MP2 result shows divergent behavior at $\Delta R_{\mathrm{BA}} = 0$, as was also observed in Fig. 3b. Although the detailed analysis may be required for the optimal determination of the Fermi level used in the DC-MP2 calculation, the authors use the Fermi level determined in the DC-HF calculation hereafter.

Finally, the present FT DC-MP2 results are compared with the DC-DM MP2 one, where the correlation energy is obtained from Eq. (9) with Eqs. (16) and (17), and the DC-HF density matrices. Figure 5 shows the buffer size dependence of the FT DC-MP2 and DC-DM MP2 energy deviations of polyene system, $C_{60}H_{62}$, with $\Delta R_{\mathrm{BA}} = 0$, The inverse temperature was fixed at $\beta = 500$ a.u. In the DC-DM MP2 calculations, the number of quadrature points was set to $\tau = 7$. For comparing with the DC-DM MP2

Table 2 The practical numbers of occupied ($N^{\alpha}_{\mathrm{occ}}$) and virtual ($N^{\alpha}_{\mathrm{vir}}$) MOs for middle and edge subsystems in the FT DC-MP2 calculations of $C_{60}H_{62}$ with $\Delta R_{\mathrm{BA}} = 0$

Subsystem		β [a.u.]				
		50	100	200	500	∞[a]
Middle	$N^{\alpha}_{\mathrm{occ}}$	128	99	72	68	66
	$N^{\alpha}_{\mathrm{vir}}$	474	434	429	428	428
	N^{α}	520	520	520	520	520
Edge	$N^{\alpha}_{\mathrm{occ}}$	70	54	39	37	36
	$N^{\alpha}_{\mathrm{vir}}$	260	238	235	235	235
	N^{α}	285	285	285	285	285

$n_b^{\mathrm{HF}} = n_b^{\mathrm{MP2}} = 6$

[a] Numbers for the integer occupation DC-MP2 calculation

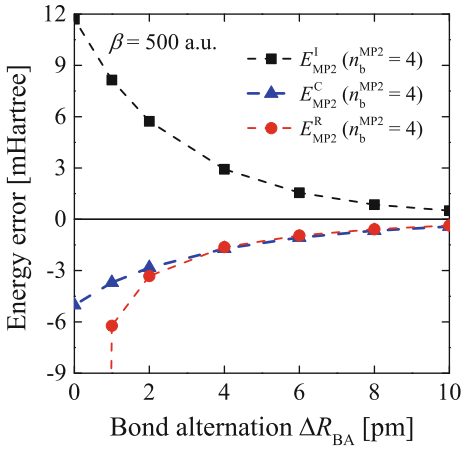

Fig. 4 The same figure as Fig. 3a but for the case that the Fermi level, ε_F, is determined using the subsystem MOs reconstructed for the DC-MP2 calculation with smaller buffer size

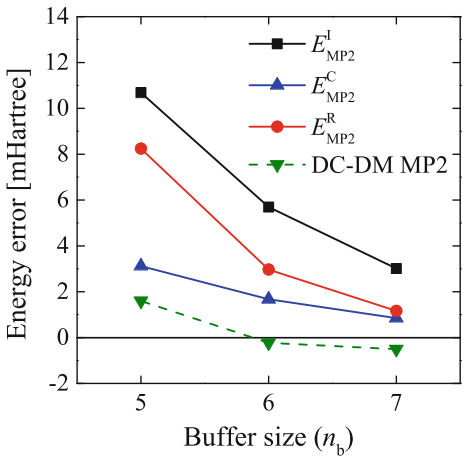

Fig. 5 Buffer size ($n_b = n_b^{HF} = n_b^{MP2}$) dependence of the FT DC-MP2 and DC-DM MP2 energy deviations of polyene system, $C_{60}H_{62}$, at $\Delta R_{BA} = 0$ and $\beta = 500$ a.u. 6-31G basis set was adopted

result, the computational details used in calculations for Fig. 5 are different from those for Fig. 3: the buffer region was fixed throughout the DC-HF and DC-MP2 calculations, i.e., $n_b^{HF} = n_b^{MP2}$, the core electrons were correlated as well as the valence ones (i.e., $N^{\alpha}_{core} = 0$ for all subsystems α), and the 6-31G basis set [53] was used. The numerical quadrature scheme used in DC-DM MP2 calculations is the same as used in the DM-MP2 calculations of benzene, mentioned in Sect. 3.1. The integer occupation DC-MP2 results are also shown for comparison. Among three subsystem-based DC-MP2 results, the conventional FT-MP2 method shows the best agreement with the zero-temperature canonical MP2 result, although the DC-DM MP2 result gives smaller energy deviation than the subsystem-based DC-MP2 method. The renormalized FT-MP2 results are also improved from the integer occupation DC-MP2 when adopting the same buffer region for DC-HF and DC-MP2 calculations. The authors again concluded that the use of FT-MP2 formulas with low electronic temperature improves the accuracy of the DC-MP2 calculations especially with the conventional FT-MP2 formalism with slight addition of the computational demands, although a moderate improvement can also be confirmed with the renormalized FT-MP2 formalism when the same buffer region is adopted for DC-HF and DC-MP2 calculations.

4 Conclusion

It was found that two different representations of density matrix (DM) MP2, which Surján originally formulated for pure state ($\beta = \infty$) [14], can be obtained from the Laplace transformation of two types of finite-temperature (FT) MP2 formulas, namely $\boldsymbol{S}^{-1}\boldsymbol{F}$ formula from the conventional FT-MP2 and $\boldsymbol{DF}$ formula from the renormalized FT-MP2. We numerically confirmed this one-to-one correspondence of FT-MP2 and DM-MP2 for benzene molecule by varying the electronic temperature β and found that the DM-MP2 energy with $\boldsymbol{S}^{-1}\boldsymbol{F}$ formula shows unfavorable behavior due to the divergent term. This fact also accounts for our previous experience [18] that the DM-MP2 calculation with $\boldsymbol{S}^{-1}\boldsymbol{F}$ formula fails to obtain approximate MP2 energy when the density matrix is approximated. We also applied the FT-MP2 energy to the subsystem MO-based divide-and-conquer (DC) MP2 method. The FT DC-MP2 energy shows better agreement with the zero-temperature canonical MP2 energy than the previous integer occupation DC-MP2 one, in spite of its tiny additional computational efforts especially for large β. For the combination of FT-MP2 and DC-MP2 method, the use of the conventional FT-MP2 formalism that directly avoids the divergent terms may be more preferable than that of the renormalized FT-MP2.

Acknowledgments The authors are grateful to Prof. Hiromi Nakai and Dr. Takeshi Yoshikawa (Waseda University) for their valuable comments. Some of the present calculations were performed using the computer facilities at Research Center for Computational Science, Okazaki, and at Research Institute for Information Technology, Kyushu University, Japan. This work was supported in part by JSPS KAKENHI Grant No. 25810011.

References

1. Helgaker T, Jørgensen P, Olsen J (2002) Molecular electronic-structure theory. Wiley, Chichester
2. Rolik Z, Szabados Á, Surján PR (2003) J Chem Phys 119:1922
3. Szabados Á, Rolik Z, Tóth G, Surján PR (2005) J Chem Phys 122:114104

4. Surján P, Rolik Z, Szabados Á, Kőhalmi D (2004) Ann Phys 13:223
5. Kobayashi M, Szabados Á, Nakai H, Surján PR (2010) J Chem Theory Comput 6:2024
6. Szabados Á, Nagy P (2011) J Phys Chem A 115:523
7. Surján PR (1999) An introduction to the theory of geminals. In: Surján PR (ed) Correlation and localization. Springer, Berlin, pp 63–88
8. Jeszenszki P, Nagy PR, Zoboki T, Szabados Á, Surján PR (2014) Int J Quantum Chem 114:1048
9. Tarumi M, Kobayashi M, Nakai H (2012) J Chem Theory Comput 8:4330
10. Møller C, Plesset MS (1934) Phys Rev 46:618
11. Shavitt I, Bartlett RJ (2009) Many-body methods in chemistry and physics: MBPT and coupled-cluster theory. Cambridge University Press, Cambridge
12. Tsuneda T (2014) Density functional theory in quantum chemistry. Springer, Tokyo
13. Engel E, Dreizler RM (2011) Density functional theory: an advanced course. Springer, Heidelberg
14. Surján PR (2005) Chem Phys Lett 406:318
15. Almlöf J (1991) Chem Phys Lett 181:319
16. Häser M (1993) Theor Chim Acta 87:147
17. Ayala PY, Scuseria GE (1999) J Chem Phys 110:3660
18. Kobayashi M, Nakai H (2006) Chem Phys Lett 420:250
19. Surján PR, Szabados Á (2011) Perturbative approximations to avoid matrix diagonalization. In: Papadopoulos MG, Zalesny R, Mezey PG, Leszczynski J (eds) Linear-scaling techniques in computational chemistry and physics: methods and applications. Springer, Dordrecht, pp 83–95
20. Kobayashi M, Nakai H (2011) Divide-and-conquer approaches to quantum chemistry: theory and implementation. In: Papadopoulos MG, Zalesny R, Mezey PG, Leszczynski J (eds) Linear-scaling techniques in computational chemistry and physics: methods and applications. Springer, Dordrecht, pp 97–127
21. Kobayashi M, Nakai H (2012) Phys Chem Chem Phys 14:7629
22. Akama T, Kobayashi M, Nakai H (2007) J Comput Chem 28:2003
23. Yang W (1991) Phys Rev Lett 66:1438
24. Yang W, Lee TS (1995) J Chem Phys 103:5674
25. Kobayashi M, Akama T, Nakai H (2006) J Chem Phys 125:204106
26. Kobayashi M, Imamura Y, Nakai H (2007) J Chem Phys 127:074103
27. Kobayashi M, Nakai H (2008) J Chem Phys 129:044103
28. Kobayashi M, Nakai H (2009) J Chem Phys 131:114108
29. Yoshikawa T, Kobayashi M, Nakai H (2013) Int J Quantum Chem 113:218
30. Bloch C (1965) Diagram expansions in quantum statistical mechanics. In: de Boer J, Uhlenbeck GE (eds) Studies in statistical mechanics, vol 3. North-Holland, Amsterdam, pp 3–211
31. Blaizot JP, Ripka G (1985) Quantum theory of finite systems. The MIT Press, Cambridge
32. Hirata S, He X (2013) J Chem Phys 138:204112
33. Kohn W, Luttinger JM (1960) Phys Rev 118:41
34. Matsubara T (1955) Prog Theor Phys 14:351
35. Thouless DJ (1957) Phys Rev 107:1162
36. Cremer D (2011) WIREs Comput Mol Sci 1:509
37. Lipparini E (2008) Modern many-particle physics, 2nd edn. World Scientific, Singapore
38. Thouless DJ (1972) The quantum mechanics of many-body systems, 2nd edn. Academic Press, New York
39. Cohen AJ, Mori-Sánchez P, Yang W (2009) J Chem Theory Comput 5:786
40. Mattuck RD (1976) A guide to Feynman diagrams in the many-body problem. McGraw-Hill, New York
41. Yoshikawa T, Kobayashi M, Nakai H (2011) Theor Chem Acc 130:411
42. Yoshikawa T, Nakai H (2015) Theor Chem Acc 134:53
43. Mezey PG (1995) J Math Chem 18:141
44. Szekeres Z, Mezey PG, Surján PR (2006) Chem Phys Lett 424:420
45. Nakai H (2002) Chem Phys Lett 363:73
46. Kobayashi M, Nakai H (2009) Int J Quantum Chem 109:2227
47. Kobayashi M, Nakai H (2013) J Chem Phys 138:044102
48. Schmidt MW, Baldridge KK, Boatz JA, Elbert ST, Gordon MS, Jensen JH, Koseki S, Matsunaga N, Nguyen KA, Su S, Windus TL, Dupuis M, Montgomery JA Jr (1993) J Comput Chem 14:1347
49. Gordon MS, Schmidt MW (2005) Advances in electronic structure theory: GAMESS a decade later. In: Dykstra CE, Frenking G, Kim KS, Scuseria GE (eds) Theory and applications of computational chemistry: the first forty years. Elsevier, Amsterdam, pp 1167–1189
50. Hariharan PC, Pople JA (1973) Theor Chim Acta 28:213
51. Sidje RB (1998) ACM Trans Math Software 24:130
52. Akama T, Kobayashi M, Nakai H (2009) Int J Quantum Chem 109:2706
53. Hehre WJ, Ditchfield R, Pople JA (1972) J Chem Phys 56:2257